

Master's Thesis

Joseph C Sajan

Effect of drift angle on added resistance of a wind assisted Ship

Supervisor: Trygve Kristiansen

Co-Supervisor: Øyvind Rabliås

Trondheim, June 2021

NTNU
Norwegian University of
Science and Technology
Faculty of Engineering Science and Technology
Department of Marine technology

**Revised
Edition**

Preface

The thesis titled 'Effect of drift angle on added resistance of wind assisted ships' is presented as part of my Master of science degree in the department of Marine Technology at NTNU. The work was carried out during spring 2021 at the Marine Technology centre in Trondheim. The advent of wind assisted ships to reduce emission and the need to explore the operational aspects of such vessels motivated me to pursue this topic for my Thesis. I believe the thesis will provide an insight on how drift angle affects the added resistance of a wind assisted ship and the capability of numerical codes to predict it. The conclusion from the study could be helpful to assist in efficient design and operation of such vessels in the future.

The thesis is a fruit of the combined effort of several people at NTNU and SINTEF Ocean. Firstly I would like to extend my gratitude to my supervisor, Professor Trygve Kristiansen who helped me in conducting the experiment and guided me through out this work with his knowledge and experience within hydrodynamics. I would also like to thank my Co- Supervisor Øyvind Rabliås for the support and suggestions he gave for my work. This thesis work would never have been possible without the help and support of people who helped me with the experiment at SINTEF Ocean. Among these were Marco Nataletti, Martin Gutsch, Terje Rosten, Trond Innset, Robert Opland and Alexander Sandnes who helped me in conducting the tests and also all other employees at SINTEF Ocean who helped in preparing the model. I would also like to extend my gratitude to Jan Roger Hoff and Anne Bruyat who guided me in using the numerical code 'VERES3D' developed at SINTEF Ocean. The experiment was conducted along with my friend and classmate Haakon Ferdinand Riedesel who is working on an another topic for his thesis. I thank Haakon for all the support and fun experience we had working on the experiment. Last but not the least I would like to thank my parents Sajan and Fiji and my partner Diana for all the support and motivation they gave me through out this period.



Joseph C Sajan

Trondheim, 12th of June 2021

Abstract

Wind assisted propulsion vessels have presented themselves as a revolutionary alternative to reduce emissions in a vessel. With the increasing regulations on emission control, many companies have started adopting wind assisted ships into their fleet. With increasing demand so does the need for a deep and better understanding of various aspects of such vessels especially into the operational aspects. This thesis aims at estimating and analyzing the added resistance of a wind assisted vessel in waves and the contribution of drift angle seen in such vessels to the added resistance in waves. This is achieved by a numerical analysis using state-of-the-art numerical panel codes used in the industry such as WAMIT, VERES3D, and VERES (ShipX) and an experimental study by a towing test using a wind assisted bulk carrier design, "SOShip" designed by SINTEF Ocean to validate the numerical results. The studies are conducted in various wave conditions simulating a wind assisted vessel with a drift angle of 0° and 9° . The numerical study also aims at creating an outlook on the capabilities of various numerical codes and methods used within the codes to predict first order motions (heave and pitch) and added resistance in various wave conditions. The thesis also includes a brief theory on how to find linear ship motions, second order mean drift loads and also covers some particular aspects in the theory used behind each of the numerical codes which are of interest for the study. The experimental study concludes that a drift angle increases the added resistance by 5-10% and the numerical study concludes that a drift angle of 9° causes a less than 5% increase in added resistance. The Experimental estimation of added resistance for shorter waves may sometimes pose large uncertainty which can lead to unreliable results of added resistance. At zero Froude number experimental added resistance estimation and numerical estimation are in good agreement. WAMIT well predicts the effect of tank walls in added resistance for zero speed test conditions. At forward speed the peak of added resistance curve along the wavelength found experimentally has a shift in comparison to the numerical results. At following sea conditions the numerical codes predict an added thrust when using some methods of finding added resistance in most of the wavelengths which contradicts the experimental results⁽¹⁾. The numerical results for added resistance in forward speed are observed to be sensitive to the changes in the panel model of the vessel which can generate misleading estimations.

Contents

Preface	2
Abstract	4
1 Introduction	26
1.1 Motivation	26
1.2 Scope of work	29
1.3 Thesis outline	29
2 Theory and Background	30
2.1 Wind assisted propulsion vessels and Added Resistance	30
2.2 Added Resistance	32
2.3 Experimental estimation of added resistance	34
2.4 Numerical estimation of added resistance	34
2.4.1 Direct Pressure Integration	35
2.4.2 Momentum Method	37
2.4.3 Radiated Energy method	39
2.5 Solving Boundary value problem	40
2.5.1 Panel method	41
2.5.2 2D or 3D	44
2.6 Asymptotic formula for short wavelength	45
2.6.1 Faltinsen's asymptotic method	45
3 Experimental study	48
3.1 Need for a experimental study	48
3.2 Experimental setup	48
3.2.1 Experiment design	48
3.2.2 Test Case Model	49
3.2.3 Environment	50
3.2.4 Wave maker limitation check	52
3.2.5 Tank wall interference check	52
3.2.6 Test conditions	54
3.2.7 Instrumentation	56
3.2.8 Test setup	64
3.2.9 Test procedure	69
3.3 Post processing	72
3.3.1 Data filtering	72
3.3.2 Time window	75
3.3.3 Extracting the final result	91
3.3.4 Generating non dimensional values	98
3.4 Uncertainty in added resistance calculation	101
4 Numerical study	104
4.1 Need for numerical study	104
4.2 What is a panel code?	104

4.3	Panel model	106
4.4	Highlights of Comparison of numerical codes	107
4.5	WAMIT	109
4.5.1	First order solutions	110
4.5.2	Methods for Added Resistance	112
4.5.3	Bodies in channels of finite width	113
4.6	VERES	114
4.6.1	First order solutions	115
4.6.2	Methods for Added Resistance in waves	118
4.7	VERES3D	119
4.7.1	First order solutions	119
4.7.2	Methods for estimation of Added Resistance in waves	122
5	Results and Discussion	124
5.1	Effect of drift angle	124
5.2	Comparison of methods	141
5.3	Wall effect	159
5.4	Asymptotic formula	162
5.5	Convergence Test	162
5.6	Panel Sensitivity	168
6	Conclusion	178
6.1	Conclusion	178
6.2	Further work	179
7	Bibliography	180
A	Emission limits	183
B	Swing Test	185
C	Time series Plots	190
D	Instrumentation	321
E	MATLAB Code	338

List of Symbols

F_n - Froude Number

α - Angle of attack

D - Drag force, Domain defined

L - Lift force

H - Heel force, wave height

β - Drift angle, incident wave angle, vessel heading

θ - Waterline inclination angle

δ - Rudder angle

λ - Incident Wavelength

C_r - Non dimensional added resistance

ρ - Density of water [kg/m^3]

g - Acceleration due to gravity [m/s^2]

B - Breadth of the vessel [m]

L_{pp} , L - Length between perpendiculars of the vessel [m]

R_{aw} , R_{add} , R_a - Added resistance of the vessel model [N]

R_T - Total longitudinal resistance on the vessel model when moving in waves [N]

R_{CW} - Calm water resistance on the vessel model [N]

F_x - Second order surge force

F_y - Second order sway force

M_z - Second order yaw moment

P - Total pressure on the vessel [N/m^2]

V - Fluid velocity [m/s], wind velocity

V_m - Ship model velocity

U - Ship velocity [m/s]

p_0 - Atmospheric pressure [N/m_2]

Z - Vertical coordinate [m]

ϕ - Total fluid velocity potential

ϕ_S - Stationary perturbation potential

ϕ_s - Fluid velocity potential that represents disturbance of incident wave due to presence of body

ϕ_F , ϕ_j , ϕ_R - Potential due to waves generated by forced motions (radiation potential)

ϕ_D - Diffraction potential
 ϕ_I - Incident wave velocity potential
 ϕ_B - Velocity potential representing disturbance due to presence of the body
 ϕ_k - Unit amplitude radiation potential K , κ - Wave number
 ζ_k - Complex amplitude of the oscillatory motion in mode k of six degrees of freedom
 c - Water line curve
 M - Mass of ship, Momentum
 ζ_r - Relative wave amplitude
 η_j - Motions along 6 degrees of freedom (DOF)
 $H(\theta)$ - Kochin function
 G - Green's function
 J_0 - Bessel Function of zero order
 η_1 - Surge amplitude
 η_2 - Sway amplitude
 η_3 - Heave amplitude
 η_4 - Roll amplitude
 η_5 - Pitch amplitude
 η_6 - Yaw amplitude
 b_{33} - Damping coefficient of vertical motion of a cross section (y, z) located x_b found by solving the first order boundary value problem.
 V_z^{*2} - Average vertical relative velocity of water particles relative to a section x_b
 ξ^* - Effective wave displacement for a cross section, which also acts as a correction factor to Froude's Hypothesis
 y_w - Half width of design waterline at section x_b
 ξ, ζ_a - Incident wave amplitude
 ω - Wave frequency
 ω_e - Wave encounter frequency
 H - Wave height
 A - Wave amplitude
 T - Wave period
 C_g - Wave Group velocity (m/s)
 L_{pp} - Length between perpendiculars

L_m - Ship model length

B_T - Tank breadth

g - Acceleration due to gravity

T_0 - Time taken for waves to reach vessel position (s)

T_1 - Time taken for waves to travel from vessel position to end of the wall near the beach (s)

T_2 - Time taken for the waves to travel from wall to the model (s)

Starttime - T_0 (s)

Endtime - t (s)

List of Figures

1.1	Enercon E-Ship1 using Flettner rotors. ⁽²⁾	27
1.2	Econonwind’s ventfoil system on DFDS cargo vessel Lysbris Seaways. ⁽³⁾	27
1.3	Flettner rotors installed on the Maersk Pelican 109,000 DWT tanker. ⁽³⁾	27
2.1	Lift generation on a foil	30
2.2	Various Wind assisted propulsion systems ^{(4),(5),(6),(7)}	30
2.3	Schematic of forces and apparent wind velocity (V) at an angle of attack of α . D-drag force, L-lift force, T- thrust force, H- heel force. ⁽²⁾	31
2.4	Drift angle β , Rudder angle δ	31
2.5	Typical Added Resistance curve of a vessel at a forward speed. The red lines indicate the limits for shorter wavelengths at $\lambda/L_{pp} = 0.5$ and the region of peak added resistance. Non dimensional added resistance Cr (Equation 2.1), Non dimensional wavelength λ/L_{pp} , λ - Wave length, L_{pp} - Length between perpendiculars of the vessel.	33
2.6	Control Volume ⁽⁸⁾ , U_n represents the velocity of the surface, it’s value depends on what surface it is. \vec{n} is the normal vector and \vec{k} is the unit vector vertical and upwards, S_∞ control surface at $\pm\infty$, S_{FS} free surface, ship hull surface S_B	37
2.7	Numerical tank models for a Non linear BVP and Linear BVP ⁽⁹⁾	41
2.8	Discretization (A)when using Rankine green function,(B)free surface green function (B)	42
2.9	Free surface elevation (XY plane) formed by a Ellipsoid moving at $Fn = 0.2$ when using zero speed free surface Green’s function ⁽¹⁰⁾ . x, y represents the distance along x, y direction in meters. The colour bar represents the the free surface elevation in meters.	43
2.10	Free surface elevation (XY plane)formed by a Ellipsoid moving at $Fn = 0.2$ when using forward speed free surface Green’s function ⁽¹⁰⁾ . x, y represents the distance along x, y direction in meters. The colour bar represents the the free surface elevation in meters.	43
2.11	Figure illustrating the division of a whole vessel into strips to find forces on each strip and integrating them along the length of the vessel to obtain the total load on the vessel using strip theory ⁽¹¹⁾	44
2.12	Figure illustrating the panel distribution of the wetted ship hull surface	44
2.13	Coordinate system in low wavelength case ⁽¹²⁾	45
3.1	SOShip vessel model in even keel condition	50
3.2	Checking wave conditions based on wave maker limitation	52
3.3	Maximum frequency at which tank interference occurs in head waves as per ITTC ⁽¹³⁾ . The Experimental values corresponds to the highest wave encounter frequency in model scale $\omega_e=14.56$ (full scale wave period= 4.9 sec and lowest wave encounter frequency in model scale $\omega_e = 3.735$ (full scale wave period=13.1sec), Tank width $B_T = 10.5m$ (Figure 3.14), Model Length $L_m = 5.938$ m, Froude number $F_n = 0.179$	53
3.4	Sailboat dynamometer ⁽¹⁴⁾	57
3.5	Sailboat dynamometer fixed on SOShip, The element fixed onto the model (top), Frame and rods which connects the dynamometer on the model to the carriage (bottom)	58
3.6	Diagram of a wave probe (left). Wave probe lowered into the water (right). Parallel rods in a wave probe are marked with a red ellipse.	59
3.7	OQUS motion capture cameras by Qualsis used for measuring motions along 6 DOF	60
3.8	OQUS cameras mounted around the model on the carriage focused on tracking the optical marker on board the model vessel	60

3.9	Position of uniaxial accelerometers on the vessel model	61
3.10	Model 4332 triaxial Accelerometer (right) used as accelerometer 16426 16316 placed in aft and fore ends(left) respectively as shown in figure 3.11	62
3.11	Position of triaxial accelerometers on the vessel model (Representative figure)	62
3.12	Three axes Rate gyro unit ⁽¹²⁾	63
3.13	Hexapod system, Symmetrie Mistral 800 ⁽¹⁵⁾ (right). Vessel mounted onto the hexapod (left),	63
3.14	Towing tank dimensions. the first 175m has a 5.8m depth and the next 85m have a 10m depth	64
3.15	Weights placed in model to achieve the design draft ensuring an even keel	64
3.16	Inclining test done to do a preliminary check of metacentric height	65
3.17	Model vessel being mounted onto the carriage through the hexapod	65
3.18	Optical markers for OQUS system. Markers used for head sea tests (top left) with aft markers covered (top right). Optical markers used for following sea tests (bottom left) with bow markers covered (bottom right)	66
3.19	Diagram of camera positions around the model vessel	66
3.20	Wave probes placed in the test setup.	67
3.21	Wave probes 3 Wave probe 4 placed near model to measure incident wave elevation. It is to be noted that during following sea conditions, wave probe 3 and wave probe 4 were switched in positions after re calibration, due to lack of cable length for one of them	67
3.22	Waves generated from a wave probe is not interfering with the model	68
3.23	Replacing center rod (Left) from sailboat dynamo meter to frame with a rod (Right) of better vertical tolerance.	68
3.24	Seakeeping Cartisean coordinate system followed as per right hand thumb rule . . .	69
3.25	An example of an unfiltered Time series plot of heave (position in z axis) for test no. CE4070 to demonstrate an empty data set interval seen in all the time series plots. The region A shows the measurements done before the wave maker generates waves which helps to record the parameters when then the water was calm before the run also referred to as zero measurements. Region B shows the empty data set where no data was recorded and region C shows the measurements recorded resumed after the pause.(in this particular example it was when the waves met the model.	69
3.26	$F_n=0$ Vessel model at 0° drift angle(Left) and vessel model at 9° drift angle(Right) . .	70
3.27	Frame which underwent torsional bending in test runs at 9° vessel heading	71
3.28	Jerking yaw motion observed in test runs at 9° vessel heading	71
3.29	$F_n=0.179$ Vessel model at 0° drift angle (Left) and vessel model at 9° drift angle . . .	71
3.30	$F_n=0.179$ Vessel model at 180° drift angle (Left) and vessel model at 189° drift angle .	71
3.31	Example of Wave probe 3 wave elevation data unfiltered (top) and filtered (bottom) for test no. CE4020 . The image is based on a random time window for easy demonstration	73
3.32	Example of heave motion data unfiltered (top) and filtered (bottom) for test no. CE4020.The image is based on a random time window for easy demonstration . . .	74
3.33	Example image of pitch motion data unfiltered (top) and filtered (bottom) set to mean value for test no. CE4020. The image is based on a random time window for easy demonstration	74
3.34	Example for longitudinal force F_x data unfiltered (top) and filtered (bottom) for test no. CE4020. The image is based on a random time window for easy demonstration	75

3.35	Wave reflections from beach interfering with the model vessel. The thicker grey lines represent the waves coming from the wave maker, the thinner red line represent the waves reflected back from the beach	76
3.36	At $F_n = 0$,Waves travelling from the model position to the beach and back to the model. T_0 Time taken for waves to reach vessel position, T_1 Time required for waves to travel from vessel position to end of the wall near the beach, T_2 Time taken for the waves to travel from wall to the model	76
3.37	Time series plots of heave (Z position [m]), pitch motions and longitudinal force F_x bounded by level 1 time window (green lines) for test no. CE2031	77
3.38	At $F_n \neq 0$,Waves travelling from the model start position to the beach and back to the moving model. Grey colour represents the model position when waves meet the model and black colour model represents the model position after covering a distance of x [m]. T_0 Time taken for waves to reach vessel position , T_1 Time taken for waves to travel from vessel position to end of the wall near the beach, T_2 Time taken for the waves to travel from wall to the model	78
3.39	Time series plots of heave (Z position [m]), pitch and longitudinal force F_x bounded by level 1 time window (green lines) for test no. CE4010	79
3.40	At $F_n \neq 0$,Waves travelling from the wave generator to the beach and then reflecting back to the model. Grey colour model represents the initial model position when waves travel 170.23 m and reach point P. [m].Black coloured model represents the model position after the waves reflect from the beach. T_0 - time when waves reach point P , T_1 - time taken for waves to travel from point P to end of the wall near the beach, T_2 - time taken for the waves to travel from wall to the model	80
3.41	Time series plots of heave (Z position (m)), pitch motions and longitudinal force F_x bounded by level 1 time window (green lines) for test no. CE6010	81
3.42	Filtered time series of longitudinal force F_x for test no. CE4010. The peaks circled in the beginning and the end of the time series shows the effects due to the band pass filtering	82
3.43	Unfiltered time series plots of the wave elevation near the ship model,heave motion(Z position) and longitudinal force F_x of test no. CE2031 in head sea condition at zero speed. The red rectangle indicates the transient region of the beginning of the measurement in the test run	83
3.44	Filtered time series plot of heave (Z position), Pitch motion and longitudinal force F_x of test no. CE2031. The blue lines marks the bounds of the level 2 time window	84
3.45	Unfiltered time series plots of the wave elevations near the ship model, heave (Z position) and longitudinal force F_x of test no. CE4010 in head sea condition. The red rectangle indicates the transient behaviour of the measured quantities in the test run.	85
3.46	Filtered time series plot of the heave motion (Z position), Pitch motion and longitudinal force F_x of test no. CE4010. The blue lines bounds of the filtering level 2 time interval window	86
3.47	Filtered time series plots of the wave elevation near the ship model, heave (Z position) and longitudinal force F_x of test no. CE6010. The red rectangle indicates the transient behaviour of the uncensored quantities in the test run	87
3.48	Filtered time series plot of heave motion (Z position), Pitch motion and longitudinal force F_x of test no. CE6010. The blue lines bounds of the filtering level 2 time interval window	88

3.49	Filtered time series plot of heave motion (Z position), Pitch motion and longitudinal force F_x of test no. CE2031. The interval highlighted red, which is intersection of the filter level 1 and the filter level 2 time windows of the measured data, is the final time window selected for this test.	89
3.50	Filtered time series plot of heave motion (Z position), Pitch motion and longitudinal force F_x of test no. CE4010. The interval highlighted red, which is intersection of the filter level 1 and level 2 time windows of the measured data, is the selected final time window of measured quantities for this test.	90
3.51	Filtered time series plot of heave motion (Z position), Pitch motion and longitudinal force F_x of test no. CE6010. The interval highlighted red, which is intersection of the filter level 1 and level 2 time windows of the measured data, is the selected final time window of measured quantities for this test.	91
3.52	Final time window of filtered time series plot of the wave elevation near the wave maker, heave motion(Z position), Pitch motion and longitudinal force F_x for test no. CE2010. The diamond markers for the heave and pitch indicate the data points corresponding to the peak values in the time series of the measured data. In case of longitudinal force all the data points every 0.005 seconds. A zoomed image between 201 th second and 202 nd second is indicated on top of the plot of the longitudinal force F_x	92
3.53	Slider positions 1,2,3,...,n considered within the final time window of the measured and filtered data of test no. CE2010 for quantitative values of Incident wave elevation, heave motion(Z position), pitch motion, longitudinal force (F_x). Each coloured rectangle represents each slider position enclosing selected 10 wave lengths (from crest to crest)	94
3.54	Calm water resistance in deep water at $F_n = 0.179$ with 0° drift angle (test no. CE4000). The first plot shows the carriage position. The second plot shows the unfiltered longitudinal force F_x , third plot shows the filtered longitudinal force F_x . The red lines in these plots points out the selected time window. Final plot shows the filtered longitudinal force F_x within the selected time window.	96
3.55	Calm water resistance at $F_n=0.179$ at 9° drift angle(test no. CE5081). The first plot shows the carriage position. The second plot shows the unfiltered longitudinal force F_x , third plot shows the filtered longitudinal force F_x . The red lines in these plots points out the selected time window. Final plot shows the filtered longitudinal force within the selected time window.	97
3.56	Comparison of non dimensional heave (RAO) obtained from heave measurements using accelerometer and Oqus system for tests at $F_n=0$, Head sea for vessel at design draft and even keel. The points marked in red circle corresponds to RAO value at non dimensional wavelength $\lambda/L = 1$. η_3 Heave amplitude, A incident wave amplitude, λ incident wavelength, L_{pp} Length between perpendiculars.	98
3.57	Comparison of heave RAO obtained from heave measurements using accelerometer and Oqus system for tests at $F_n=0.179$, Head sea at design draft and even keel. The points marked in red circle corresponds to RAO value at non dimensional wavelength $\lambda/L = 0.3$. η_3 Heave amplitude, A wave amplitude, λ incident wavelength, L_{pp} Length between perpendiculars.	99

3.58	Comparison of heave RAO obtained from heave measurements using accelerometer and Oqus system for tests at $F_n=0.179$, Following sea at design draft and even keel. The points marked in red circle corresponds to RAO value at non dimensional wavelength $\lambda/L = 0.5$. η_3 Heave amplitude, A wave amplitude, λ incident wavelength, L_{pp} Length between perpendiculars.	99
3.59	Added Resistance plot from experimental values at $F_n = 0.179$, drift angle = 0° in head sea waves at design draft and even keel, with error bar showing the standard deviation of averages at each slider position. Non dimensional added resistance $C_r = \text{Added resistance}/(\rho g A^2 \frac{B^2}{L_{pp}})$, λ incident wave length, L_{pp} Length between perpendiculars	101
4.1	Flow chart showing the general procedure used in numerical codes to find first order solutions and second order loads.	106
4.2	3D panel model of SOShip used for numerical analysis	107
4.3	Coordinate system used for numerical calculations in WAMIT when the origin of local coordinate system was assumed in the origin of global coordinate system. β is the wave heading, $\beta=180^\circ$ represents head sea	109
4.4	Channel of width w defined with walls on both sides of the body	113
4.5	Coordinate system used for numerical calculations in ShipX when the origin of local coordinate system was assumed in the origin of global coordinate system. β is the direction angle of incident waves, $\beta=0^\circ$ represents head sea	114
4.6	Control surfaces and fluid domain considered around a 2D strip	118
4.7	Coordinate system used for numerical calculations in VERES3D when the origin of local coordinate system was assumed in the origin of global coordinate system. β is direction angle of incident waves, $\beta=0^\circ$ represents head sea	119
4.8	Control surface defined around the vessel (figure for representation, not accurate by dimensions)	122
5.1	Added Resistance curves from Experimental results at $F_n = 0$ for 0° and 9° drift angle. λ - Wavelength, L - Length between perpendiculars, $C_r = Ra/(\rho g A^2 \frac{B^2}{L_{pp}})$ - non dimensional added resistance, Ra - Added resistance	124
5.2	Added Resistance curves from Numerical results using WAMIT at $F_n=0$ for 0° and 9° drift angle with 5% uncertainty marked as error bars. λ - Wavelength, L - Length between perpendiculars, $C_r = Ra/(\rho g A^2 \frac{B^2}{L_{pp}})$ - non dimensional added resistance, Ra - Added resistance	125
5.3	Added Resistance curves from Numerical results using WAMIT, VERES3D and experimental results at $F_n=0$ for 0° and 9° drift angle with measurement uncertainty marked as error bars. λ - Wavelength, L - Length between perpendiculars, $C_r = Ra/(\rho g A^2 \frac{B^2}{L_{pp}})$ - non dimensional added resistance, Ra - Added resistance	126
5.4	Heave RAO from Experimental results at $F_n=0$ for 0° and 9° drift angle with measurement uncertainty as error bars. η_3 - Heave amplitude, A - Wave amplitude, λ - Wavelength, L - Length between perpendiculars	127
5.5	Heave RAO from Numerical results obtained in WAMIT, VERES3D and Experimental results at $F_n=0$ for 0° and 9° drift angle with measurement uncertainty as error bars. η_3 - Heave amplitude, A - Wave amplitude, λ - Wavelength, L - Length between perpendiculars	128
5.6	Pitch RAO from Experimental results at $F_n=0$ for 0° and 9° drift angle with measurement uncertainty as error bars. η_5 - Pitch amplitude, k - wave number, A - Wave amplitude, λ - Wavelength, L - Length between perpendiculars	129

5.7	Pitch RAO from Numerical results obtained in WAMIT, VERES3D and Experimental results at $F_n=0$ for 0° and 9° drift angle with measurement uncertainty as error bars. η_5 - Pitch amplitude, k - wave number, A - Wave amplitude, λ - Wavelength, L - Length between perpendiculars	130
5.8	Transverse mean drift force curve from Experimental and Numerical results of WAMIT at $F_n=0$ for 0° and 9° drift angle. λ - Wavelength, L - Length between perpendiculars, $C_r = F_y/(\rho g A^2 \frac{B^2}{L_{pp}})$ - non dimensional transverse drift force, F_y - Mean transverse drift force	131
5.9	Vessel model at 0° (left) and 9° (right) at $F_n = 0$ in wave length corresponding to non dimensional wavelength $\lambda/L = 1.6$. The waves generated at 0° and 9° are similar. No separation effects are observed in presence of a drift angle.	132
5.10	Added Resistance curves from Experimental results at $F_n=0.179$ for 0° and 9° drift angle	133
5.11	Added Resistance curves from Numerical results using ShipX (VERES) and VERES3D at $F_n=0.179$ for 0° and 9° drift angle	134
5.12	Heave RAO from Experimental results at $F_n=0.179$ for 0° and 9° drift angle	135
5.13	Heave RAO from Numerical values using VERES3D, ShipX(VERES) and Experimental results at $F_n=0.179$ for 0° and 9° drift angle	135
5.14	Pitch RAO from Experimental results at $F_n=0.179$ for 0° and 9° drift angle	136
5.15	Pitch RAO from Numerical values using VERES3D, ShipX(VERES) and Experimental results at $F_n=0.179$ for 0° and 9° drift angle	136
5.16	Vessel at $F_n=0.179$ with 0° (left) and 9° (right) drift angles in wavelength corresponding to $\lambda/L = 1.4$. No notable separation is observed.	137
5.17	Transverse mean drift force curve from Numerical results of VERES3D and Experimental results at $F_n=0.179$ for 0° and 9° drift angle. λ - Wavelength, L - Length between perpendiculars, $C_r = F_y/(\rho g A^2 \frac{B^2}{L_{pp}})$ - non dimensional transverse drift force, F_y - Mean transverse drift force	138
5.18	Comparison of Transverse mean drift force curve at $F_n=0$ and $F_n=0.179$ with Numerical results from VERES3D for $F_n=0.179$ and WAMIT results for $f_n=0$ and Experimental results at both speeds for 0° and 9° drift angle. λ - Wavelength, L - Length between perpendiculars, $C_r = F_y/(\rho g A^2 \frac{B^2}{L_{pp}})$ - non dimensional transverse drift force, F_y - Mean transverse drift force	139
5.19	Added Resistance curves from Experimental results at $F_n=0.179$ at following sea for 0° and 9° drift angle	140
5.20	Added Resistance curves from Experimental results and Numerical results using WAMIT (3D panel code), ShipX(VERES) (2D panel code using strip theory) and VERES3D (3D panel code) at $F_n=0$, Drift angle= 0° . DPI - Direct pressure integration method, Momentum- Momentum method. λ - Wavelength, L - Length between perpendiculars, $C_r = Ra/(\rho g A^2 \frac{B^2}{L})$ - non dimensional added resistance, Ra - Added resistance	141
5.21	Added Resistance curves from Experimental results Numerical results using WAMIT (3D panel code), ShipX(VERES) (2D panel code using strip theory) and VERES3D (3D panel code) at $F_n=0$, Drift angle= 9° . DPI - Direct pressure integration method, Momentum- Momentum method. λ - Wavelength, L - Length between perpendiculars, $C_r = Ra/(\rho g A^2 \frac{B^2}{L})$ - non dimensional added resistance, Ra - Added resistance	142

5.22	Heave RAO from Experimental and Numerical results using WAMIT (3D panel code), ShipX(VERES) (2D panel code using strip theory) and VERES3D (3D panel code) at $F_n=0$, Drift angle= 0° . λ - Wavelength, L - Length between perpendiculars, η_3 - Heave amplitude, A - Wave amplitude	143
5.23	Heave RAO from Experimental and Numerical results using WAMIT (3D panel code), ShipX(VERES) (2D panel code using strip theory) and VERES3D (3D panel code) at $F_n=0$, Drift angle= 9° . λ - Wavelength, L - Length between perpendiculars, η_3 - Heave amplitude, A - Wave amplitude	144
5.24	Pitch RAO from Experimental results and Numerical results using WAMIT (3D panel code), ShipX(VERES) (2D panel code using strip theory) and VERES3D (3D panel code) at $F_n=0$, Drift angle= 0° . λ - Wavelength, L - Length between perpendiculars, η_5 - Pitch amplitude, k - Wave number, A - Wave amplitude	145
5.25	Pitch RAO from Experimental results and Numerical results using WAMIT (3D panel code), ShipX(VERES) (2D panel code using strip theory) and VERES3D (3D panel code) at $F_n=0$, Drift angle= 9° . λ - Wavelength, L - Length between perpendiculars, η_5 - Pitch amplitude, k - Wave number, A - Wave amplitude	146
5.26	Added Resistance curves from Experimental Numerical results using ShipX(VERES) (2D panel code using strip theory) and VERES3D (3D panel code) at $F_n=0.179$, Drift angle= 0° . DPI - Direct pressure integration method, Momentum- Momentum method. λ - Wavelength, L - Length between perpendiculars, $C_r = Ra/(\rho g A^2 \frac{B^2}{L})$ - non dimensional added resistance, Ra - Added resistance	147
5.27	Added Resistance curves from Experimental results Numerical results using ShipX(VERES) (2D panel code using strip theory) and VERES3D (3D panel code) at $F_n=0.179$, Drift angle= 9° . DPI - Direct pressure integration method, Momentum- Momentum method. λ - Wavelength, L - Length between perpendiculars, $C_r = Ra/(\rho g A^2 \frac{B^2}{L})$ - non dimensional added resistance, Ra - Added resistance	148
5.28	Heave RAO from Experimental and Numerical results using ShipX(VERES) (2D panel code using strip theory) and VERES3D (3D panel code) at $F_n = 0.179$, Drift angle= 0° . λ - Wavelength, L - Length between perpendiculars, η_3 - Heave amplitude, A - Wave amplitude	149
5.29	Heave RAO from Experimental and Numerical results using ShipX(VERES) (2D panel code using strip theory) and VERES3D (3D panel code) at $F_n = 0.179$, Drift angle= 9° . λ - Wavelength, L - Length between perpendiculars, η_3 - Heave amplitude, A - Wave amplitude	150
5.30	Deck slamming observed at $\lambda/L = 1.4$	150
5.31	Stern slamming observed at $\lambda/L = 1.4$	151
5.32	Pitch RAO from Experimental results and Numerical results using ShipX(VERES) (2D panel code using strip theory) and VERES3D (3D panel code) at $F_n=0.179$, Drift angle= 0° . λ - Wavelength, L - Length between perpendiculars, η_5 - Pitch Amplitude, k - Wave number, A - Wave amplitude	151
5.33	Pitch RAO from Experimental results and Numerical results using ShipX(VERES) (2D panel code using strip theory) and VERES3D (3D panel code) at $F_n=0.179$, Drift angle= 9° . λ - Wavelength, L - Length between perpendiculars, η_5 - Pitch amplitude, k - Wave number, A - Wave amplitude	152

5.34	Added Resistance curves from Experimental and Numerical results using ShipX(VERES) (2D panel code using strip theory) and VERES3D (3D panel code) at $F_n=0.179$, Drift angle= 0° . DPI - Direct pressure integration method, Momentum (CS)- Momentum method using user defined control surface. λ - Wavelength, L - Length between perpendiculars, $C_r = Ra/(\rho g A^2 \frac{B^2}{L})$ - non dimensional added resistance, Ra - Added resistance	153
5.35	Added Resistance curves from Experimental and Numerical results using VERES3D (3D panel code) at $F_n=0.179$, Drift angle= 0° . DPI - Direct pressure integration method, Momentum (CS)- Momentum method using user defined control surface. λ - Wavelength, L - Length between perpendiculars, $C_r = Ra/(\rho g A^2 \frac{B^2}{L})$ - non dimensional added resistance, Ra - Added resistance	154
5.36	Added Resistance curves from Experimental and Numerical results using ShipX(VERES) (2D panel code using strip theory) and VERES3D (3D panel code) at $F_n=0.179$, Drift angle= 9° . DPI - Direct pressure integration method, Momentum (CS)- Momentum method using user defined control surface. λ - Wavelength, L - Length between perpendiculars, $C_r = Ra/(\rho g A^2 \frac{B^2}{L})$ - non dimensional added resistance, Ra - Added resistance	155
5.37	Added Resistance curves from Experimental and Numerical results using VERES3D (3D panel code) at $F_n=0.179$, Drift angle= 9° . DPI - Direct pressure integration method, Momentum (CS)- Momentum method using user defined control surface. λ - Wavelength, L - Length between perpendiculars, $C_r = Ra/(\rho g A^2 \frac{B^2}{L})$ - non dimensional added resistance, Ra - Added resistance	155
5.38	Heave motion RAO from Experimental and Numerical results using ShipX(VERES) (2D panel code using strip theory) and VERES3D (3D panel code) at $F_n=0.179$, Drift angle= 0° . λ - Wavelength, L - Length between perpendiculars, η_3 - Heave amplitude, A - Wave amplitude	156
5.39	Heave RAO from Experimental and Numerical results using ShipX(VERES) (2D panel code using strip theory) and VERES3D (3D panel code) at $F_n=0.179$, Drift angle= 9° . λ - Wavelength, L - Length between perpendiculars, η_3 - Heave amplitude, A - Wave amplitude	157
5.40	Pitch RAO from Experimental and Numerical results using ShipX(VERES) (2D panel code using strip theory) and VERES3D (3D panel code) at $F_n=0.179$, Drift angle= 0° . λ - Wavelength, L - Length between perpendiculars, η_5 - Pitch Amplitude, k - Wave number, A - Wave amplitude	158
5.41	Pitch RAO from Experimental and Numerical results using ShipX(VERES) (2D panel code using strip theory) and VERES3D (3D panel code) at $F_n=0.179$, Drift angle= 9° . λ - Wavelength, L - Length between perpendiculars, η_5 - Pitch amplitude, k - Wave number, A - Wave amplitude	158
5.42	Heave RAO from Experimental and Numerical results using WAMIT (3D panel code) with and without wall effect at $F_n = 0$, Drift angle= 0° . λ - Wavelength, L - Length between perpendiculars, η_3 - Heave Amplitude, A - Wave amplitude	159
5.43	Pitch RAO from Experimental results and Numerical results using WAMIT (3D panel code) with and without wall effect at $F_n=0$, Drift angle= 0° . λ - Wavelength, L - Length between perpendiculars, η_5 - Pitch Amplitude, A - Wave amplitude	160

5.44	Added Resistance curves from Experimental and Numerical results using WAMIT(3D panel code) with and without wall effect at $F_n=0$, Drift angle= 0° . DPI - Direct pressure integration method, Momentum- Momentum method. λ - Wavelength, L - Length between perpendiculars, $C_r = Ra/(\rho g A^2 \frac{B^2}{L})$ - non dimensional added resistance, Ra - Added resistance	161
5.45	Added Resistance curves from Experimental results and Numerical results using VERES3D (3D panel code) at $F_n = 0.179$, Drift angle= 0° using Direct pressure integration alone and combined with results using Faltinsens's asymptotic formula(Refer 2.6). DPI - Direct pressure integration method. λ - Wavelength, L - Length between perpendiculars, $C_r = Ra/(\rho g A^2 \frac{B^2}{L})$ - non dimensional added resistance, Ra - Added resistance	162
5.46	Convergence test for Added Resistance curve using results from WAMIT (3D panel code) at $F_n=0$, Drift angle= 0° . The added resistance curves were obtained using direct pressure integration. The increasing number of panels in the legend represents the approximate number of panels in the geometry used for obtaining the corresponding curve λ - Wavelength, L - Length between perpendiculars, $C_r = Ra/(\rho g A^2 \frac{B^2}{L})$ - non dimensional added resistance, Ra - Added resistance.	163
5.47	Convergence test for Added Resistance using results from WAMIT (3D panel code) at $F_n=0.0$, Drift angle= 0° . The added resistance curves were obtained using Momentum Method. The increasing number of panels in the legend represents the approximate number of panels in the geometry used for obtaining the corresponding curve λ - Wavelength, L - Length between perpendiculars, $C_r = Ra/(\rho g A^2 \frac{B^2}{L})$ - non dimensional added resistance, Ra - Added resistance	163
5.48	Convergence test for Heave RAO using results from WAMIT (3D panel code) at $F_n=0$ in head sea condition, Drift angle= 0° . The number of panels in the legend represents the approximate number of panels in the geometry used for obtaining the corresponding curve λ - Wavelength, L - Length between perpendiculars, η_3 - Heave Amplitude, k - Wave number, A - Wave amplitude	164
5.49	Convergence test for pitch RAO using results from WAMIT (3D panel code) at $F_n=0.0$, Drift angle= 0° . The number of panels in the legend represents the approximate number of panels in the geometry used for obtaining the corresponding curve λ - Wavelength, L - Length between perpendiculars, η_5 - Pitch Amplitude, k - Wave number, A - Wave amplitude	165
5.50	Convergence test for Added Resistance using results from VERES3D (3D panel code) at $F_n=0.179$, Drift angle= 0° . The added resistance curves were obtained using direct pressure integration. The number of panels in the legend represents the approximate number of panels in the geometry used for obtaining the corresponding curve λ - Wavelength, L - Length between perpendiculars, $C_r = Ra/(\rho g A^2 \frac{B^2}{L})$ - non dimensional added resistance, Ra - Added resistance	166
5.51	Convergence test for Pitch motion RAO using results from WAMIT (3D panel code) at $F_n=0$, Drift angle= 0° . The number of panels in the legend represents the approximate number of panels in the geometry used for obtaining the corresponding curve λ - Wavelength, L - Length between perpendiculars, η_3 - Heave Amplitude, k - Wave number, A - Wave amplitude	167

5.52	Convergence test for Pitch motion RAO using results from VERES3D (3D panel code) at Fn=0.179, Drift angle=0°. The number of panels in the legend represents the approximate number of panels in the geometry used for obtaining the corresponding curve λ - Wavelength, L - Length between perpendiculars, η_5 - Pitch Amplitude, k - Wave number, A - Wave amplitude	168
5.53	Three different types of ship body discretization based on difference in the panels at transom.(A) First geometry file does not include transom panels, (B) Second geometry file includes all panels on the transom, (C) Third geometry file excludes some small panels	169
5.54	Sensitivity test for Added Resistance in waves using results from WAMIT (3D panel code) at Fn=0, Drift angle=0°. The added resistance curves were obtained using direct pressure integration. Each curve represents the result for each type of geometry file used. λ - Wavelength, L - Length between perpendiculars, $C_r = Ra/(\rho g A^2 \frac{B^2}{L})$ - non dimensional added resistance, Ra - Added resistance	170
5.55	Sensitivity test for Added Resistance using results from WAMIT (3D panel code) at Fn=0, Drift angle=0°. The added resistance curves were obtained using Momentum method . Each curve represents the result for each type of geometry file used. λ - Wavelength, L - Length between perpendiculars, $C_r = Ra/(\rho g A^2 \frac{B^2}{L})$ - non dimensional added resistance, Ra - Added resistance	171
5.56	Sensitivity test for Heave RAO using results from WAMIT (3D panel code) at Fn=0, Drift angle=0°. Each curve represents the result for each type of geometry file used. λ - Wavelength, L - Length between perpendiculars, η_3 - Heave Amplitude, k - Wave number, A - Wave amplitude	171
5.57	Sensitivity test for Pitch RAO using results from WAMIT (3D panel code) at Fn=0, Drift angle=0°. Each curve represents the result for each type of geometry file used. λ - Wavelength, L - Length between perpendiculars, η_5 - Pitch Amplitude, k - Wave number, A - Wave amplitude	172
5.58	Sensitivity test for Added Resistance by direct pressure integration using results from VERES3D (3D panel code) at Fn=0.179, Drift angle=0°. Each curve represents the result for each type of geometry file used. λ - Wavelength, L - Length between perpendiculars, $C_r = Ra/(\rho g A^2 \frac{B^2}{L})$ - non dimensional added resistance, Ra - Added resistance	173
5.59	Sensitivity test for added resistance in waves using results from VERES3D (3D panel code) at Fn=0.179, Drift angle=0°. The added resistance curves were obtained using Momentum method referred to as control surface in the legend, where user defined the control surface. Each curve represents the result for each type of geometry file used. λ - Wavelength, L - Length between perpendiculars, $C_r = Ra/(\rho g A^2 \frac{B^2}{L})$ - non dimensional added resistance, Ra - Added resistance	174
5.60	Sensitivity test for Heave motion RAO using results from VERES3D (3D panel code) at Fn=0.179, Drift angle=0°. Each curve represents the result for each type of geometry file used. λ - Incident wavelength, L - Length between perpendiculars, η_3 - Heave Amplitude, k - Wave number, A - Wave amplitude	175
5.61	Sensitivity test for Pitch RAO using results from VERES3D (3D panel code) at Fn=0.179, Drift angle=0°. Each curve represents the result for each type of geometry file used. λ - Wavelength, L - Length between perpendiculars, η_5 - Pitch Amplitude, k - Wave number, A - Wave amplitude	176

A.1	MARPOL Annex VI NO _x emission limits ⁽¹⁶⁾ n=rpm	183
A.2	MARPOL Annex VI NO _x emission limits ⁽¹⁶⁾	183
A.3	MARPOL Annex VI fuel sulphur limits ⁽¹⁶⁾	183
A.4	MARPOL Annex VI fuel sulphur limits ⁽¹⁶⁾	184
B.1	Swing test	189

List of Tables

2.1	Classification of methods for added resistance	35
3.1	Physical model versus Numerical model ⁽¹⁷⁾	48
3.2	Principal particulars of SOShip (Model scale 1:32)	50
3.3	Wave conditions for the test. H - Wave height, T - Wave period, λ - Wave length, L_{pp} - Length between perpendicular=190m. (8xxx is a common wave number series convention used for documenting wave conditions at SINTEF Ocean)	51
3.4	Maximum frequency at which tank interference occurs in head waves, Tank breadth B_T , Model length L_m , Highest wave frequency ω , acceleration due to gravity $g=9.81\text{m/s}^2$, F_n - Froude number, ω_e - Encounter wave frequency	53
3.5	Experiment run list with full scale parameters. Wave Period $T(\text{sec})$, Wavelength $\lambda(\text{m})$, Wave frequency $\omega(\text{rad/sec})$, Wave encounter frequency $\omega_e(\text{rad/s})$, Wave height $H(\text{m})$, Vessel heading $\beta(\text{degree})$, Vessel speed U (m/s)	54
3.6	Design limits of dynamometer	58
3.7	Average wave elevation, heave (Z position), pitch and longitudinal force (F_x) from their average (standard deviation for pitch) values at each slider position shown in figure 3.53 for test no. CE2010	95

1 Introduction

1.1 Motivation

As per the fourth greenhouse gas (GHG) emissions study 2020⁽¹⁸⁾, emissions including Carbon dioxide (CO₂), Methane(CH₄) and Nitrogen oxide (NO_x) of total shipping have increased from 977 million tonnes in 2012 to 1076 million tonnes in 2018(9.6% increase). This brings the share of global shipping emissions in global anthropogenic emissions increased from 2.76% in 2012 to 2.89% in 2018. Emissions are projected to increase to 90-130% of 2008 emissions by 2050. With a mission to reduce global emissions, in 1997 the International convention for the prevention of pollution from ships (MARPOL) adopted Annex VI titled “Regulation for the Prevention of Air Pollution from Ships” which limits the Sulphur oxides (SO_x), Nitrogen oxides (NO_x) contained in ships exhaust gas and prohibits deliberate emissions of ozone-depleting substances (ODS). The emission limits are commonly referred to in terms of Tiers (Tier I, Tier II, Tier III). On 1 July 2010, the revised regulations which were more stringent came into force. As per the assessments by MEPC 70, the fuel oil standard requires a 0.5% (percentage by mass) Sulphur limit which is effective from 1 January 2020, and in the Emission control areas (ECA) SO_x and particulate matter is limited to 0.1% (percentage by mass) from 1 January 2015. Tier III emission limits are now required for NO_x emissions from a marine diesel engine on or after January 2016⁽¹⁹⁾. The emission limits can be seen in Appendix A. In 2005 IMO had identified the North Sea as a SO_x Emission Control Area which makes it more difficult for shipping activities in the North Sea. It has become a great challenge for designers and ship owners to cope up with these regulations as it calls for change in fuel, engine technology, or installation of new exhaust gas cleaning systems. As per an article written by a DNV expert low Sulphur content in fuels becomes the root cause for ignition and combustion problems and the increased catalytic fines and abrasives damage the engine. DNV has also questioned the market availability of sufficient low Sulphur bunkers due to the addition of North Sea SECA. An operational problem DNV has identified is the difficulty of timing a change over to fuel required to enter and operate within a SECA.⁽²⁰⁾ As designers and engine manufacturers squeeze out the maximum limits of efficiency of an engine and hull design, we will be out of options as the regulations get more and more stringent, which is why we are now in search of alternative propulsion systems. This is where wind assisted propulsion system gains importance.

Wind was the primary source of propulsion energy for ships even from the ages of ancient Egyptians. Until the advent of combustion engines, between the 19th and the early 20th centuries, it was the only method of propulsion used for ships. With the increased demand for better solutions for reducing emissions from combustion based propulsion systems, wind powered vessels have stepped back into the industry. Wind assisted propulsion was a concept that was studied in the 1980s for the US merchant marine. Today a lot of research is being done on the design and operation of wind assisted propulsion vessels. This technology makes use of the thrust developed from wind capturing devices (Figure 2.2) like sails, kites, or rotors along with the thrust from the propellers thereby reducing the load on engines and thus reducing the amount of fuel consumed in a voyage. Sails have been told to give up to 15% annual fuel saving.⁽²¹⁾ Using a kite system gave fuel savings up to 21% at speed of 15 knots.⁽²²⁾ A type of rigid sails called Walker Wingsail on a 7000 DWT bulk carrier gave an average fuel saving up to 8% and up to 15-20% under favourable conditions.⁽²³⁾ Fuel savings of such large numbers have brought in the interest of numerous shipping companies to use wind assisted propulsion for their vessels. 3600-DWT general cargo ship Ankie by Van Dam Shipping, the ferry Copenhagen by Scandlines, general cargo vessel Tharsis by Tharsis Sea-River Shipping are some of

the examples.⁽²⁴⁾Some of the vessels which already in operation can be seen in figures 1.1,1.2and 1.3.



Figure 1.1: Enercon E-Ship1 using Flettner rotors.⁽²⁾



Figure 1.2: Econonwind’s ventfoil system on DFDS cargo vessel Lysbris Seaways.⁽³⁾



Figure 1.3: Flettner rotors installed on the Maersk Pelican 109,000 DWT tanker.⁽³⁾

With increasing demand and popularity in the industry, so does the importance for a deeper

understanding on various aspects of vessels using wind assisted propulsion.

Efficiency is a key aspect of the design of a vessel. The pursuit of achieving efficient designs that possess a lower rate of fuel consumption has brought advanced hull designs and engine designs over the past. Each vessel is designed based on calm water conditions but in reality, an ocean going vessel spends her life in waves, currents, and winds causing speed loss and reduction in operational efficiency.⁽⁹⁾ The ship performance degradation is reported to be 15-30% of the power required in calm water conditions.⁽²⁵⁾ This loss in efficiency when operating at sea is caused due to the added resistance experienced by a vessel when in operation. During the power estimation for the design of a vessel, the added resistance is accounted for by an additional 15% power as a sea margin, but in reality, this cannot precisely account for the actual power required and hence can under predict or over predict the requirement. Proper estimation of added resistance has its benefits which can be listed as follows⁽²⁶⁾

- Proper evaluation of additional power requirement
- More efficient design in operating conditions that meets IMO criteria for Energy Efficiency Design Index (EEDI) and Energy Efficiency Operational Index (EEDO)
- Effective planning of voyage and facilitate decision on weather routing

When talking about wind assisted propulsion systems it becomes more interesting. In comparison to a conventional ship, a vessel using wind assisted propulsion experiences larger wind forces and also posses an inherent drift angle and rudder angle to compensate for the large side forces it experiences.⁽²⁷⁾ This, in turn, affects the added resistance on such vessels. To what magnitude does it affect the added resistance? Should it be considered as an important factor during engine power estimation for wind assisted ships? The new Ship Performance Index (SPI) proposed by IMO includes the requirement of estimating added resistance through model tests or equivalent formulas with considerable accuracy.⁽²⁸⁾ Having more companies switching to wind assisted ships and the increasing demand for the proper estimation of added resistance, a detailed study into added resistance of wind assisted propulsion vessels and the various methods and tools available today to estimate added resistance of a vessel is inevitable.

The Thesis primarily aims at studying the added resistance of wind-assisted propulsion vessels with and without a drift angle in a head sea and in following sea conditions at various wavelengths in deep water condition. A detailed study into the added resistance also opens up possibilities to later develop designs that reduce added resistance and also to adapt operational strategies that ensure the least added resistance and provide maximum efficiency.

The objectives of the Thesis can be summarized as follows

- Present an overview on various methods to find added resistance
- Comparison of added resistance on a vessel with and without a drift angle using experimental results and numerical results
- Investigation of change in added resistance in head sea and following sea at different wavelengths
- Evaluating the capabilities and limitations of numerical codes in predicting added resistance with and without a drift angle in head sea and following sea conditions

- Investigating how reflections from tank wall affects the added resistance results at a zero speed condition.

1.2 Scope of work

The Thesis studies the effect of drift angle in added resistance of wind assisted ships by simulating selected conditions using a physical model and numerical model. Many factors contribute to the added resistance of a wind assisted ship such as rudder angle, wind loads above the waterline, etc. In reality, there are wind assisted propulsion devices mounted on top of a wind assisted ship vessel, but the physical model used for the study do not use any such wind propulsion devices instead simply simulates the drift angle by an oblique towing test, thereby only considering the contribution from drift angle to added resistance. The study is also confined to a single vessel design and a single value of drift angle. Therefore the results from this study cannot represent all the ships using wind assisted propulsion and for any drift angle. The conclusion of this study is based on a single non zero Froude number ($F_n=0.179$). The study is targeted at displacement type vessels with Froude number, $F_n \leq 0.28$. Due to limited time available for testing, it was not possible to conduct repetition tests which would have helped to assess the levels of uncertainty of the measurement. Therefore, a complete uncertainty analysis is not done on the test measurements. The numerical analysis is based on numerical codes which operate based on potential fluid flow theory. Therefore it does not include the viscous effects seen in reality.

1.3 Thesis outline

The study is done using a design of an optimized bulk carrier (SOShip) with wind-assisted propulsion by SINTEF Ocean. An experimental study is conducted based on a towing test and a numerical study is done using state-of-the-art numerical codes such as WAMIT, VERES3D, and VERES used in the industry.

The core of the report can be split into 4 parts. It begins with the basic concepts on wind assisted propulsion vessels and drift angle on such vessels, then we dive deep into the theory on what added resistance is and on how to find added resistance using various methods. The second part of the thesis describes the experimental study which includes the test setup, instrumentation, data extraction, and post-data processing. In the third part, we will talk about various numerical codes with some selected theory used in the code which is of particular interest for this study which will give a brief idea of how these codes generate the results we are interested in. Finally, we have the results and discussion part where we analyze the experimental and numerical results together and present the findings based on the theory learned.

2 Theory and Background

In this section, the theory of various aspects, which includes basics on wind assisted propulsion, added resistance and methods to find it, and also briefly about wall effect observed in experimental tests is presented. The theory used behind various numerical codes is presented in section 4. The theories presented in this section are well-established. A brief description of various aspects is included to support the analysis done later in the report.

2.1 Wind assisted propulsion vessels and Added Resistance

Wind assisted propulsion relies on absorbing wind energy using various devices so that it could provide an additional thrust along with the thrust generated from the propeller, which helps in maintaining or enhancing the performance of vessels with lesser fuel consumption. Most of the devices work on the principle of a foil where a lift is generated in presence of a flow over the foil as in figure 2.1.

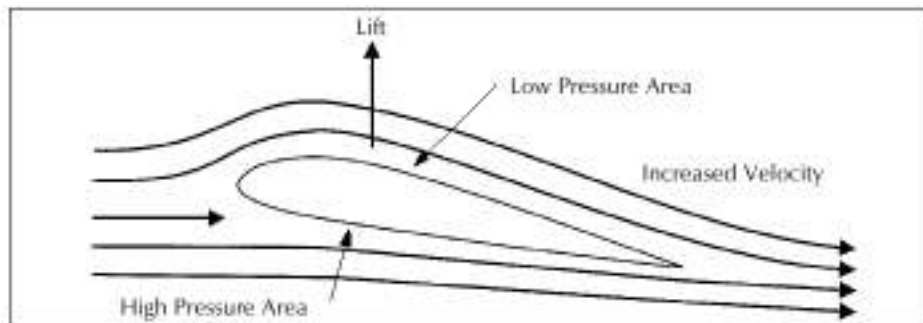


Figure 2.1: Lift generation on a foil

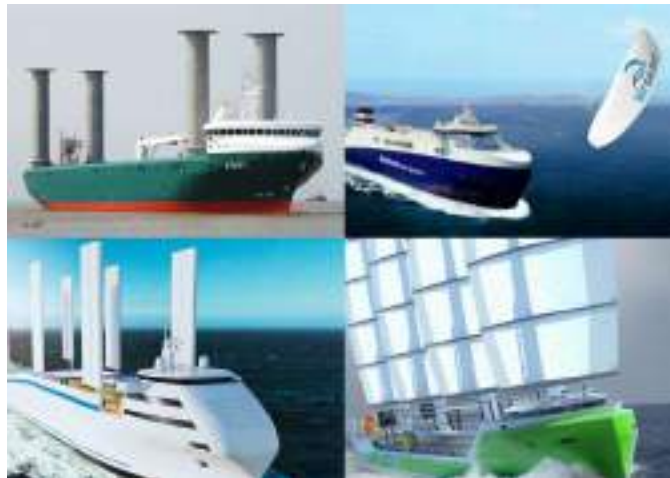


Figure 2.2: Various Wind assisted propulsion systems^{(4),(5),(6),(7)}

There are different kinds of devices used for this purpose, for example, wings, sails, and rotors as seen in figure 2.2. There are also concepts of using a kite that relies on wind drag force acting on the kite which can be also seen in figure 2.2.

Contrary to the conventional propulsion system where the thrust is along the longitudinal axis of the vessel, in the case of wind assisted propulsion vessels, the thrust act in a direction perpendicular to the inflow just as in a foil. When considering the forces on the vessel due to wind, there exists a drag force (D), and a lift force (L) which in turn generates a thrust force (T) and heel force (H) on the vessel (H)⁽²⁾ as shown in figure 2.3.

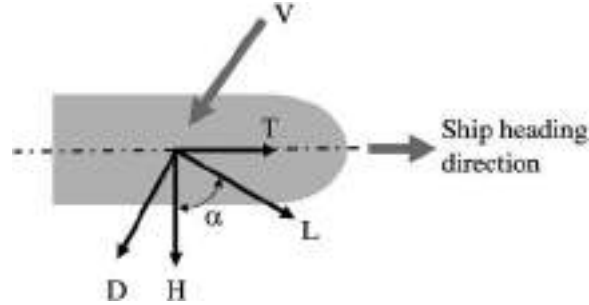


Figure 2.3: Schematic of forces and apparent wind velocity (V) at an angle of attack of α . D-drag force, L-lift force, T- thrust force, H- heel force. ⁽²⁾

The forces and moments on a wind assisted propulsion vessel can be divided to 1) Aerodynamic forces and moments due wind loads on hull and superstructure 2)Hydrodynamic forces and moments due to drag and lift forces on the hull and on the rudder.⁽²⁷⁾ The side forces in presence of a wind assisted propulsion system will be larger in comparison to a conventional ship. This is compensated by a drift angle of the hull and a rudder angle, which causes increase in added resistance of the vessel which affects the performance of the vessel. Therefore for a proper performance prediction of a wind assisted ship, it is essential to accurately predict the added resistance of the vessel.

There are two additional sources of added resistance for a wind assisted ship and they are

- Drift angle of the hull (β)
- Rudder angle (δ)

Drift angle at any point along the length of the ship is defined as the angle between the centerline of the ship and the tangent to the path of the point considered⁽²⁹⁾ as seen in figure 2.4. This study focuses on studying the added resistance and the change in added resistance due to the drift angle of the hull of wind assisted ships.

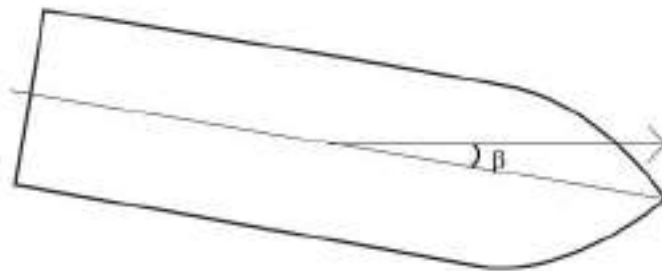


Figure 2.4: Drift angle β , Rudder angle δ

2.2 Added Resistance

Resistance estimation is one of the key factors that determine the total power requirement for a vessel. Resistance is defined as the horizontal force a vessel experiences when moving in calm water. Wave resistance and viscous resistance are two major components that contribute to the total resistance. Wave resistance is due to the energy spent as the vessel makes waves as it moves in calm water. Viscous resistance is due to the viscosity of water which causes tangential or normal stresses on the vessel, that the vessel has to overcome to move forward in calm water. Many other components contribute to the total resistance which is presented in detail.⁽³⁰⁾ In reality, a vessel operates in presence of waves, winds, and currents causing speed loss and reduced efficiency in operation when compared to that predicted efficiency in calm water conditions. Considering the effect of waves alone, a vessel is exposed to unsteady wave loads due to the incident regular waves and diffracted waves from herself. Nonlinear second order mean wave loads acts on the vessel due to the imposed regular incident wavefield and vessel motions. The effect of the mean second order wave drift loads can be observed when a floating object slowly drifts along the direction of the incident regular wave field. If we had considered only linear forces which are directly proportional to the amplitude of the wave the floating object would have simply been oscillating at its position, but the existence of a drift force along with the waves causes it to slowly drift along the direction of the waves. The mean longitudinal component of this wave drift load on a floating vessel is defined as the added resistance on the vessel due to waves.⁽³¹⁾ Wind and current also cause added resistance on a vessel, but this is not investigated in this study since the focus is on added resistance due to waves.

While the other excitation forces on a vessel, that causes first order motions along the 6 degrees of freedom, are linear (directly proportional to the amplitude of the wave) added resistance is a second-order force (proportional to the square of the wave amplitude). The experimental results exhibits a relationship between added resistance and square of wave amplitude.⁽²⁵⁾ As already mentioned drift forces depend on the waves generated by the vessel, thus it is related to the wave making capability of a body. Figure 2.5 shows a typically added resistance curve of vessel that shows a variation of added resistance with wavelength.

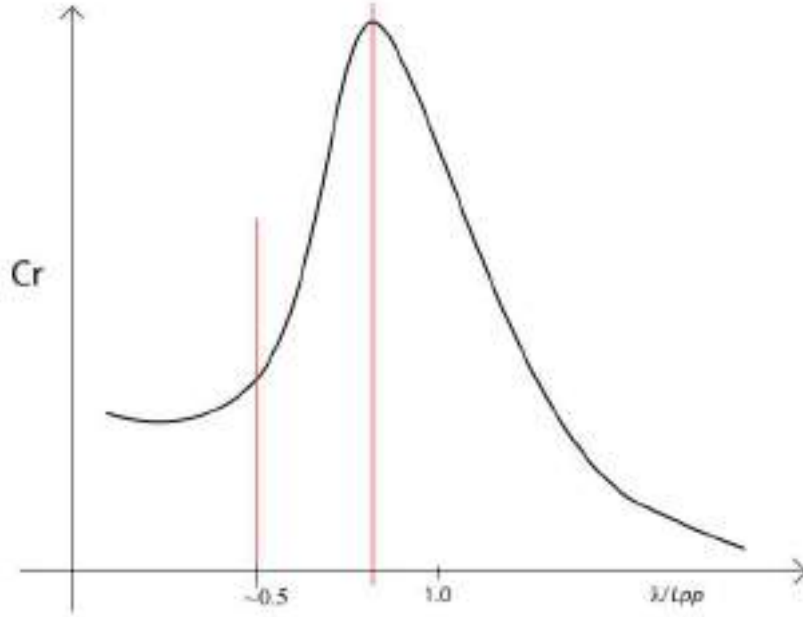


Figure 2.5: Typical Added Resistance curve of a vessel at a forward speed. The red lines indicate the limits for shorter wavelengths at $\lambda/L_{pp} = 0.5$ and the region of peak added resistance. Non dimensional added resistance Cr (Equation 2.1), Non dimensional wavelength λ/L_{pp} , λ - Wave length, L_{pp} - Length between perpendiculars of the vessel.

A typical added resistance curve plots the non dimensional added resistance, Cr which is defined as in equation 2.1 along the non dimensional wavelength λ/L_{pp} .

$$\frac{R_{aw}}{\rho g A^2 (B^2 / L_{pp})} \quad (2.1)$$

R_{aw} - Added resistance [N]

ρ - Density of water [kg/m^3]

g - Acceleration due to gravity [m/s^2]

B - Breadth of the vessel [m]

L_{pp} - Length between perpendiculars of the vessel [m]

From the plot, it is clear that added resistance increases in the range of $\lambda/L_{pp} < 1$ and after it reaches a particular peak value it decreases with further increase in a wavelength where $\lambda/L_{pp} > 1$. At $\lambda/L_{pp} < 0.5$ the waves are small compared to the length of the vessel. With smaller waves, there is more number reflections from the bow, which makes bow reflections the dominating in contribution to the added resistance at this range of wavelengths. The peak of the added resistance curve is associated with the ship motions. At Froude number $Fn=0$ the peak is seen closer to $\lambda/L_{pp} \sim 1$. At a forward speed, the peak is observed between $0.5 < \lambda/L_{pp} < 1$. Heave motion and pitch motion generate the largest waves compared to other motions of a vessel. As added resistance

is related to the wave-making capability of a vessel, the heave and pitch motions of a vessel largely influence the added resistance of a vessel. As the wavelengths become larger ($\lambda/L_{pp} > 1$) the added resistance decreases and become negligible. In larger wavelengths, the waves generated by the vessel are negligible thereby reducing the added resistance on the vessel.

2.3 Experimental estimation of added resistance

Experimentally added resistance is estimated as the difference between the total longitudinal resistance on a vessel moving in waves at a particular speed and the calm water resistance at that particular speed, as defined in equation 2.2

$$R_{aw} = R_T - R_{CW} \quad (2.2)$$

R_{aw} - Added resistance of the vessel model [N]

R_T - Total longitudinal resistance on the vessel model when moving in waves [N]

R_{CW} - Calm water resistance on the vessel model [N]

The resistance on a vessel can be estimated by a towing test where a scaled model of the vessel is towed in calm water or in waves generated by a wavemaker at the end of the tank. It is also possible to perform a self-propelled test and then measure the resistances on the vessel. A detailed description of the procedure for finding the added resistance from a towing test can be found in section 3.

2.4 Numerical estimation of added resistance

Potential flow theory is an established model to represent fluid flow. There are numerous researchers with numerous numerical models to find added resistance. They are different from each other based on the assumptions and approximations used in their formulation. When using potential flow theory, even though it is possible to use a second order potential, when dealing with mean drift loads, second order potential does not have any influence as they give a mean value of zero.⁽³²⁾ So linear potential fluid flow theory is sufficient for numerical modeling of fluid flow when studying added resistance. The basic formulation for finding added resistance can be split into two and they are 1) Solving the first order boundary value problem (BVP) to obtain linear vessel motions and loads 2) Finding the added resistance using the linear vessel motions obtained. Each model is different from the other based on how these two parts are dealt with. In general, a possible classification for various numerical models can be classified based on 1) How they solve the boundary value problem (BVP) to find the total velocity potential 2) Methods used for finding added resistance using the first order solutions. The classification based on how the boundary value problem is not presented in this report, instead of a general description of BVP and finding its solution is presented in section 2.5. The methods used to find added resistance can be classified into 3

- Direct pressure integration
- Momentum method
- Radiated energy method

Based on this classification some of the well known numerical models for finding added resistance by various researchers can be classified as in table 2.1.

Table 2.1: Classification of methods for added resistance

Direct Pressure Integration	Momentum	Radiated Energy
Havelock ⁽³³⁾	Maruo ⁽³⁴⁾	Gerritsma and Beukelman ⁽³⁵⁾
Faltinsen et al ⁽³²⁾	Joosen ⁽³⁶⁾	
Salvensen et al ⁽³⁷⁾	Newman ⁽³⁸⁾	
Kim et al ⁽²⁶⁾	Kim et al ⁽²⁶⁾	

Further in this section a brief description on each of the three methods based on the one numerical model using the method is given. The direct pressure integration is explained based on the formulation by Faltinsen⁽³²⁾, momentum method is explained based on the formulation by Newman⁽³⁸⁾ and radiated energy method is based on the formulation by Gerritsma and Beukelman⁽³⁸⁾.

2.4.1 Direct Pressure Integration

As the name suggests this method is based on finding the added resistance by directly integrating the pressure acting on the vessel. This method is also referred to as Near field method. From the total pressure acting on a vessel, considering the components of pressure that contribute to the mean drift force and integrating the longitudinal components of those oscillating pressure components over the wetted surface area of the hull will generate the total longitudinal mean drift force on the vessel.

Faltinsen⁽³²⁾ had presented his formulation to find added resistance using pressure integration as follows.

The total pressure that acts on a ship can be written using the Bernoulli's equation (Equation 2.3)

$$P = p_0 + \rho gz - \rho \frac{\partial \phi}{\partial t} - \rho \frac{V^2}{2} + \rho \frac{U^2}{2} \quad (2.3)$$

P - Total pressure on the vessel [N/m^2]

V - Fluid velocity [m/s]

U - Ship velocity [m/s]

p_0 - Atmospheric pressure [N/m_2]

Z - Vertical coordinate [m]

ρ - Fluid density [kg/m^3]

The total velocity potential of the fluid around the vessel can be written as

$$\phi = Ux + \phi_S + \phi_I + \phi_F + \phi_D \quad (2.4)$$

where $Ux + \phi_S$ is the steady contribution

U - Ship velocity [m/s]

ϕ_S - Stationary perturbation potential

ϕ_F - Potential due to waves generated by forced motions (radiation potential)

ϕ_D - Diffraction potential

Neglecting the contribution from ϕ_S , using the total velocity potential ϕ the pressure on the vessel can be written as

$$P = p_0 - \rho g z - \rho \frac{\partial \phi}{\partial t} - \rho U \frac{\partial \phi}{\partial x} - \frac{\rho}{2} \left(\frac{\partial \phi^2}{\partial x} + \frac{\partial \phi^2}{\partial y} + \frac{\partial \phi^2}{\partial z} \right) \quad (2.5)$$

The total velocity potential can be written as sum of first order potential (directly proportional to wave amplitude) and second order potential (proportional to the square of the wave amplitude)

$$\phi \sim \phi_1 + \phi_2 \quad (2.6)$$

Using Taylor expansion the total pressure including the first order and second order velocity potential equation 2.5 can be written as

$$P_s = P_0 - \rho g z - \rho \left(\frac{\partial \phi_1}{\partial t} + U \frac{\partial \phi_1}{\partial x} \right) - \rho \left(\frac{\partial \phi_2}{\partial t} + U \frac{\partial \phi_2}{\partial x} \right) - \rho (\eta_2 + x\eta_6 - z\eta_4) \frac{\partial}{\partial y} \left(\frac{\partial \phi_1}{\partial t} + U \frac{\partial \phi_1}{\partial x} \right) - \rho (\eta_3 - x\eta_5 - y\eta_4) \frac{\partial}{\partial z} \left(\frac{\partial \phi_1}{\partial t} + U \frac{\partial \phi_1}{\partial x} \right) - \frac{\rho}{2} \left(\frac{\partial \phi_1^2}{\partial x} + \frac{\partial \phi_1^2}{\partial y} + \frac{\partial \phi_1^2}{\partial z} \right) \quad (2.7)$$

After considering the contribution of each term in equation 2.7 to added resistance it can be seen that $\rho g z$ is just the vertical force on the vessel but above $z=0$ the free surface evolution causes the variation of body wetted surface and thus it contributes to the added resistance. The linear pressure term $\rho \left(\frac{\partial \phi_1}{\partial t} + U \frac{\partial \phi_1}{\partial x} \right)$ contributes to added resistance when we consider the correct wetted area of the ship hull according to second order theory. The term $\rho \left(\frac{\partial \phi_2}{\partial t} + U \frac{\partial \phi_2}{\partial x} \right)$ gives a mean force of zero and thus doesn't contribute to added resistance. The terms of pressure due to the body motions and oscillating fluid also contribute to the added resistance. Considering all the components of pressure that contribute to the longitudinal mean force, Faltinsen derived the following expression for added resistance

$$F_x = \int_c \left(\frac{\rho g}{2} \zeta_r^2 \right) n_1 ds - \omega_e^2 M \overline{\eta_3 \eta_5} + \omega_e^2 M \overline{(\eta_2 - z_G \eta_4) \eta_6} + \rho \int_{S_B} \left(\rho (\eta_2 + x\eta_6 - z\eta_4) \frac{\partial}{\partial y} \left(\frac{\partial \phi_1}{\partial t} + U \frac{\partial \phi_1}{\partial x} \right) \Big|_m - \rho (\eta_3 - x\eta_5 - y\eta_4) \frac{\partial}{\partial z} \left(\frac{\partial \phi_1}{\partial t} + U \frac{\partial \phi_1}{\partial x} \right) \Big|_m + \frac{\rho}{2} \left(\frac{\partial \phi_1^2}{\partial x} + \frac{\partial \phi_1^2}{\partial y} + \frac{\partial \phi_1^2}{\partial z} \right) \right) n_1 ds \quad (2.8)$$

c - Water line curve

F_x - Second order surge force(Added resistance)

M - Mass of ship

$|_m$ - Implies the quantity about mean position

z_G - Vertical coordinate of Center of Gravity

ζ_r - Relative wave amplitude

$$\zeta_r = \zeta - (\eta_3 - x\eta_5 + y\eta_4) \quad (2.9)$$

η_j - Motions along 6 degrees of freedom (DOF)

Based on the comparison of results using direct pressure method ⁽⁴¹⁾, at shorter wavelengths ($\lambda/L < 0.5$) pressure integration seems to give unstable results and also it over estimates the peak added resistance at wavelengths close to the vessel length. Direct pressure integration have proven to give good results in vessels with larger block coefficient. In shorter wavelengths direct pressure integration do give better results compared to radiated energy method and in longer waves ($\lambda/L > 1.0$) it gives better results than momentum method.

2.4.2 Momentum Method

Momentum method is based on the principle of conservation of fluid momentum about a control surface around the vessel enclosing the control volume which is the considered fluid domain Ω .

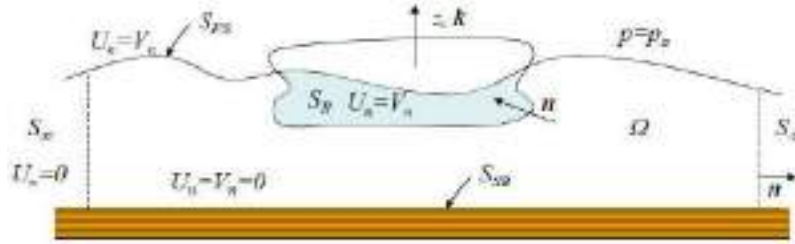


Figure 2.6: Control Volume⁽⁸⁾, U_n represents the velocity of the surface, it's value depends on what surface it is. \vec{n} is the normal vector and \vec{k} is the unit vector vertical and upwards, S_∞ control surface at $\pm\infty$, S_{FS} free surface, ship hull surface S_B

The control surface assumed at $\pm\infty$ does not necessarily need to be located very far away, it can be assumed at a finite distance from the hull that will account for all the effects. The following description on using momentum method is based on the formulation by Newman (1967)⁽³⁸⁾

With the assumption of an inviscid, incompressible fluid, The velocity Vector of the fluid \vec{V} satisfies the Euler's equation of motion (Equation 2.10)

$$\frac{\partial \vec{V}}{\partial t} + (\vec{V} \cdot \nabla) \vec{V} = -\nabla(p/\rho + gz) \quad (2.10)$$

The velocity vector also satisfies the continuity equation(Equation 2.11)

$$\nabla \cdot \vec{V} = 0 \quad (2.11)$$

The Rate of change of momentum, M about the volume Ω can be written as

$$\frac{dM}{dt} = \frac{d}{dt} \rho \int \int \int \vec{V} d\Omega \quad (2.12)$$

$$\frac{dM}{dt} = \rho \int \int \int \frac{\partial \vec{V}}{\partial t} d\Omega + \rho \int \int \vec{V} U_n dS \quad (2.13)$$

Using equation 2.10 and equation 2.11, equation 2.12 can be rewritten as

$$\frac{dM}{dt} = -\rho \int \int \left(\frac{P}{\rho} + gz \right) n + \vec{V} (V_n - U_n) ds \quad (2.14)$$

When finding added resistance, the rate of change of momentum along x axis is of interest and thus neglecting the terms including gravity and considering the velocity component along x , V_x

$$\frac{dM_x}{dt} = - \int \int_{S_B + S_{FS} + S_\infty} P n_1 ds + \rho V_x (V_n - U_n) \quad (2.15)$$

where n_1 is the direction cosine with direction of unit vector \vec{n} taken as positive out of the closed surface.

The force integrated along the body surface S_B is the added resistance which is $F_x = \int \int_{S_B} P_1 ds$. Eliminating the free surface leaves the equation as an integral over the control surface at infinity.

$$\overline{F_x} = \overline{\int \int_{S_\infty} (P \cos(n, x) + \rho V_x V_n) ds} \quad (2.16)$$

The control surface is then considered to have a large cylinder around the vessel at infinity with depth at infinity, so that the contribution from sea bed can be neglected. Using polar coordinates with $x = R \cos \theta$ and $y = R \sin \theta$ equation 2.16 can be rewritten as

$$F_x = - \overline{\int \int_{S_\infty} [p \cos \theta + \rho V_R (V_R \cos \theta - V_\theta \sin \theta)] R d\theta dz} \quad (2.17)$$

Further on assuming the wave amplitude (ζ_a is small and retaining contribution to the forces and moment which are of second order in the incident wave amplitude

The velocity components V_R and V_θ can be defined as $V_R = Re \frac{\partial \phi}{\partial x} e^{-i\omega t}$ $V_\theta = Re \frac{1}{R} \frac{\partial \phi}{\partial \theta} e^{-i\omega t}$

where $\phi = \phi_B + \phi_I$

ϕ_I - Incident wave velocity potential

ϕ_B - Velocity potential representing disturbance due to presence of the body

K - Wave number

$$V_R = \operatorname{Re} \frac{\partial \phi}{\partial x} e^{-i\omega t} \quad V_\theta = \operatorname{Re} \frac{1}{R} \frac{\partial \phi}{\partial \theta} e^{-i\omega t} \quad (2.18)$$

$$\phi_B = \left(\frac{K}{2\pi R} \right)^{\frac{1}{2}} H(\pi + \theta) \exp(Kz + iKR + i\pi/4) + O(R^{-3/2}) \quad (2.19)$$

where $H(\theta)$ called the Kochin function is defined as

$$H(\theta) = \int \int_{S_B} \left(\frac{\partial \phi_B}{\partial n} - \phi_B \frac{\partial}{\partial n} \right) \exp(Kz + iKx \cos \theta + iK_y \sin \theta) ds \quad (2.20)$$

The momentum method is a widely used method as it is quite robust in comparison to the pressure integration method as it is not too sensitive to the wave diffraction near the hull surface. As per the study by Arribas⁽²⁵⁾ In short waves ($\lambda/L < 0.5$) the added resistance values are more stable, but it seen to tend towards zero in very short waves which is mainly because the method does not consider diffraction effects which becomes the dominating waves for added resistance in short waves. The peak values are predicted quite well once the wave generation is captured properly by the model. Momentum method also gives good results fro slender ships. In longer waves ($\lambda/L > 1.0$) the added resistance values are sometimes underestimated.

2.4.3 Radiated Energy method

The basic principle behind this method is to relate the added resistance on a vessel to the energy contained by the damping waves radiated away from the ship. Faltinsen⁽³²⁾ had expressed his opinion that the rational basis behind this method is not clear, but it is used in codes like VERES for added resistance estimation. Gerritsma and Journee⁽³⁹⁾ had published an improved method applicable to oblique seas. This section describes the method with reference to the formulation by Geritsma and Beukelman⁽³⁵⁾.

The energy radiated, P during one wave encounter period T will be

$$P = \int_0^T \int_L b_{33} V_z^{*2} dx_b dt \quad (2.21)$$

b_{33} - Damping coefficient of vertical motion of a cross section (y, z) located x_b found by solving the first order boundary value problem.

V_z^{*2} - Average vertical relative velocity of water particles relative to a section x_b

Relative vertical velocity of water, V_z is

$$V_z = \omega_e \left(Z_a - x_b \theta_a + \frac{U \theta_a}{\omega_e} \right) - \omega_n \xi^* \quad (2.22)$$

U - Ship speed

ξ^* - effective wave displacement for a cross section, which also acts as a correction factor to Froude's Hypothesis

$$\xi^* = \xi \left[1 - \frac{k}{y_w} \int_{-T}^0 y_b \exp(kz_b) dz_b \right] \quad (2.23)$$

(y_b, z_b) - points of the section at x_b

y_w - Half width of design waterline at section x_b

ξ - Wave amplitude without modification

V_z^* is harmonic function with amplitude V_z and encounter frequency ω_e , therefore the mean energy radiated is

$$P = \int_L b_{33} V_z^2 dx_b \quad (2.24)$$

Work done by added resistance $= F_x(V + c)T = F_x\lambda =$ Energy radiated, therefore added resistance is given by

$$F_x = \frac{\pi}{\omega_e \lambda} \int_L b_{33} V_z^2 dx_b \quad (2.25)$$

Radiated energy method gives better results in shorter waves in comparison to longer waves. This is because of its sensitivity to relative motion. In longer waves the relative motion is very small which makes it difficult for this method to accurately predict the added resistance⁽²⁵⁾. It does lack numerical stability in numerical waves. The peak values are also captured quite well using this method.

2.5 Solving Boundary value problem

The total fluid velocity potential ϕ can be defined as

$$\phi = Ux + (\phi_I + \phi_j + \phi_D) \quad (2.26)$$

ϕ_I - Incident wave potential

ϕ_D - Diffraction potential

ϕ_j - Radiation potential

U - Ship velocity

The incident wave potential can be defined in deep water conditions using Airy theory. So finding the total velocity potential requires finding the radiation potential and diffraction potential. This can be achieved by solving a boundary value problem (BVP). In a boundary value problem a numerical wave tank is defined enclosing a control volume, bounded by control surfaces. These control surfaces can be modelled by defining boundary conditions that the fluid potential have to fulfill. A BVP can be further simplified into a linear boundary value problem which makes the model more simple yet

still effective. Using a linear model the boundary conditions can be defined on the mean position of the surfaces rather than the instantaneous position used in non linear BVP (Refer figure 2.7).

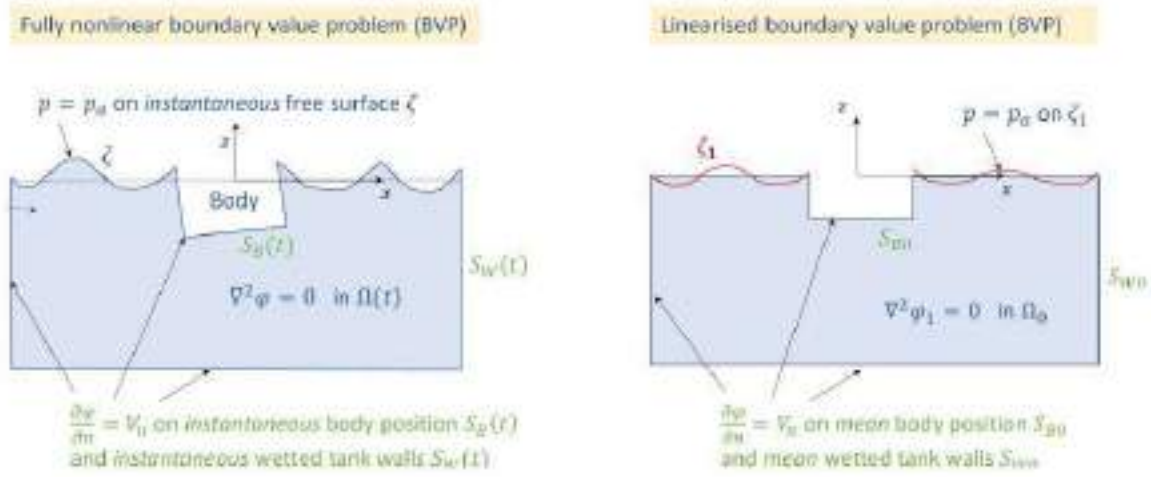


Figure 2.7: Numerical tank models for a Non linear BVP and Linear BVP⁽⁹⁾.

Defining a BVP, includes defining the governing equations and the boundary conditions. When talking about the BVP for the current study on a vessel in waves, the governing equation and boundary conditions can be summed up as follows.

The fluid velocity potential must obey the Laplace equation defined as

$$\nabla^2 \phi = 0 \quad (2.27)$$

The free surface of the control volume is defined by the combined free surface and dynamic boundary condition which states the fluid particles on the free surface stays on the free surface and the pressure on the free surface is equal to the atmospheric pressure. The free surface in a zero speed condition is different from the free surface in a forward speed condition. Therefore free surface condition can be defined for a zero speed condition or a forward speed. The surface of the vessel is defined by the body boundary condition which states that the fluid particles do not penetrate the body. The radiation conditions is also used which defines that the energy from the disturbance of the body is carried away into infinite distance.

2.5.1 Panel method

Boundary element method (BEM) or panel method is a useful technique to solve a boundary value problem. This method divides the body into panels or elements and then distribute sources and sinks along these panels in such a way that to represent the flow around the model. The velocity potential can be obtained by solving an integral equation formulated using Green's second identity. Green's second identity defines a relationship based on two scalar functions. The scalar functions can be considered as the Green's function, G and the fluid velocity potential, ϕ . If we define a domain as D then the integral equation can be written as in equation 2.28.

$$\int_D (G\nabla^2\phi - \phi\nabla^2G)dV = \int \int_{\partial D} (G\nabla\phi - \phi\nabla G)dS \quad (2.28)$$

Finding the appropriate green's function plays an important role in finding the solution for the defined BVP. This is also the main element which differentiates the numerical models formulated by various researchers. Based on the numerical models present until now, the following two types of green's function are the most widely used functions.

- Rankine function
- Free surface Green's function

The Rankine green's function is relatively simple and could accommodate a variety of linear and non linear free surface boundary conditions⁽⁴⁰⁾, but using a Rankine approach requires the need to discretize both the free surface and the body (at infinite depth and when control surfaces at the sides are located at infinity). Where as in case of a free surface green's function which already satisfies the free surface condition, the function becomes complex, but only the body needs to be discretized as shown in figure 2.8. Therefore Rankine approach requires larger computational effort than free surface green function.

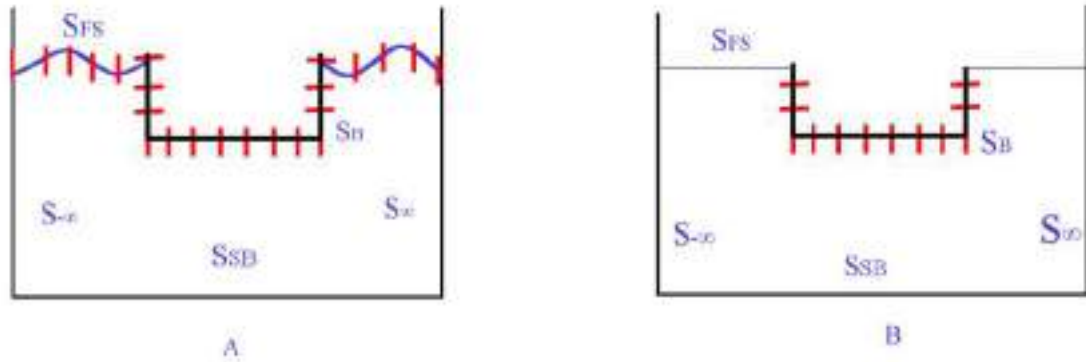


Figure 2.8: Discretization (A) when using Rankine green function, (B) free surface green function (B)

Based on the type of free surface Green's function used it is of two types.

- Zero speed free surface Green's function
- Forward speed free surface Green's function

The type of free surface Green's function used determines how the free surface can be modelled. For example⁽¹⁰⁾ if we consider an submerged Ellipsoid at Froude number of 0.2 (which is simple geometry similar to that of a ship) figure 2.9 illustrates the free surface modelled when using a zero speed free surface condition and figure 2.10 illustrates the free surface modelled when using a forward speed free surface green's function.

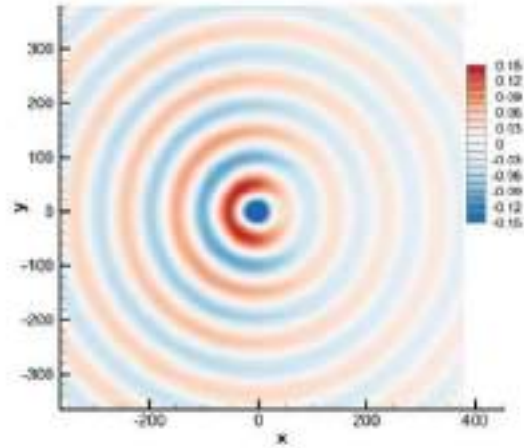


Figure 2.9: Free surface elevation (XY plane) formed by a Ellipsoid moving at $F_n = 0.2$ when using zero speed free surface Green's function⁽¹⁰⁾. x, y represents the distance along x, y direction in meters. The colour bar represents the the free surface elevation in meters.

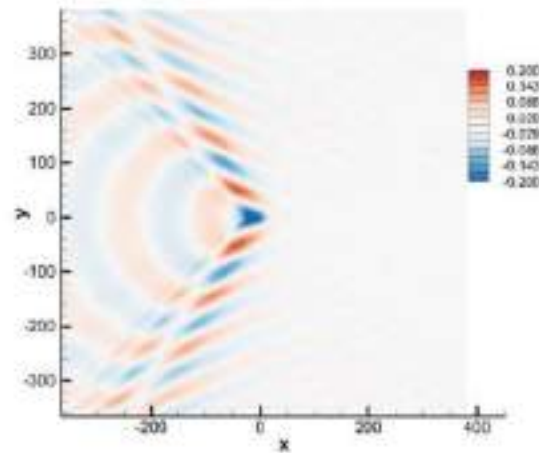


Figure 2.10: Free surface elevation (XY plane)formed by a Ellipsoid moving at $F_n = 0.2$ when using forward speed free surface Green's function⁽¹⁰⁾. x, y represents the distance along x, y direction in meters. The colour bar represents the the free surface elevation in meters.

Once the integral equation is solved, the radiation potential and the diffraction potential are obtained, combining it with the incident potential known for deep water waves the total potential is obtained. With the total velocity potential , we can apply Bernoulli's equation to obtain the total hydrodynamic force which consists of the excitation forces, added mass and damping forces. Using the restoring coefficients that depend on the hydrostatic vessel parameters the equation of motion can be solved which will give the motions of the vessel.

2.5.2 2D or 3D

Solving the BVP can be dealt as a 2D problem or a 3D problem. It can also be solved by a 2D+t approach. When the BVP is dealt in 2D, the whole vessel is divided into thin strips. Each strip is then divided to line segments and BVP is solved for each strip by distributing two dimensional sources and dipoles in each element. Once the forces on each strip is obtained using the solution from the BVP it is integrated along the length of the vessel to obtain the total load and corresponding motions of the whole vessel. This is based on the principle of strip theory. Strip theory is a linear theory based on the assumption that the body is slender and the encounter frequencies are high. The theory also assumes that effect from one strip does not affect the other.

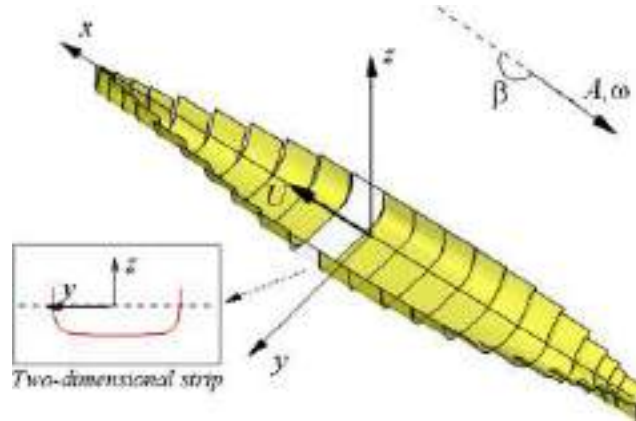


Figure 2.11: Figure illustrating the division of a whole vessel into strips to find forces on each strip and integrating them along the length of the vessel to obtain the total load on the vessel using strip theory⁽¹¹⁾

Alternatively the BVP can be solved as a 3D problem, where the whole vessel is divided into panels and the BVP is solved for the whole vessel by distributing singularities at the center of each panels.



Figure 2.12: Figure illustrating the panel distribution of the wetted ship hull surface

2.6 Asymptotic formula for short wavelength

Wavelengths which are less than half of the vessel length can be referred as short wavelengths. When considering the lifetime of a vessel, most of the waves it experiences are short wavelengths. Therefore these wavelengths are of particular interest from an operational perspective. In these ranges of wavelengths, the ship motions are negligible thus the added resistance in these wavelengths are dominated by wave reflections. Estimation of added resistance in shorter wave lengths poses its own challenges. Experimental estimation of added resistance in shorter waves are difficult because of instability in shorter waves and experimental uncertainty⁽⁴¹⁾. The usual Numerical estimations also fail to predict added resistance accurately in short waves. Researchers have been developing numerical formulations specifically for short wave conditions. Faltinsen⁽³²⁾ have formulated an expression for added resistance in short waves. Later Fuji and Takashi⁽⁴²⁾ had introduced slight modification on this formula, but none of the modification have brought any significant difference from the results based on Faltinsen’s method⁽⁴¹⁾. A brief description on Faltinsen’s formulation for added resistance at shorter waves is presented in the following section

2.6.1 Faltinsen’s asymptotic method

Faltinsen⁽⁴¹⁾ have formulated an expression for added resistance in this short waves referred to as the asymptotic expression using the principle of pressure integration. This formulation gives comparatively good results in case of vessels with blunt forms at Froude numbers less than 0.2. According to Faltinsen⁽⁴¹⁾ since the wave lengths are small and decays exponentially and it is only the part of the ship close to the waterplane that will affect the flow field and we may replace the ship by a stationary, vertical, infinitely long cylinder with a cross section equal to the waterplane area of the ship. He neglects the wave induced motions as the wavelengths are small ($\lambda/L < 0.5$) and also assumes the change in water plane area is small over a wavelength. He defines the equation assuming steady flow parallel to the wall and incident waves does not reach the so called shadow region as seen in figure 2.13. Since we neglect wave induced motions the velocity potential at non shadow region can be given as $\phi = Vs + \phi_I + \phi_D$, where s is defined in the local coordinate system in figure 2.13 and $V = U \cos\theta$ is the steady fluid velocity.

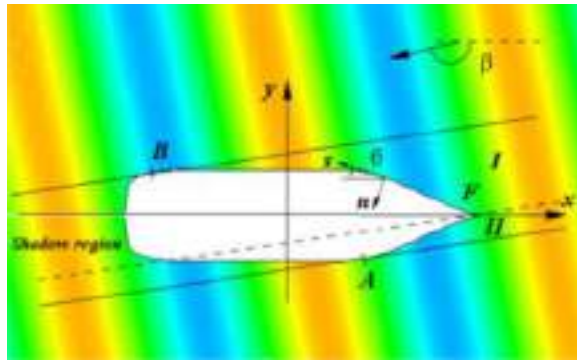


Figure 2.13: Coordinate system in low wavelength case⁽¹²⁾

As per above assumptions the added resistance in case of short wavelengths can be written as

$$R_{add} = 0.5\rho g\zeta_a^2 \int_L (\sin^2(\theta - \beta) + \frac{2\omega U}{g}[1 + \cos\theta\cos(\theta - \beta)])n_1 dL \quad (2.29)$$

where

$$n_1 = \sin\theta$$

θ - waterline inclination angle

β - incident wave angle

ζ_a - incident wave amplitude

3 Experimental study

3.1 Need for a experimental study

Estimating second order loads like added resistance becomes challenging as they are non linear in nature and sensitive to many factors. The reliability of the estimations depends on how well we are simulating the conditions we are interested in. Numerical modelling and physical modelling(model testing) are the two methods we use to model realistic operating conditions of investigated body. A numerical model is confined within the theories and computer power available today. It does give us accurate results, but only within its validity limits which are bound by certain assumptions and simplifications. Currently there are numerous numerical codes that estimate added resistance with their own models to represent reality, but we still have not come down to a general model which accurately represents all cases, especially when it comes down to studying a vessel with forward speed. Whereas a physical model is more capable of capturing all kinds of physical phenomena .Table 3.1 by Aage C⁽¹⁷⁾ points out the advantages of using a physical model from a numerical model. Even though the paper was published in 1992 and since then there have been drastic improvement in using numerical models, when it comes to estimating second order loads such as added resistance, physical models are still considered more reliable and thus used as a means for verification of numerical estimation. Therefore in order to validate the numerical results an experimental study needs to be performed. However it is to be noted that in case of short waves, even model tests poses large uncertainty in measurement of added resistance, which will be discussed further in the report.

Table 3.1: Physical model versus Numerical model⁽¹⁷⁾

Qualities	Physical models	Numerical models
<i>Representation</i>	Very Good	Limited by available theories and computer power
<i>Accuracy</i>	Good	Good within validity limits
<i>Scale Effects</i>	Yes	No
<i>Reliability</i>	Very good	Risk of human errors
<i>Credibility</i>	Very good	Prima facie not good
<i>Flexibility</i>	Not good	Good
<i>Execution</i>	Long	Low with standard programs
<i>Cost</i>	High	Development cost high

3.2 Experimental setup

3.2.1 Experiment design

As mentioned the quality of the experimental model depends on how well we can simulate the case of interest. In this study a wind assisted propulsion displacement type of vessel moving in regular waves in deep water is to be modelled to study the added resistance in waves. Only the added resistance due to the drift angle is of interest in this study, and thus other sources like wind, rudder angle are not be incorporated in the experiment.

Added resistance can be found experimentally by finding the difference between the time averaged total resistance (in a particular wave condition and vessel speed) and the still water resistance (at the particular vessel speed). A towing test can be used to measure the total resistance on a model vessel.

There are two towing methods: the constant thrust test (model free to surge) and the constant speed test (surge motion mode restricted). The constant thrust test requires complicated devices where as the constant speed test does not require complicated device but it gives large oscillatory signals of force⁽⁴³⁾. But C. M-Park et al⁽⁴³⁾ points out that both the methods give nearly identical results affecting the added resistance. Therefore a constant speed towing test along with waves generated by a wave maker is sufficient to physically model a vessel moving in waves. Froude scaling is followed to scale down the full scale parameters to model scale parameters. For the current study the model is restricted in surge, sway, yaw and roll motion modes even though these mode of motions can affect the added resistance. The model is allowed to heave and pitch motion modes. The drift angle can be simulated by means of an oblique tow test, where the vessel is set at the required angle and then towed. This can be achieved by means of a hexapod system. More details about the hexapod system will be presented further in the report.

As per ITTC⁽⁴⁴⁾ a deep water environment can be modelled by tank with $h/T > 4$ and a vessel speed less than $0.5(gh)^{1/2}$ where acceleration due to gravity $g = 9.81m/s^2$, h is water depth, T is model vessel draught. The towing tank at Sintef Ocean gives a minimum $h/T = 5/0.343 = 14.5$ which is greater then required and $0.5(gh)^{1/2} = 0.5(9.81 * 5)^{1/2} = 7.0m/s$ which is greater than our model speed of $1.36m/s$. So the towing tank at Sintef Ocean provides us with the right conditions for modelling a deep water condition.

For a complete study along with resistance, quantities like all six degrees of motion, the regular incident wave elevation at the model, the wave elevation of the waves generated and the carriage speed and position are to be measured. This calls for instruments like force transducers, accelerometers, wave probes which are capable of measuring these quantities accurately and generate a time series of all the quantities of interest for each test run, along with cameras and a computer system to record data and control the carriage. The detailed description on instruments used for this experiment is presented further in the report.

Since we have decided upon on how we we can model our test case, a more detailed description of the vessel model, the environment, the instrumentation used for the test is discussed further in this section.

3.2.2 Test Case Model

When analyzing the total number of ships in the world merchant fleet as of January 1 2020, 21.8% are bulk carriers, making it the vessel type with second largest number of vessel⁽⁴⁵⁾. Bulk carriers have the second largest contribution of the total CO₂ emissions which amounts to 19% ⁽⁴⁶⁾. With larger deck space compared to other vessels bulk carriers becomes a suitable vessel design for wind assisted propulsion. Therefore this study is based on an bulk carrier vessel optimized for wind assisted propulsion designed by Sintef Ocean called SOShip with a scale factor of 1:32 (Figure 3.1). The principal parameters of the vessel can be found in Table 3.2.

sea state ⁽⁴¹⁾ and thus it is included in the current study. Based on the ITTC recommendation and particular interests of this study wavelengths from $0.2 L_{pp}$ to $2.0 L_{pp}$ are used in the test. When considering wave steepness, the waves should not be too steep which might cause wave breaking. The higher the amplitude the larger the forces. ITTC recommends to keep wave steepness constant around 0.02 throughout all the wavelengths⁽¹³⁾. It was thus decided to use a wave steepness of 0.025. It is to be noted that it was not possible to perform tests at all desired wavelengths due to lack of time and test setup limitations. Based on the desired wavelengths and wave steepness the following wave conditions in Table 3.3 were used for the tests.

Table 3.3: Wave conditions for the test. H - Wave height, T - Wave period, λ - Wave length, L_{pp} - Length between perpendicular=190m. (8xxx is a common wave number series convention used for documenting wave conditions at SINTEF Ocean)

Wave Series no.	Test type	H(m)	T(s)	λ/L_{pp}
8000	Reg	0.95	4.9	0.2
8010	Reg	1.43	6.0	0.3
8020	Reg	1.90	7.0	0.4
8030	Reg	2.38	7.8	0.5
8040	Reg	2.85	8.5	0.6
8050	Reg	3.33	9.2	0.7
8060	Reg	3.80	9.9	0.8
8070	Reg	4.04	10.2	0.85
8080	Reg	4.28	10.5	0.9
8090	Reg	4.51	10.8	0.95
8100	Reg	4.66	10.9	0.98
8110	Reg	4.75	11.0	1
8120	Reg	4.85	11.1	1.02
8130	Reg	4.99	11.3	1.05
8140	Reg	5.23	11.6	1.1
8150	Reg	5.46	11.8	1.15
8160	Reg	5.70	12.1	1.2
8170	Reg	6.18	12.6	1.3
8180	Reg	6.65	13.1	1.4
8190	Reg	7.60	14.0	1.6
8200	Reg	8.55	14.8	1.8
8210	Reg	9.50	15.6	2

Other aspects that were considered while selecting the wave conditions includes checking the limitations of the wave maker and the possibility of tank wall interference.

3.2.4 Wave maker limitation check

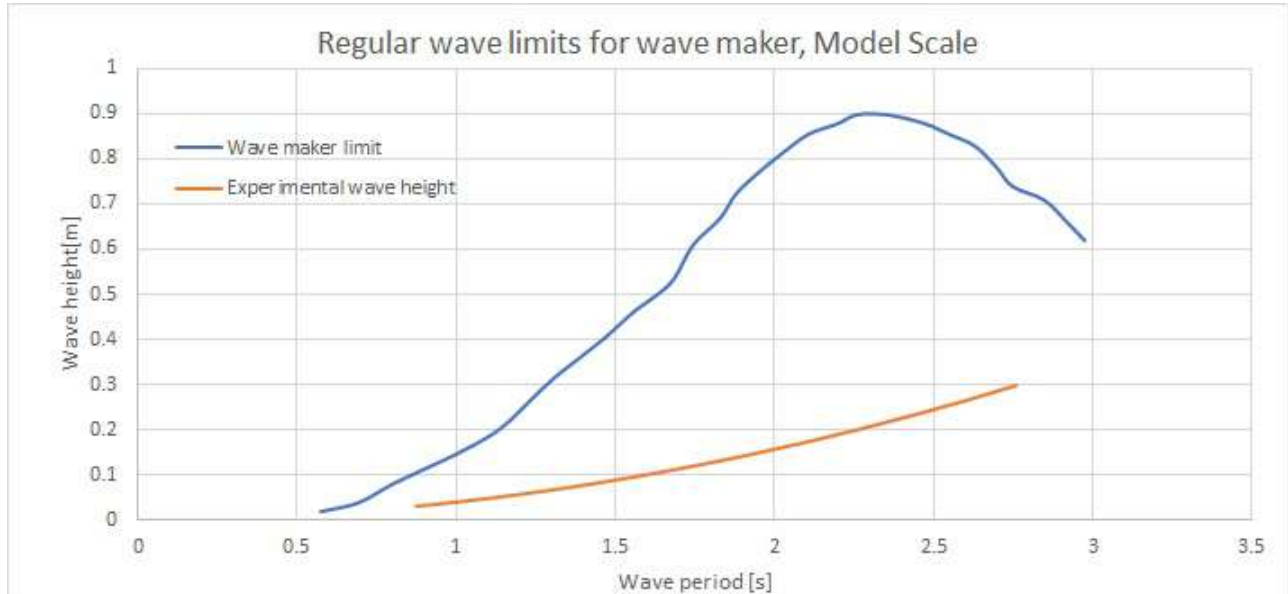


Figure 3.2: Checking wave conditions based on wave maker limitation

In Figure 3.3 since the wave conditions decided (red curve) is within the wave maker limit (blue curve) provided by SINTEF Ocean, all the wave conditions decided can be generated by the wave maker.

3.2.5 Tank wall interference check

During model tests in a towing tank, there is possibility of waves from the model to reflect from the tank wall and interfere with model giving wrong results. This tank wall interference can depend on wave frequency, model size and model speed. ITTC have given the following table (Table 3.4) where a dimensionless form of a relationship between model length, tank breadth, Froude number and highest wave frequency at which interference may occur in head waves⁽¹³⁾. This table was used checked for possibility of tank wall interference based on the decided parameters of the experiment (Figure 3.3). It was observed that the experimental conditions were within the limits of possibility tank wall interference.

Table 3.4: Maximum frequency at which tank interference occurs in head waves, Tank breadth B_T , Model length L_m , Highest wave frequency ω , acceleration due to gravity $g=9.81\text{m/s}^2$, F_n - Froude number, ω_e - Encounter wave frequency

B_T/L_m	$F_n\omega_e\sqrt{(L_m/g)}$
0.5	0.635
0.75	0.458
1.00	0.378
1.25	0.335
1.5	0.309
1.75	0.292
2.0	0.280
2.25	0.271
2.5	0.265
2.75	0.260
3.0	0.255
3.25	0.252
3.5	0.249
3.75	0.247
4.0	0.245

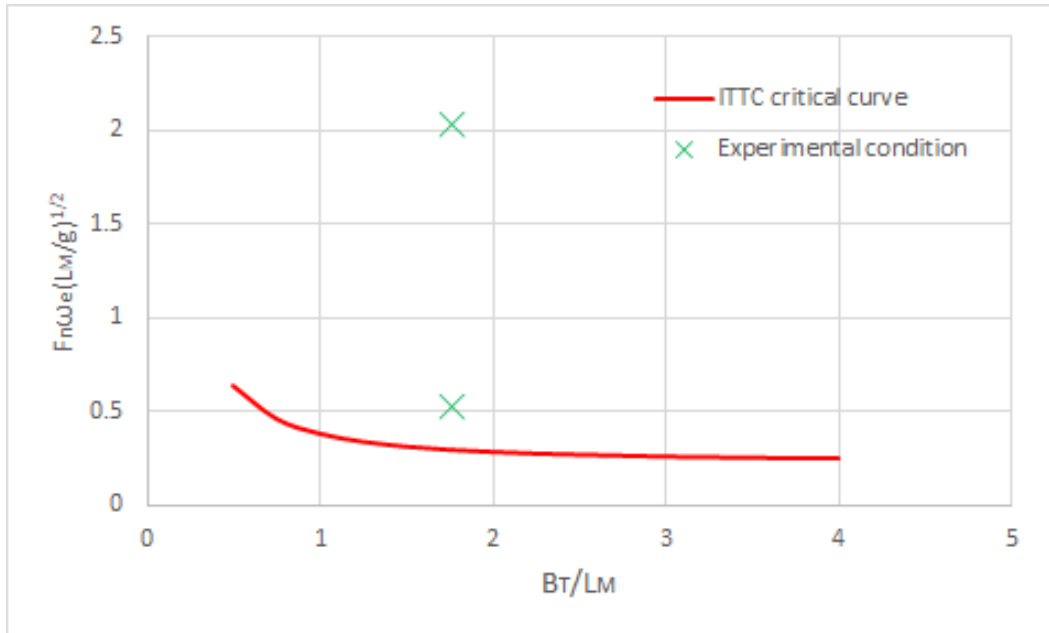


Figure 3.3: Maximum frequency at which tank interference occurs in head waves as per ITTC⁽¹³⁾. The Experimental values corresponds to the highest wave encounter frequency in model scale $\omega_e=14.56$ (full scale wave period= 4.9 sec and lowest wave encounter frequency in model scale $\omega_e = 3.735$ (full scale wave period=13.1sec), Tank width $B_T = 10.5\text{m}$ (Figure 3.14), Model Length $L_m = 5.938$ m, Froude number $F_n = 0.179$

Since the value of $F_n \omega_e \sqrt{L_m/g}$ corresponding to the lowest wave encounter frequency and largest wave encounter frequency in the conditions decided is above the critical limit, there will not be any tank wall interference in head sea. In our test case we are also performing the test conditions with a 9 degree drift angle. Even though this drift angle causes a change in the projected width of the model, since it is very small it is expected not to give drastic difference from head sea conditions when considering tank wall interference. In this experiment a tests are also conducted at $F_n = 0$. In this case the model will experience the wave reflections from the side walls of the tank. This could affect the results and thus a study on tank wall interference at $F_n = 0$ is conducted in section 5.3.

3.2.6 Test conditions

A tabulated form of all the tests performed is presented in table 3.3. A more detailed description for selecting each test condition is presented in this section.

The test was performed for two different froude numbers (Fn), $F_n = 0$ and $F_n = 0.179$. The concept of added resistance becomes more interesting when a vessel moves with a forward speed, it is only then we are concerned about issues like speed loss and fuel consumption. Drift forces also exists for vessel without forward speed, but this is of more concern for moored vessels or platforms. There are two reason for including a zero speed condition in this study: Firstly, the numerical codes we have at present have already proven to give good results at a zero speed condition as a zero speed free surface green function could solve the velocity potential in this condition. Therefore performing a set of tests at zero speed and comparing it with the numerical codes can be helpful in detecting large errors from instruments or from the test setup. This gives better confidence on the reliability of all the tests. Secondly, this also presents the opportunity to investigate about how the reflections of waves from the tank walls affect the results. The numerical code WAMIT version 7.3 have the capability of predicting this numerically and thus can be used for detecting tank wall effects by comparing it with the experimental results.

To evaluate the effect of a drift angle, tests were performed at drift angles of 0° and 9° . Due to lack of time it was only possible to perform a single case of non zero drift angle. When selecting the drift angle care had to be taken to make sure it was not too small such that the effects of drift angle were not easily visible, and not too large that would cause flow separation on the hull bringing other forces into the picture which a potential theory based numerical code could not produce. It is to be noted that at a drift angle other modes of motions affect the waves generated by the vessel and thus affects the added resistance. This is not being investigated for now. Jarle et al⁽⁴⁸⁾ had published a study on Drift forces on wingsails and flettner rotors. Based on their study which used drift angle ranges from 2° to 10° and suggestions from my supervisor and experienced personnel at Sintef Ocean a 9° drift angle was selected for the test. The effect of drift angle was measured by means of oblique towing in head sea (vessel heading= 9°) and in following sea (vessel heading= 189°) wave conditions at $F_n = 0.179$. Following sea condition was not used for tests at $F_n = 0$ due to lack of time.

Table 3.5: Experiment run list with full scale parameters. Wave Period T (sec), Wavelength λ (m), Wave frequency ω (rad/sec), Wave encounter frequency ω_e (rad/s), Wave height H (m), Vessel heading β (degree), Vessel speed U (m/s)

Test Series no.	T	λ	λ/L_{pp}	ω	ω_e	H	β	U
CE2000	7	76.504	0.40	0.898	0.898	1.9	0	0

<i>CE2001(rep)</i>	7	76.504	0.40	0.898	0.898	1.9	0	0
<i>CE2010</i>	7.8	94.990	0.50	0.806	0.806	2.38	0	0
<i>CE2020</i>	9.2	132.149	0.70	0.683	0.683	3.33	0	0
<i>CE2031</i>	10.5	172.134	0.91	0.598	0.598	4.28	0	0
<i>CE2040</i>	11	188.919	0.99	0.571	0.571	4.75	0	0
<i>CE2050</i>	12.1	228.591	1.20	0.519	0.519	5.7	0	0
<i>CE2060</i>	13.1	267.936	1.41	0.480	0.480	6.65	0	0
<i>CE2070</i>	14	306.017	1.61	0.449	0.449	7.6	0	0
<i>CE2071</i>	8.5	112.805	0.59	0.739	0.739	2.85	0	0
<i>CE3000</i>	7	76.504	0.40	0.898	0.898	1.9	9	0
<i>CE3010</i>	7.8	94.990	0.50	0.806	0.806	2.38	9	0
<i>CE3020</i>	9.2	132.149	0.70	0.683	0.683	3.33	9	0
<i>CE3030</i>	10.5	172.134	0.91	0.598	0.598	4.28	9	0
<i>CE3040</i>	11	188.919	0.99	0.571	0.571	4.75	9	0
<i>CE3050</i>	12.1	228.591	1.20	0.519	0.519	5.7	9	0
<i>CE3051(rep)</i>	12.1	228.591	1.20	0.519	0.519	5.7	9	0
<i>CE3060</i>	13.1	267.936	1.41	0.480	0.480	6.65	9	0
<i>CE3070</i>	14	306.017	1.61	0.449	0.449	7.6	9	0
<i>CE4000</i>	Calm water run						0	7.71
<i>CE4010</i>	4.9	37.487	0.20	1.282	2.575	0.95	0	7.71
<i>CE4020</i>	6	56.207	0.30	1.047	1.909	1.43	0	7.71
<i>CE4030</i>	7	76.504	0.40	0.898	1.531	1.9	0	7.71
<i>CE4040</i>	7.8	94.990	0.50	0.806	1.316	2.38	0	7.71
<i>CE4050</i>	8.5	112.805	0.59	0.739	1.169	2.85	0	7.71
<i>CE4060</i>	9.2	132.149	0.70	0.683	1.050	3.33	0	7.71
<i>CE4070</i>	9.9	153.024	0.81	0.635	0.951	3.8	0	7.71
<i>CE4080</i>	10.2	162.439	0.85	0.616	0.914	4.04	0	7.71
<i>CE4090</i>	10.5	172.134	0.91	0.598	0.880	4.28	0	7.71
<i>CE4100</i>	10.8	182.111	0.96	0.582	0.848	4.51	0	7.71
<i>CE4110</i>	10.9	185.499	0.98	0.576	0.838	4.66	0	7.71
<i>CE4120</i>	11	188.919	0.99	0.571	0.828	4.75	0	7.71
<i>CE4130</i>	11.1	192.369	1.01	0.566	0.818	4.85	0	7.71
<i>CE4140</i>	11.3	199.364	1.05	0.556	0.799	4.99	0	7.71
<i>CE4150</i>	11.6	210.090	1.11	0.542	0.772	5.23	0	7.71
<i>CE4160</i>	11.8	217.397	1.14	0.532	0.755	5.46	0	7.71
<i>CE4170</i>	12.1	228.591	1.20	0.519	0.731	5.7	0	7.71
<i>CE4180</i>	12.6	247.874	1.30	0.499	0.694	6.18	0	7.71
<i>CE4190</i>	13.1	267.936	1.41	0.480	0.660	6.65	0	7.71
<i>CE5000</i>	6	56.207	0.30	1.047	1.898	1.43	9	7.71
<i>CE5010</i>	7	76.504	0.40	0.898	1.523	1.9	9	7.71
<i>CE5020</i>	7.8	94.990	0.50	0.806	1.309	2.38	9	7.71
<i>CE5030</i>	8.5	112.805	0.59	0.739	1.163	2.85	9	7.71
<i>CE5040</i>	9.2	132.149	0.70	0.683	1.045	3.33	9	7.71
<i>CE5050</i>	9.9	153.024	0.81	0.635	0.947	3.8	9	7.71

<i>CE5060</i>	10.5	172.134	0.91	0.598	0.876	4.28	9	7.71
<i>CE5070</i>	11	188.919	0.99	0.571	0.824	4.75	9	7.71
<i>CE5080</i>	11.6	210.090	1.11	0.542	0.769	5.23	9	7.71
<i>CE5081</i>	Calm water run						9	7.71
<i>CE5090</i>	12.1	228.591	1.20	0.519	0.729	5.7	9	7.71
<i>CE5100</i>	13.1	267.936	1.41	0.480	0.658	6.65	9	7.71
<i>CE6000</i>	6	56.207	0.30	1.047	0.185	1.43	180	7.71
<i>CE6010</i>	7	76.504	0.40	0.898	0.264	1.9	180	7.71
<i>CE6020</i>	7.8	94.990	0.50	0.806	0.296	2.38	180	7.71
<i>CE6030</i>	8.5	112.805	0.59	0.739	0.310	2.85	180	7.71
<i>CE6031(rep)</i>	8.5	112.805	0.59	0.739	0.310	2.85	180	7.71
<i>CE6040</i>	9.2	132.149	0.70	0.683	0.316	3.33	180	7.71
<i>CE6050</i>	9.9	153.024	0.81	0.635	0.318	3.8	180	7.71
<i>CE6060</i>	10.5	172.134	0.91	0.598	0.317	4.28	180	7.71
<i>CE6070</i>	11	188.919	0.99	0.571	0.315	4.75	180	7.71
<i>CE6080</i>	11.6	210.090	1.11	0.542	0.311	5.23	180	7.71
<i>CE6090</i>	12.1	228.591	1.20	0.519	0.307	5.7	180	7.71
<i>CE6100</i>	13.1	267.936	1.41	0.480	0.299	6.65	180	7.71
<i>CE6110</i>	14	306.017	1.61	0.449	0.290	7.6	180	7.71
<i>CE7010</i>	7	76.504	0.40	0.898	0.272	1.9	189	7.71
<i>CE7040</i>	9.2	132.149	0.70	0.683	0.321	3.33	189	7.71
<i>CE7050</i>	9.9	153.024	0.81	0.635	0.322	3.8	189	7.71
<i>CE7060</i>	10.5	172.134	0.91	0.598	0.320	4.28	189	7.71
<i>CE7070</i>	11	188.919	0.99	0.571	0.318	4.75	189	7.71

3.2.7 Instrumentation

This section discusses the various instruments used for measurements for the experiment. Before we talk about the instruments, we begin by discussing a parameter called sampling frequency.

Sampling frequency

Sampling frequency defines the number of samples or data points obtained in a second. It is important to have sufficient sampling frequency to identify the proper change of a parameter with time. A low sampling frequency might predict a completely different behaviour for the parameter of interest with respect to time.

Therefore the resolution must be large enough to record the proper change of a parameter with respect to time. Having very large sampling frequencies will help us to capture the change with better accuracy, but it comes with a price. As sampling frequency increases the storage capacity required for the data also increases⁽⁴⁹⁾. This limits us from selecting very large sampling frequencies. Based on experience from previous tests done at SINTEF Ocean, in the current study all the instruments except the motion capture camera system (OQUS) used a sampling frequency of 200 Hz, which tells

us that a data point is recorded every 0.005 second. For the OQUS system, a sampling frequency of 50 Hz was used which corresponds to data point recorded at every 0.02 seconds.

There are various types of instruments available today that helps in measuring various parameters in an experiment. Usually instruments are designed to generate an analog voltage or current signal which is linearly proportional to the measured parameter⁽⁴⁹⁾. In general the system required for performing measurements includes⁽⁴⁹⁾:

- The transducers
- Amplifiers
- Filters(analog and/or digital)
- Data storage unit
- Cabling between the different components

So along with the instruments for measurement we require a computer system for data acquisition and multiple other systems for purposes such as wave generation and carriage control.

Further in this section, we will discuss about the various instruments used for measuring required parameters for the study.

Sailboat Dynamometer

The sailboat dynamometer helps us in measuring the longitudinal force and transverse force on the model. This instrument utilizes load cells in it to measure the force on the model. For the current study the sailboat dynamometer developed by Wolfson Unit was utilized. Figure 3.4 shows us a clear image of various elements in a sailboat dynamometer. It consists of an element with three connector posts that is fixed onto the model as seen in figure 3.5. The post in the center consists of the load cell used for measuring the longitudinal force on the model. The other posts, located towards the fore end and aft end measure the transverse force at the fore and aft respectively. The design limits of the sailboat dynamometer is given in table 3.6. More details on the sailboat dynamometer can be found in appendix D



Figure 3.4: Sailboat dynamometer⁽¹⁴⁾



Figure 3.5: Sailboat dynamometer fixed on SOShip, The element fixed onto the model (top), Frame and rods which connects the dynamometer on the model to the carriage (bottom)

Table 3.6: Design limits of dynamometer

Parameter	Range	Resolution
<i>Heel (deg)</i>	+/- 40	2.5
<i>Leeway (deg)</i>	+/- 8	infinite
<i>Heave (mm)</i>	+/- 400	infinite
<i>Pitch (degrees)</i>	+/-7.5	infinite
<i>Drag WOL 21 (N)</i>	+1590 -1364	infinite
<i>Side force FWD WOL 20 (N)</i>	+1384 -1649	infinite
<i>Side force Aft WOL 22 (N)</i>	+1433 -1403	infinite
<i>Roll Moment (Nm)</i>	+/-2000 nominal	infinite
<i>Yaw Moment (Nm)</i>	+/- 2400 nominal	infinite

There are three rods that goes through a metal frame. This setup helps in connecting the model to the carriage. The frame is mounted on the carriage, in our case it was mounted onto the carriage through the hexapod system. The rods are inserted through this frame into the three connector posts and a locking mechanism at the top prevents the rod from to come out from the frame in extreme cases of vessel motion. Care was taken to ensure that this locking mechanism did not touch the frame during the test runs as it would affect the results. The dynamometer is a sensitive instrument

and thus even a minor problem in the assembly can give large error in the results. For example the tolerance between the rod and the frame can affect the results in a drastic way. During the preparation tests it was observed that, when the longer set of rods were used, the rod in the middle was the cause for wrong measurements due to unsuitable tolerance between the rod and the frame. It was then replaced with an another rod of suitable tolerance before the test runs as shown in figure 3.23.

Wave probes

Wave elevation is measured using wave probes. It consists of two parallel rods on which a voltage is applied as in figure 3.6. The wave probes are then lowered into the water. The water between the two rods then act as a conductor medium between the rods. Based on the elevation of the free surface the resistance varies (A higher elevation creates lesser resistance) thereby varying the current. Measuring this current can then be used to estimate surface elevation.

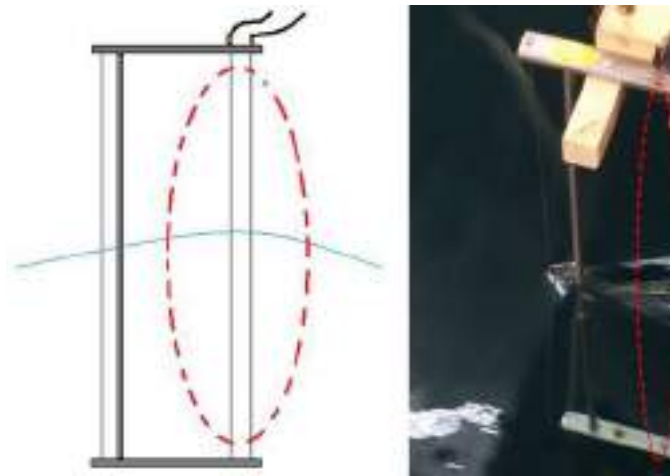


Figure 3.6: Diagram of a wave probe (left). Wave probe lowered into the water (right). Parallel rods in a wave probe are marked with a red ellipse.

Four wave probes were used for the tests in this experimental study. Two wave probes were placed near the wave maker to measure the waves generated and two wave probes were placed near to the model for measuring incident waves as shown in figure 3.20. The wave probes were made at SINTEF Ocean. The wave probes were calibrated before mounting onto the carriage. The wave probes near the model had to be re-calibrated when it changed positions for head sea and following sea tests. The accuracy of a wave probe depends on various factors like how old the calibration is, the change in tank water temperature since calibration, impurities in the water etc. A freshly calibrated wave probe used in the test is told to give an accuracy around 1%.

Motion capture cameras

Motion capture cameras helps us to capture the motion of a body with respect to time by tracking markers placed on the object. A vessel has 6 degrees of freedom in total. For this study the vertical motions such as heave and pitch are to be measured. Other motions such as surge, sway, roll and yaw are also to be measured to ensure the vessel was restricted in such motions during the tests. It is to be noted that numerical codes do not allow this restriction bringing a minor difference

in the conditions simulated. The company Qualis has developed Oqus range of cameras , which is the new platform for their motion capture systems (Figure 3.7). These range of cameras were the primary instruments used for measuring the vessel motions during the tests. The facilitate high speed, high resolution recording with real time marker generation. The system has minimal latency which facilitates faster transmission to the system and visualisation using their software. The camera measures the vessel motions by tracking optical markers on the object. In this test three ball shaped silver reflectors were placed on the model at three different levels, which acted similar to light emitting diodes for an optical system.



Figure 3.7: OQUS motion capture cameras by Qualis used for measuring motions along 6 DOF

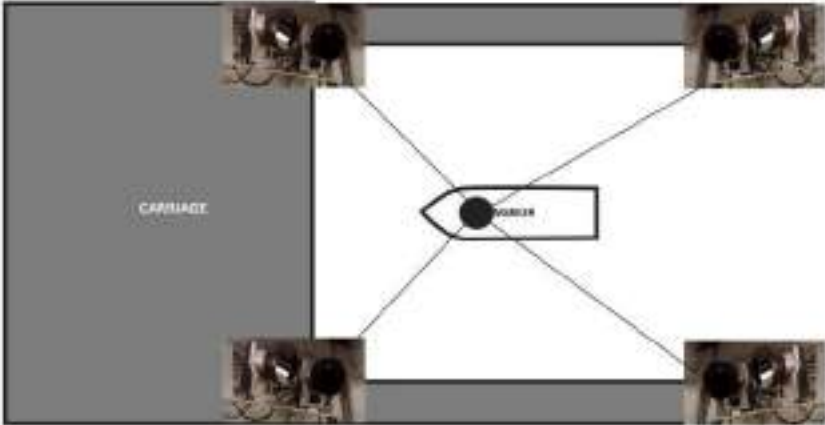


Figure 3.8: OQUS cameras mounted around the model on the carriage focused on tracking the optical marker on board the model vessel

The accuracy of the OQUS system depends on various factors like distance from cameras to the markers, the number of cameras used, other reflections in the surroundings, calibration and the type of lens used in the camera. A minimum of two cameras are used to read the position of each marker. For this test 8 cameras placed around the model at four corners, with 2 each on one corner (refer figure 3.8). The OQUS was pre calibrated and as part of test preparation, it was made sure there were no other reflections in the surrounding environment. The OQUS system used for the test has a measuring accuracy of ± 0.5 to ± 1.5 mm for displacements and ± 0.01 to ± 0.03 deg for angles as per SINTEF. This provides us with acceptable accuracy for measuring rigid body vessel motions. More specifications of OQUS cameras can be found in appendix D.

Accelerometer

Accelerometer is a tool that can be used to measure acceleration of a body in its own rest frame⁽⁵⁰⁾. They are used in many application from phones to structural monitoring. In the current study the main purpose of the accelerometers was to record the acceleration which can then be used to obtain the motion of the vessel. Even though OQUS was seen as the primary instrument for measuring motions in this experiment, this can be used as an extra instrument for recording motions, especially in case of any possible high frequency motions. In this experiment 2 types of accelerometers were used,

1. Uniaxial accelerometer

It measures acceleration along z axis. It was manufactured at SINTEF Ocean. 2 accelerometers of this type were used with one at the fore end and the other at the aft end as shown in figure 3.9. More specifications about the accelerometer can be found in the calibration certificate in appendix D

- Accelerometer 20642
- Accelerometer 20645

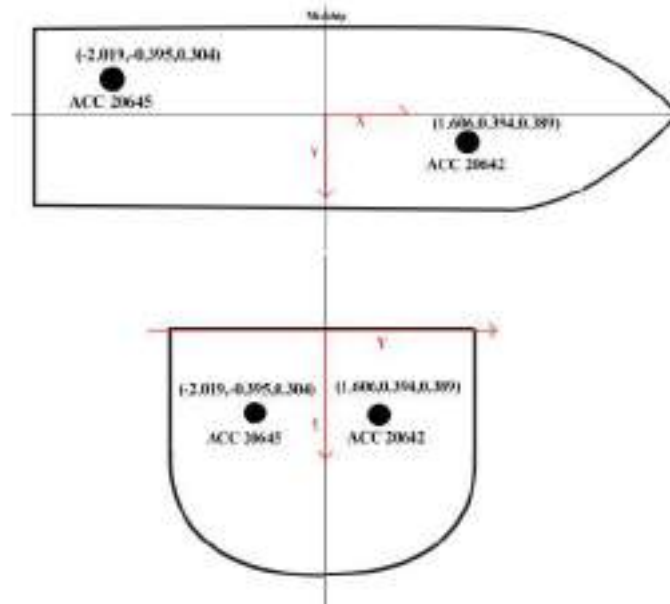


Figure 3.9: Position of uniaxial accelerometers on the vessel model

2. Triaxial accelerometers

It measures acceleration along x, y and z axis. For this test we have used the Model 4332 accelerometer (Figure 3.10).It offers both static and dynamic response. It has dynamic range of $\pm 2g \pm 5g$. It also incorporates a 50 Hz low pass filter. Two accelerometers of this type were used in the test and placed in the model at position as shown in figure 3.11. More specifications about the accelerometer can be found in Appendix D

- Accelerometer 16426
- Accelerometer 16316



Figure 3.10: Model 4332 triaxial Accelerometer (right) used as accelerometer 16426 16316 placed in aft and fore ends(left) respectively as shown in figure 3.11

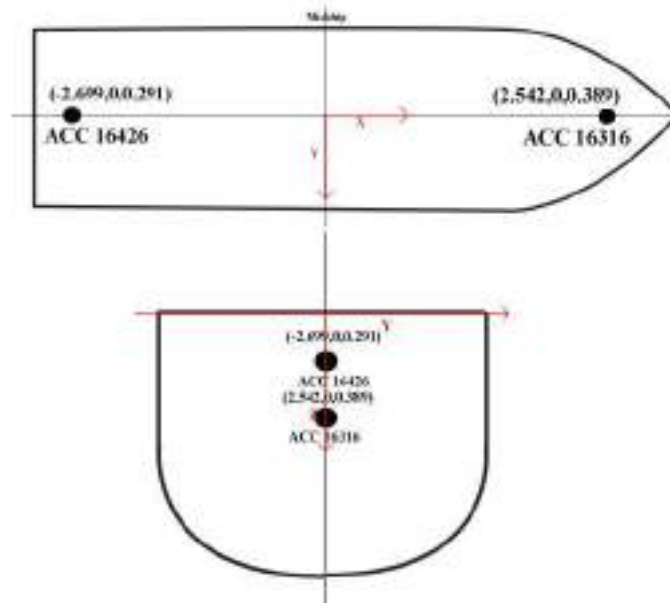


Figure 3.11: Position of triaxial accelerometers on the vessel model (Representative figure)

Rate Gyro

A rate gyro helps to record the rate of change of angle with time. This helps us to record the rate of change of pitch which could be also used for finding the pitch motion. This could help as a backup to be sure that OQUS results are dependable. It could also help to monitor the roll and yaw motions to see if it is restricted properly. For this test a rate gyro developed by SAAB, capable of measuring angular rotation rate along all the three axes, was used (Figure 3.12). More specifications on the unit is presented in appendix D.



Figure 3.12: Three axes Rate gyro unit⁽¹²⁾

Hexapod

The hexapod system, Symmetrie Mistral 800 (Figure 3.13), used for the test was a product of the company called Mistral. Mistral hexapods is a dynamic system capable of providing 6 degrees of freedom. It has a total payload capacity of 1 tonne with an accuracy of 0.5mm. For the current study the hexapod facilitated for easily changing the vessel heading between 0°, 9°, 180° and 189° for each test by simply turning the model to the required position for each test. Once the heading was set all the motions of the hexapod were restricted. The use of hexapod helped in reducing loss of time and effort that would have occurred for mounting the model in various heading angles. Using a hexapod it was just a matter of minutes to turn the model to the required heading angle for each test.



Figure 3.13: Hexapod system, Symmetrie Mistral 800⁽¹⁵⁾(right). Vessel mounted onto the hexapod (left),

3.2.8 Test setup

As mentioned the towing test was performed at the towing tank at Sintef Ocean. The tank parameters are defined as in Figure 3.14. The largest wavelength to be used in model scale dimensions is 8.373m corresponding to a full scale wave period of 13.1sec. Therefore the towing length enables to have more than the minimum 10 encounters that ITTC recommends when measuring motions⁽¹³⁾. The depth is sufficient for simulating deep water condition as already mentioned in section 3.2.1.

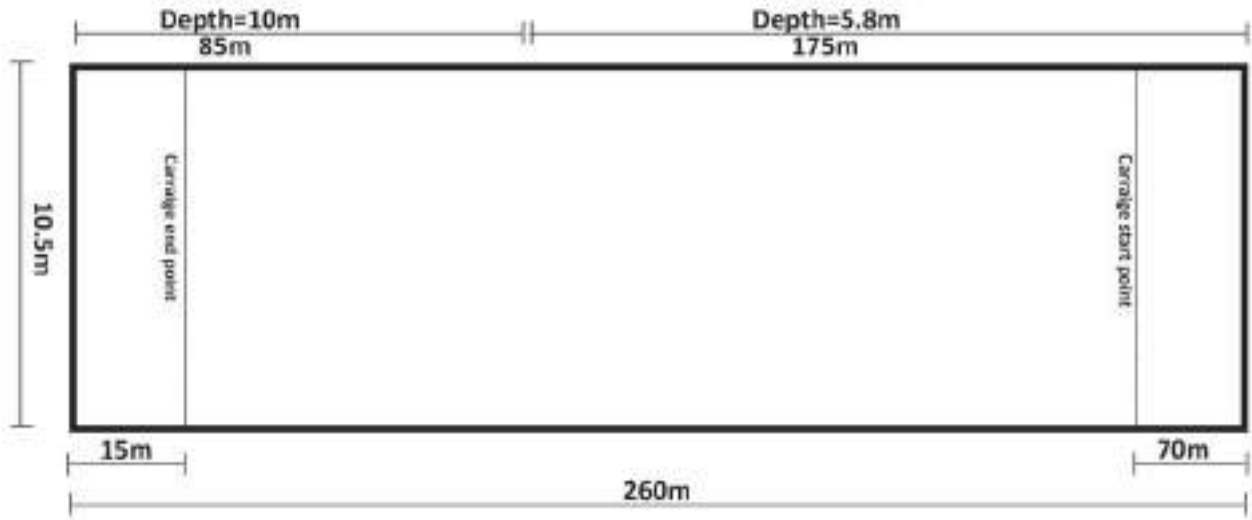


Figure 3.14: Towing tank dimensions. the first 175m has a 5.8m depth and the next 85m have a 10m depth

The model was painted, marked and the essential instruments were mounted on board, and was ballasted using weights to acquire design draft. The weights were placed ensuring even keel without any trim or heel angle (Figure 3.15).



Figure 3.15: Weights placed in model to achieve the design draft ensuring an even keel

A basic inclining test (Figure 3.17) was performed to have a rough check whether the transverse metacentric height of the model was close to that of the expected value of 2.5m in full scale (0.078 m in model scale).



Figure 3.16: Inclining test done to do a preliminary check of metacentric height

A swing test was performed after the experiment to get an accurate estimation on position of center of gravity and the radius of gyration in pitch. The swing test results and pictures(Figure B.1) is presented in Appendix B. The vessel was then mounted on the carriage through the hexapod with all the instruments such as accelerometers, gyro and the force transducers installed within it. All the instruments had been calibrated before the test

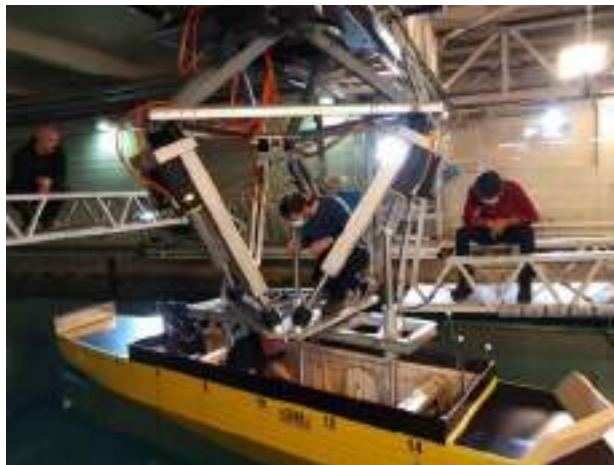


Figure 3.17: Model vessel being mounted onto the carriage through the hexapod

The pre calibrated OQUS system mounted around the model on the carriage helped in measuring the motions of the model using silver coloured optical marker on the vessel. Two set of optical markers were placed on the model to facilitate head sea test and following sea test measurements. For the head sea tests the markers at the bow were used and the one at the aft was covered with a

black plastic sheet. For the following sea markers at the aft were used and the markers at the bow were covered with a black plastic sheet. (Figure 3.18)



Figure 3.18: Optical markers for OQUS system. Markers used for head sea tests (top left) with aft markers covered (top right). Optical markers used for following sea tests (bottom left) with bow markers covered (bottom right)

Four video cameras were mounted around the model on the carriage as in Figure 3.19. They helped in recording the whole tests which was useful in careful and close observation and post processing of the test runs from different angles especially at the bow and the stern where there is significant wave radiation and slamming.

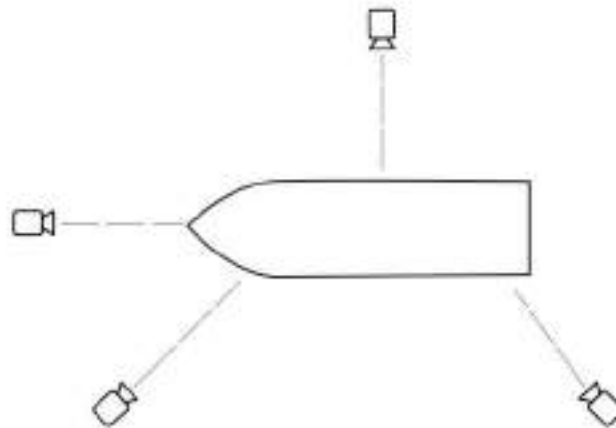


Figure 3.19: Diagram of camera positions around the model vessel

In order to measure the wave elevation, two wave probes were placed near to the wave maker and two wave probes were placed near the model. An ultra sound wave probe was placed on the carriage to measure the wave elevation to act as a backup to check incident wave elevation as seen in Figure 3.20. When placing the wave probes care had to be take to ensure the waves generated from the wave maker did not interfere with the model (Figure 3.22). The wave probes near the model had to

be placed as close as possible to the model to ensure we get the best value of incident wave elevation on the model. Based on the visual observation in the documentation runs, the wave probes were fixed at both sides of the vessel, not too far away from the model and not too close to the tank walls as seen in Figure 3.21.

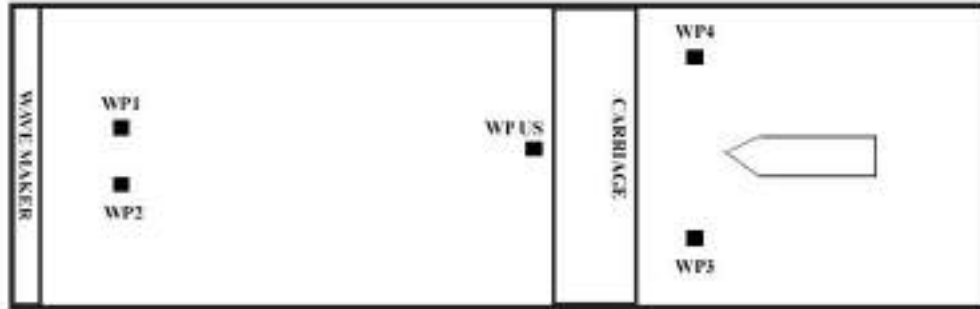


Figure 3.20: Wave probes placed in the test setup.



Figure 3.21: Wave probes 3 Wave probe 4 placed near model to measure incident wave elevation. It is to be noted that during following sea conditions, wave probe 3 and wave probe 4 were switched in positions after re calibration, due to lack of cable length for one of them

The test began with preparation runs to check whether the instruments were working well and the setup itself is ready for the run. Static tests were done by pushing and pulling the vessel to different directions to check the direction of longitudinal force and transverse force in the system. The direction of moment was checked by placing weights on port and starboard side. Then a test run at model speed corresponding to $Fn = 0.179$ (15 knots (7.71m/s) in full scale) was done. It was noted that the longitudinal force was not giving a proper oscillating value as expected. It exhibited close to flat zero reading instead of a crest in the time series plot, whereas the troughs were behaving as expected. It was deduced that the error was due to some mechanical connection between the carriage and the model. After multiple trials it was found that the rod in the center among the three rods which is connected to the sailboat dynamo meter was causing this mechanical issue therefore it was replaced with new rod which was shorter (Figure 3.23). Since the new rod was shorter very large wave amplitudes could not be used for the runs as there was possibility for the rod to fall off the frame or the locking mechanism (used to prevent such fall off) to collide with the frame during the test. The hexapod height was also adjusted to avoid the collision between the metal frame and



Figure 3.22: Waves generated from a wave probe is not interfering with the model

the vessel due to large heave motions. The tests began when all the instruments were rechecked and the directions were aligning to that of the desired coordinate system (Figure 3.24).



Figure 3.23: Replacing center rod (Left) from sailboat dynamo meter to frame with a rod (Right) of better vertical tolerance.



Figure 3.24: Seakeeping Cartesian coordinate system followed as per right hand thumb rule

3.2.9 Test procedure

Including the preparation runs all the test runs were done in a period of 6 days. For every test condition in the beginning a zero measurement is recorded which records all the parameters which is paused and then later resumed at another point of time which depends on the wave heading. It is to be noted that this creates an interval of empty data set in all the time series plot as seen in figure 3.25

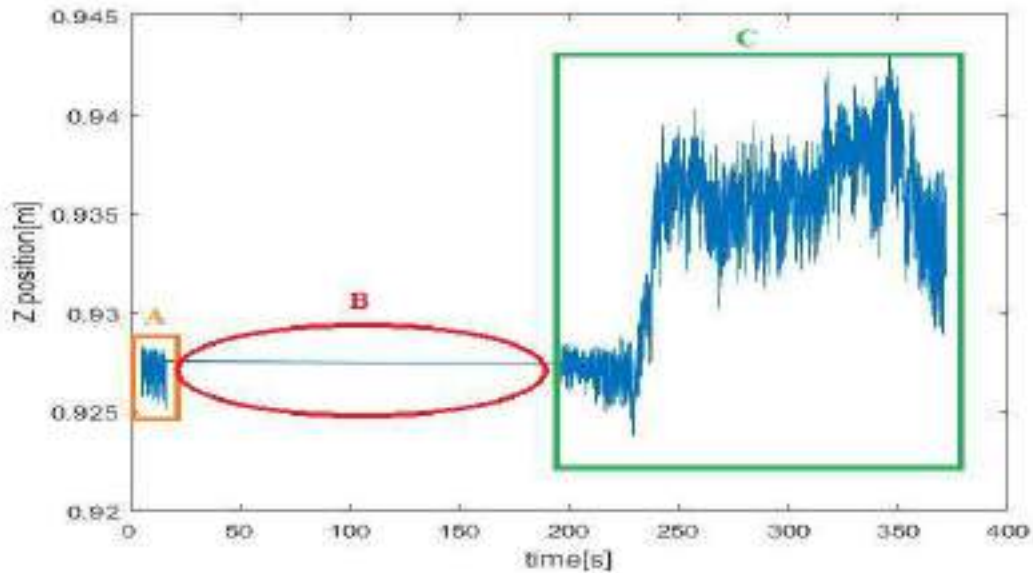


Figure 3.25: An example of an unfiltered Time series plot of heave (position in z axis) for test no. CE4070 to demonstrate an empty data set interval seen in all the time series plots. The region A shows the measurements done before the wave maker generates waves which helps to record the parameters when then the water was calm before the run also referred to as zero measurements. Region B shows the empty data set where no data was recorded and region C shows the measurements recorded resumed after the pause.(in this particular example it was when the waves met the model.

The tests began with the zero speed test conditions (test series no. 2000-3070). For test CE2000 the

model vessel was at the carriage starting point (refer Figure 3.14). This point did not seem to be a ideal position for zero speed test as the depth was not constant along the length of the model and due to probable wave reflections from the tank wall at the the starting end of the tank in case the beach does not absorb all the waves perfectly. So the test was repeated after moving the vessel to the carriage position 116.1m . As seen in Table 3.2.6 nine different wave conditions were used at a 0° drift angle 8 different wave conditions were used at a 9° drift angle. As the wave maker started generating the waves all the measurements were recorded from the point when the first wave from the wavemaker reached near the carriage (about 10 - 15 meters ahead of the vessel model) . All the required parameters as presented in section 5, were recorded for about 70 - 80 wave encounters. The average waiting time between each runs for the water to be calm before the next run was close to 20 minutes. The passive wave dampeners along the side of the tanks were used to dampen out the waves in the tank and disturbances along the depth of the tank. The dampeners were lifted up onto the surface during the waiting period and lowered down into the water during the test run. After the test runs in 0° , the hexapod system was used to turn the model 9° (Figure 3.26. The procedure were repeated just as in zero degree drift angle. The average waiting time between the runs were roughly 30 minutes as the waves were taking longer to dampen out. At the end the model was turned again to 0° to obtain an extra data point near the peak of the added resistance curve.



Figure 3.26: $F_n=0$ Vessel model at 0° drift angle(Left) and vessel model at 9° drift angle(Right)

After the tests at zero speed condition, the carriage was taken back to the starting point position at 70m length of the tank to begin the tests with $F_n = 0.179$. The tests began with the conditions with 9° vessel heading (Figure 3.29). The carriage speed was set to 15 knots full scale speed corresponding to 1.36m/s model scale speed. For tests CE5000 and CE5010 the carriage started to tow the model and the instruments started recording data when the first wave reached near the end of the carriage ahead of the model. Later for all the other tests the model started moving and the instruments started recording data when the first wave hit the model. It was noticed that at 9° drift angle, the frame between the hexapod and the dynamometer rods (marked in figure 3.27) was undergoing torsional bending and the hexapod was exhibiting a small jerking rotatory motion (as marked in figure 3.28). After checking the transverse forces and yaw motion plots corresponding to these runs, it was concluded to ignore this and continue the tests as these problems do not affect the results drastically and it would have taken one or two days to fix this issue, which will significantly reduce valuable time interval reserved for the experiments.



Figure 3.27: Frame which underwent torsional bending in test runs at 9°vessel heading

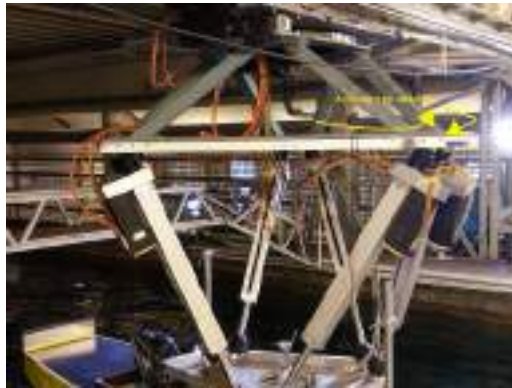


Figure 3.28: Jerking yaw motion observed in test runs at 9°vessel heading



Figure 3.29: $F_n=0.179$ Vessel model at 0°drift angle (Left) and vessel model at 9°drift angle



Figure 3.30: $F_n=0.179$ Vessel model at 180°drift angle (Left) and vessel model at 189°drift angle

Next the runs at 0°heading were done for $F_n = 0.179$ (Figure 3.29). At longer wavelengths ($\lambda/L > 1.0$) there was a large run up of water in the bow region and slamming of bow and stern.

After the head sea tests the model was turned 180° (Figure 3.30) for the following sea tests and the aft optical markers were revealed hiding the bow optical markers. This time the model starts from the tank length position of 238.4 m. When the first wave from the wave generator reached at particular point by visual observation the model started to be towed. Considering the distance covered by the wave within the time the model started to move in all the following sea tests, the average distance of this point from the wave maker was calculated to be 170.23 m (See Figure 3.40). After the tests with heading of 180° the vessel was turned to heading of 189° (Figure 3.30) using the hexapod and the final test runs were done just as at 180° heading. Due to lack of time for testing only few test runs were completed and thus a very few data points for analysis for tests at 189° heading are available.

Along with the tests in waves, calm water runs were also performed for the test conditions with forward speed which is used for finding the added resistance in waves. Test no. CE4000 corresponds to the calm water run with 0° drift angle at $F_n = 0.179$ and CE5081 corresponds to calm water run with 9° drift angle at $F_n = 0.179$.

3.3 Post processing

The output measured from each instrument is recorded in the system through various channels. The total data are extracted as a binary file (or in other file formats) which is then used in post processing analysis using programming platforms such as MATLAB. MATLAB was used in processing experimental data in this study. As per the binary files in this experiment there were 75 channels with data on each physical quantity. For this study we are more interested in quantities such as wave elevation at the wave maker, incident wave elevation, vessel motions (pitch, heave), longitudinal force (F_x), transverse force (F_y) versus time intervals. We also check quantities such as surge, yaw, sway and roll to ensure are restricted during the test. This also allows us to check whether the ship model alignment was correct or not.

Post processing analysis can be briefly summarized as follows. Firstly from the recorded the time series data we extract have to be filtered to remove unwanted noise and undesirable frequencies within the output. Once the records are filtered we select the desired time window which would represent the results of a test condition properly. By doing so the transient disturbances in the recorded set of data are also removed. The data set is now shorter and consists of relevant data points. The next step depends on what kind of output we need from the time series data set. We can use the data set in any way such that we could use the results to come to conclusions on the particular physical quantity in a particular test condition. For example in case of longitudinal force we find the average force within the time span using the data points within this range. In this study as mentioned earlier, the focus in this study is given to longitudinal force and vertical motions. Therefor in the following section a more detailed description of how each of these physical quantities were analysed is presented.

3.3.1 Data filtering

In an experimental data set of a physical quantity there can be unwanted frequencies which can give wrong results or misleading conclusions. It is therefore important to clear out unwanted frequencies from data set. Band pass filtering is common technique used to filter out such unwanted frequencies. A band pass filter helps to extract the frequencies within the specified frequency range excluding unwanted higher or lower frequencies.

Further this section presents details on filtering the quantities such as wave elevation, heave, pitch, longitudinal force and transverse force for the analysis.

Wave elevation

The wave probes near the vessel model had to be filtered. In the analysis the frequency of interest is the wave encounter frequency and therefore the lower and upper limits for frequencies to be filtered were used as 0.8 and 1.2 times the wave encounter frequency(Figure 3.31).

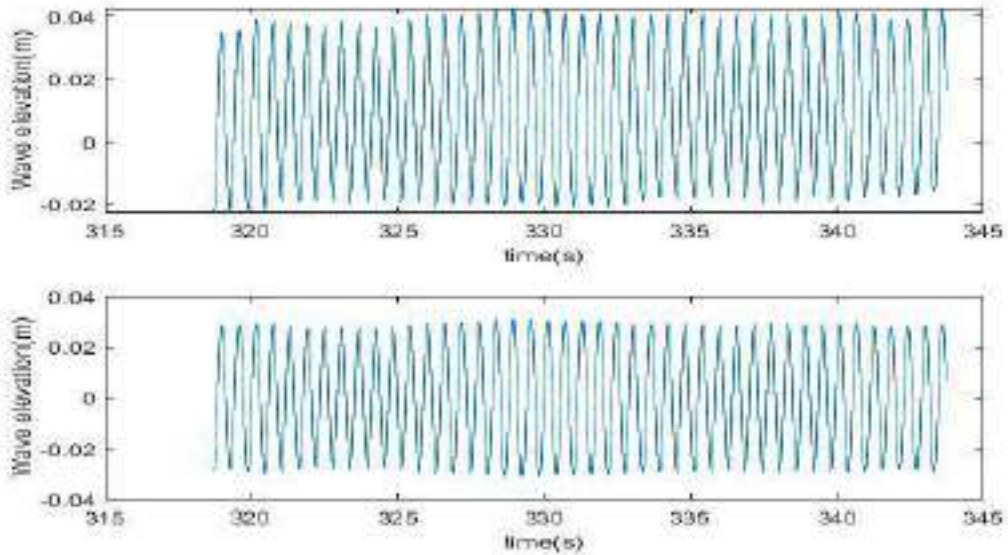


Figure 3.31: Example of Wave probe 3 wave elevation data unfiltered (top) and filtered (bottom) for test no. CE4020 . The image is based on a random time window for easy demonstration

Heave & Pitch motion

The analysis studies first order motions which are directly proportional to the wave elevation of the first order regular wave field in deep water and so the lower and upper limits for frequencies to be filtered were used as 0.8 and 1.2 time the wave encounter frequency. The output from OQUS was utilized for the analysis as OQUS system have already proven its capability in measuring motions accurately for many experiments (Figure 3.32 and Figure 3.33).

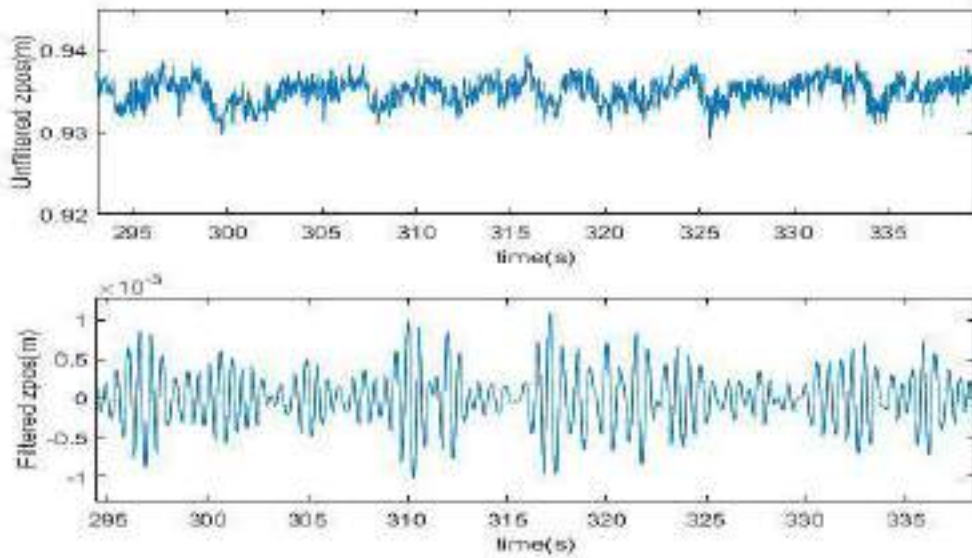


Figure 3.32: Example of heave motion data unfiltered (top) and filtered (bottom) for test no. CE4020. The image is based on a random time window for easy demonstration

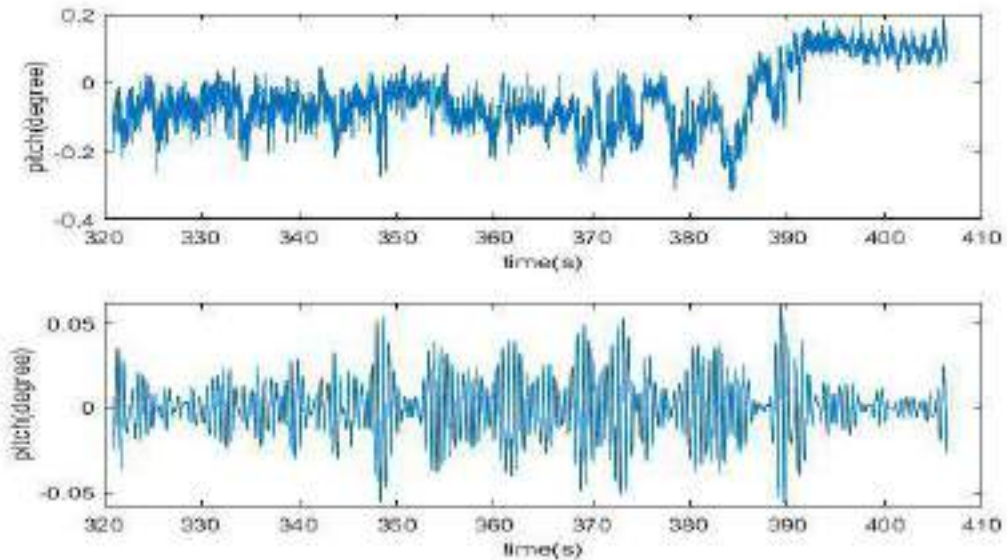


Figure 3.33: Example image of pitch motion data unfiltered (top) and filtered (bottom) set to mean value for test no. CE4020. The image is based on a random time window for easy demonstration

Force

In case of the longitudinal force the average value is to be estimated. Based on experience a frequency band from 0 to 0.05 is used for filtering longitudinal force (Figure 3.34), which provides a basic idea on the average longitudinal force in a test run. Towards the beginning and the end of the record

there is large values in the filtered data as seen in figure 3.34. This is due to the end effect that occurs when applying a band pass filter.

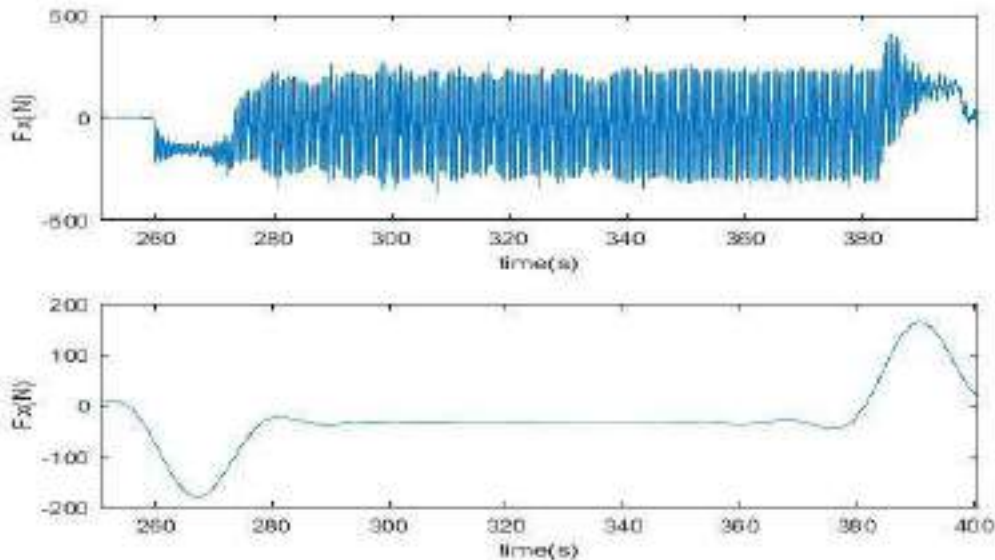


Figure 3.34: Example for longitudinal force F_x data unfiltered (top) and filtered (bottom) for test no. CE4020. The image is based on a random time window for easy demonstration

3.3.2 Time window

Selecting the right time window plays a major role in experimental data analysis. A time window that simulated the condition in the best way possible is expected to give the correct results. A time window must include as many encounters as possible to ensure a good amount of data at a constant speed. There are some instances that prevent us from simulating the right conditions in towing test like the transient stage at the beginning and the end of test run, unwanted noise, unexpected interference or motions during the tests. A single spike in the reading can drastically affect the average value from that time window. Therefore selecting a proper time window plays a major role in the accuracy of the results. In this analysis 3 different levels of time window have been used to select the best representative values of the measured quantities versus time interval. This section talks about the criteria used for selecting the time windows and demonstrates it through the results of three tests, CE2031, CE4010 and CE6010 where each represent zero speed condition, head sea condition with forward speed and following sea with forward speed respectively.

Level 1- Basin wall reflection

The waves generated travels from the wave maker to the beach at the other end of the the tank. A beach does not absorb all the waves to a 100%, some of them get reflected back to the other side. If the vessel model is not moving fast enough these reflected waves can interfere with the model which brings in additional forces and motions on the model (Figure 3.35). These same waves can also get reflected back again from the wave maker end and interfere with the model again. Therefore the first level of time window is based on selecting a time interval before the reflected waves interfere with the model.

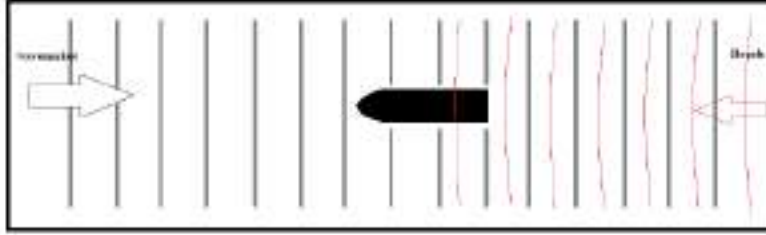


Figure 3.35: Wave reflections from beach interfering with the model vessel. The thicker grey lines represent the waves coming from the wave maker, the thinner red line represent the waves reflected back from the beach

Since reflected waves cannot be easily detected from the measured data, this time window is calculated manually for each wave condition and vessel speed condition using the group velocity $C_g(m/s)$ of the waves. In this first level of time window the end of the time window is controlled by the point when wave reflection meets the vessel. The start point of the time window is not of priority in this window. We can categorize all the test to the following three types

1. $F_n = 0$, Head sea condition

The model is positioned at 116.1m away from the beach end. The starting point (T_0) of the time window can be set to the point when the waves meet the model as it is when the data recording starts. The end point of the time window (t) is when the waves reflected from the beach hit the model, which at zero speed is the time a wave takes to travel to the beach from the model and then back onto the model as shown in figure 3.36.

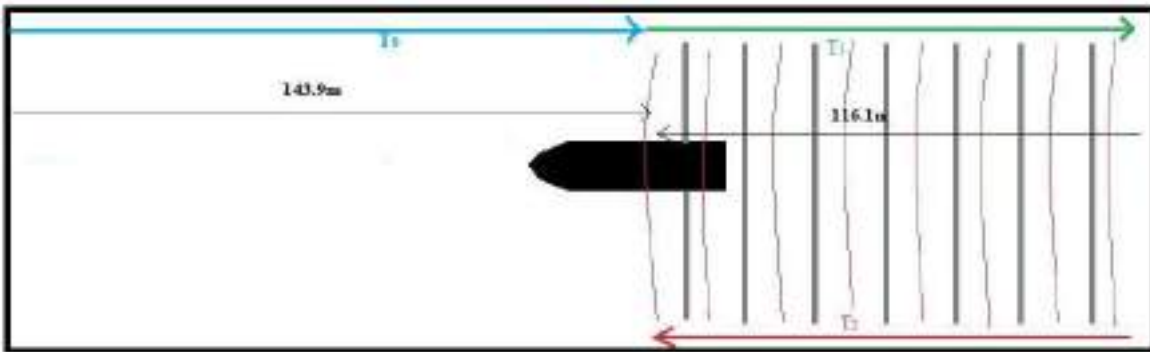


Figure 3.36: At $F_n = 0$, Waves travelling from the model position to the beach and back to the model. T_0 Time taken for waves to reach vessel position, T_1 Time required for waves to travel from vessel position to end of the wall near the beach, T_2 Time taken for the waves to travel from wall to the model

$$T_0 = \frac{143.9m}{C_g}, T_1 = \frac{116.1m}{C_g}, T_2 = \frac{116.1m}{C_g}, t = T_0 + T_1 + T_2 \quad (3.1)$$

C_g - Wave Group velocity(m/s)

T_0 - Time taken for waves to reach vessel position (s)

T_1 - Time taken for waves to travel from vessel position to end of the wall near the beach (s)

T_2 - Time taken for the waves to travel from wall to the model (s)

$Starttime - T_0$ (s)

$Endtime - t$ (s)

For example figure 3.37 shows a time series plots and a selected level 1 time window between the green lines for a particular test in head sea at zero speed.

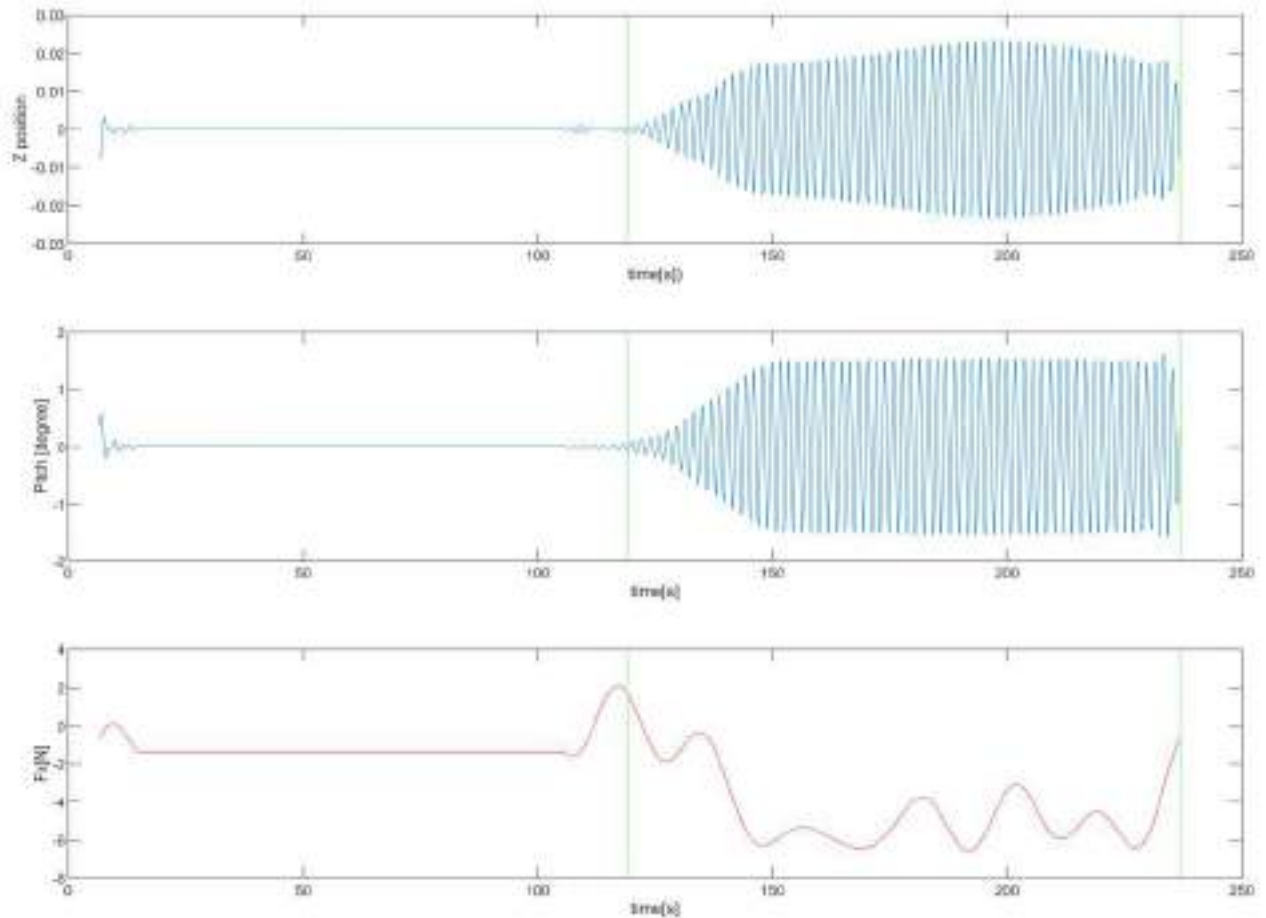


Figure 3.37: Time series plots of heave (Z position [m]), pitch motions and longitudinal force F_x bounded by level 1 time window (green lines) for test no. CE2031

2. $F_n \neq 0$, Head Sea condition

This time as the waves from the wave maker meet the model, the model vessel moves forward with a velocity (Figure 3.38) from its start position (70m away from beach side) and have covered a distance of x meter by the time the wave meets the tank wall. Therefore T_2 depends on the relative velocity between the model and the waves. If the group velocity of the waves are lesser than the model

velocity, then the waves do not catch up. In that case the end point of the time window can simply be defined as the time when the test ends. The starting point (T_0) of the time window can be set to the point when the model starts to be towed.

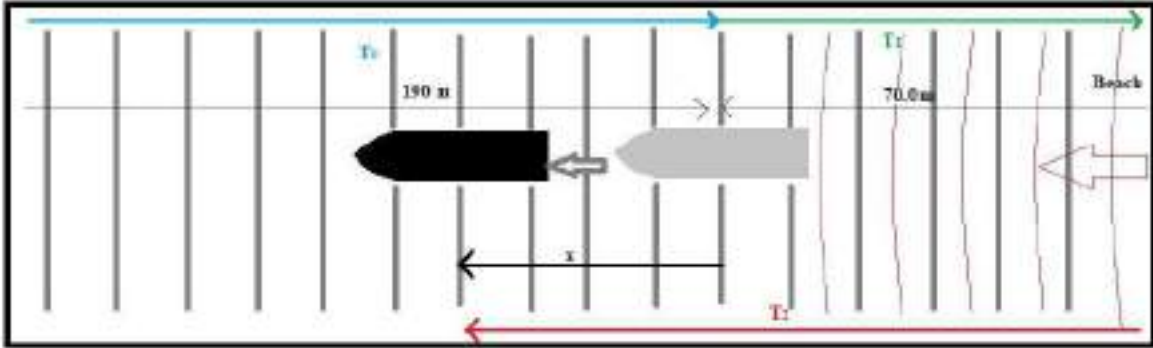


Figure 3.38: At $Fn \neq 0$, Waves travelling from the model start position to the beach and back to the moving model. Grey colour represents the model position when waves meet the model and black colour model represents the model position after covering a distance of x [m]. T_0 Time taken for waves to reach vessel position, T_1 Time taken for waves to travel from vessel position to end of the wall near the beach, T_2 Time taken for the waves to travel from wall to the model

$$T_0 = \frac{190m}{C_g}, T_1 = \frac{70m}{C_g}, \quad (3.2)$$

If $C_g > V_m$

$$T_2 = \frac{x + 70m}{C_g - V_m} \quad (3.3)$$

$$t = T_0 + T_1 + T_2 \quad (3.4)$$

Else

$$t = \text{End time of test} \quad (3.5)$$

V_m - Model ship speed(m/s)

C_g - Wave Group velocity(m/s)

T_0 - Time taken for waves to reach vessel position

T_1 - Time taken for waves to travel from vessel position to end of the wall near the beach (s)

T_2 - Time taken for the waves to travel from wall to the model (s)

Starttime – T_0 (s)

Endtime – t (s)

For example, figure 3.39 shows a time series plots and a selected level 1 time window between the green lines for a particular test in head sea at forward speed corresponding to $F_n=0.179$.

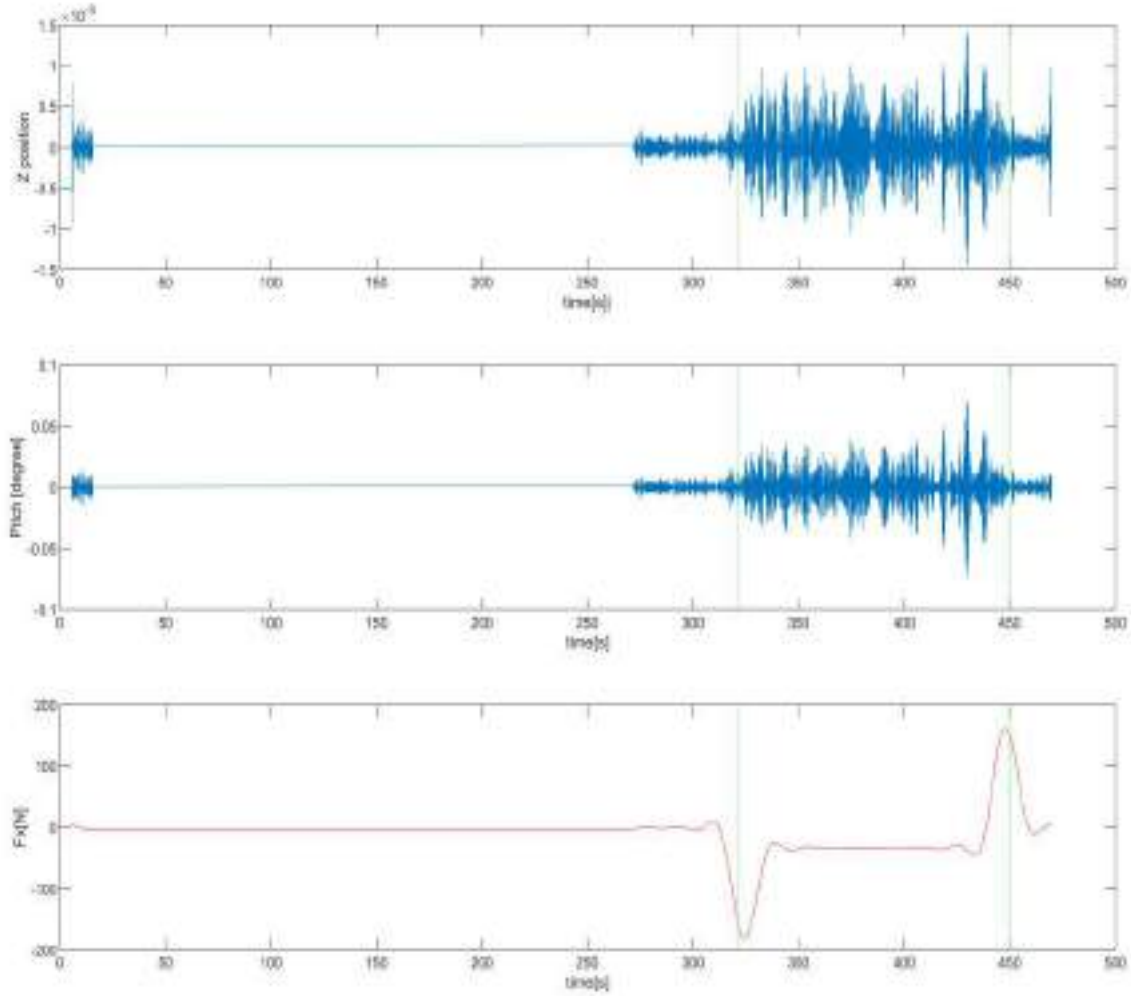


Figure 3.39: Time series plots of heave (Z position [m]), pitch and longitudinal force F_x bounded by level 1 time window (green lines) for test no. CE4010

3. $F_n \neq 0$, Following Sea condition

In the following sea condition, the model started moving when the wave reached roughly a particular distance denoted by P in Figure 3.40. This was done based on visual observation and thus point P is different for each test condition. The start point of this time window is when the model starts moving from its position of 238.4m. The waves need to travel the rest of the distance to the beach and then back to the model. If the vessel reaches the end of its run before the reflected waves touches the vessel the endpoint will be taken as the end of test time.

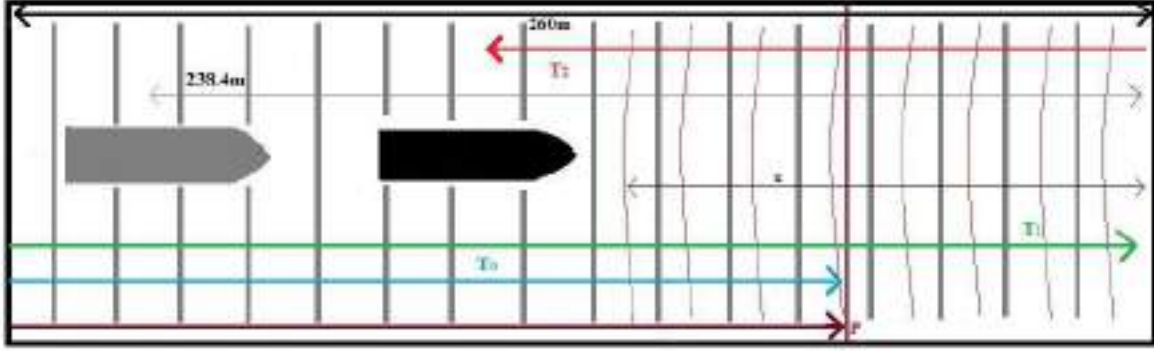


Figure 3.40: At $Fn \neq 0$, Waves travelling from the wave generator to the beach and then reflecting back to the model. Grey colour model represents the initial model position when waves travel 170.23 m and reach point P. [m]. Black coloured model represents the model position after the waves reflect from the beach. T_0 - time when waves reach point P, T_1 - time taken for waves to travel from point P to end of the wall near the beach, T_2 - time taken for the waves to travel from wall to the model

$$T_0 = \text{Time at which model starts}, T_1 = \frac{260m}{C_g}, \quad (3.6)$$

$$x = (T_1 - T_0)C_g \quad (3.7)$$

$$T_2 = \frac{238.4 - x}{C_g + V_m} \quad (3.8)$$

$$t = T_0 + T_2 \quad (3.9)$$

C_g - Wave Group velocity(m/s)

V_m - Model speed(m/s)

x - Distance travelled by the wave by the time model starts moving (m)

T_0 - Time taken for waves to reach vessel position (s)

T_1 - Time taken for waves to travel from vessel position to end of the wall near the beach (s)

T_2 - Time taken for the waves to travel from wall to the model (s)

Starttime – T_0 *Endtime* – t

For example figure 3.41 shows a time series plots and a selected level 1 time window between the green lines for a particular test in following sea at forward speed corresponding to $Fn = 0.179$.

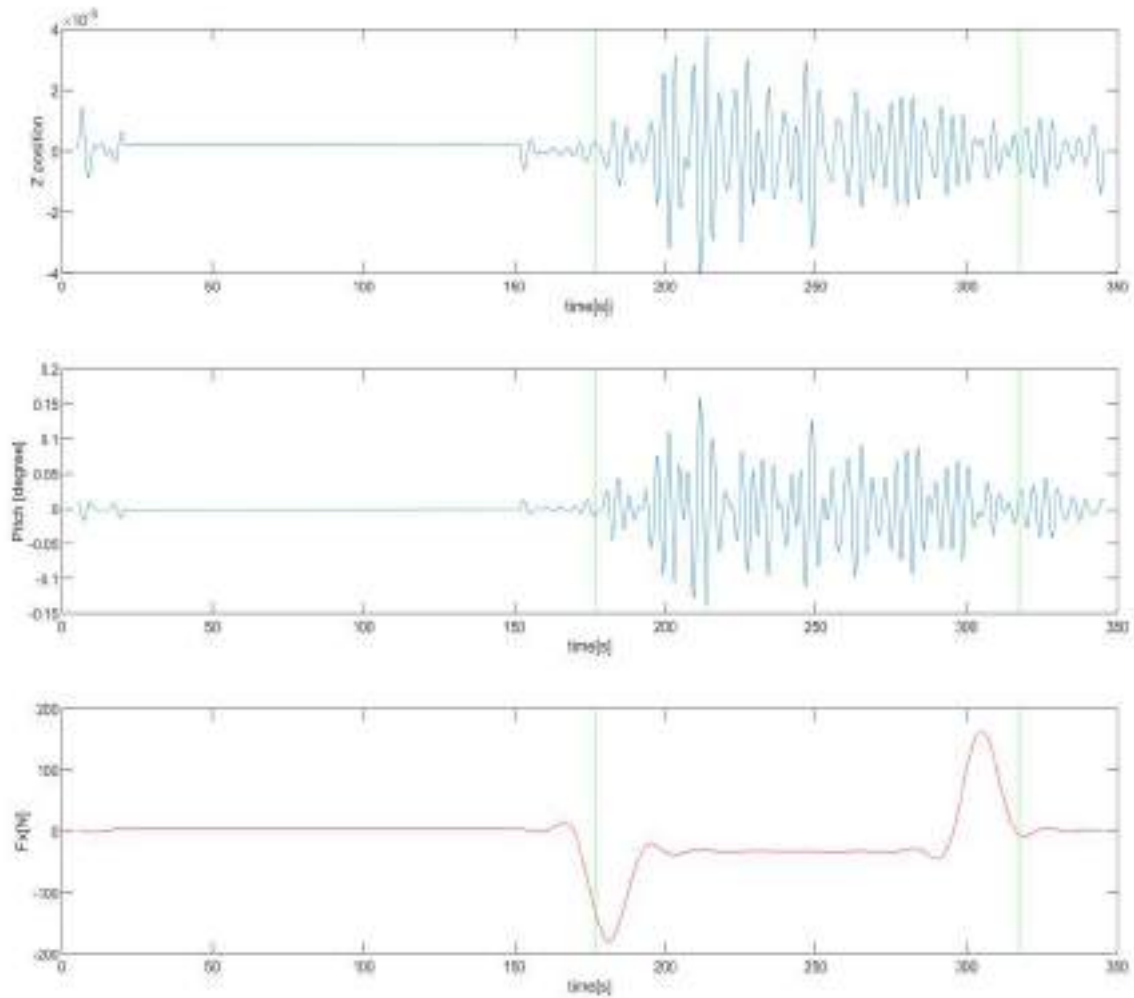


Figure 3.41: Time series plots of heave (Z position (m)), pitch motions and longitudinal force F_x bounded by level 1 time window (green lines) for test no. CE6010

Level 2 - Removing Transient values

In every test a transient stage in the measurements from sources like acceleration or deceleration of the model vessel or the moment when the wave just hits the vessel is always present. As the steady state measurements represents the area of interest for the current study, we need to remove this transient behaviour from data set. This level of time window includes two factors. The first factor is to select a time window excluding the transient stage in the time series data. Secondly, when we filter the force measurement using the band pass filter, it causes a large increase or decrease in the beginning and in the end of the series as shown in figure 3.42. This is due to an end effect when using a band pass filter. The stated behaviour will affect the estimation of mean force and therefore they need to be removed from the measured quantities.

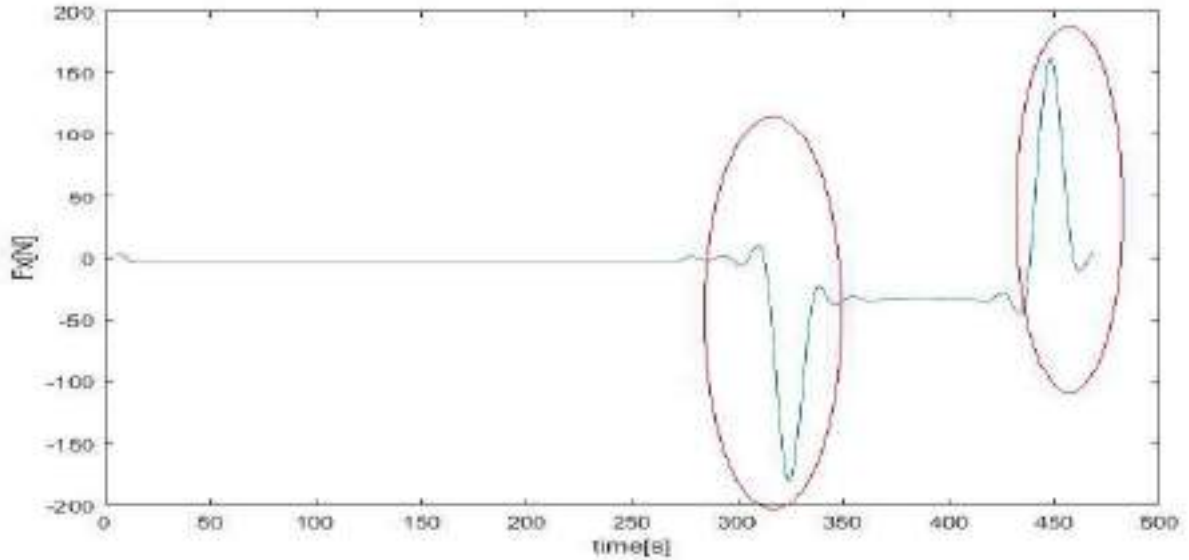


Figure 3.42: Filtered time series of longitudinal force F_x for test no. CE4010. The peaks circled in the beginning and the end of the time series shows the effects due to the band pass filtering

In the following, the discussion related to the removal of the transient behavior of the measured quantities in respect to different combinations of Froude numbers and incident regular wave field conditions is provided.

1. $F_n = 0$, Head sea condition

At $F_n = 0$, the transient behaviour of measured quantities is seen when the first waves meet the model. Figure 3.43 which shows some parameters recorded for a zero speed test run, clearly demonstrates this region in a red rectangle. If we consider longitudinal force as an example, it can be seen that the force keeps on increasing until a certain point of time after the first waves meet the model. Then after 200 seconds the values have to have a stable and steady region. Since the data measurement was stopped along with the wave maker the transient region at the end of the measurement records is not seen in most of the zero speed tests. Next, the band pass filter is applied by the filtering level 2 in order to exclude the peak values which can be observed in the filtered longitudinal force (Figure 3.44). When the time series of all the results are observed it can be seen that the first transient region comes to an end at an average time span of about about 56 seconds before the measurements are stopped and the transient region in the end starts at an average time span of about 2.5 seconds before the measurements are stopped. So the required time interval must be between this region. Therefore a time window spanning from the first wave crest (recorded at the wave probe near the model) after the first transient region and after the peak value in filtered F_x , to the last wave crest before the second transient region begins and the point where the second peak value for filtered F_x is seen, thus selected for all the tests done at $F_n = 0$. Figure 3.44 is an another example that clearly demonstrates the selected time window.

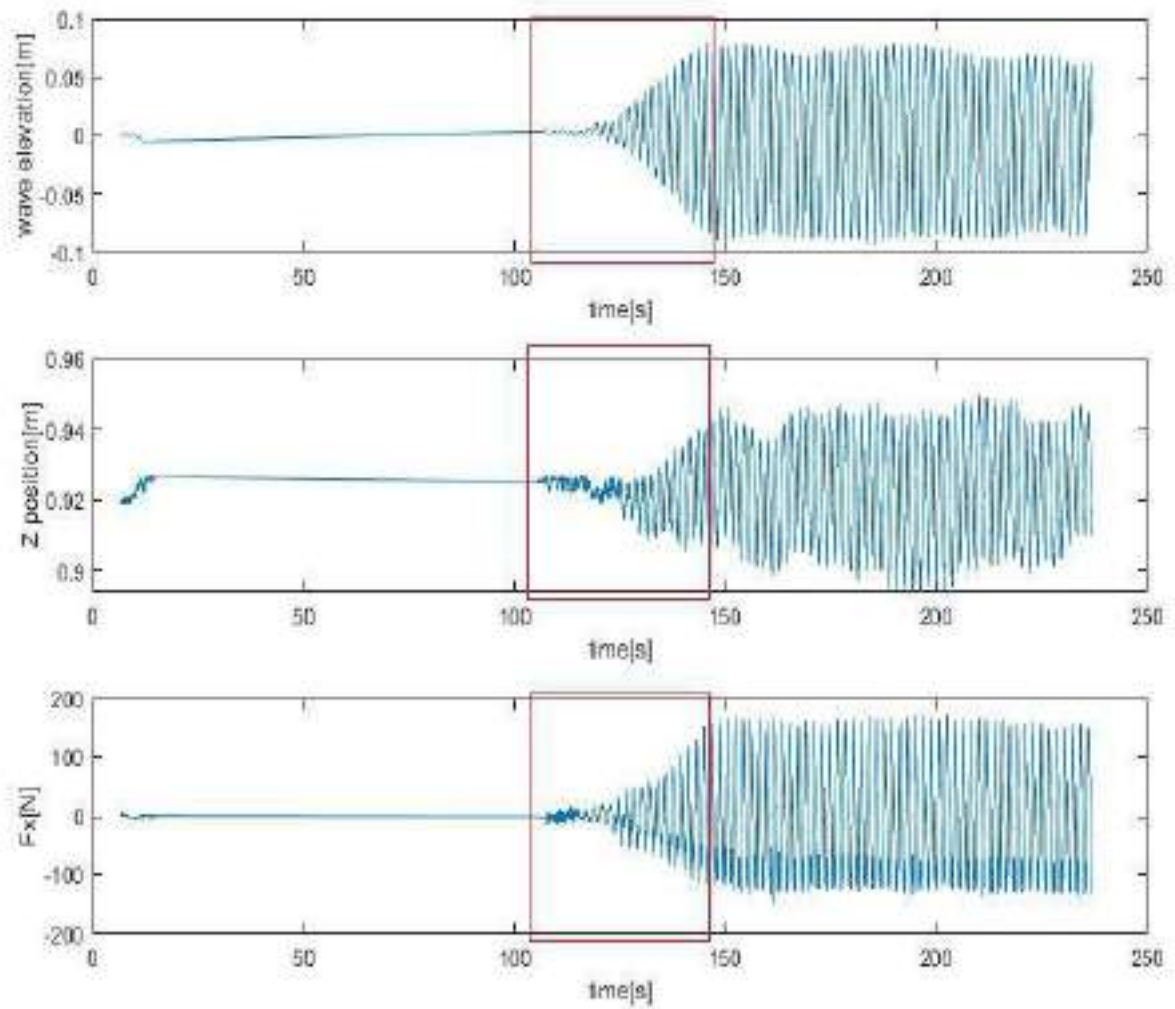


Figure 3.43: Unfiltered time series plots of the wave elevation near the ship model, heave motion (Z position) and longitudinal force F_x of test no. CE2031 in head sea condition at zero speed. The red rectangle indicates the transient region of the beginning of the measurement in the test run

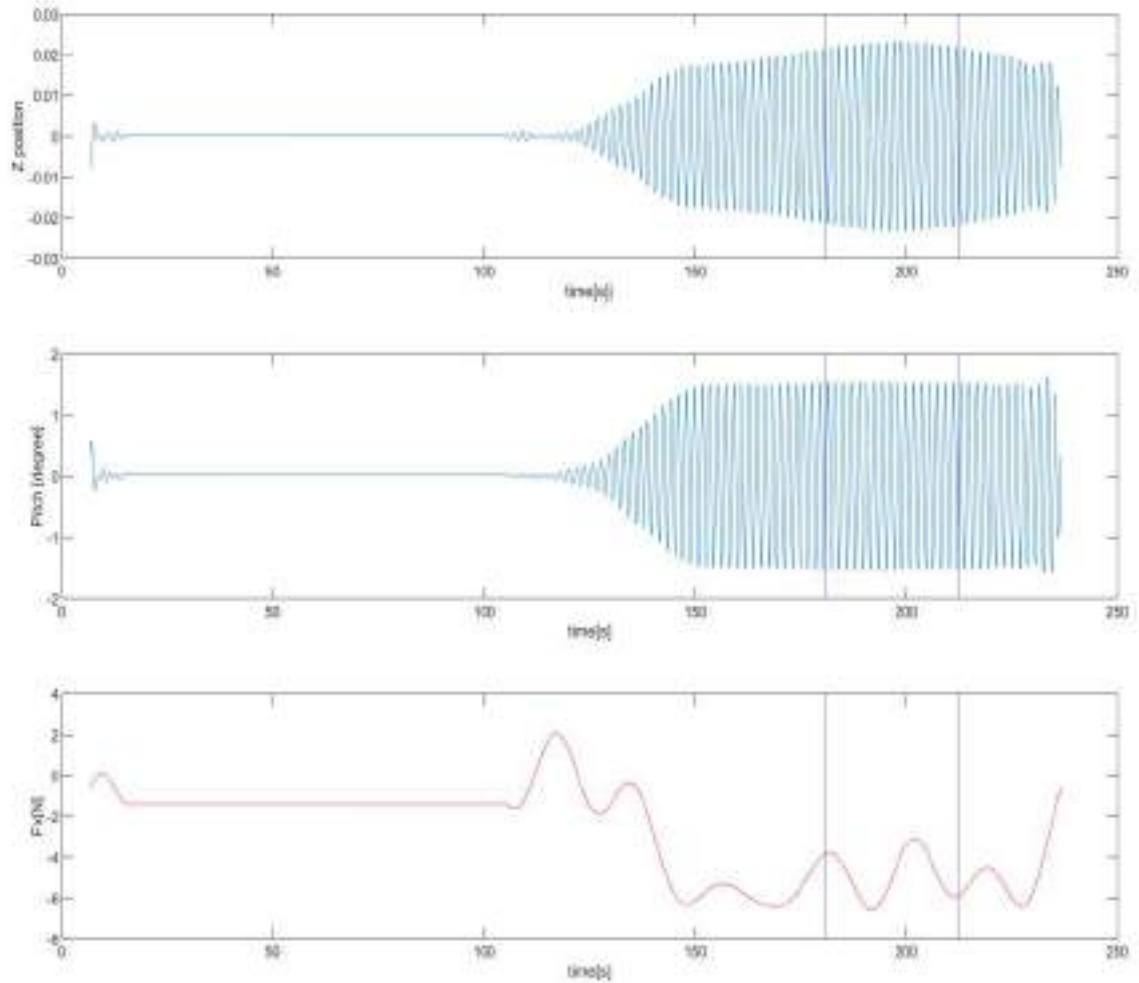


Figure 3.44: Filtered time series plot of heave (Z position), Pitch motion and longitudinal force F_x of test no. CE2031. The blue lines marks the bounds of the level 2 time window

2. $F_n \neq 0$, Head Sea condition

When the ship model is towed in head sea condition, the acceleration at the beginning of the tow and the deceleration of the carriage at the end of the tow adds to the transient observed in measurements seen in the previous zero speed case. This can be clearly seen in figure 3.45. Based on experience, to filter out this transient region we need to consider a time interval after a few encounters in the beginning and before a few encounters at the end. We also need to eliminate the interval where the peaking in filtered longitudinal force F_x as shown in Figure 3.46. The mentioned interval are different for each of the generated waves and thus we need to formulate a common criteria that can filter out the transient regions. It was observed that in between the carriage position of 110 m and 200 m, all the test runs gave a transient free interval with a minimum of 50 wave encounters (can

also be seen in figure 3.45). Therefore an easy way to achieve this is to select the time interval of crest to crest measurements of the incident wave when the carriage was between these positions. Based on this a second level of time windows has been applied for all the tow tests at head sea with a forward speed. Figure 3.46 clearly demonstrates the selected time window.

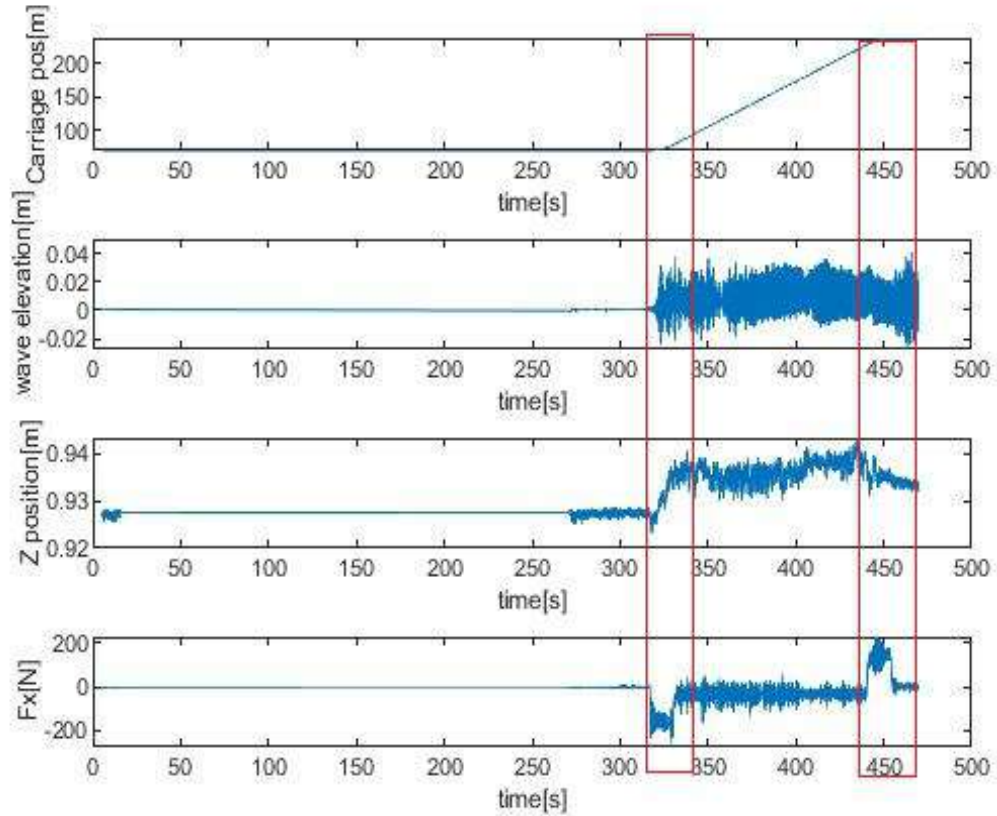


Figure 3.45: Unfiltered time series plots of the wave elevations near the ship model, heave (Z position) and longitudinal force F_x of test no. CE4010 in head sea condition. The red rectangle indicates the transient behaviour of the measured quantities in the test run.

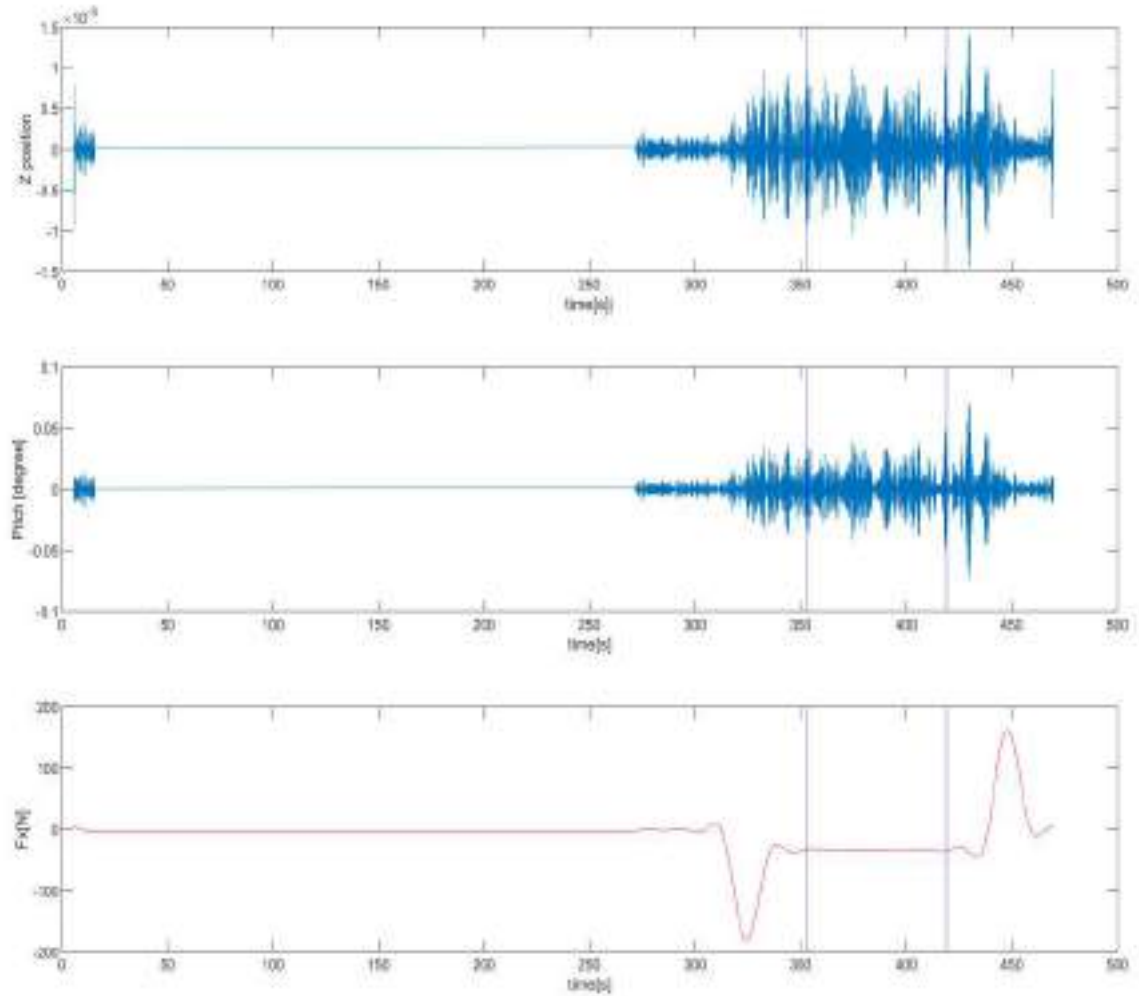


Figure 3.46: Filtered time series plot of the heave motion (Z position), Pitch motion and longitudinal force F_x of test no. CE4010. The blue lines bounds of the filtering level 2 time interval window

3. $F_n \neq 0$, Following Sea condition

Just as in case of head sea there are two transient regions due to the acceleration and deceleration of the ship model along with the transient behaviour of the measured quantities as a wave front met by the ship model belonging to the time interval which need to be removed. This removal process is carried out by considering the filtered measured value of the the longitudinal force F_x (seen figure 3.48). Since this condition is similar to that of the head sea condition with forward speed, it has been decided to use the same criteria for filtering process except that here we consider the first incident wave crest after the carriage has passed the carriage position of 200 m till the final incident wave crest before the carriage position of 110 m. Figure 3.48 clearly demonstrates the selected time window.

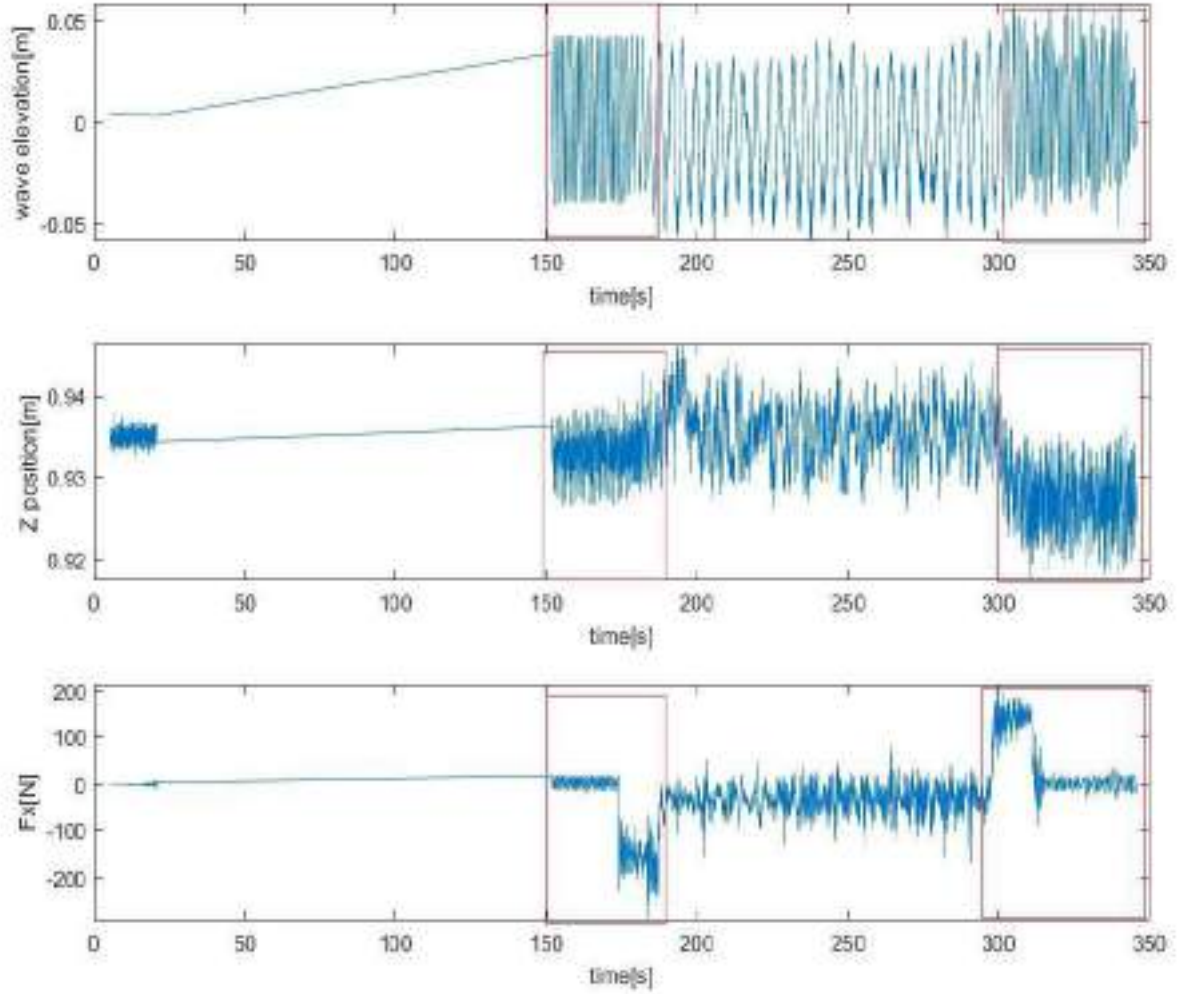


Figure 3.47: Filtered time series plots of the wave elevation near the ship model, heave (Z position) and longitudinal force F_x of test no. CE6010. The red rectangle indicates the transient behaviour of the uncensored quantities in the test run

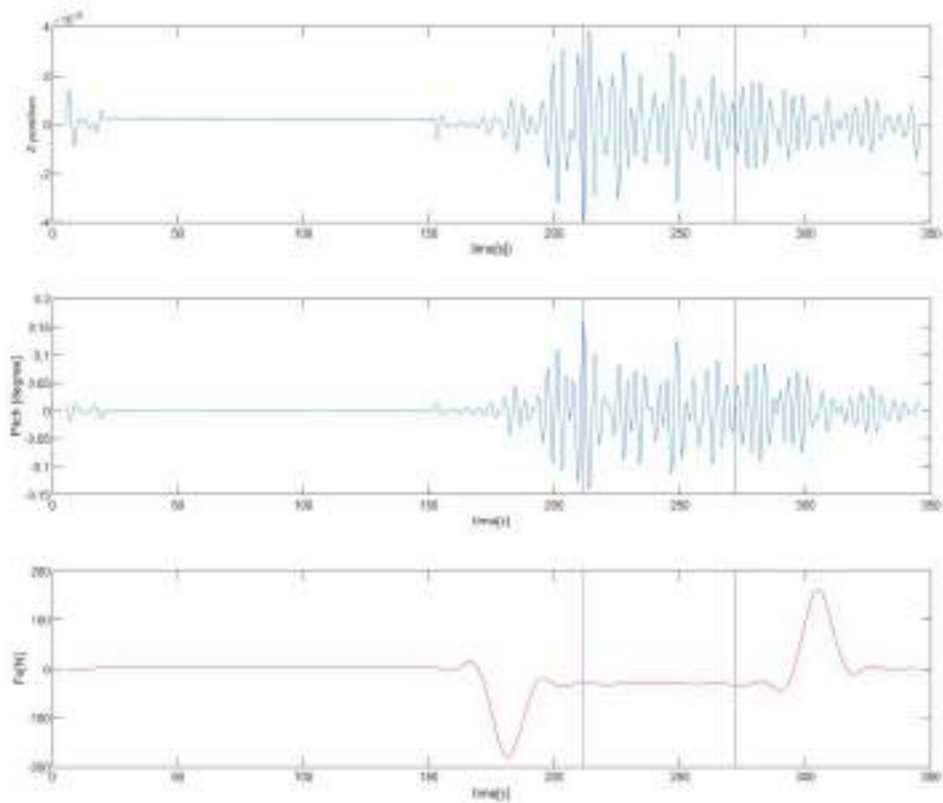


Figure 3.48: Filtered time series plot of heave motion (Z position), Pitch motion and longitudinal force F_x of test no. CE6010. The blue lines bounds of the filtering level 2 time interval window

Level 3-Visual observation and final time window

After bounding the data using the two time interval windows as in previous discussion, the intersection of both the time windows were then selected as the final time interval of the measured quantities suitable for further analysis. The time series of all the tests were also checked visually for any unusual readings or further change required in the final time window to select the best possible interval of the measured data. Figure 3.49, 3.50 and 3.51 shows the final time window selected for the tests CE2031, CE4010 and CE6010.

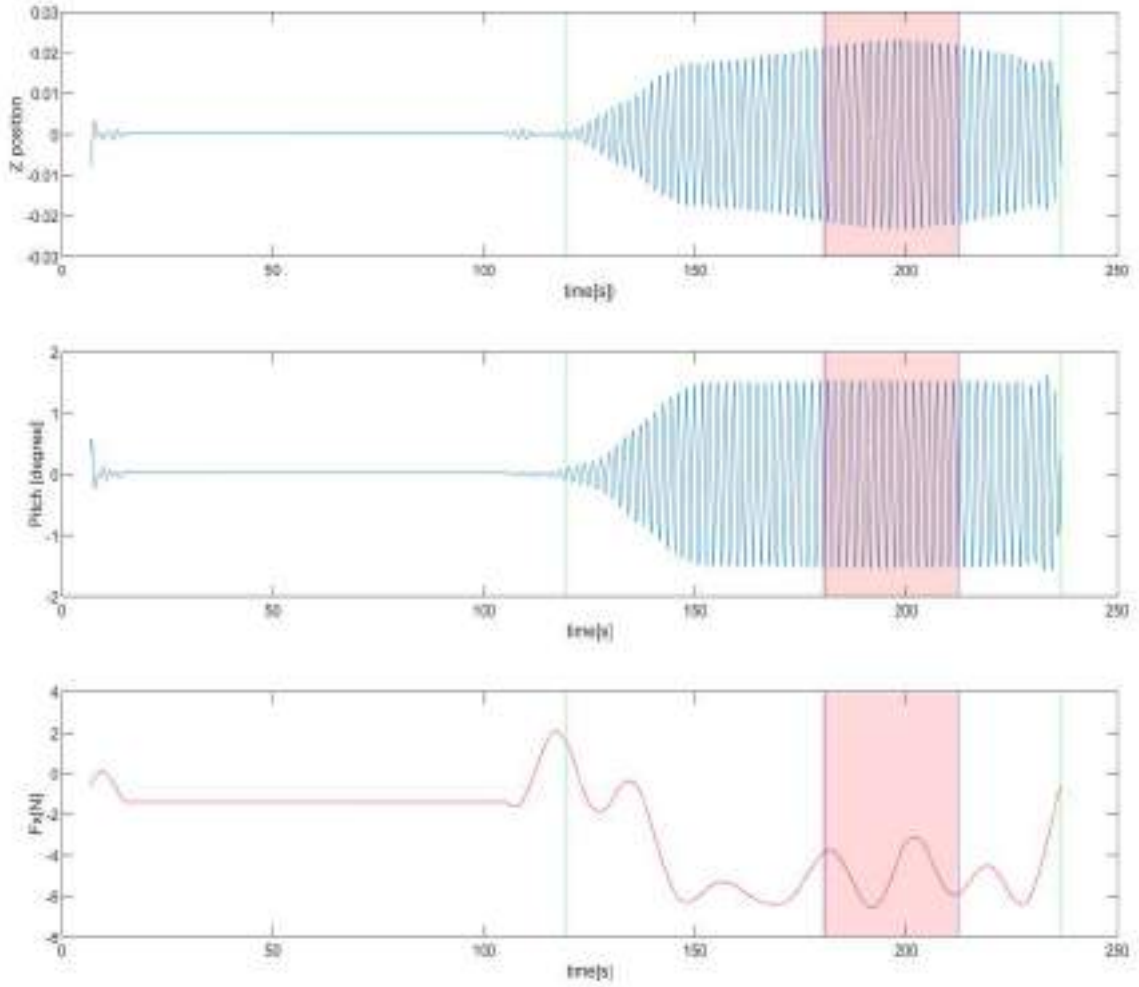


Figure 3.49: Filtered time series plot of heave motion (Z position), Pitch motion and longitudinal force F_x of test no. CE2031. The interval highlighted red, which is intersection of the filter level 1 and the filter level 2 time windows of the measured data, is the final time window selected for this test.

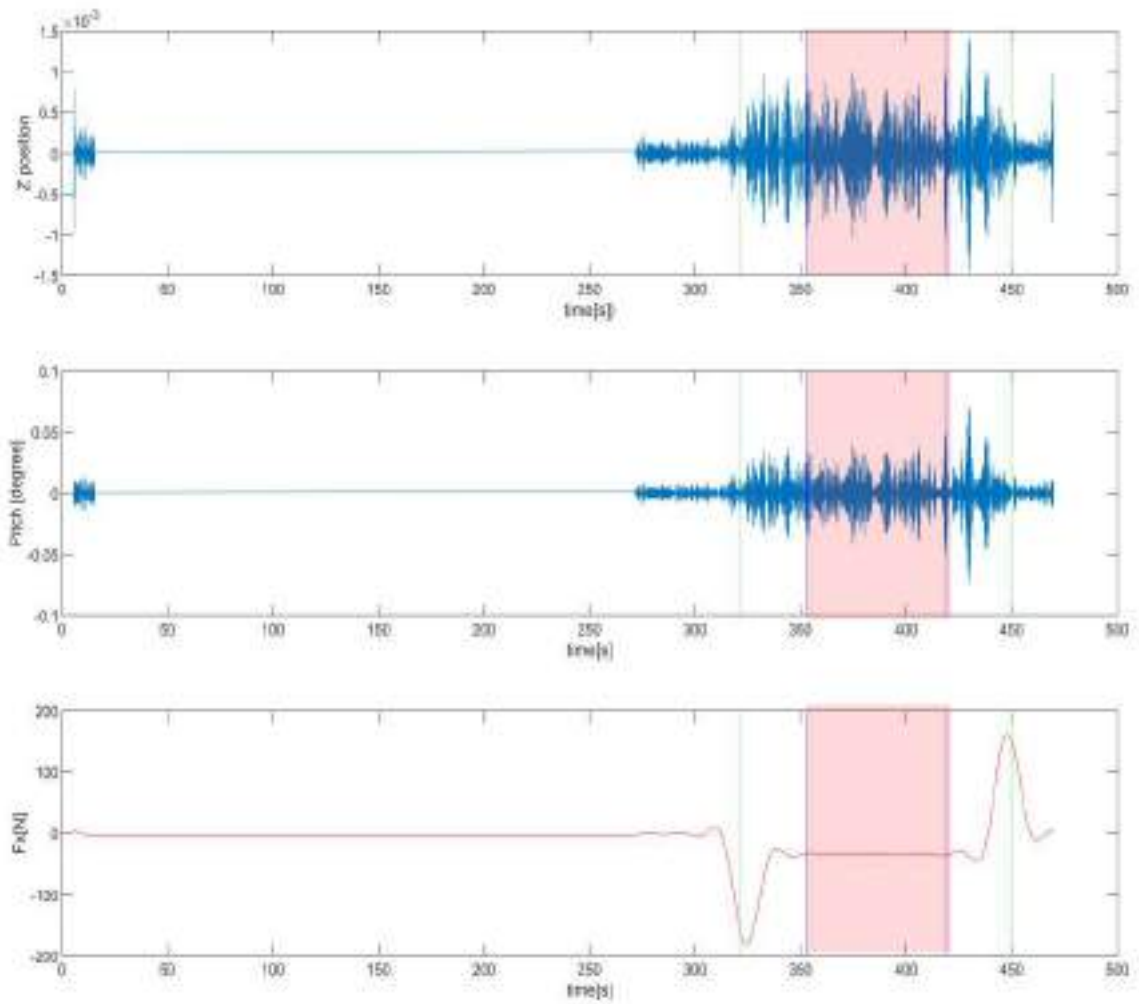


Figure 3.50: Filtered time series plot of heave motion (Z position), Pitch motion and longitudinal force F_x of test no. CE4010. The interval highlighted red, which is intersection of the filter level 1 and level 2 time windows of the measured data, is the selected final time window of measured quantities for this test.

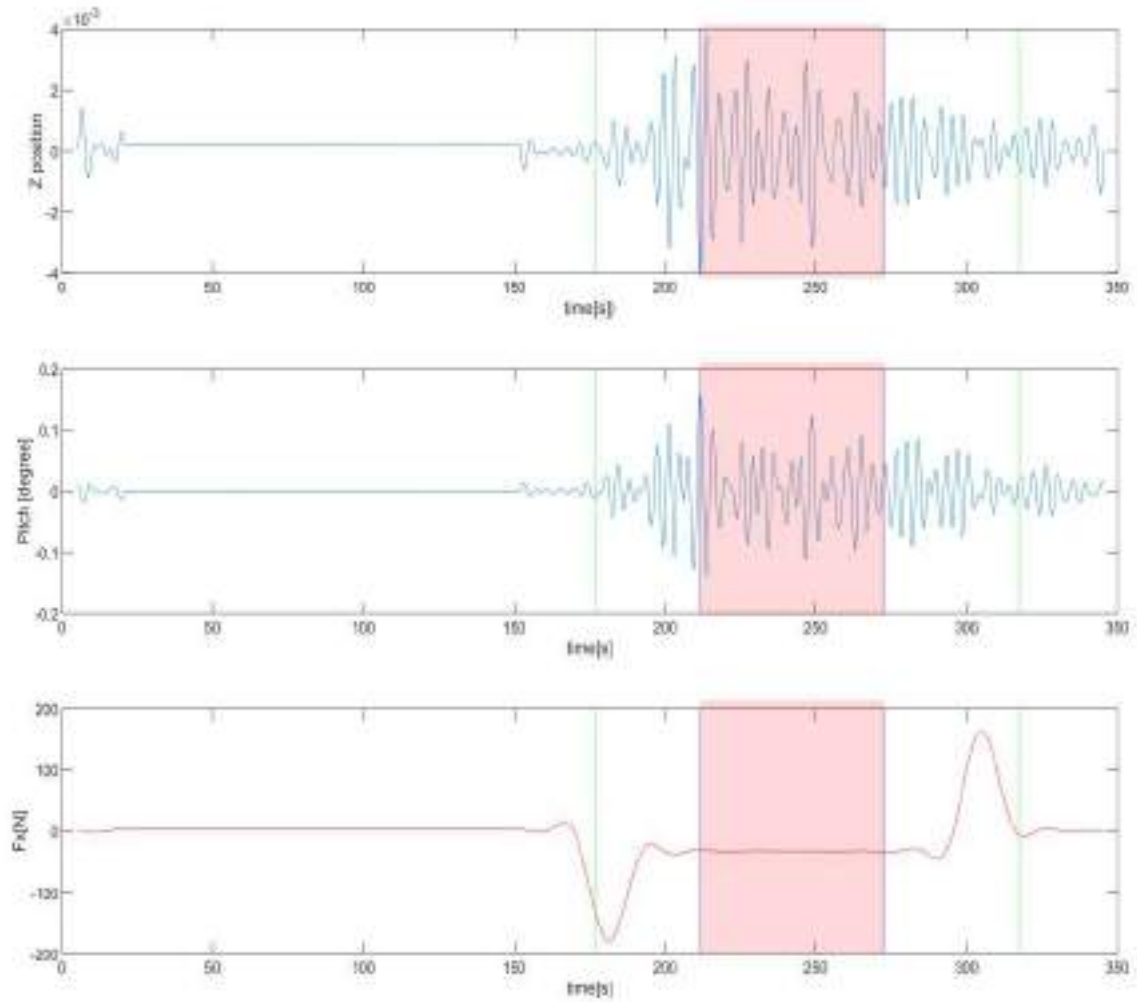


Figure 3.51: Filtered time series plot of heave motion (Z position), Pitch motion and longitudinal force F_x of test no. CE6010. The interval highlighted red, which is intersection of the filter level 1 and level 2 time windows of the measured data, is the selected final time window of measured quantities for this test.

3.3.3 Extracting the final result

When the measurements from each instrument are reduced according to the above described filtering levels to a selected range of data, for each incident wave frequency, measured values for parameters like the heave and pitch motions, longitudinal and transverse forces and other parameters of interest are extracted for each test run. For this purpose the standard deviation of the measured data points within the measured interval is used for extracting the pitch motion. For other measured parameters of interest the arithmetic averaging of the data points within the measured intervals of data is used. It is to be noted that when considering the average of forces we find the average of all the data points within the time interval whereas when considering motions such as heave or pitch and also

when considering the wave amplitude, we only find the average (or standard deviation) of the data points corresponding to the peaks in a time series as marked in figure 3.52

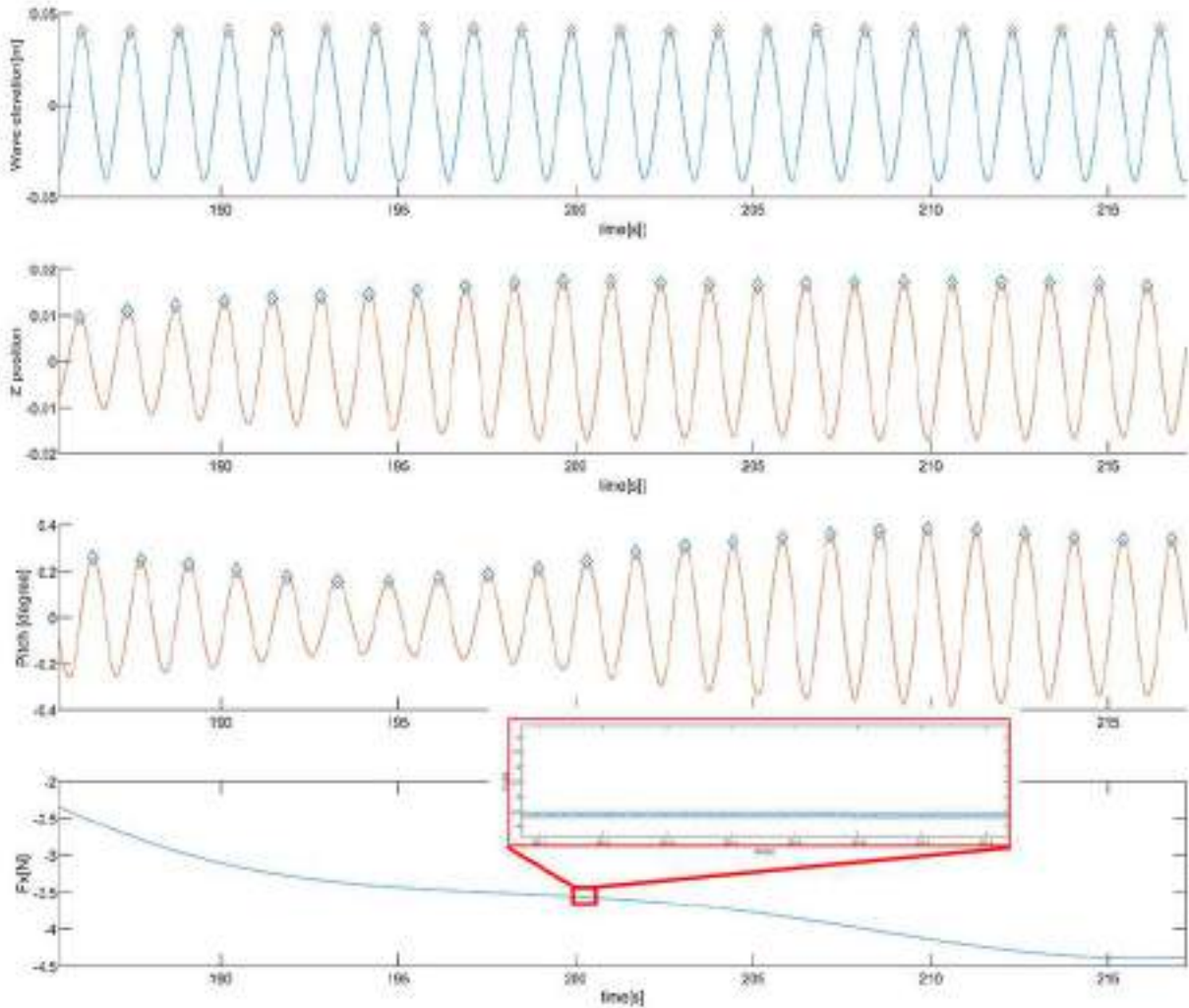


Figure 3.52: Final time window of filtered time series plot of the wave elevation near the wave maker, heave motion (Z position), Pitch motion and longitudinal force F_x for test no. CE2010. The diamond markers for the heave and pitch indicate the data points corresponding to the peak values in the time series of the measured data. In case of longitudinal force all the data points every 0.005 seconds. A zoomed image between 201th second and 202nd second is indicated on top of the plot of the longitudinal force F_x

Even though the final time window consists of a steady state data set, there are still small variations in the measurement estimates. Sometimes these differences can be quite significant and this can affect the average (or standard deviation). For example referring to figure 3.52 it can be seen that within the final time interval the value of force and other vertical motions is different for each generated incident wave frequency.

Therefore instead of finding the simple average(or standard deviation) of the entire data set together in the selected time interval, we applied the novel procedure of sliding arithmetic average of the final measured and filtered data set. Based on previous experience only 10 wave encounters are considered at a time. Firstly we consider the first 10 wave encounters within the interval. After we get the arithmetic average (or standard deviation) from the first 10 wave encounters we find the arithmetic average(or standard deviation) of next 10 wave encounters starting from the second wave encounter in the total interval. This continues until we cover the last 10 wave encounters in the time interval. This is equivalent to a slider of fixed width (10 wave encounters) moving along the time series interval with a fixed difference between them corresponding to one single wave length directly proportional to the incident regular deep water waves accounted for in this study. So currently for a single test condition we have a set of arithmetic averages (or standard deviations). The average of all those values will be the result we wanted and at the same time we now can have an uncertainty range based on smaller time windows in the whole interval for each test. Based on test CE2010 figure 3.53 clearly illustrates how the analysis described above works. In the figure each coloured rectangle marked 1, 2, 3.. n represents a slider position in the time series. For example, slider 1 (violet colour) includes the first 10 wave encounters in the total time interval, slider 2(cyan colour) includes the next 10 encounters starting fro the second wave encountered in the total time interval. Similarly we have n slider positions until the last 10 encounters are considered. The wave encounters in the record after the last ten are ignored. Table 3.7 shows the average value of wave elevation,heave and longitudinal force measurements and standard deviation of pitch motion measurement at each slider position. It also consists of the final arithmetic average value estimates for all slider positions in the final data sets which is later used for the study during comparison with the numerically obtained results.

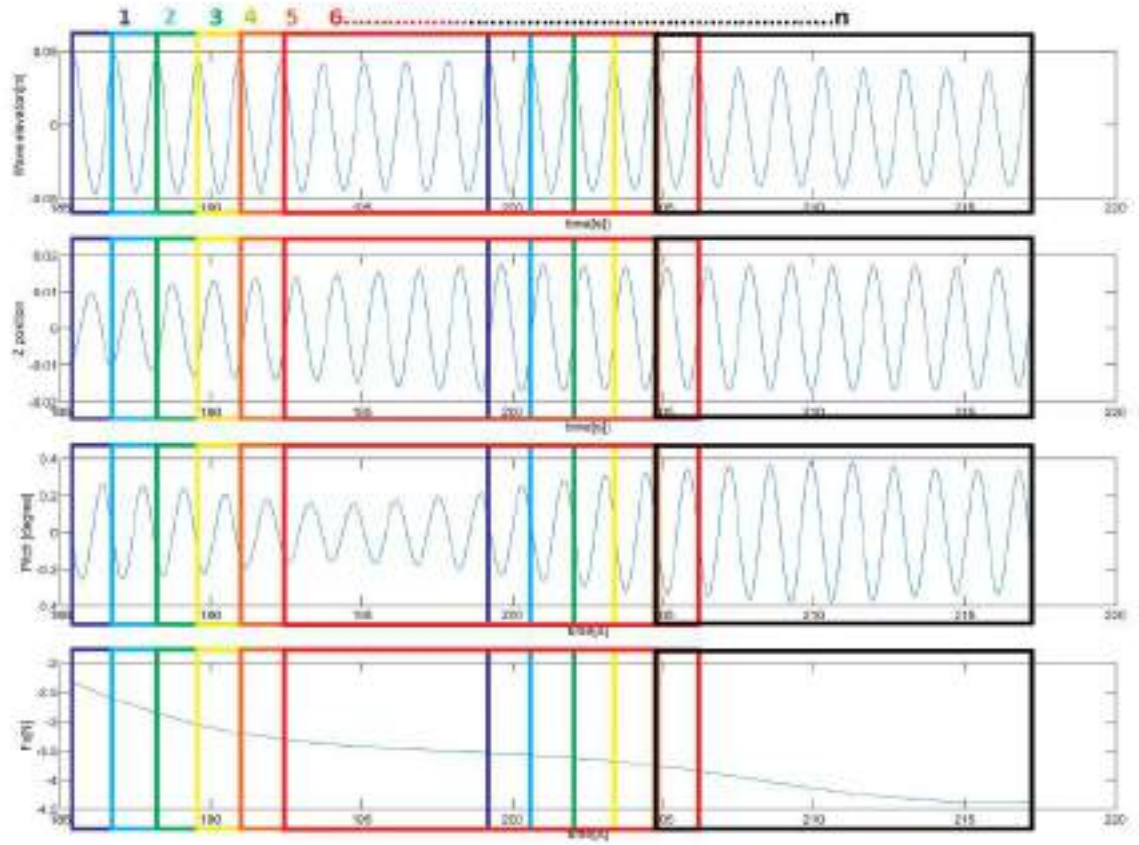


Figure 3.53: Slider positions 1,2,3,...,n considered within the final time window of the measured and filtered data of test no. CE2010 for quantitative values of Incident wave elevation, heave motion(Z position), pitch motion, longitudinal force (F_x). Each coloured rectangle represents each slider position enclosing selected 10 wave lengths (from crest to crest)

Table 3.7: Average wave elevation,heave (Z position),pitch and longitudinal force (Fx) from their average (standard deviation for pitch) values at each slider position shown in figure 3.53 for test no. CE2010

Slider no.	Wave elevation (m)	Z position (m)	pitch (deg)	Fx (N)
1	0.044868	0.013619	0.036991	-3.18224
2	0.044511	0.014382	0.034786	-3.28914
3	0.044426	0.01501	0.040969	-3.37395
4	0.044244	0.015488	0.0528	-3.44258
5	0.043924	0.015836	0.064242	-3.50122
6	0.043577	0.016114	0.071936	-3.55582
7	0.04327	0.016376	0.074315	-3.6113
8	0.042948	0.016624	0.072558	-3.67091
9	0.042553	0.016809	0.067482	-3.73632
10	0.042091	0.016894	0.058243	-3.80799
11	0.041567	0.016905	0.044991	-3.8849
12	0.040977	0.016878	0.031897	-3.96463
13	0.040378	0.016825	0.023279	-4.04359
14	0.040019	0.016757	0.019117	-4.11769
Arithmetic Average	0.042811	0.016037	0.049543	-3.65588

The above presented analysis is performed by developing a computer program using MATLAB software package. Other than longitudinal force, vertical motions, generated wave elevation and incident wave elevation, other parameters like yaw moment, transverse force were also extracted to be used for analysis. The time series plot generated from all the test runs is outlined in appendix C.

Calm water resistance

This study is focused on added resistance on the vessel in each test condition. As mentioned previously the added resistance in waves is the difference between the total resistance of the ship in waves and her calm water resistance taken at the same forward speed when the ship advances at the same heading course. The forces were filtered to remove unwanted frequencies as it was done for other longitudinal forces mentioned in the previous sections. Once the forces were filtered a time window was selected based on towing carriage position to remove the transient stage in the measurement that occurs as the vessel starts to move or stop. Based on visual observation, it was seen that in between the carriage positions 105 m and 195 m, the transient were excluded and the end due to bandpass filtering for longitudinal force were also excluded as seen in figures 3.54 and 3.55

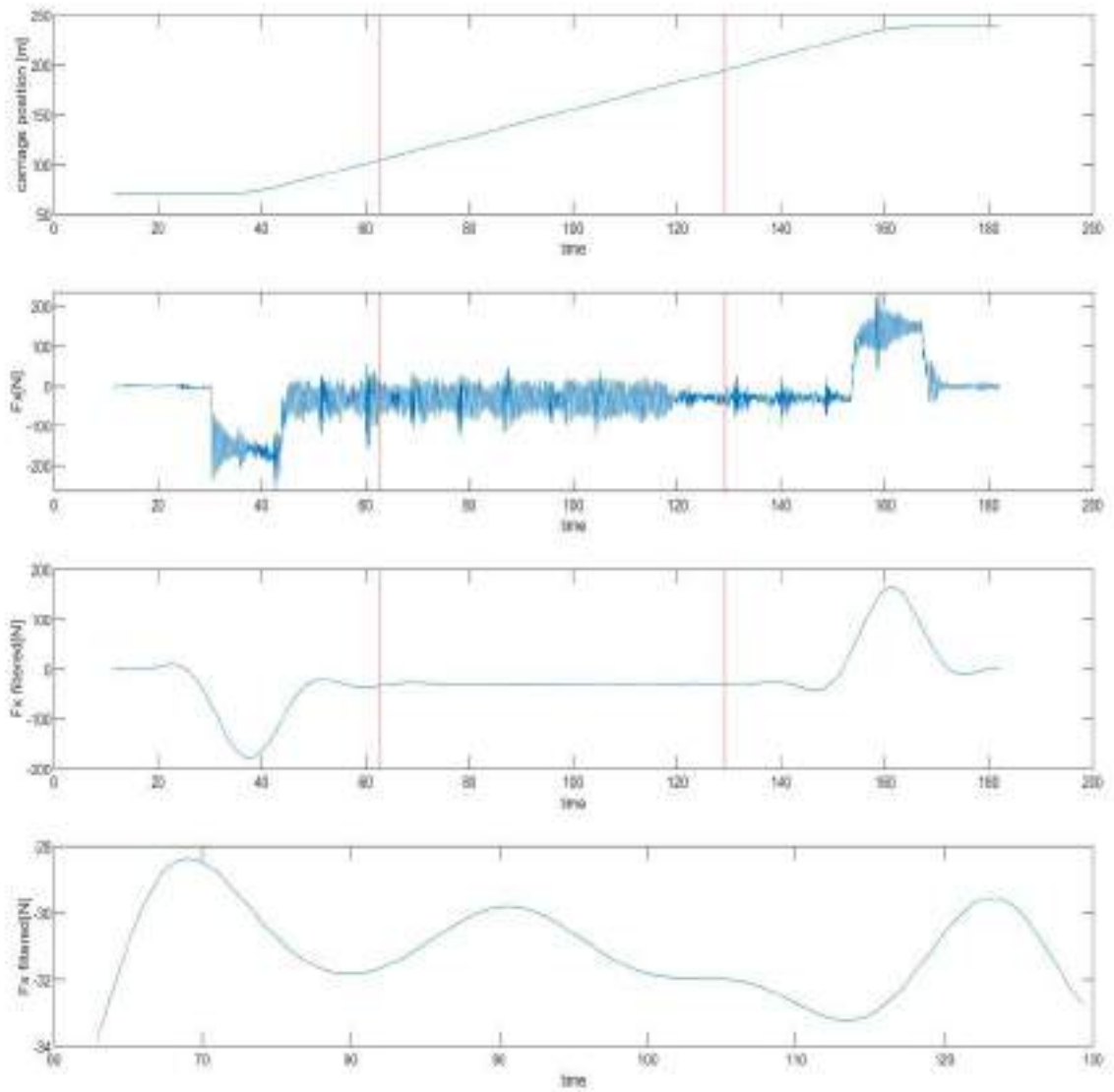


Figure 3.54: Calm water resistance in deep water at $Fn = 0.179$ with 0° drift angle (test no. CE4000). The first plot shows the carriage position. The second plot shows the unfiltered longitudinal force F_x , third plot shows the filtered longitudinal force F_x . The red lines in these plots points out the selected time window. Final plot shows the filtered longitudinal force F_x within the selected time window.

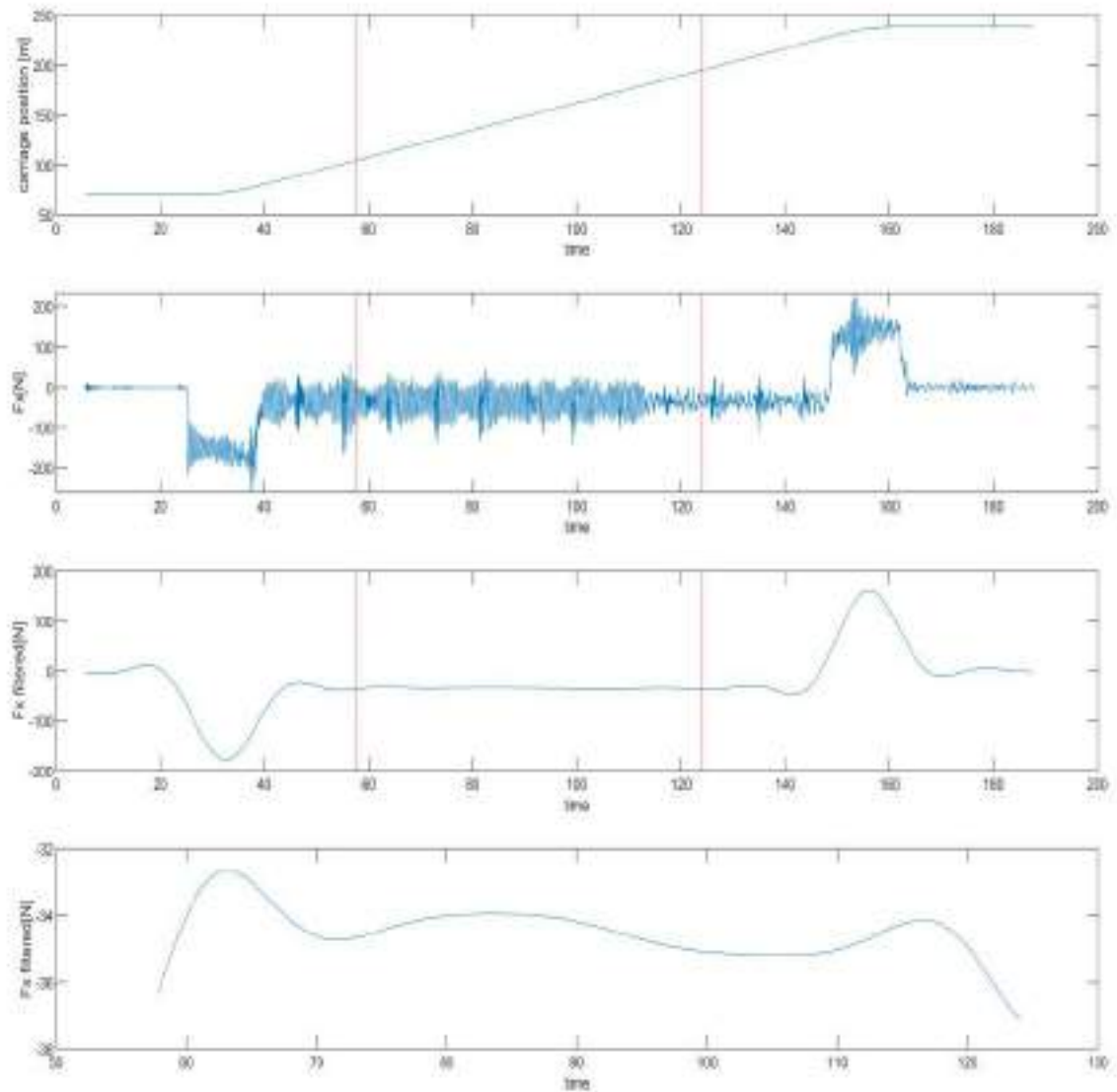


Figure 3.55: Calm water resistance at $F_n=0.179$ at 9° drift angle (test no. CE5081). The first plot shows the carriage position. The second plot shows the unfiltered longitudinal force F_x , third plot shows the filtered longitudinal force F_x . The red lines in these plots points out the selected time window. Final plot shows the filtered longitudinal force within the selected time window.

From the selected time window the average force in longitudinal x F_x has been found from the filtered time series of the mentioned force. For test no. CE4000 the calm water resistance was found to be -31.3 N and for test no. CE5081 the calm water resistance was found to be equal to -34.3 N. The added resistance in waves is the difference between the total longitudinal force in waves and the calm water resistance. Therefore in the study for all the test conditions with $F_n=0.179$ and drift

angle of 0° (head sea and following sea), is found as the difference between the total longitudinal force measured and the measured calm water resistance in test CE4000 (-31.3 N) which corresponds to the same conditions. Similarly for all test conditions with $F_n = 0.179$ and drift angle of 9° (head sea and following sea) we find the difference between the total longitudinal force in x direction and the calm water resistance measured in test CE35081 (-34.3 N) where $F_n = 0$ and drift angle is 9° .

3.3.4 Generating non dimensional values

The obtained value of longitudinal force in x direction F_x , transverse force F_y , yaw moment M_z , heave motion η_3 pitch motion η_5 and other parameters as per the need, were made non dimensional which facilitates comparisons during analysis.

Vessel motions

Translatory ship motions are defined by the non dimensional response amplitude operators (RAO) presents the ratio between the ship motions and the incident wave amplitude ζ_a . To obtain the RAO of vessel motions for the experiment, the response amplitude found is divided by the wave amplitude measured by the wave probes at the wave maker. The incident wave amplitude is required but the wave amplitudes near to the model was not selected as the wave probes near the model may be measuring reflected waves from the tank wall or waves from the model itself which will not provide the right measurement for the real incident waves. It was already mentioned in the previous section on instrumentation that we had used an accelerometer that could be used to obtain motions along with the Oqus system. A comparison of heave RAO's obtained using measurements from accelerometer and Oqus system is presented for head sea condition for $F_n = 0$ and head sea and following sea conditions at $F_n = 0$ and $F_n = 0.179$ in figures 3.56, 3.57 and 3.58

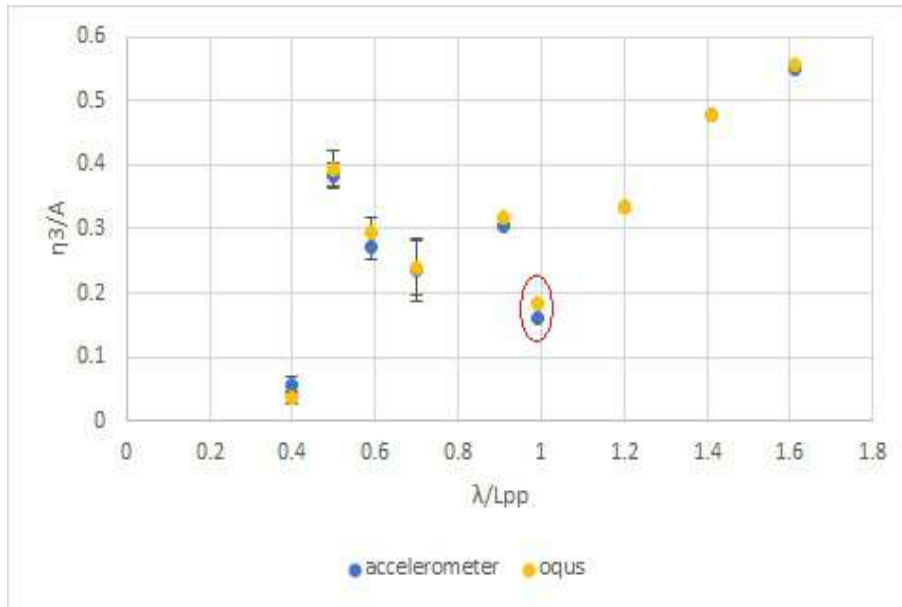


Figure 3.56: Comparison of non dimensional heave (RAO) obtained from heave measurements using accelerometer and Oqus system for tests at $F_n=0$, Head sea for vessel at design draft and even keel. The points marked in red circle corresponds to RAO value at non dimensional wavelength $\lambda/L = 1$. η_3 Heave amplitude, A incident wave amplitude, λ incident wavelength, L_{pp} Length between perpendiculars.

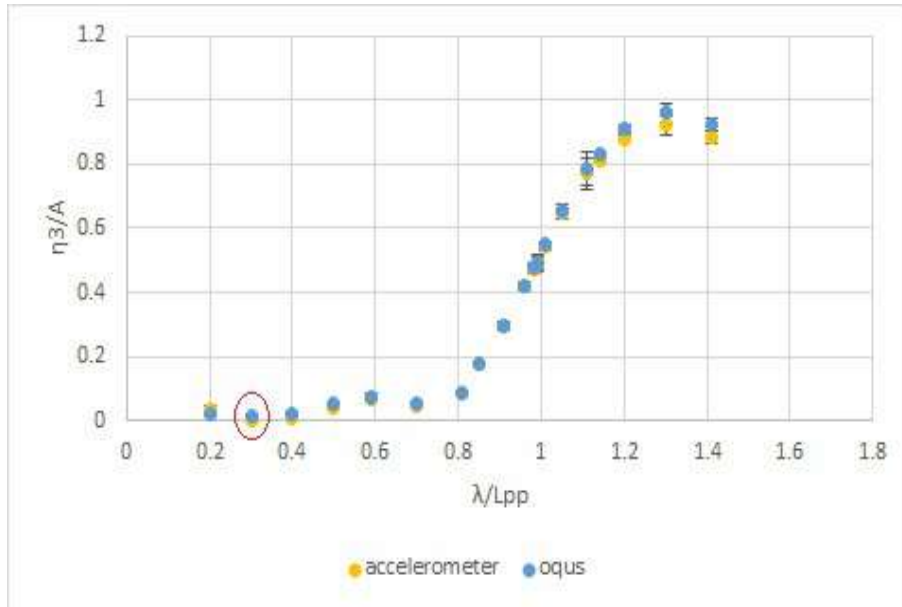


Figure 3.57: Comparison of heave RAO obtained from heave measurements using accelerometer and Oqus system for tests at $F_n=0.179$, Head sea at design draft and even keel. The points marked in red circle corresponds to RAO value at non dimensional wavelength $\lambda/L = 0.3$. η_3 Heave amplitude, A wave amplitude, λ incident wavelength, L_{pp} Length between perpendiculars.

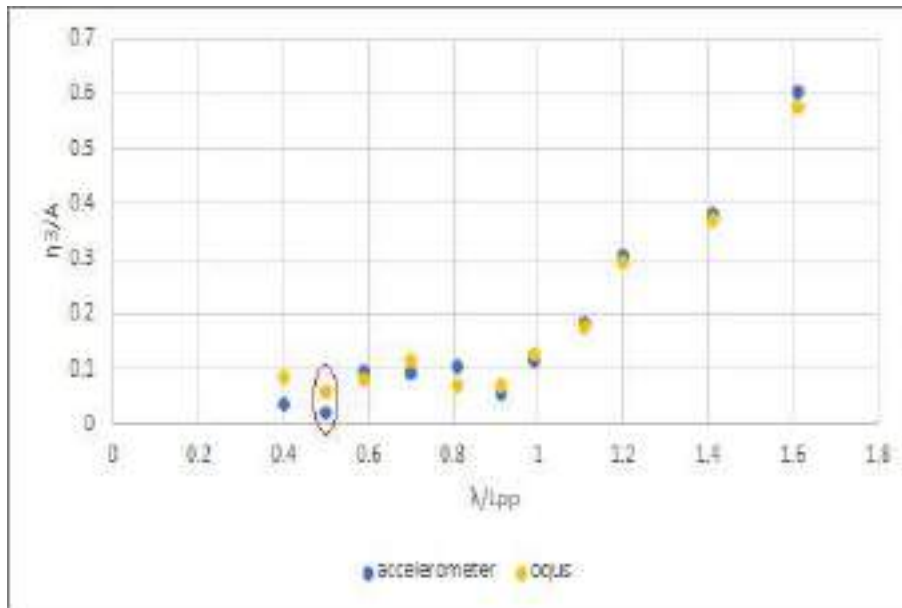


Figure 3.58: Comparison of heave RAO obtained from heave measurements using accelerometer and Oqus system for tests at $F_n=0.179$, Following sea at design draft and even keel. The points marked in red circle corresponds to RAO value at non dimensional wavelength $\lambda/L = 0.5$. η_3 Heave amplitude, A wave amplitude, λ incident wavelength, L_{pp} Length between perpendiculars.

It can be seen that for most of the conditions, the heave RAO values have a difference of less than

5%, but at some conditions it can be seen that the values are different. For example in figures 3.56, 3.57 and 3.58 the points marked with the red circle correspond to few such points which have difference of 13.8%, 77.39% and 62.76% in their values respectively. Larger difference is mostly observed for smaller heave motions for head sea conditions. This is also evident for many test conditions in following sea conditions which in general has relatively smaller motions. The reason for this variation between Oqus and accelerometers is not found. Oqus system easily gives all 6 DOF directly, whereas for an accelerometer we need to integrate the acceleration measured twice to obtain the motion and also we need to use the position of accelerometers on the model along with the linear motions to obtain angular motions. The Oqus and accelerometers are showing similar trends in their measurements. The Oqus system has also proven it's capabilities in motion measurement from other tests performed at SINTEF. Due to all the reasons pointed out above, the measurements from the Oqus system were used for generating the RAO's using the experimental values. It is to be noted that the points in the RAO also include an error bar based on the standard deviation of averages measured in each slider position as already mentioned before.

Forces

In case of drift forces in surge or sway we make the force non dimensional by dividing the force with the following factor as in equation 3.10 to obtain a non dimensional value for force.

$$\rho g A^2 \frac{B^2}{L_{pp}} \quad (3.10)$$

where ρ is water density , g is acceleration due to gravity , B is breadth of the model and L_{pp} is the length between perpendiculars of the model and A is the wave amplitude. Using the factor the non dimensional experimental values for added resistance and second order transverse forces were formulated for all the test. On the plot the standard deviation based on the averages measured at each slider position (as seen in figure 3.53) is marked on each value of added resistance as an error bar. This uncertainty is called measurement uncertainty (refer section 3.4). For example the added resistance plot at $Fn = 0.179$ with zero degree drift angle for head sea condition is obtained as in figure 3.59

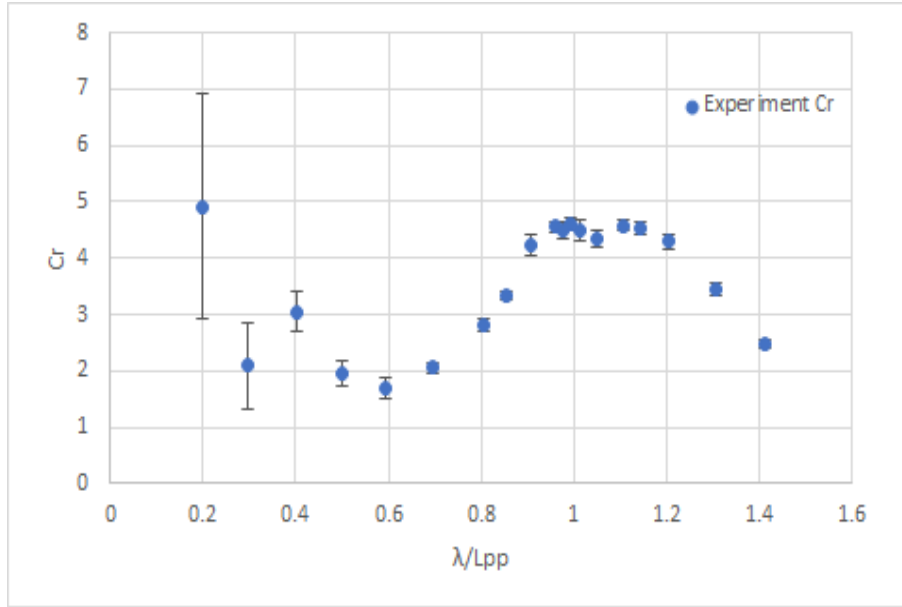


Figure 3.59: Added Resistance plot from experimental values at $Fn = 0.179$, drift angle = 0° in head sea waves at design draft and even keel, with error bar showing the standard deviation of averages at each slider position. Non dimensional added resistance $C_r = \text{Added resistance}/(\rho g A^2 \frac{B^2}{L_{pp}})$, λ incident wave length, L_{pp} Length between perpendiculars

Similarly the added resistance plot for all the test conditions are obtained. The study also analyses the yaw moment M_z and the sway force F_y in the presence of a drift angle.

3.4 Uncertainty in added resistance calculation

In the current study due to lack of time test repetitions were not conducted which prevented us from performing a precision error calculation. Therefore this section list out the probable sources of uncertainty based on the uncertainty analysis⁽⁵¹⁾ in an added resistance test using KVLCC2 ship model. Even though all the sources of uncertainty were not evaluated for this test, Mass uncertainty and Measurement uncertainty were evaluated.

The sources of uncertainty in an added resistance test can be divided into groups as follows

- *Basic Instrument uncertainty:* This uncertainty is associated with the uncertainty in the instrument used to measure or calibrate the experimental devices. This uncertainty can affect all the subsequent measurements in the test.
- *Mass uncertainty:* This is based on the uncertainty based on the mass distribution of the vessel. This uncertainty is already calculated in the current study from the swing test results presented in appendix B. The distance from the keel to the centre of gravity can have a standard deviation of 0.65%.
- *Calibration uncertainty:* It stands for the sources of uncertainties during the calibration process which includes uncertainty of calibration standard, uncertainty of misalignment and uncertainty of curve fitting

- *Measurement uncertainty:* This error is based on the uncertainty when we extract the data from the recorded time series. This is already done during the post processing using the sliding mean method as already described in section 3.3.3
- *Data reduction equation uncertainty:* The variables measured will have an uncertainty this is passed down into the experimental result through data reduction equation. For example the transfer function of added resistance was formulated from the amplitude which was measured. So the uncertainty in amplitude affect the uncertainty of the transfer function.

Based on the uncertainty evaluation for the experiment using KVLCC2 ship model⁽⁵¹⁾, In short waves ($\lambda/L < 0.5$) added resistance measurements have approximately 16% uncertainty at 95% confidence interval, for $\lambda/L = 1.1$ the added resistance have approximately 9% uncertainty at 95% confidence interval and upto 60% uncertainty at 95% confidence for long wavelengths. Similarly heave RAO had a 5% uncertainty and pitch RAO had 7.5% uncertainty as per the study on KVLCC2 ship model. Even though the uncertainty for the experiment performed in the current study cannot be the same as that given by Park et al⁽⁵¹⁾, it will serve as a reference to have an estimate on probable levels of uncertainty in our model test.

4 Numerical study

4.1 Need for numerical study

Even though experiments help to create a physical model which simulates the required condition, closer to reality, it lacks flexibility. As already mentioned in table 3.1 execution of experiments are costly and resources and time consuming process. Therefore it does not economically and pragmatically justify to estimate the added resistance using an experiment for every new ship design. When it comes to investigating the effect of changing a parameter or finding results of added resistance for wide range of incident wave periods, a ship model which is flexible and relatively cheaper is required. When considering the current study as an example, many of the test conditions that were planned were not conducted due to lack of time and test setup limitations, which in turn reduced the number data points available for analysis. This is where the importance of numerical models comes in. A numerical model helps us to simulate test conditions far quicker than an experiment, enabling us to investigate numerous test conditions as we desire. It enables us to bring changes to model parameters or environment for further investigation with lesser effort, time and cost. This motivates researchers to keep developing numerous numerical models that could simulate reality to the best extent as possible. These are the same reasons that motivated this study to use existing numerical models for analysis.

There are numerous numerical models and numerous panel codes that exist today that help us to find first order and second order solutions as already mentioned in the theory. In the current study, state of the art industrial panel codes such as WAMIT, VERES and VERES3D are used to perform the numerical analysis. The following sections discuss about the basic theory behind each tool and on how these tools were used for this numerical study.

4.2 What is a panel code?

Finding the first order and second order motions and loads is essential to ensure safe operation of a marine structure such as ship, offshore platform etc. Mentioned parameters are obtained from the total velocity potential which includes the incident wave potential ϕ_I , radiation potential ϕ_j and diffraction potential ϕ_D . As already discussed in section 2 the radiation potential and the diffraction potential can be obtained by solving a boundary value problem (BVP). Solving the first order BVP will help to generate the first order solutions which is then used to find second order nonlinear mean wave loads using various methods formulated (for example momentum method⁽³⁸⁾). Panel method, also known as boundary element method based on potential flow theory, is the most common technique to solve a boundary value problem. In this method we divide the whole body into elements and then distribute sinks and sources in each element along the body that would represent the fluid flow around the body. The unknown strength of these sources or sinks are then found which in turn gives the fluid velocity potential around the vessel. To find a solution for the velocity potential the method uses a mathematical tool called Green's function and appropriate boundary conditions defined in the control volume considered. Generally each numerical code that exist today are different from each other based on the Green's function it uses and the boundary condition it uses. Numerical codes can also be differentiated based on whether the panel method uses panels on 2D strips of the vessel (which later is applied for the whole length by using strip theory) or panels on the whole 3D model.

There are many numerical codes that exist today that use panel methods to perform this task and

such codes are generally referred to as panel codes. As panel codes are based on potential fluid flow theory, it has their own limitations based on the assumptions of potential fluid flow theory. The amplitude of oscillation of the body and the fluid is assumed to be small relative to the cross sectional dimension of the body, the effect of flow separation is neglected and it only predicts damping due to radiation of surface waves. Even though they have such limitations panel codes are widely used in the industry as it gives reasonable results in less time, reducing cost and increasing flexibility.

Panel codes have been proven to be more effective at zero Froude numbers, for example WAMIT is a state of the art numerical code well known and widely used in the industry for analysis at zero Froude number. Numerous companies and researchers are still developing better numerical codes that could predict the first order and second order solutions accurately at a non zero Froude number. VERES and VERES3D developed at SINTEF Ocean are two of many numerical codes available today that could predict both first order and second order solutions at non zero Froude number. In this numerical study we will use WAMIT, VERES, and VERES3D to conduct a numerical analysis of first order motions and second order drift forces and motions which are of particular interest.

The general flow of work to find first order solutions and the second order mean longitudinal force in x direction for all codes can be generalized as shown in the flow chart in figure 4.1. Firstly the total fluid velocity potential ϕ is to be obtained. This is achieved by solving the boundary value problem using the the integral equation method which gives the diffraction wave potential ϕ_d and the radiated wave potentials ϕ_j , that obeys the defined boundary conditions.

The integral equation method defines an integral equation based on green's second identity which uses two scalar functions (Refer equation 2.28).

Using a suitable Green's function the velocity potential (radiation potential or diffraction potential) which fulfills the boundary conditions is formulated by solving the Green's second identity.

Using the total fluid velocity potential the total hydrodynamic force which includes the excitation force and the added mass and damping force is found. The restoring coefficient is formulated using the ship geometry. Using these quantities in the equation of motion, the vessel motions can be formulated. Once the first order body motions are obtained, they together with the values of the first order velocity potentials mentioned previously are used for estimation of added resistance in waves. Each numerical code is different from each other mainly in the boundary conditions, the green's function used in the integral equation and in the methods used for finding added resistance.

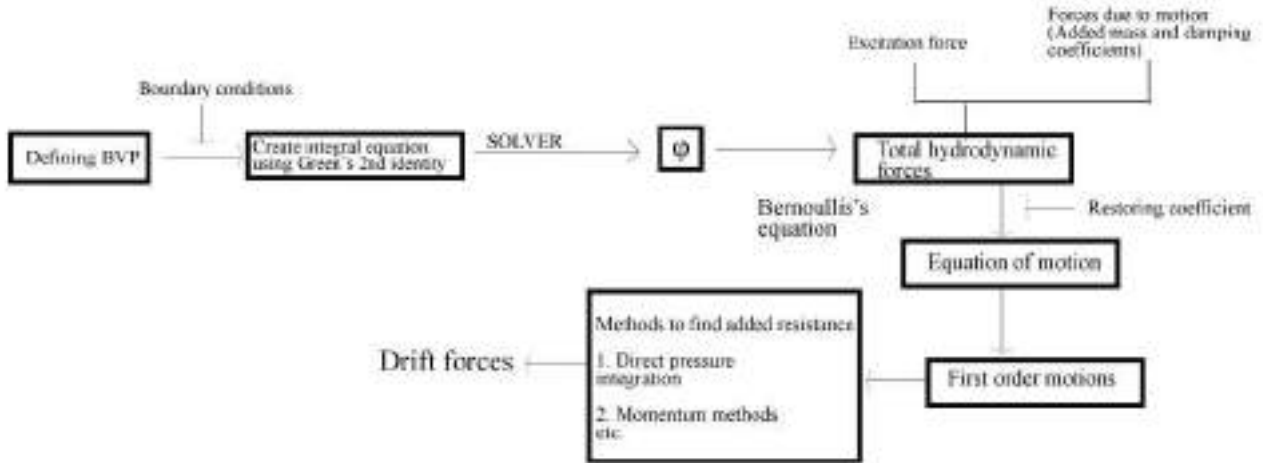


Figure 4.1: Flow chart showing the general procedure used in numerical codes to find first order solutions and second order loads.

4.3 Panel model

The first and foremost requirement to begin a numerical analysis using any of the numerical codes is a panel model of the vessel. For 3D panel codes the submerged geometry is to be divided into panels, where the basic singularities are to be distributed. In the current study the design software called Rhinoceros 3D and its feature (Quadmesh) which had been used to create a quadratic mesh of the whole body based on target number of mesh elements that is given as input. Using this feature the panel model of the vessel was created as seen in figure 4.2. The panel size is an important parameter that influences the quality of the results. The number of panels was decided based on a grid convergence test which is discussed later in the section for results. The panel model created was then exported into the required geometry format used in different numerical codes. VERES is based on 2D strip theory and it is implemented through a platform called ShipX, where the paneling is done within the platform.



Figure 4.2: 3D panel model of SOShip used for numerical analysis

Further in the report a brief description of the theory used in each code to find first order solutions, i.e the ship motions and velocity potentials, and added resistance is shown along with the numerical results of the mentioned parameters for the studied ship models. Therefore, in the following the focus will be given to the exemplification of the differences which are present between the applied numerical methods in this work.

4.4 Highlights of Comparison of numerical codes

For a reader familiar with the numerical codes this section highlights the basic differences between the three numerical codes used which are of interest for this study.

WAMIT

- 3D panel code
- Use zero speed free surface boundary condition
- Uses zero speed free surface Green's function when solving BVP
- Need to descritize the body alone
- Can use Direct pressure integration (Near field), Momentum method (Far field) and momentum method using user defined control surface (require geometry file for control surface)
- Only possible for analysis at $Fn = 0$

VERES (ShipX)

- 2D panel code
- Include forward speed in free surface boundary condition
- Uses Rankine's Green's function when solving BVP
- Need to descritize the body and free surface

- Can use Direct pressure integration (Near field), Gerritsma and Beukelmann method (Far field method)
- Possible for analysis at Froude numbers $Fn = 0$ and $Fn > 0$

VERES3D

- 3D panel code
- Uses zero speed free surface boundary condition
- Uses zero speed free surface Green's function when solving BVP
- Need to descritize the body alone
- Can use Direct pressure integration (Near field), Momentum method (Far field) and momentum method using user defined control surface (require or control surface parameter to control distance of cylindrical control surface around the vessel)
- Possible for analysis at Froude numbers $Fn = 0$ and $Fn > 0$

Further in the following sections we describe these highlights in detail for each numerical code.

4.5 WAMIT

WAMIT is one of the most widely used numerical software tool used today in the industry to analyze wave interaction with various kinds of marine structures which includes vessels, offshore platforms and other structures. It is program capable for performing analysis at Froude number $Fn = 0$. Furthermore the software is based on linear and second order potential theory. It uses the panel method to solve for velocity potential and fluid pressure on submerged surfaces of the bodies. After finding solutions for the diffraction problem and radiation problem separately it is used to obtain hydrodynamic coefficients, exciting forces, response amplitude operators, pressure and fluid velocity, mean drift forces and moments ⁽⁵²⁾. Along with the required inputs it requires the panel geometry file (discretized wetted surface of the free surface piercing body) in *'gdf'* format. One of the important advantage of using Wamit version 7 is that , it can include tank wall effects by means of defining a channel around the vessel. This will be discussed further in the report in the section on wall effects.

Further in this section the basic summary on how WAMIT formulates the first order solutions and second order forces is presented. The theory discussed further in the section is referenced from the theory manual for WAMIT⁽⁵³⁾.

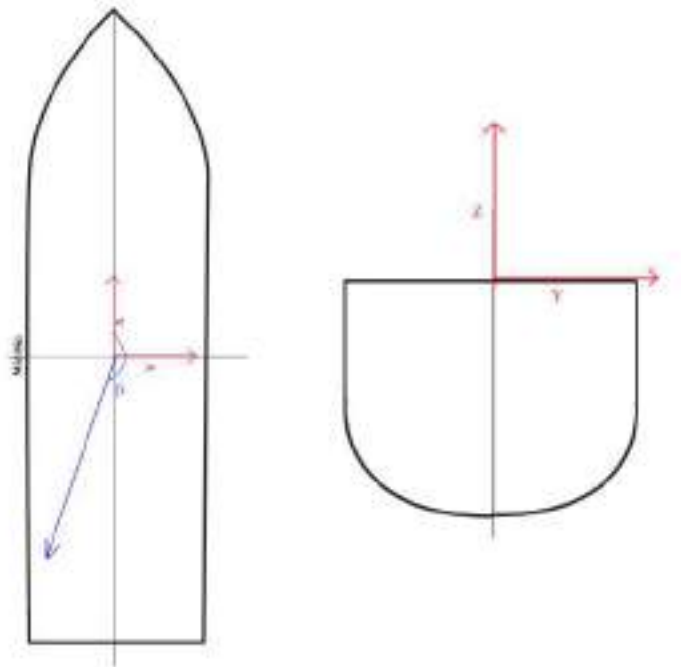


Figure 4.3: Coordinate system used for numerical calculations in WAMIT when the origin of local coordinate system was assumed in the origin of global coordinate system. β is the wave heading, $\beta=180^\circ$ represents head sea

WAMIT allows the user to give the position of the local coordinate system with respect to the global coordinate system. For the current study the origin of the local and global coordinate systems are the same as in figure 4.3

4.5.1 First order solutions

Total velocity potential, ϕ is defined as

$$\phi = \phi_I + \phi_s + \phi_R \quad (4.1)$$

where

ϕ_I - Incident wave velocity potential

ϕ_s - Fluid velocity potential that represents disturbance of incident wave due to presence of body

ϕ_R - Radiation wave velocity potential

$\phi_I + \phi_s$ can be referred as diffraction wave velocity potential ϕ_D

The incident wave potential in infinite water depth can be defined as

$$\phi_I = \frac{igA}{\omega} e^{\kappa z} e^{-i\kappa(x\cos\beta + y\sin\beta)} \quad (4.2)$$

g - acceleration due to gravity

A - Wave amplitude

ω - circular wave frequency

β - wave heading (the angle of incidence to the positive x axis)

κ - wave number = $\frac{\omega^2}{g} = \nu$

$$\phi_R = i\omega \sum_{k=1}^6 \phi_k \zeta_k \quad (4.3)$$

ζ_k - Complex amplitude of the oscillatory motion in mode k of six degrees of freedom

ϕ_k - Unit amplitude radiation potential

The BVP can be defined as follows

The total velocity potential ϕ obeys the Laplace equation

$$\nabla^2 \phi = 0 \quad (4.4)$$

Boundary conditions

1. *Free surface boundary condition on $z=0$*

Since WAMIT is used for analysis at $Fn = 0$, the free surface boundary condition defined in equation 4.5 can be termed as a zero speed free surface condition.

$$g \frac{\partial \phi}{\partial z} - \omega^2 \phi = 0 \quad (4.5)$$

2. Sea bottom boundary condition on $z \rightarrow -\infty$

$$\nabla\phi = 0 \quad (4.6)$$

3. Body boundary condition on mean position of the hull

For radiation potential

$$\frac{\partial\phi_k}{\partial n} = n_k \quad (4.7)$$

For diffraction potential

$$\frac{\partial\phi_D}{\partial n} = 0 \quad \frac{\partial\phi_s}{\partial n} + \frac{\partial\phi_I}{\partial n} = 0 \quad (4.8)$$

If wall effects (tank wall effects) are considered, on the walls

$$\frac{\partial\phi}{\partial n} = 0 \quad (4.9)$$

4. Radiation condition

The scattering and radiation potentials are subject to a radiation condition. It states that the wave energy from the disturbance of the body is carried away to all directions in the far field.

Integral equation & Green's function

The BVP is solved by using the integral equation method (refer equation 2.28). The integral equations are defined as follows

For the unit amplitude radiation potential ϕ_k , the integral equation can be defined as

$$2\pi\phi_k(x) + \int \int_{S_B} d\xi\phi_k(\xi) \frac{\partial G(\xi; x)}{\partial n_\xi} = \int \int_{S_B} d\xi n_k G(\xi; x) \quad (4.10)$$

For diffraction potential

$$2\pi\phi_D(x) + \int \int_{S_B} d\xi\phi_D(\xi) \frac{\partial G(\xi; x)}{\partial n_\xi} = 4\pi\phi_I(x) \quad (4.11)$$

ξ - coordinate of the point considered $(\varepsilon, \eta, \varsigma)$

The green's function is defined as the velocity potential at a point x due to a point source of strength -4π located at the point ξ . It satisfies the zero speed free surface boundary condition and radiation conditions mentioned above, because of which it will only be required to descritize the body alone and not the free surface. The Green's function in infinite depth used in WAMIT can be defined as

$$G(x; \xi) = \frac{1}{r} \frac{1}{r'} + \frac{2\nu}{\pi} \int_0^\infty dk \frac{e^{k(z+\varsigma)}}{k - \nu} J_0(kR) \quad (4.12)$$

where r and r' are defined as follows

$$r^2 = (x - \varepsilon)^2 + (y - \eta)^2 + (z - \varsigma)^2 \quad (4.13)$$

$$r^2 = (x - \varepsilon)^2 + (y - \eta)^2 + (z + \varsigma)^2 \quad (4.14)$$

$$\frac{\omega^2}{g} = \nu$$

J_0 - Bessel Function of zero order

As shown in figure 4.1 once the first order BVP is solved and the total velocity potential is obtained the Bernoulli's equation is used to find the total hydrodynamic pressure and consequently the hydrodynamic forces and moments acting on the body from which the added mass and damping coefficients are generated. The restoring coefficients are also obtained from analysing the hydrostatic force on the vessel. Solving the equation of motion then generates the first order solutions.

WAMIT presents the output for motions in dimensionless RAO's. If η_j represents the motion along one axis, then the motion outputs are of the format as seen in equation 4.15

$$\bar{\eta}_j = \frac{\eta_j}{A/L^n} \quad (4.15)$$

$n = 0$ for $i = 1 - surge, 2 - sway, 3 - heave$

$n = 1$ for $i = 4 - roll, 5 - pitch, 6 - yaw$

where A is the wave amplitude of 1 m, L is the input for characteristic length (ULEN) defined in the geometry file (.gdf).

4.5.2 Methods for Added Resistance

WAMIT provides three different methods to find added resistance.

- Pressure Integration
- Momentum method
- Control surface momentum flux method

More details on pressure integration and momentum method can be seen in section 2. The third method is based on a user defined control surface around the vessel. This requires a separate geometry file for the control surface. It gives the advantage when the body is not smooth and it has sharp corners but it also increases the run time. In this study pressure integration and momentum method are used for finding the added resistance in waves.

Along with other wave loads, the mean drift forces are also presented non dimensionless as per equation 4.16

$$\bar{F}_j = \frac{F_j}{\rho g A^2 L K} \quad (4.16)$$

g - Acceleration due to gravity given as input (GRAV) in the geometry file (.gdf)

A - Wave amplitude

L - Characteristic length(ULEN) input in the geometry file (.gdf)

$K = 1$ for $i = 1, 2, 3$ and $K = 2$ for $i = 4, 5, 6$

In the current study the longitudinal and transverse forces were made non dimensional using the non dimensional factor as shown in equation 3.10. Therefore for ease of comparison of results presented in section 5, the non dimensional value of forces in WAMIT were converted to the non dimensional value using the factor in 3.10.

4.5.3 Bodies in channels of finite width

Starting from WAMIT Version 7.2, the code facilitates including the effects due to presence of walls on both sides that act as a channel of finite width. It is only possible if the body is within the domain of $channelwidth/2$ and at wave headings of 0° and 180° . The only required parameter is the channel width, w shown in figure 4.4. The body is then assumed at the centre of the channel. This feature includes hydrodynamic analysis of the interaction between the body and the wall.

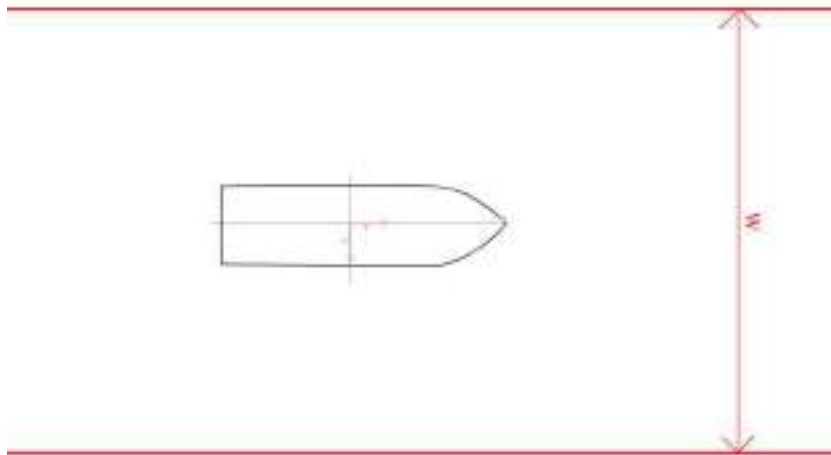


Figure 4.4: Channel of width w defined with walls on both sides of the body

4.6 VERES

VERES is accessible as a software package plug-in for estimation of vessel motions in the software platform named SHipX developed by SINTEF Ocean. It is used for calculation of global loads and motions at both zero and non zero Froude numbers. Unlike a 3D panel code, VERES works based on 2D strip theory. Using the principles of strip theory the loads are estimated for each strips and then integrated along the whole length to obtain the 3D loads on the whole vessel. VERES is based on linear potential fluid flow theory. The theory assumes the wave amplitudes are small compared to the characteristic length of the vessel, the wave steepness is small as to avoid wave breaking and the linear motions and loads have the same frequency as the wave. However viscous effect for roll damping can be included for rolling through empirical formulas. As per assumptions in strip theory, the vessel is assumed to be slender and symmetric about the center line. The hull is assumed to be close to wall-sided at the free surface. In VERES it is possible to use strip theory formulation of Salvenden,tuck Faltinsen⁽⁵⁴⁾ or the high speed theory formulation of Faltinsen Zhao⁽⁵⁵⁾. This study uses strip theory formulation that facilitates the possibility to learn about its capabilities in estimating first order ship motions and mean drift loads,in particular added resistance in waves in comparison to 3D panel codes. The following theory is a basic summary covering the required aspects relevant for the current study from the theory manual of VERES⁽⁵⁶⁾.

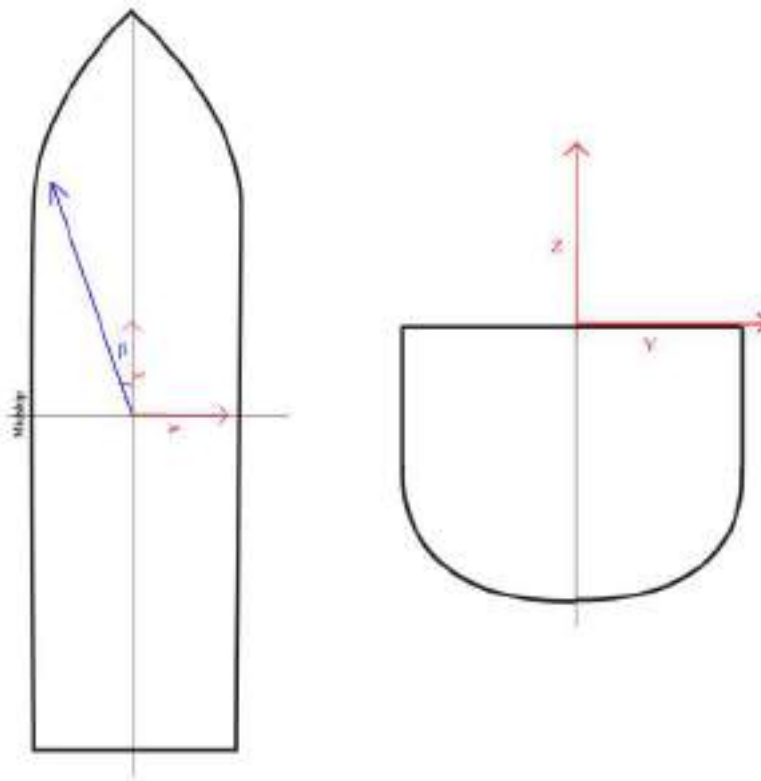


Figure 4.5: Coordinate system used for numerical calculations in ShipX when the origin of local coordinate system was assumed in the origin of global coordinate system. β is the direction angle of incident waves, $\beta=0^\circ$ represents head sea

ShipX platform uses the left handed coordinate system as seen in figure 4.5 for the user. As per the

Manual⁽⁵⁶⁾, VERES internally uses right handed coordinate system.

4.6.1 First order solutions

The total fluid velocity potential is defined as

$$\phi = [Ux + \phi_S] + (\phi_I + \phi_D + \sum_{j=1}^6 \phi_j \eta_j e^{i\omega t}) \quad (4.17)$$

$[Ux + \phi_S]$ - Steady contribution with U the forward speed of the Ship

$(\phi_I + \phi_D + \sum_{j=1}^6 \phi_j \eta_j)$ - Complex amplitude of unsteady velocity potential

ϕ_I - Incident wave potential

ϕ_D - Diffraction potential

ϕ_j - contribution to velocity potential from j^{th} mode of motion

$\phi_I + \phi_s$ can be referred as diffraction wave potential ϕ_D

The incident wave potential in infinite depth can be written as

$$\phi_I = \frac{igA}{\omega_0} e^{\kappa z} e^{-i\kappa(x\cos\beta + y\sin\beta)} \quad (4.18)$$

ω_0 - Incident wave frequency

Encounter frequency $\omega = \omega_0 + \kappa U \cos\beta$

The BVP can be defined as follows

The total velocity potential ϕ obeys the Laplace equation

$$\nabla^2 \phi = 0 \quad (4.19)$$

Boundary conditions

1. Free surface boundary condition on $z=0$

For steady perturbation potential, ϕ_S

$$U^2 \frac{\partial^2 \phi_S}{\partial x^2} + g \frac{\partial \phi_S}{\partial z} = 0 \quad (4.20)$$

For incident wave potential ϕ_I , diffraction potential ϕ_D and oscillatory potential components $\phi_j, j = 1, 2, \dots, 6$

$$\left[(i\omega + U \frac{\partial}{\partial x})^2 + g \frac{\partial}{\partial z} \right] \phi_I = 0 \quad (4.21)$$

$$\left[(i\omega + U \frac{\partial}{\partial x})^2 + g \frac{\partial}{\partial z} \right] \phi_D = 0 \quad (4.22)$$

$$\left[(i\omega + U \frac{\partial}{\partial x})^2 + g \frac{\partial}{\partial z} \right] \phi_j = 0 \quad (4.23)$$

It can be noted that in comparison to the zero speed free surface condition used in WAMIT, VERES uses a free surface condition which includes forward speed U .

2. Body boundary condition on mean position of the body

For steady perturbation potential, ϕ_S

$$\frac{\partial}{\partial n}(Ux + \phi_S) = 0 \quad (4.24)$$

For incident wave potential and diffraction wave potential

$$\frac{\partial \phi_I}{\partial n} + \frac{\partial \phi_D}{\partial n} = 0 \quad (4.25)$$

For oscillatory velocity potential due to motions

$$\frac{\partial \phi_j}{\partial n} = i\omega n_j - Um_j \quad (4.26)$$

where generalised normal n_j , is defined by

$$\vec{n} = (n_1, n_2, n_3)$$

$$\vec{r} \times \vec{n} = (n_4, n_5, n_6)$$

with $\vec{r} = (x, y, z)$ as the position vector with respect to the origin of the coordinate system. \vec{n} is the outward unit normal vector pointing into the fluid

$$(m_1, m_2, m_3) = \vec{m} = (\vec{n} \cdot \nabla) \nabla(x + \frac{1}{U} \phi_S)$$

$$(m_4, m_5, m_6) = \vec{r} \times \vec{m} - \nabla(x + \frac{1}{U} \phi_S)$$

$$m_j = 0 \quad j = 1, 2, 3, 4$$

$$m_5 = n_3, m_6 = -n_2$$

Simplified Boundary conditions

Following the low speed formulation the oscillatory potential ϕ_j can be simplified by splitting into a speed independent and speed dependent part as in equation 4.27

$$\phi_j = \phi_j^0 - \frac{U}{i\omega} \phi_j^U \quad (4.27)$$

ϕ_j^0 is the speed independent term and ϕ_j^U is the speed dependent term. The speed dependent term can be further written in terms of the speed independent term thus giving a simplified version of the boundary conditions in terms of speed independent terms as shown below.

Body boundary condition

Equation 4.26 can be written as

$$\phi_j = \phi_j^0 \quad j = 1, 2, 3, 4 \quad (4.28)$$

$$\phi_5 = \phi_5^0 - \frac{U}{i\omega} \phi_3^0 \quad (4.29)$$

$$\phi_6 = \phi_6^0 - \frac{U}{i\omega} \phi_2^0 \quad (4.30)$$

Free surface boundary condition

Similarly the free surface boundary condition on $z=0$ in equation 4.23 for ϕ_j can be written as

$$\left[(i\omega + U \frac{\partial}{\partial x})^2 + g \frac{\partial}{\partial z} \right] \phi_j^0 = 0 \quad (4.31)$$

Integral Equation & Green's function

Green's Second identity using suitable green's function and total velocity potential as the two scalar functions, creates an integral equation which is solved to find the unknown total velocity potential over a closed surface containing the body surface, the free surface and a control surface far away from the body as in figure 4.6. In VERES the integral equation considering a single strip where r is the distance from the source/sink point considered to the centre of the panel or element being considered can be defined as in equation 4.32

$$-2\pi\phi = \int_S \left[\phi \frac{\partial \log(r)}{\partial n} - \log(r) \frac{\partial \phi}{\partial n} \right] dS \quad (4.32)$$

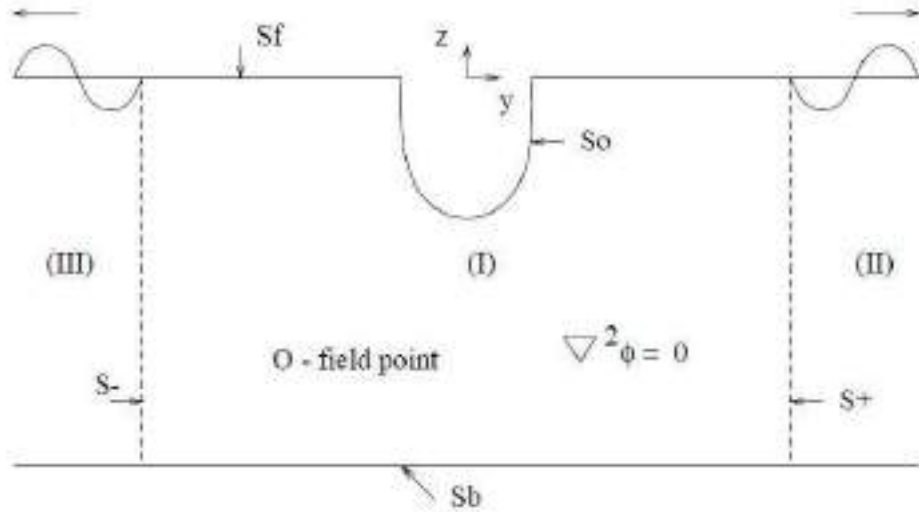


Figure 4.6: Control surfaces and fluid domain considered around a 2D strip

The green's function used here is

$$G = \log r \quad (4.33)$$

This is a Rankine 2D source Green's function as described in section 2.5.1. The free surface and the body has to be discretized into 2D elements, which will be done by ShipX.

Once the total velocity potential is formulated the total hydrodynamic forces and first order motions are obtained.

ShipX presents the motion output as non dimensional RAO's.

4.6.2 Methods for Added Resistance in waves

There are two possible methods in Shipx to find added resistance.

If the global loads are calculated using strip theory

- Gerritsma and Beukelman method

If the global loads are calculates using pressure integration

- Gerritsma and Beukelman method
- Pressure Integration

The use of pressure integration for calculation of global loads is not clearly understood and therefore the study uses Geritsma and Beukelman method for added resistance based on strip theory formulation.

The added resistance outputs are available in non-dimensional format using the same non dimensional factor used for the experimental results as shown in equation 3.10.

4.7 VERES3D

VERES3D is a newly developed 3D panel code by SINTEF Ocean. It is capable of estimating first order motions, loads and second order drift forces at zero and non zero Froude number. VERES3D is based on linear potential fluid flow theory under the assumptions, small wave amplitude compared to the characteristic dimensions of the body with small motions, the wave steepness is small which prevents waves from breaking, the linear dynamic forces oscillate harmonically with the same frequency as the incident regular wave excitation force. Further in this section a basic summary from the VERES3D user manual ⁽⁵⁷⁾ covering the aspects relevant for the current study is presented.

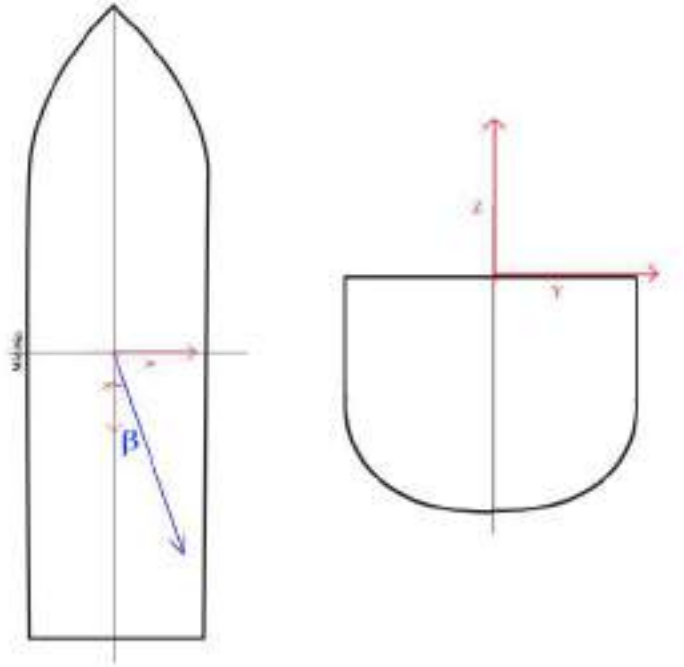


Figure 4.7: Coordinate system used for numerical calculations in VERES3D when the origin of local coordinate system was assumed in the origin of global coordinate system. β is direction angle of incident waves, $\beta=0^\circ$ represents head sea

For the current study the origin of the local coordinate system was positioned at the origin of the global coordinate system as in figure 4.7.

4.7.1 First order solutions

The total velocity potential ϕ is defined as

$$\phi = \bar{\phi} - Ux + \phi_0 + \phi_7 + \sum_{j=1}^6 \phi_j \eta_j \quad (4.34)$$

$\bar{\phi}$ - Steady velocity potential due to disturbance of incident steady flow due to presence of the body

U - Forward speed of the vessel

ϕ_0 - Incident wave potential

ϕ_7 - Velocity potential of scattered disturbance of the incident wave

Diffraction wave potential can be defined as $\phi_D = \phi_0 + \phi_7$

ϕ_j - Radiation wave potential

Incident wave potential at infinite depth can be defined as

$$\phi_0 = \frac{g\zeta_a}{\omega_0} e^{vz} e^{i(vxcos\beta + vysin\beta + \omega t)} \quad (4.35)$$

Encounter frequency $\omega = \omega_0 + \kappa U \cos\beta$

$$v = \frac{\omega_0^2}{g}$$

The BVP can be defined as follows

The total velocity potential obeys the Laplace equation

$$\nabla^2 \phi = 0 \quad (4.36)$$

Boundary conditions

1. *Body boundary conditions on mean position of the vessel*

For diffraction potential

$$\frac{\partial \phi_D}{\partial n} = 0 \quad (4.37)$$

or

$$\frac{\partial \phi_0}{\partial n} + \frac{\partial \phi_7}{\partial n} = 0 \quad (4.38)$$

For Radiation potential

$$\frac{\partial \phi_j}{\partial n} = i\omega n_j + M_j \quad (4.39)$$

Unit normal n_j can be defined as

$$n_j = n_1, n_1, n_2, n_3 \text{ for } j=1,2,3$$

$$n_j = [x, y, z]^T \times [n_1, n_1, n_2, n_3]^T \text{ for } j=4,5,6$$

The M represents simplified way to account for interaction with steady part of velocity potential for steady fluid flow. For slender body becomes as,

$$M_j =$$

$$M_1 = 0, M_2 = 0, M_3 = 0, M_4 = 0, M_5 = +Un_3, M_6 = -n_2U$$

2. Free surface condition on $z=0$

The total velocity potential must fulfill the free surface boundary condition shown below

$$-\omega^2\phi + g\frac{\partial\phi}{\partial z} = 0 \quad (4.40)$$

It can be observed that even though VERES3D is used for analysis at non zero Froude number the free surface condition corresponds to that of a zero speed free surface condition which predicts circular waves rather than the wave train behind a moving vessel.

Integral Equation & Green's function

The integral equation formulated from Green's second identity is used for solving for the radiation potential $\phi_{1,2,..6}$ and potential of scattered disturbance of the incident wave ϕ_7 in VERES3D and it is defined as

$$\int \int_{S_B} (G\frac{\partial\phi_j}{\partial n} - \phi_j\frac{\partial G}{\partial n})dS = -4\pi\phi_j(x_1, y_1, z_1) \quad j = 1, 2, \dots, 7 \quad (4.41)$$

where (x_1, y_1, z_1) here is the singular point where the distance from source to the point $r = 0$

The zero speed Green function used by VERES3D is given by Telste and Noblesse⁽⁵⁸⁾. The non dimensionless Green function is defined as

$$\hat{G} = \frac{1}{\hat{r}} + \frac{1}{\hat{r}_1} + 2f(R_0(h, v) - i\pi J_0(h)e^v) \quad (4.42)$$

Where

$$\rho = \sqrt{(\hat{x} - \hat{\xi})^2 + (\hat{y} - \hat{\eta})^2}$$

$$\hat{r} = \sqrt{\rho^2 + (\hat{z} - \hat{\zeta})^2}$$

$$\hat{r}_1 = \sqrt{\rho^2 + (\hat{z} + \hat{\zeta})^2}$$

$$h = f\rho$$

$$v = f(\hat{z} + \hat{\zeta})$$

$$d = \sqrt{h^2 + v^2} = f\hat{r}_1$$

J_0 - Bessel function of first kind

R_0 - Real functions expressed in terms of different integral representation, asymptotic expansions, ascending series, Taylor series and Haskind integral representations by Telste and Noblesse⁽⁵⁸⁾.

$$\hat{x} = [x/l, y/l, z/l]^T$$

$$\hat{\xi} = [\xi/l, \eta/l, \zeta/l]^T$$

l - Some reference length

Once the total velocity potential is obtained, then the first order forces and motions are calculated. The results are made non dimensional by dividing the result with the wave amplitude. For the current study the wave amplitude was taken to be 1m.

4.7.2 Methods for estimation of Added Resistance in waves

VERES3D provides 3 different methods to calculate second order drift forces.

- Direct Pressure Integration method (Near field method)
- Momentum method (Far field method)
- Control surface method

For the control surface method a cylindrical control surface is defined around the vessel (Refer figure 4.8). The distance of the control surface from the body can be given as input by the user along longitudinal and transverse directions of the vessel by using control surface parameters. Control surface parameters of (1,1) as defined in the input files represents the control surface at the position of the body. For the current study the influence of control surface distance over the results were conducted and the recommended parameters of 1.2, 1.5 were used for the analysis. This means the control surface has a longitudinal span of 1.2 times the L_{pp} of the vessel and a transverse span of 1.5 times the breadth of the vessel.

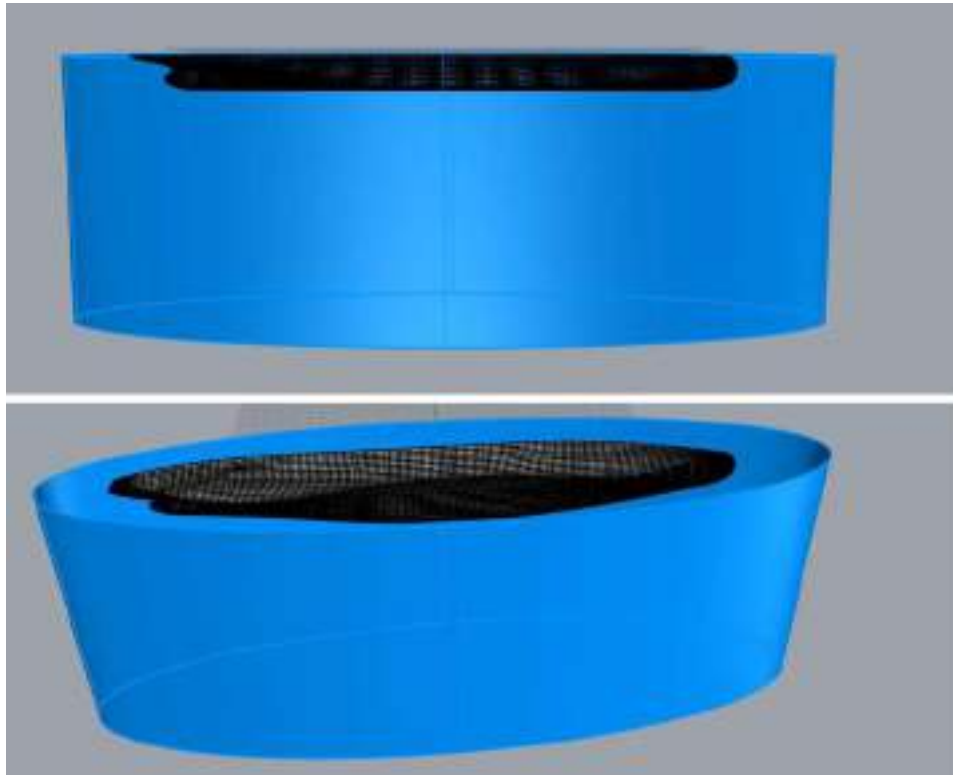


Figure 4.8: Control surface defined around the vessel (figure for representation, not accurate by dimensions)

5 Results and Discussion

5.1 Effect of drift angle

1. $F_n=0$

Added Resistance

In this section we compare the added resistance, heave RAO and pitch RAO of SoShip with and without a drift angle based on experimental and numerical results. The section focuses on making a conclusion of what difference the drift angle causes in the results. The numerical result by a numerical code presented in this section is based on the method which gave the best results within the code. The analysis on whether the numerical codes were able to predict the results effectively will be discussed further in section 5.2

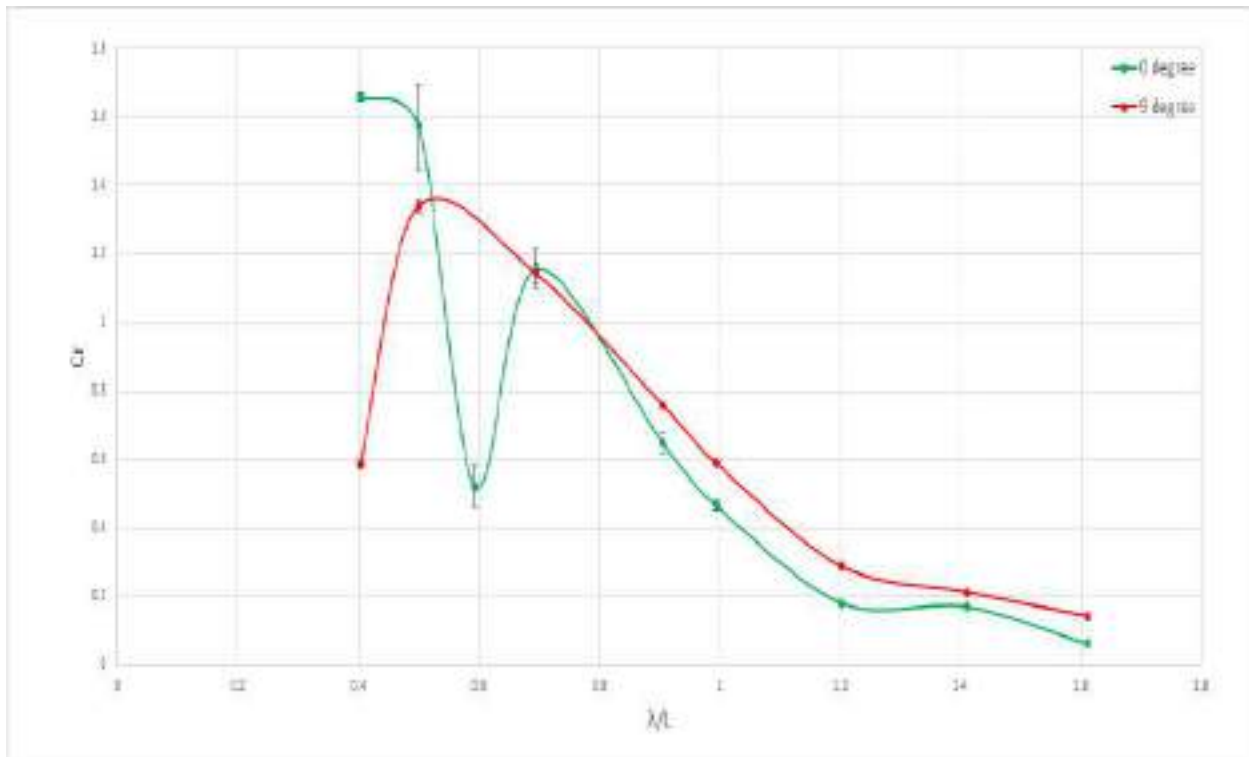


Figure 5.1: Added Resistance curves from Experimental results at $F_n = 0$ for 0° and 9° drift angle. λ - Wavelength, L - Length between perpendiculars, $C_r = Ra/(\rho g A^2 \frac{B^2}{L_{pp}})$ - non dimensional added resistance, Ra - Added resistance

The Plot in figure 5.1 represents the added resistance curve from experimental results at $F_n = 0$ for 0° and 9° along different wavelengths. It is to be noted that the tests at 0° drift angle has an extra data point at $\lambda/L = 0.6$ where as the tests at 9° drift angle do not have a data point at this wavelength as no test was done at this wavelength due to lack of time. This particular data point is of particular interest and it will be dealt later in section 5.3. At larger wavelengths the added resistance is observed to be a bit higher, but as discussed in section 3.4, with reference to a value of uncertainty based on the studies by Park et al⁽⁵¹⁾, we can assume a minimum 5% uncertainty in the

measurements for 0° and 9° drift angle test cases as shown in figure 5.2. From figure 5.2 it is clear that in general the added resistance with and without drift angle are not significantly different from each other at $Fn = 0$ based on experimental results. When comparing the numerical results with and without a drift angle, a difference of less than 5% is observed at $0.5 < \lambda/L < 1.2$. In smaller wavelengths this difference increases up to 10%. When analysing the experimental results excluding the shorter wavelengths where the uncertainty is higher and also excluding the point at $\lambda/L = 0.6$, at $0.5 < \lambda/L < 1.2$ the difference in added resistance predicted with and without a drift angle ranges from 5 - 10%. In the experimental results (figure 5.1) at shorter wavelengths ($\lambda/L < 0.5$) the measured added resistance is significantly different from each other (upto 64% difference), but considering the larger uncertainty seen in short wavelengths as pointed out in section 2.6 it is not possible to make a conclusive statement from these results for shorter waves. Uncertainty exists at longer wavelengths and this difference is approximately 10%.

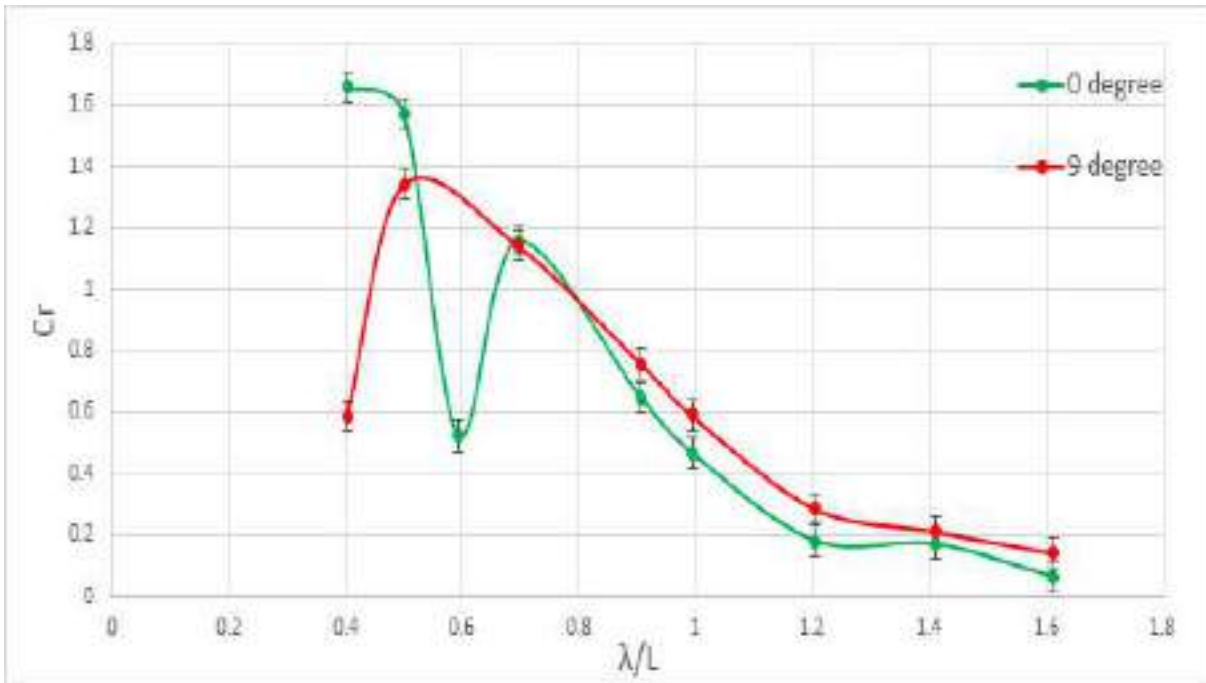


Figure 5.2: Added Resistance curves from Numerical results using WAMIT at $Fn=0$ for 0° and 9° drift angle with 5% uncertainty marked as error bars. λ - Wavelength, L - Length between perpendiculars, $C_r = Ra/(\rho g A^2 \frac{B^2}{L_{pp}})$ - non dimensional added resistance, Ra - Added resistance

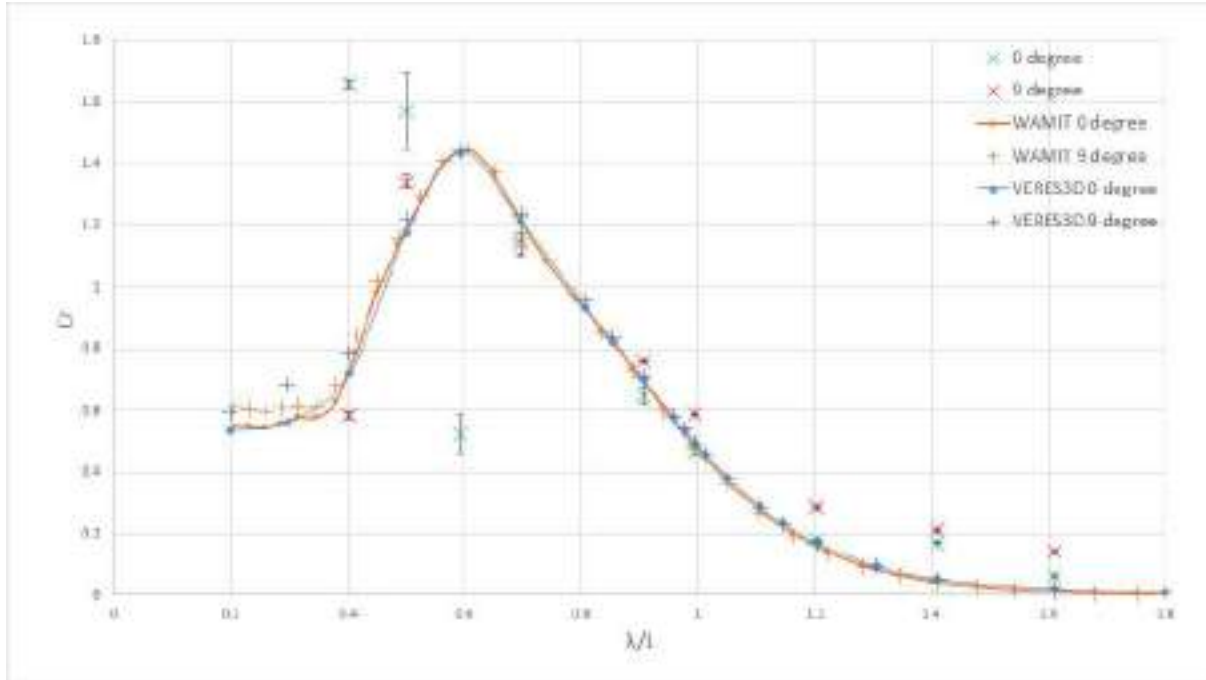


Figure 5.3: Added Resistance curves from Numerical results using WAMIT, VERES3D and experimental results at $F_n=0$ for 0° and 9° drift angle with measurement uncertainty marked as error bars. λ - Wavelength, L - Length between perpendiculars, $C_r = Ra/(\rho g A^2 \frac{B^2}{L_{pp}})$ - non dimensional added resistance, Ra - Added resistance

Figure 5.3 illustrates the numerical results obtained from the numerical codes- WAMIT and VERES3D for test conditions with $F_n = 0$ and drift angles of 9° and 0° . Similar to the experimental results, the numerical code also predicts that generally the added resistance are not significantly different with and without a drift angle. In shorter wavelengths the numerical codes predicts that 9° drift angle causes 10% more added resistance when compared to the case without a drift angle. Since the added resistance values were similar the heave and pitch motions are also expected to be similar, as added resistance depends on the wave generated by the vessel and heave and pitch motions generates the largest waves.

Heave RAO

Figure 5.4 illustrates the heave (η_3) RAO obtained from experimental results at $F_n=0$ for 0° and 9° drift angles. Corresponding to the added resistance heave value at 9° drift is slightly higher than at 0° drift angle. Considering an uncertainty of 5% based on a reference value from Park et al 's analysis (refer section in 3.4) it can be concluded that the heave RAO at 0° and 9° drift angles are not significantly different from each other. The results from numerical codes also provides the same results with and without a drift angle as seen in figure 5.5.

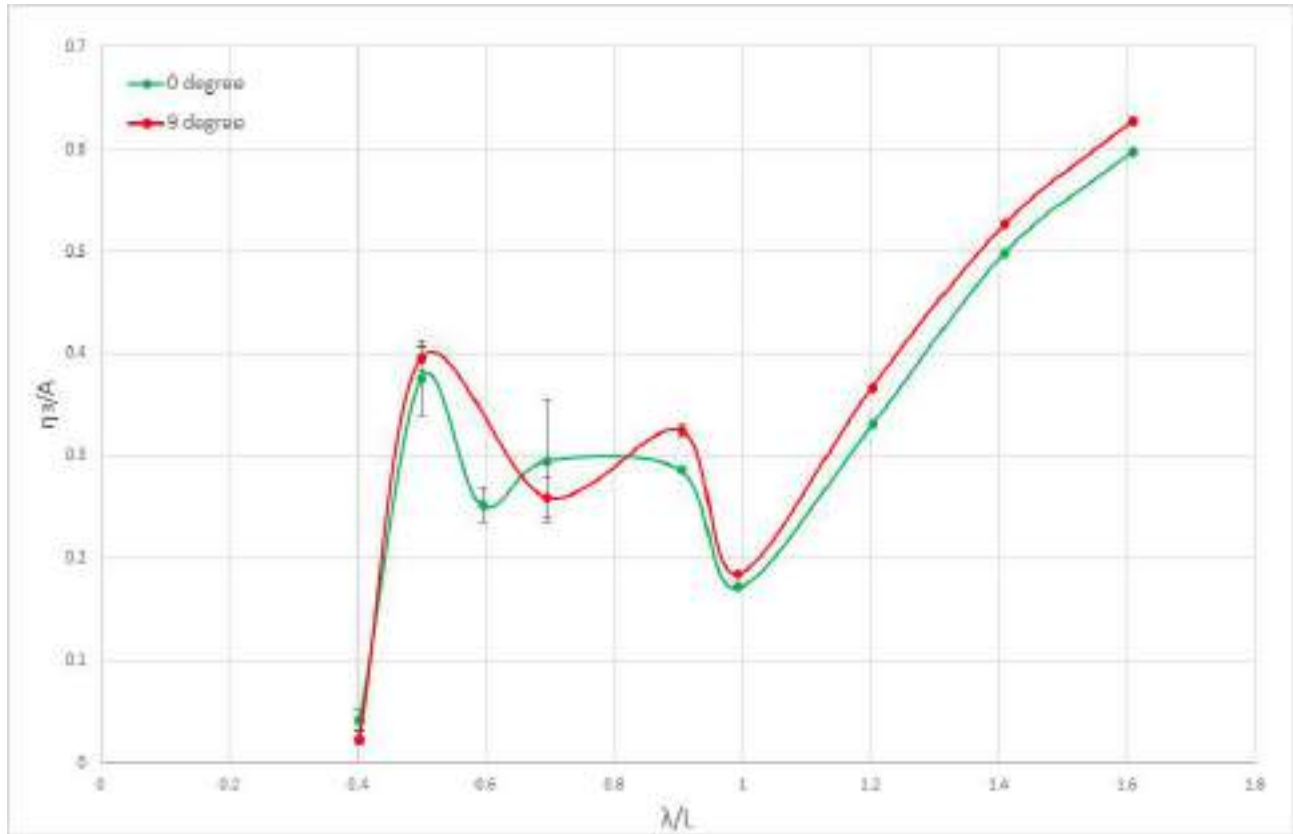


Figure 5.4: Heave RAO from Experimental results at $F_n=0$ for 0° and 9° drift angle with measurement uncertainty as error bars. η_3 - Heave amplitude, A - Wave amplitude, λ - Wavelength, L - Length between perpendiculars

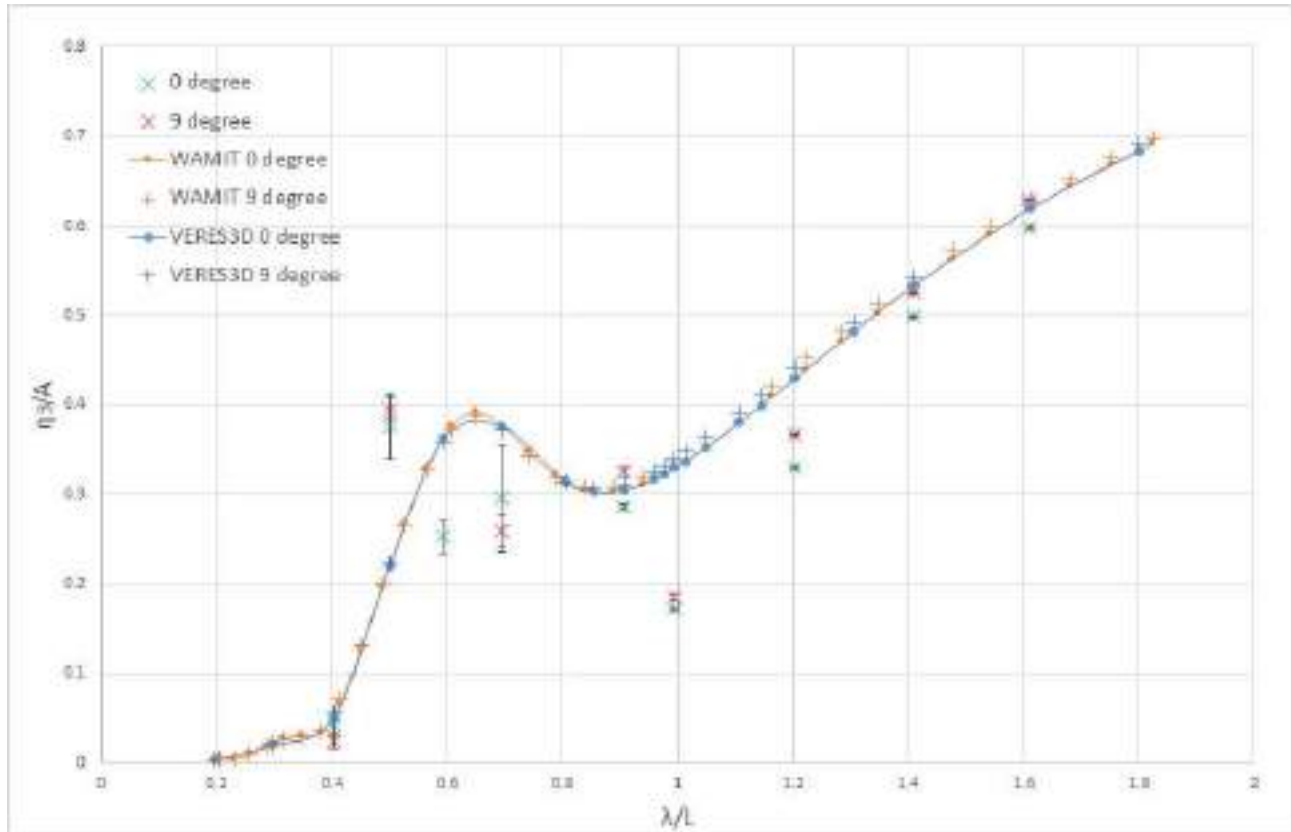


Figure 5.5: Heave RAO from Numerical results obtained in WAMIT, VERES3D and Experimental results at $F_n=0$ for 0° and 9° drift angle with measurement uncertainty as error bars. η_3 - Heave amplitude, A - Wave amplitude, λ - Wavelength, L - Length between perpendiculars

Pitch RAO

Figure 5.6 illustrates the pitch RAO obtained from experimental results at $F_n=0$. It can be concluded that the pitch RAO at 0° and 9° drift angles are not significantly different from each other. The results from numerical codes also provides the same results with and without a drift angle as seen in figure 5.7. As expected heave and pitch motions are also similar with and without drift angle.

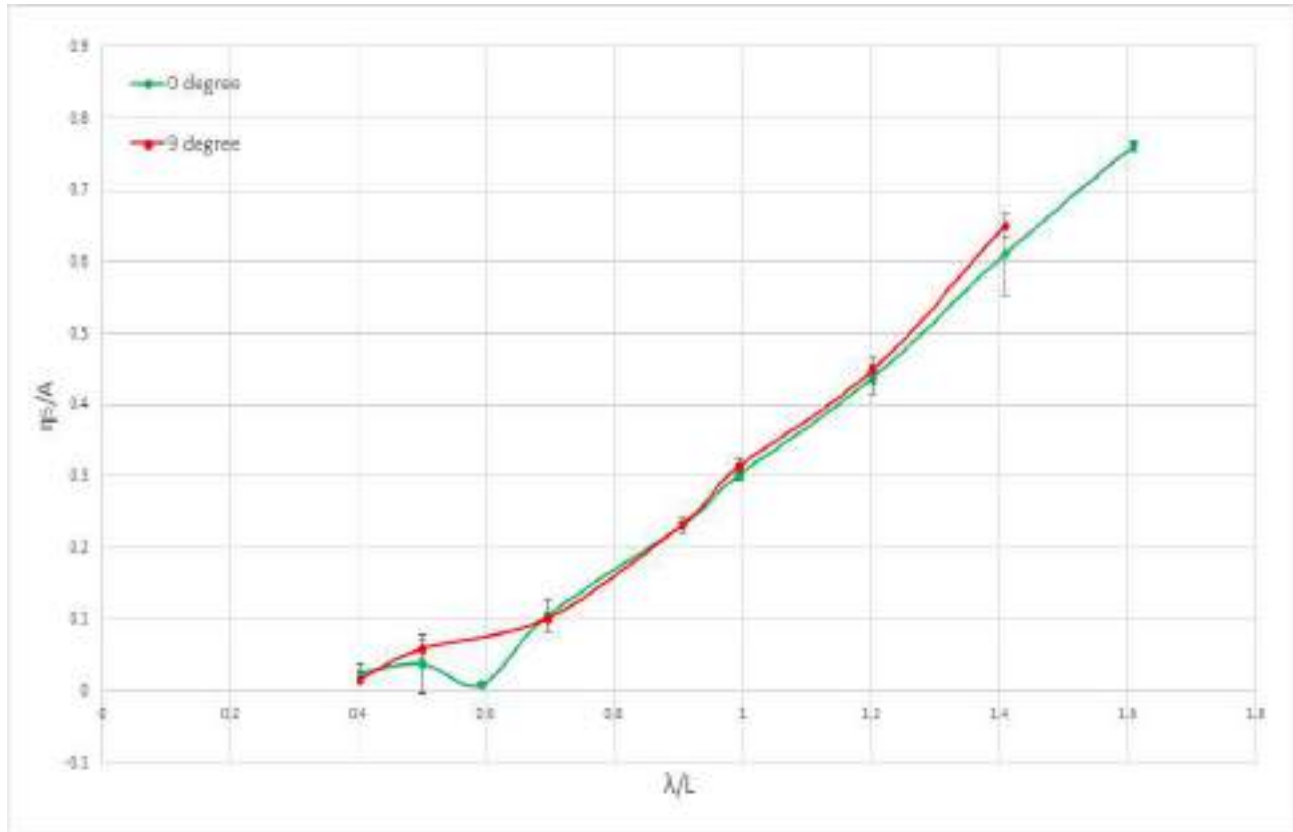


Figure 5.6: Pitch RAO from Experimental results at $F_n=0$ for 0° and 9° drift angle with measurement uncertainty as error bars. η_5 - Pitch amplitude, k - wave number, A - Wave amplitude, λ - Wavelength, L - Length between perpendiculars

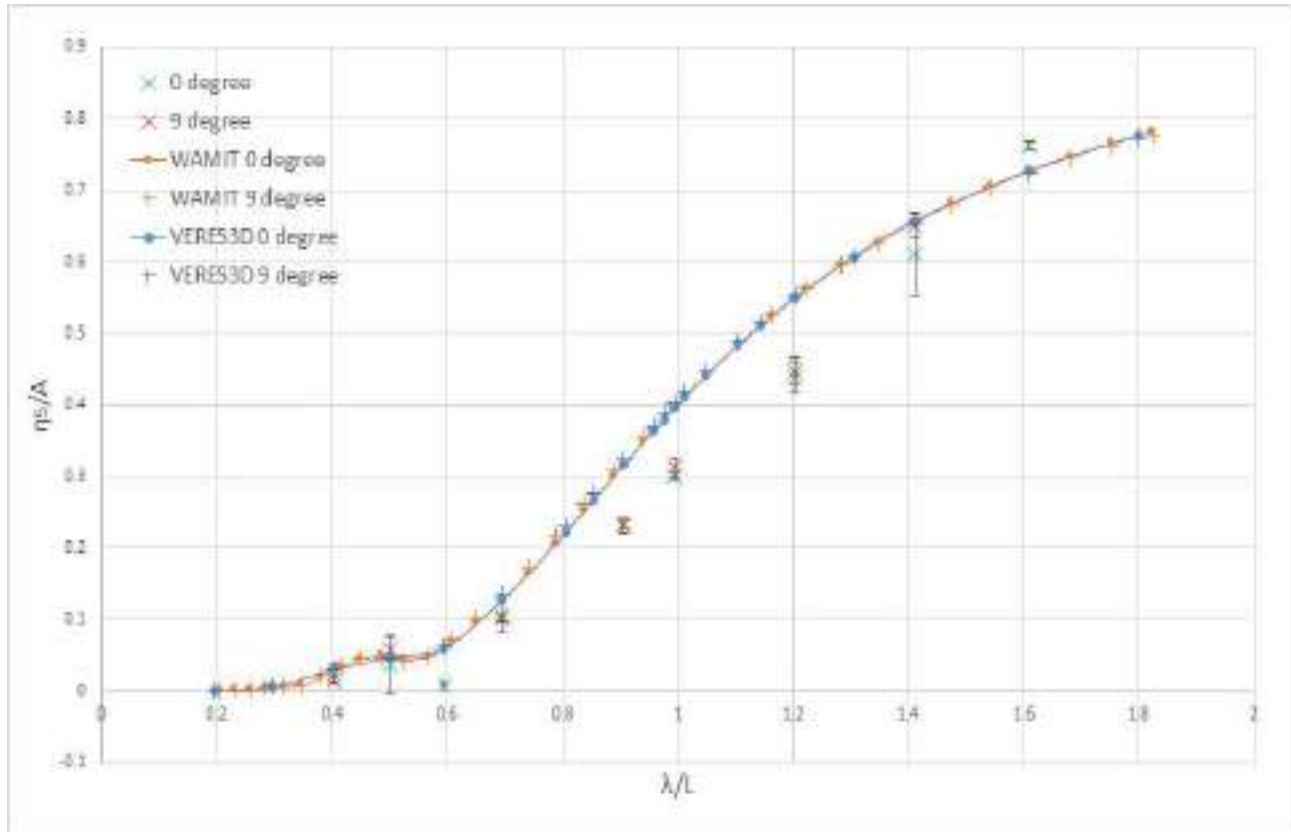


Figure 5.7: Pitch RAO from Numerical results obtained in WAMIT, VERES3D and Experimental results at $Fn=0$ for 0° and 9° drift angle with measurement uncertainty as error bars. η_5 - Pitch amplitude, k - wave number, A - Wave amplitude, λ - Wavelength, L - Length between perpendiculars

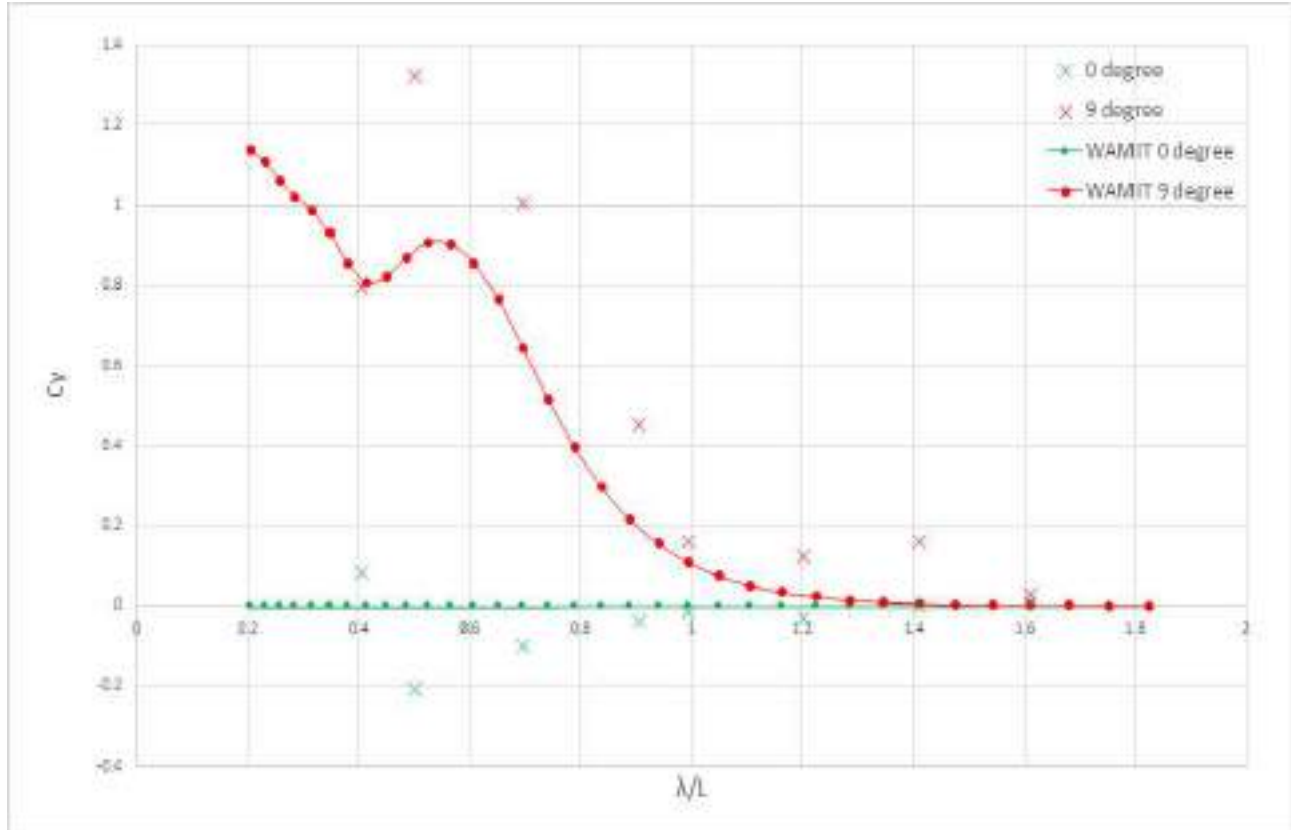


Figure 5.8: Transverse mean drift force curve from Experimental and Numerical results of WAMIT at $F_n=0$ for 0° and 9° drift angle. λ - Wavelength, L - Length between perpendiculars, $C_r = F_y / (\rho g A^2 \frac{B^2}{L_{pp}})$ - non dimensional transverse drift force, F_y - Mean transverse drift force

Mean transverse drift force

Figure 5.8 represents the variation of mean transverse force F_y measured from the experiments and obtained numerically from the applied numerical codes. At zero degree drift angle for the case of non dimensional incident wavelength $\lambda/L > 0.5$ the transverse force is near to zero. The uncertainty of measurements in shorter waves should account for the fluctuating values which becomes positive at $\lambda/L = 0.4$. At 9 degree drift angle the transverse mean drift force show a significant increase at $\lambda/L < 1.0$. The mean drift forces are comparable to the longitudinal drift forces measured at $F_n=0$. This trend is also evident in the numerical results. It is observed that the numerical code underestimates the forces in comparison to the experimental results in most of the wavelengths. Transverse mean forces can become relevant especially in case of vessels involved in marine operations such as installation or cargo transfer operations. More repetition tests are necessary to further confirm the uncertainty of the experimental measurements.

Based on the above presented numerical results and experimental results, it can be concluded that at Froude number $F_n = 0$, drift angle β does not affect the added resistance significantly. At zero speed no notable separation effects were observed. The vessel motions were similar with and without the drift angle in the current test conditions. At 9° the waves generated from the vessel were not very different from that without a drift angle. This is illustrated from the experiment in figure 5.9

which shows the vessel in the largest wave used for zero speed tests. Thus the added resistance results were also similar.



Figure 5.9: Vessel model at 0° (left) and 9° (right) at $Fn = 0$ in wave length corresponding to non dimensional wavelength $\lambda/L = 1.6$. The waves generated at 0° and 9° are similar. No separation effects are observed in presence of a drift angle.

2. $F_n=0.179$ Head Sea

Added resistance

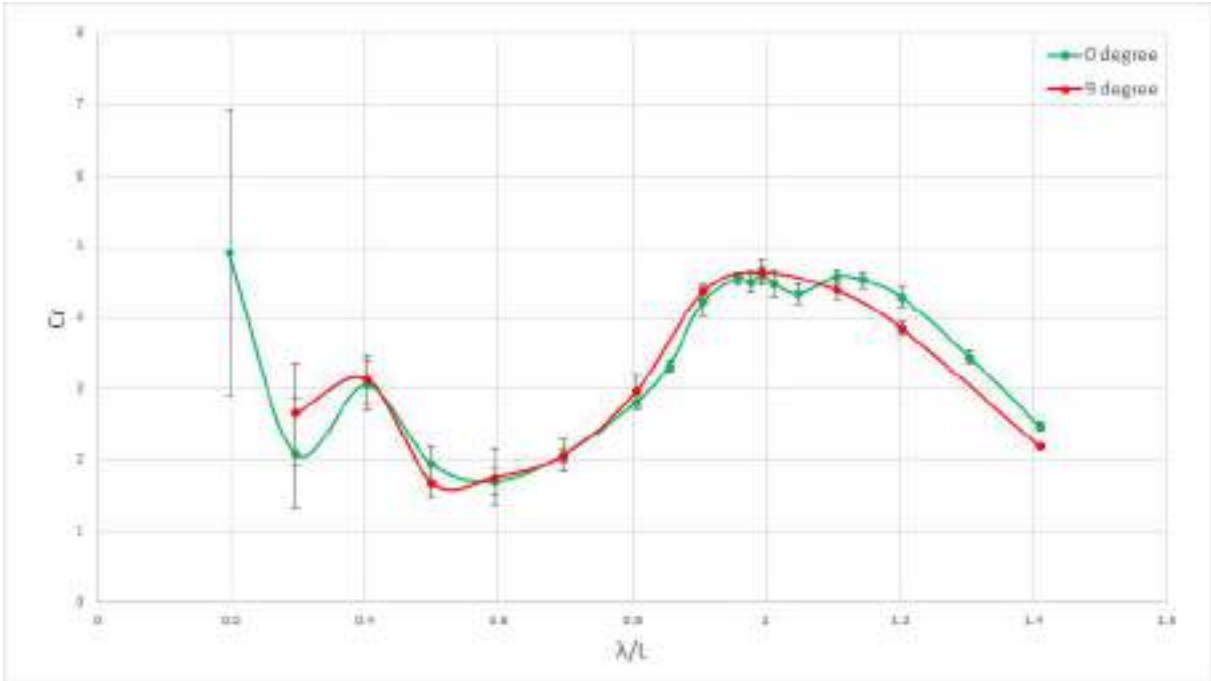


Figure 5.10: Added Resistance curves from Experimental results at $F_n=0.179$ for 0 °and 9°drift angle

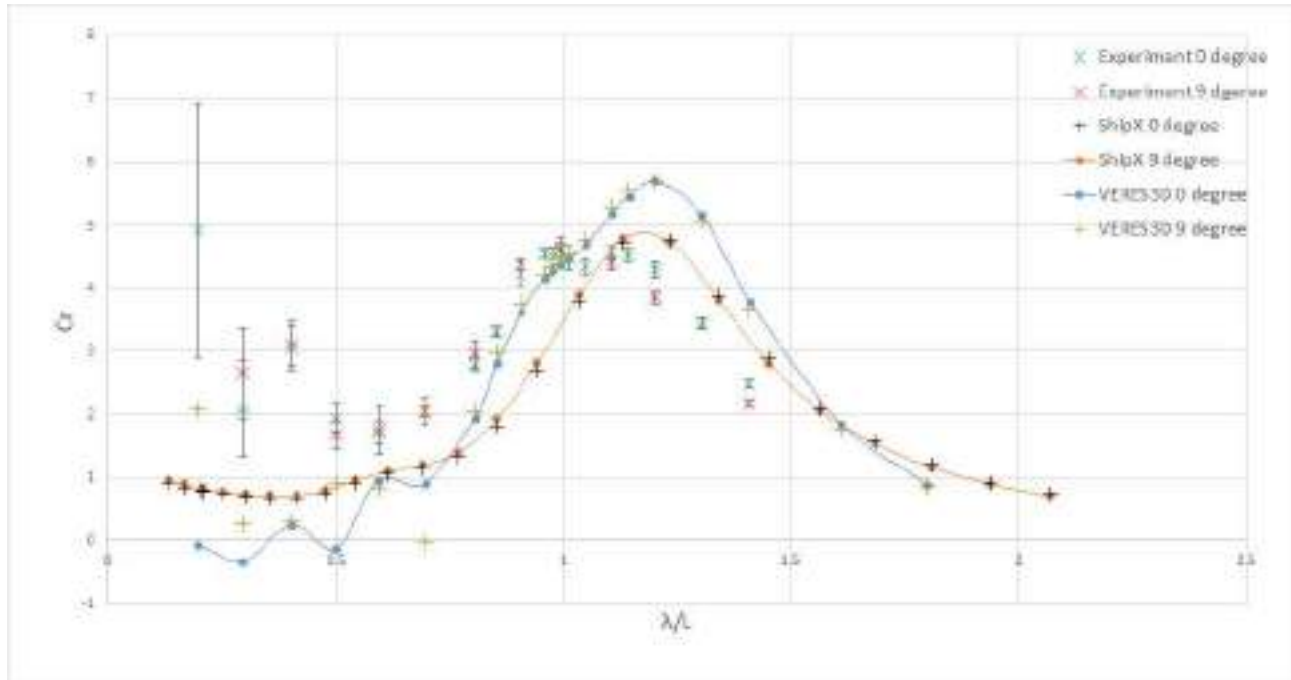


Figure 5.11: Added Resistance curves from Numerical results using ShipX (VERES) and VERES3D at $F_n=0.179$ for 0° and 9° drift angle

Figure 5.10 illustrates the experimental results of added resistance with and without a drift angle at $F_n=0.179$. It is clearly seen that apart from the data points at shorter waves which poses a large uncertainty, the added resistance measured do not have a significant difference. When analysing the numerical results in figure 5.11 when considering a single tool the results with and without drift angle generates similar values. When comparing the numerical results with and without a drift angle, a different of less than 5% is observed. When analysing the experimental results excluding the shorter wavelengths where the uncertainty is higher, at $0.5 < \lambda/L < 1.2$ the difference in added resistance predicted with and without a drift angle is less than 5%. At longer wavelengths where the experimental uncertainty increases and this difference increases to 10%.

Heave RAO

From the heave RAO's obtained experimentally (Figure 5.11) and numerically (Figure 5.13) using two different tools, it is seen that the RAO curves give similar values with and without a drift angle.

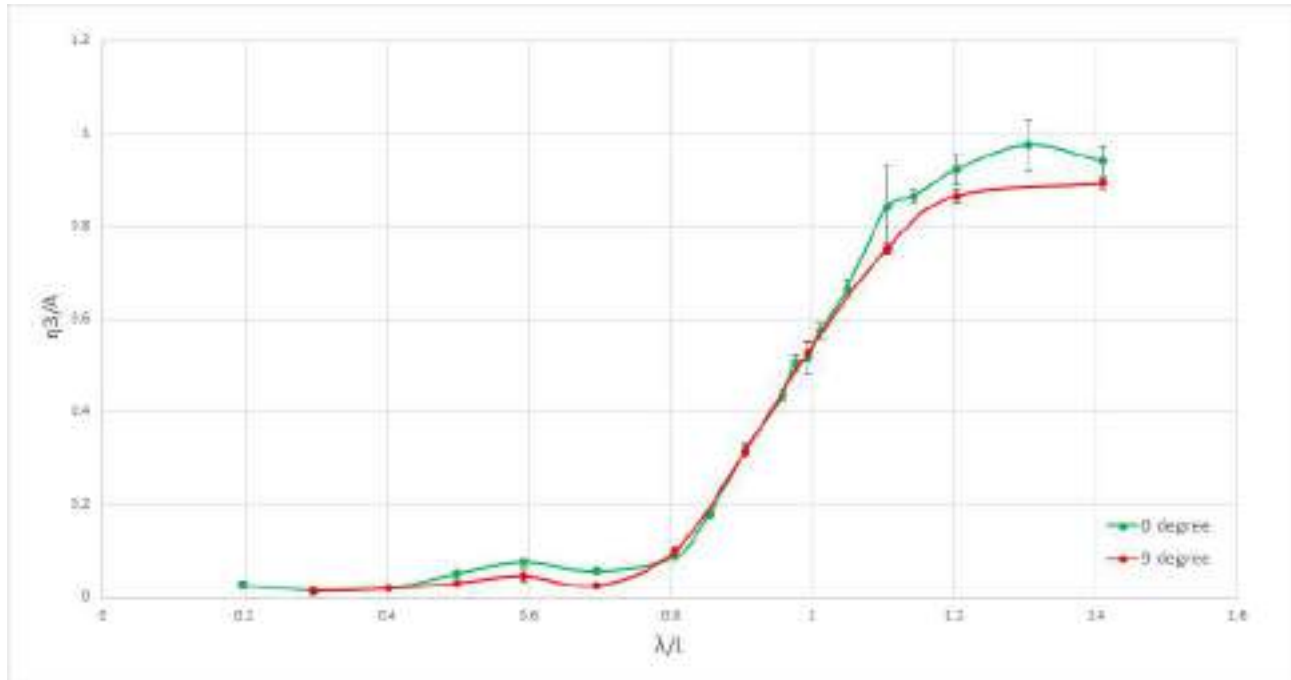


Figure 5.12: Heave RAO from Experimental results at $F_n=0.179$ for 0° and 9° drift angle

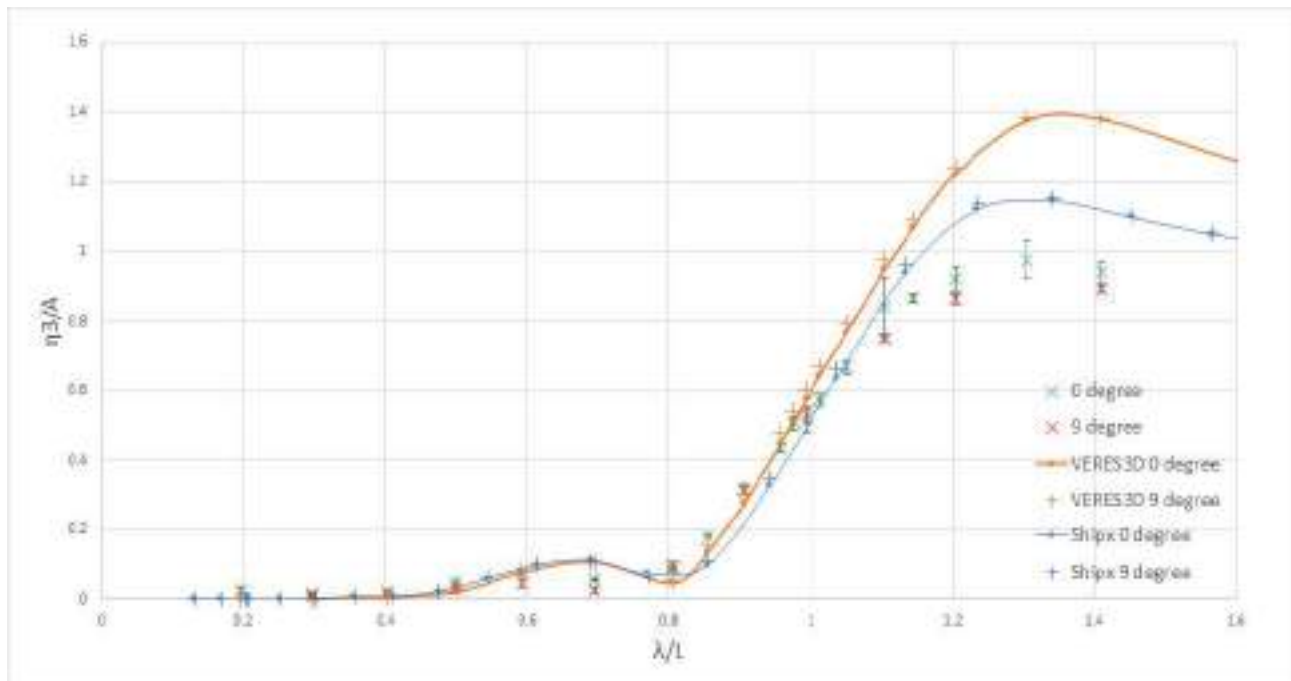


Figure 5.13: Heave RAO from Numerical values using VERES3D, ShipX(VERES) and Experimental results at $F_n=0.179$ for 0° and 9° drift angle

Pitch RAO

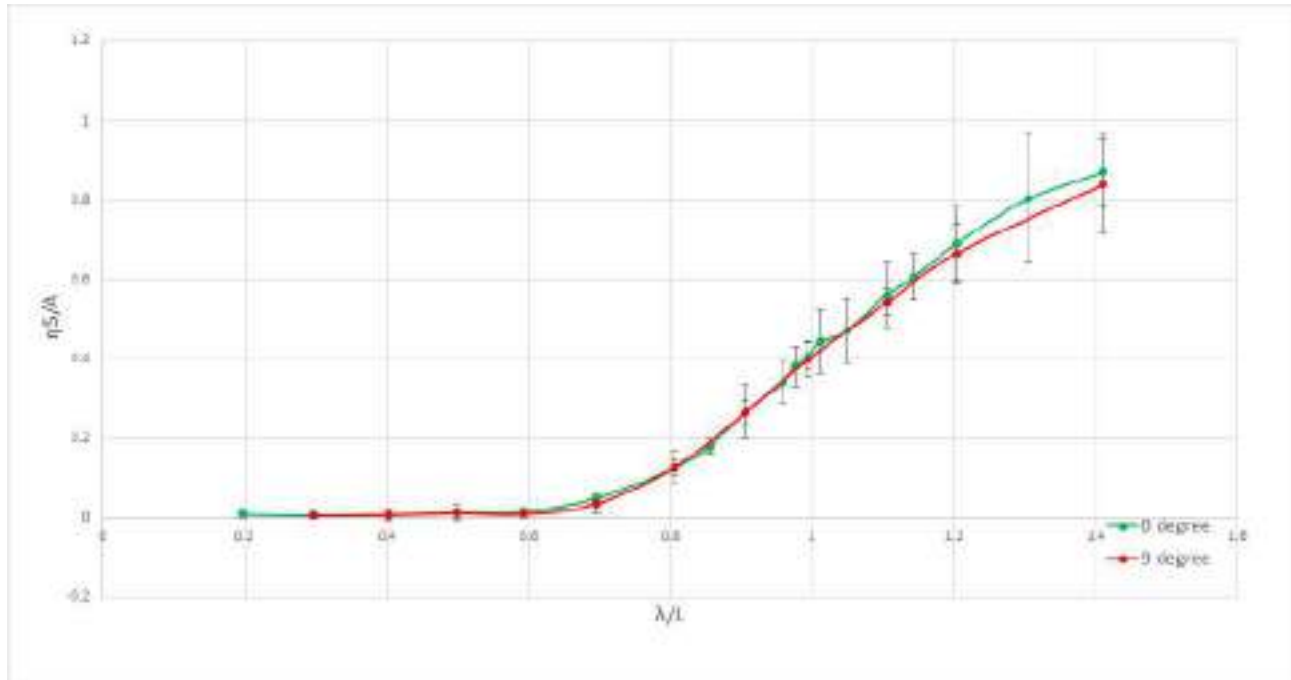


Figure 5.14: Pitch RAO from Experimental results at $F_n=0.179$ for 0° and 9° drift angle

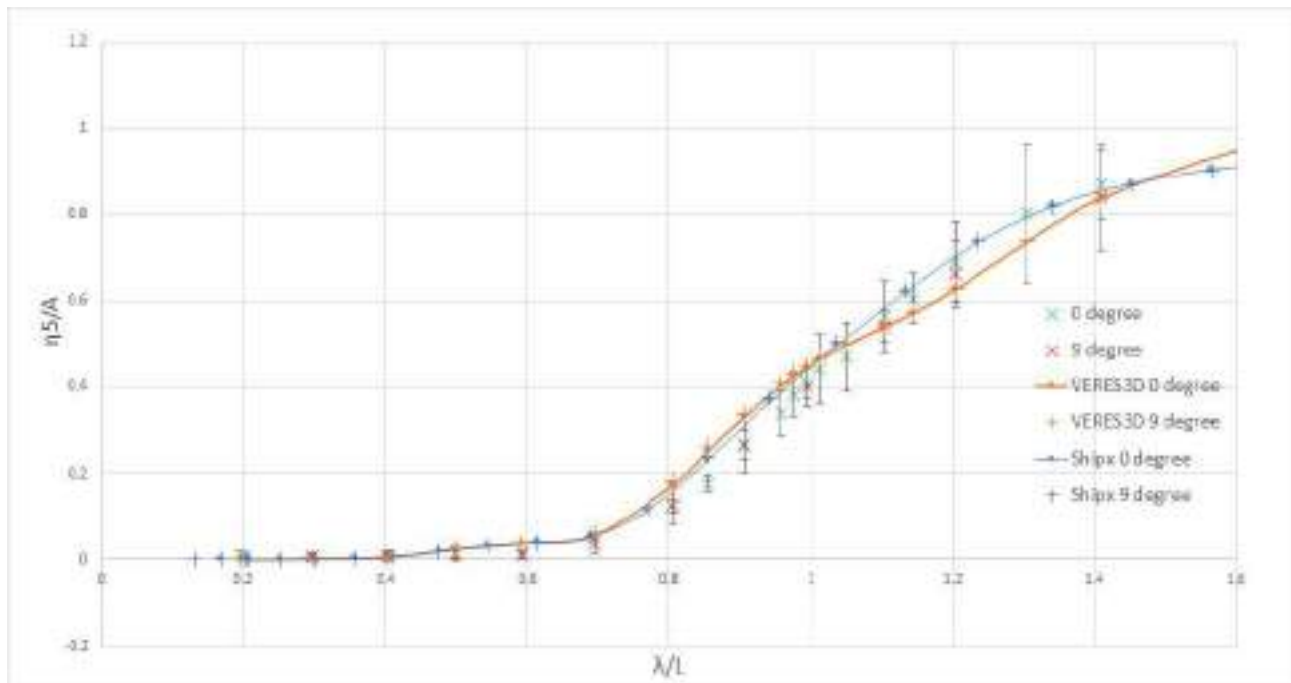


Figure 5.15: Pitch RAO from Numerical values using VERES3D, ShipX(VERES) and Experimental results at $F_n=0.179$ for 0° and 9° drift angle

From the pitch RAO's obtained experimentally (Figure 5.14) and numerically (Figure 5.15) using

two different tools, it is seen that the RAO curves give similar values with and without a drift angle.

Heave and pitch generates the largest waves compared to other motions. Since the heave and pitch RAO exhibit similar values the added resistance is also expected to exhibit similar values with and without drift angle as already seen in the added resistance curve. This strengthens the conclusion that drift angle of 9° does not affect the added resistance.

Mean transverse drift force

The mean transverse drift force F_y measured in the experiment and the results from the numerical code, VERES3D is presented in figure 5.17. Considering 0° drift angle, in the experimental results at shorter waves it is seen that the first data point marked 'A' in the figure shows a largely negative value instead of a value close to zero, it also has a large measurement uncertainty. Based on the general uncertainty of measurements in shorter waves and the measurement uncertainty observed the data point at shorter wavelength can be neglected from the study as a unreliable measurement. From the overall plot for 0° drift angle, it is observed that both the experimental and numerical results point to a approximate zero mean transverse drift as expected. At 9° drift angle the experimental and numerical values are different from each other with significant difference in shorter waves and longer waves. Keeping aside the longer and shorter waves where the uncertainty is higher, the wavelengths in the region $0.5 < \lambda/L < 1.2$ shows a larger sway drift force. In comparison with the tests at $Fn=0$ as illustrated in figure 5.18 it is observed that for experimental values at longer wavelengths ($\lambda/L > 1$) the sway drift forces are almost zero with and without a forward speed. When considering the numerical results, WAMIT also predicts this reduction of added resistance to zero as wavelength increases. As wavelength increases the waves generated by the vessel becomes negligible and correspondingly the mean sway drift force also reduces. VERES3D is exhibiting a larger value in longer wavelengths. VERES3D in general is predicting an unstable curve. At wavelengths $0.4 < \lambda/L < 1$ the experimental values exhibit a mean drift force 2 to 5 times the force for forward speed in comparison to the zero speed sway drift force. WAMIT predicts this curve reasonable well for $Fn=0$, but VERES3D underestimates this mean sway drift force. It is to be verified by test repetition whether the values are large because of experimental uncertainty and therefore a conclusion cannot be made of whether the numerical codes predicted the sway drift force accurately in this range of wavelength. It is to be noted that there was no notable separation effect caused due to the drift angle which would have affected the experimental values as illustrated in figure 5.17.



Figure 5.16: Vessel at $Fn=0.179$ with 0° (left) and 9° (right) drift angles in wavelength corresponding to $\lambda/L = 1.4$. No notable separation is observed.

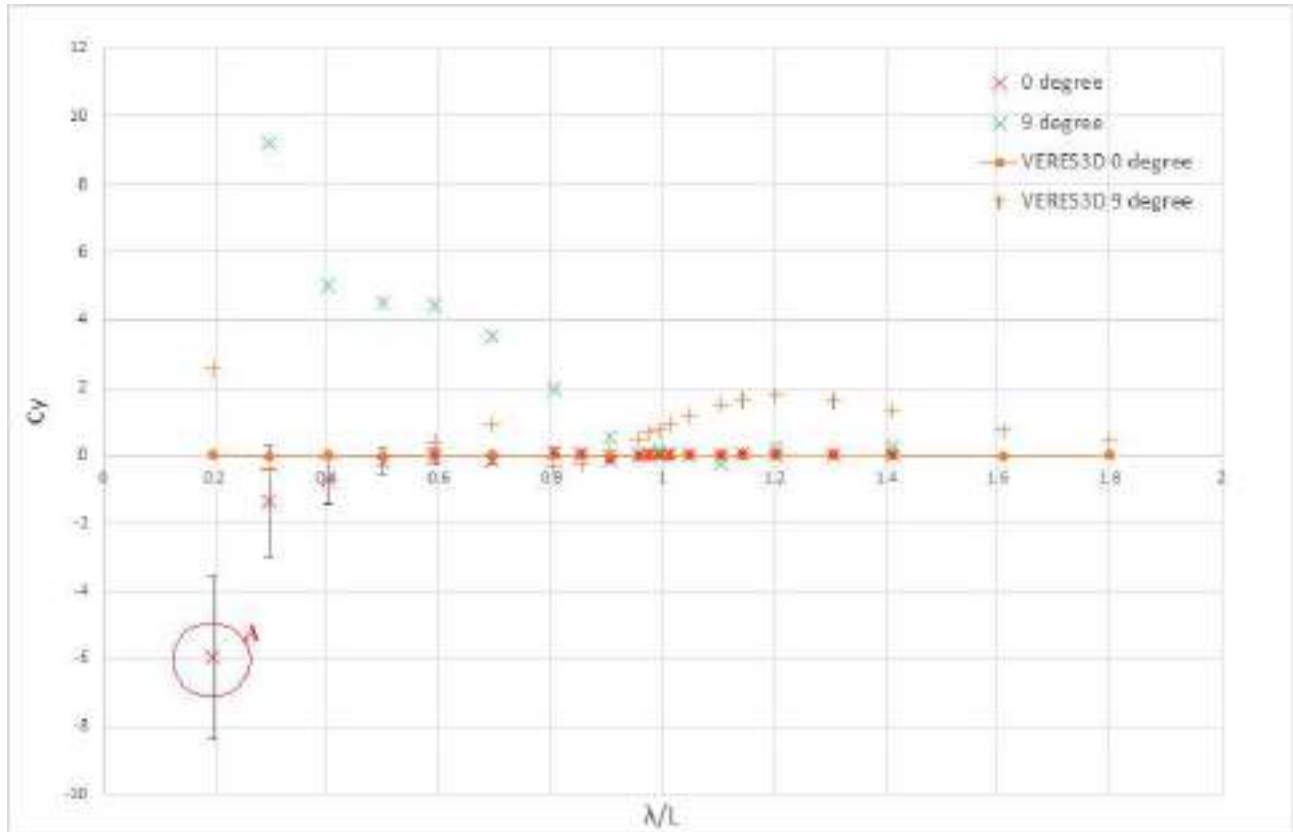


Figure 5.17: Transverse mean drift force curve from Numerical results of VERES3D and Experimental results at $F_n=0.179$ for 0° and 9° drift angle. λ - Wavelength, L - Length between perpendiculars, $C_r = F_y / (\rho g A^2 \frac{B^2}{L_{pp}})$ - non dimensional transverse drift force, F_y - Mean transverse drift force

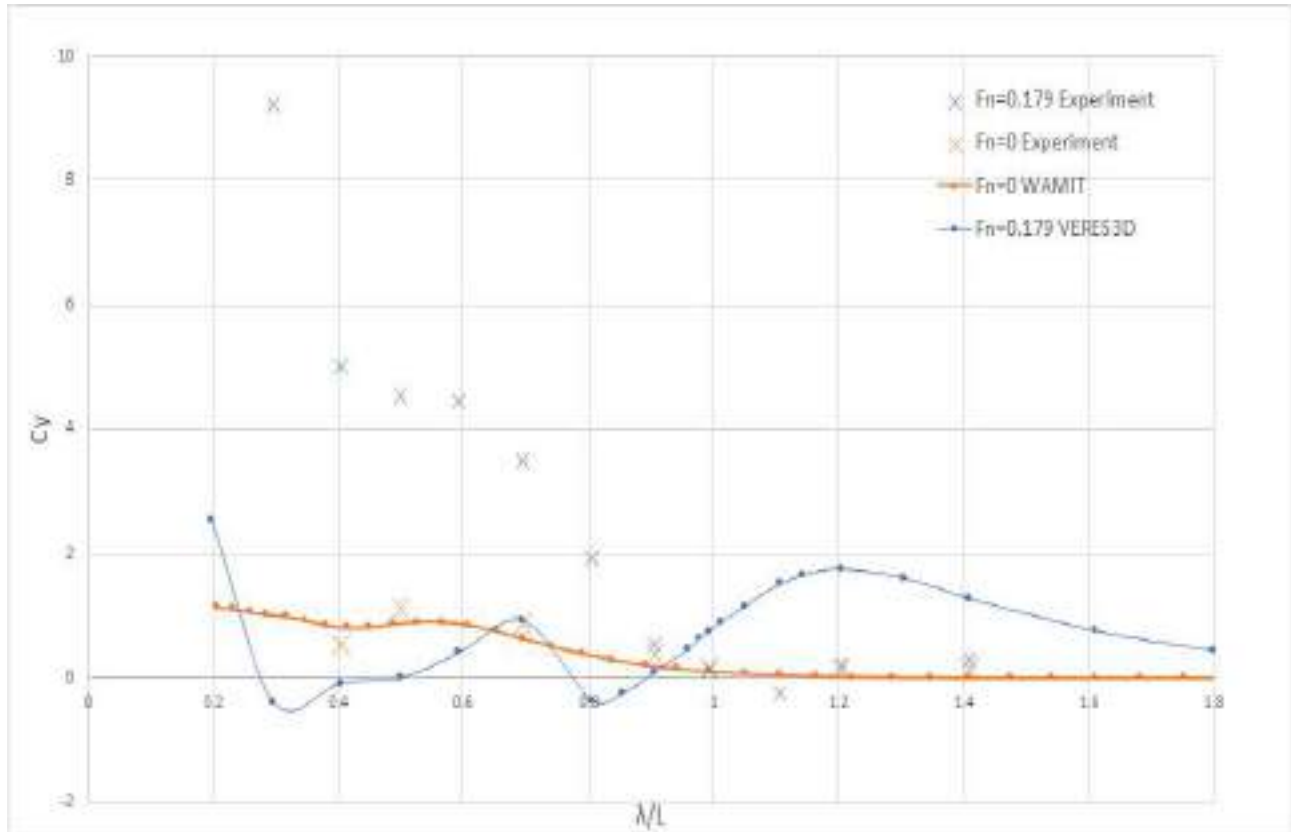


Figure 5.18: Comparison of Transverse mean drift force curve at $F_n=0$ and $F_n=0.179$ with Numerical results from VERES3D for $F_n=0.179$ and WAMIT results for $F_n=0$ and Experimental results at both speeds for 0° and 9° drift angle. λ - Wavelength, L - Length between perpendiculars, $C_r = F_y / (\rho g A^2 \frac{B^2}{L_{pp}})$ - non dimensional transverse drift force, F_y - Mean transverse drift force

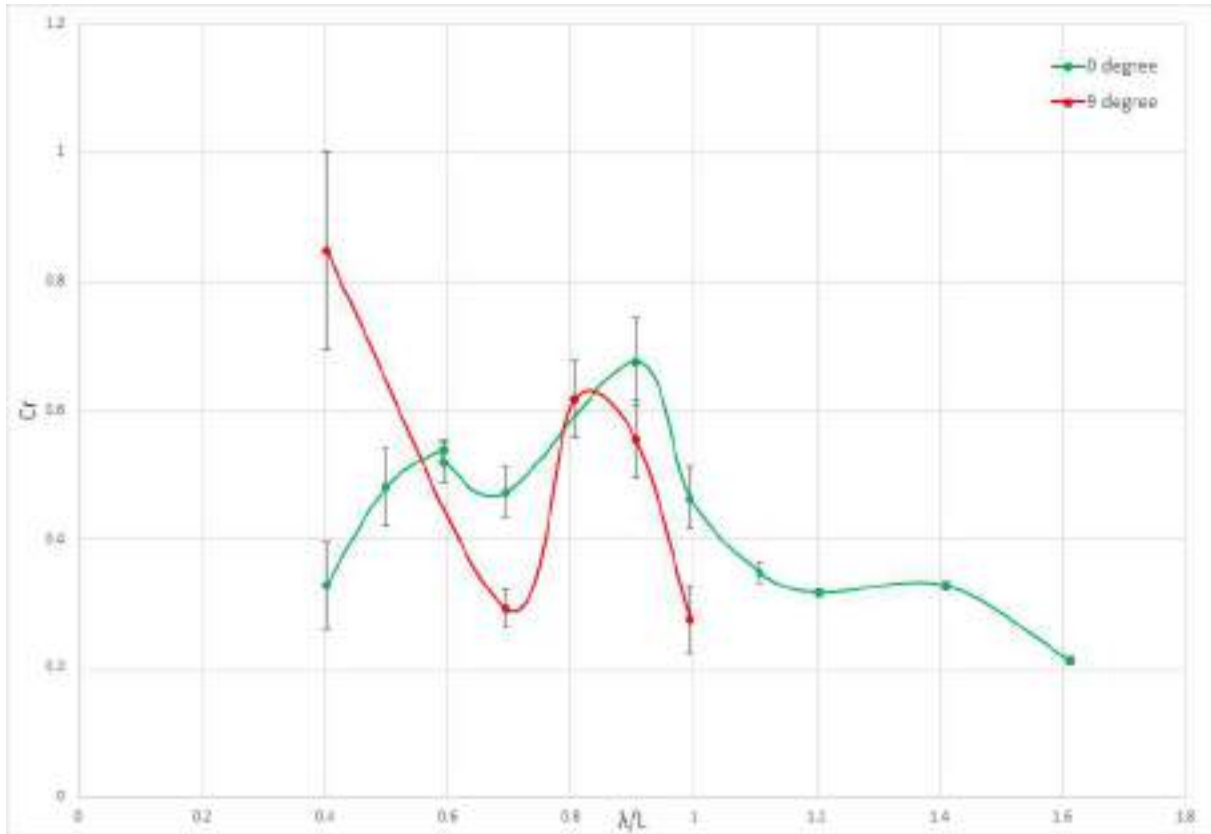


Figure 5.19: Added Resistance curves from Experimental results at $F_n=0.179$ at following sea for 0° and 9° drift angle

3. $F_n=0.179$ Following Sea

Due to lack of time only 5 test runs were completed at a drift angle in following sea condition, out of which only 2 data points are in short wavelengths which exhibit large measurement uncertainty. From figure 5.19 it is observed that the measurement uncertainty is very large for all the data points. The numerical codes contradicts the experimental results which is discussed in section 5.2. Therefore a proper conclusion cannot be made about the effect of drift angle in following sea condition.

5.2 Comparison of methods

This section focuses on comparing the added resistance in waves and ship motion RAO's obtained using various methods used in various tools (WAMIT,VERES,VERES3D). This analysis will provide insight into the capabilities of various codes and methods used in predicting added resistance in waves at various conditions by validating them with the experimental results.

1. $F_n=0$, Drift angle= 0° , 9° , Head Sea

Added Resistance

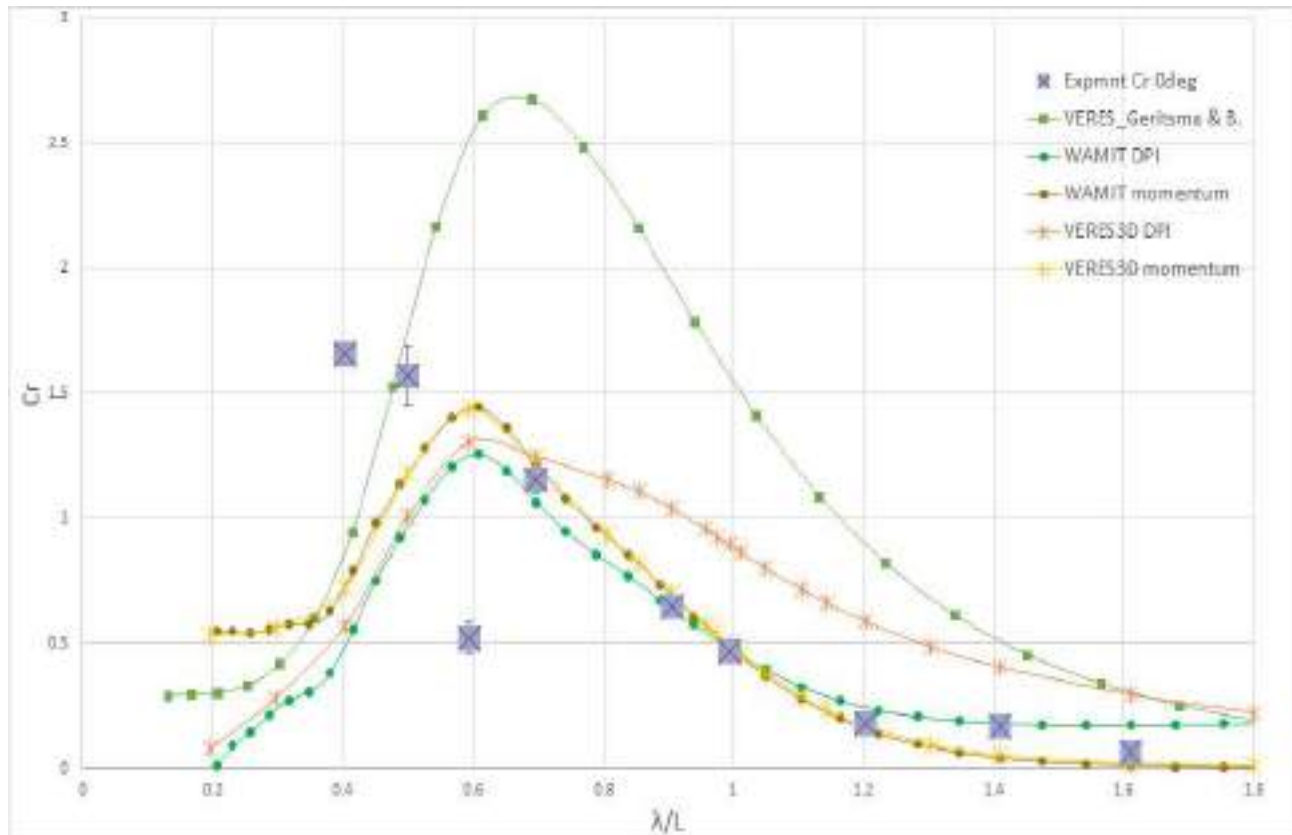


Figure 5.20: Added Resistance curves from Experimental results and Numerical results using WAMIT (3D panel code), ShipX(VERES) (2D panel code using strip theory) and VERES3D (3D panel code) at $F_n=0$, Drift angle= 0° . DPI - Direct pressure integration method, Momentum- Momentum method. λ - Wavelength, L - Length between perpendiculars, $C_r = Ra/(\rho g A^2 \frac{B^2}{L})$ - non dimensional added resistance, Ra - Added resistance

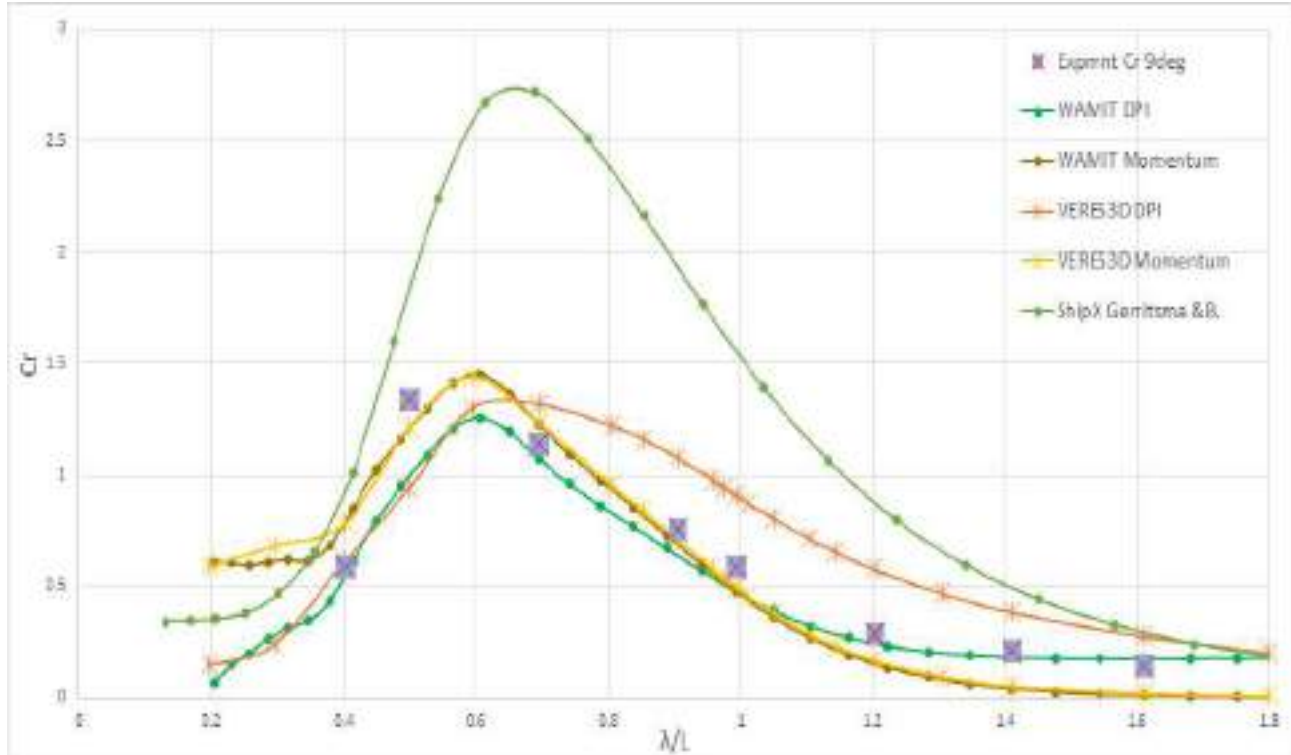


Figure 5.21: Added Resistance curves from Experimental results Numerical results using WAMIT (3D panel code), ShipX(VERES) (2D panel code using strip theory) and VERES3D (3D panel code) at $F_n=0$, Drift angle= 9° . DPI - Direct pressure integration method, Momentum- Momentum method. λ - Wavelength, L - Length between perpendiculars, $C_r = Ra/(\rho g A^2 \frac{B^2}{L})$ - non dimensional added resistance, Ra - Added resistance

Figure 5.20 provides the added resistance curves at $F_n = 0$ in head sea waves with a drift angle of zero degree obtained from the experimental results and numerical results. In general, momentum method using WAMIT and VERES3D predicts the closest value to the experiments. The results from VERES using Gerritsma Beukelman method (Section 2.4.3) to find added resistance, exhibits that numerical results overestimate the added resistance compared to the experimental results. At $\lambda/L > 0.6$ WAMIT and VERES3D predicts the results reasonably well. When using momentum method both the mentioned software packages slightly over estimate the peak value and it is also observed that the peak values predicted by the numerical codes are slightly shifted to lower wavelengths at $\lambda/L \sim 0.6$ compared to the peak obtained from experimental results at $\lambda/L \sim 0.7$. The experimental results at $\lambda/L = 0.6$ has very low value compared to all the numerical results. This is dealt with in section 5.3. It is observed that VERES3D using direct pressure integration overestimate the added resistance at most wavelengths, but using pressure integration method, VERES3D and WAMIT predicts the magnitude of peak value quite well but at a different wavelength. At smaller wavelengths $\lambda/L < 0.5$ there is a significant difference of up to 150% between the numerical and experimental results. As already mentioned in section 2.6 measurements in short wavelengths are difficult to measure accurately due to instability and experimental uncertainty. Therefore, the measurements in this range is believed to have some error. The possibility of wall reflections to affect the results is also to be checked, which is discussed in section . Similar type of observations valid for the zero degree drift angle are also observed for the case when the drift angle is equal to 9° as shown in figure 5.21.

Heave RAO

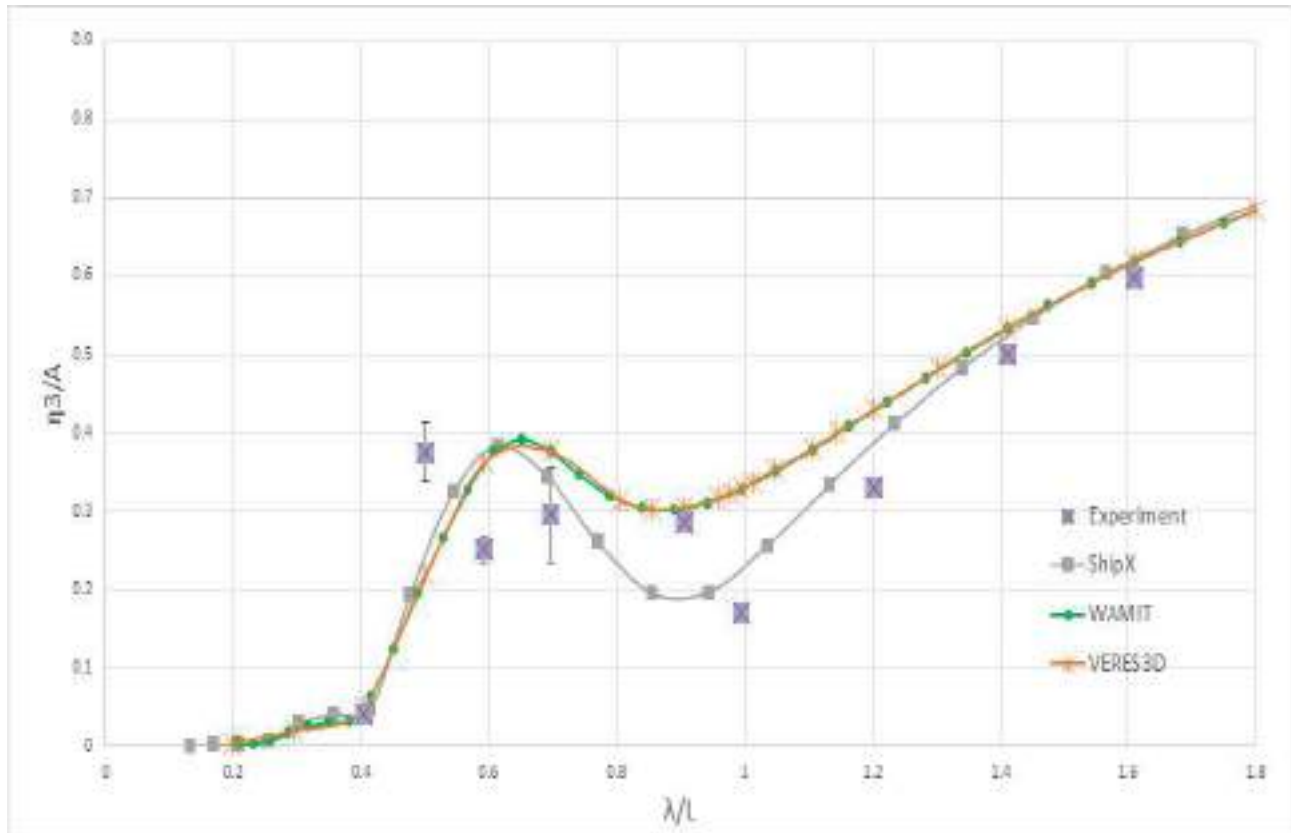


Figure 5.22: Heave RAO from Experimental and Numerical results using WAMIT (3D panel code), ShipX(VERES) (2D panel code using strip theory) and VERES3D (3D panel code) at $F_n=0$, Drift angle= 0° . λ - Wavelength, L - Length between perpendiculars, η_3 - Heave amplitude, A - Wave amplitude

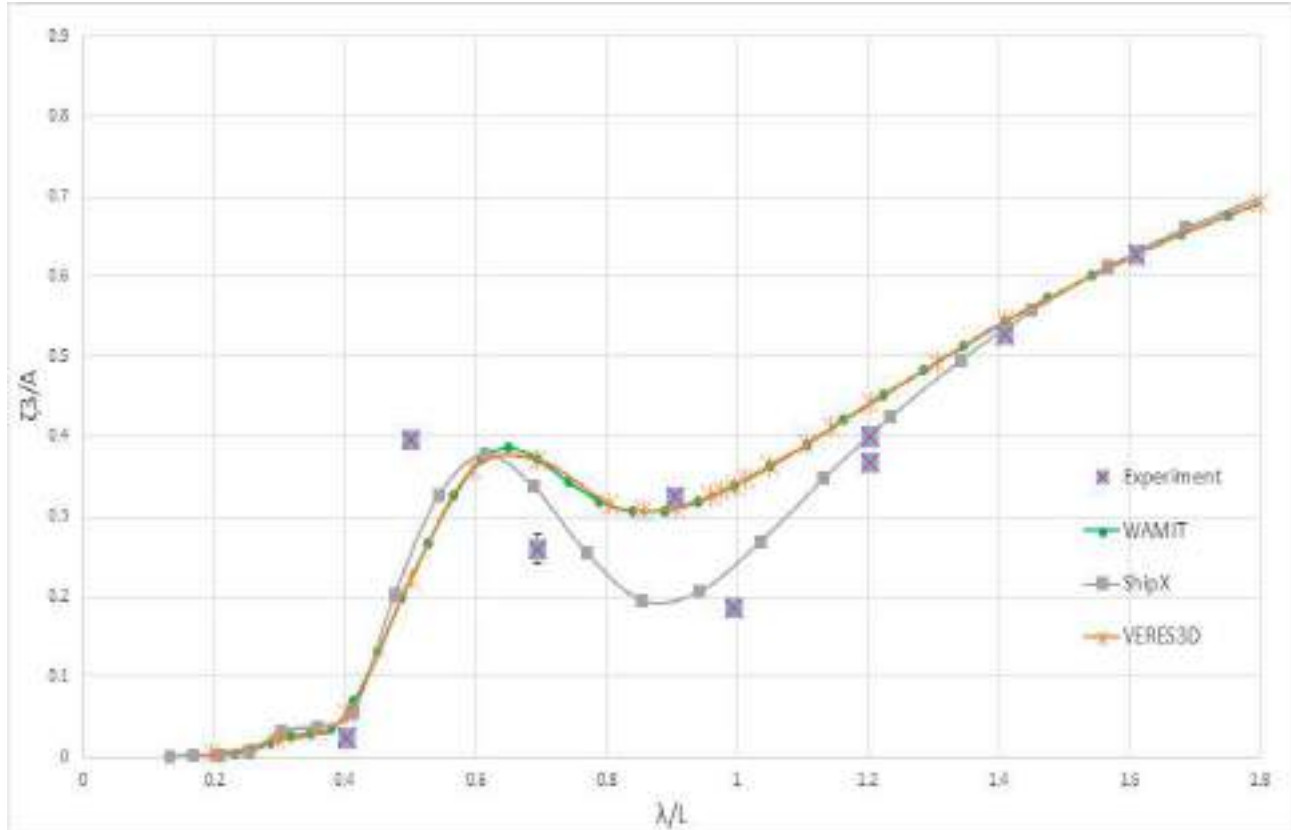


Figure 5.23: Heave RAO from Experimental and Numerical results using WAMIT (3D panel code), ShipX(VERES) (2D panel code using strip theory) and VERES3D (3D panel code) at $F_n=0$, Drift angle= 9° . λ - Wavelength, L - Length between perpendiculars, η_3 - Heave amplitude, A - Wave amplitude

In general the experimental values are a 5% to 20% smaller than the numerical results, especially at non dimensional wavelength $\lambda/L = 1$ where there is a 48% difference between numerical and experimental results. Uncertainty in measurements and negligence of viscous effect by numerical codes contribute to these differences. One of the important observation is that the heave RAO also exhibits a peak near $\lambda/L \sim 0.6$ as in added resistance which shows the relation between wave making capability of the vessel and RAO. The expected peak was at $\lambda/L \sim 1$. Just as in the added resistance curve there is a decrease in value at $\lambda/L = 0.6$ in the experimental values. Strip theory based code, VERES predicts the results quite well. The 3D panel codes VERES3D and WAMIT predicts similar values which is close to the experimental value. The observations for heave RAO is the same as without drift angle for tests with a drift angle of 9° as presented in figure 5.23.

Pitch RAO

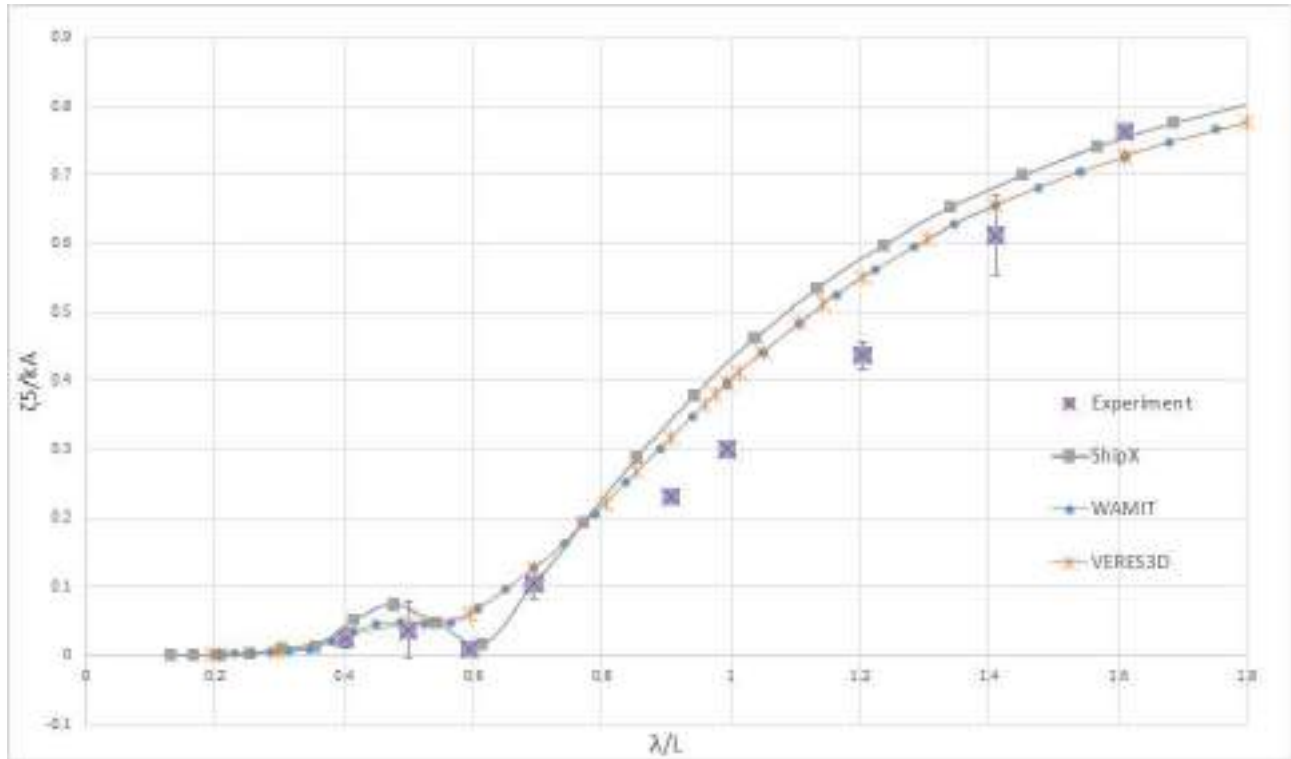


Figure 5.24: Pitch RAO from Experimental results and Numerical results using WAMIT (3D panel code), ShipX(VERES) (2D panel code using strip theory) and VERES3D (3D panel code) at $F_n=0$, Drift angle= 0° . λ - Wavelength, L - Length between perpendiculars, η_5 - Pitch amplitude, k - Wave number, A - Wave amplitude

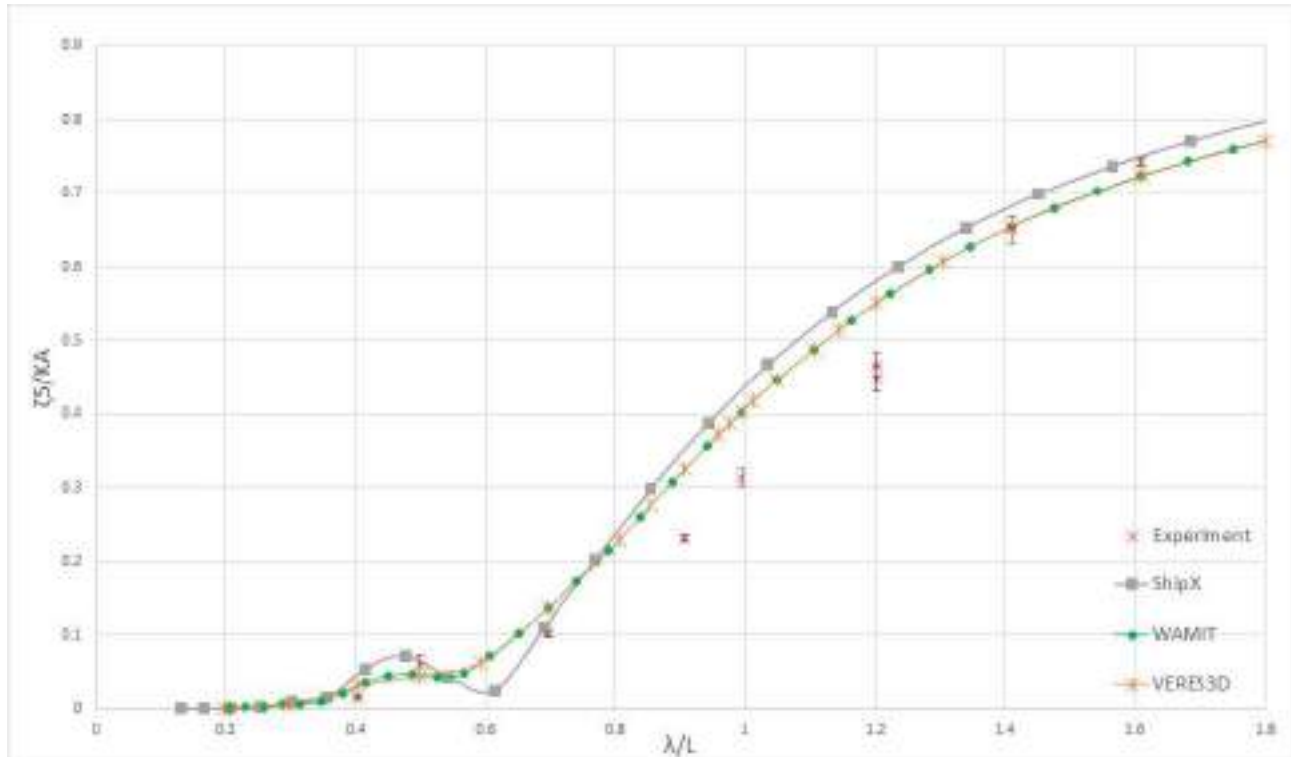


Figure 5.25: Pitch RAO from Experimental results and Numerical results using WAMIT (3D panel code), ShipX(VERES) (2D panel code using strip theory) and VERES3D (3D panel code) at $F_n=0$, Drift angle= 9° . λ - Wavelength, L - Length between perpendiculars, η_5 - Pitch amplitude, k - Wave number, A - Wave amplitude

It is observed that the experimental values are a 5%-15% smaller than the values predicted by the numerical codes. Taking into account possible uncertainty in measurements, it can be pointed out that the numerical codes predict pitch motion similar to the experimental values. A possible reason for smaller experimental values is because of the fact that numerical codes do not consider viscous effects. Repeated tests are recommended to analyse the data more vividly. The observations for Pitch motion RAO is the same as without drift angle for tests with a drift angle of 9° as presented in figure 5.25.

2. $F_n=0.179$, Drift angle= 0° , 9° , Head Sea

Added resistance

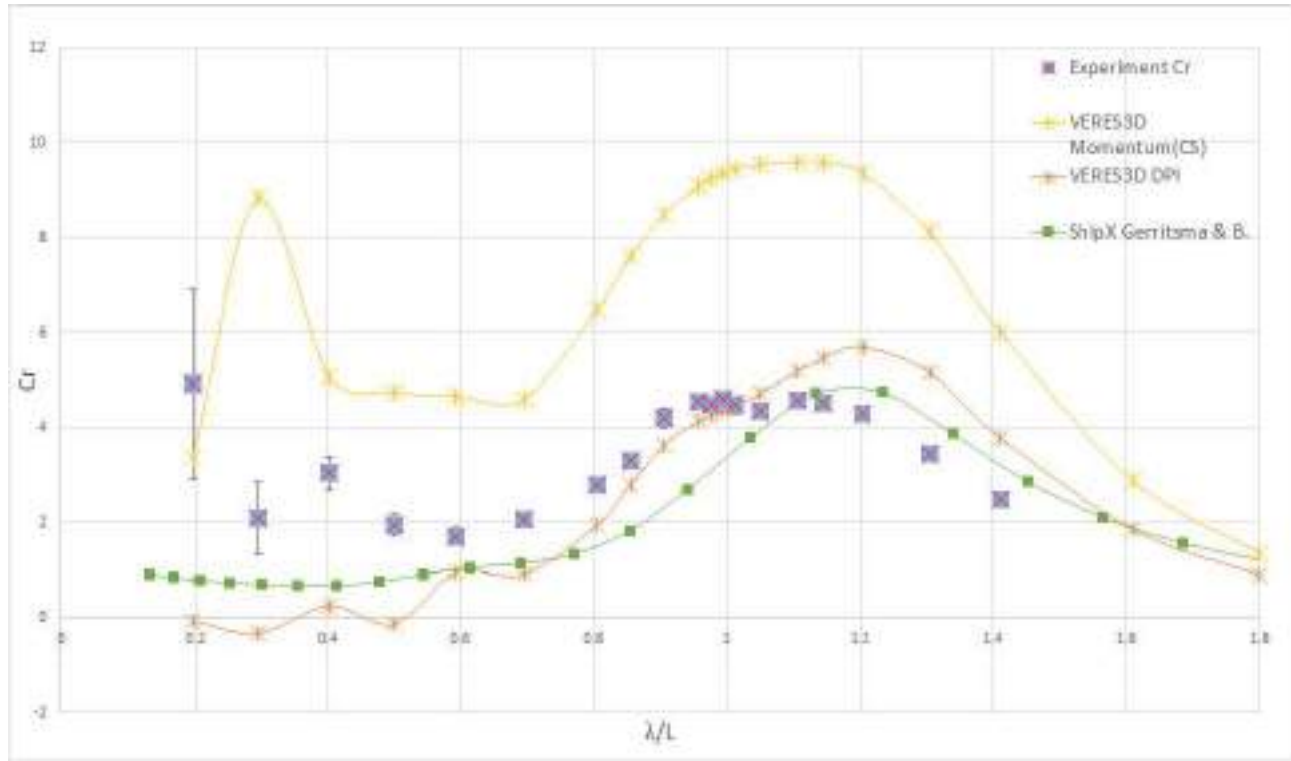


Figure 5.26: Added Resistance curves from Experimental Numerical results using ShipX(VERES) (2D panel code using strip theory) and VERES3D (3D panel code) at $F_n=0.179$, Drift angle= 0° . DPI - Direct pressure integration method, Momentum- Momentum method. λ - Wavelength, L - Length between perpendiculars, $C_r = Ra/(\rho g A^2 \frac{B^2}{L})$ - non dimensional added resistance, Ra - Added resistance

Figure 5.26 provides the added resistance curves at $F_n=0.179$ with 0° drift angle. It is observed that using the momentum method based on the user defined control surface in VERES3D is over estimating the added resistance by 200%. This is clearly an error indicating that the code has not captured the waves generated by the vessel accurately. The 3D panel code (VERES3D) also overestimates the added resistance peak by 20% when using direct pressure integration. The 2D code VERES predicts a peak value close to the measured value in the experiment, But all the numerical codes predict the peak at $\lambda/L \sim 1.2$, where as the experimental peak is located at $\lambda/L = 1.0$. The reason for this shift is not determined. In shorter waves the 3D panel code exhibits unstable values and the experimental values exhibit larger uncertainty. The same observations is made for the results at 9° drift angle illustrated in figure 5.27.

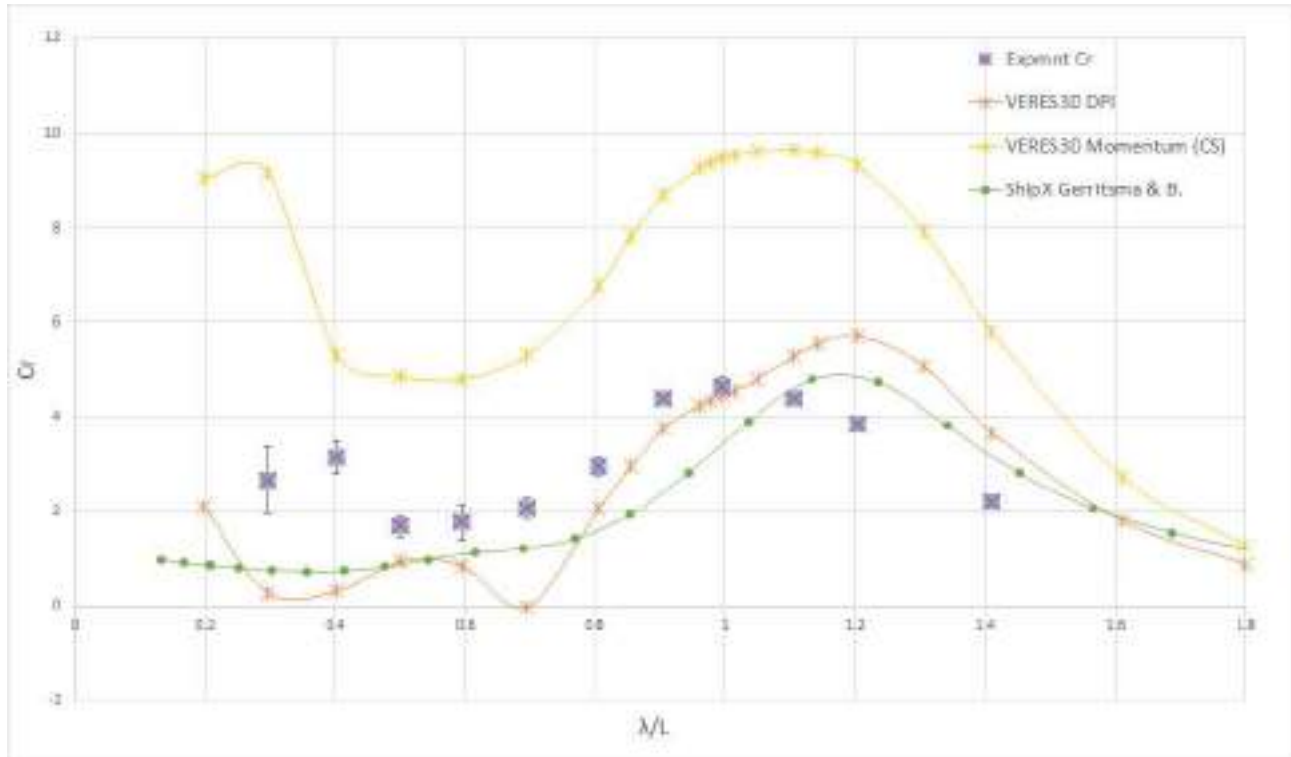


Figure 5.27: Added Resistance curves from Experimental results Numerical results using ShipX(VERES) (2D panel code using strip theory) and VERES3D (3D panel code) at $F_n=0.179$, Drift angle= 9° . DPI - Direct pressure integration method, Momentum- Momentum method. λ - Wavelength, L - Length between perpendiculars, $C_r = Ra/(\rho g A^2 \frac{B^2}{L})$ - non dimensional added resistance, Ra - Added resistance

Heave RAO

Analysing the heave motion RAO in figure 5.28, it is clearly observed that both the numerical software packages used overestimate the heave RAO at the peak (VERES3D by 40% and ShipX by 20%). Both the codes predict the heave RAO with sufficient accuracy for $\lambda/L < 1.2$. This is also observed for the tests with the drift angle illustrated in figure 5.29. One of the contribution for the lower value of heave is the effect of viscosity in the experiment which the codes do not include as they are based on the potential fluid flow theory. But the contribution from viscosity is not expected to contribute to the entire difference. It was also observed that at longer wavelengths the bow was coming out of the water and slamming back into the water with water splashing onto the deck as seen in figure 5.30. Similar slamming motion was also observed in the stern 5.31. Therefore there are other reasons not yet concluded for this difference between numerical and experimental results at non dimensional wavelength $\lambda/L > 1.1$.

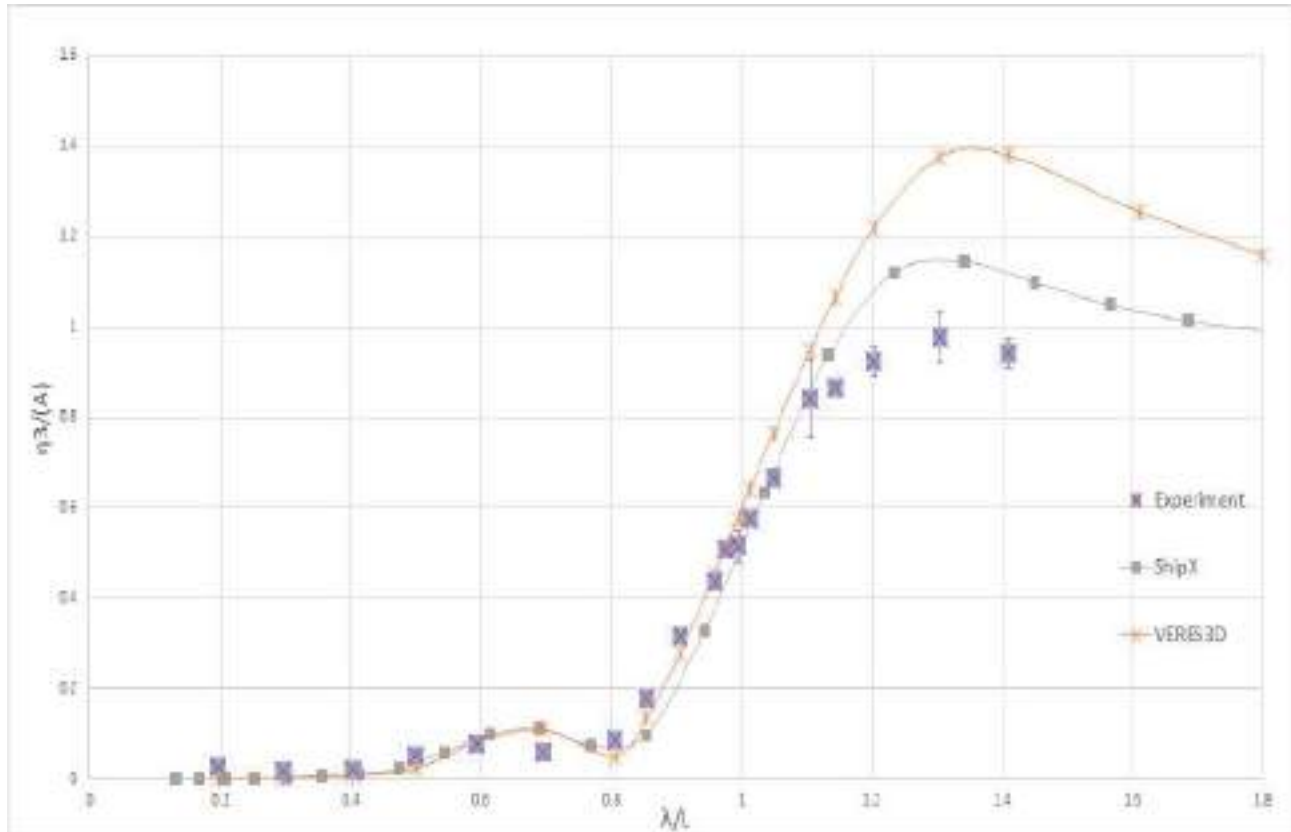


Figure 5.28: Heave RAO from Experimental and Numerical results using ShipX(VERES) (2D panel code using strip theory) and VERES3D (3D panel code) at $Fn = 0.179$, Drift angle= 0° . λ - Wavelength, L - Length between perpendiculars, η_3 - Heave amplitude, A - Wave amplitude

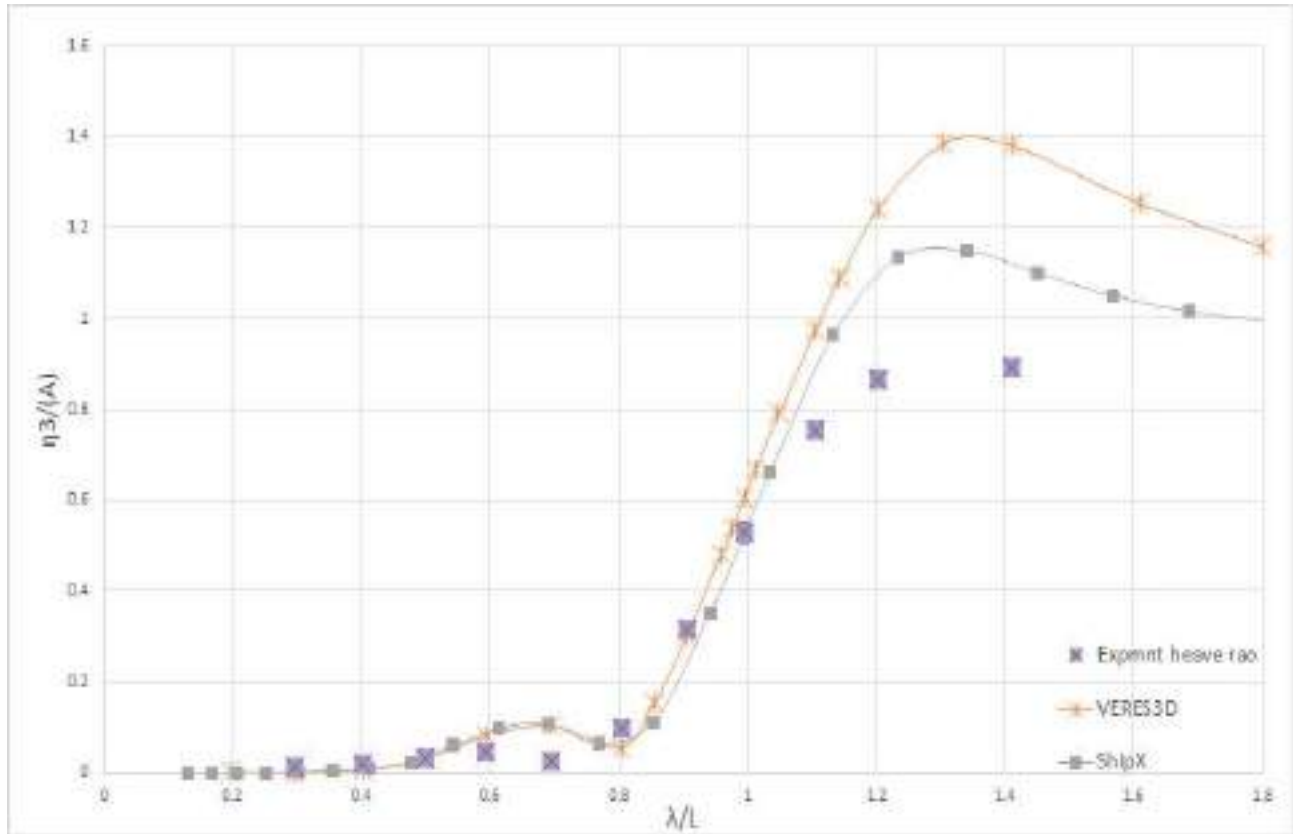


Figure 5.29: Heave RAO from Experimental and Numerical results using ShipX(VERES) (2D panel code using strip theory) and VERES3D (3D panel code) at $F_n = 0.179$, Drift angle= 9° . λ - Wavelength, L - Length between perpendiculars, η_3 - Heave amplitude, A - Wave amplitude



Figure 5.30: Deck slamming observed at $\lambda/L = 1.4$



Figure 5.31: Stern slamming observed at $\lambda/L = 1.4$

Pitch RAO

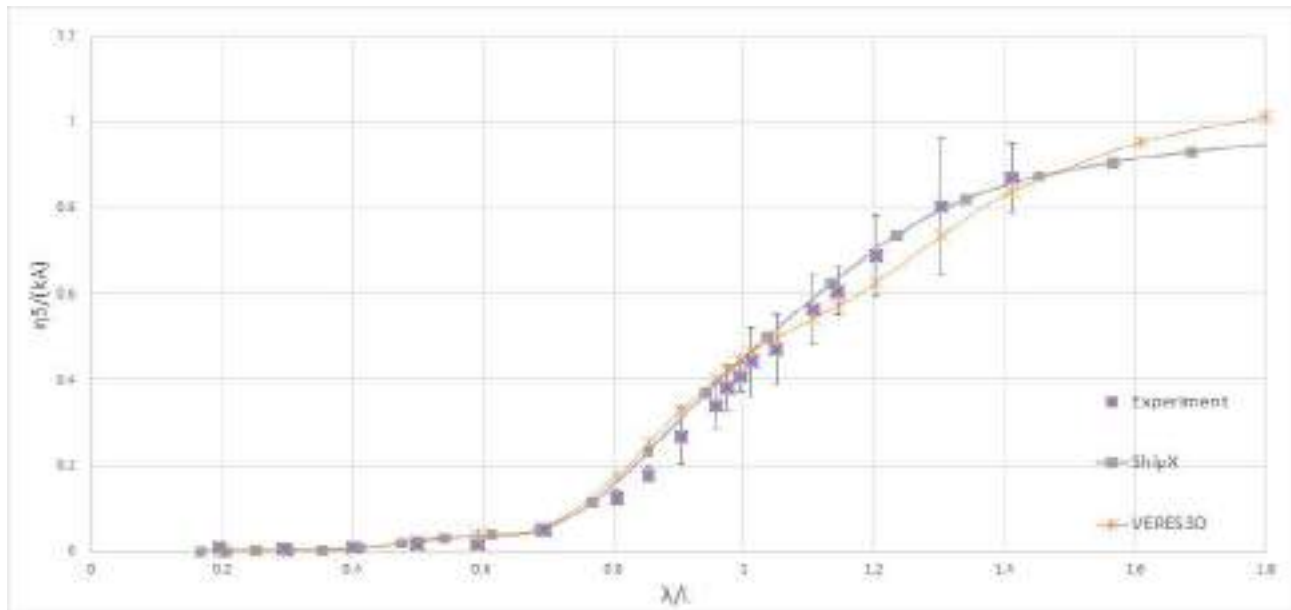


Figure 5.32: Pitch RAO from Experimental results and Numerical results using ShipX(VERES) (2D panel code using strip theory) and VERES3D (3D panel code) at $F_n=0.179$, Drift angle= 0° . λ - Wavelength, L - Length between perpendiculars, η_5 - Pitch Amplitude, k - Wave number, A - Wave amplitude

From figure 5.32 and figure 5.33 it is clear that the pitch motion is well predicted by the codes with and without a drift angle at forward speed in head sea waves. The measurement uncertainty is higher at larger wavelengths.

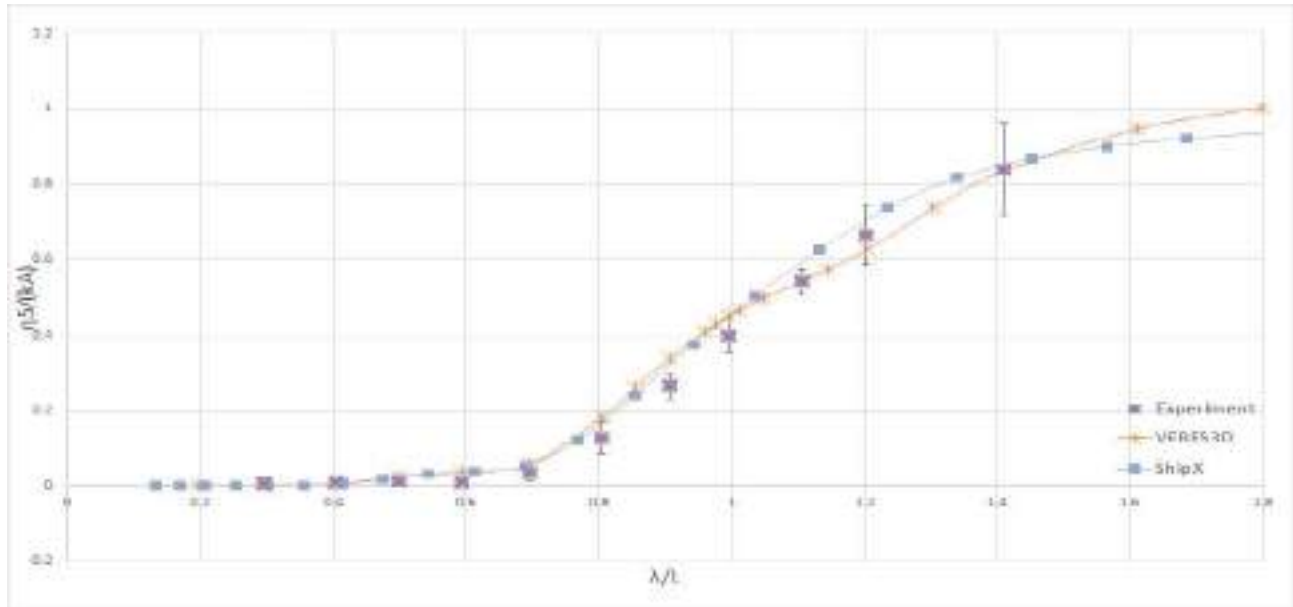


Figure 5.33: Pitch RAO from Experimental results and Numerical results using ShipX(VERES) (2D panel code using strip theory) and VERES3D (3D panel code) at $F_n=0.179$, Drift angle= 9° . λ - Wavelength, L - Length between perpendiculars, η_5 - Pitch amplitude, k - Wave number, A - Wave amplitude

3. $F_n=0.179$, Drift angle= 0° , 9° , Following Sea

Added Resistance

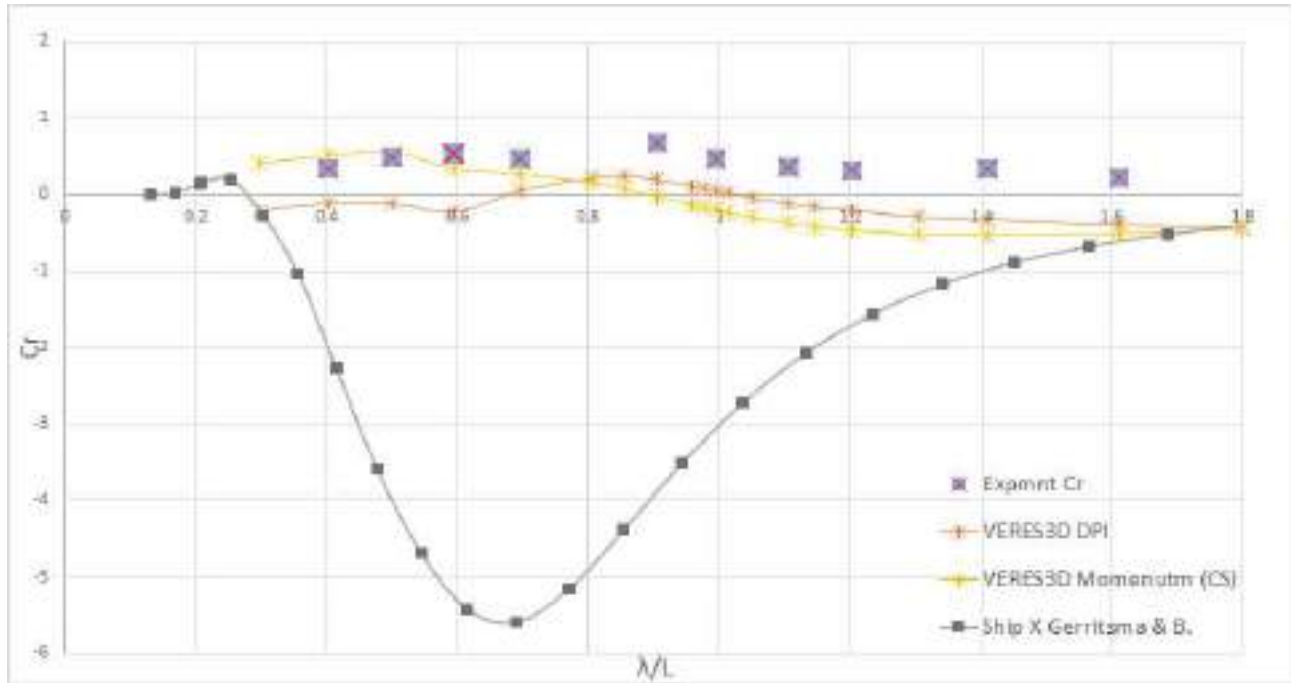


Figure 5.34: Added Resistance curves from Experimental and Numerical results using ShipX(VERES) (2D panel code using strip theory) and VERES3D (3D panel code) at $F_n=0.179$, Drift angle= 0° . DPI - Direct pressure integration method, Momentum (CS)- Momentum method using user defined control surface. λ - Wavelength, L - Length between perpendiculars, $C_r = Ra/(\rho g A^2 \frac{B^2}{L})$ - non dimensional added resistance, Ra - Added resistance

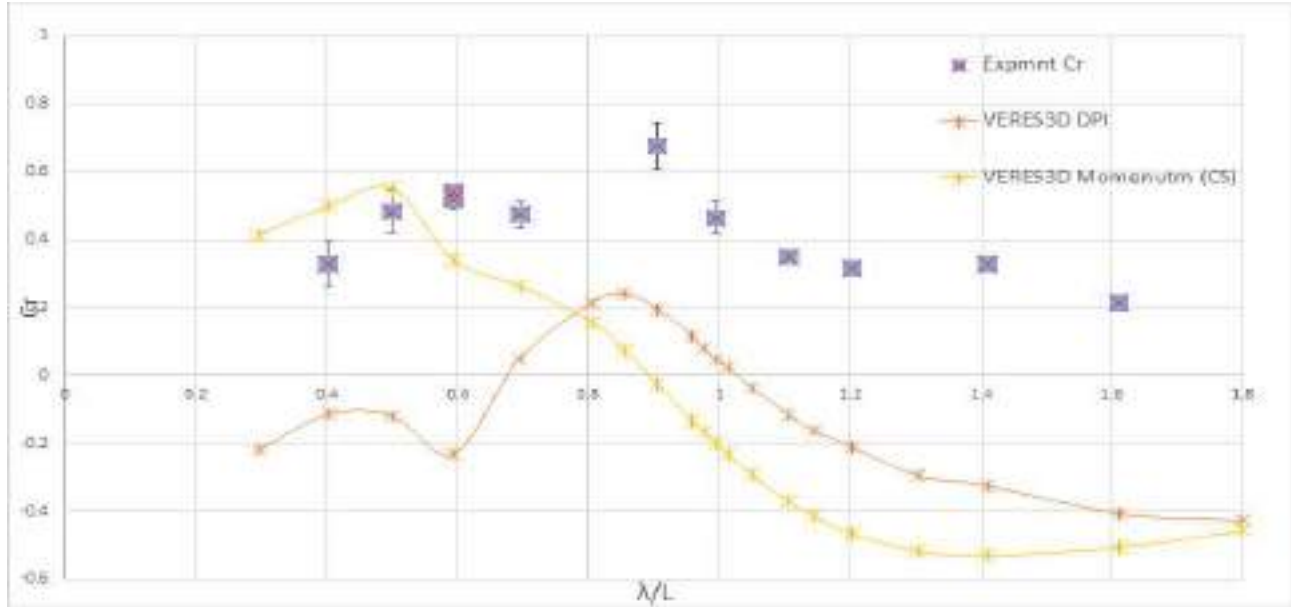


Figure 5.35: Added Resistance curves from Experimental and Numerical results using VERES3D (3D panel code) at $F_n=0.179$, Drift angle= 0° . DPI - Direct pressure integration method, Momentum (CS)- Momentum method using user defined control surface. λ - Wavelength, L - Length between perpendiculars, $C_r = Ra/(\rho g A^2 \frac{B^2}{L})$ - non dimensional added resistance, Ra - Added resistance

Figure 5.34 illustrates the added resistance on the vessel at $F_n=0.179$ in following sea with no drift angle. When it comes to following sea, none of the numerical codes seems to predict added resistance in waves well, in fact in most of the wavelengths the codes predict added thrust. An added thrust implies that the vessel would require very less power to move along in following sea waves, But as seen from the experimental values, this is not the case. It is quite clear from the figure that ShipX (VERES) which uses 2D strip theory, clearly predicts an added thrust instead of an added resistance which contradicts the experimental results. 2D strip theory is a high frequency theory and assumes the vessel is slender. In the case of following sea, the encounter frequency is very low and the vessel is also not strictly slender. Due to these reasons strip theory cannot accurately predict the hydrodynamic coefficients. Methods like Gerritsma and Beukelman method is a far field based method, which is highly dependent on wave induced damping terms for added resistance prediction. The inaccurate hydrodynamic coefficients causes in accurate prediction of radiation forces and hence wrong results for added resistance⁽¹⁾. Focusing more on the other methods illustrated in figure, it is evident that the 3D panel code (VERES3D) also predicts added thrusts in most of the wavelengths, especially in longer wavelengths. The magnitude of peak is smaller by approximately 4-5 times in comparison to added resistance in head sea. The peak measured is also in between $0.9 < \lambda/L < 1$ just as the added resistance in head sea.

The presence of a drift angle of 9° in figure 5.36 and figure 5.37 do not produce significant change and produces the same conclusions as for a 0° drift angle. Due to lack of time only few test runs were done for following sea waves with drift angle.

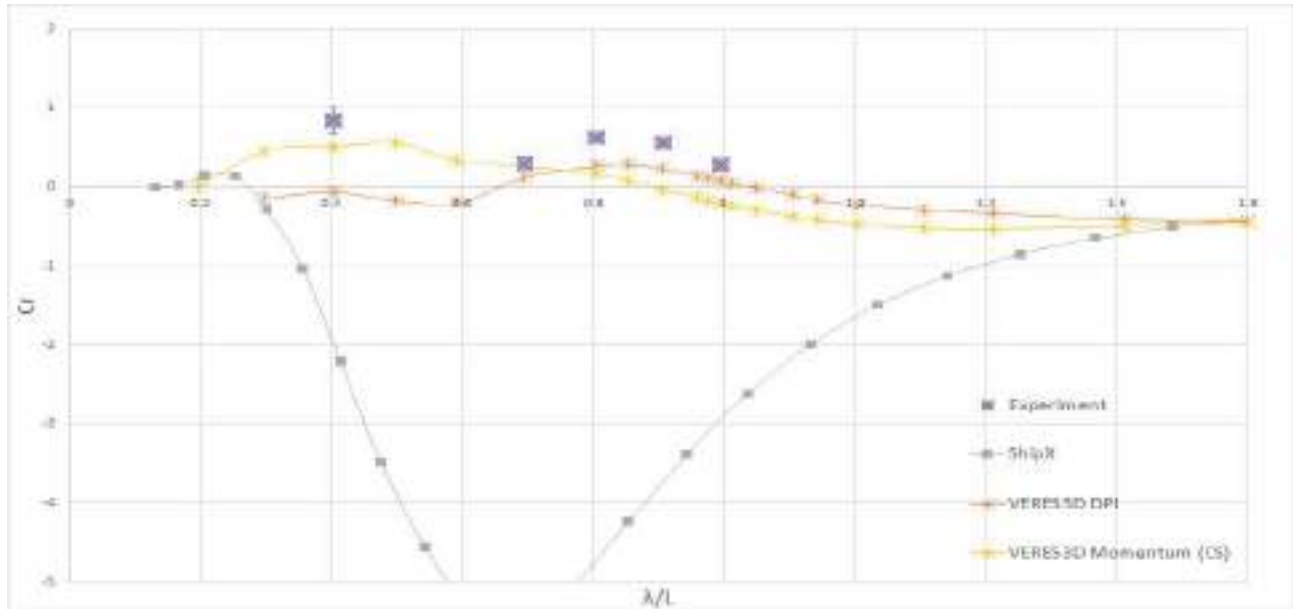


Figure 5.36: Added Resistance curves from Experimental and Numerical results using ShipX(VERES) (2D panel code using strip theory) and VERES3D (3D panel code) at $F_n=0.179$, Drift angle= 9° . DPI - Direct pressure integration method, Momentum (CS)- Momentum method using user defined control surface. λ - Wavelength, L - Length between perpendiculars, $C_r = Ra/(\rho g A^2 \frac{B^2}{L})$ - non dimensional added resistance, Ra - Added resistance

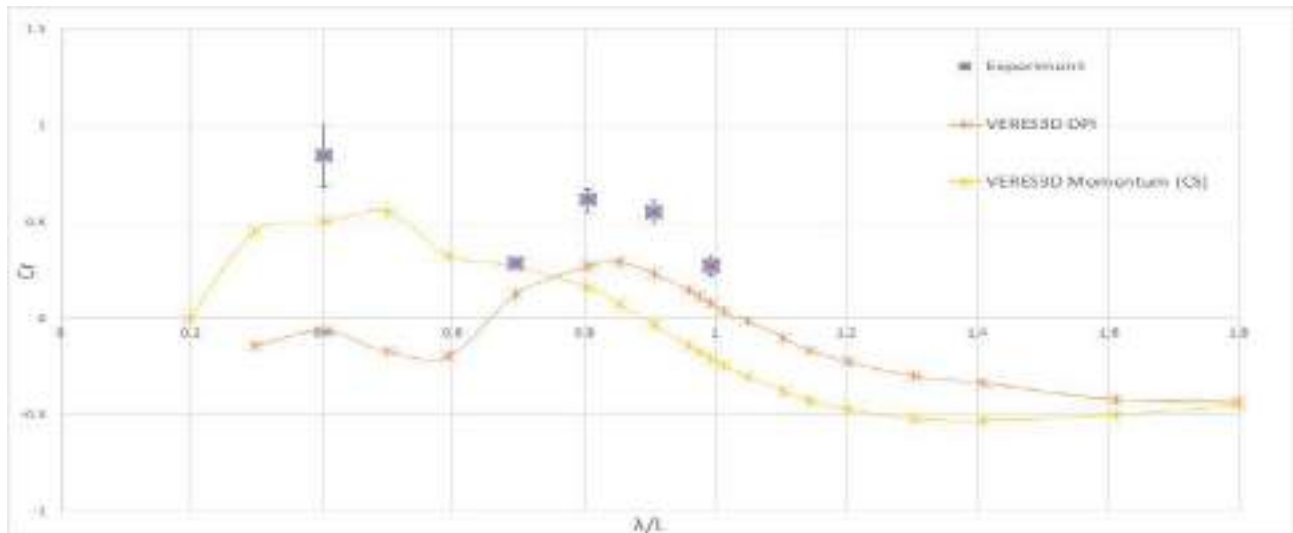


Figure 5.37: Added Resistance curves from Experimental and Numerical results using VERES3D (3D panel code) at $F_n=0.179$, Drift angle= 9° . DPI - Direct pressure integration method, Momentum (CS)- Momentum method using user defined control surface. λ - Wavelength, L - Length between perpendiculars, $C_r = Ra/(\rho g A^2 \frac{B^2}{L})$ - non dimensional added resistance, Ra - Added resistance

Heave RAO

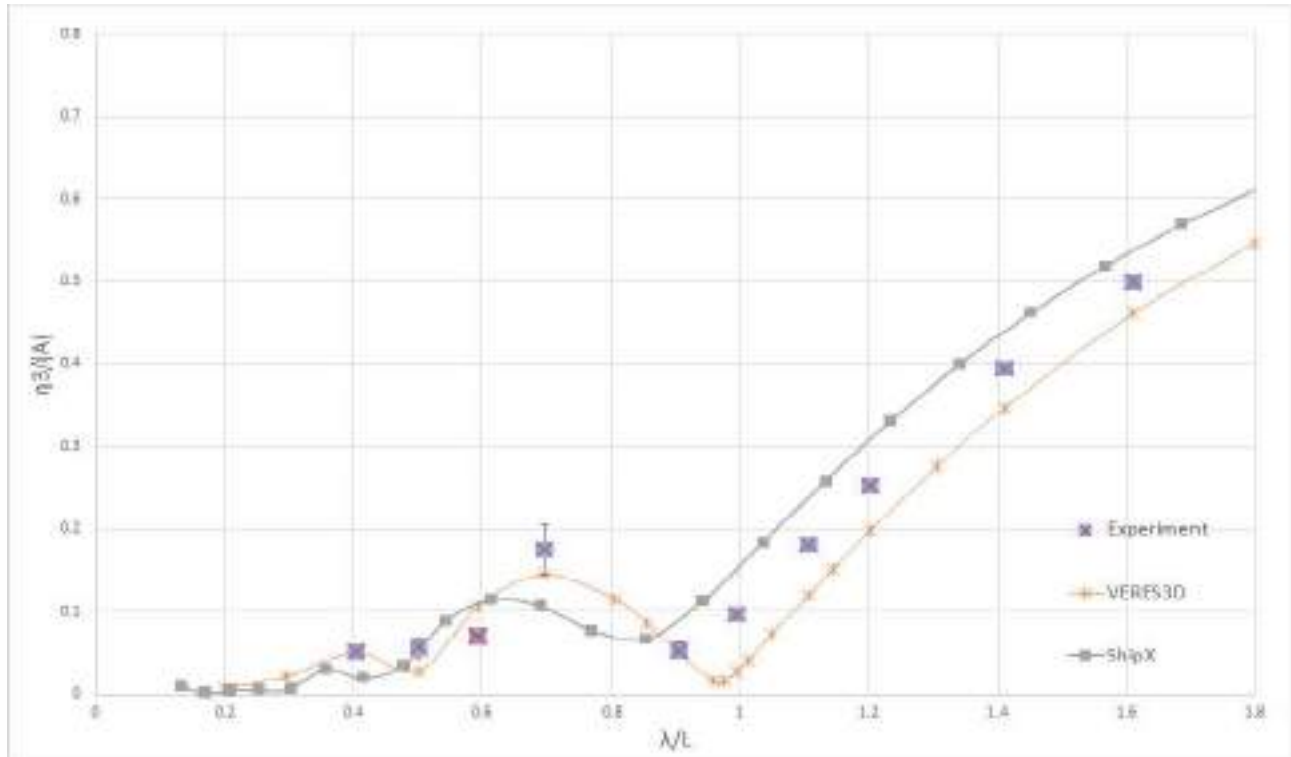


Figure 5.38: Heave motion RAO from Experimental and Numerical results using ShipX(VERES) (2D panel code using strip theory) and VERES3D (3D panel code) at $F_n=0.179$, Drift angle= 0° . λ - Wavelength, L - Length between perpendiculars, η_3 - Heave amplitude, A - Wave amplitude

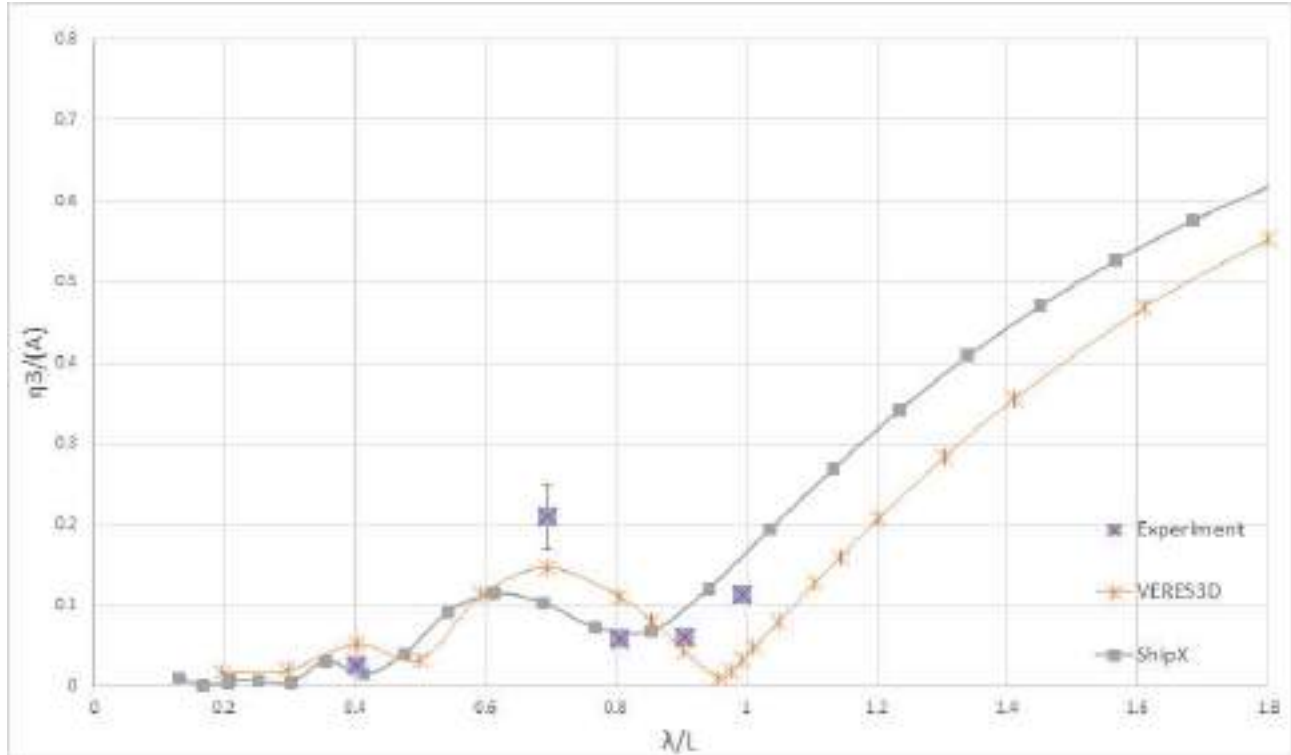


Figure 5.39: Heave RAO from Experimental and Numerical results using ShipX(VERES) (2D panel code using strip theory) and VERES3D (3D panel code) at $F_n=0.179$, Drift angle= 9° . λ - Wavelength, L - Length between perpendiculars, η_3 - Heave amplitude, A - Wave amplitude

When examining the heave RAO for figure 5.38 (drift angle= 0°) and figure 5.39(drift angle= 9°) it is observed that the heave motion in following sea is approximately half the heave motion compared in head sea conditions. The numerical codes predict the experimental values within a 20% difference. ShipX predicts the heave approximately 20% higher and VERES3D predicts it approximately 20% lower. Accounting for the experiment uncertainty due to small motions, it can be concluded that the Shipx (VERES-2D panel code) and VERES3D (3D panel code) fairly predicted the heave motion. Half of the number of wavelengths tested had wave velocities less than the model velocity and half of the waves had wave velocities greater than that of the model. During the experiment based on visual observation, the vessel motions were very small and surfing was not observed.

Pitch RAO

Just as for heave, the pitch motion observed in figure 5.40 and figure 5.41 were approximately half compared to that observed in head sea conditions in figure 5.32. Figure 5.40 and figure 5.41 also illustrates that in general the numerical codes predict a higher pitch motion. VERES3D predicts upto 20% larger pitch motion at $\lambda/L = 1.6$ and ShipX predicts 28.8% larger pitch motions.

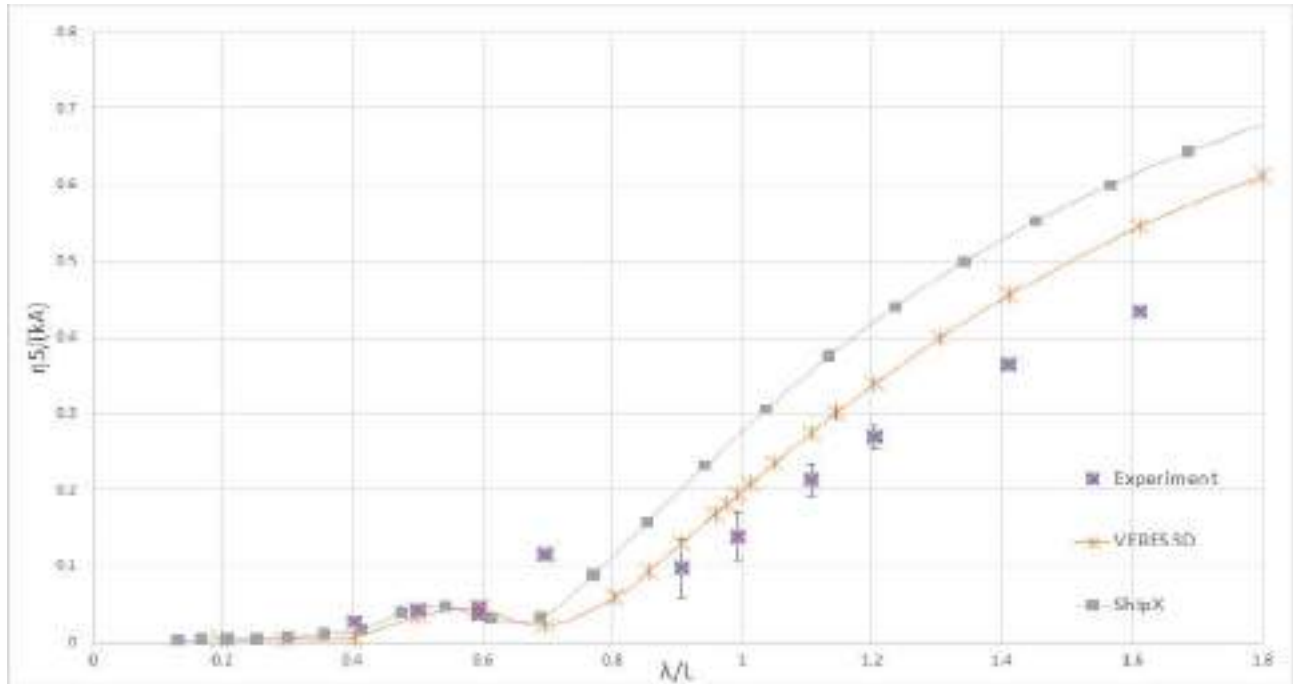


Figure 5.40: Pitch RAO from Experimental and Numerical results using ShipX(VERES) (2D panel code using strip theory) and VERES3D (3D panel code) at $F_n=0.179$, Drift angle= 0° . λ - Wavelength, L - Length between perpendiculars, η_5 - Pitch Amplitude, k - Wave number, A - Wave amplitude

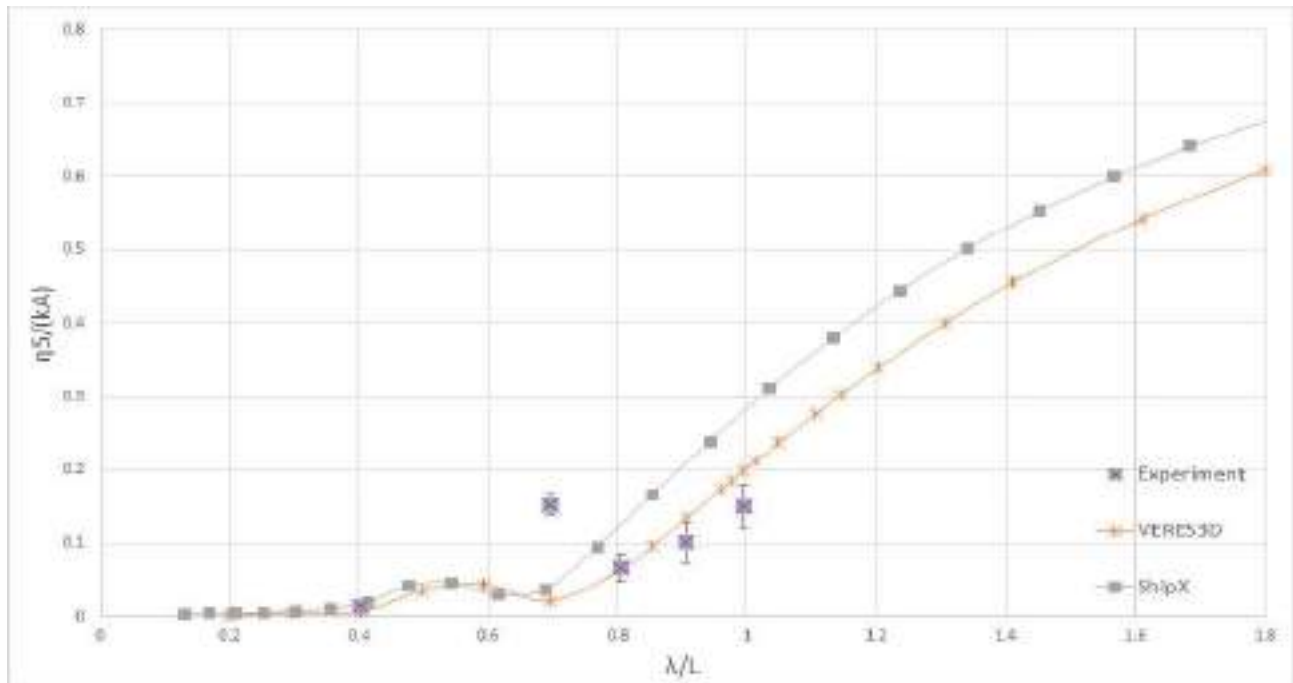


Figure 5.41: Pitch RAO from Experimental and Numerical results using ShipX(VERES) (2D panel code using strip theory) and VERES3D (3D panel code) at $F_n=0.179$, Drift angle= 9° . λ - Wavelength, L - Length between perpendiculars, η_5 - Pitch amplitude, k - Wave number, A - Wave amplitude

5.3 Wall effect

As mentioned in section 3.2.5, during execution of tests at $F_n = 0$ in head sea condition, the model vessel is bound to experience tank wall reflections from both sides. These reflections can affect the results if they are relatively large. If the tank walls are assumed to be perfectly reflecting and the body is symmetric, a wave resonance motion can occur about the center line when the tank width becomes equal to a integer multiple of the wavelength⁽⁵⁹⁾ as in equation 5.1

$$w = n \times \lambda \quad (5.1)$$

where w is the tank width (refer figure 4.4), λ is the incident wavelength used for the test and $n = 1, 2, 3, \dots$

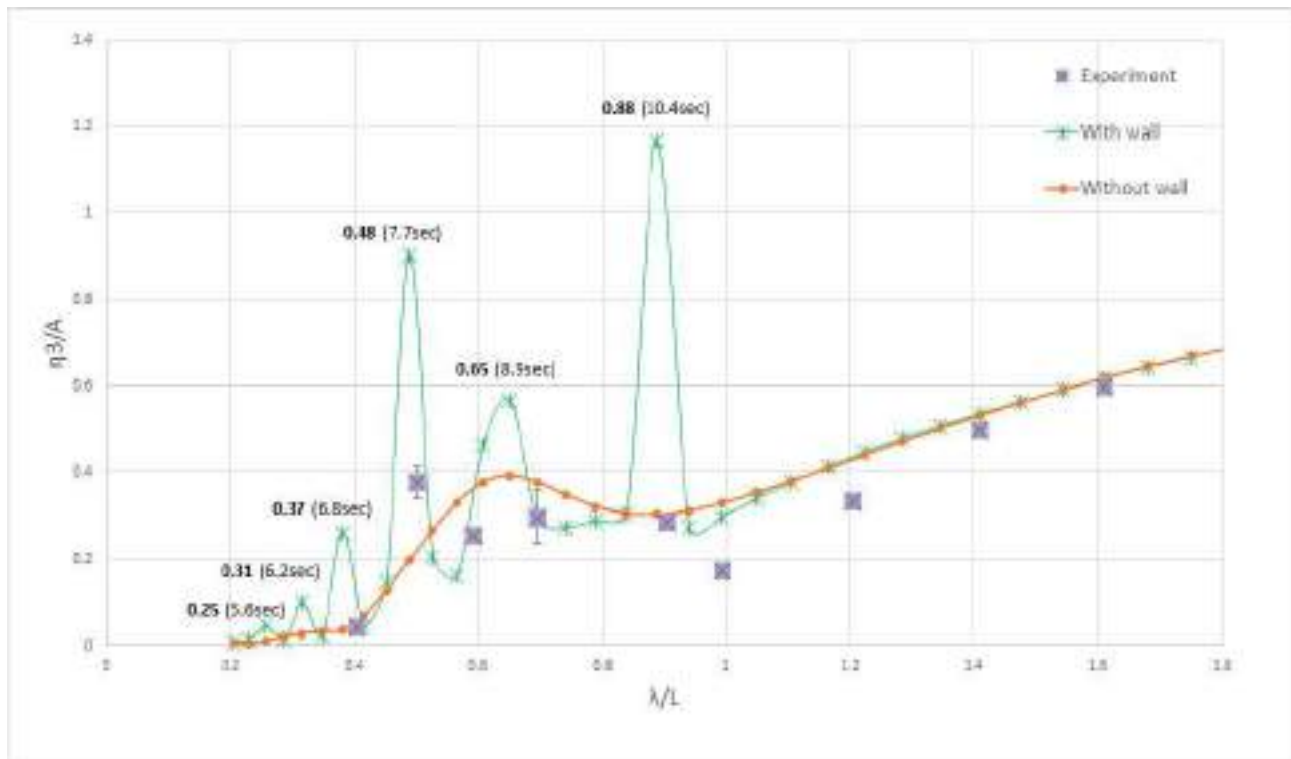


Figure 5.42: Heave RAO from Experimental and Numerical results using WAMIT (3D panel code) with and without wall effect at $F_n = 0$, Drift angle = 0° . λ - Wavelength, L - Length between perpendiculars, η_3 - Heave Amplitude, A - Wave amplitude

Figure 5.42 provides experimental values plotted against the numerical results from WAMIT, with and without tank wall effects. From the numerical results using the wall it is identified that there are significant spikes in the results. These spikes are not seen when we exclude wall effect as seen from the orange curve. At some points for example, at $\lambda/L = 0.88$ where the largest spike is seen, the wavelength (λ) is 168.8m and $2 \times \lambda = 337.7$ m which is close to the full scale tank width of 336. Therefore these spikes in the heave motion RAO is concluded to form due to presence of walls. In the experiment these spikes are not clearly visible as the effects that occur due to wave resonance

are too small to cause significantly large heave motions. In the pitch motion RAO (Figure 5.43) some of the spikes are visible at the same values of λ/L .

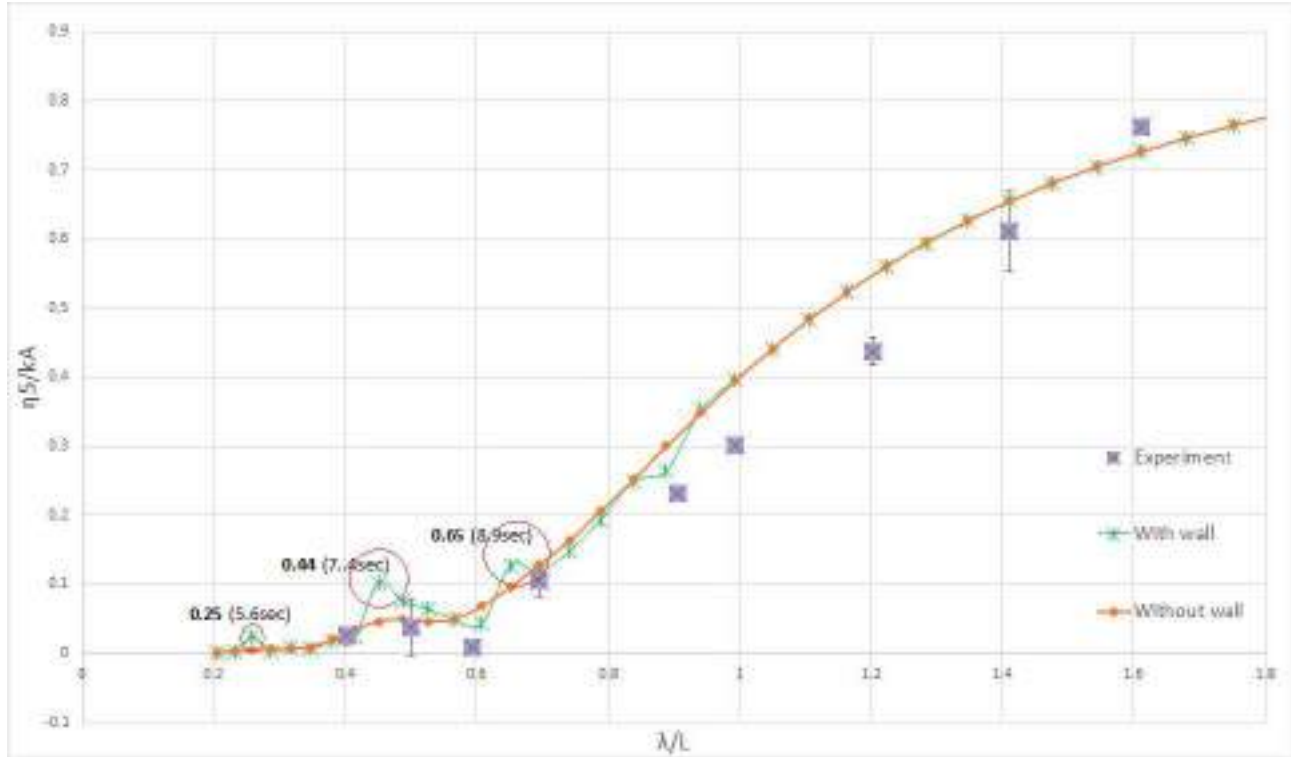


Figure 5.43: Pitch RAO from Experimental results and Numerical results using WAMIT (3D panel code) with and without wall effect at $F_n=0$, Drift angle= 0° . λ - Wavelength, L - Length between perpendiculars, η_5 - Pitch Amplitude, A - Wave amplitude

Analysing the added resistance curve in figure 5.44 for the same test conditions, it is seen that the points marked 'A', 'B', 'C' and 'D' correspond to the spikes seen in heave RAO. At point 'A' 'B' and 'C' there are spike in added resistance results and at point 'D' there is decrease in added resistance. Analysing the experimental values it can be seen that the points follow the same trend as predicted by the code (WAMIT). Due to large uncertainty of measurement the experimental value corresponding to $\lambda/L = 0.4$ may or may not be due to wall effect. For other data points it is seen that the experimental values correspond to the numerical values, especially for the point at $\lambda/L = 0.6$. The added resistance measured at $\lambda/L = 0.6$ was exhibiting an unusual dip in the added resistance curve. Since the numerical code predicts the dip at the exact same point that corresponds to a wavelength that create wave resonance effect, it can be concluded that the major contribution for the decrease in added resistance at $\lambda/L = 0.6$ is the hydrodynamic interaction between the body and the tank wall. It was also observed that the numerical analysis using wall effect predicted the added resistance gradually goes to zero in longer wavelengths, where as analysis without wall effect did not show such behaviour.

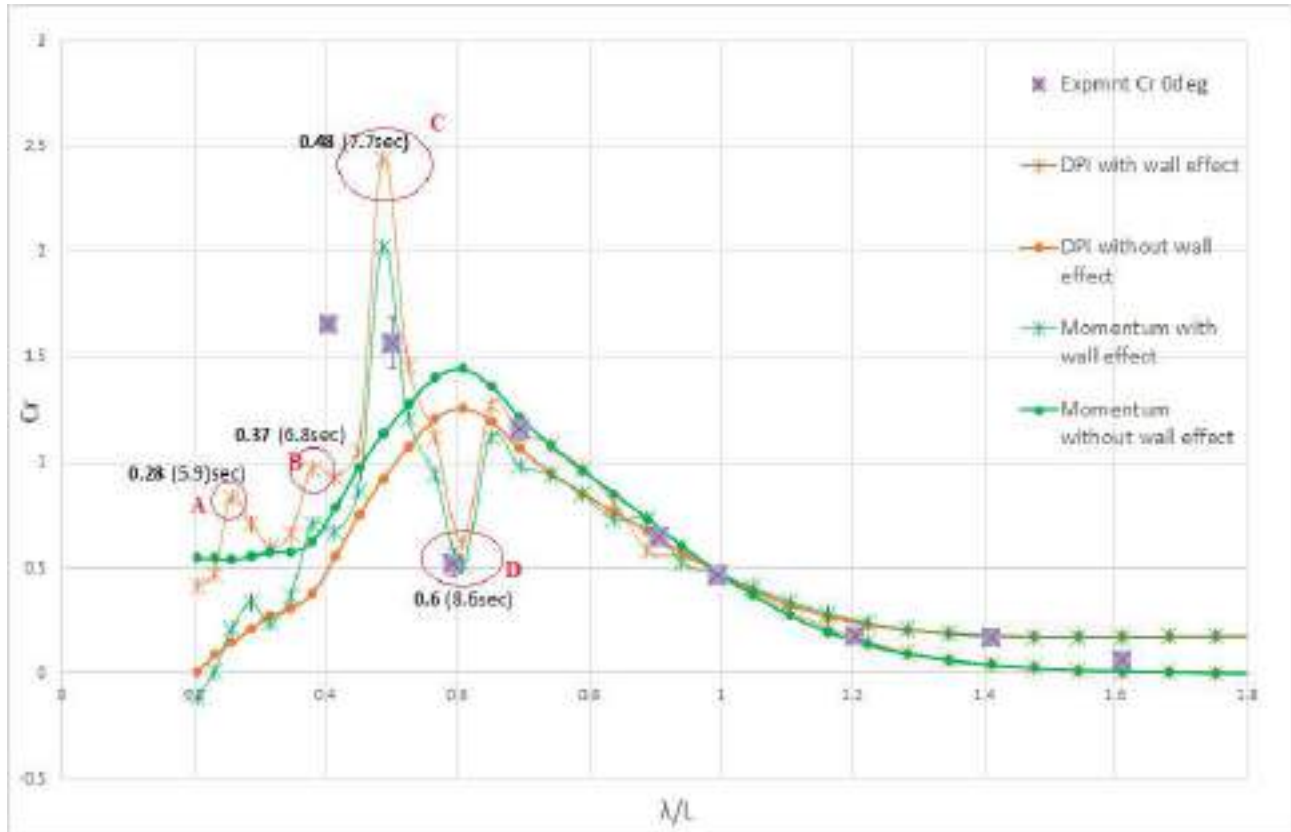


Figure 5.44: Added Resistance curves from Experimental and Numerical results using WAMIT(3D panel code) with and without wall effect at $F_n=0$, Drift angle= 0° . DPI - Direct pressure integration method, Momentum- Momentum method. λ - Wavelength, L - Length between perpendiculars, $C_r = Ra/(\rho g A^2 \frac{B^2}{L})$ - non dimensional added resistance, Ra - Added resistance

5.4 Asymptotic formula

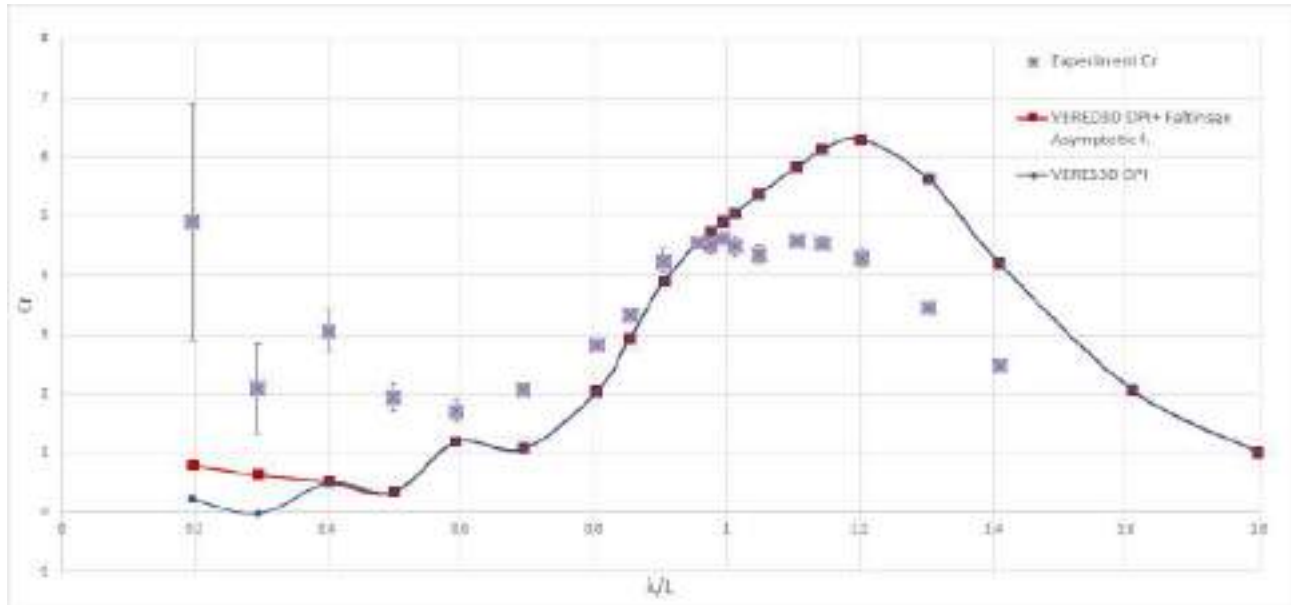


Figure 5.45: Added Resistance curves from Experimental results and Numerical results using VERES3D (3D panel code) at $F_n = 0.179$, Drift angle= 0° using Direct pressure integration alone and combined with results using Faltinsen's asymptotic formula(Refer 2.6). DPI - Direct pressure integration method. λ - Wavelength, L - Length between perpendiculars, $C_r = Ra/(\rho g A^2 \frac{B^2}{L})$ - non dimensional added resistance, Ra - Added resistance

The added resistance curve in figure 5.45 is made from combining the added resistance found using Faltinsen's asymptotic formula for added resistance in short waves (refer section 2.6.1) until $\lambda/L = 0.4$ and direct pressure integration results for $\lambda/L > 0.4$. It is observed that Faltinsen's formula predicts a higher value compared to the results from using the direct pressure integration results alone. Since the experimental results exhibit large uncertainty in the this range of wavelengths, it is not possible to arrive at a proper conclusion whether the numerical results predict the added resistance accurately in this study.

5.5 Convergence Test

This section analyses the change in first order heave and pitch motions and added resistance in waves in head sea condition with increasing number of panels in the panel model used for numerical analysis.

1.WAMIT

Added Resistance

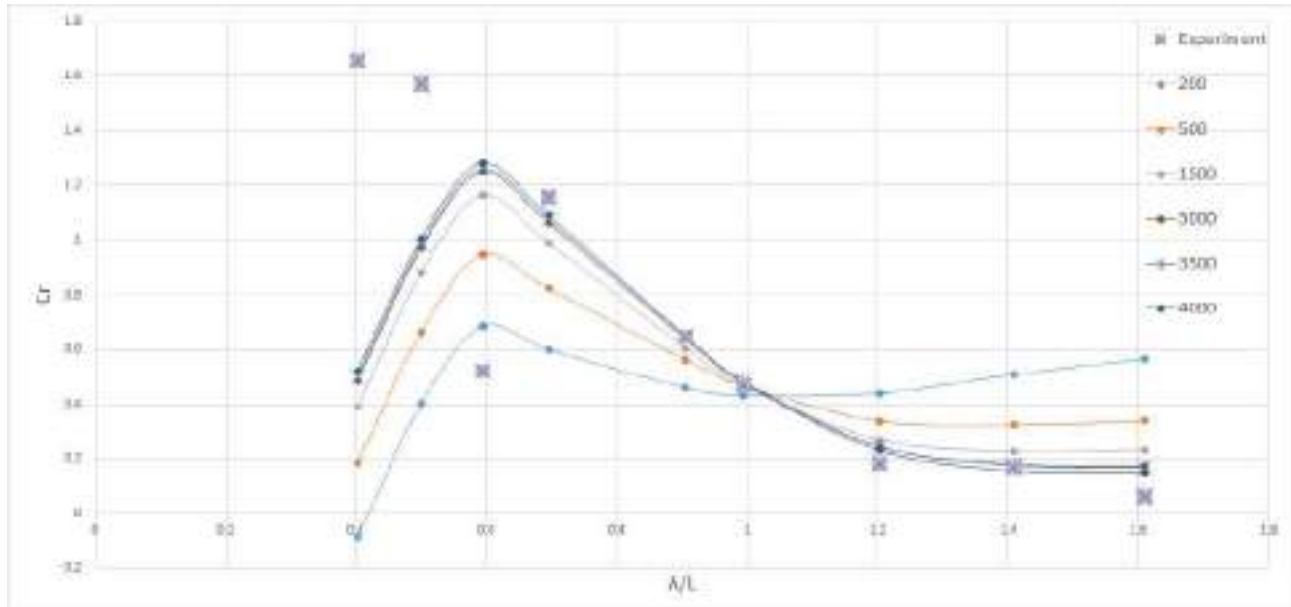


Figure 5.46: Convergence test for Added Resistance curve using results from WAMIT (3D panel code) at $F_n=0$, Drift angle= 0° . The added resistance curves were obtained using direct pressure integration. The increasing number of panels in the legend represents the approximate number of panels in the geometry used for obtaining the corresponding curve λ - Wavelength, L - Length between perpendiculars, $C_r = Ra/(\rho g A^2 \frac{B^2}{L})$ - non dimensional added resistance, Ra - Added resistance.

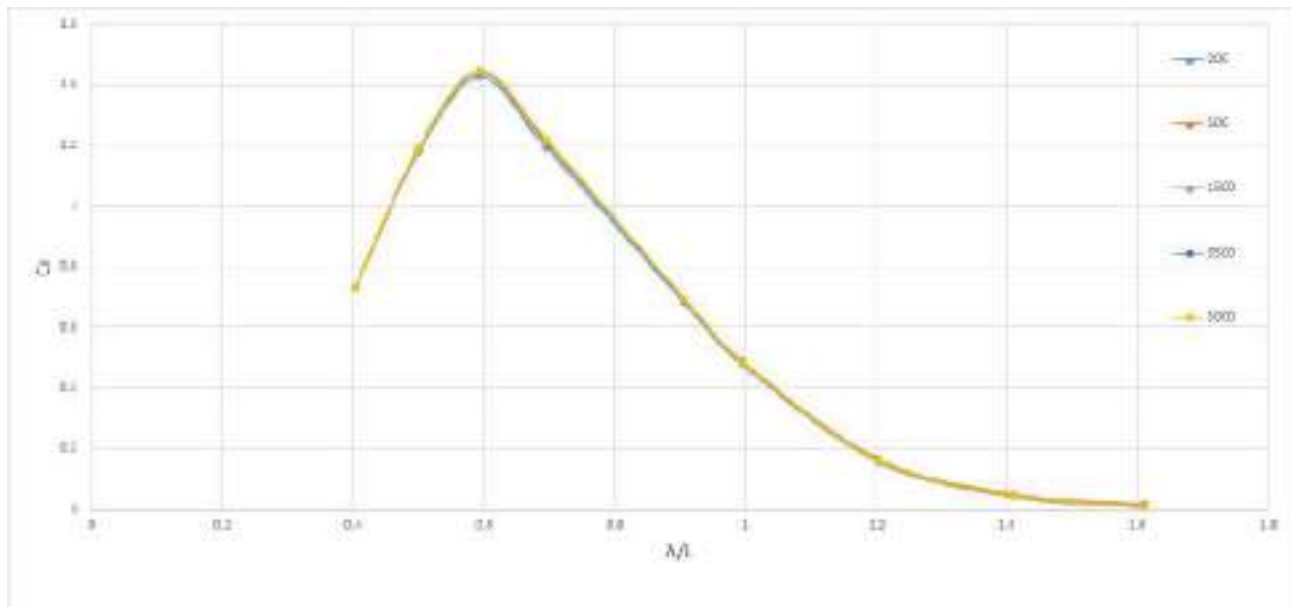


Figure 5.47: Convergence test for Added Resistance using results from WAMIT (3D panel code) at $F_n=0.0$, Drift angle= 0° . The added resistance curves were obtained using Momentum Method. The increasing number of panels in the legend represents the approximate number of panels in the geometry used for obtaining the corresponding curve λ - Wavelength, L - Length between perpendiculars, $C_r = Ra/(\rho g A^2 \frac{B^2}{L})$ - non dimensional added resistance, Ra - Added resistance

Figure 5.46 provides the added resistance curves at $F_n=0$ obtained using direct pressure integration method (Near field) in WAMIT for panel models with number of panels varying from 200 to 4000. From the figure it is observed that as the number of panels increases, the added resistance curve get closer to the experimental results. With less number of panels the added resistance is underestimated at wavelengths that correspond to $\lambda/L = 1$ and the added resistance is overestimated for longer waves with non dimensional wavelength $\lambda/l > 1$. AT $\lambda/L = 1$ all the panel models exhibit the same result which is in good agreement with the experimental results. When using the momentum method for finding added resistance as illustrated in figure 5.47 it can be concluded that, at $F_n=0$ the momentum method is not sensitive to the number of panels of the body and thus facilitates us to obtain reasonable results at less computational time. Even though the largest number of panels gave the best result, for the current study approximately 3000 panels were used in the panel model for numerical analysis in WAMIT as it was the optimal choice for number of panels based on accuracy within common engineering, computational time and resources used.

Heave motion RAO & Pitch motion RAO

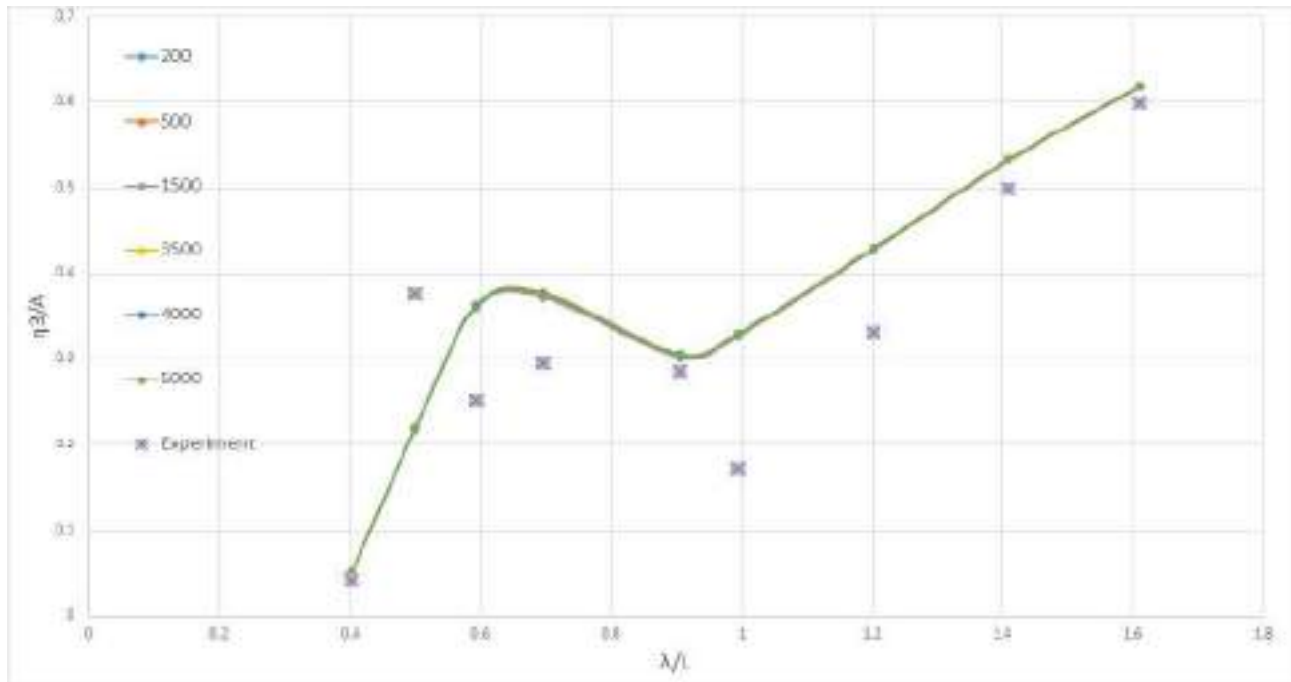


Figure 5.48: Convergence test for Heave RAO using results from WAMIT (3D panel code) at $F_n=0$ in head sea condition, Drift angle= 0° . The number of panels in the legend represents the approximate number of panels in the geometry used for obtaining the corresponding curve λ - Wavelength, L - Length between perpendiculars, η_3 - Heave Amplitude, k - Wave number, A - Wave amplitude

When analysing the heave motion RAO in figure 5.48 and the pitch motion RAO in figure 5.49 it is clearly observed that the first order heave and pitch motions are not sensitive to the number of panels used for discretization. Therefore, if only the first order motions are of interest at $F_n = 0$, a lower number of panels can be used in the 3D panel code WAMIT.

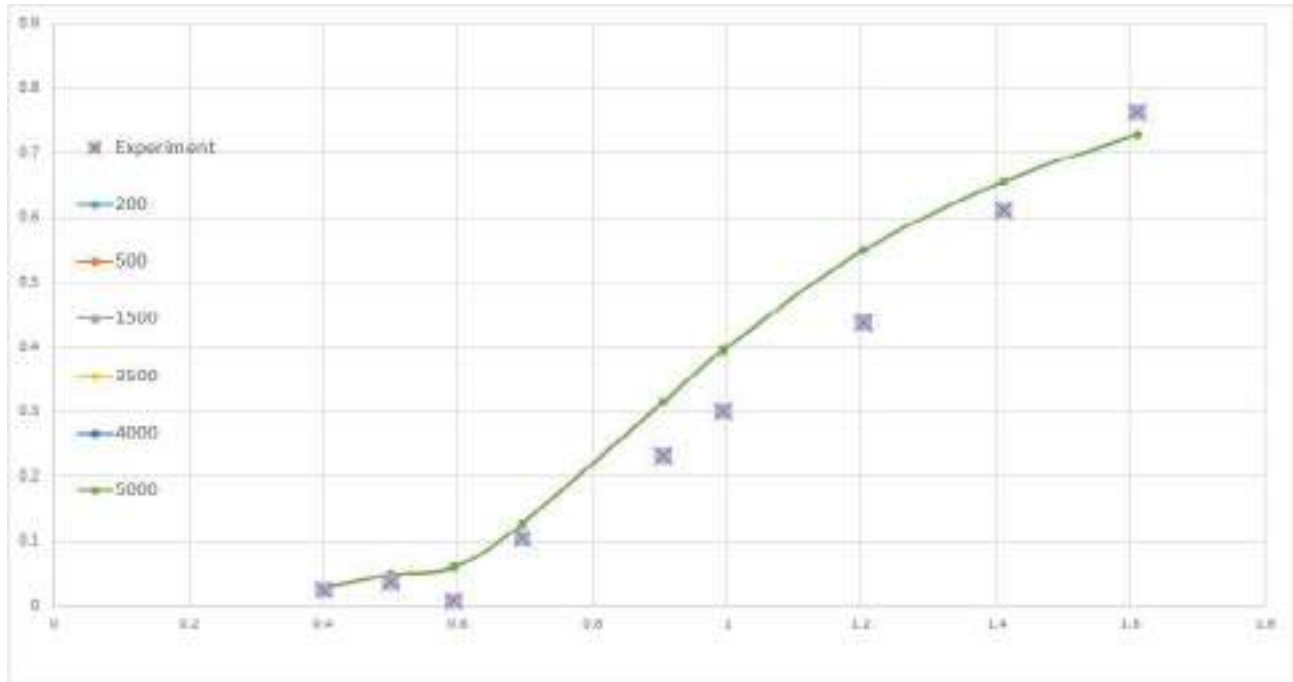


Figure 5.49: Convergence test for pitch RAO using results from WAMIT (3D panel code) at $F_n=0.0$, Drift angle= 0° . The number of panels in the legend represents the approximate number of panels in the geometry used for obtaining the corresponding curve λ - Wavelength, L - Length between perpendiculars, η_5 - Pitch Amplitude, k - Wave number, A - Wave amplitude

2. VERES3D

Added Resistance

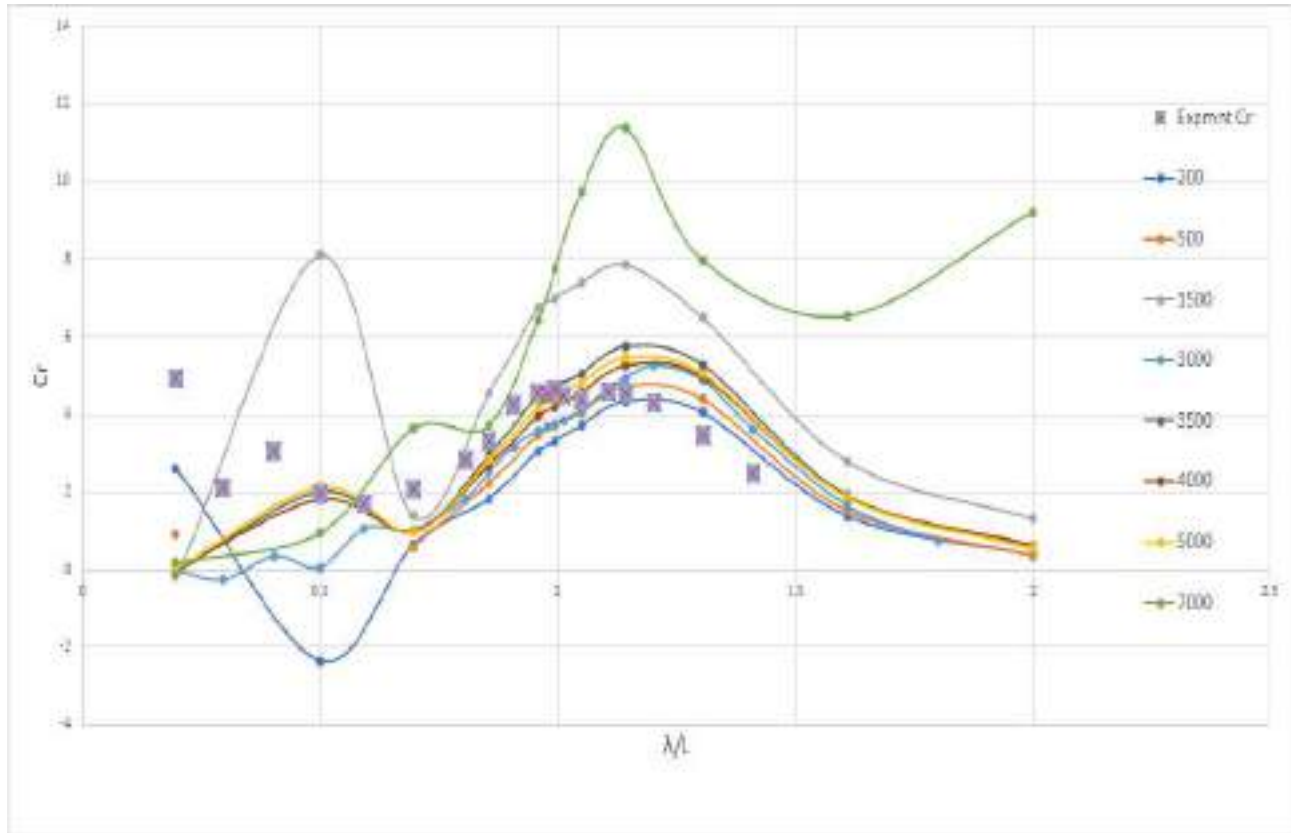


Figure 5.50: Convergence test for Added Resistance using results from VERES3D (3D panel code) at $F_n=0.179$, Drift angle= 0° . The added resistance curves were obtained using direct pressure integration. The number of panels in the legend represents the approximate number of panels in the geometry used for obtaining the corresponding curve λ - Wavelength, L - Length between perpendiculars, $C_r = Ra/(\rho g A^2 \frac{B^2}{L})$ - non dimensional added resistance, Ra - Added resistance

Figure 5.50 provides the added resistance curves at $F_n=0.179$ obtained using direct pressure integration in VERES3D using panel models with various number of panels ranging from 200 to 7000 as shown in the legend. From the plot it is observed that the added resistance results varies with the number of panels used. The accuracy of the results do not exhibit a linear relationship with the number of panels. When 200 panels were used the results in shorter waves were predicting an unstable result. This is concluded to be because the panels are too large to properly pick up the diffracted waves in shorter wavelengths. When the panel number was 7000 the results were exhibiting very large values, pointing to the possibility of singularity at some point on the model as the panels became too small. The sensitivity of the result to the panels is further analysed in section 5.6. The current study used a model with approximately 3000 panels, but the convergence study points to a possibility of better results at shorter wave lengths by using approximately 4000 panels.

Heave motion RAO and Pitch motion RAO

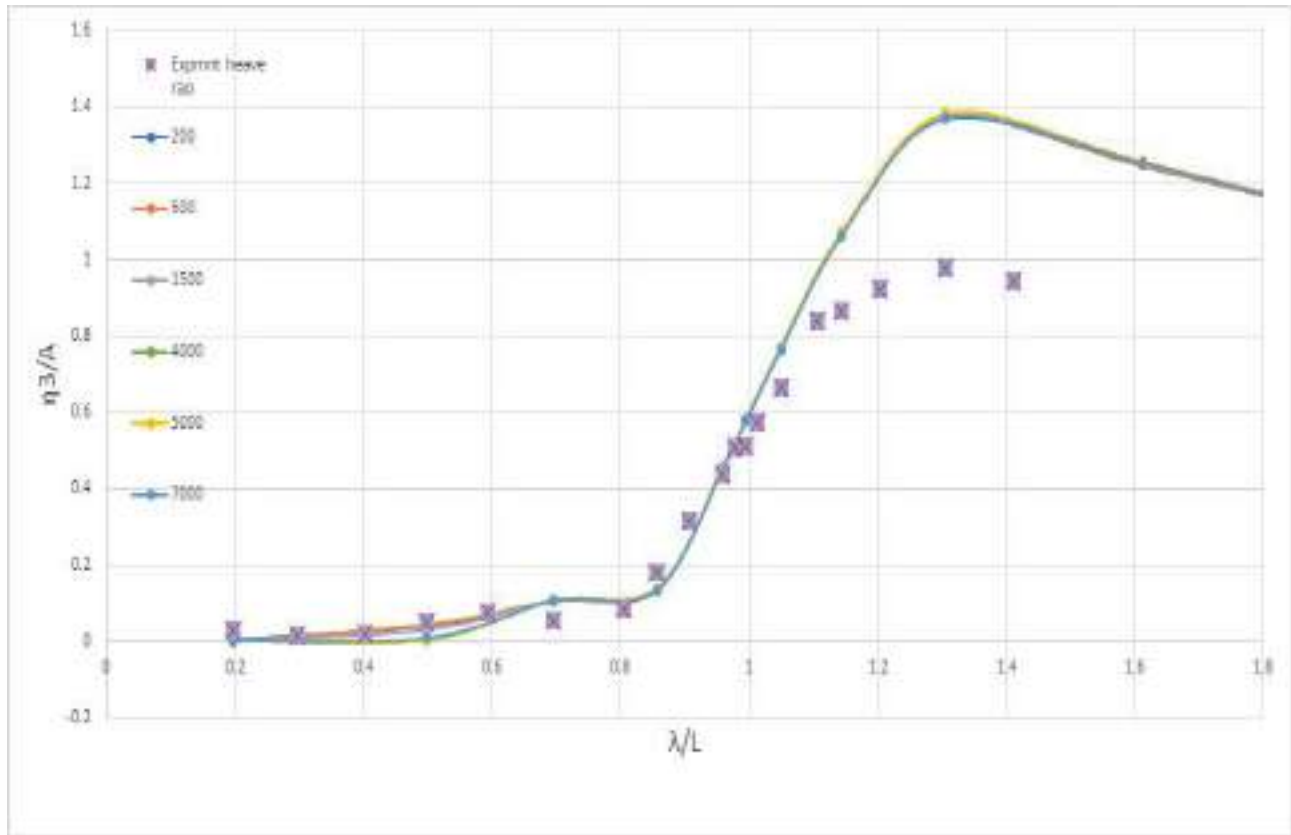


Figure 5.51: Convergence test for Pitch motion RAO using results from WAMIT (3D panel code) at $F_n=0$, Drift angle= 0° . The number of panels in the legend represents the approximate number of panels in the geometry used for obtaining the corresponding curve λ - Wavelength, L - Length between perpendiculars, η_3 - Heave Amplitude, k - Wave number, A - Wave amplitude

By analysing figures 5.51 and 5.52 it can be concluded that the first order heave and pitch motions are not sensitive to the number of panels used. It is also observed that when using 500 panels the pitch motion is over estimated at non dimensional wavelength of $\lambda/L = 0.5$. Therefore it is recommended to use reasonable number of panels that would agree to generate reasonable results for added resistance in waves and linear ship motions.

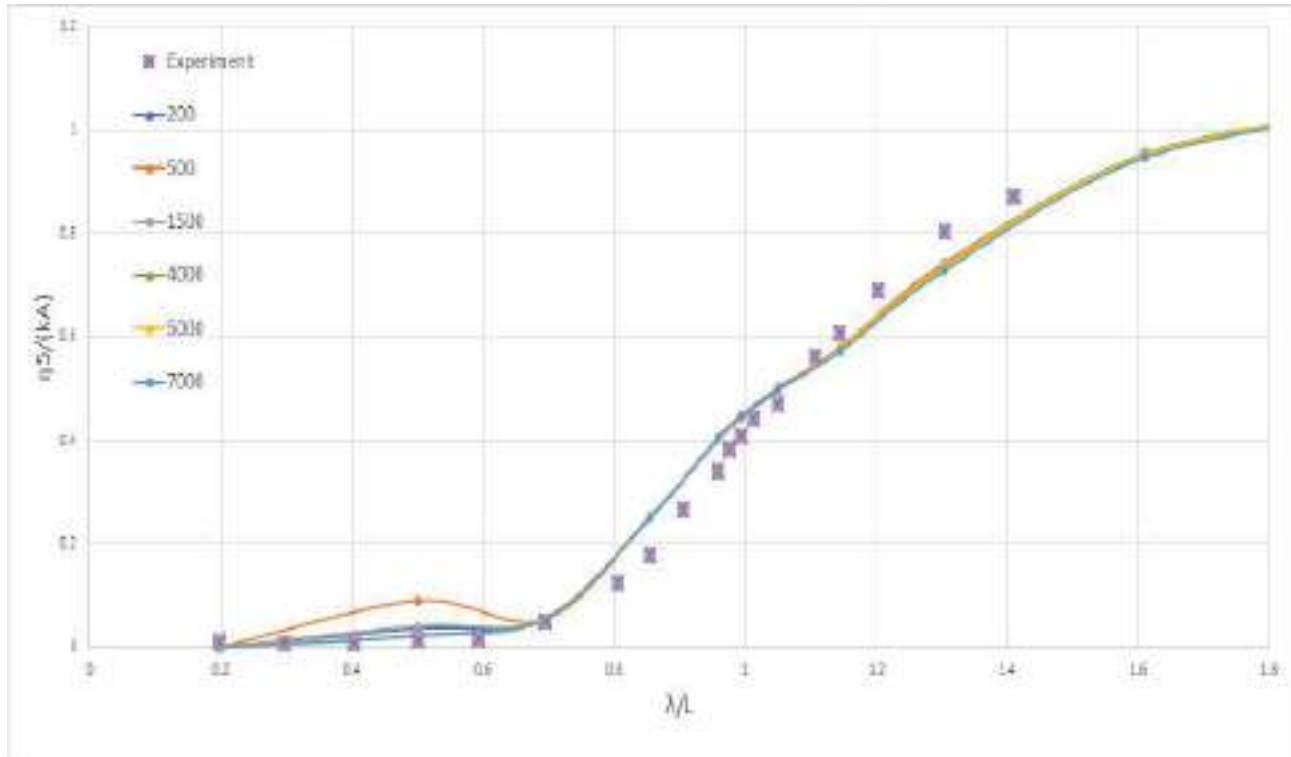


Figure 5.52: Convergence test for Pitch motion RAO using results from VERES3D (3D panel code) at $F_n=0.179$, Drift angle= 0° . The number of panels in the legend represents the approximate number of panels in the geometry used for obtaining the corresponding curve λ - Wavelength, L - Length between perpendiculars, η_5 - Pitch Amplitude, k - Wave number, A - Wave amplitude

5.6 Panel Sensitivity

In VERES3D it was observed that the convergence test did not show a linear relationship with the number of panels and the results. In figure 5.26 the results also seemed a bit unstable, this motivated to perform a sensitivity check by using geometric models by bringing some changes in the panels in an attempt to find any probable points singularities. Figure 5.53 shows the symmetric half of three different panel models, 'A', 'B' and 'C' used for this sensitivity check. The model is different from each other based on the panels used in the transom of the vessel. Model 'A' does not have any panels in the transom and the stern tube is not a closed by panels, Model 'B' includes all panels on the transom and model 'C' has some of its panels removed which were too slender. Based on the three type of discretization the added resistance and first order heave and pitch motions were found numerically in VERES3D and presented in this section.

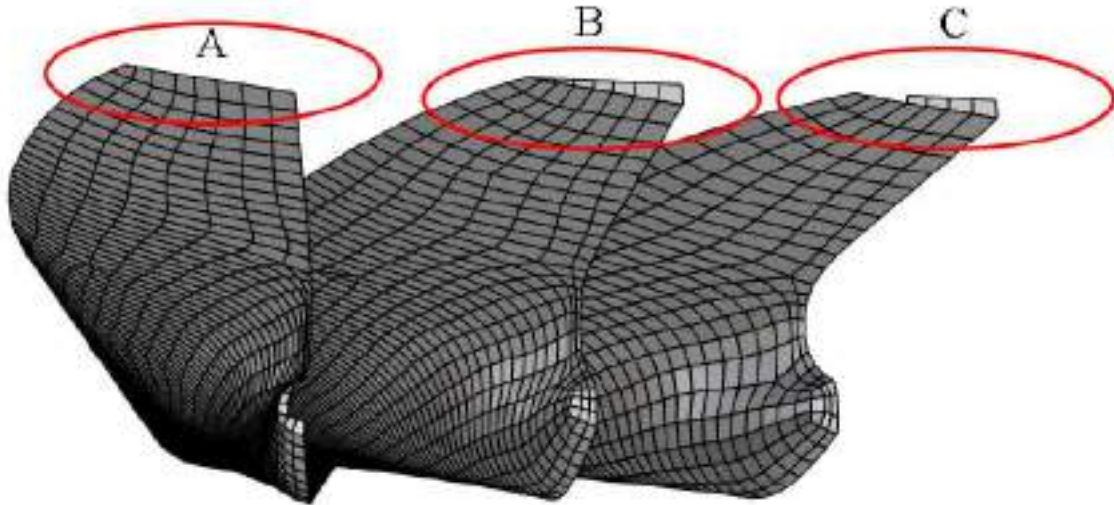


Figure 5.53: Three different types of ship body discretization based on difference in the panels at transom. (A) First geometry file does not include transom panels, (B) Second geometry file includes all panels on the transom, (C) Third geometry file excludes some small panels

1. $F_n=0$, Head sea

Figure 5.54 illustrates the added resistance curve at $F_n=0$ using direct pressure integration. Direct pressure integration is a method which is sensitive to the panel size as already seen in figure 5.46. From figure 5.54 it is observed that for $\lambda/L < 0.6$ all the three panel models generate similar values. At larger wavelengths $\lambda/L > 0.6$ the model without transom panels (A) predict 84% higher added resistance which is 20% higher than that predicted by the other type of discretization of the body. The added resistance of the model with transom (B) and the model with panels removed (C) predict 68% higher than the experimental values. Removing panels from the transom reduced added resistance where it gave values closer to the experimental values but the absence of transom created large difference in added resistance. Therefore, the slender panels at the transom were affecting the results. Where as when using the momentum method by using a user defined control surface, the presence or absence of panels do not seem to affect the results as seen in figure 5.55.

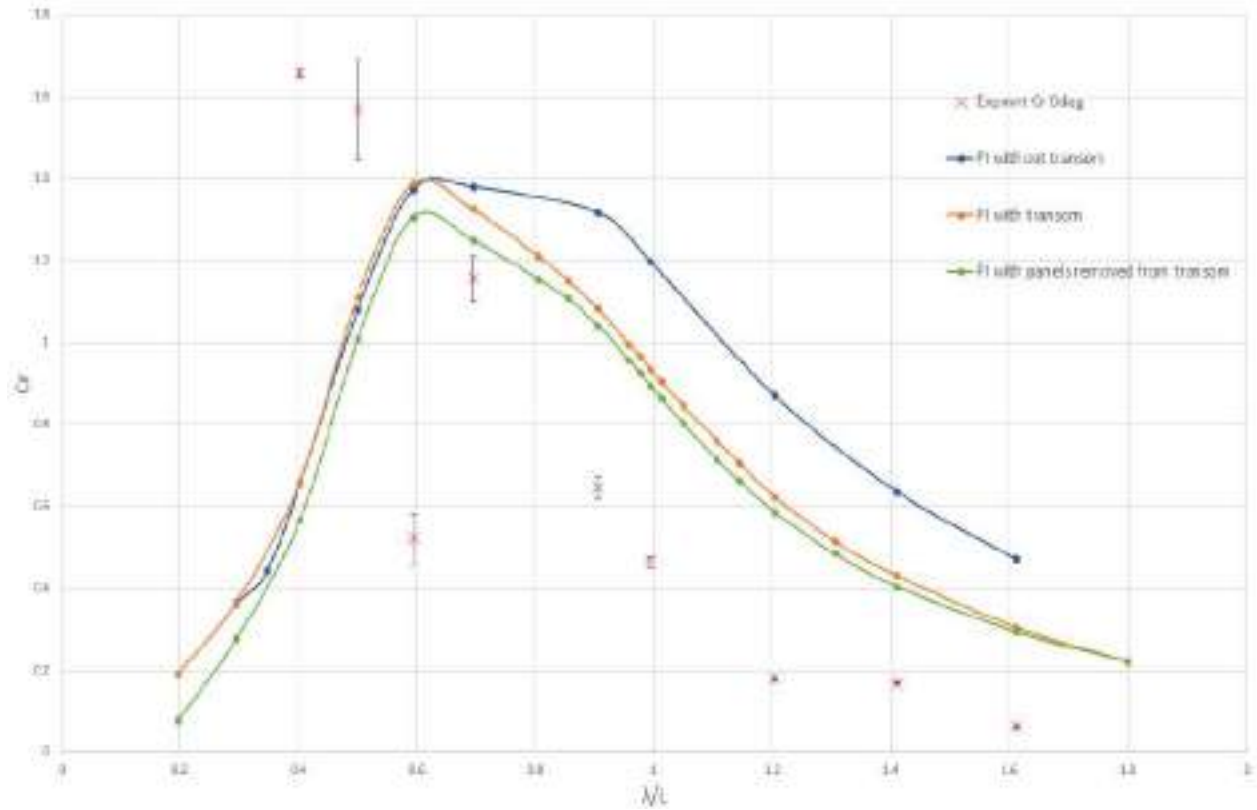


Figure 5.54: Sensitivity test for Added Resistance in waves using results from WAMIT (3D panel code) at $F_n=0$, Drift angle= 0° . The added resistance curves were obtained using direct pressure integration. Each curve represents the result for each type of geometry file used. λ - Wavelength, L - Length between perpendiculars, $C_r = Ra/(\rho g A^2 \frac{B^2}{L})$ - non dimensional added resistance, Ra - Added resistance

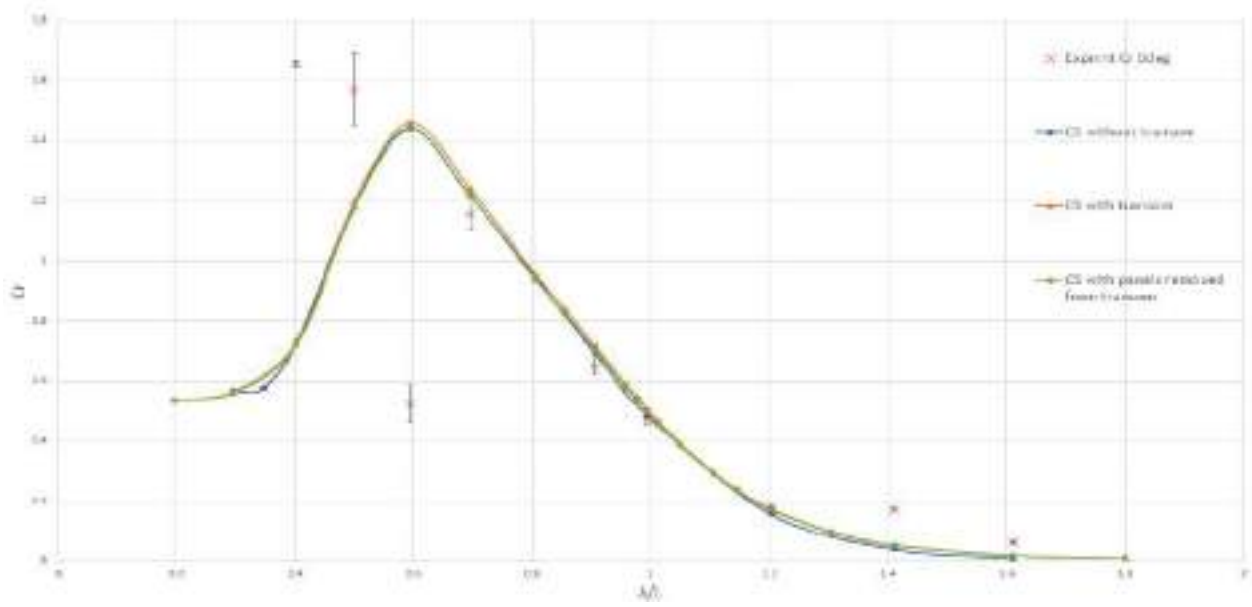


Figure 5.55: Sensitivity test for Added Resistance using results from WAMIT (3D panel code) at $F_n=0$, Drift angle= 0° . The added resistance curves were obtained using Momentum method . Each curve represents the result for each type of geometry file used. λ - Wavelength, L - Length between perpendiculars, $C_r = Ra/(\rho g A^2 \frac{B^2}{L})$ - non dimensional added resistance, Ra - Added resistance

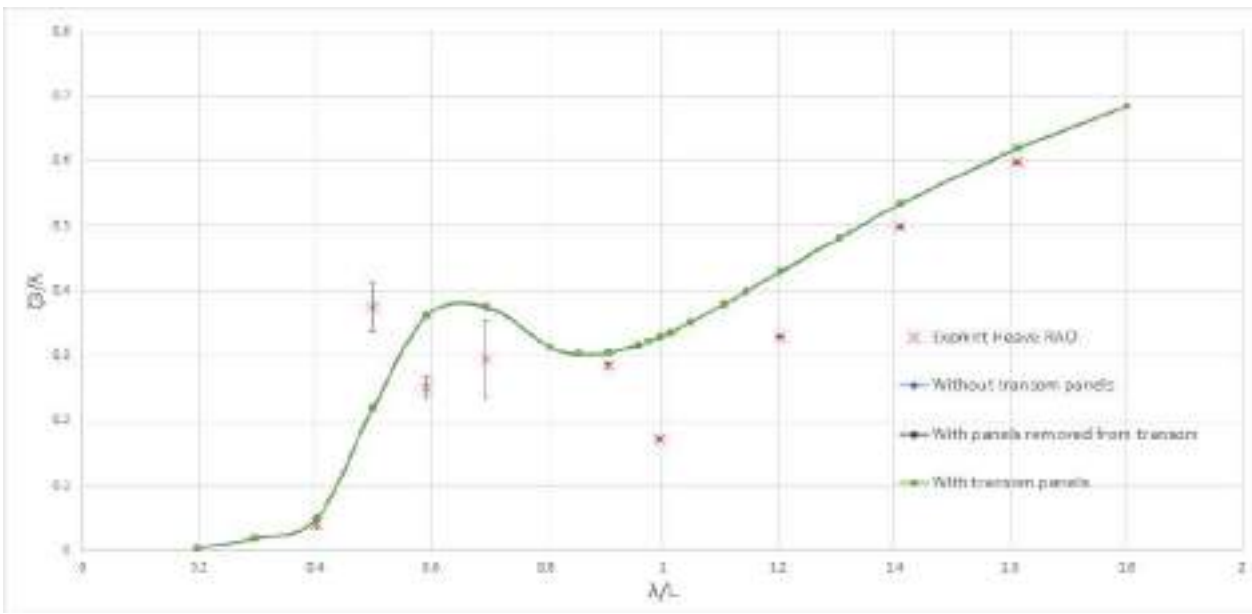


Figure 5.56: Sensitivity test for Heave RAO using results from WAMIT (3D panel code) at $F_n=0$, Drift angle= 0° . Each curve represents the result for each type of geometry file used. λ - Wavelength, L - Length between perpendiculars, η_3 - Heave Amplitude, k - Wave number, A - Wave amplitude

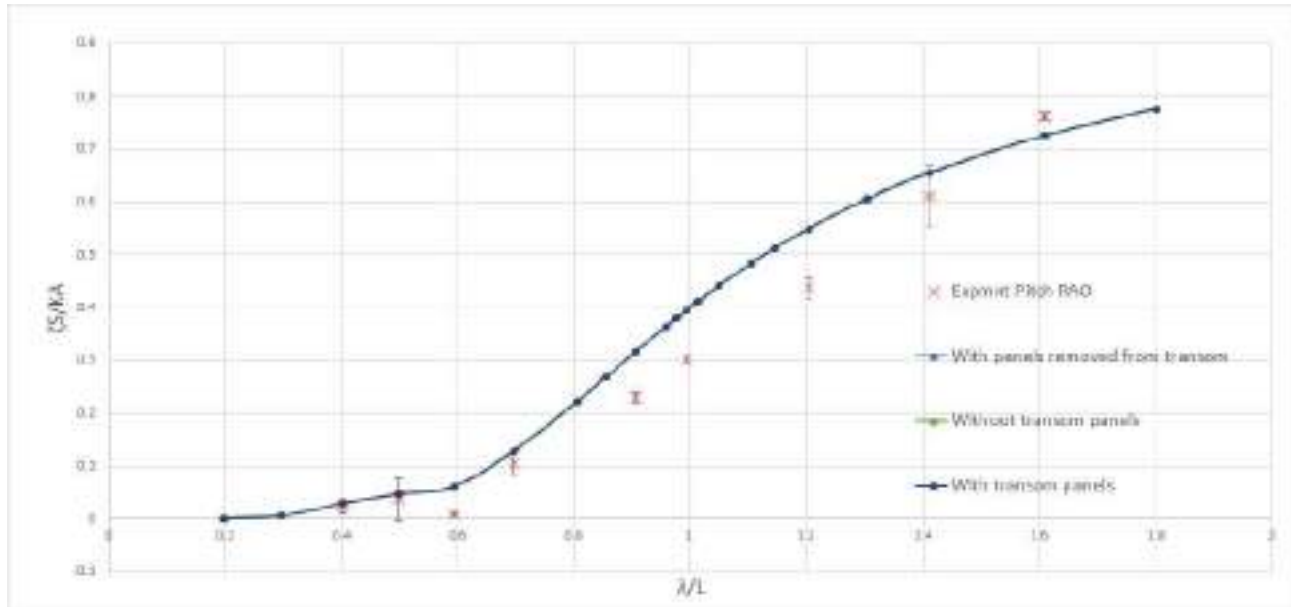


Figure 5.57: Sensitivity test for Pitch RAO using results from WAMIT (3D panel code) at $F_n=0$, Drift angle= 0° . Each curve represents the result for each type of geometry file used. λ - Wavelength, L - Length between perpendiculars, η_5 - Pitch Amplitude, k - Wave number, A - Wave amplitude

When analysing the first order heave RAO presented in figure 5.56 and pitch RAO presented in figure 5.57 it is observed that the modification of panels in transom do not affect the results.

2. $F_n=0.179$, Head sea

In case of added resistance using pressure integration for a forward speed the observations are similar to that at zero speed (Figure 5.58). Results without the transom had the largest values than all other type of discretization, removing some panels gives similar but slightly higher results to that with the transom.

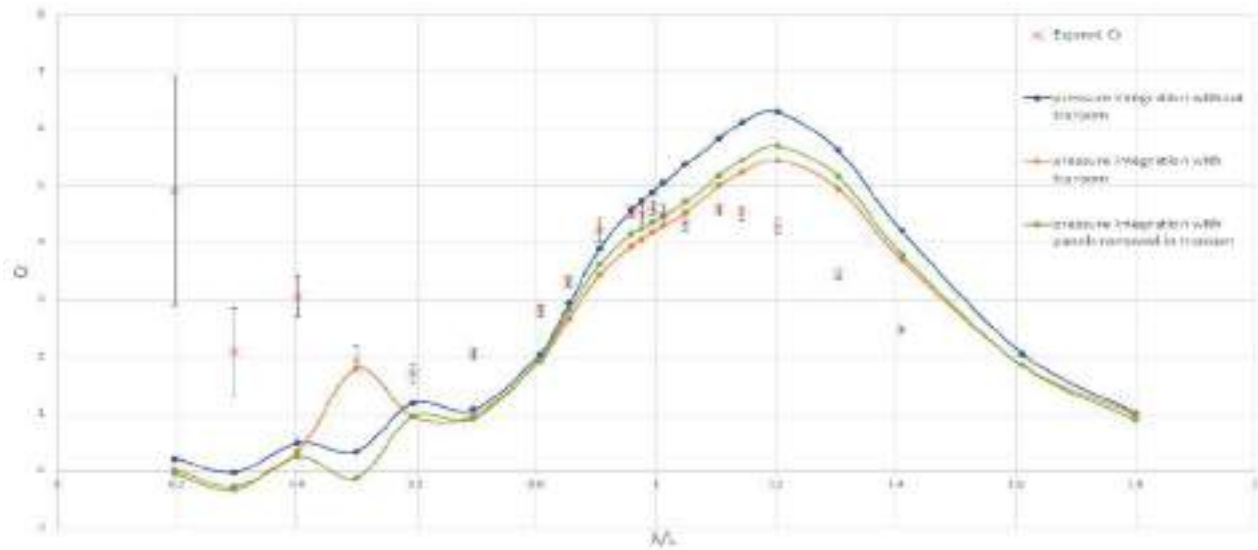


Figure 5.58: Sensitivity test for Added Resistance by direct pressure integration using results from VERES3D (3D panel code) at $F_n=0.179$, Drift angle= 0° . Each curve represents the result for each type of geometry file used. λ - Wavelength, L - Length between perpendiculars, $C_r = Ra/(\rho g A^2 \frac{B^2}{L})$ - non dimensional added resistance, R_a - Added resistance

The most interesting results is when using the momentum method with the user defined control surface in test cases with a forward speed as illustrated in figure 5.59. All the results from three of the panel geometries overestimate the results to a large magnitude. Full discretization of the ship transom stern with quadrilateral panels provides largest results, removing some panels reduced added resistance by half and removing all the transom panels reduced it by half again. Since the direct pressure integration results were not showing error of such large magnitude it was clear that it was not just an issue of panel size. The zero speed results exhibited no sensitivity to the body discretization using a momentum methods. Whereas results with a forward speed exhibited sensitivity to the discretization. Momentum methods depends a lot on how well the wave generation was predicted. Errors of such large error points out the possibility that the numerical code is not capturing the waves generated appropriately in this particular case. The exact reason is not determined.

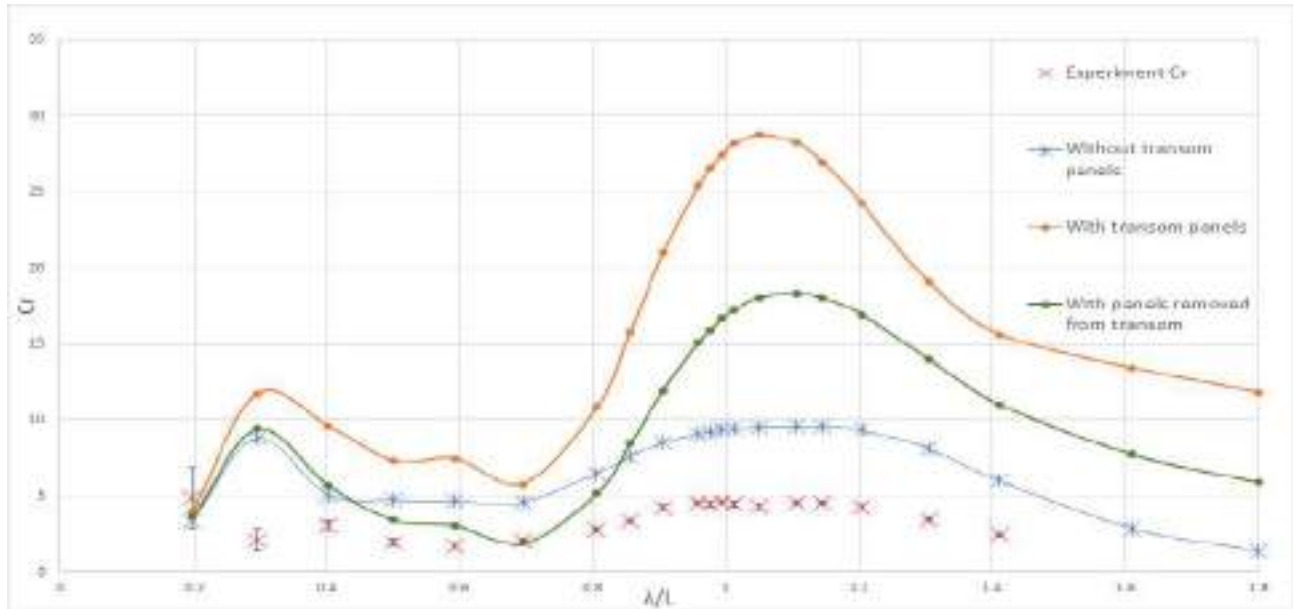


Figure 5.59: Sensitivity test for added resistance in waves using results from VERES3D (3D panel code) at $F_n=0.179$, Drift angle= 0° . The added resistance curves were obtained using Momentum method referred to as control surface in the legend, where user defined the control surface. Each curve represents the result for each type of geometry file used. λ - Wavelength, L - Length between perpendiculars, $C_r = Ra/(\rho g A^2 \frac{B^2}{L})$ - non dimensional added resistance, Ra - Added resistance

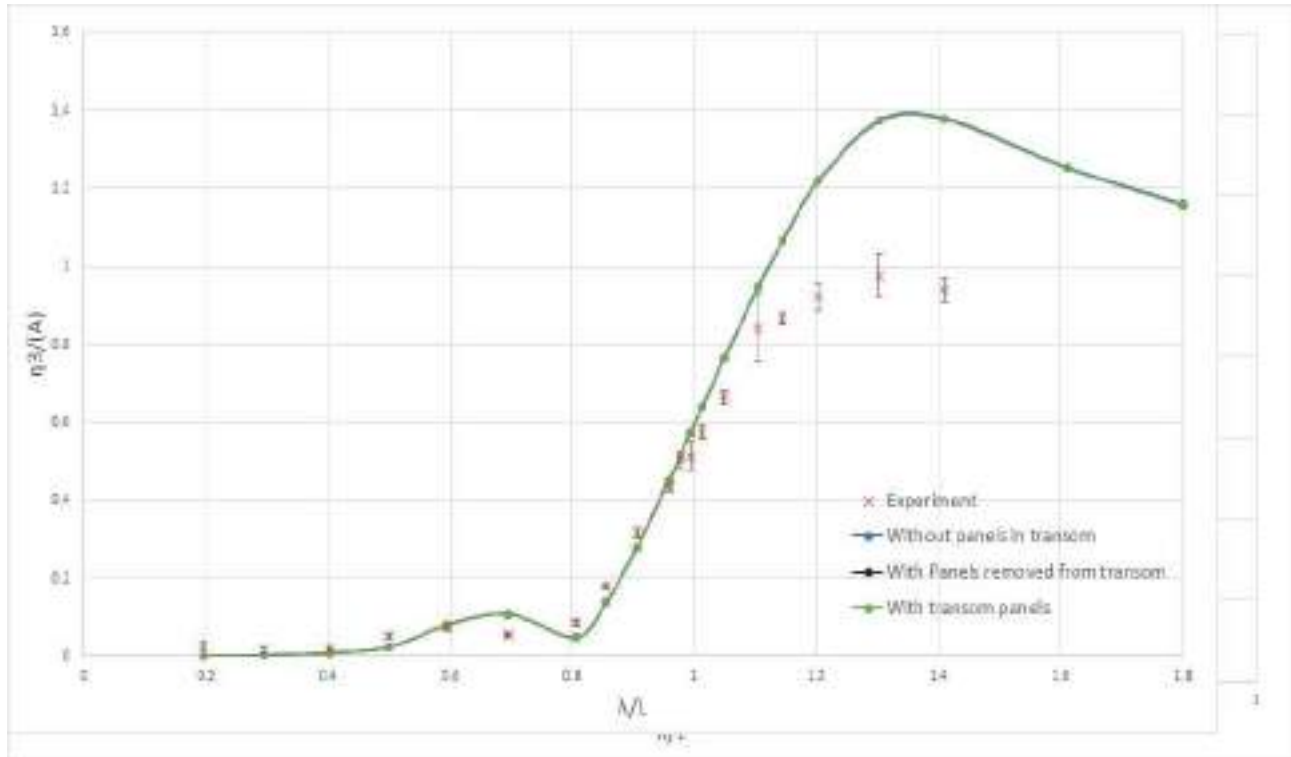


Figure 5.60: Sensitivity test for Heave motion RAO using results from VERES3D (3D panel code) at $F_n=0.179$, Drift angle= 0° . Each curve represents the result for each type of geometry file used. λ - Incident wavelength, L - Length between perpendiculars, η_3 - Heave Amplitude, k - Wave number, A - Wave amplitude

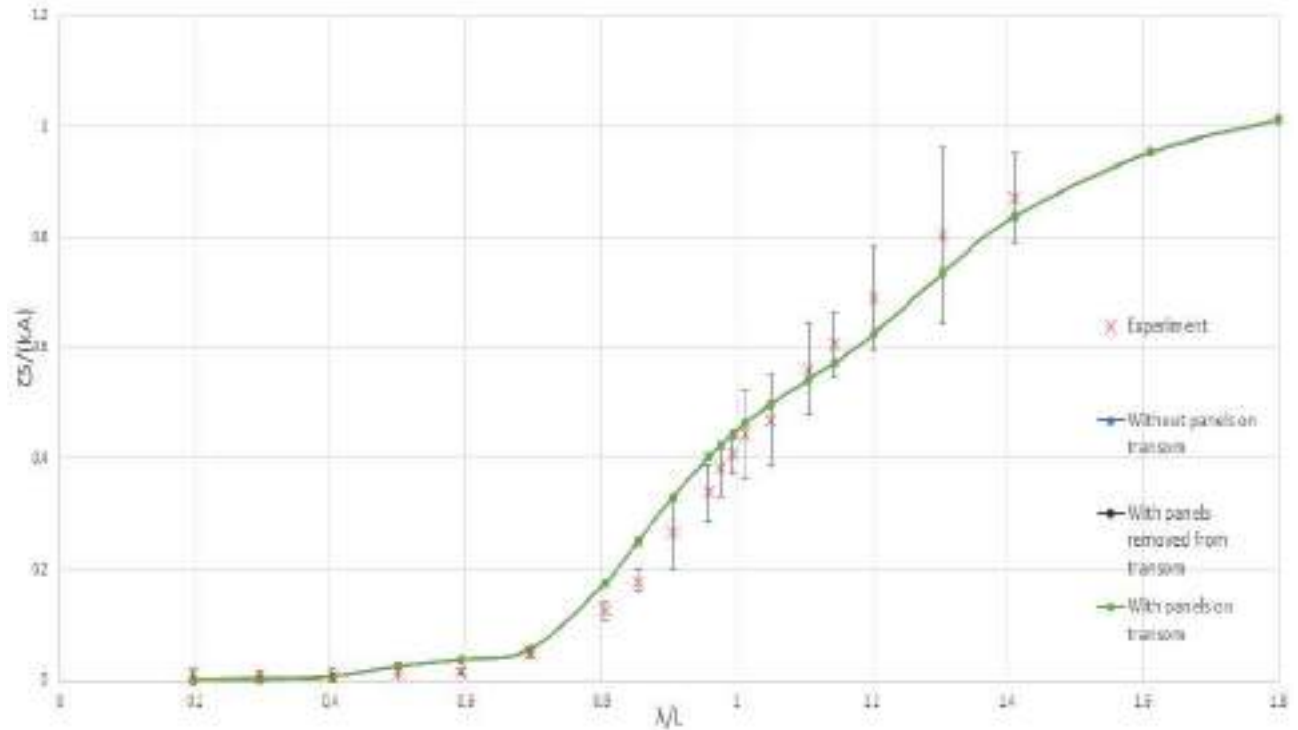


Figure 5.61: Sensitivity test for Pitch RAO using results from VERES3D (3D panel code) at $F_n=0.179$, Drift angle= 0° . Each curve represents the result for each type of geometry file used. λ - Wavelength, L - Length between perpendiculars, η_5 - Pitch Amplitude, k - Wave number, A - Wave amplitude

Figure 5.60 and figure 5.61 concludes that first order heave and pitch motions are not affected by changes in transom panel just as observed in the case where $F_n=0$.

From this sensitivity study, it is evident that even though first order motions are less effected by panel model variations, second order forces are very much dependent on the discretization of the wetted part of the ship hull with quadrilateral panels. Minor differences in the panel model can generate large differences in the added resistance estimations.

6 Conclusion

6.1 Conclusion

This thesis primarily aimed at studying the effect of drift angle on added resistance in waves of a wind assisted ship based on a wind assisted bulk carrier design named SOShip by Sintef Ocean. This study has been performed by accounting for the pre-selected drift angles of 0° and 9° in wavelengths from 0.2 to 1.8 times the vessel length in head sea and following sea conditions. An experimental study was conducted through a towing test at Sintef Ocean, Trondheim, Norway. A numerical analysis was performed using state of the art panel codes used in the industry such as WAMIT, VERES3D and VERES. A theoretical investigation into the theory used behind each numerical software packages has been carried out in order to find how each is different from each other and how it affects the results. The thesis also focused on creating an outlook on the capability on numerical codes to predict added resistance in various conditions. The effect of tank walls on estimation of first order linear heave and pitch motions and added resistance in waves during tests at $Fn = 0$ was also pursued using the experimental results and the results from the numerical software package WAMIT.

Based on the experimental results at $Fn = 0$ in interval of non dimensional wavelengths corresponding to $0.5 < \lambda/L < 1.2$ at head sea condition, it has been observed that a drift angle of 9° increases the added resistance of the vessel upto 5 - 10% and at Froude number $Fn = 0.179$ it increases upto 5%. In wavelengths corresponding to $\lambda/L > 1.2$, the experiments exhibit a increase of 10% in added resistance in presence of a drift angle of 9° . The numerical results for $Fn = 0$ and $Fn = 0.179$ at $\lambda/L > 0.5$ in head sea condition exhibits a increase of less than 5% in added resistance at 9° drift angle. The peak of added resistance curve was observed at $\lambda/L \sim 0.6$ at $Fn=0$ and $\lambda/L \sim 1.2$ at $Fn=0.179$.

The experimental results at shorter wavelengths where diffraction effects are dominant ($\lambda/L < 0.5$) has a large uncertainty, which makes it difficult to use the experimental values for validation of numerical results. At $Fn = 0$ the 3D panel codes predict the added resistance reasonably well with 10 - 15% accuracy in the wavelength corresponding to $\lambda/L > 0.6$. At shorter wavelengths tank wall effects were identified using the experimental results and results from WAMIT V7 including wall effects. The interaction between the tank wall increased the added resistance at some points and decreased the added resistance particularly at $\lambda/L = 0.6$. The tank wall effects were not easily detectable in heave and pitch RAO in the experimental results. The 2d panel code VERES (ShipX) using Gerritsma and Beukelman method overestimated the peak by more than 100%. At $Fn = 0.179$ in head sea the added resistance curve predicted by the numerical codes predicts a shift in the added resistance curve with peak values at $\lambda/L \sim 1.2$ whereas the experimental peaks were observed at $\lambda/L \sim 1$. ShipX using Gerritsma and Beukelman predicted a peak value with magnitude similar to that obtained by experiments. VERES3D using direct pressure integration method predicted a peak value of magnitude $\sim 20\%$ higher than the experiment. The momentum method in VERES3D using the user defined control surface over estimated the added resistance by more than 200%. Based on a sensitivity check of the panels it was concluded that at forward speed the waves generated by the vessel are not properly captured by the code which originates from the issues with the panelling.

In following sea at $Fn = 0.179$ all the numerical software packages predict a negative added resistance i.e an added thrust which contradicts the experimental results which estimates about 10% of added resistance seen in head sea condition. In 2D panel code VERES it was due to the limitation of strip

theory to predict hydrodynamic coefficients at low encounter frequency. The reason why 3D panel code VERES3D predict a wrong result is not yet determined. This conclusion based on experimental results for following regular wave field condition is very relevant from an operational perspective which might mislead the ship operation based on the numerical results.

Another interesting observation based on the analysis of experimental and numerical results of Heave RAO points out that at $\lambda/L > 1.1$ the numerical codes over estimate the heave (ShipX by 20% and VERES3D by 40%) compared to the numerical results. Viscous effects and slamming motions at these wavelengths were determined to be two of the possible contributions to this decrease in experimental values.

6.2 Further work

The major drawback of the conducted experimental study was the lack of an uncertainty analysis which would have clearly defined the uncertainty in the experimental values. A proper precision error calculation can provide a better picture of the results, especially at shorter waves and longer regular deep water waves. Test repetitions focusing on shorter waves, longer waves and wavelengths corresponding to the peak value of added resistance can further increase the reliability of the experimental results. Due to lack of time only few test runs were completed in following sea conditions, especially in presence of a drift angle. More data points can provide better conclusions on added resistance in following sea condition and effect of drift angle in added resistance.

The conducted numerical study was based on linear potential fluid flow theory which neglects viscous effects. A further study using CFD based tools is recommended to obtain numerical results including viscous effects. This can also provide an outlook on the benefits of using a potential fluid flow theory based code which is less resources and time demanding demanding to find added resistance in waves on a vessel. The discretization of the wetted portion of the ship hull with quadrilateral first order panels used in VERES3D generates issues when using the control surface based method. A more detailed study on finding the source of this issue could be used a guideline for further simulation in the future.

This study focused on the effect of a drift angle of 9° and 0° . More drift angles are to be studied to arrive at a general conclusion for effect of drift angles on added resistance of a vessel.

We focused on just the contribution of drift angle seen in wind assisted propulsion vessels. There are other factors that contribute to increasing the added resistance in waves of wind assisted vessels such as rudder angle and added resistance due to wind above the water line. A model test simulating all the effects individually or simultaneously would provide the total picture about the added resistance in waves on wind assisted ships which could be used for design and operation of such kind of vessels in the upcoming future.

7 Bibliography

- [1] Mingyu Kim, Olgun Hizir, Osman Turan Sandy Day Atilla Incecik: *Estimation of added resistance and ship speed loss in a seaway*.
- [2] Ruihua LU, Jonas W.Ringsberg: *Ship energy performance study of three wind-assisted ship propulsion technologies including a parametric study of the flettner rotor technology*. 2019.
- [3] Excell, Jon: *The rise of the wind ships*. theengineer.co.uk/wind-ships-marine-propulsion/.
- [4] <https://theloadstar.com/wind-technology-could-give-shipping-lines-double-digit-fuel-savings/>.
- [5] <https://cleantechnica.com/2018/09/11/airbus-seawing-kite-sails-to-cut-fuel-costs-for-cargo-ships-20/>.
- [6] <https://www.dnv.com/expert-story/maritime-impact/Wind-ships-ahead.html?cookie-consent=1>.
- [7] <https://www.tudelft.nl/en/3me/research/check-out-our-science/will-steel-sails-make-ships-more-sustainable>.
- [8] Greco, Marilena: *Tmr 4215: Sea loads lecture notes*.
- [9] *Tmr 4182: Marine dynamics ntnu*.
- [10] Hoff, Jan Roger: *Calculation of added resistance submerged ellipsoid, adopted from presentation as part of developing veres3d*.
- [11] Dong-Min Park, Yonghwan kim, Min Guk Seo Jaehoon Lee: *Study on added resistance of a tanker in head waves at different drafts*.
- [12] *Fiber optic gyro (fog) - stability under pressure*. <https://www.saab.com/products/fiber-optic-gyro-products>.
- [13] ITTC: *Ittc- recommended procedures and guidelines, testing ad extrapolation methods loads and responses, seakeeping and seakeeping experiments*. 2017.
- [14] *Dynamometry*. <http://www.wumtia.soton.ac.uk/products/dynamometry>.
- [15] *Sirius hexapod*. <https://symetrie.fr/en/hexapods/sirius/>.
- [16] *Imo marine engine regulations*. <https://dieselnet.com/standards/inter/imo.php>.
- [17] Aage, C.: *Relevance of model testing in irregular seas and current, proc. of omae 1992*. 1992.
- [18] Organisation, International Maritime: *Fourth imo ghc study 2020*. 2021.
- [19] Organisation, International Maritime: *Prevention of air-pollution from ships*. <https://www.imo.org/en/OurWork/Environment/Pages/Air-Pollution.aspx>.
- [20] News, Gard: *Marpol annex vi-new risks and challenges for owners and charterers*. 2007.
- [21] Clauss GF, Siekmann H, Tampier BG: *Simulation of the operation of wind-assisted cargo ships.hauptversammlung der schiffbautechnischen gesellschaft*. 2007.

- [22] Schlaak M, Kreutzer R, Elsner R: *Simulating possible savings of the skysails-system on international merchant ship fleets*. 2009.
- [23] Greenport: *Windsail:energy saving solution?* <https://www.greenport.com/news101/energy-and-technology/windsail-energy-saving-solution>.
- [24] Buitendijk, Mariska: *Wind assisted ship propulsion puts the sail back into sailing*. <https://www.swzmaritime.nl/news/2021/04/08/wind-assisted-ship-propulsion-puts-the-sail-back-into-sailing/?gdpr=accept>.
- [25] Arribas, F.: *Some methods to obtain the added resistance of a ship advancing in waves*. *ocean eng.* 34(7),946-955. 2007.
- [26] Mingyu Kim, Olgun hizir, Osman Turan Atilla Incecik: *numerical studies on added resistance and motions of kvlcc2 in head sea for various ship speeds*. 2017.
- [27] Fabian Tillig, Jonas W. Ringerg: *Design, operation and analysis of wind assisted cargo ships*. 2020.
- [28] IMO: *Prevention of air pollution from ships[c]. marine environment protection committee, international maritime organization (imo).oslo, norway*. 2008.
- [29] K.J Rawson, E.C Tupper: *Basic ship theory (fifth edition)*. 2001.
- [30] Larsson L, H. Raven: *The principles of naval architecture series:ship resistance and flow*. sname. 2010.
- [31] Afshar, Mostafa Amini: *Towards predicting the added resistance of slow ships in waves*. 2014.
- [32] Odd M Faltinsen, Knut J Minsaas, Nicolas Liapis Svein O SkØrdal: *Prediction of resistance and propulsion of a ship in a seaway*. 1980.
- [33] T.H, Havelock: *The resistance of a ship among waves*. *proc. r. soc.lond. ser. a math. phys.sci.*,299-308. 1937.
- [34] Maruo H., Ishii T.: *Calculation of added resistance in head sea waves by means of a simplified formula*. 1976.
- [35] Gerritsma J., Beukelam W.: *Analysis of resistance increase in waves of a fast cargo ship*. 1972.
- [36] W.P.A., Joosen: *Added resistance in waves*. in: *Proceedings of the sixth symposium on naval hydrodynamics, washington*. 1966.
- [37] Salvensen N, Tuck E.O, Faltinsen O.M: *Ship motions and sea loads sname 104 119-137*. 1970.
- [38] Newman., J.N: *The drift force and moment on ships in waves*.
- [39] Gerritsma J., Journee J.M, J: *Proc. 15th ittc part 2 pg 70*. 1978.
- [40] Newman., J.N: *The quest for three dimensional theory of ship wave interactions*.
- [41] Guo Bing-jie, Steen Svere, title =.
- [42] Fujii H., Takahashi T.: *Experimental study on the resistance increase of a ship in regular oblique waves*. 1975.

- [43] Cong-Min Park, Jaehoon lee, Yonghwan Kim: *uncertainty analysis for added resistance experiment of kvlcc2 ship*. 2014.
- [44] ITTC: *Ittc-recommended procedures and guidelines, testing and extrapolation methods manoeuvrability free running model tests*. 2008.
- [45] *Number of ships in the world merchant fleet as of january 1 by type*. <https://www.statista.com/statistics/264024/number-of-merchant-ships-worldwide-by-type/>.
- [46] Naya Olmer, Brya Comer, Biswajoy Roy Xiaoli Mao Dan Rutherford: *Greenhouse gas emissions from global shipping,2013-2015, icct*. 2017.
- [47] Faltinsen, O.M: *Sea Loads on ships and offshore structures*. Cambridge University press, 1990.
- [48] Jarle A. Kramer, Sverre Steen, Luca Savio: *Drift forces-wingsails vs flettner rotors*. 2016.
- [49] Steen, Sverre: *Tmr7 experimental methods in marine hydrodynamics- lecture notes*. 2014.
- [50] *Accelerometer*. <https://en.wikipedia.org/wiki/Accelerometer>.
- [51] Dong-Min Park, Jaehoon Lee, Yonghwan kim: *Uncertainty analysis for added resistance experiment of kvlcc2 ship*.
- [52] *Wamit*. <https://www.wamit.com/techdescription.htm>.
- [53] Lee, C. H.: *Wamit theory manual*. 1995.
- [54] Salvensen, N., Tuck E.O Faltinsen O.: *Ship motions and sea loads. in transactions of the society of naval architects and marine engineers vol 78 pp.-250-287*. 1970.
- [55] Faltinsen, O.M, Zhao R: *Numerical predictions of ship motions at high forward speed*. 1970.
- [56] Dariusz Fathi, Jan Roger Hoff: *Shipx vessel responses (veres)*. 2004.
- [57] Anne bruyat, Martin Gutsch, Jan Roger Hoff: *Veres3d user manual*. 2020.
- [58] Telste, J.G, Noblesse F.: *Numerical evaluation of the green function of water wave radiation and diffraction. journal of ship research, vol.3*. 1986.
- [59] Inc., WAMIT: *Wamit user manual version 7.3*.

Appendices

Appendices

A Emission limits

Tier	Date	NO _x Limit, g/kWh		
		n < 130	130 ≤ n < 2000	n ≥ 2000
Tier I	2000	17.0	45 · n ^{-0.2}	9.8
Tier II	2011	14.4	44 · n ^{-0.23}	7.7
Tier III	2016†	3.4	9 · n ^{-0.2}	1.96

† In NO_x Emission Control Areas (Tier II standards apply outside ECAs).

Figure A.1: MARPOL Annex VI NO_x emission limits ⁽¹⁶⁾ n=rpm

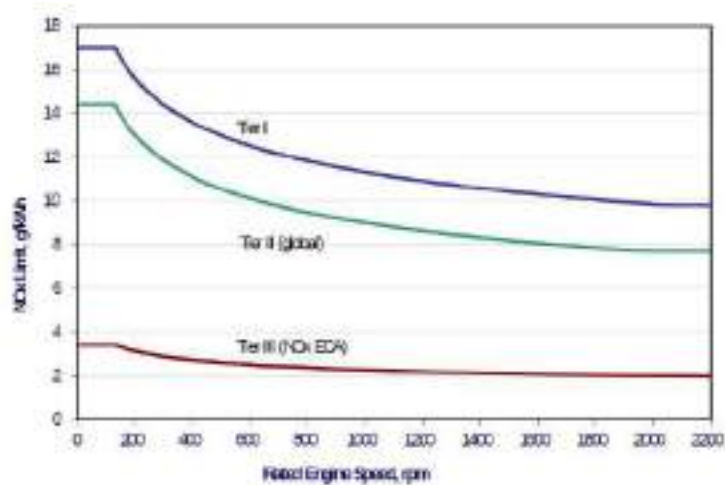


Figure A.2: MARPOL Annex VI NO_x emission limits ⁽¹⁶⁾

Date	Sulfur Limit in Fuel (% m/m)	
	SO _x ECA	Global
2000	1.5%	4.5%
2010.07	1.0%	3.5%
2012		
2015	0.1%	0.5%
2020		

Figure A.3: MARPOL Annex VI fuel sulphur limits ⁽¹⁶⁾

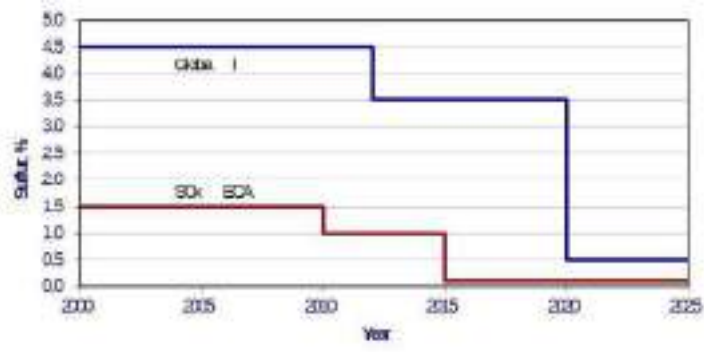


Figure A.4: MARPOL Annex VI fuel sulphur limits ⁽¹⁶⁾

B Swing Test

Resultater fra krengeprøve/vipping av M3246A (SO-skip)

fredag 01.02.2021. ballastering og krengeprøve

Modellen har et deplasement på 1493,2 kg. Seilbåtdynamometer er montert i modellen. Den testes uten ror og uten propell. Propellhylse er plagget igjen. Dummylodd for stenger er plassert under hengslingspunkter i selvbåtdynamometeret. Modellen ble lastet til deplasementet på 1493,2kg. Har ikke fått noen spec, men fikk beskjed om å prøve å laste modellen slik at Ryy blir tilnærmet 25% av Lpp. Lastingen blir skjønnsmessig plassert etter dette. Jeg fikk beskjed om å oppnå en GM på mellom 2 og 3 meter i fullskala. Krengeprøve viser GM på 85mm. Dette er før vi erstatter dummylodd med stenger. Regner om dummyvekta til riktig høyde som gir en GM på 76mm. Dette gir en GM i fullskala på 2,432m.

Torsdag 18.02.2021 og fredag 19.02.2021. kontrollvipping

Etter forsøk ble modellen vippet i pitch. Jeg vippet først modellen med all last i modellen. Av erfaring vet jeg at en så tung modell vil gi unøyaktige vippedata på grunn av friksjon i vippe. Jeg tok ut 400kg av modellen og vippet på nytt. Regnet så inn disse 400 kiloene i ettetid, og sammenlignet med første vipping. Ser at det er noe avvik. Jeg bruker derfor resultater fra siste vipping som endelig.

Alle data inkl. bilder er lagret

23.02.2021

Trond Innset

Results from heeling test/swingtest of M3246A (SO-ship)

01.02.2021. ballasting and heeling test

The model has a displacement of 1493.2 kg. Sailboat dynamometer is mounted in the model. It is tested without rudder and without propeller. Propeller sleeve is plugged. Dummy weights for rods are located under hinge points in the seal boat dynamometer. The model was loaded to the displacement of 1493.2kg. I have not received any spec, but was told to try to load the model so that Ryy is approximately 25% of Lpp. The loading is discretionarily placed after this. I was told to achieve a GM between 2 and 3 meters in full scale. Heeling test shows GM at 85mm. This is before we replace dummy weights with rods. Converts the dummy weight to the correct height which gives a GM of 76mm. This gives a full-scale GM of 2,432m.

Thursday 18.02.2021 and Friday 19.02.2021. swing-test

After the tests in the Towing tank, I did swing-test in pitch for the model. I first did swing-test with all the weight in the model. From experience I know that such a heavy model will give inaccurate lash data due to friction in the lash. I took out 400kg from the model and did new swing test. I calculatet these 400 kilos into the model again, and compared to the first test. I see that there is some discrepancy. I therefore use results from the last test as final.

All data including images are stored

23.02.2021

Trond Innset

Vektsdata for modeller

MT-K4-S105 Rev.08

Prosjektnr.: Modellnr.: M3246A
 Prosjekttittel: SO-skip Skala : 32,00000
 Tetthetsforhold: 1,000 saltvann/ferskvann
 Lastekondisjon : KVL

X-akse : positive forward

Y-akse :

Z-akse : positive upwards

Origo: AP/CL/BL

SKROG		Fullskala	Modellskala	Målt modell	Avvik (%)
Lengde, Lpp	m	190,000	5,938		
Bredde, B	m		0,000		
Dypgang akter, TA	m	11,000	0,344		
Dypgang forut, TF	m	11,000	0,344		
Deplasement, totalt	tonn, kp	48927,6	1493,2		
Vertikalkomp. stigerør	tonn, kp		0,0		
Vertikalkomp. ankerliner	tonn, kp		0,0		
KG inkl. vertikalkomp.	m	11,191	0,350		
XCOG inkl. vertikalkomp.	m	99,388	3,106		
YCOG inkl. vertikalkomp.	m	0,000	0,000		

FAIRLEAD-KOORDINATER: FULLSKALA		X	Y	Z
Stigerør	m			
Ankerliner	m			

VIPPING		Fullskala	Modellskala	Målt modell	Avvik (%)	
KG ekskl. vertikalkomp.	m	11,191	0,350	0,352	0,65	fra krengeprøve
XCOG ekskl. vertikalkomp.	m	99,388	3,106	3,103	-0,09	ballansert i vippa
YCOG ekskl. vertikalkomp.	m	0,000	0,000			
Vekt ekskl. vertikalkomp.	tonn, kp	48928	1493,2	1490,300	-0,19	veid i vippa
Ixx ekskl. vertikalkomp.	t m2/kg m2	0	0,0			
Iyy ekskl. vertikalkomp.	t m2/kg m2	110392898	3290,0	2661,829	-19,09	resultat fra vipping
Izz ekskl. vertikalkomp.	t m2/kg m2	0	0,0			
Rxx ekskl. vertikalkomp.	m					
Ryy ekskl. vertikalkomp.	m	47,500	1,484	1,336	-10,00	resultat fra vipping
Rzz ekskl. vertikalkomp.	m					

KRENGEPRØVE		Fullskala	Modellskala	Målt modell	Avvik (%)	
Vekt inkl. vertikalkomp.	tonn, kp	48929,2	1493,200	1493,20	0,00	fra krengeprøve
GMxx inkl. vertikalkomp.	m	2,500	0,078	0,076	-2,72	
GMyy inkl. vertikalkomp.	m					
Txx med vekter	s					
Tyy med vekter	s					

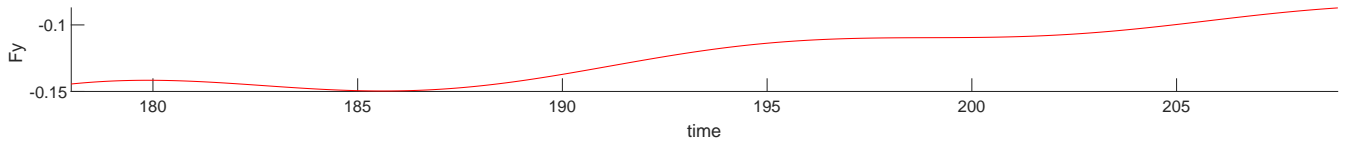
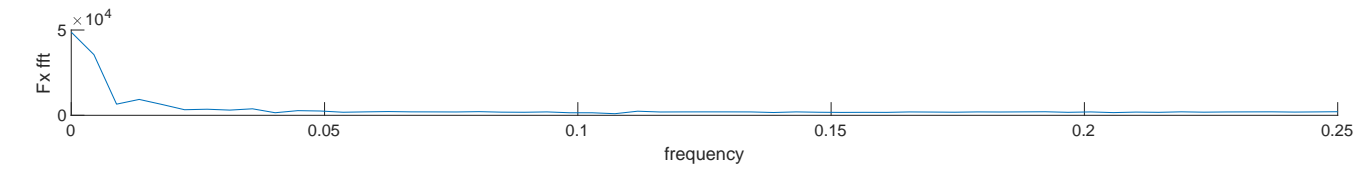
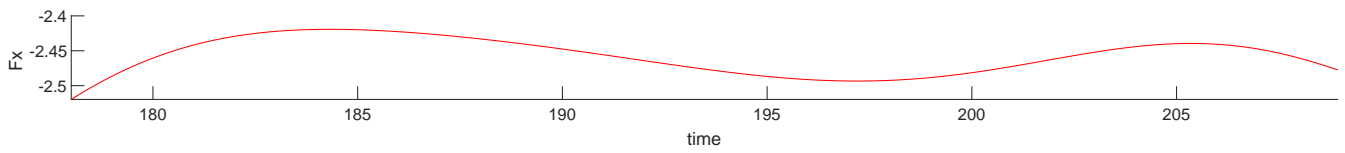
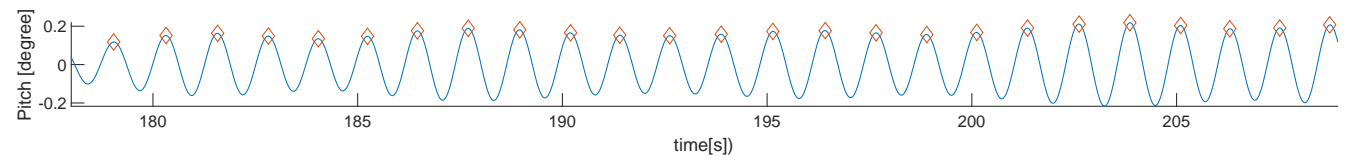
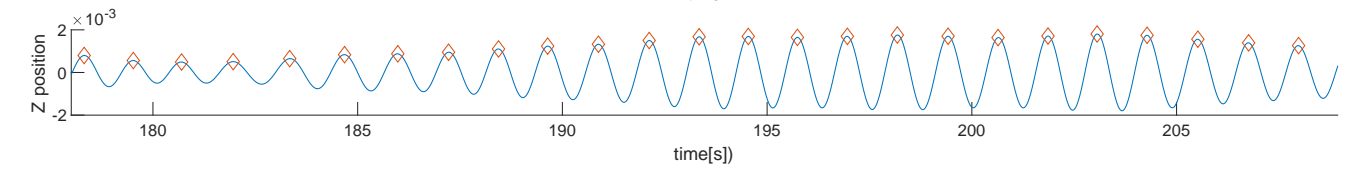
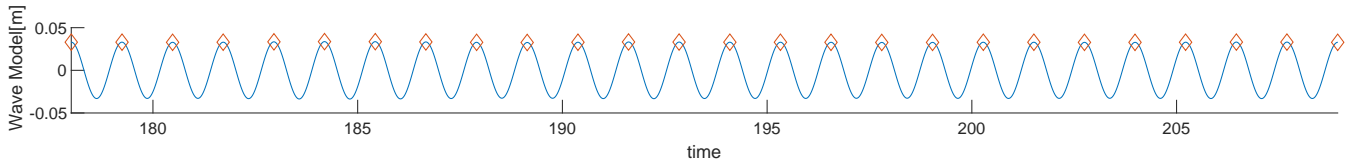
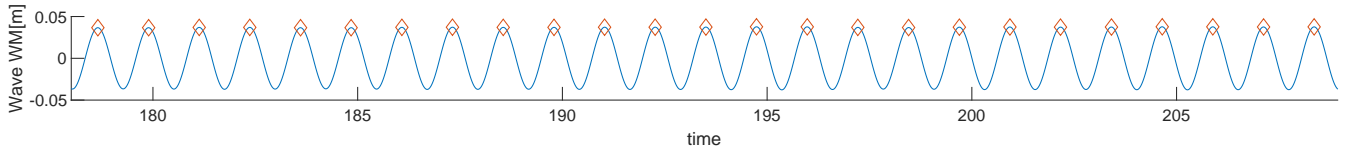


Figure B.1: Swing test

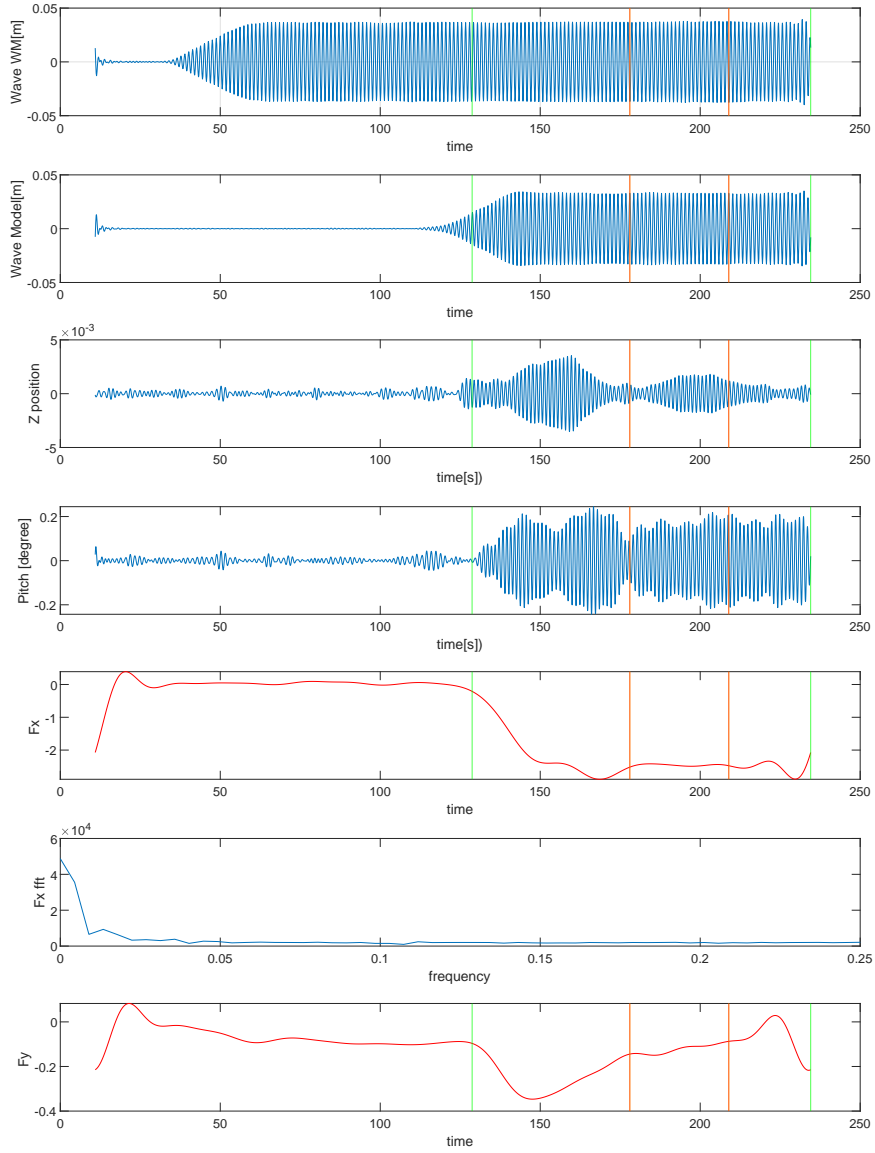
C Time series Plots

In this section all the time series plot from the test runs are presented. Two pages are provided for each page. The first page consists of the filtered time series with the time windows marked on the plot. The second page consists of the time series plots of the required parameters within the final time window, In the plots *WaveWm* represents the wave elevation measured at the wave maker, *WaveModel* represents the wave elevation measured near the model, *Z* position represents the heave motion of the vessel, *Pitch* represent the pitch motion of the vessel, *Fx* represents the longitudinal force measured, *Fxfft* represents the Fourier transformed longitudinal force and *Fy* represents the total transverse force on the vessel.

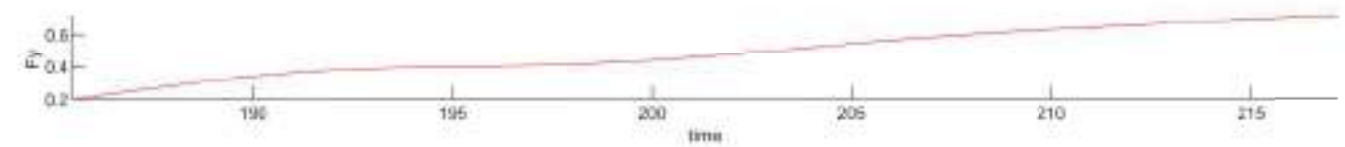
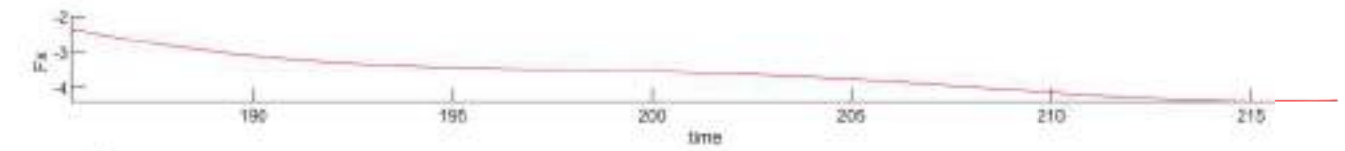
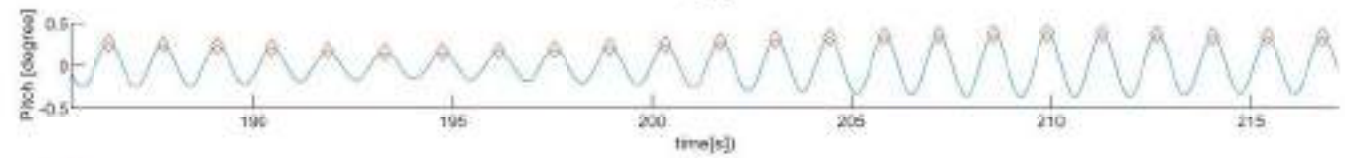
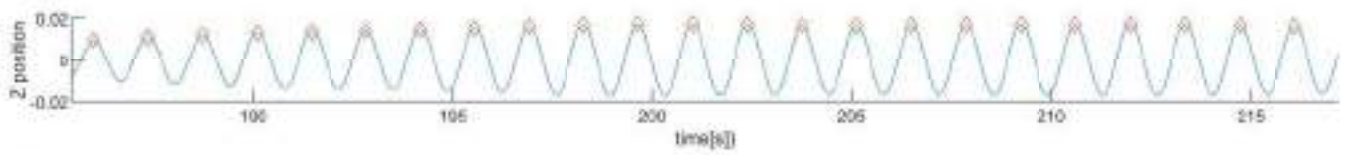
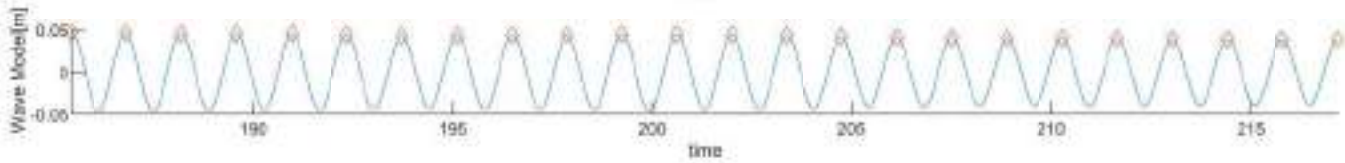
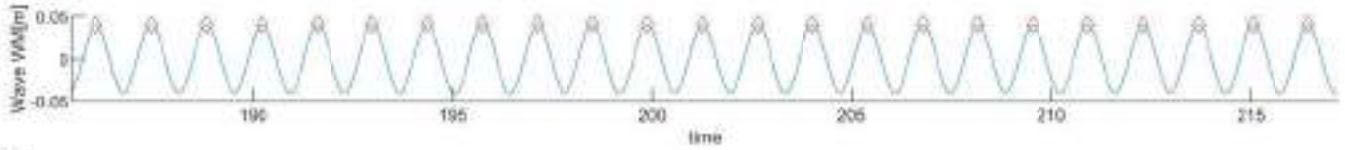
CE2001 Period(s):7 Lamda/L:0.4 Drift angle(deg):0 Speed(m/s):0



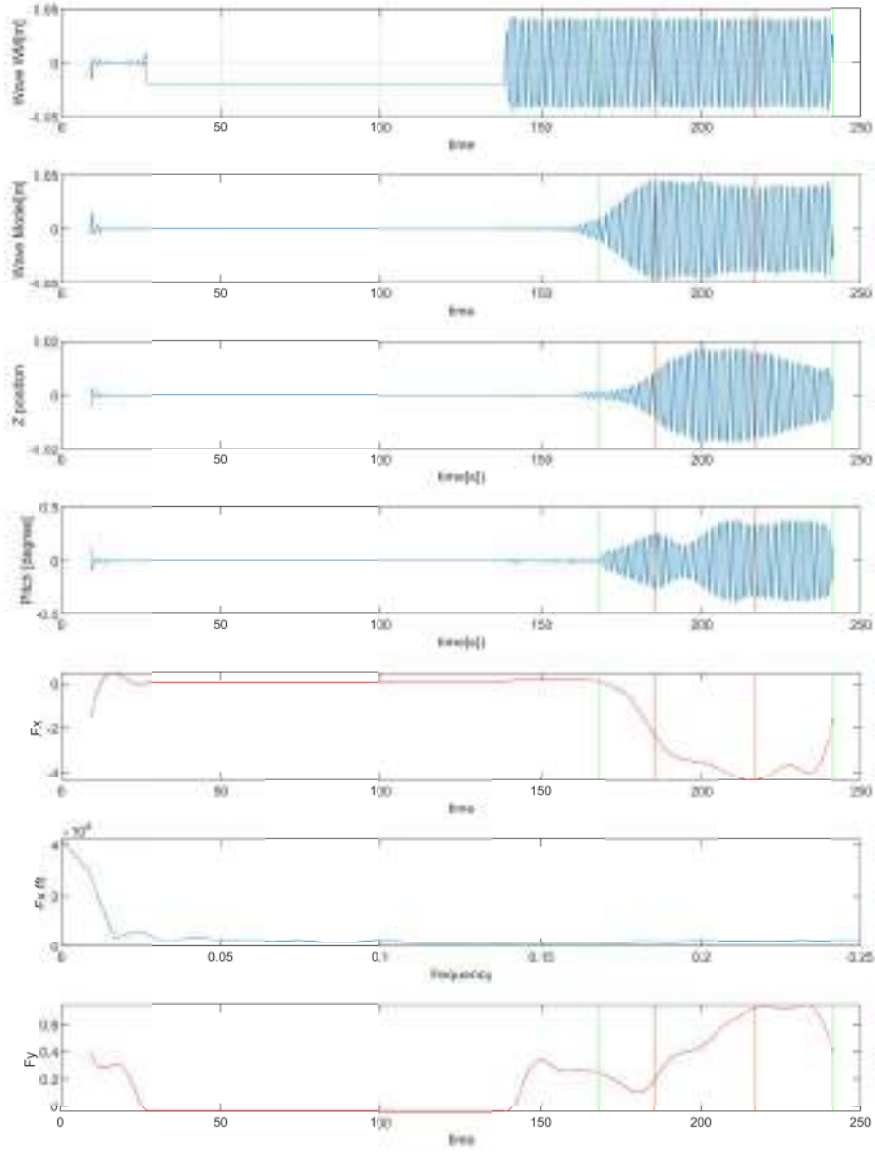
CE2001 Period(s):7 Lamda/L:0.4 Drift agle(deg):0 Speed(m/s):0



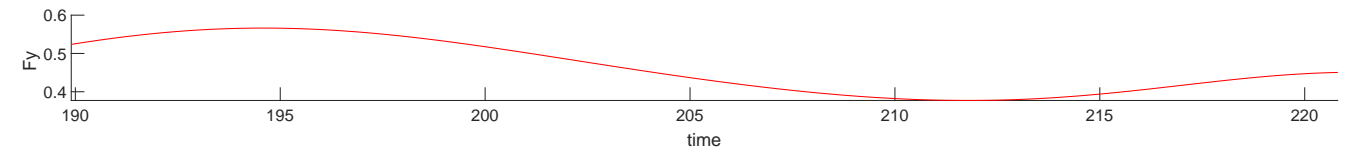
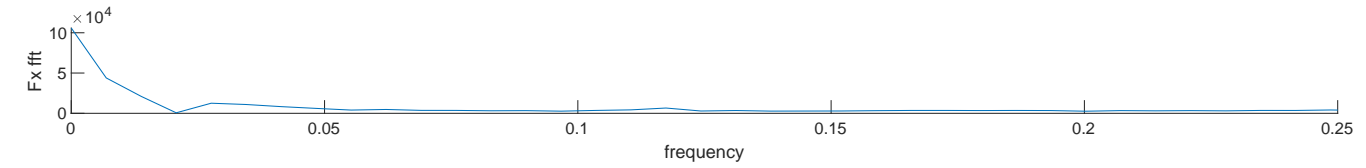
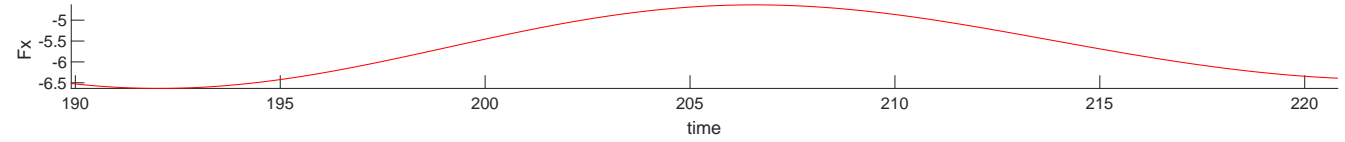
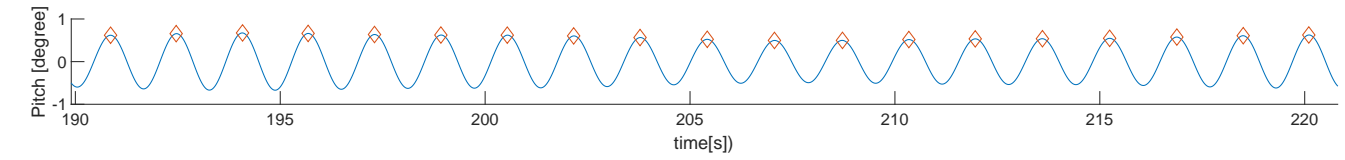
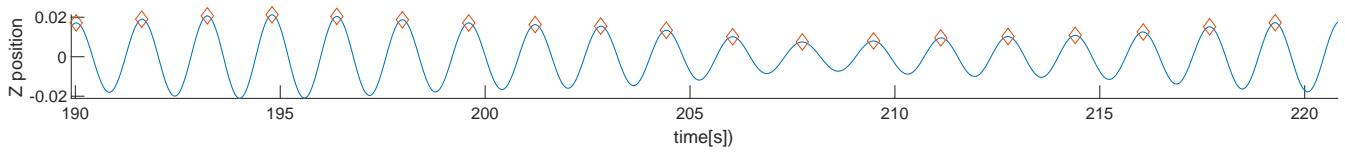
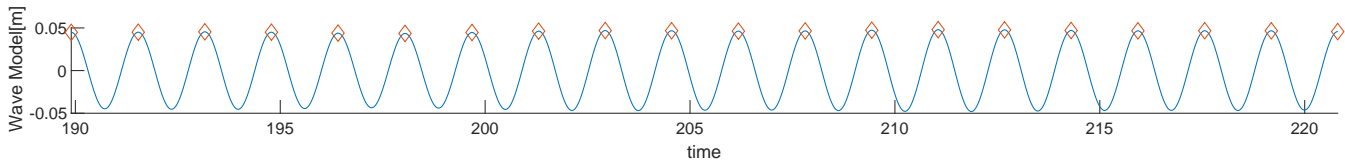
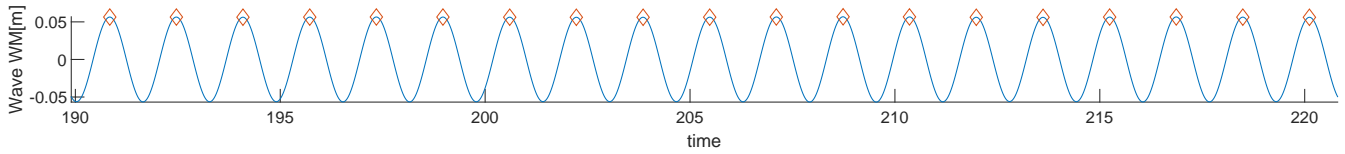
CE2010 Period(s):7.8 Lamda/L:0.5 Drift angle(deg):0 Speed(m/s):0



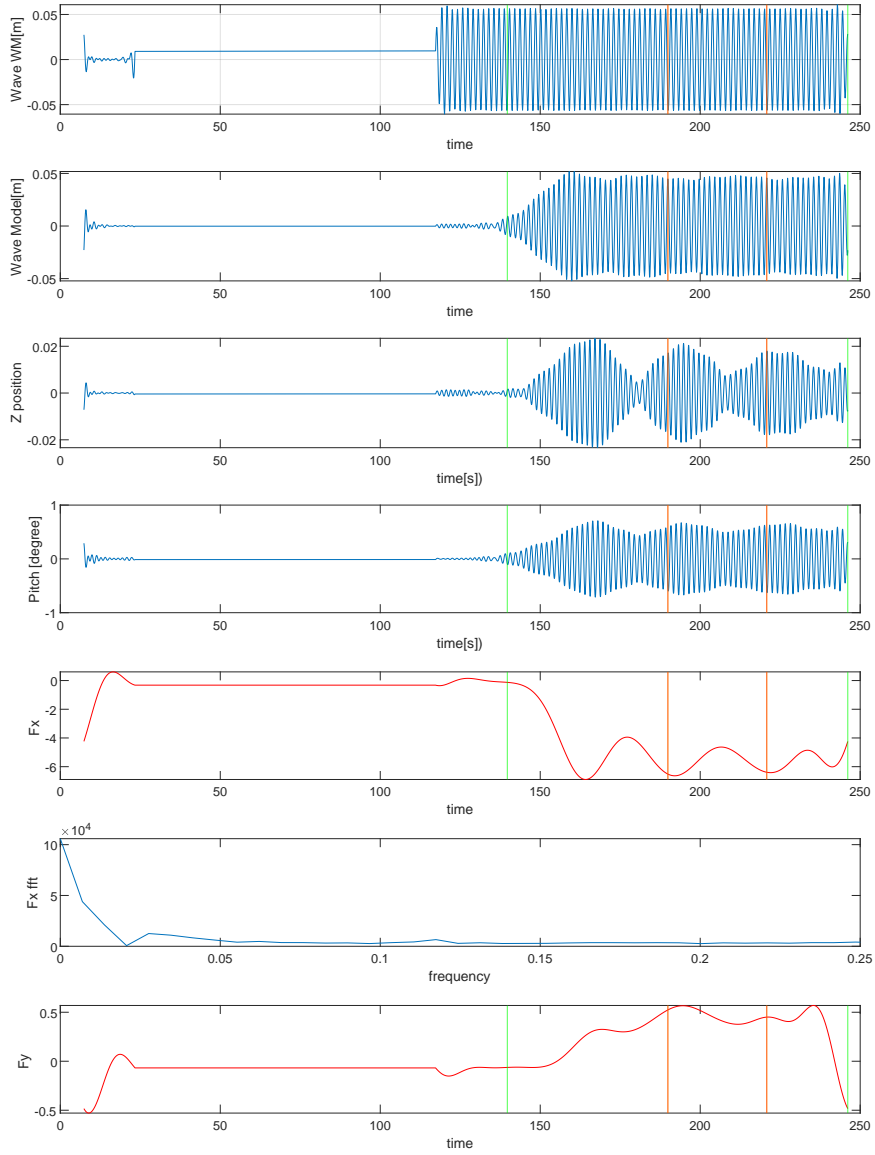
CE2010 Period(s):7.8 Lambda:L:0.5 Drift angle(deg):0 Speed(m/s):0



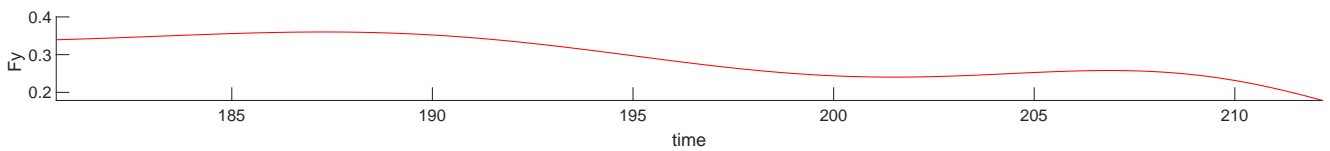
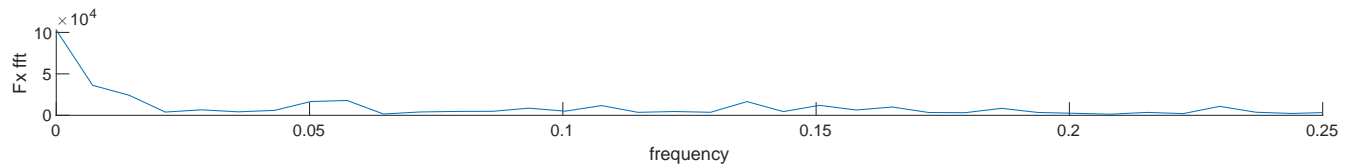
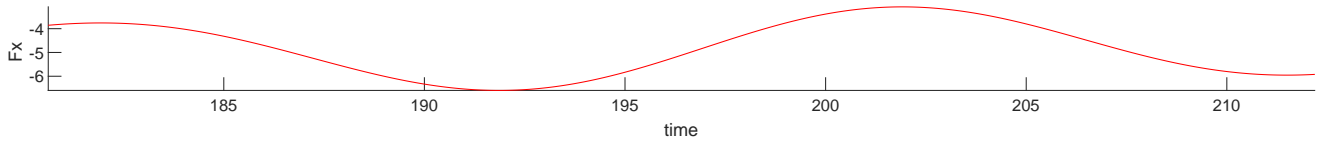
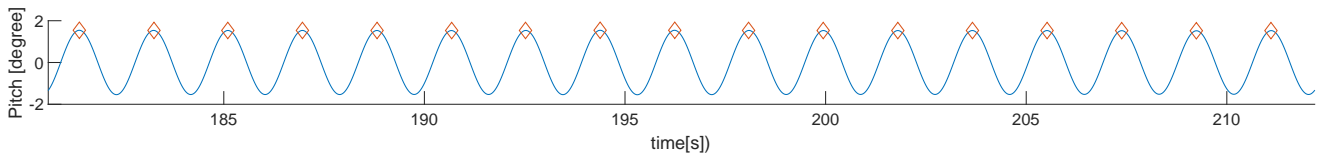
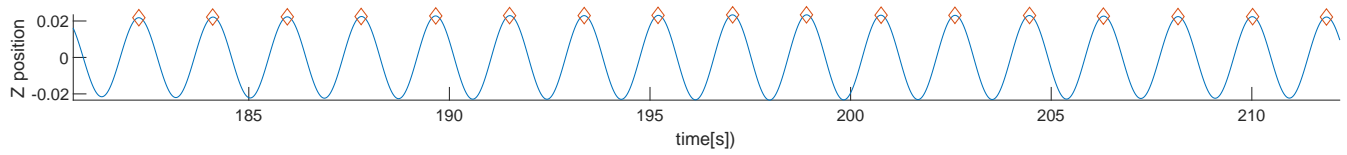
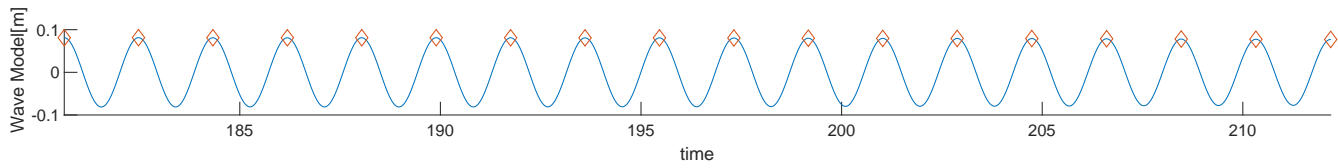
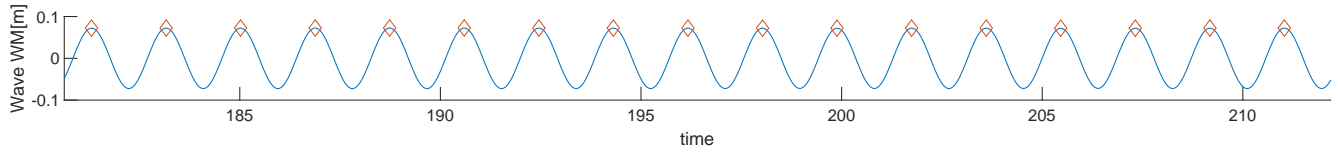
CE2020 Period(s):9.2 Lamda/L:0.7 Drift agle(deg):0 Speed(m/s):0



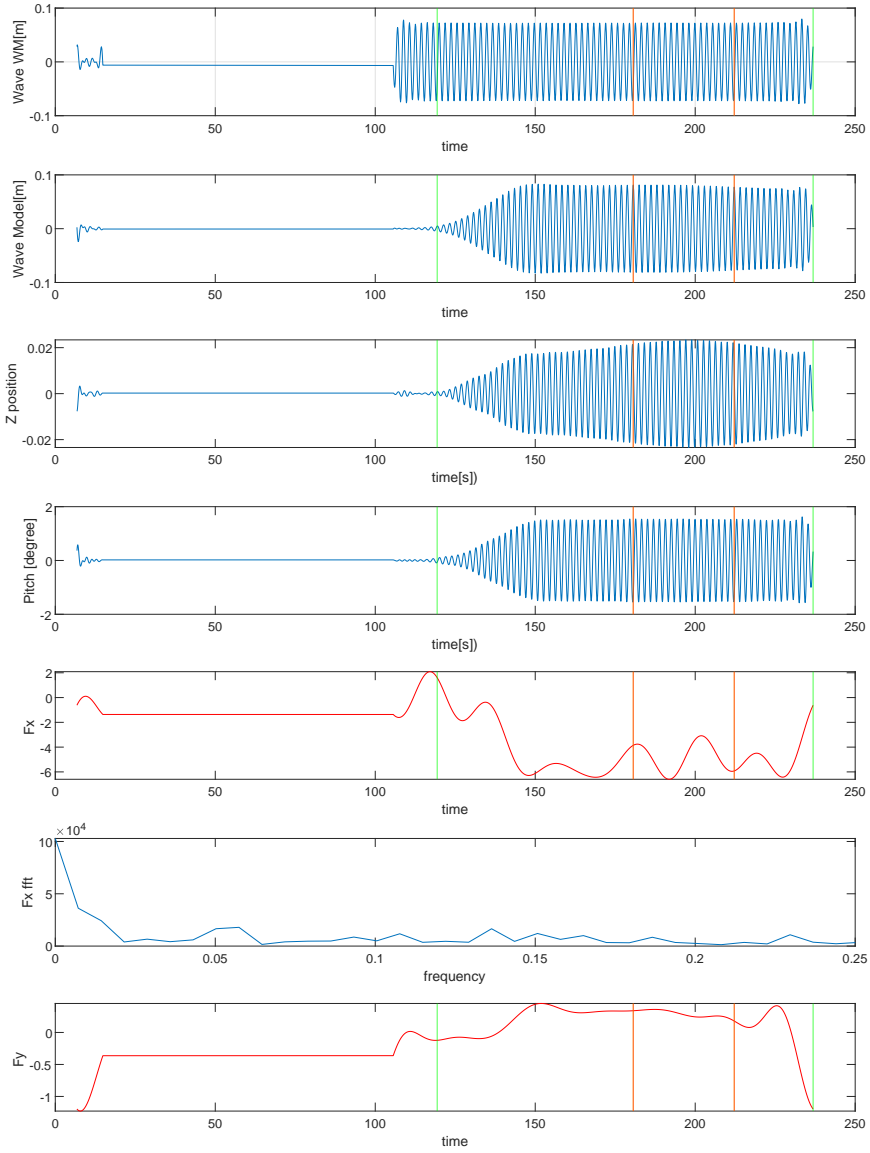
CE2020 Period(s):9.2 Lamda/L:0.7 Drift agle(deg):0 Speed(m/s):0



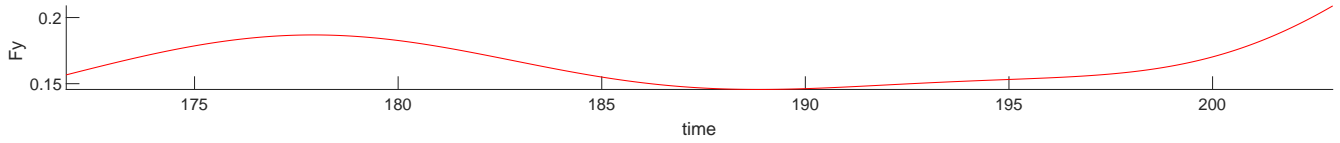
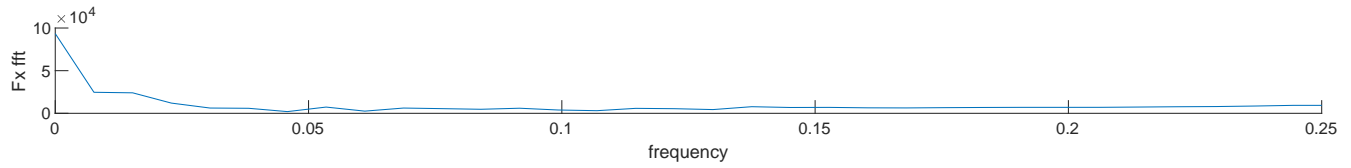
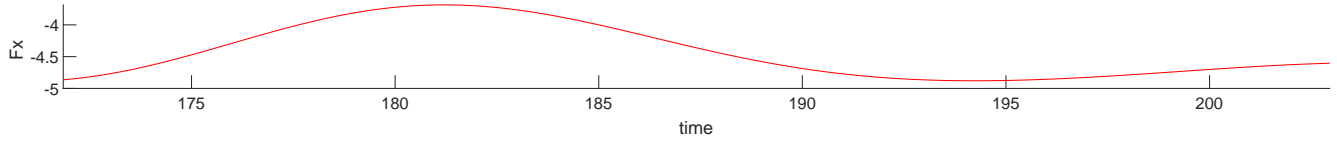
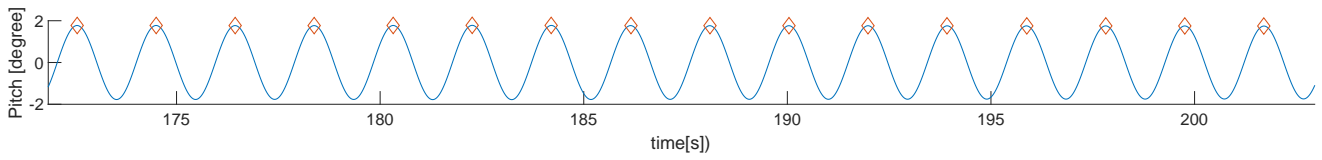
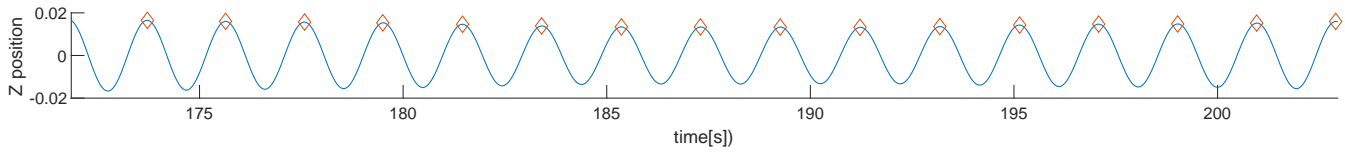
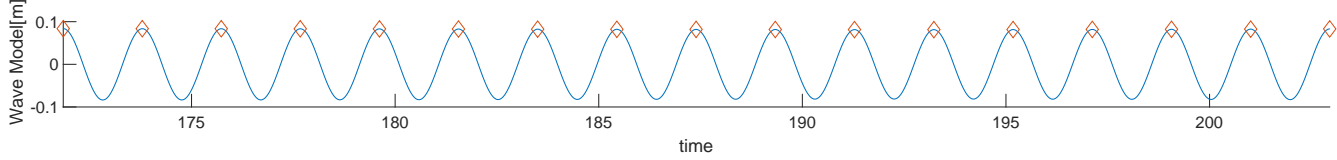
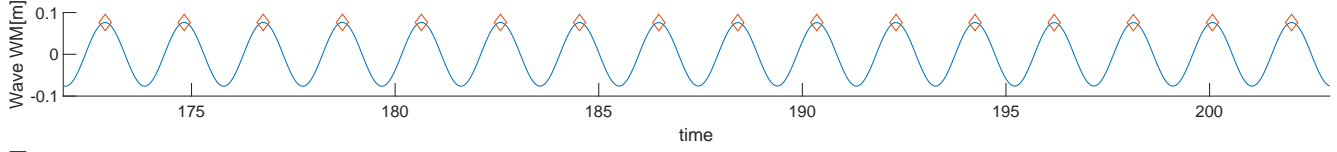
CE2031 Period(s):10.5 Lamda/L:0.91 Drift agle(deg):0 Speed(m/s):0



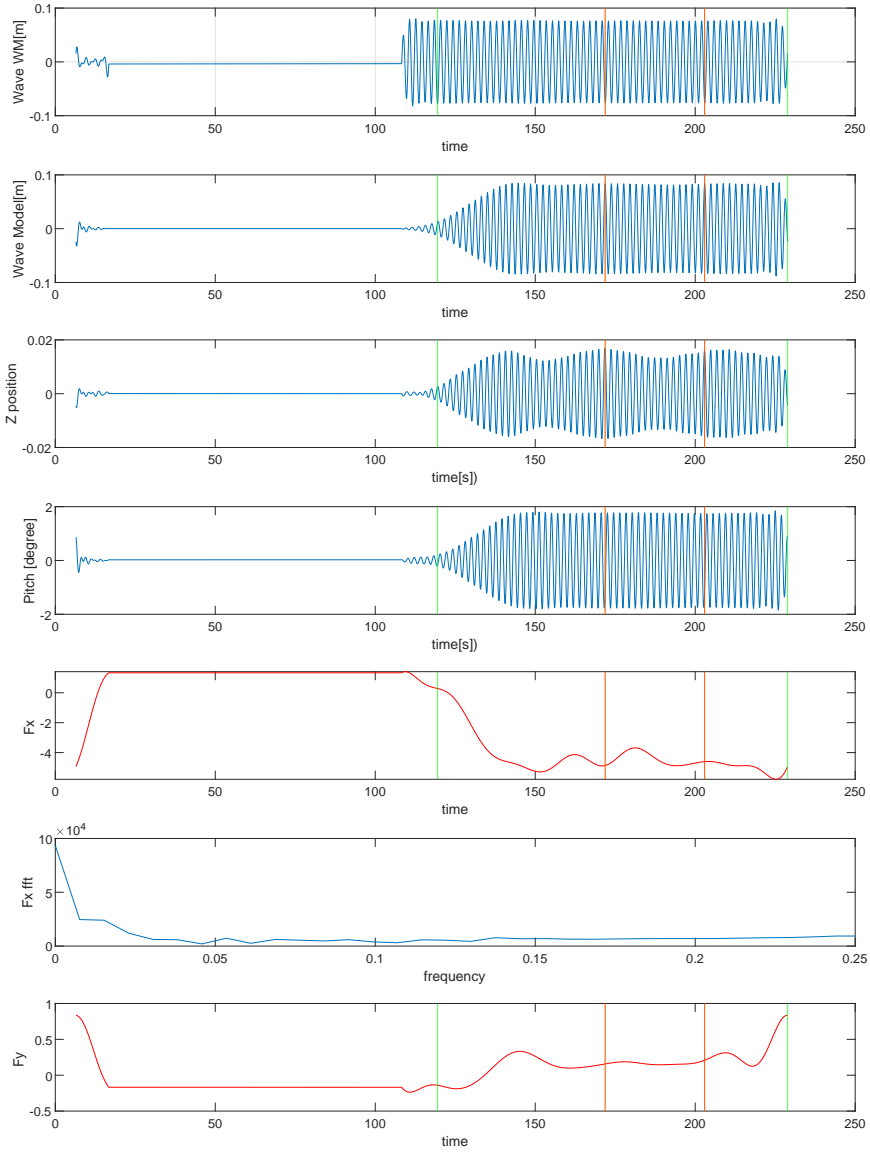
CE2031 Period(s):10.5 Lamda/L:0.91 Drift angle(deg):0 Speed(m/s):0



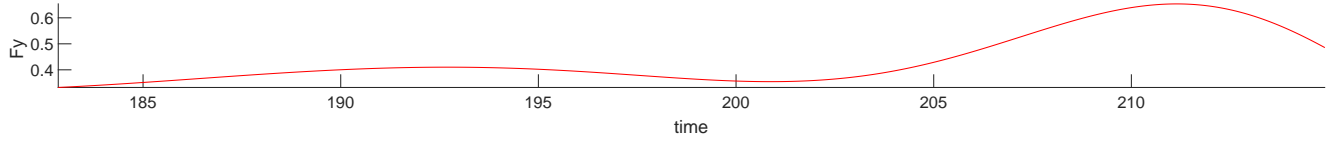
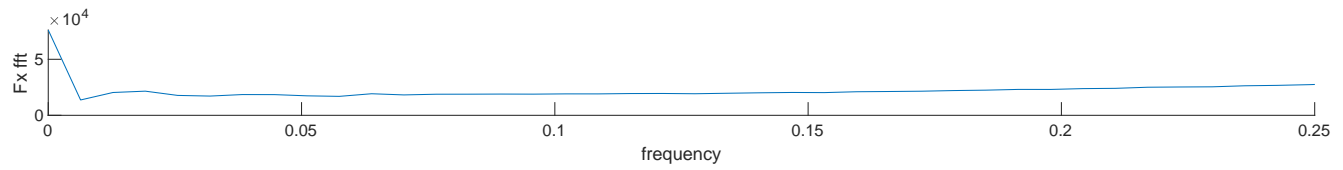
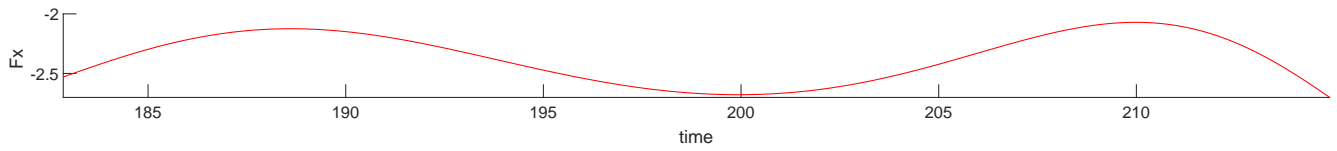
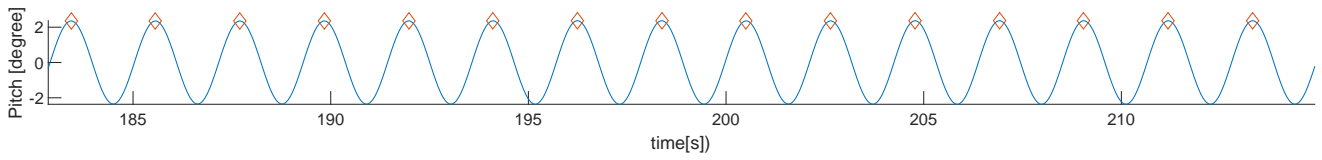
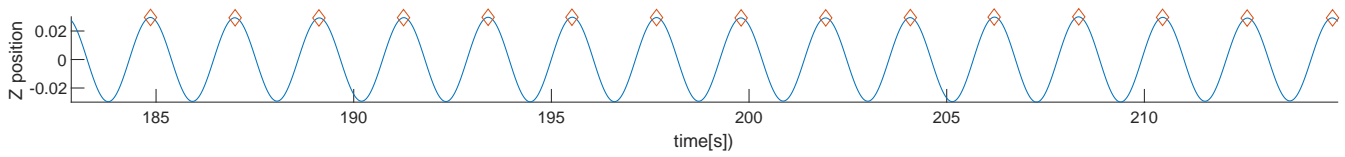
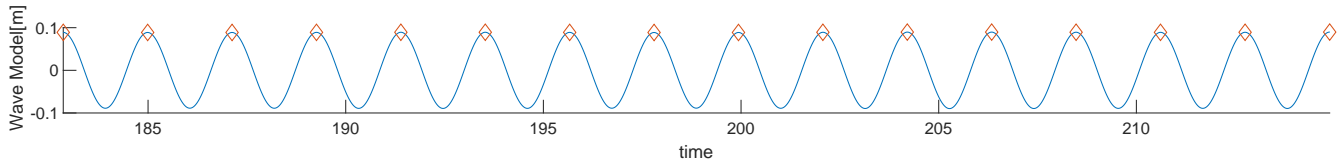
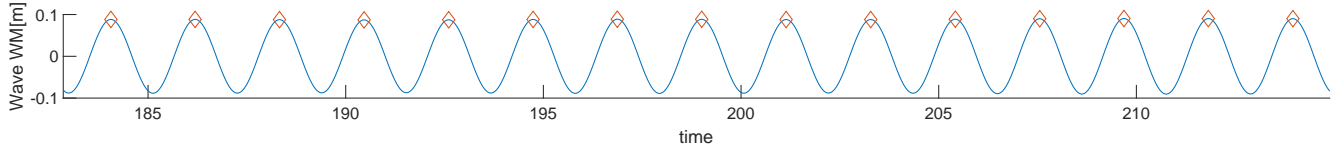
CE2040 Period(s):11 Lamda/L:0.99 Drift agle(deg):0 Speed(m/s):0



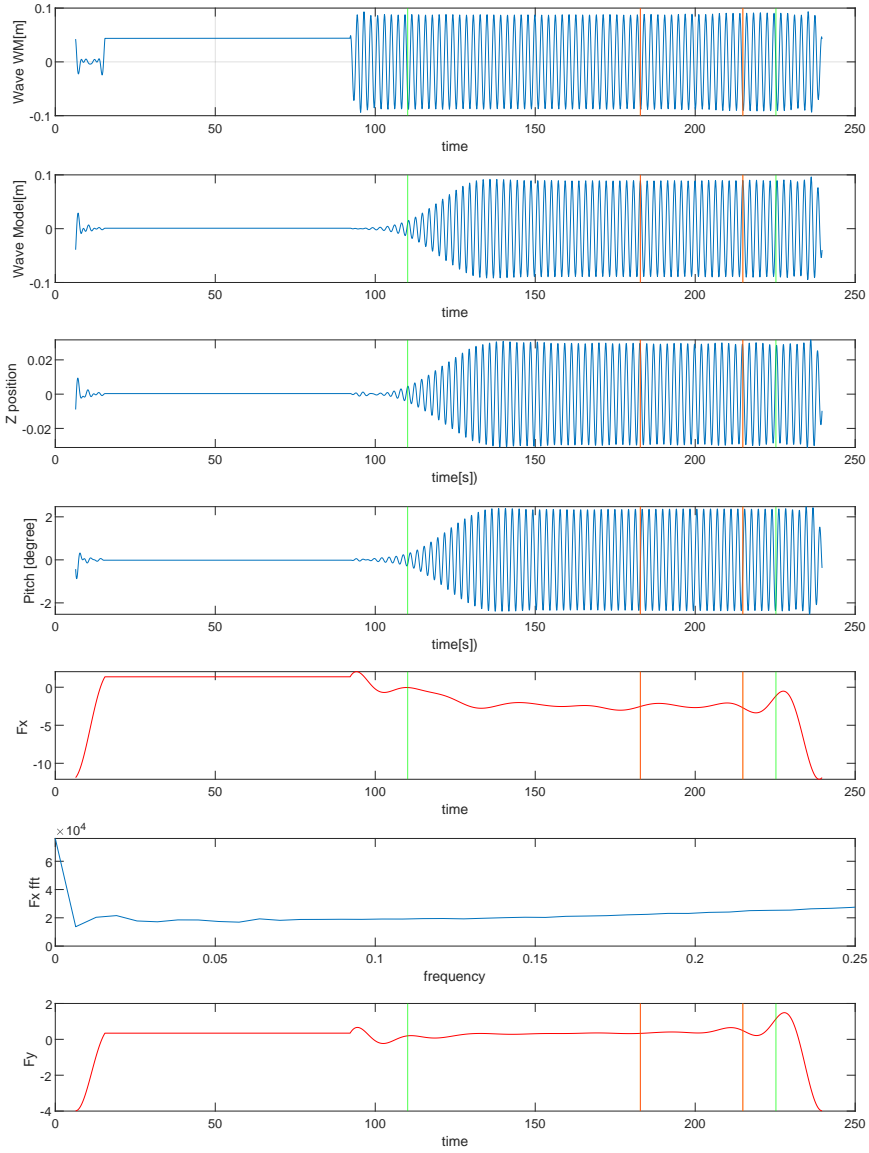
CE2040 Period(s):11 Lamda/L:0.99 Drift aple(deg):0 Speed(m/s):0



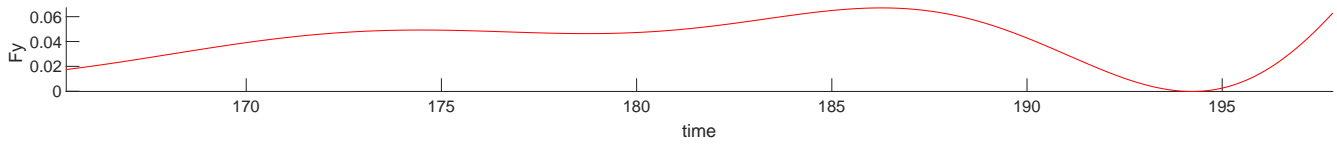
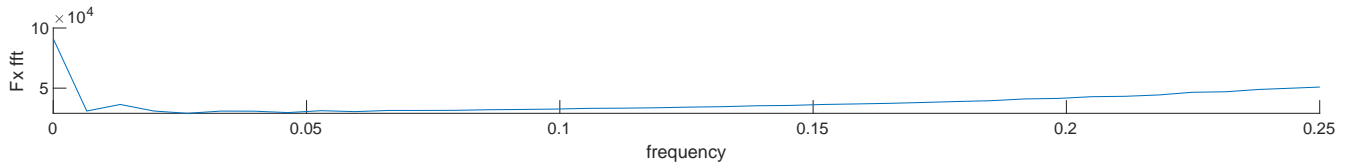
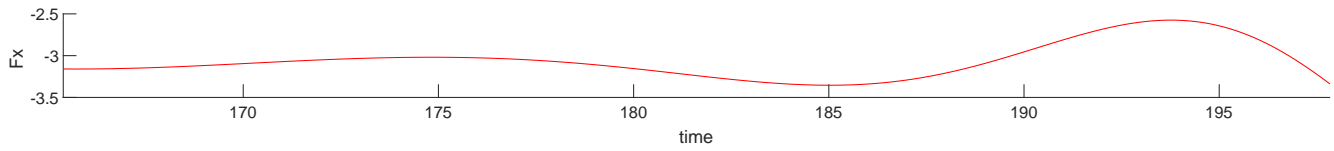
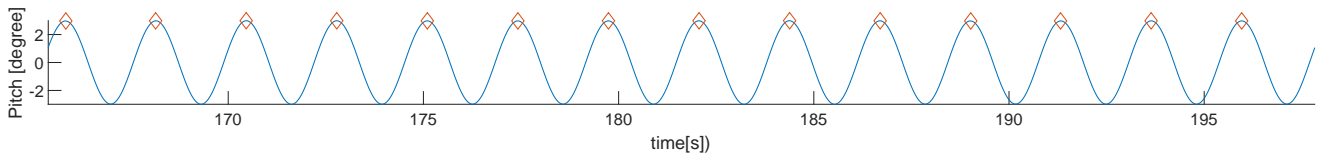
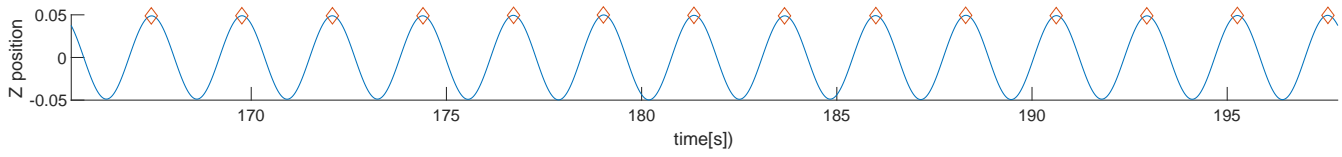
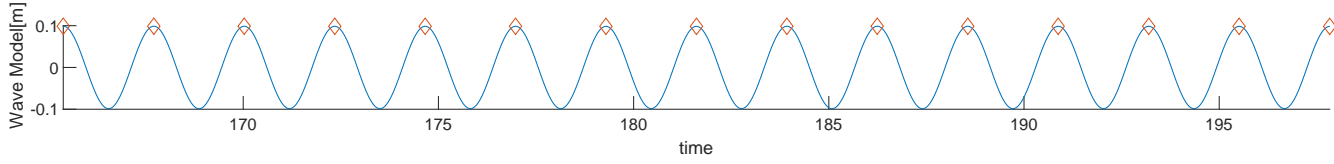
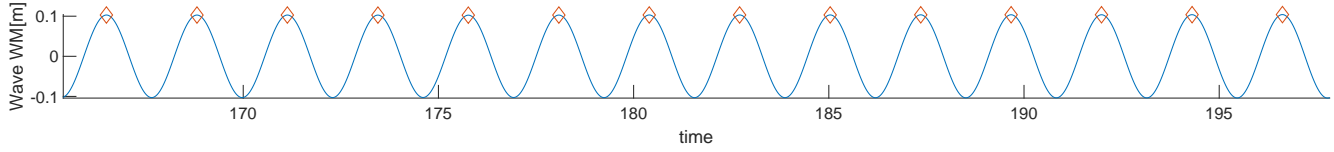
CE2050 Period(s):12.1 Lamda/L:1.2 Drift agle(deg):0 Speed(m/s):0



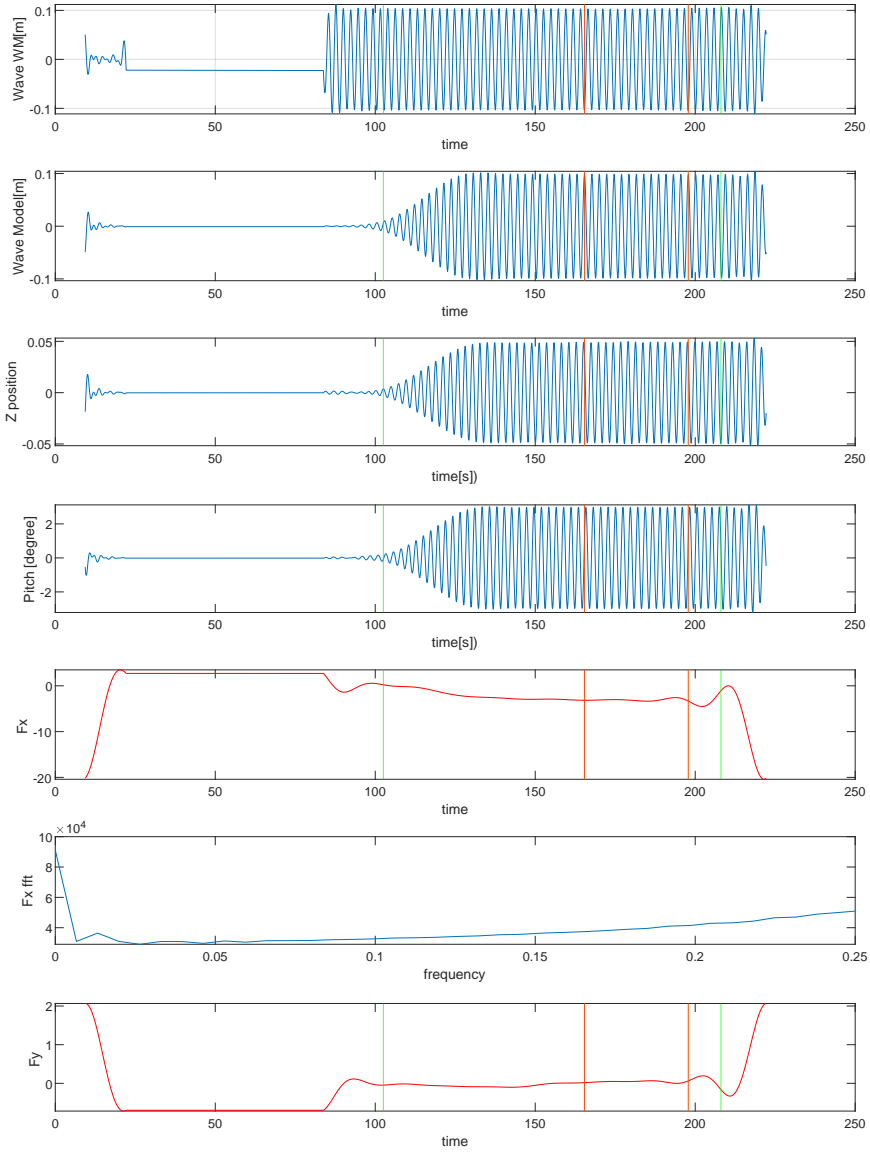
CE2050 Period(s):12.1 Lamda/L:1.2 Drift aple(deg):0 Speed(m/s):0



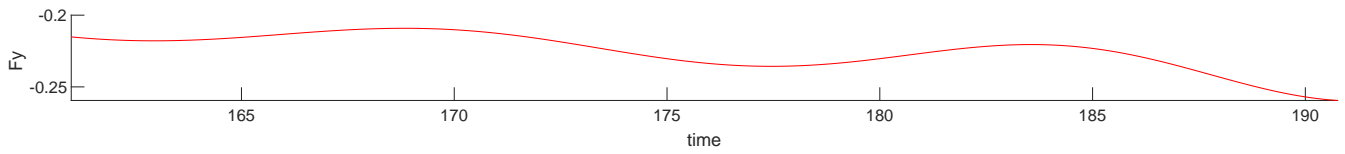
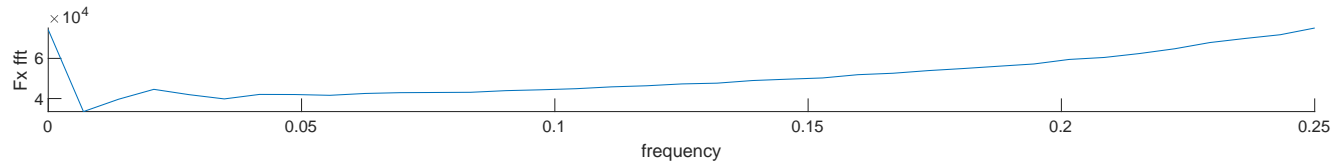
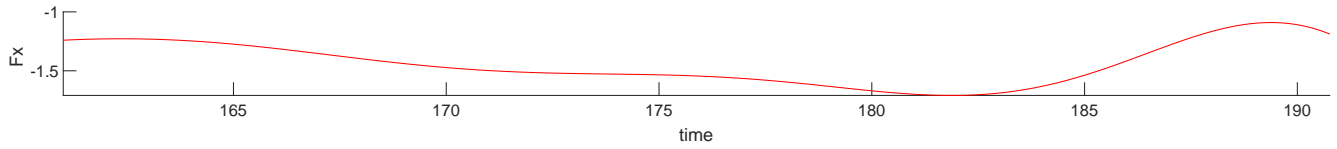
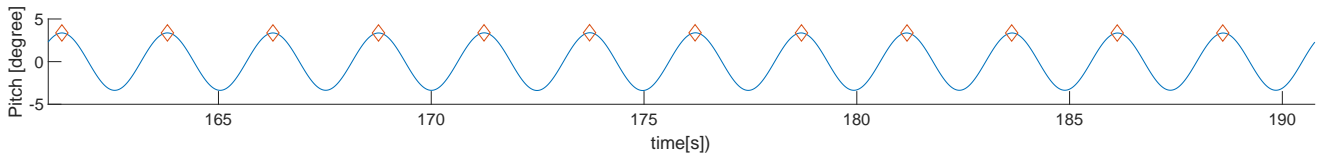
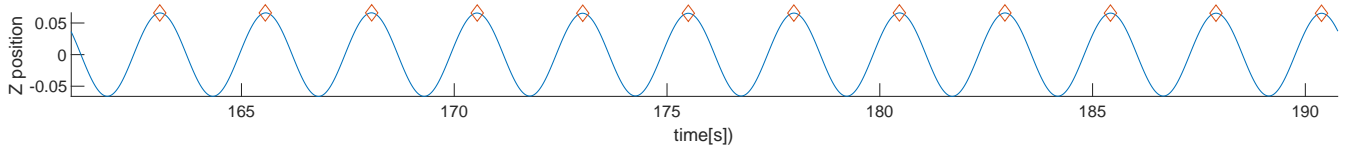
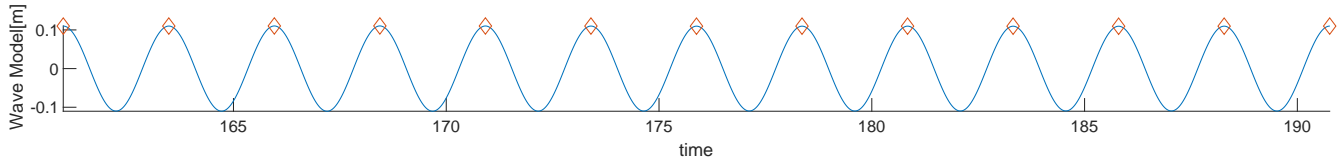
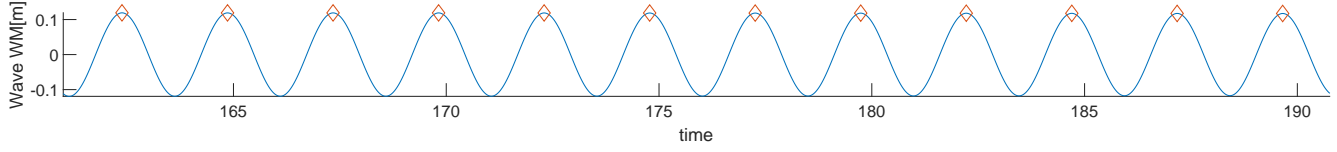
CE2060 Period(s):13.1 Lamda/L:1.41 Drift agle(deg):0 Speed(m/s):0



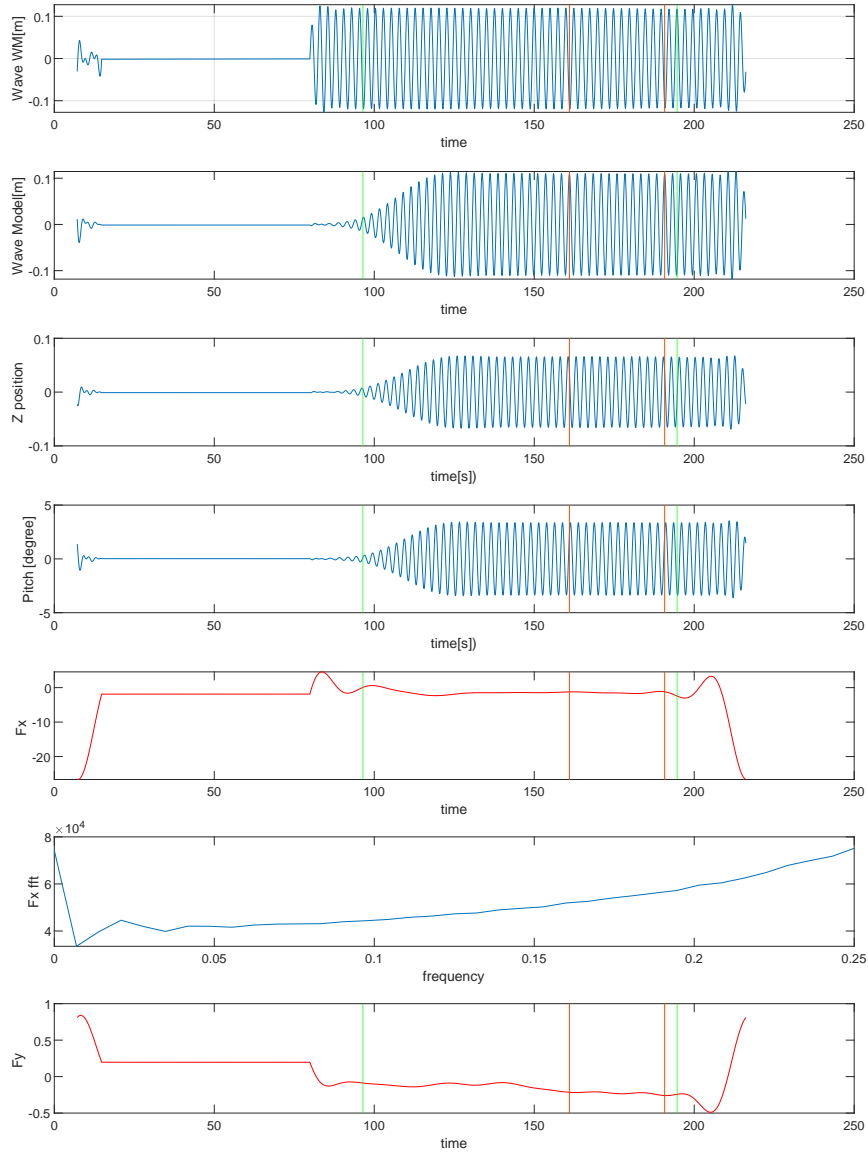
CE2060 Period(s):13.1 Lamda/L:1.41 Drift angle(deg):0 Speed(m/s):0



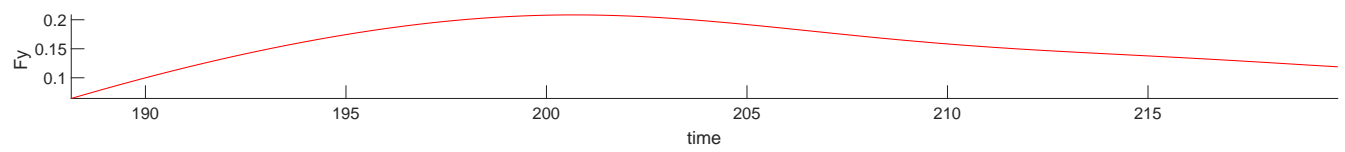
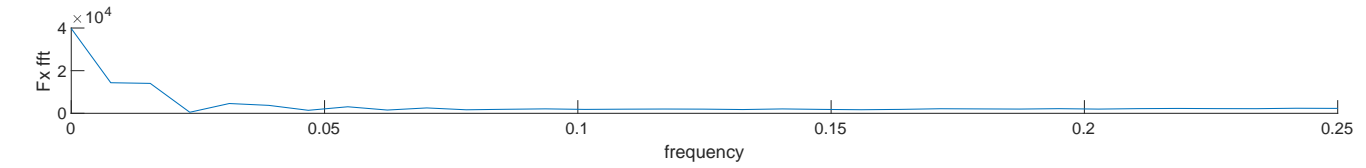
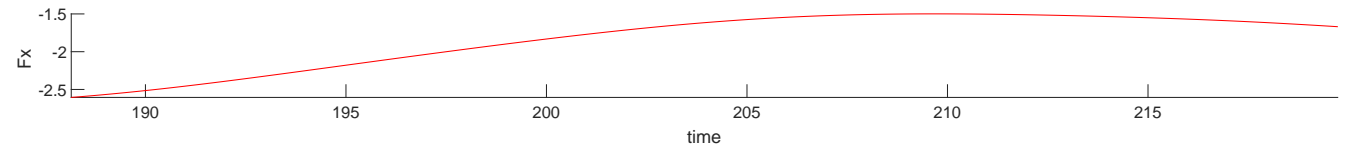
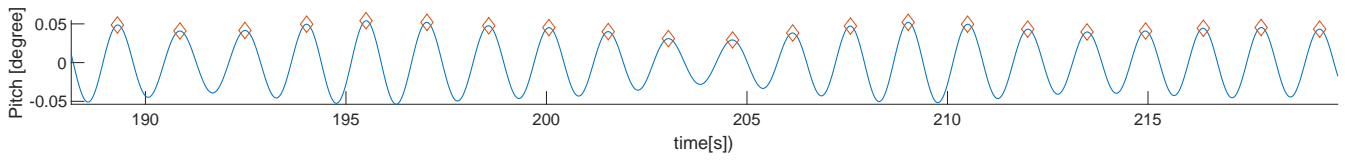
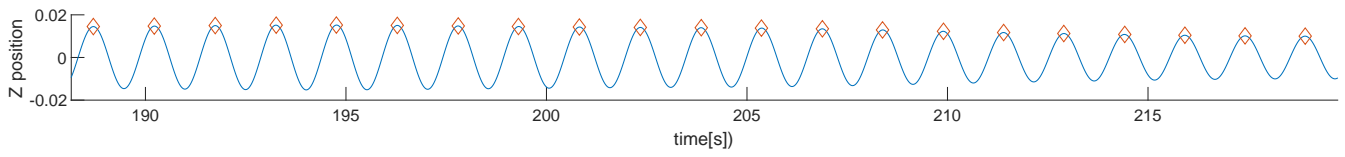
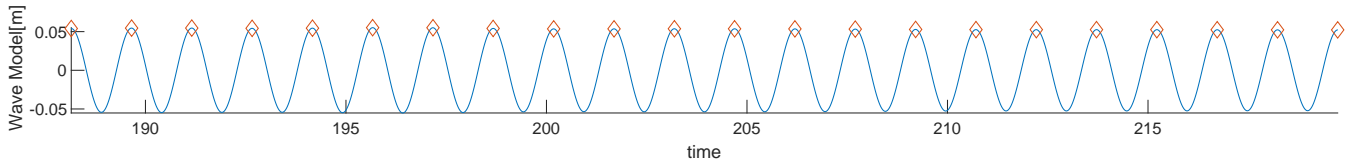
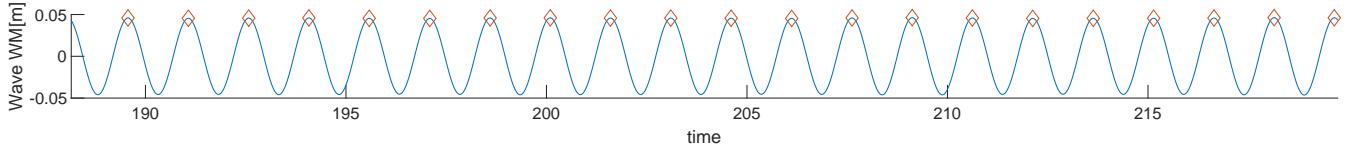
CE2070 Period(s):14 Lamda/L:1.61 Drift agle(deg):0 Speed(m/s):0



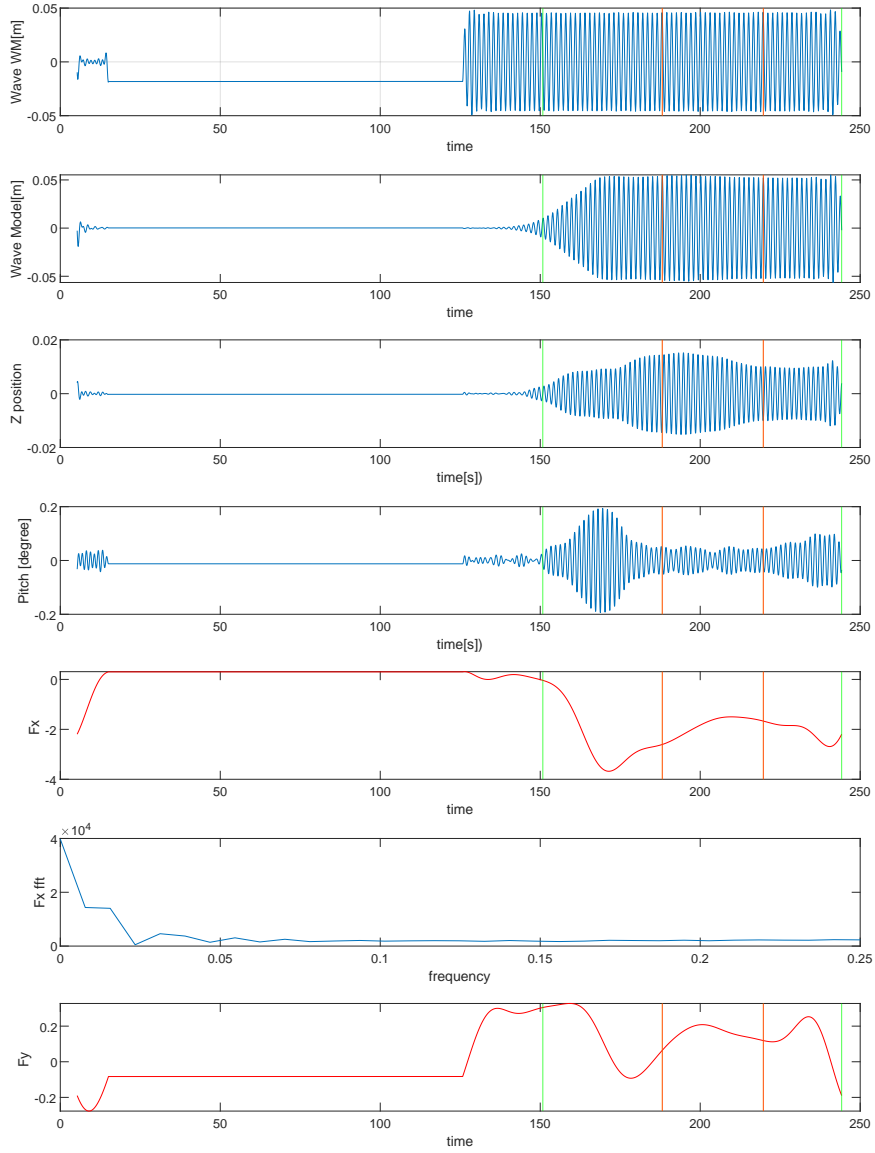
CE2070 Period(s):14 Lamda/L:1.61 Drift angle(deg):0 Speed(m/s):0



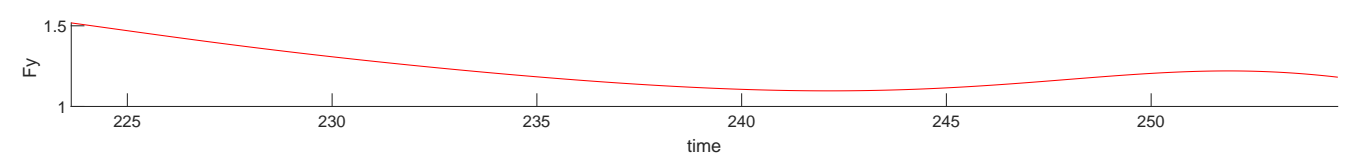
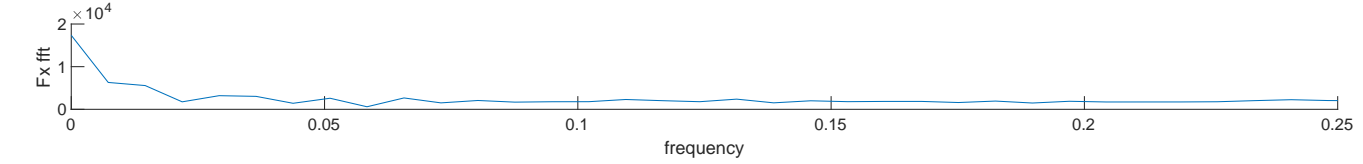
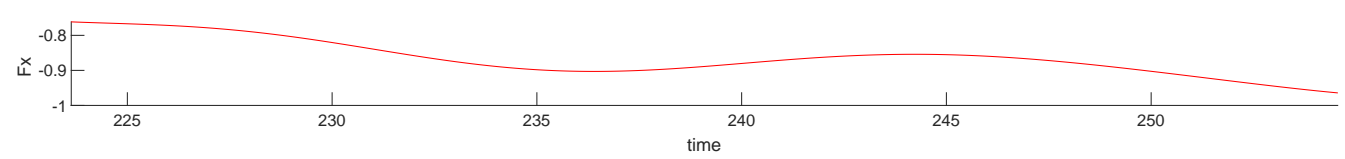
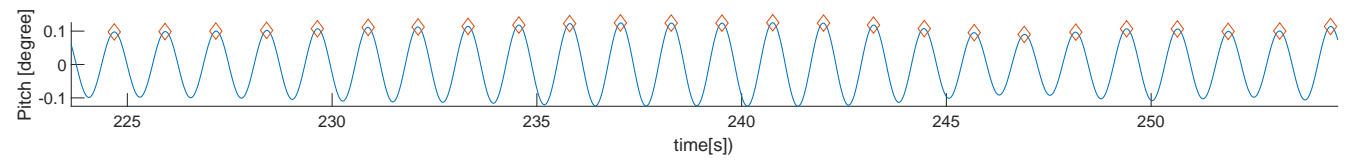
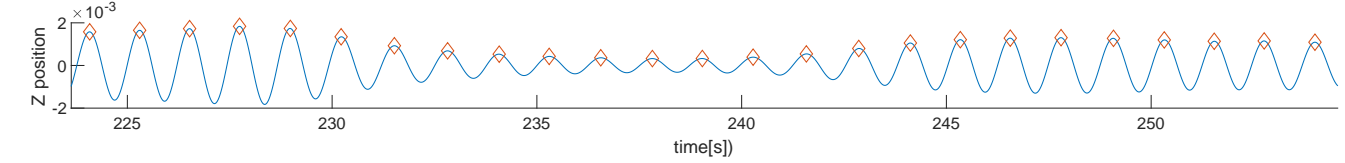
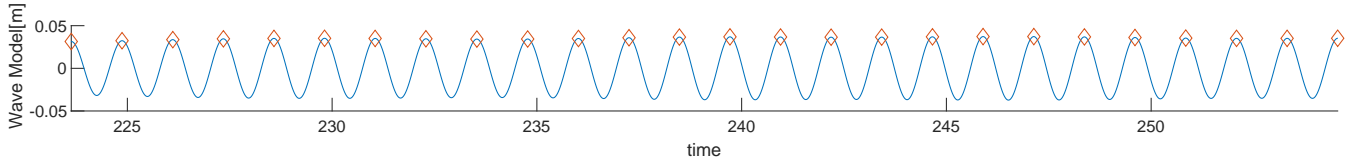
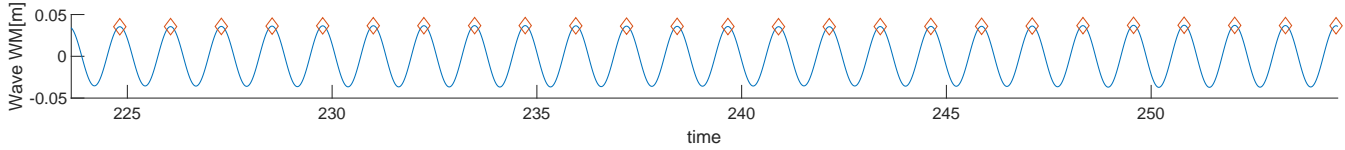
CE2071 Period(s):8.5 Lamda/L:0.59 Drift agle(deg):0 Speed(m/s):0



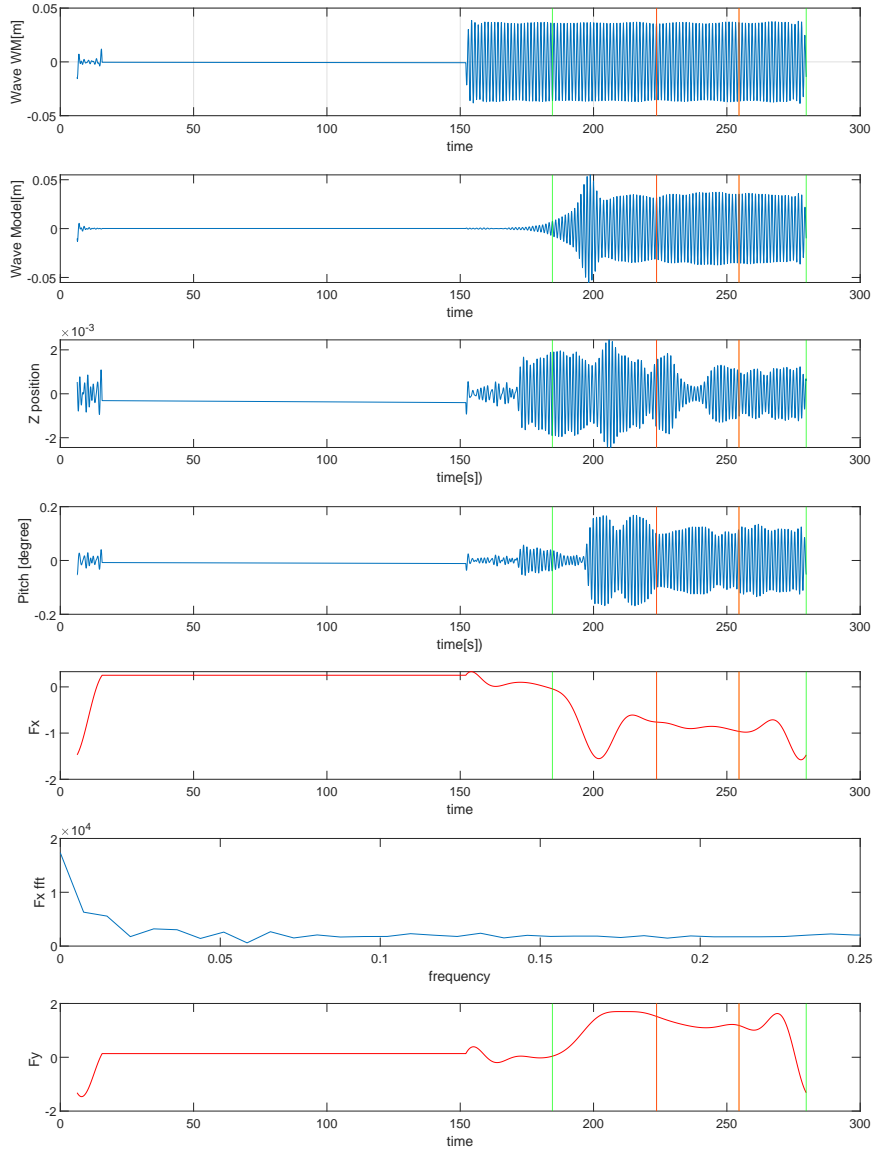
CE2071 Period(s):8.5 Lamda/L:0.59 Drift angle(deg):0 Speed(m/s):0



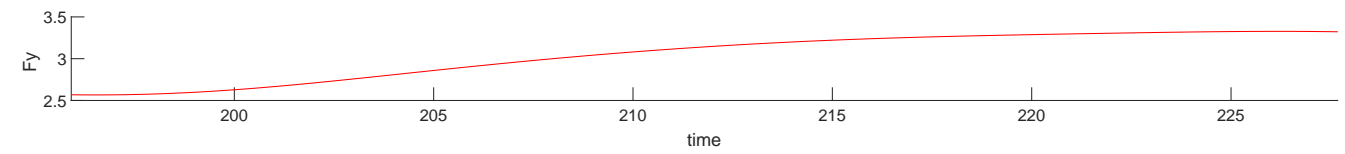
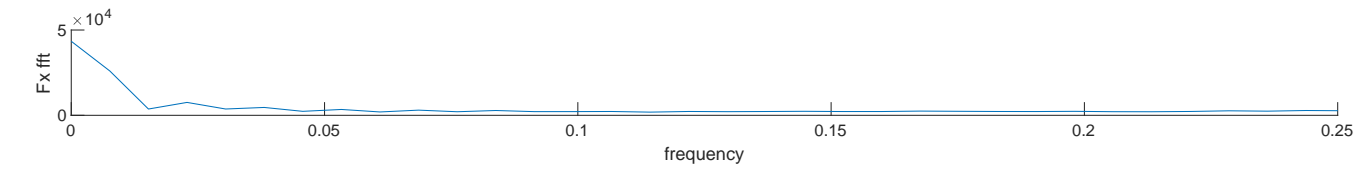
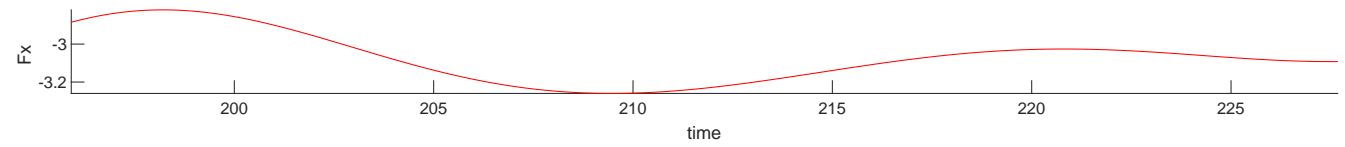
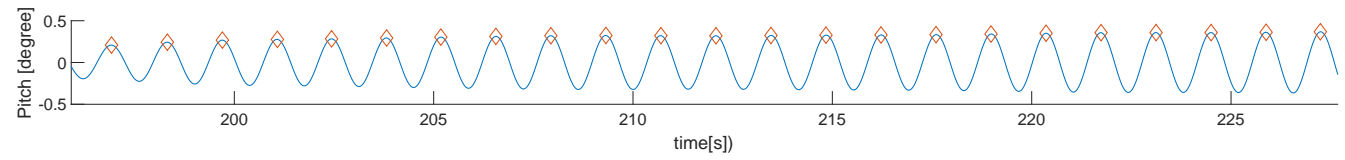
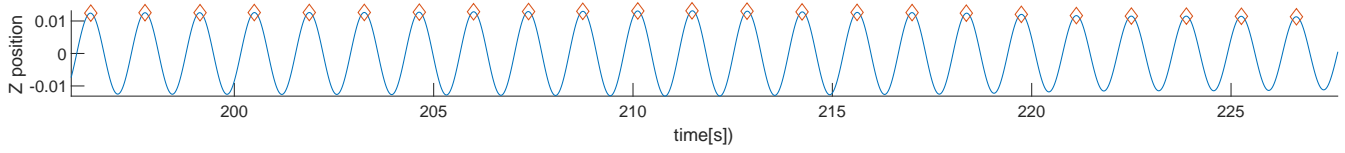
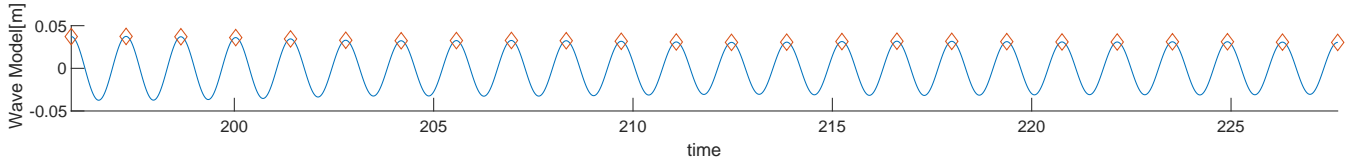
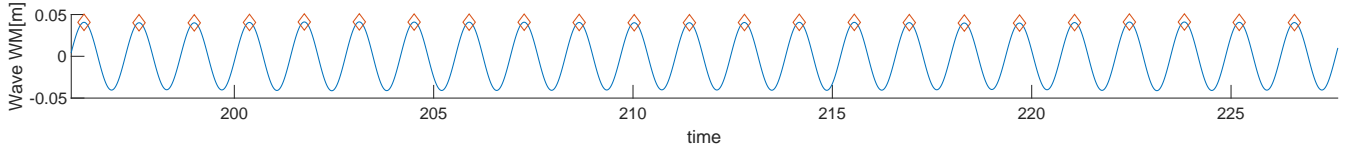
CE3000 Period(s):7 Lamda/L:0.4 Drift angle(deg):9 Speed(m/s):0



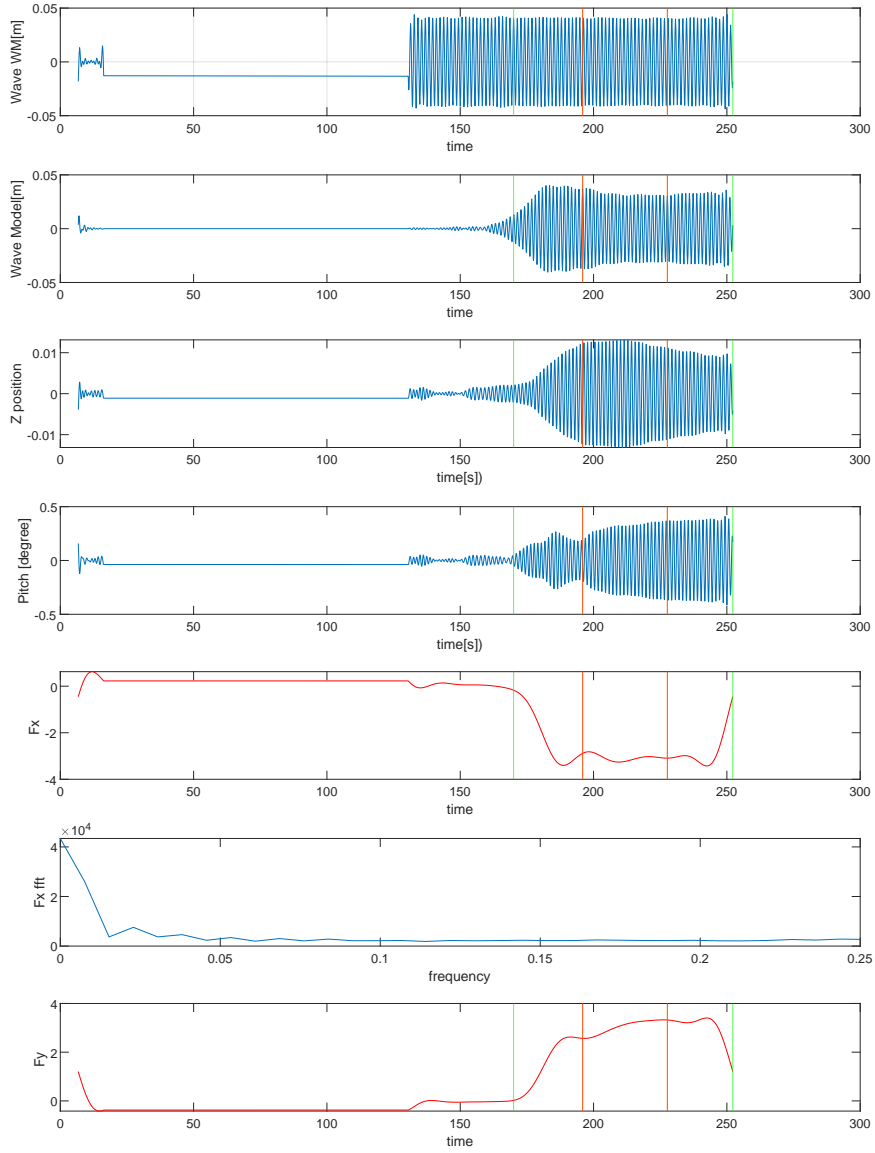
CE3000 Period(s):7 Lamda/L:0.4 Drift agle(deg):9 Speed(m/s):0



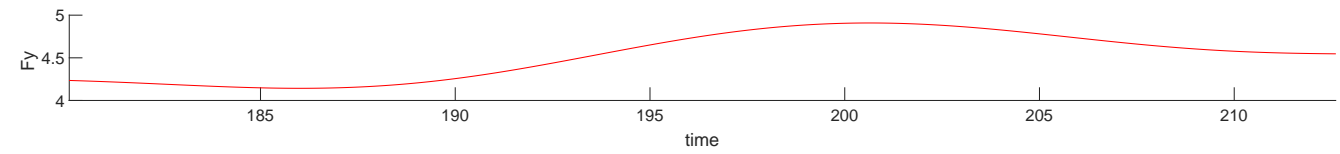
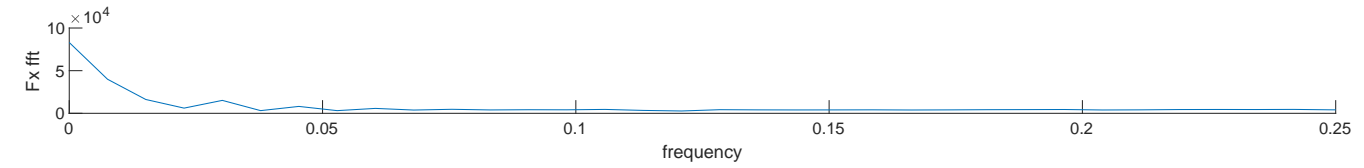
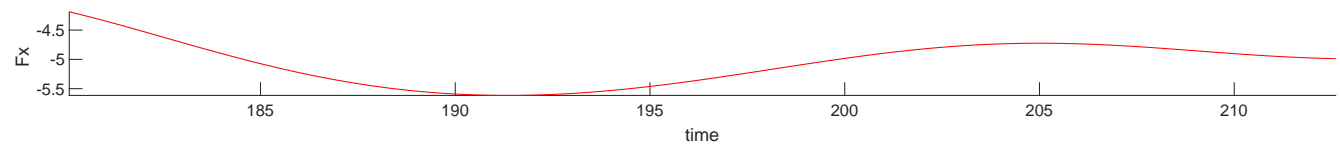
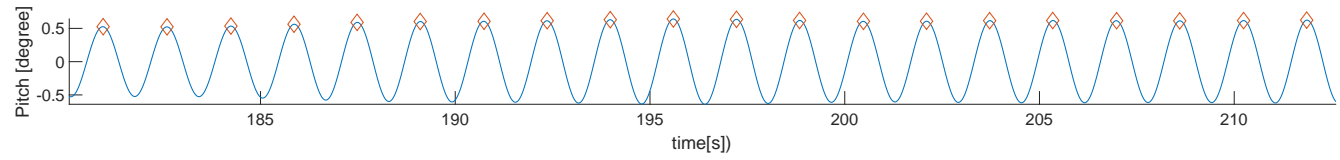
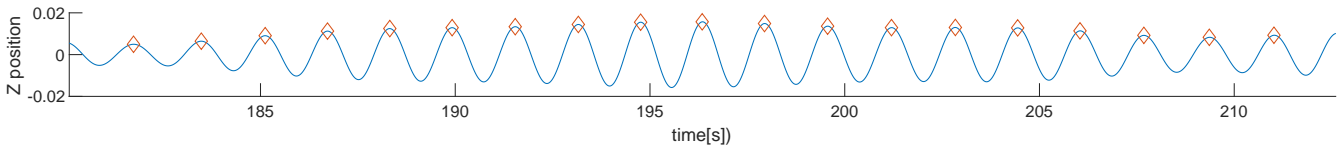
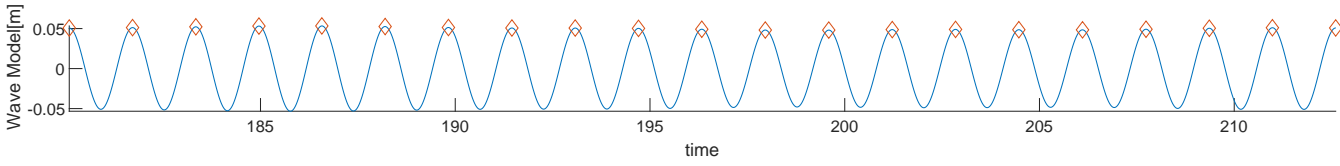
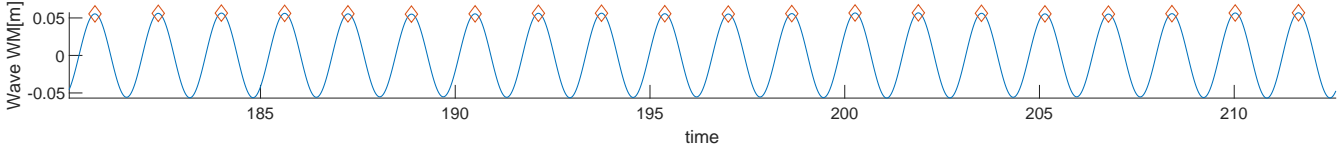
CE3010 Period(s):7.8 Lamda/L:0.5 Drift agle(deg):9 Speed(m/s):0



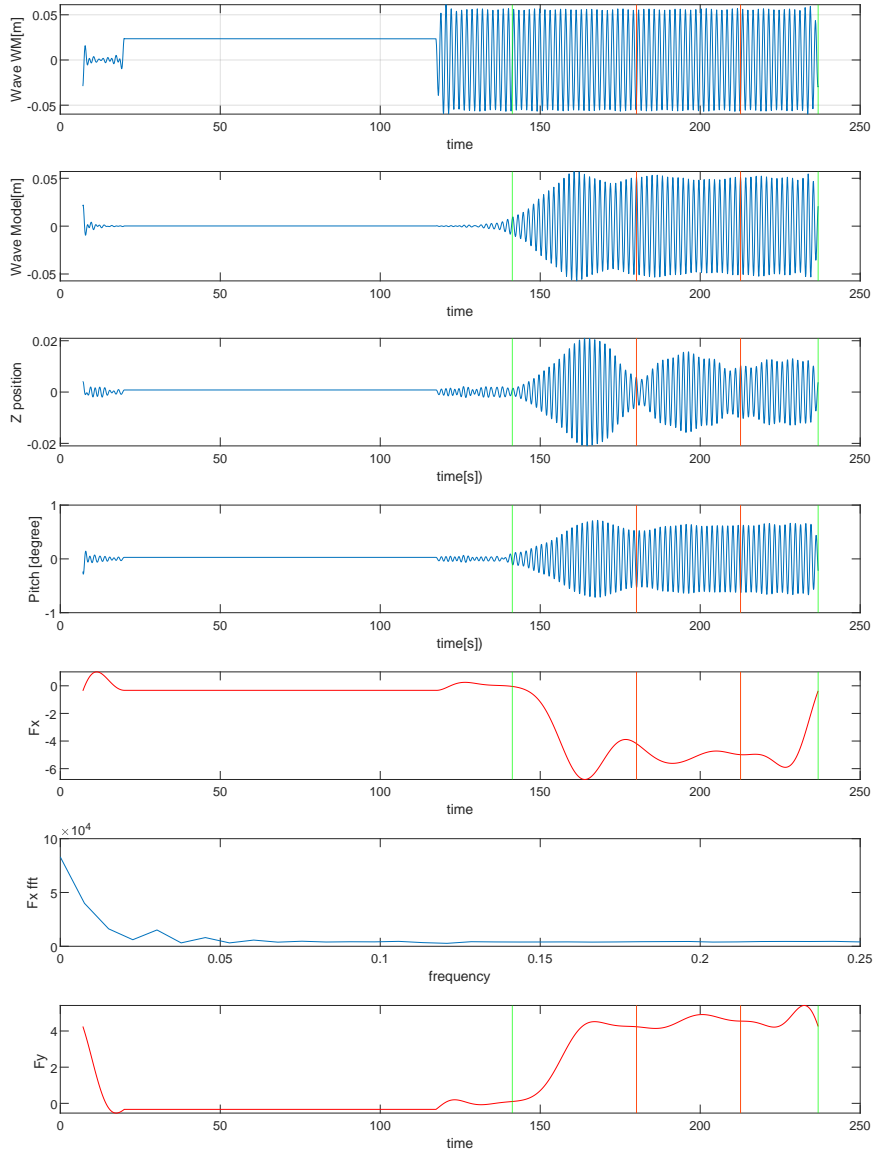
CE3010 Period(s):7.8 Lamda/L:0.5 Drift angle(deg):9 Speed(m/s):0



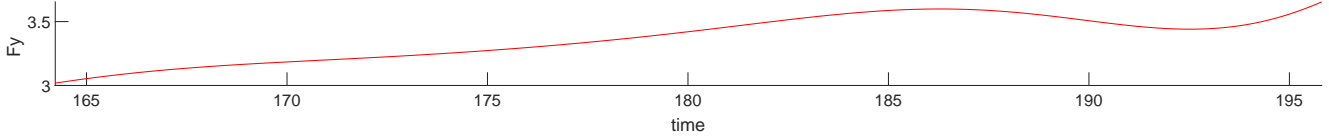
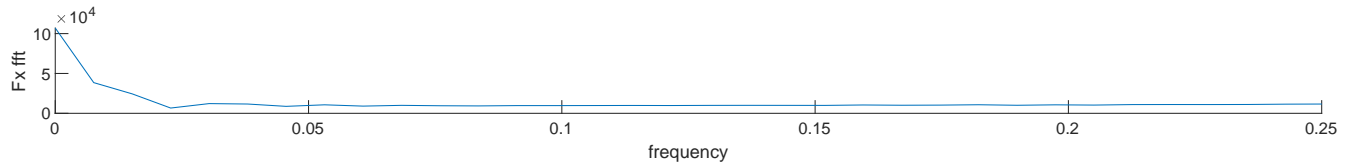
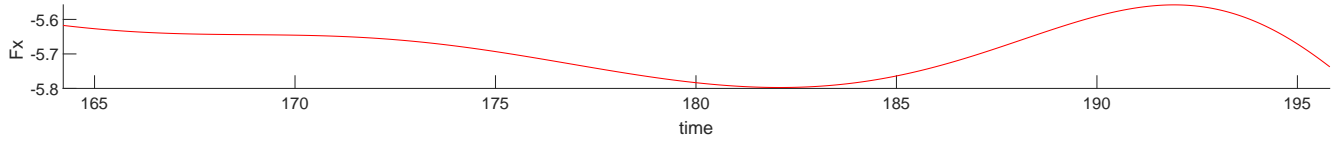
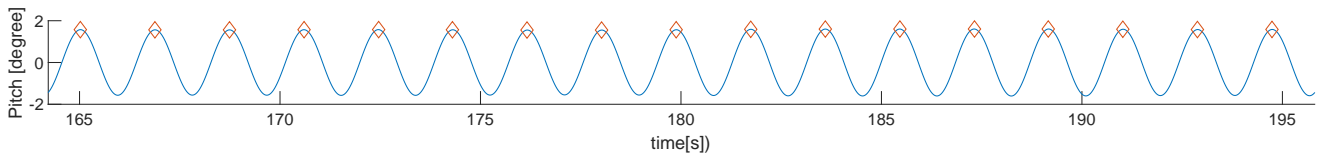
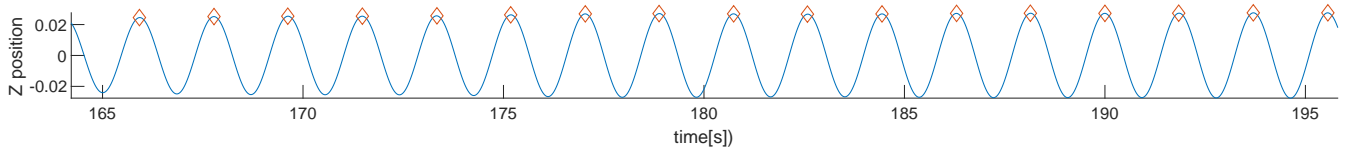
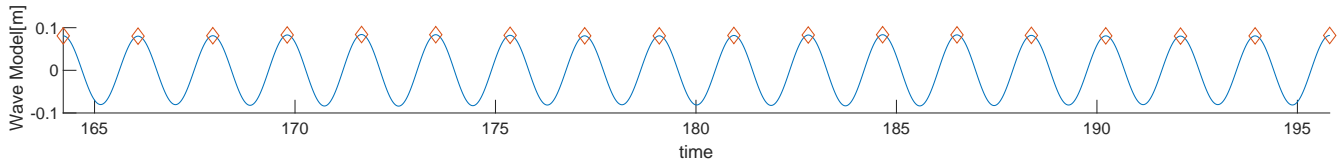
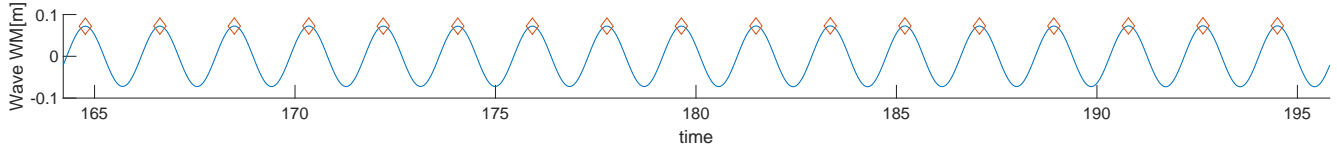
CE3020 Period(s):9.2 Lamda/L:0.7 Drift agle(deg):9 Speed(m/s):0



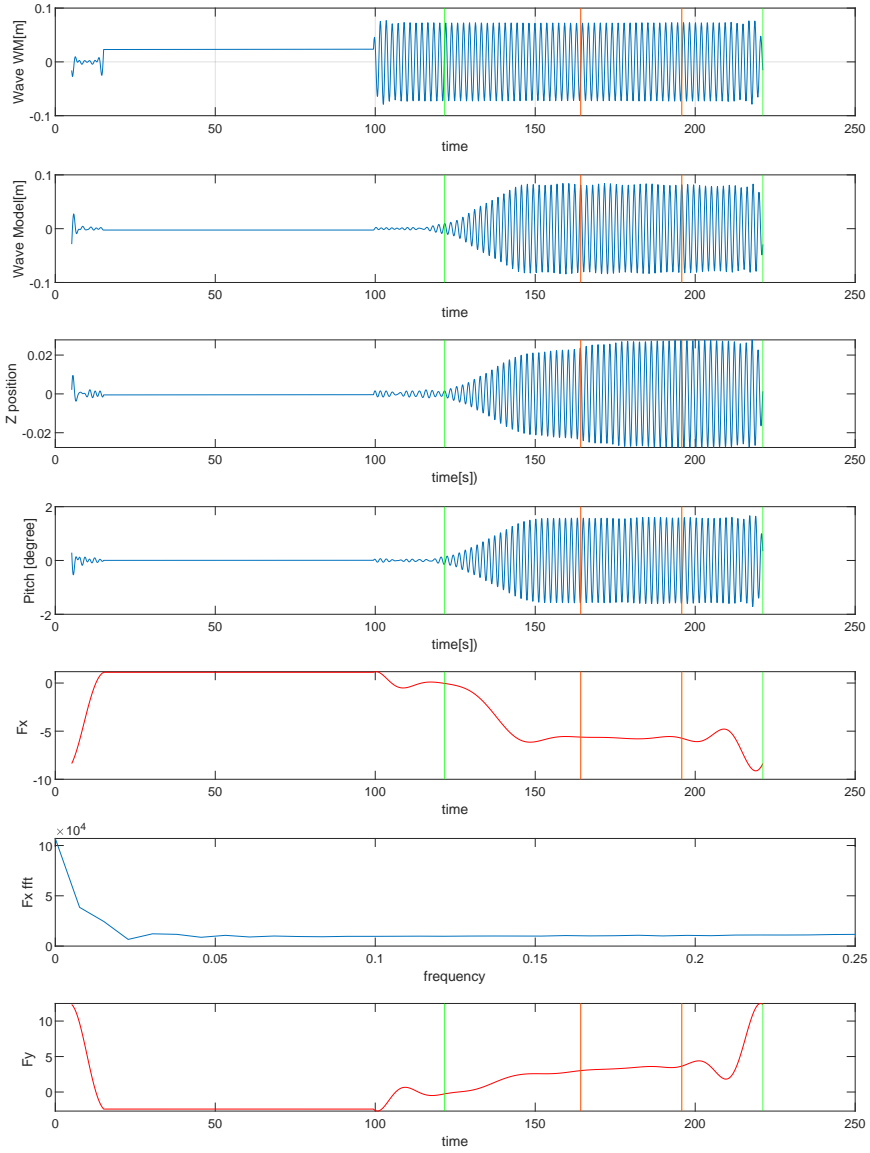
CE3020 Period(s):9.2 Lamda/L:0.7 Drift angle(deg):9 Speed(m/s):0



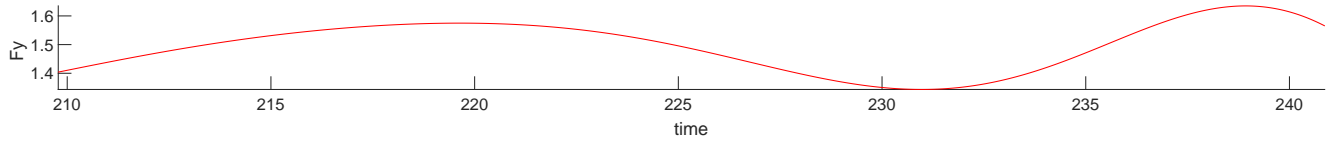
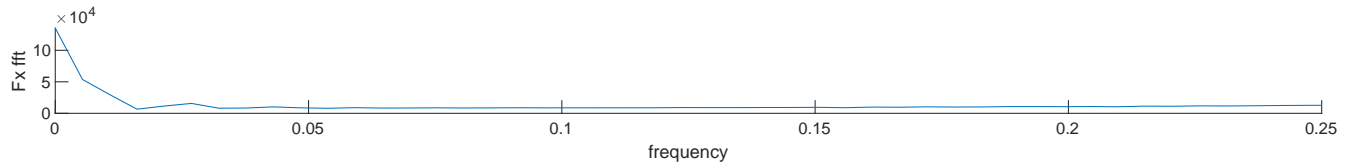
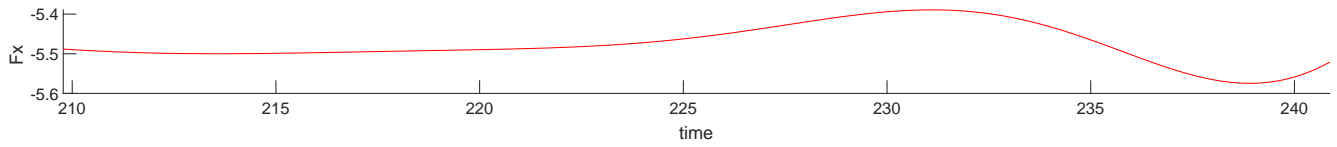
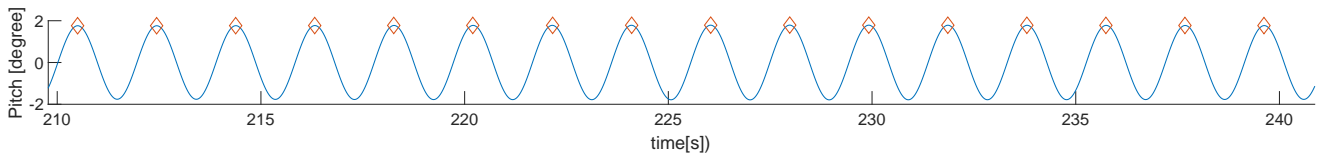
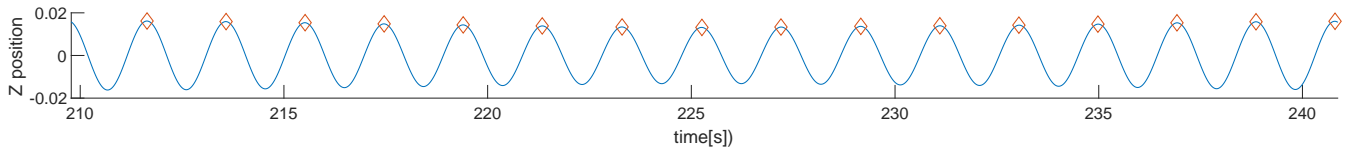
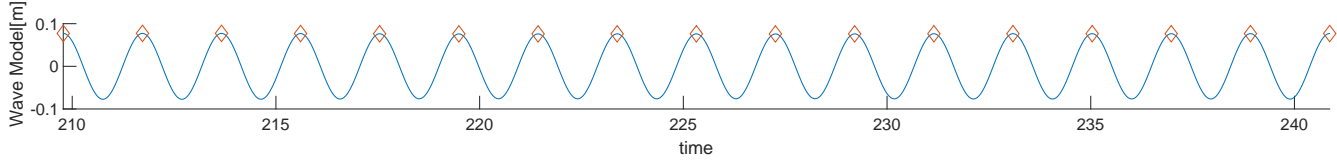
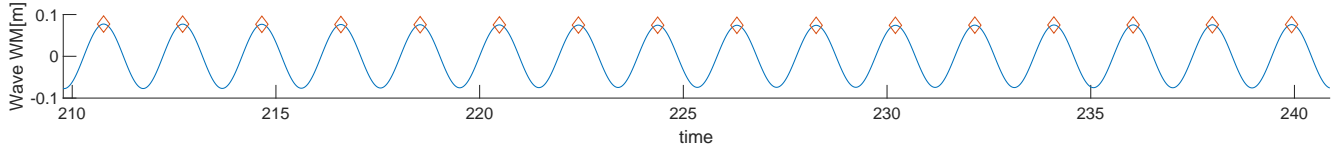
CE3030 Period(s):10.5 Lamda/L:0.91 Drift agle(deg):9 Speed(m/s):0



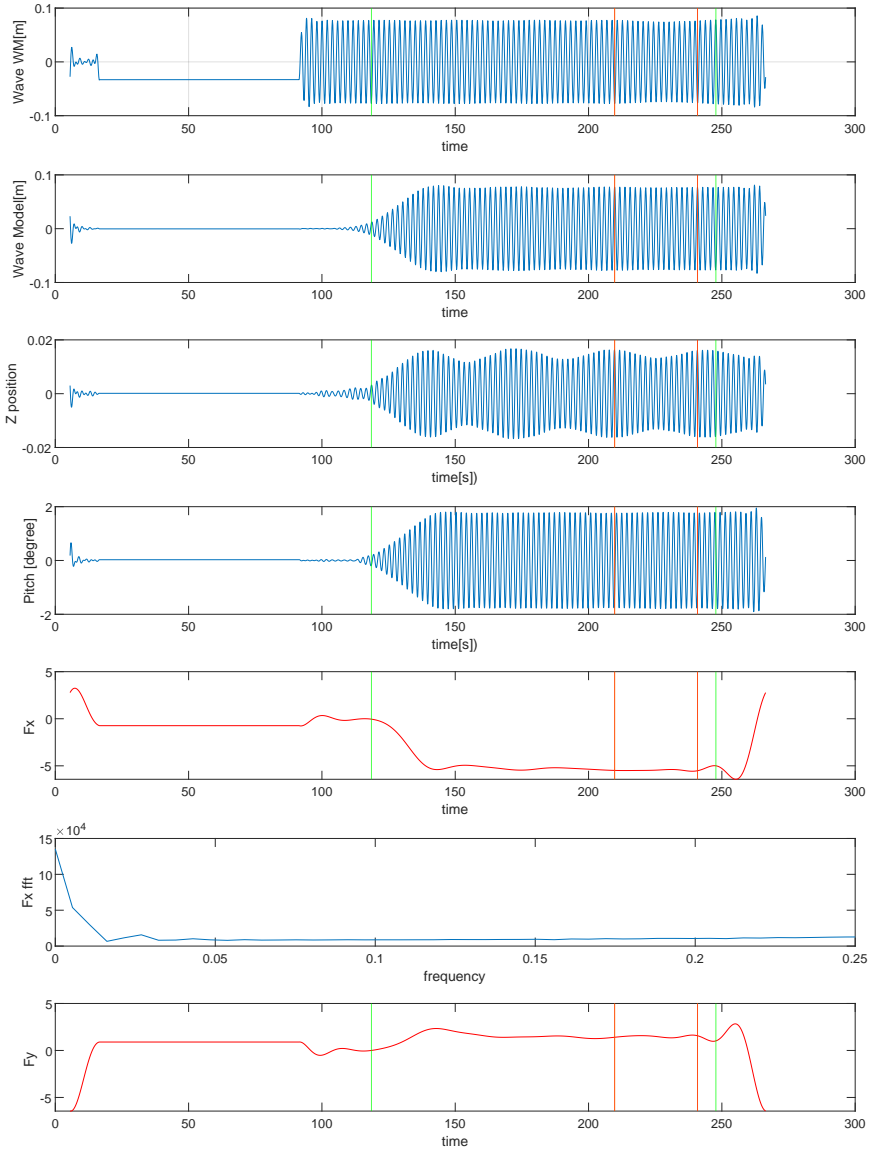
CE3030 Period(s):10.5 Lamda/L:0.91 Drift angle(deg):9 Speed(m/s):0



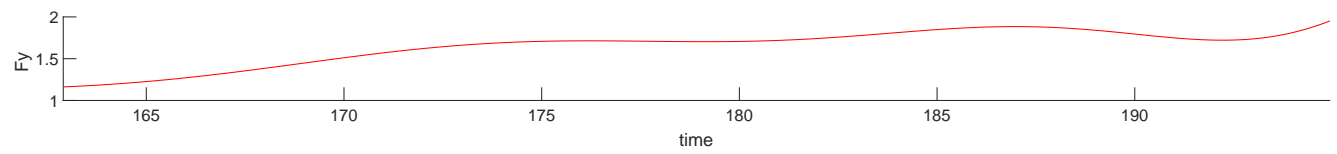
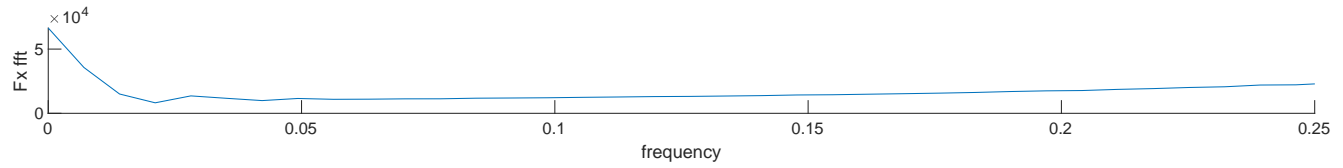
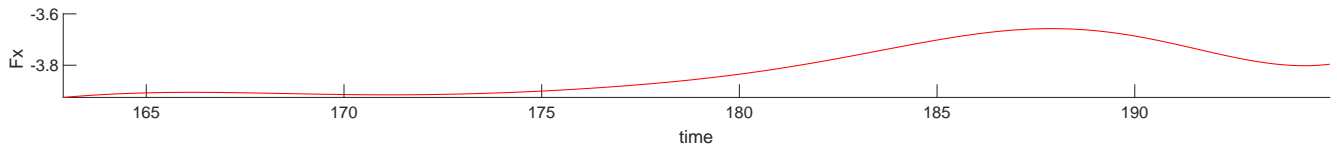
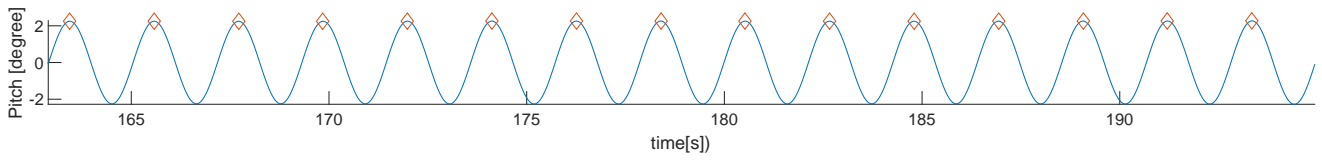
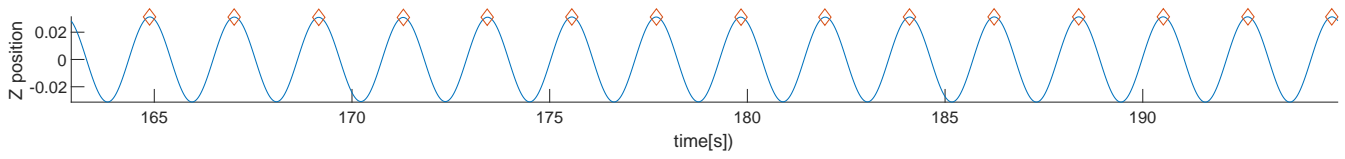
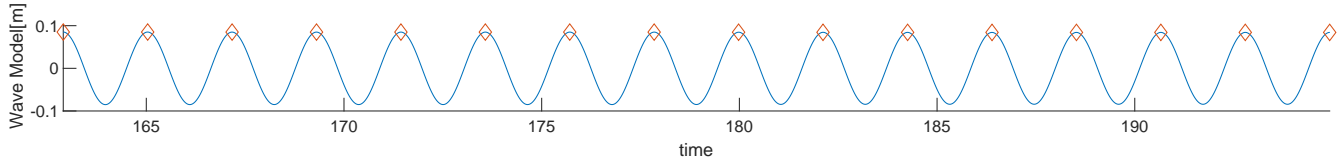
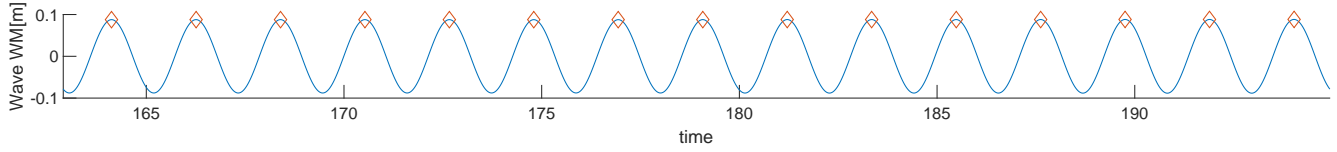
CE3040 Period(s):11 Lamda/L:0.99 Drift agle(deg):9 Speed(m/s):0



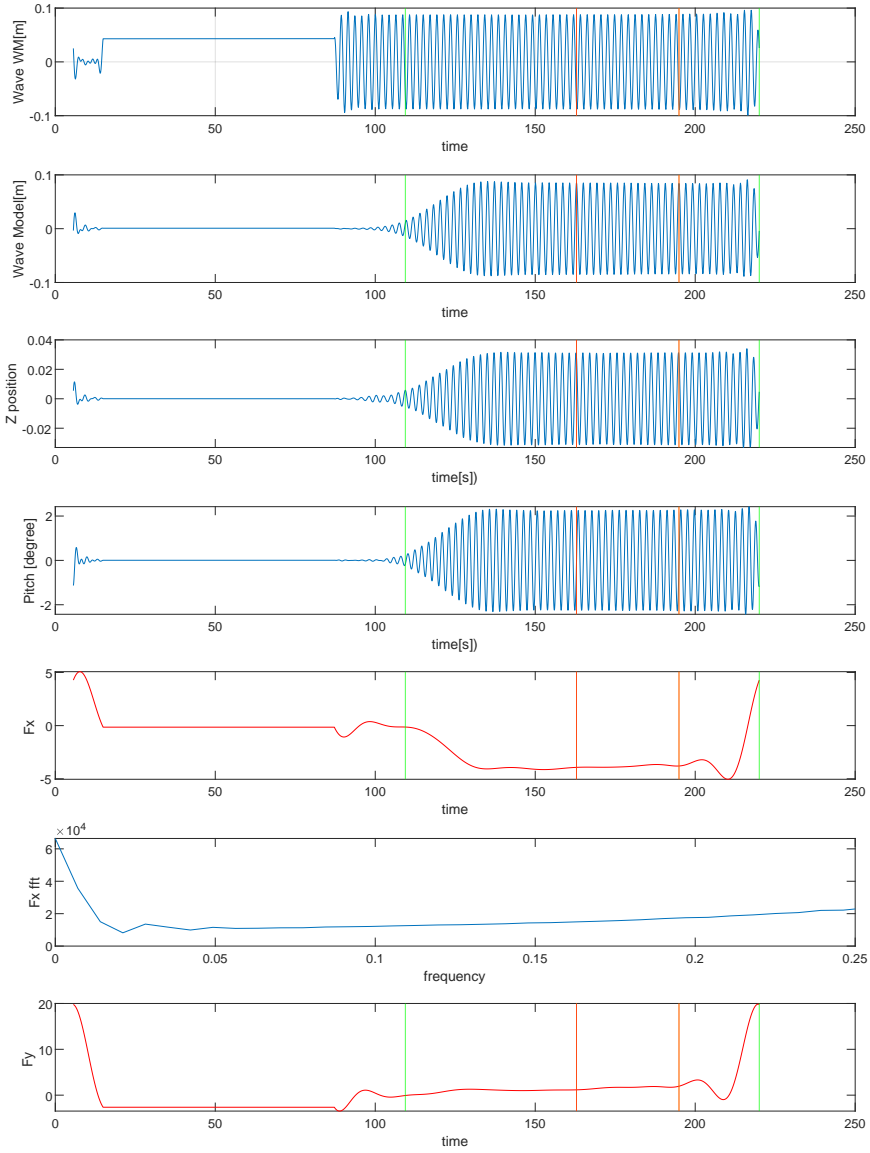
CE3040 Period(s):11 Lamda/L:0.99 Drift angle(deg):9 Speed(m/s):0



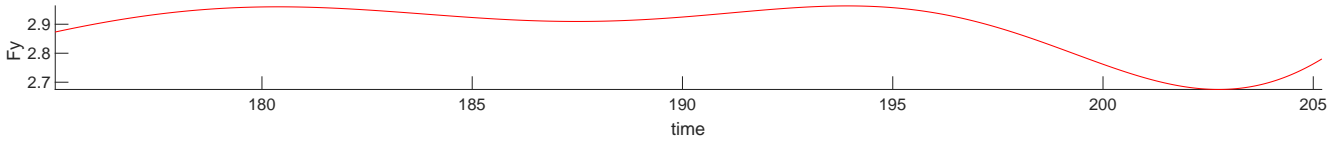
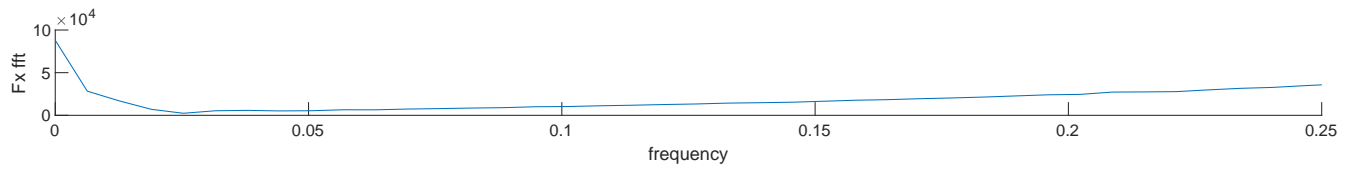
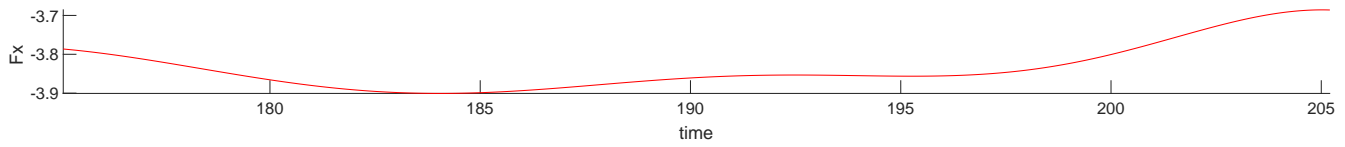
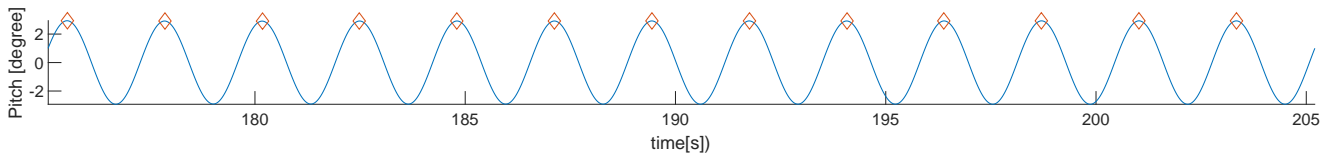
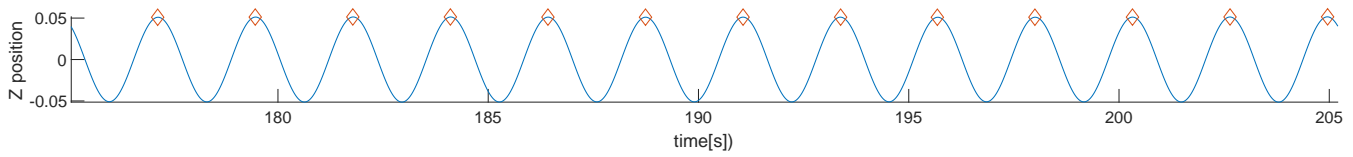
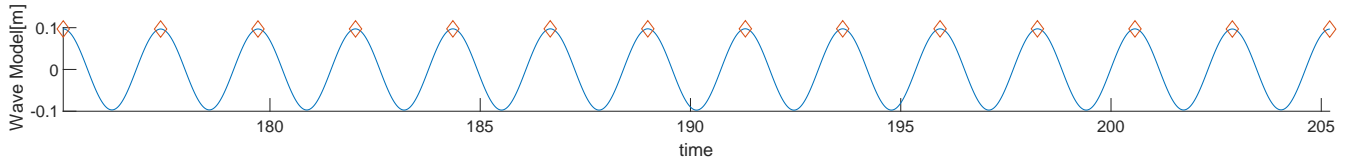
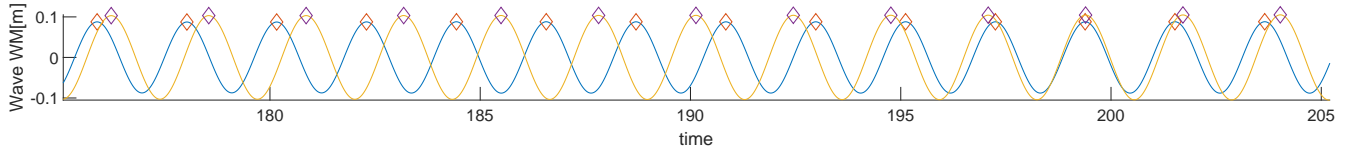
CE3050 Period(s):12.1 Lamda/L:1.2 Drift agle(deg):9 Speed(m/s):0



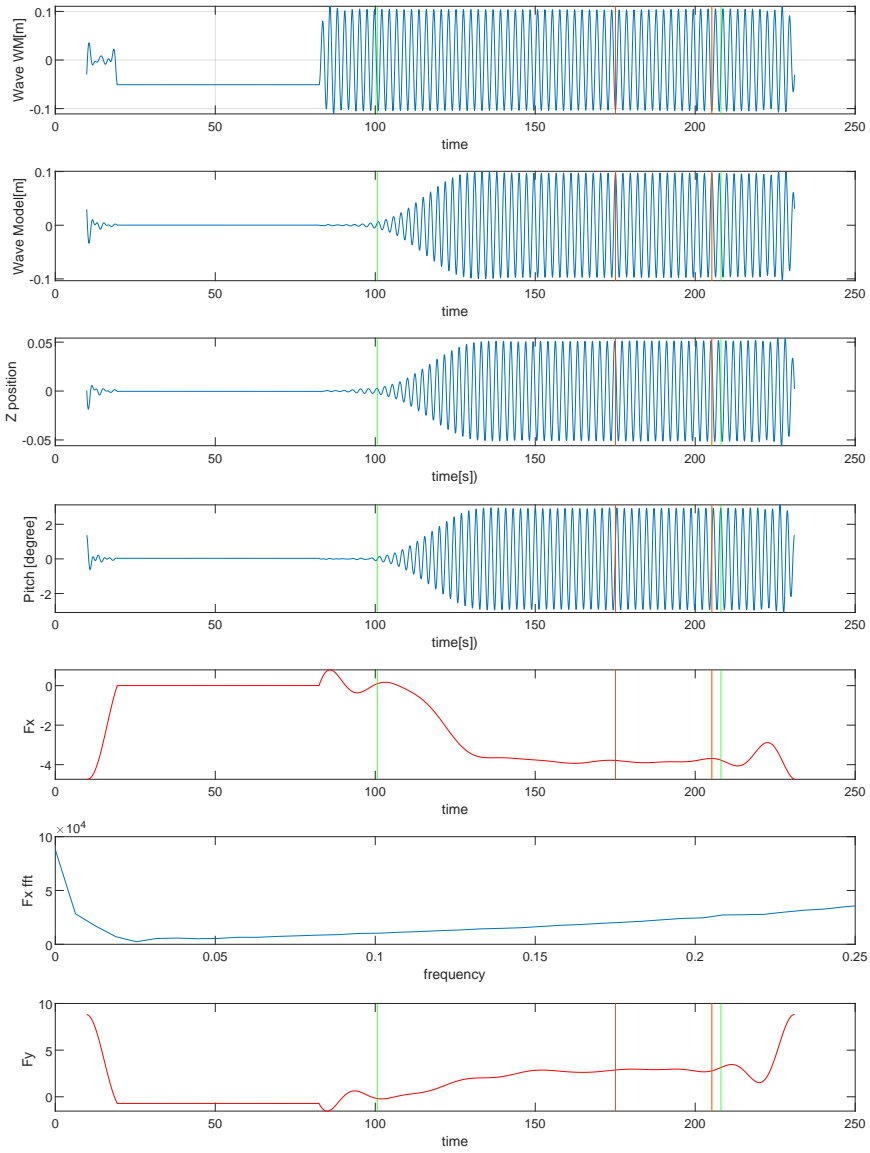
CE3050 Period(s):12.1 Lamda/L:1.2 Drift agle(deg):9 Speed(m/s):0



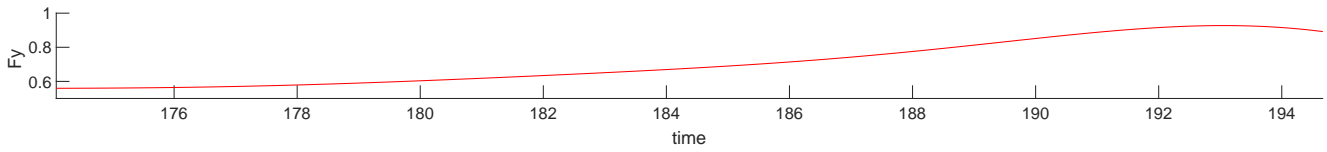
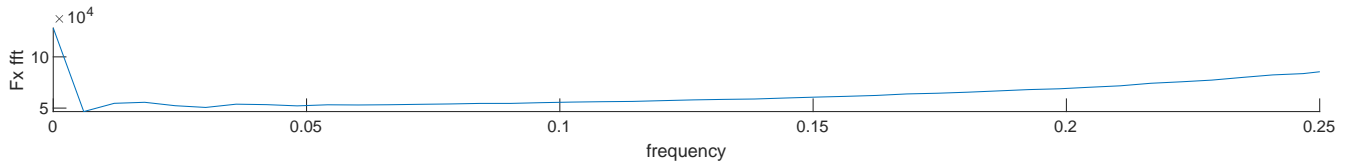
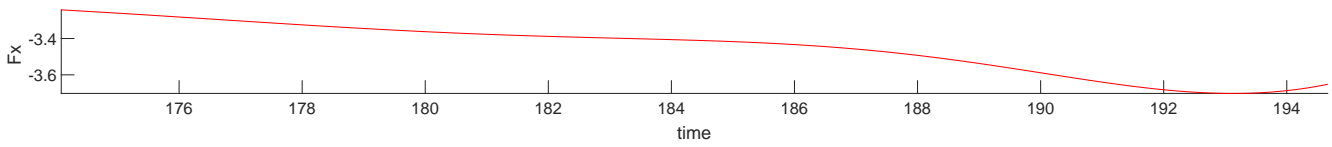
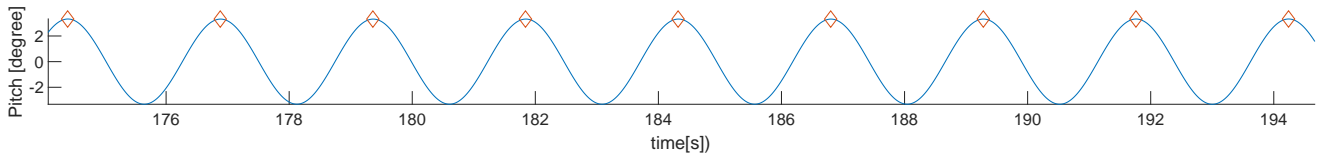
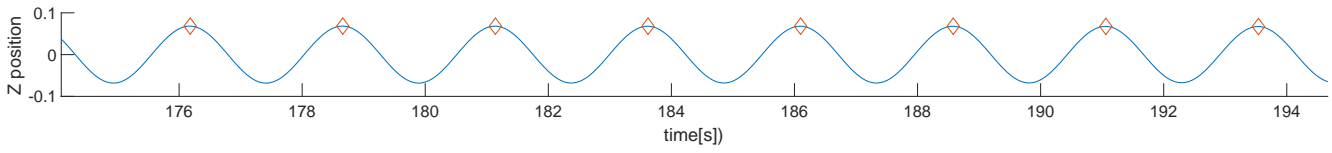
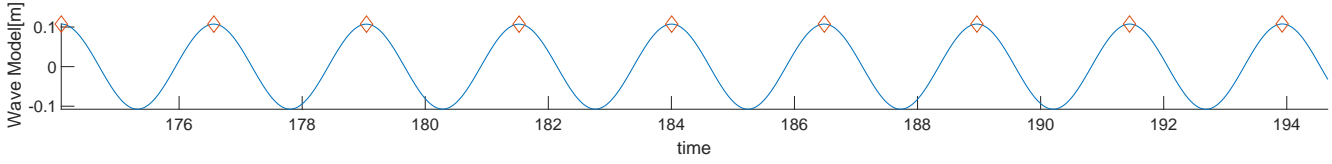
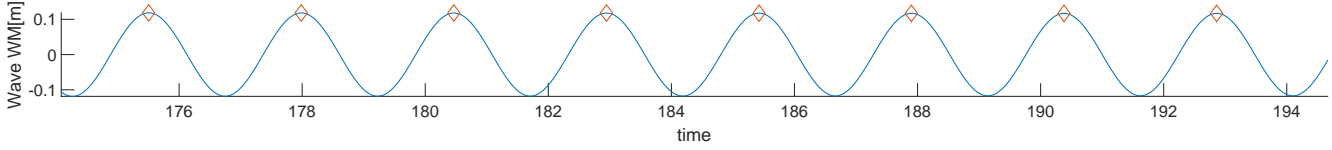
CE3060 Period(s):13.1 Lamda/L:1.41 Drift agle(deg):9 Speed(m/s):0



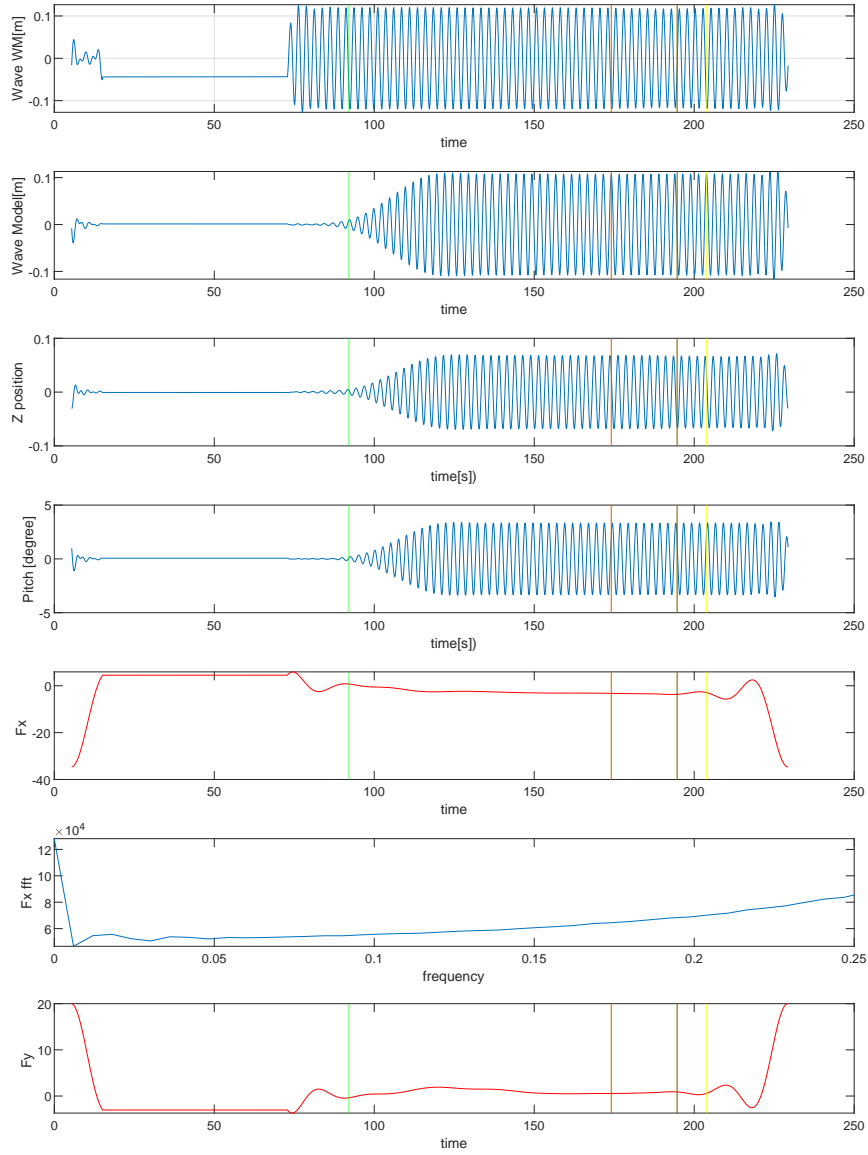
CE3060 Period(s):13.1 Lamda/L:1.41 Drift angle(deg):9 Speed(m/s):0



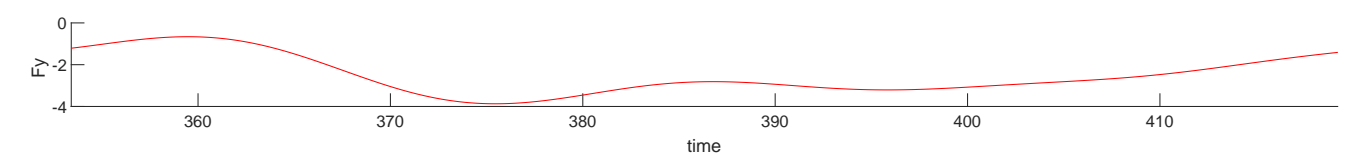
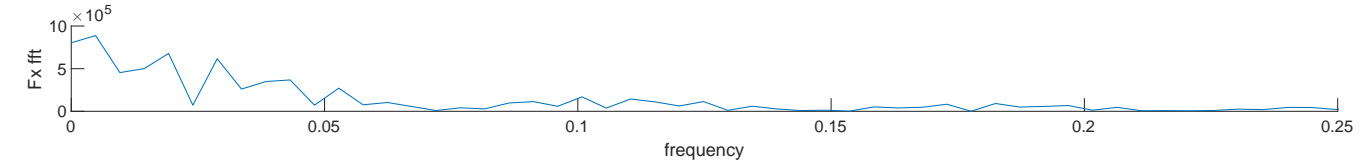
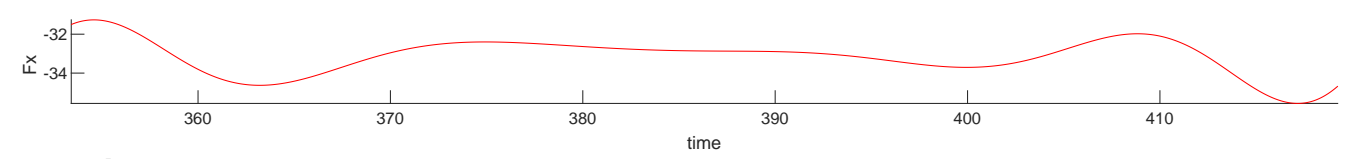
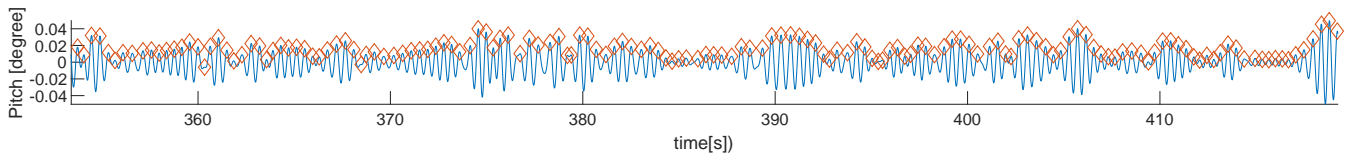
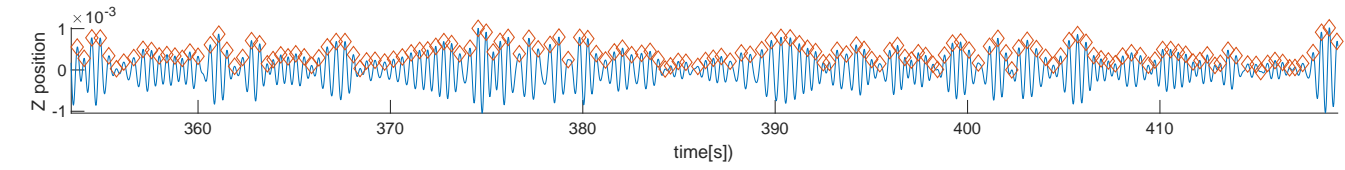
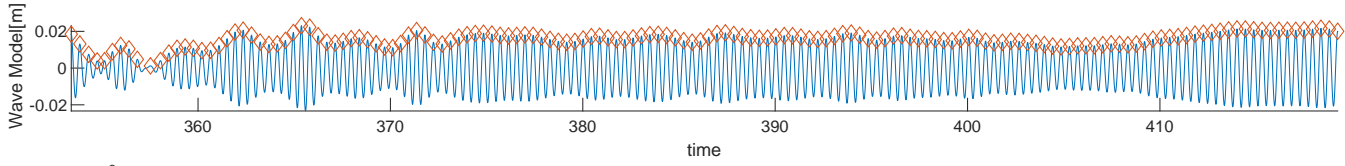
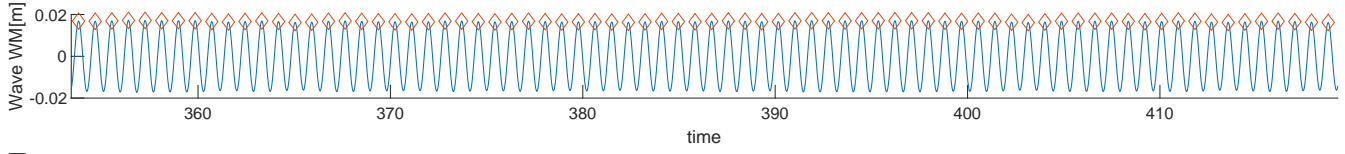
CE3070 Period(s):14 Lamda/L:1.61 Drift agle(deg):9 Speed(m/s):0



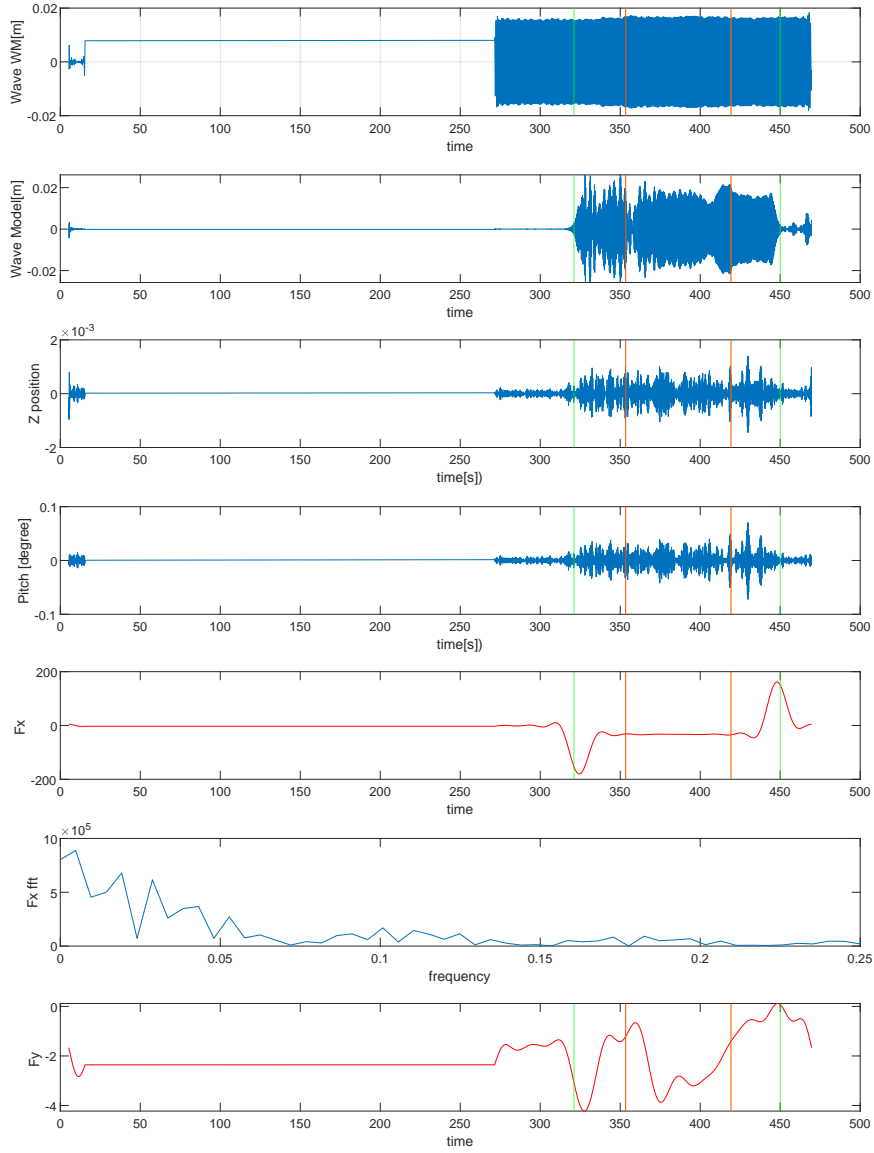
CE3070 Period(s):14 Lamda/L:1.61 Drift angle(deg):9 Speed(m/s):0



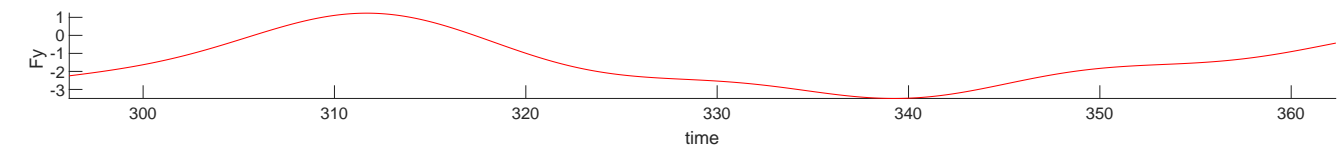
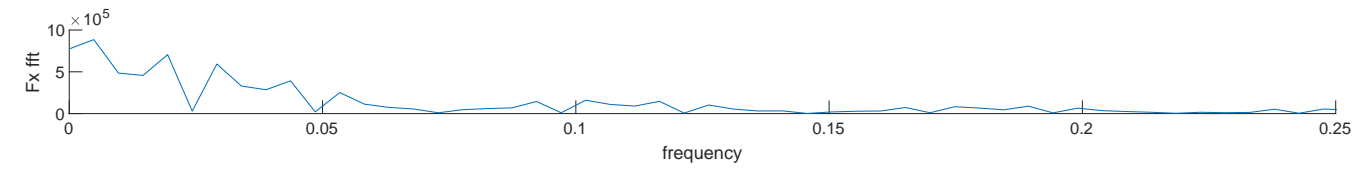
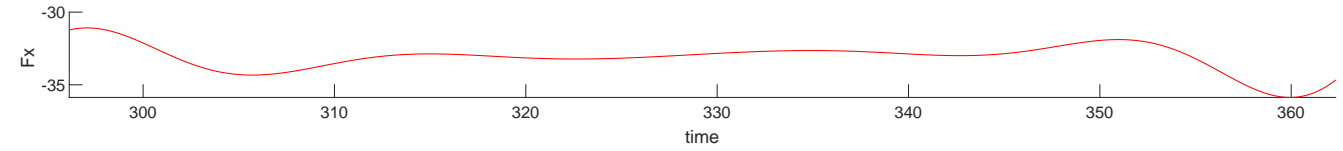
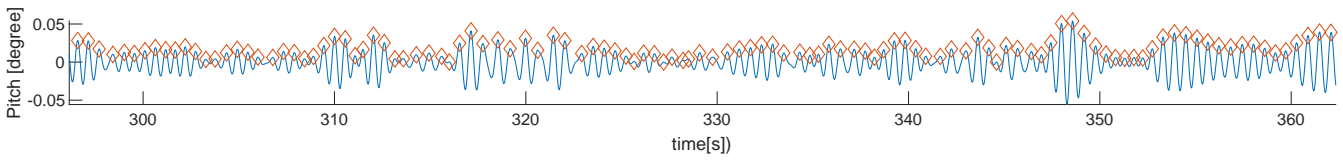
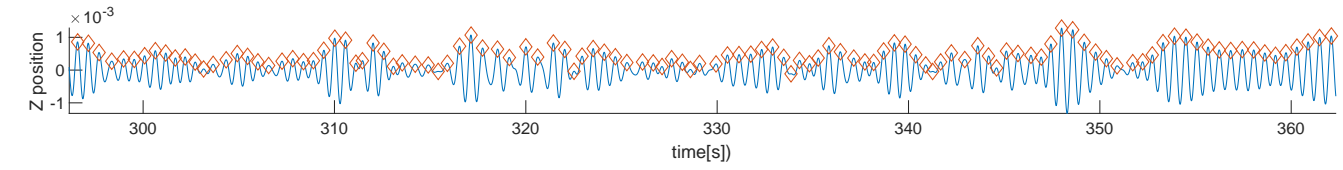
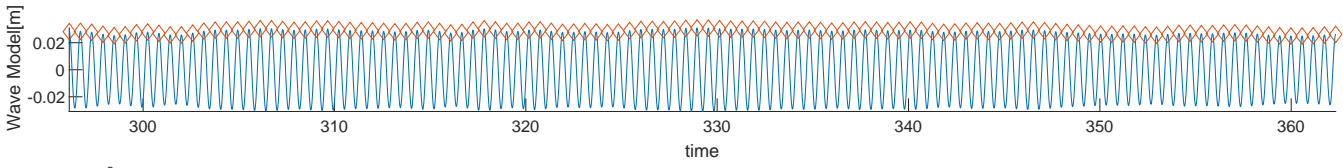
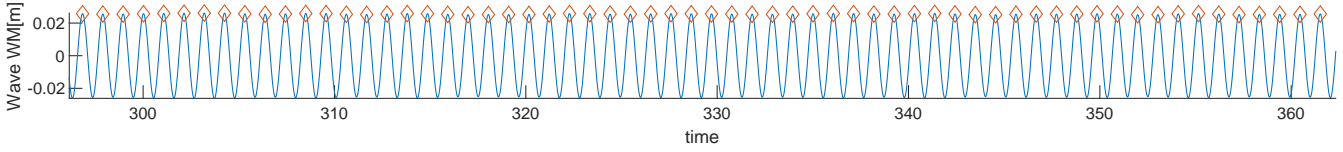
CE4010 Period(s):4.9 Lamda/L:0.2 Drift agle(deg):0 Speed(m/s):7.71



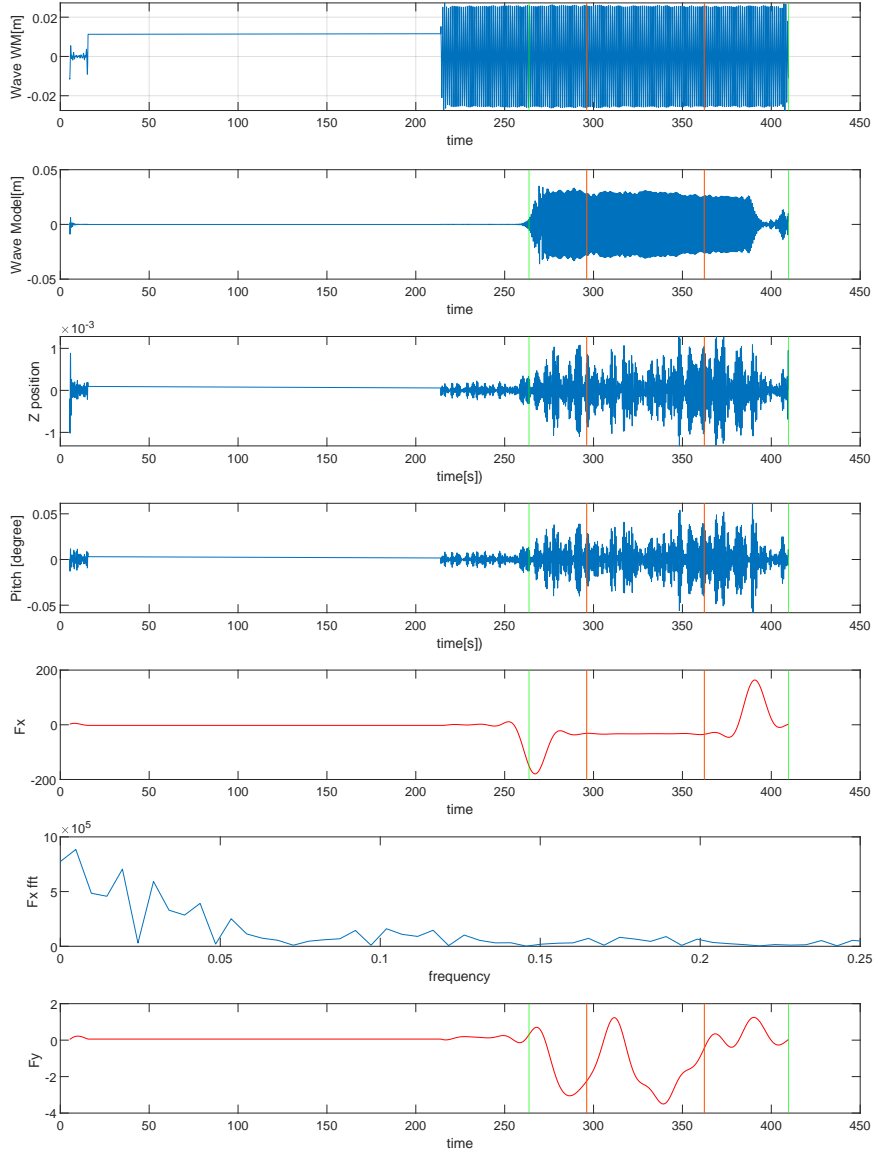
CE4010 Period(s):4.9 Lamda/L:0.2 Drift agle(deg):0 Speed(m/s):7.71



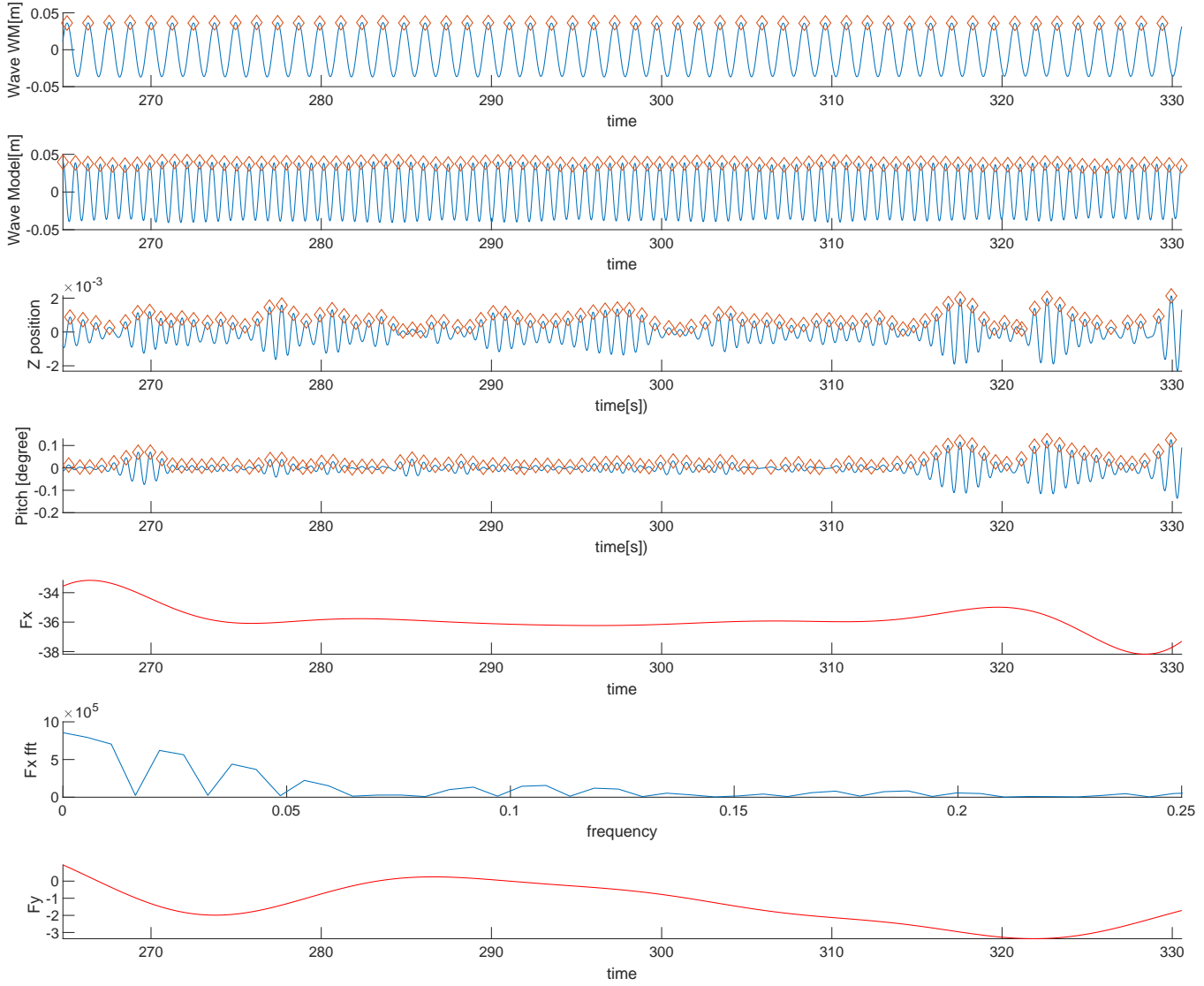
CE4020 Period(s):6 Lamda/L:0.3 Drift agle(deg):0 Speed(m/s):7.71



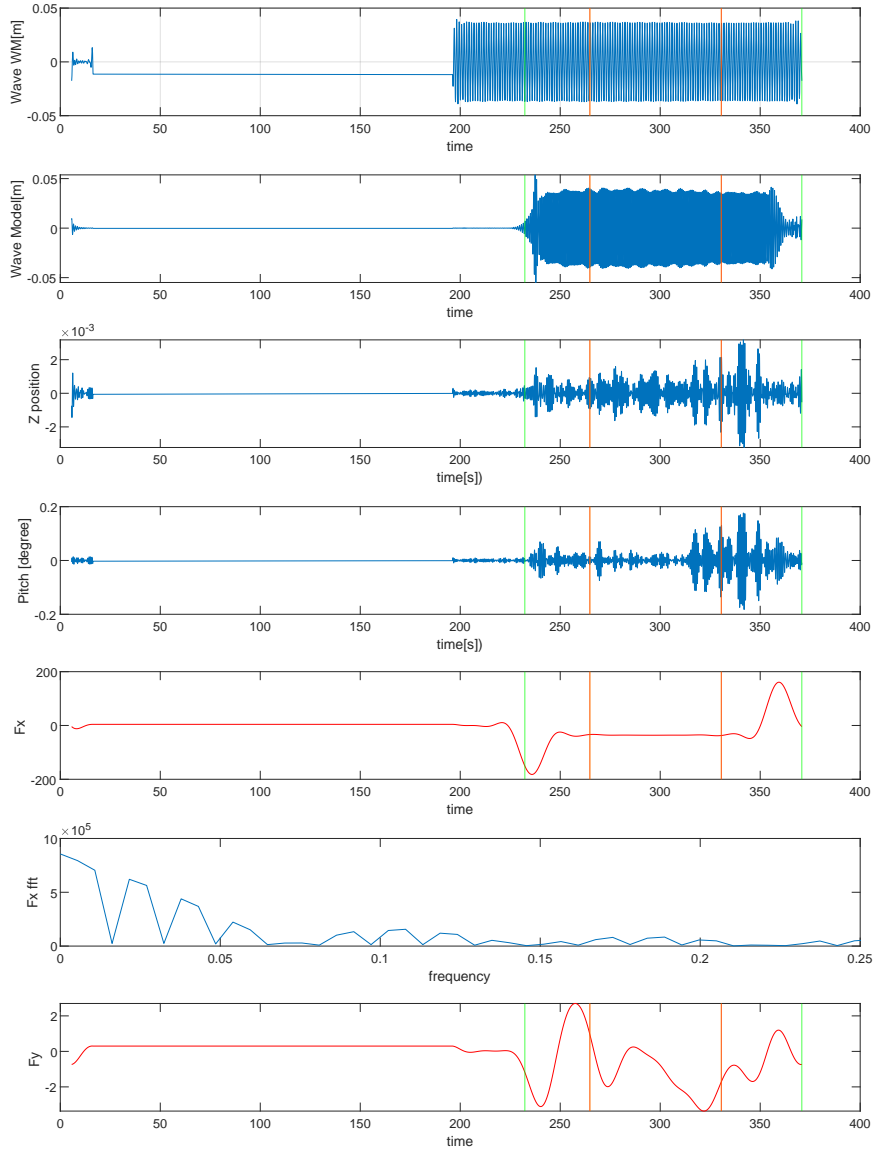
CE4020 Period(s):6 Lamda/L:0.3 Drift angle(deg):0 Speed(m/s):7.71



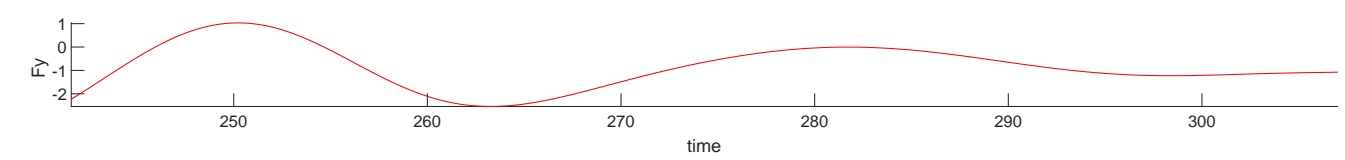
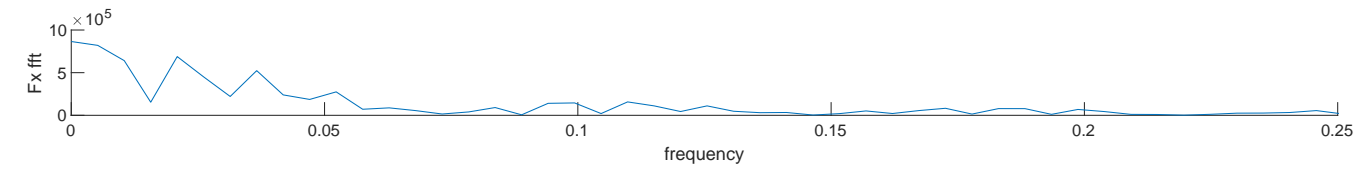
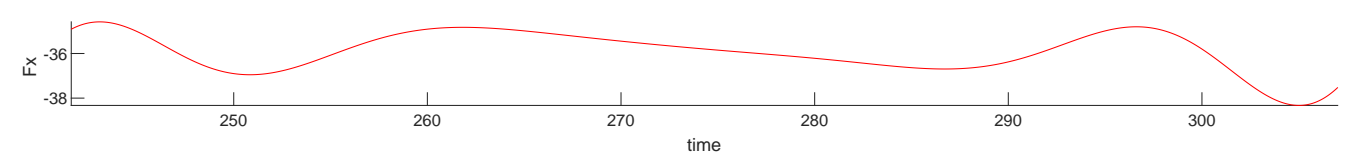
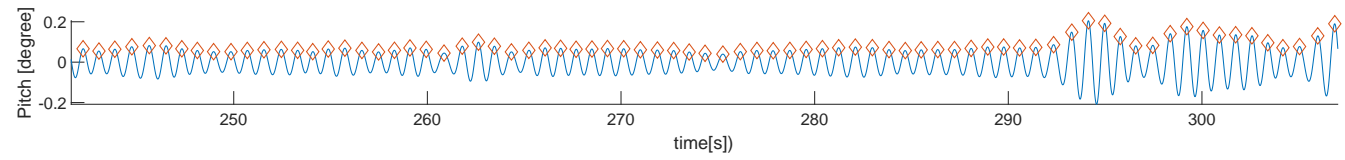
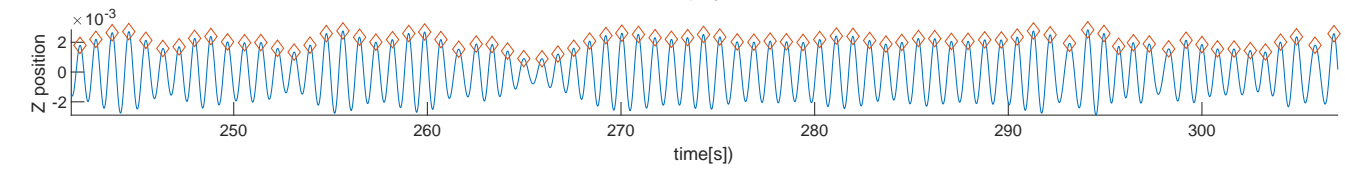
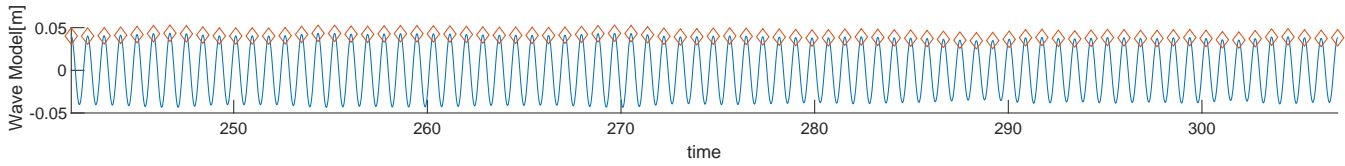
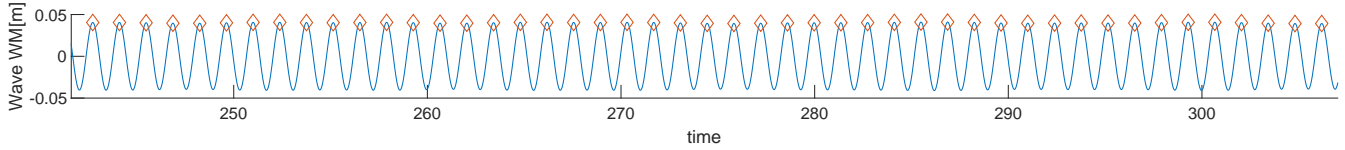
CE4030 Period(s):7 Lamda/L:0.4 Drift agle(deg):0 Speed(m/s):7.71



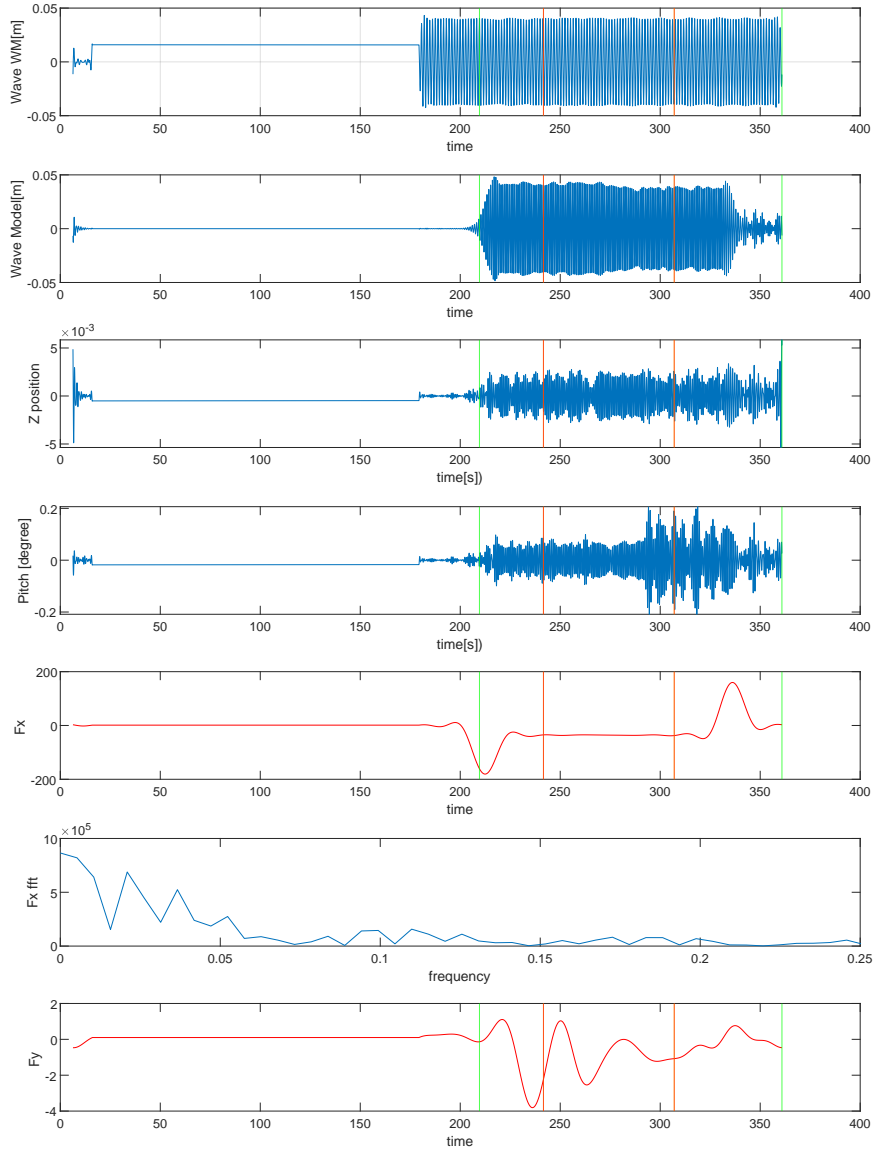
CE4030 Period(s):7 Lamda/L:0.4 Drift angle(deg):0 Speed(m/s):7.71



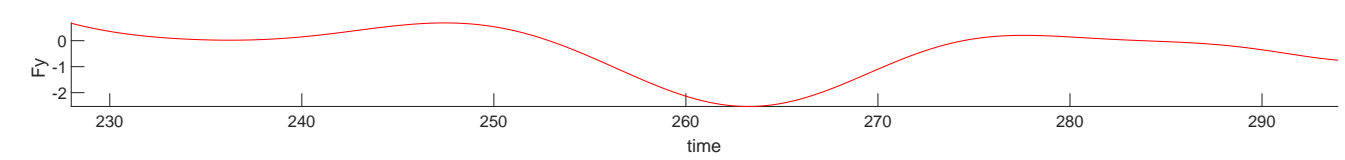
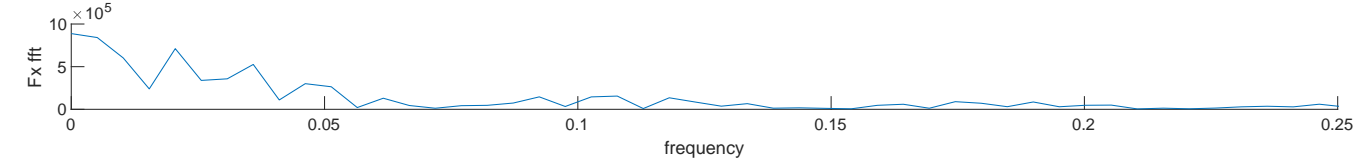
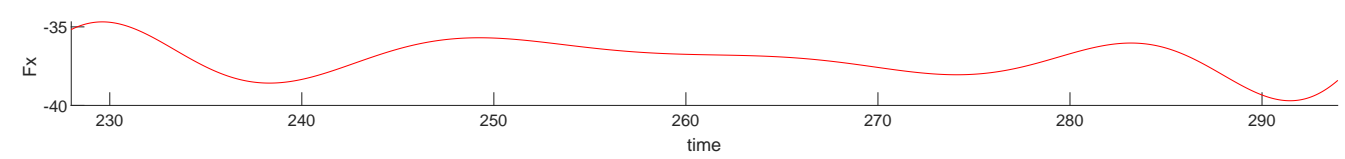
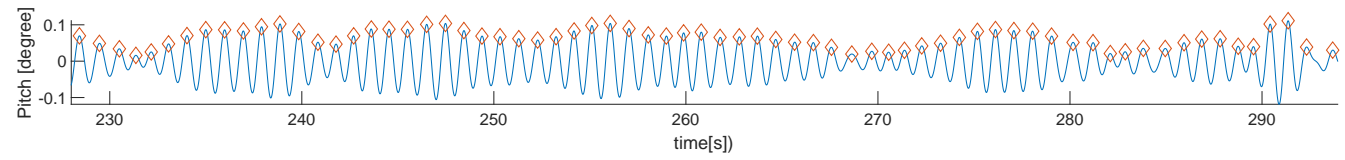
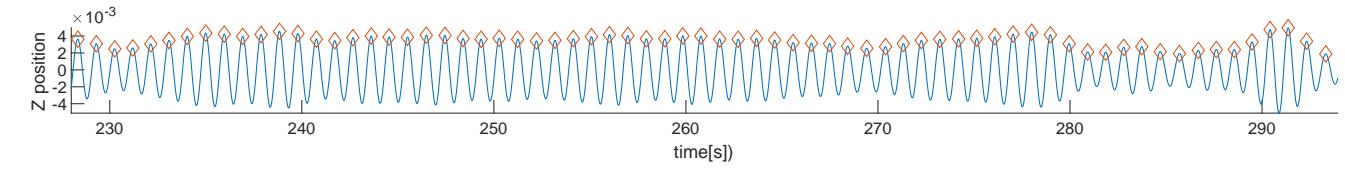
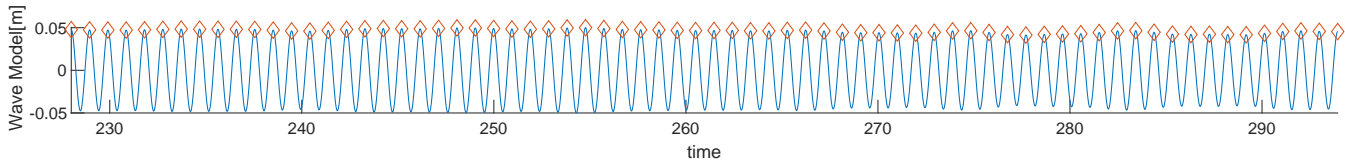
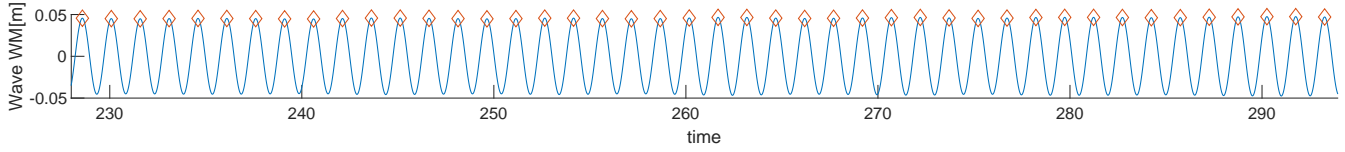
CE4040 Period(s):7.8 Lamda/L:0.5 Drift agle(deg):0 Speed(m/s):7.71



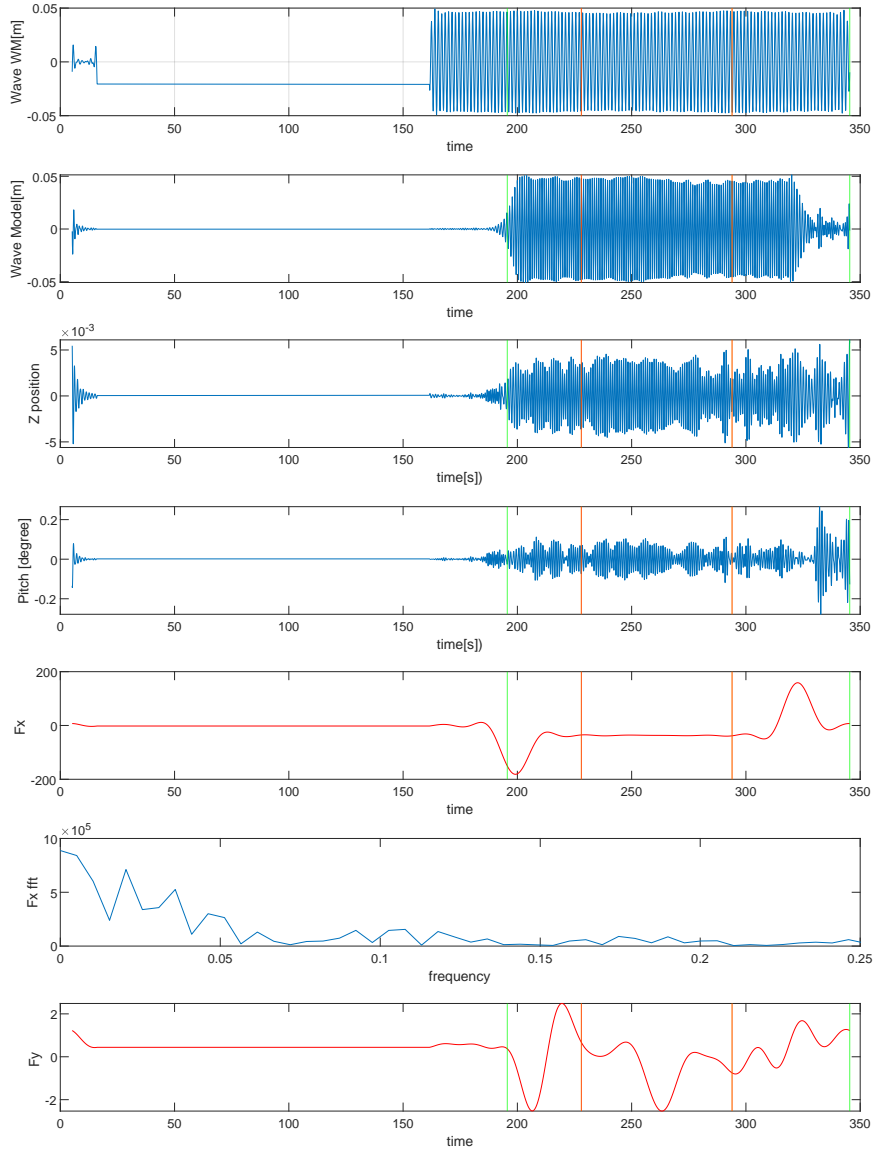
CE4040 Period(s):7.8 Lamda/L:0.5 Drift agle(deg):0 Speed(m/s):7.71



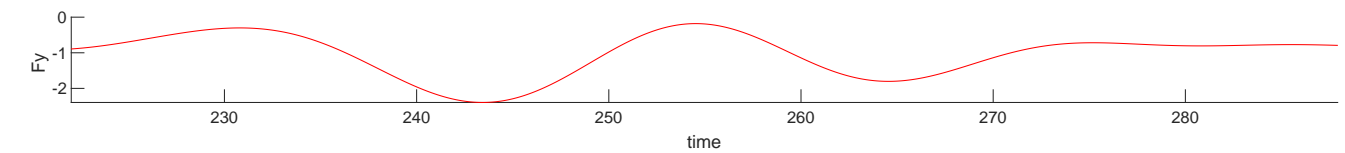
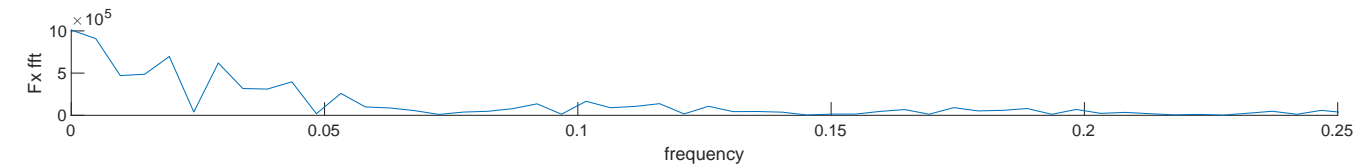
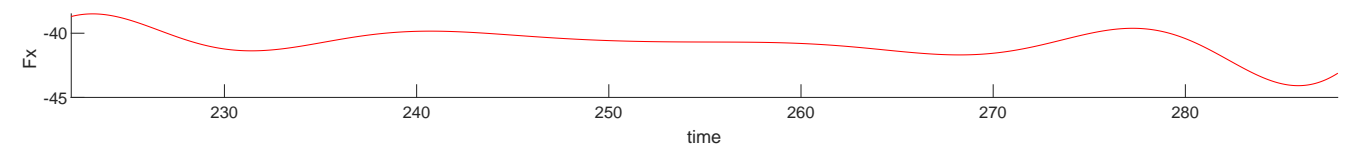
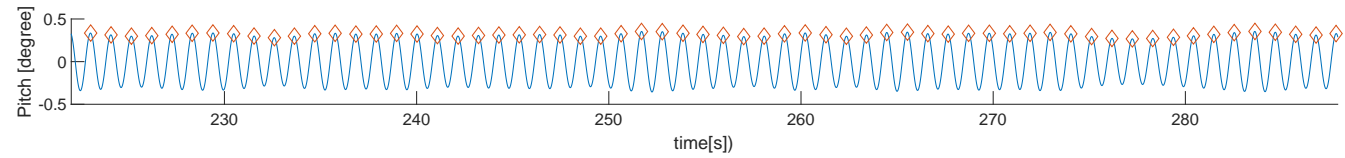
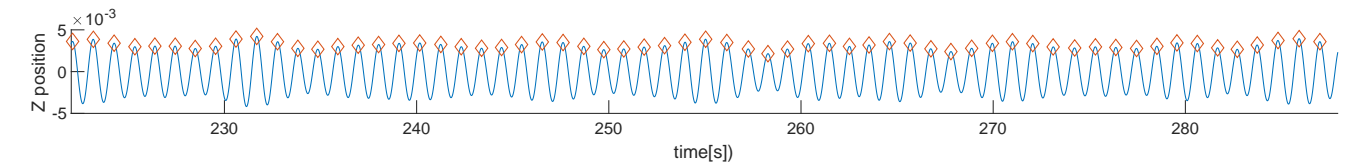
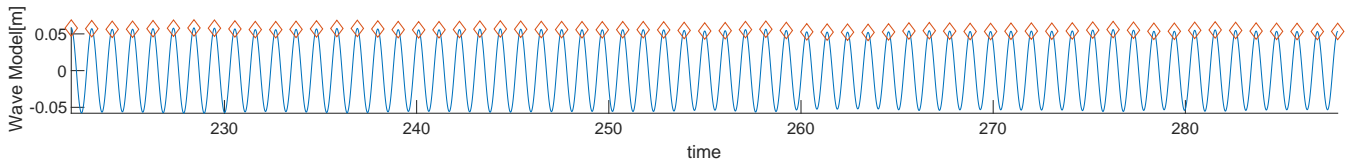
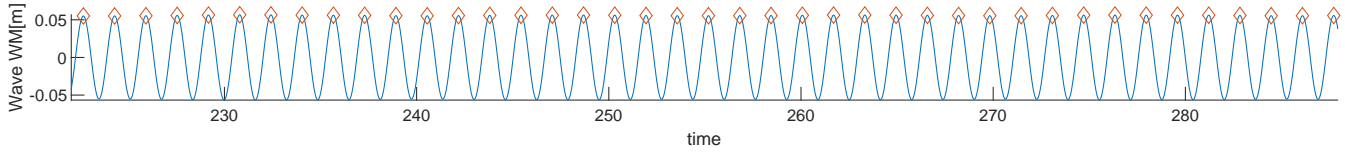
CE4050 Period(s):8.5 Lamda/L:0.59 Drift agle(deg):0 Speed(m/s):7.71



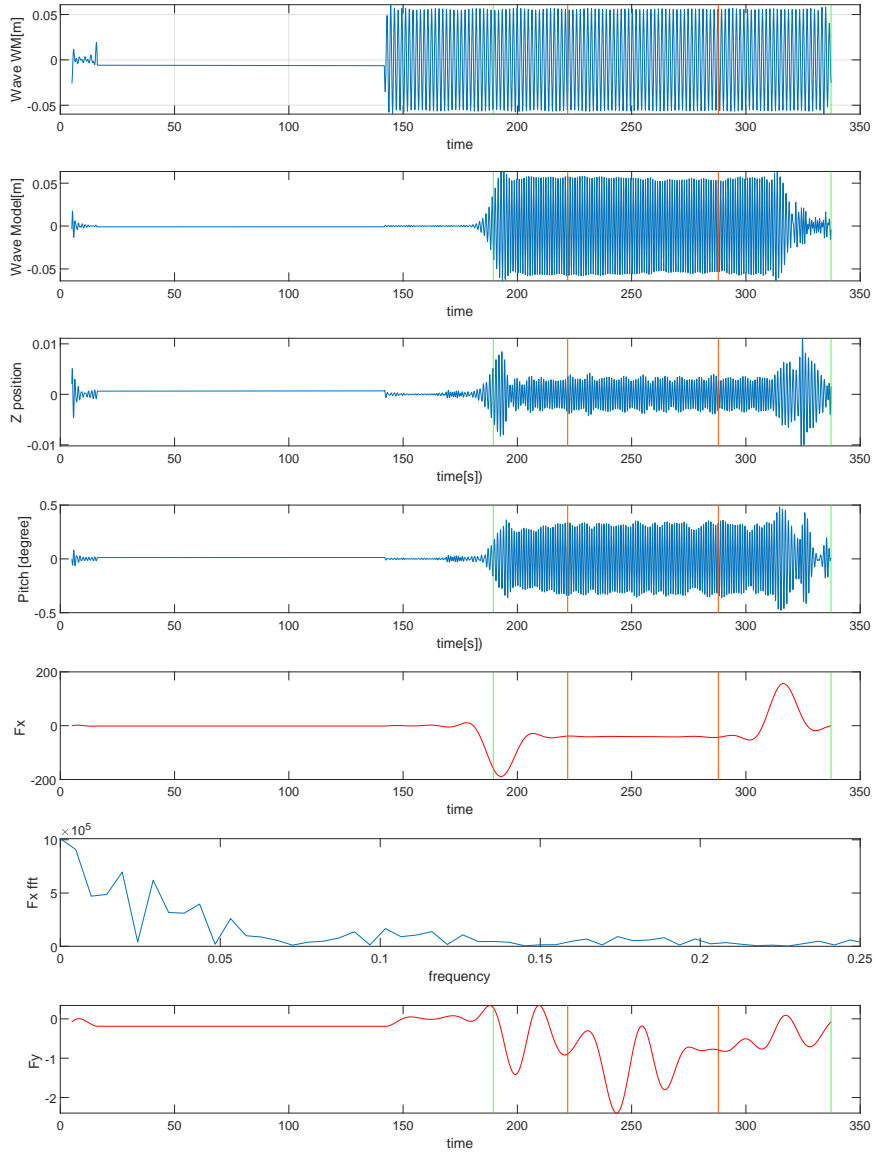
CE4050 Period(s):8.5 Lamda/L:0.59 Drift agle(deg):0 Speed(m/s):7.71



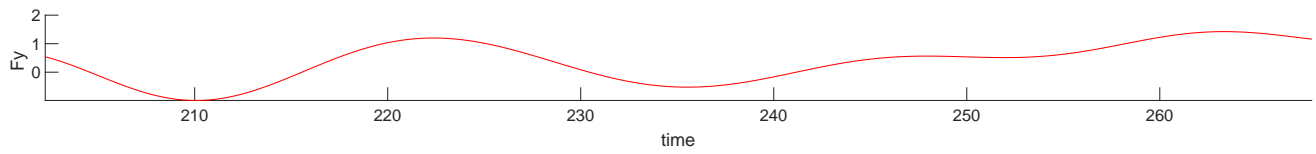
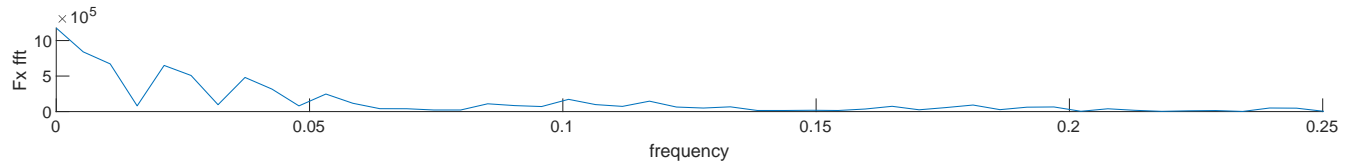
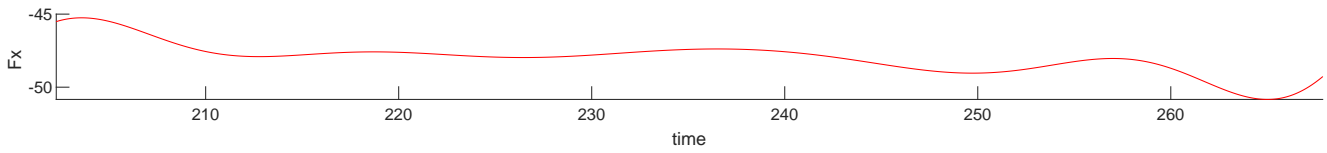
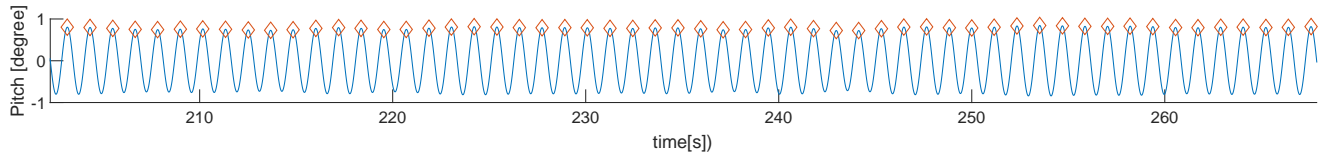
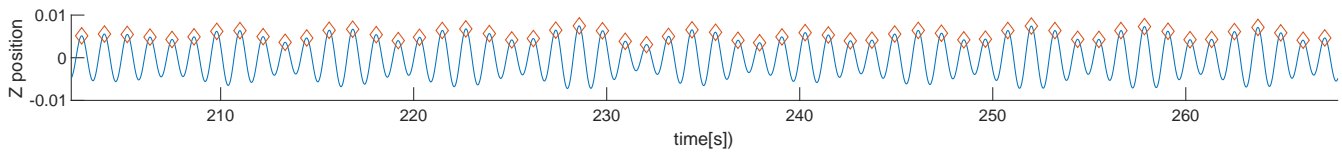
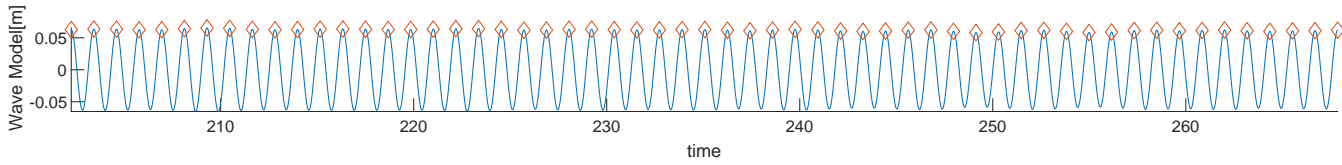
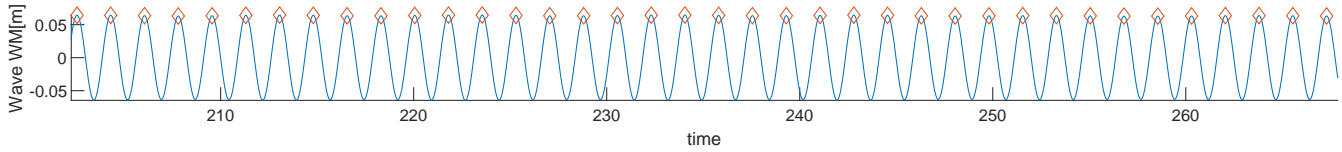
CE4060 Period(s):9.2 Lamda/L:0.7 Drift agle(deg):0 Speed(m/s):7.71



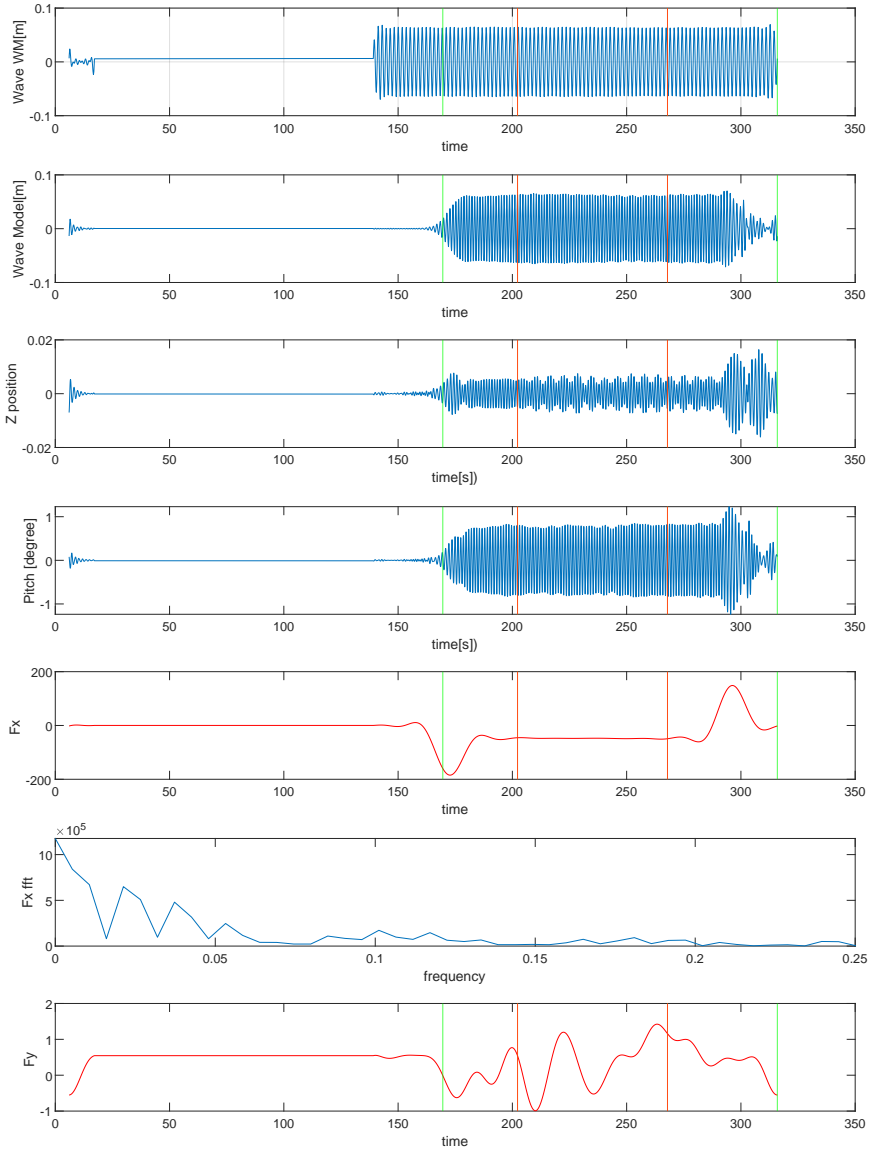
CE4060 Period(s):9.2 Lamda/L:0.7 Drift agle(deg):0 Speed(m/s):7.71



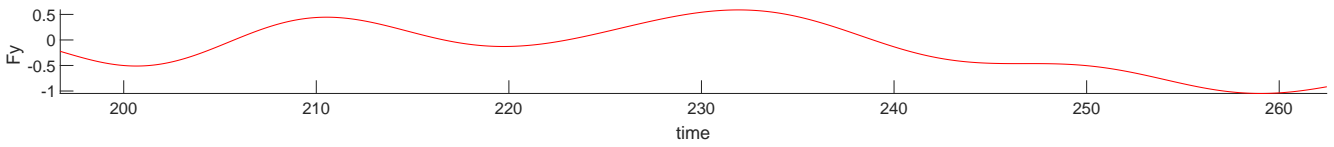
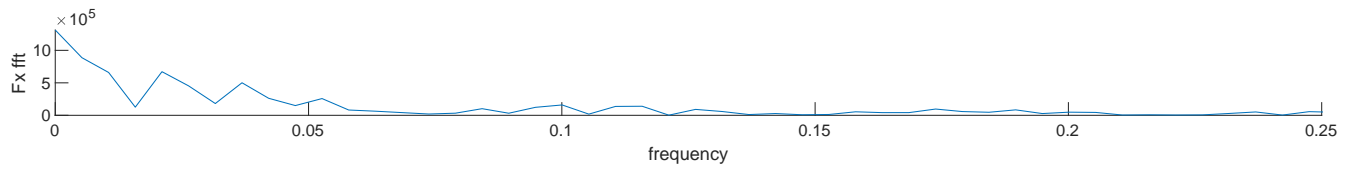
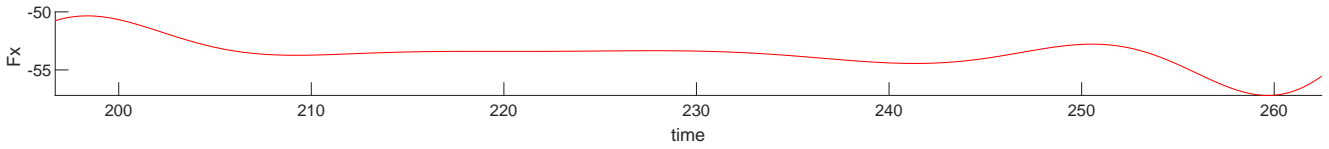
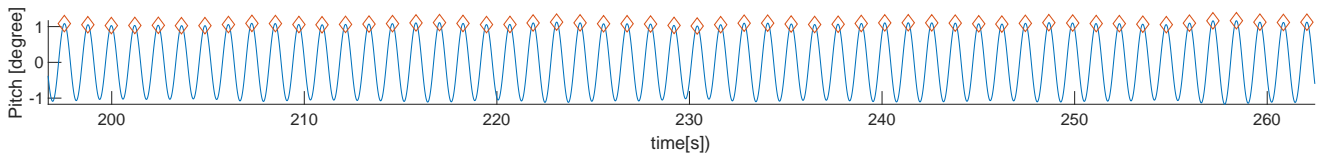
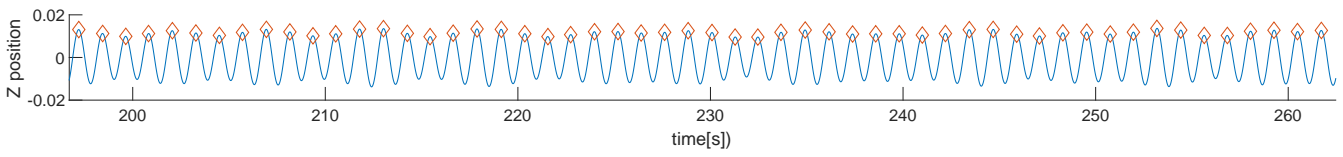
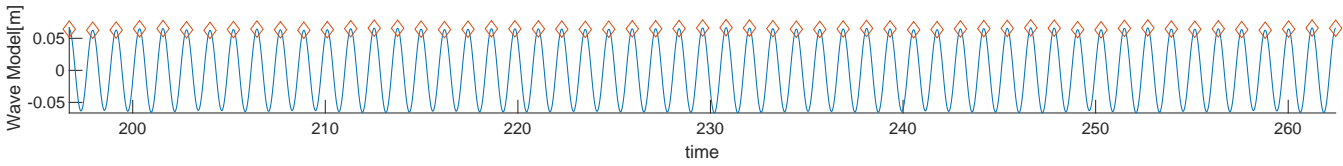
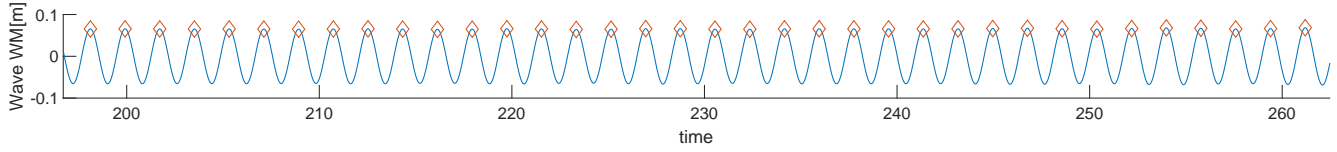
CE4070 Period(s):9.9 Lamda/L:0.81 Drift agle(deg):0 Speed(m/s):7.71



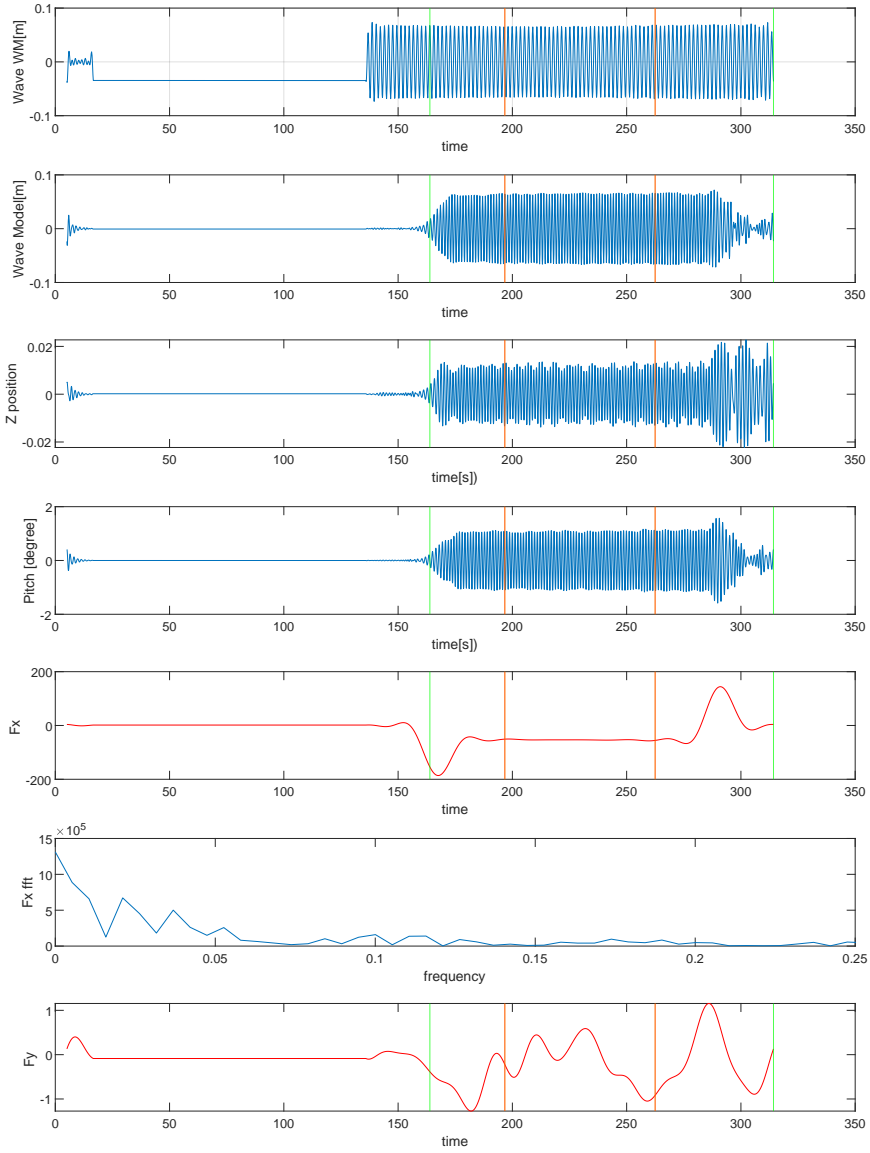
CE4070 Period(s):9.9 Lamda/L:0.81 Drift agle(deg):0 Speed(m/s):7.71



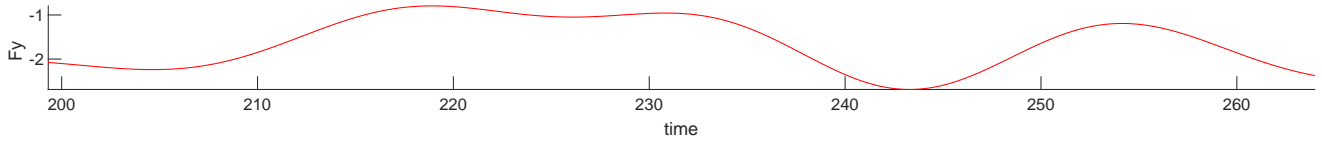
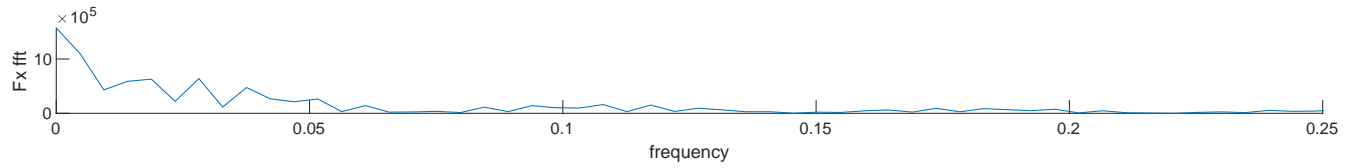
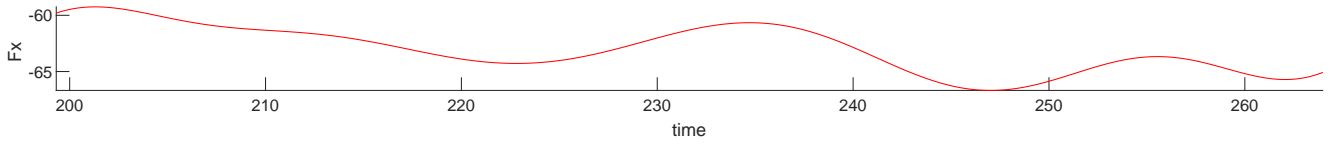
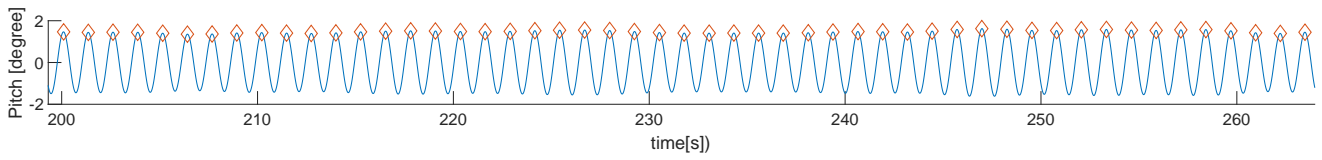
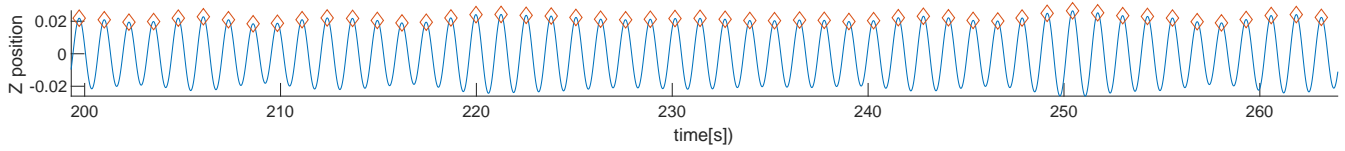
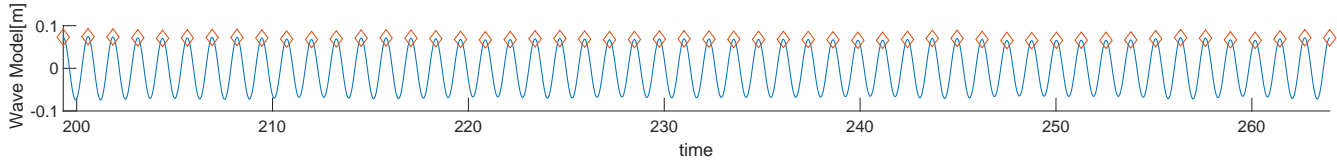
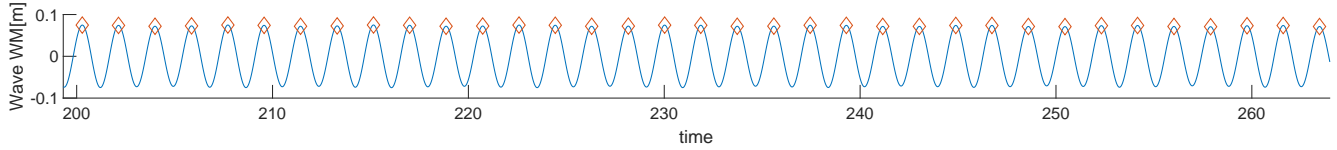
CE4080 Period(s):10.2 Lamda/L:0.85 Drift agle(deg):0 Speed(m/s):7.71



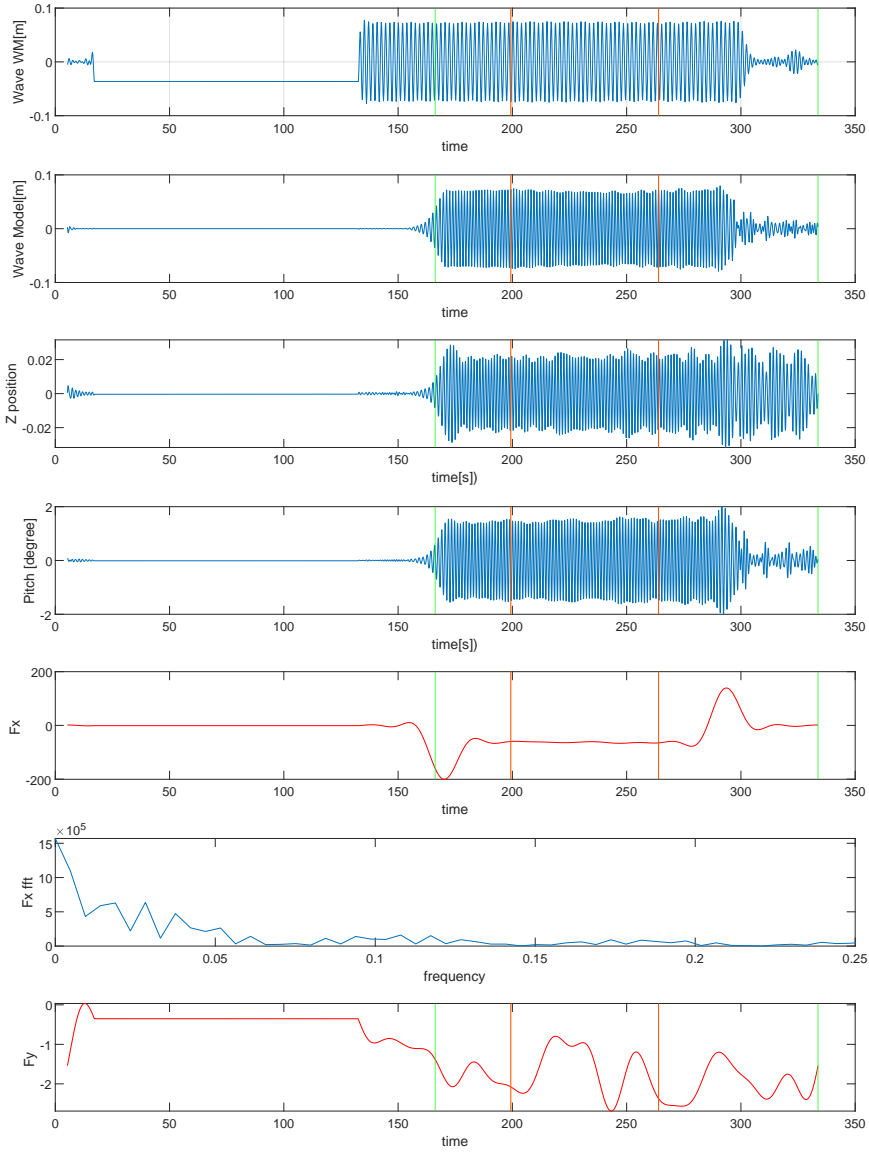
CE4080 Period(s):10.2 Lamda/L:0.85 Drift angle(deg):0 Speed(m/s):7.71



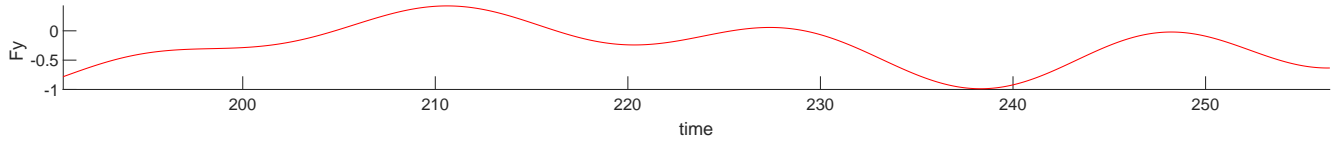
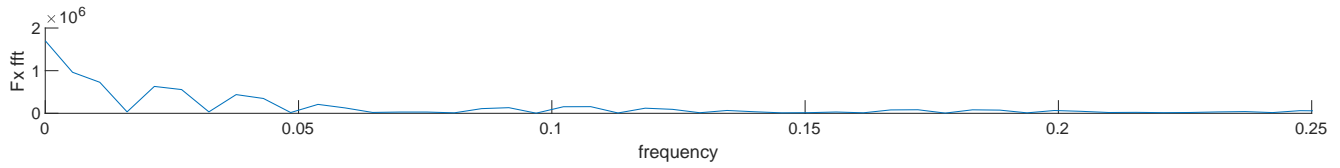
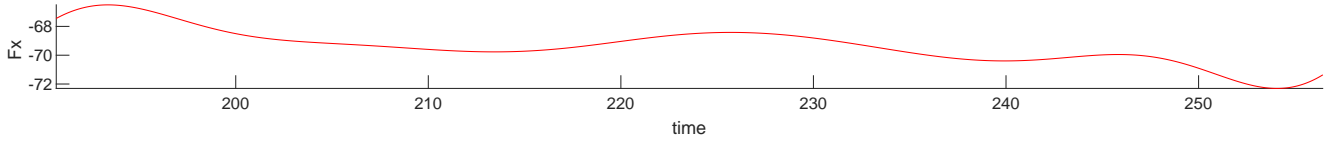
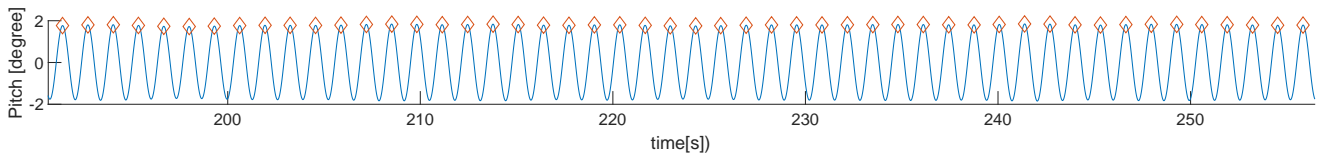
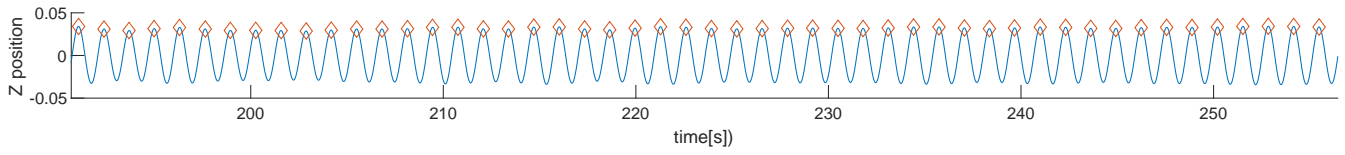
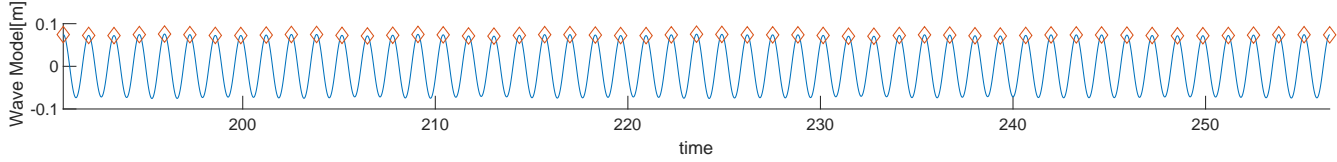
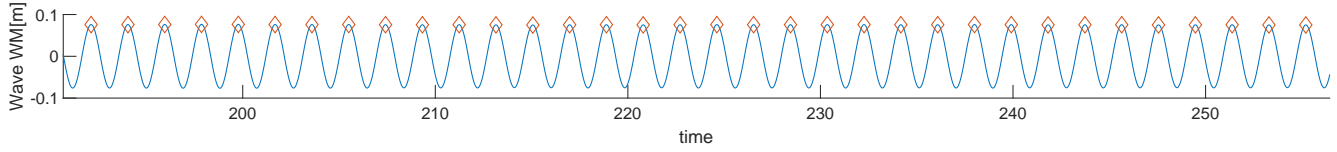
CE4090 Period(s):10.5 Lamda/L:0.91 Drift agle(deg):0 Speed(m/s):7.71



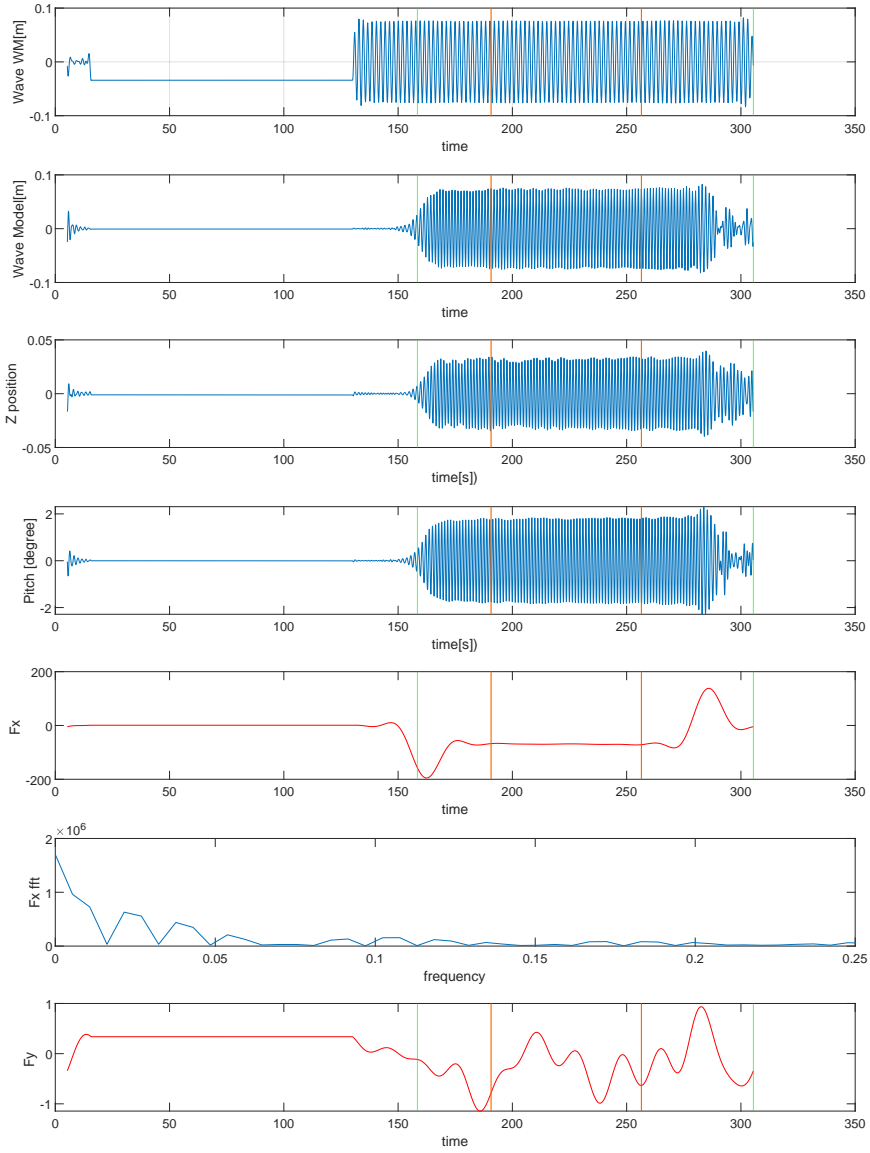
CE4090 Period(s):10.5 Lamda/L:0.91 Drift angle(deg):0 Speed(m/s):7.71



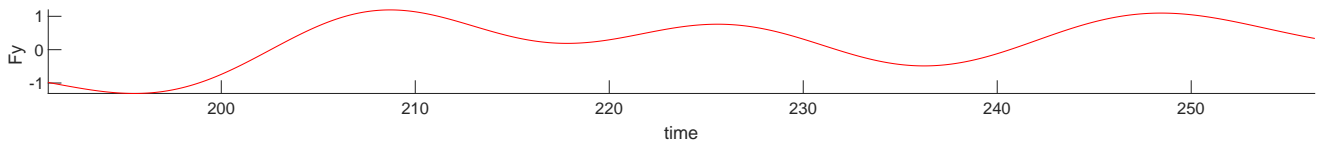
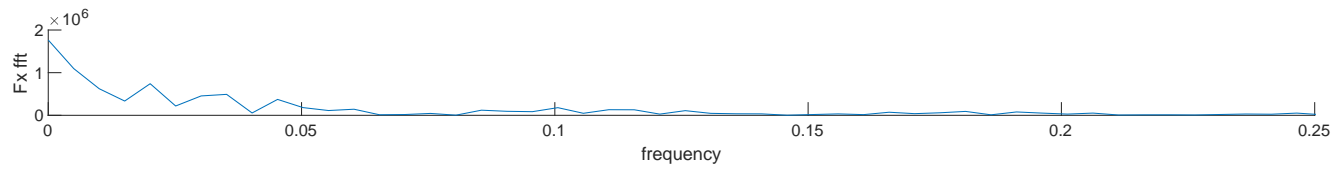
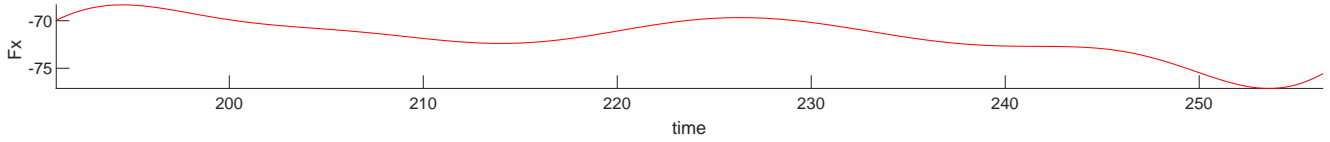
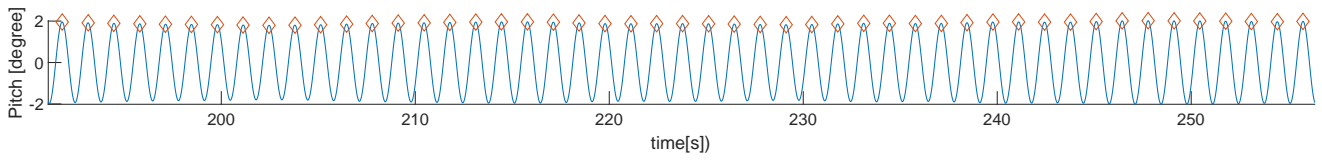
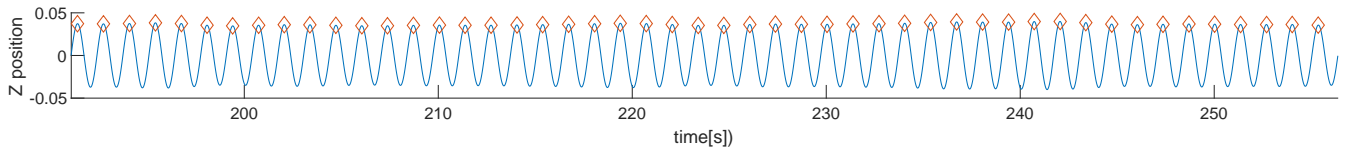
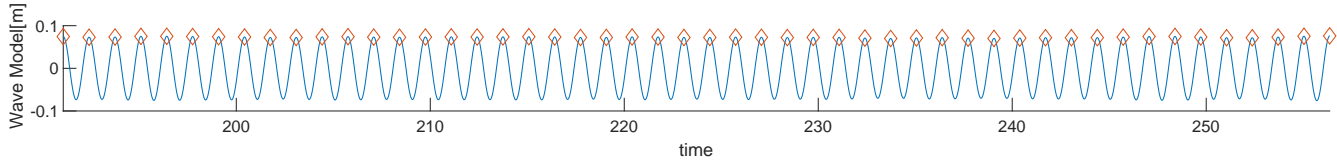
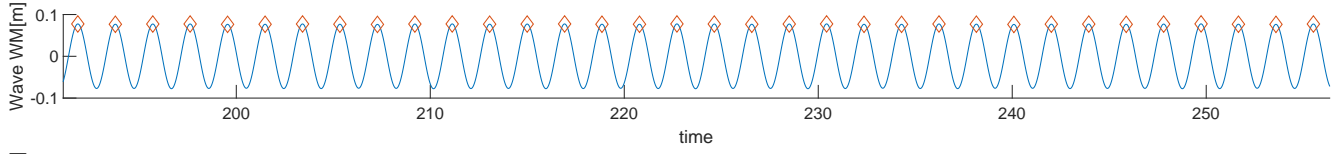
CE4100 Period(s):10.8 Lamda/L:0.96 Drift agle(deg):0 Speed(m/s):7.71



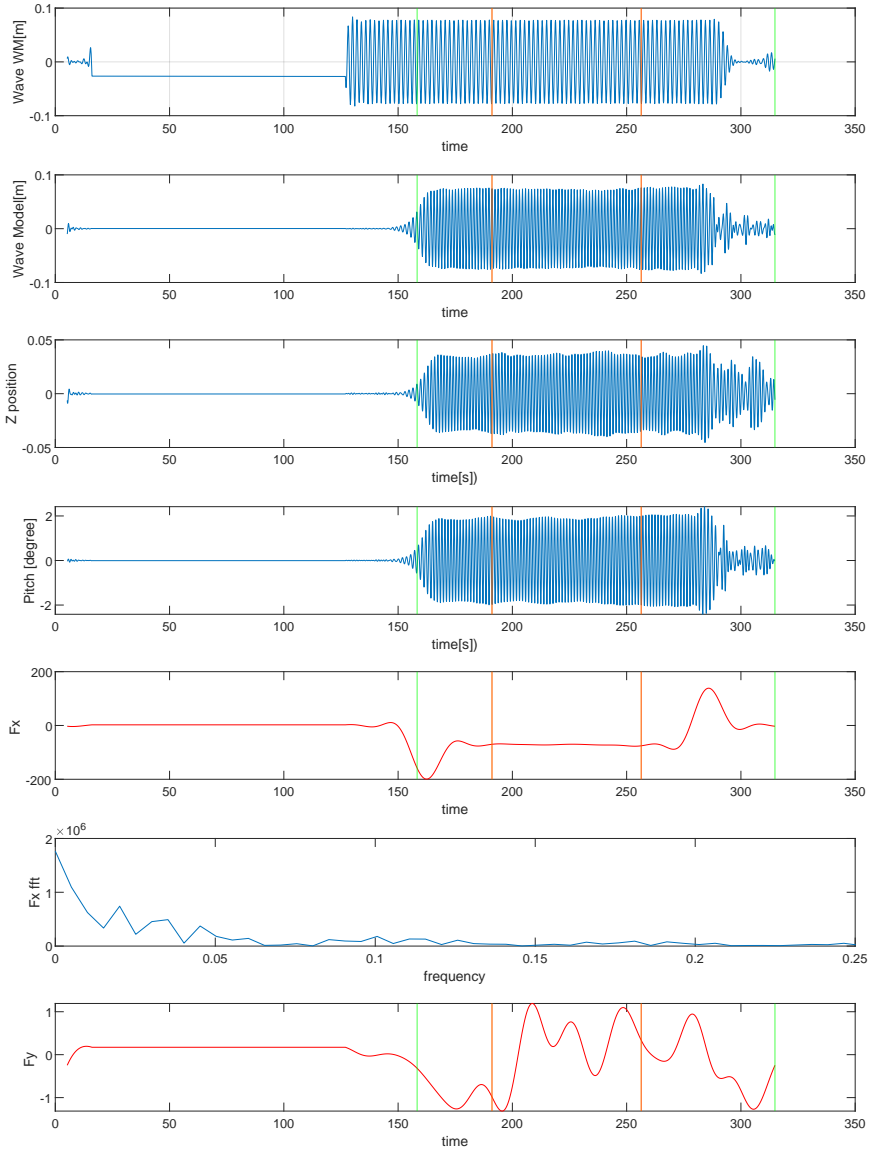
CE4100 Period(s):10.8 Lamda/L:0.96 Drift angle(deg):0 Speed(m/s):7.71



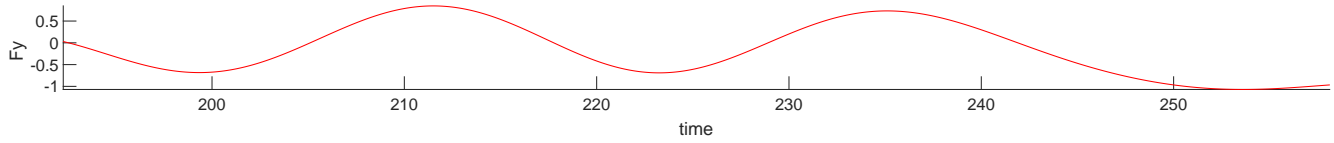
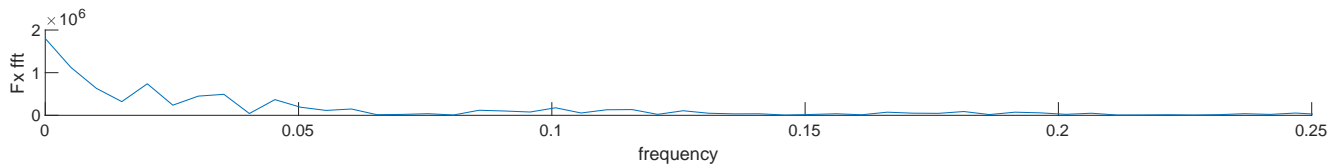
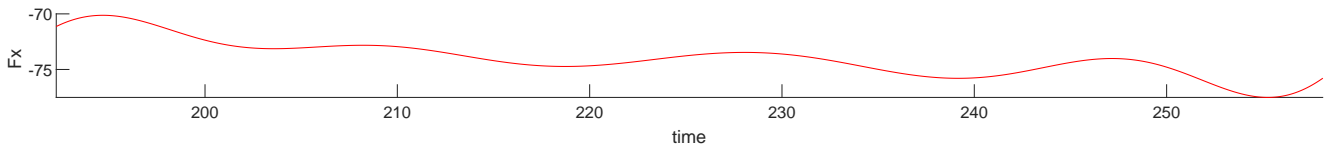
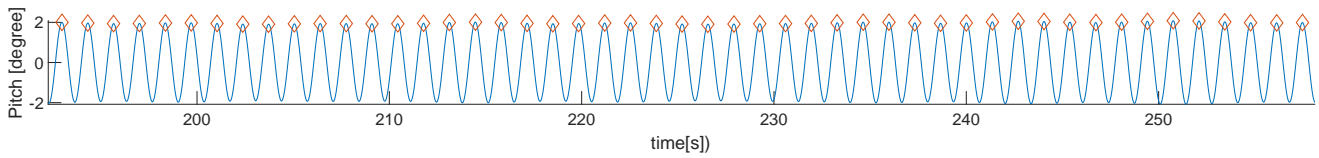
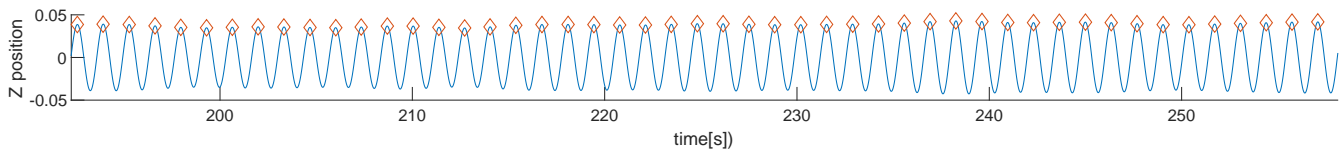
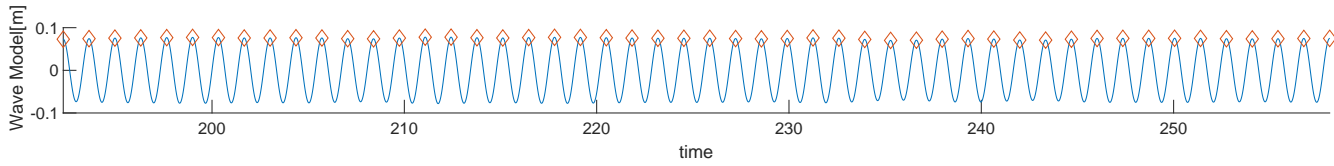
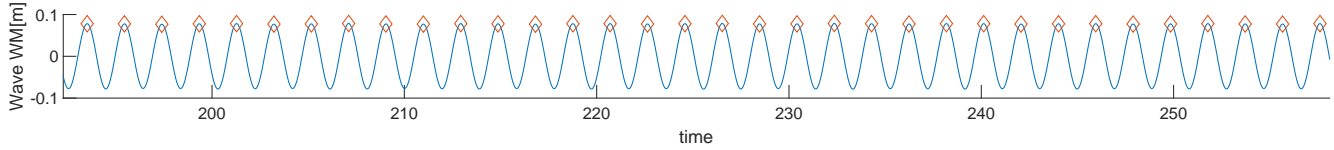
CE4110 Period(s):10.9 Lamda/L:0.98 Drift agle(deg):0 Speed(m/s):7.71



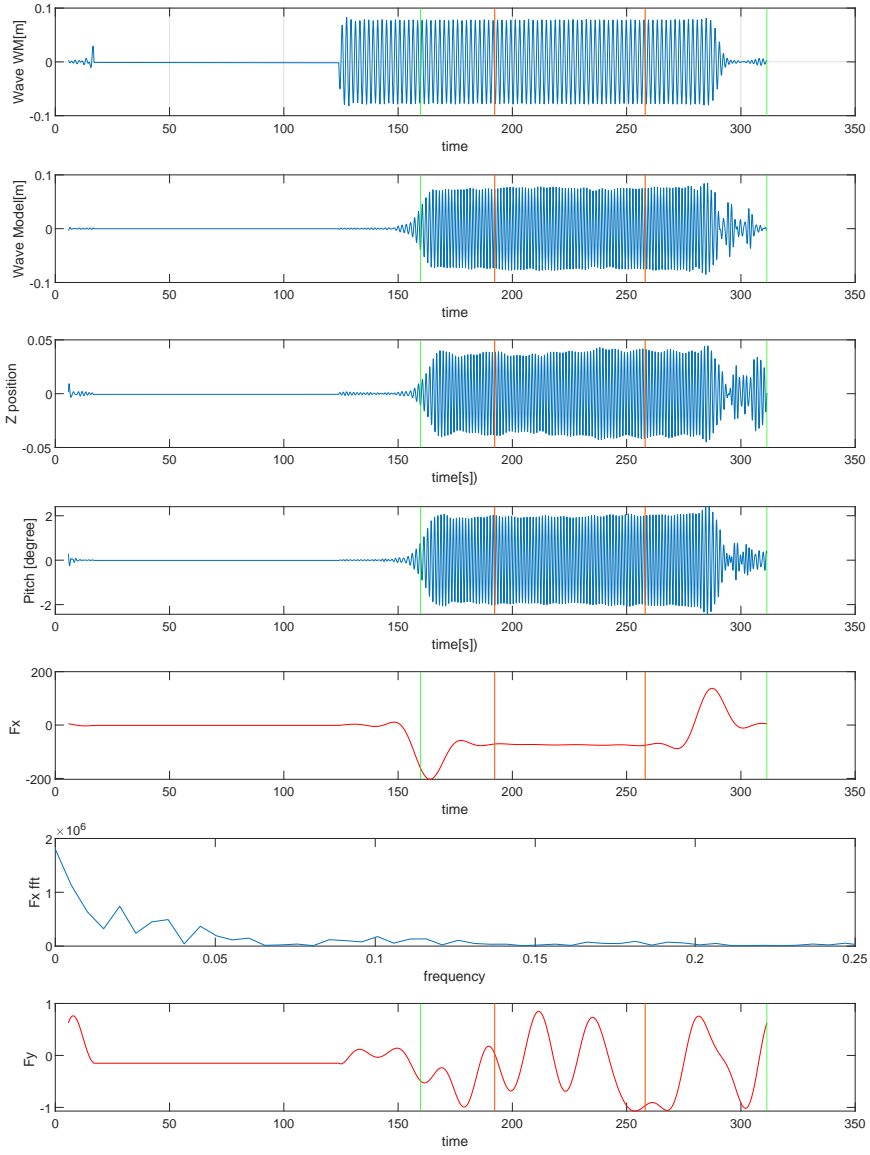
CE4110 Period(s):10.9 Lamda/L:0.98 Drift angle(deg):0 Speed(m/s):7.71



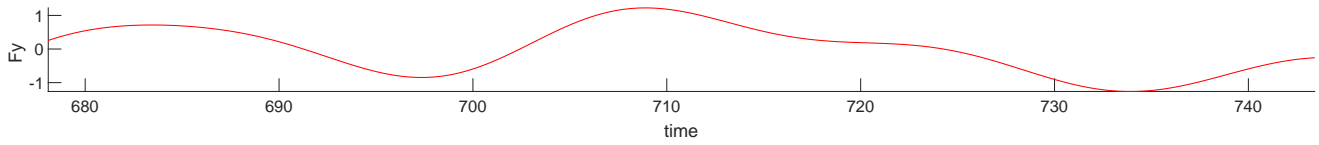
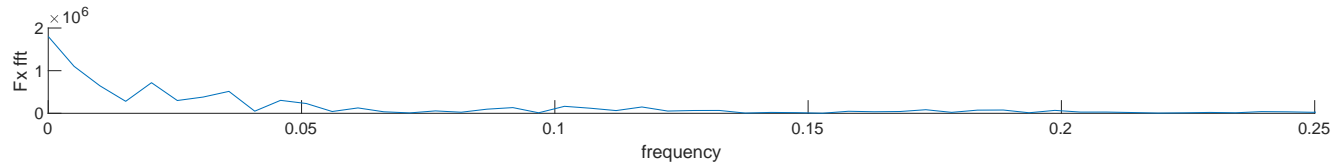
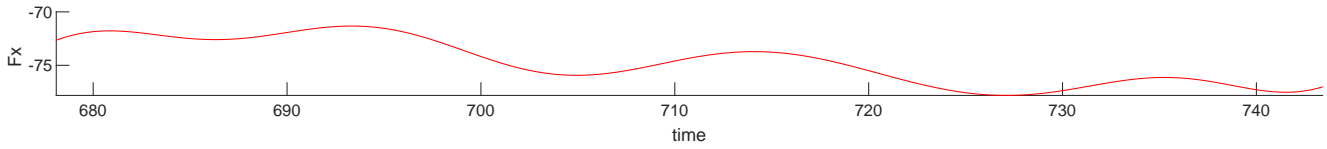
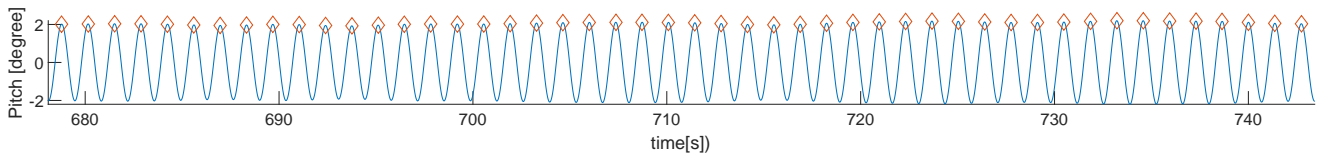
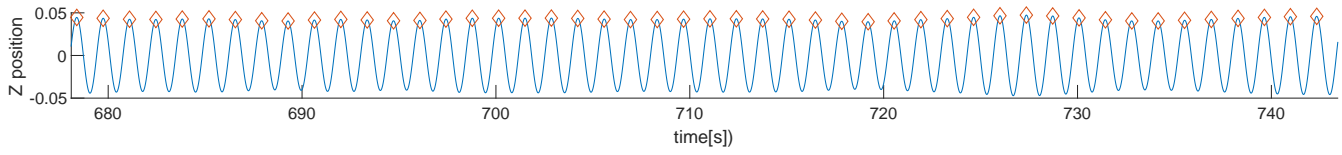
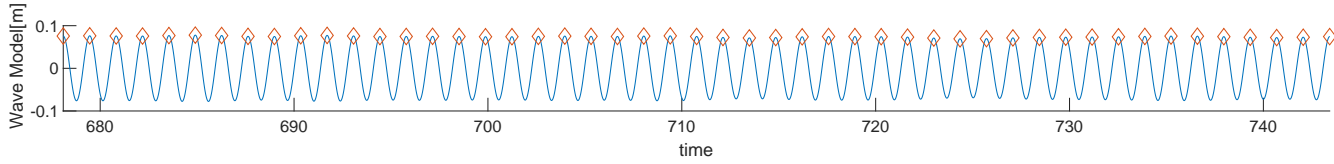
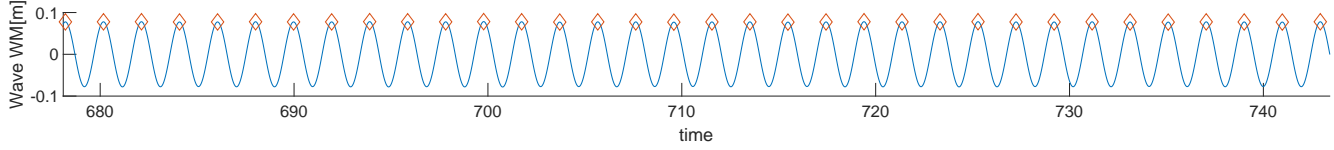
CE4120 Period(s):11 Lamda/L:0.99 Drift agle(deg):0 Speed(m/s):7.71



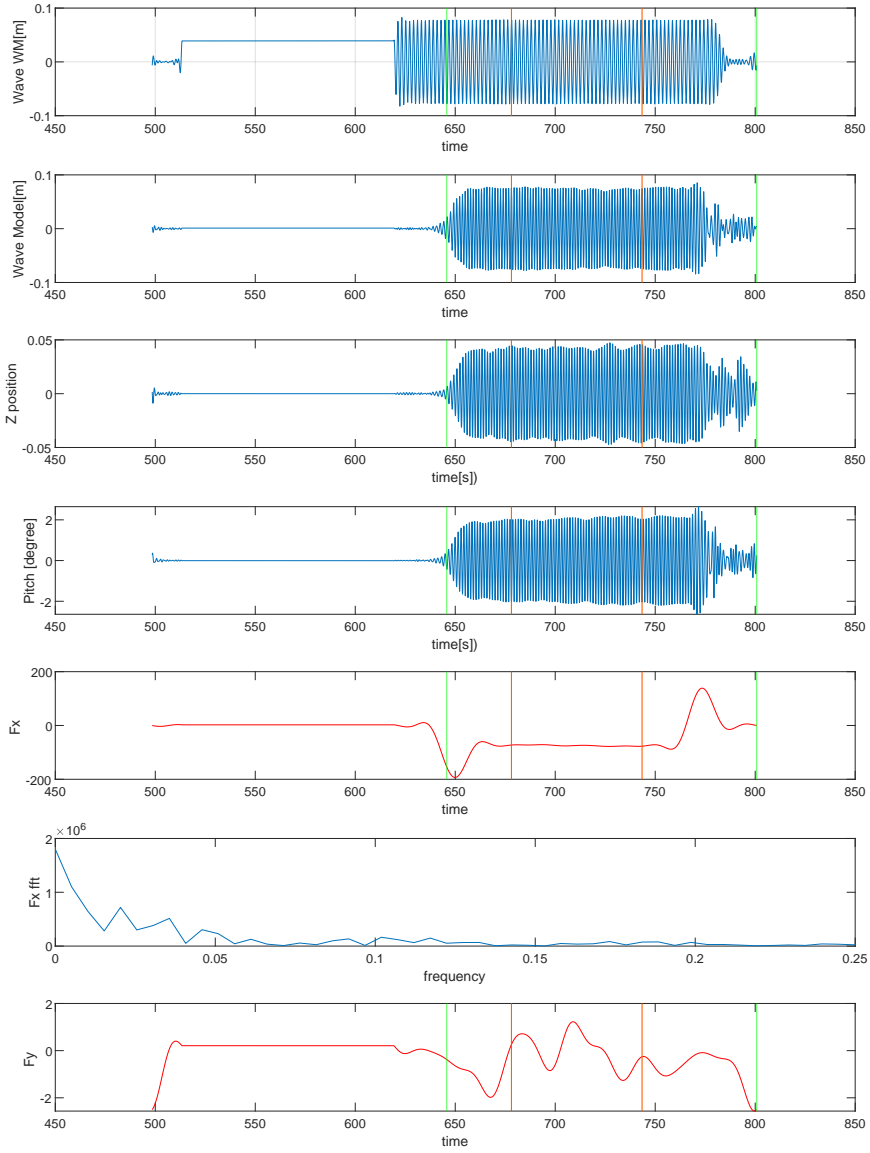
CE4120 Period(s):11 Lamda/L:0.99 Drift angle(deg):0 Speed(m/s):7.71



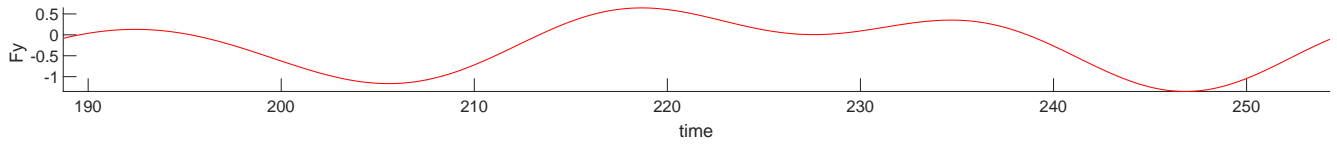
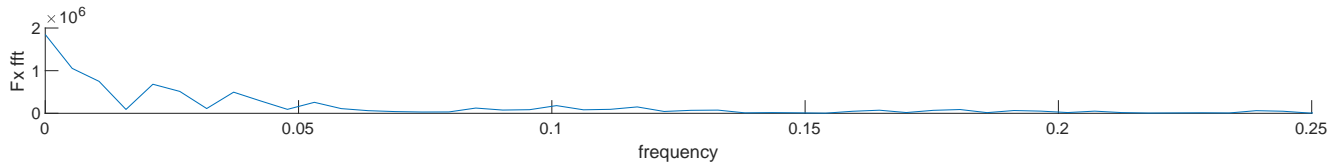
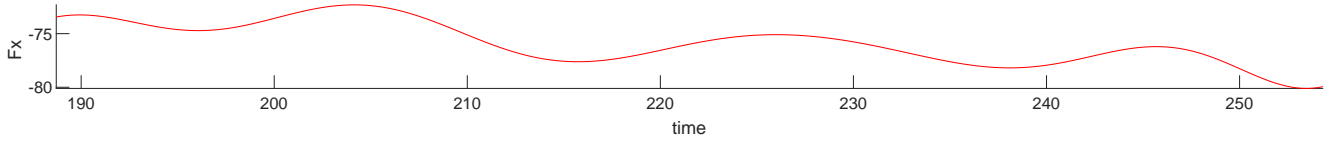
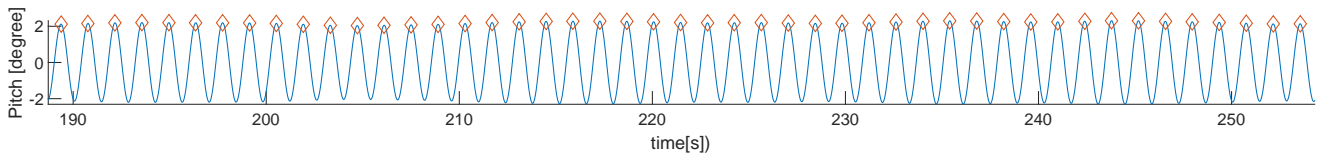
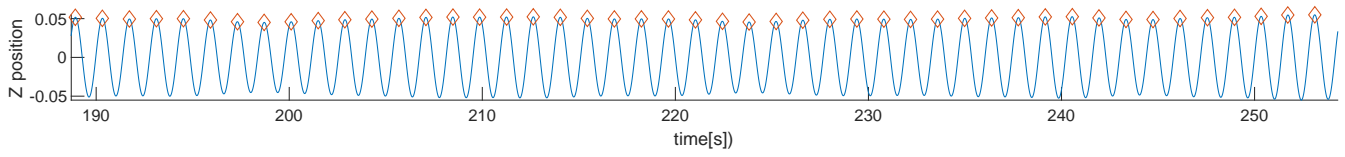
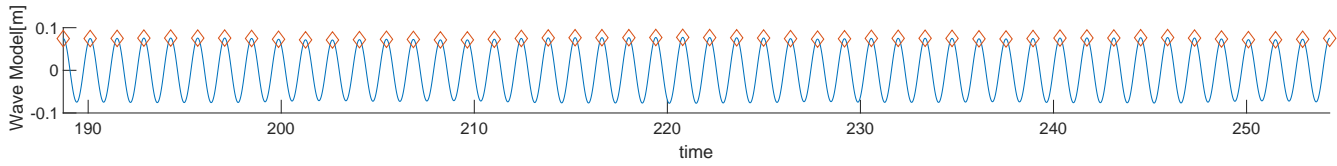
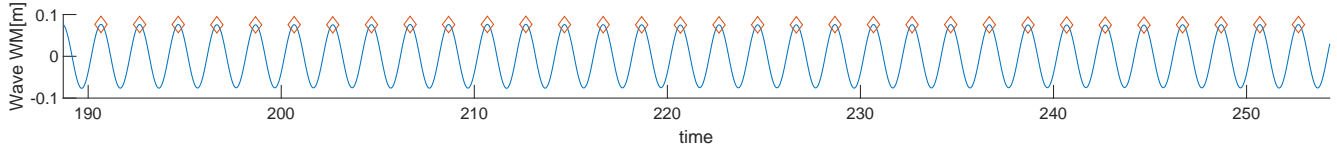
CE4130 Period(s):11.1 Lamda/L:1.01 Drift agle(deg):0 Speed(m/s):7.71



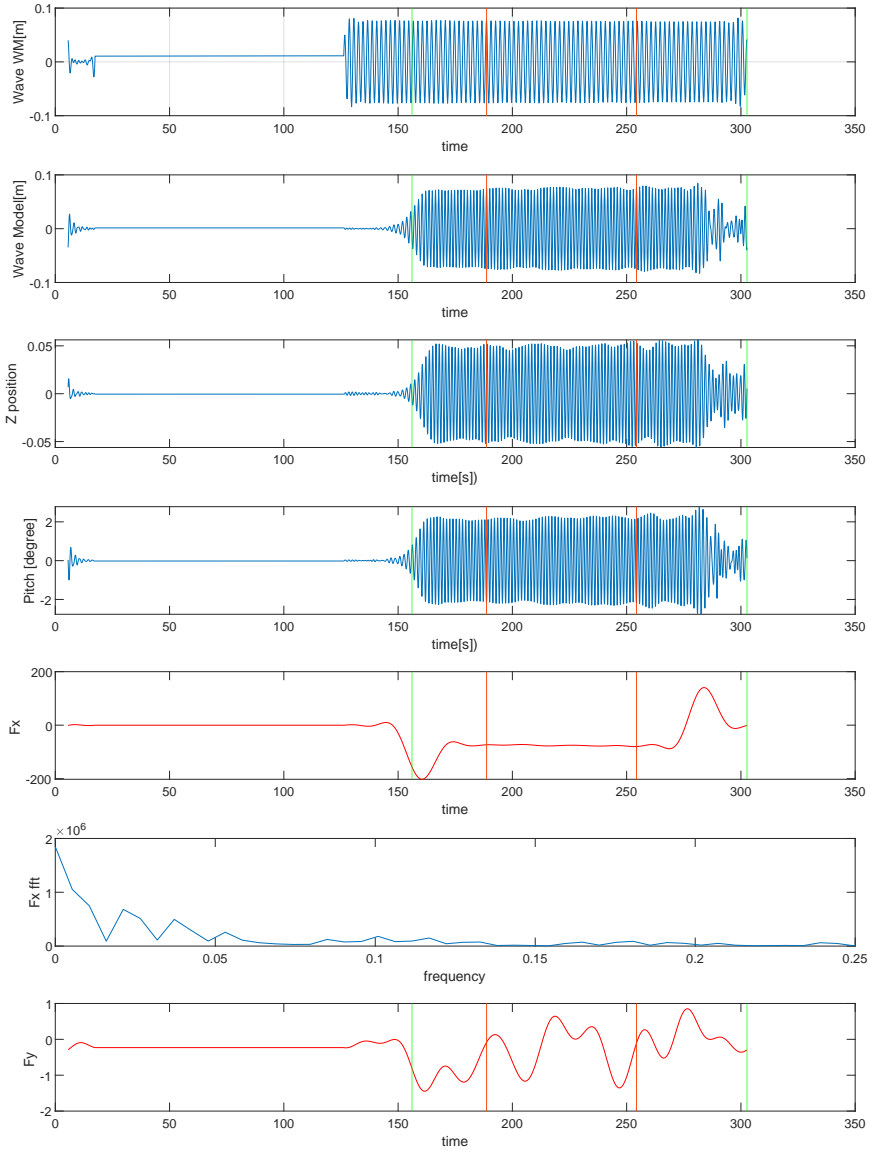
CE4130 Period(s):11.1 Lamda/L:1.01 Drift angle(deg):0 Speed(m/s):7.71



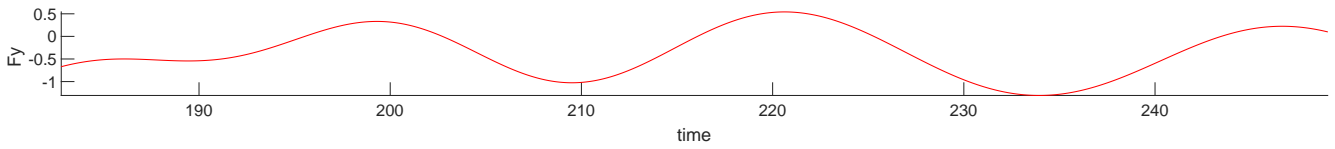
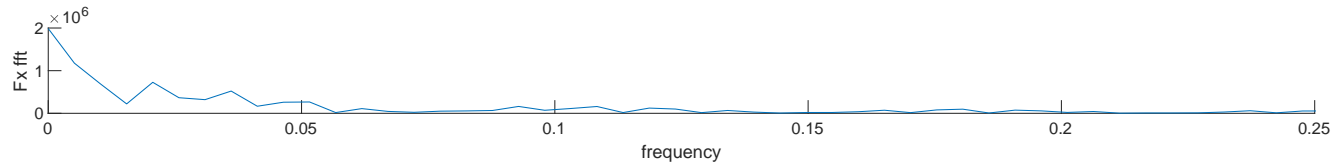
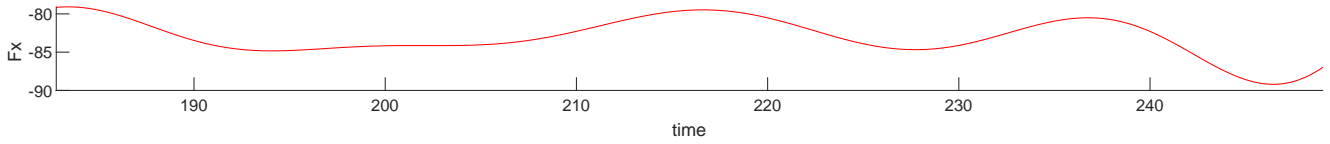
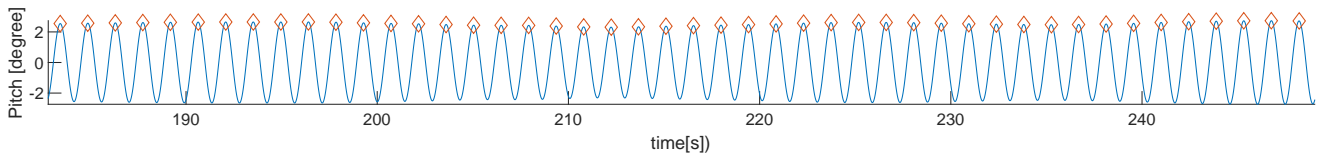
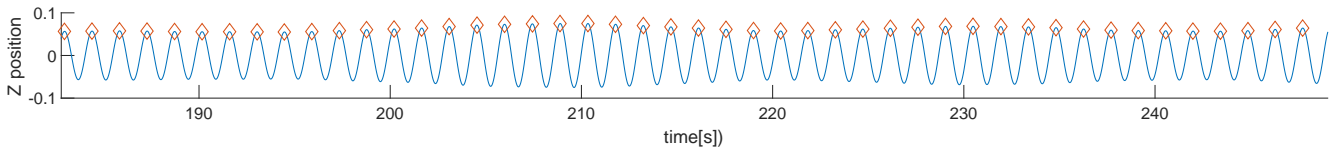
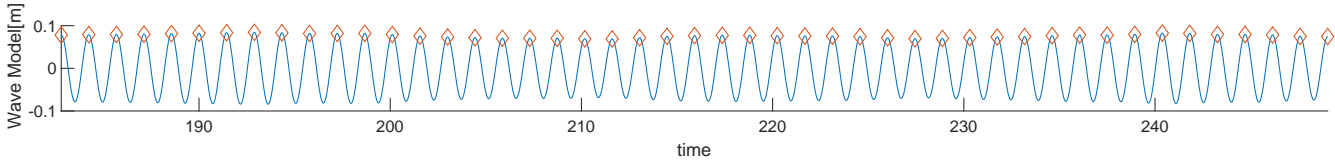
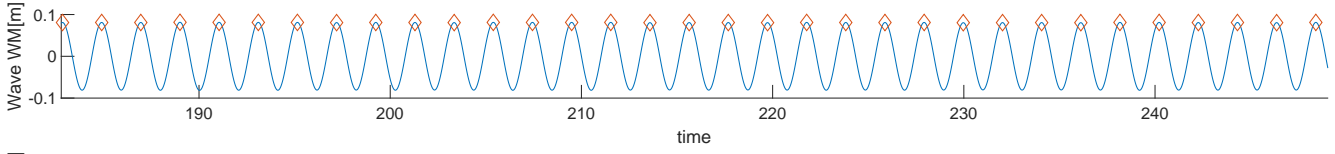
CE4140 Period(s):11.3 Lamda/L:1.05 Drift agle(deg):0 Speed(m/s):7.71



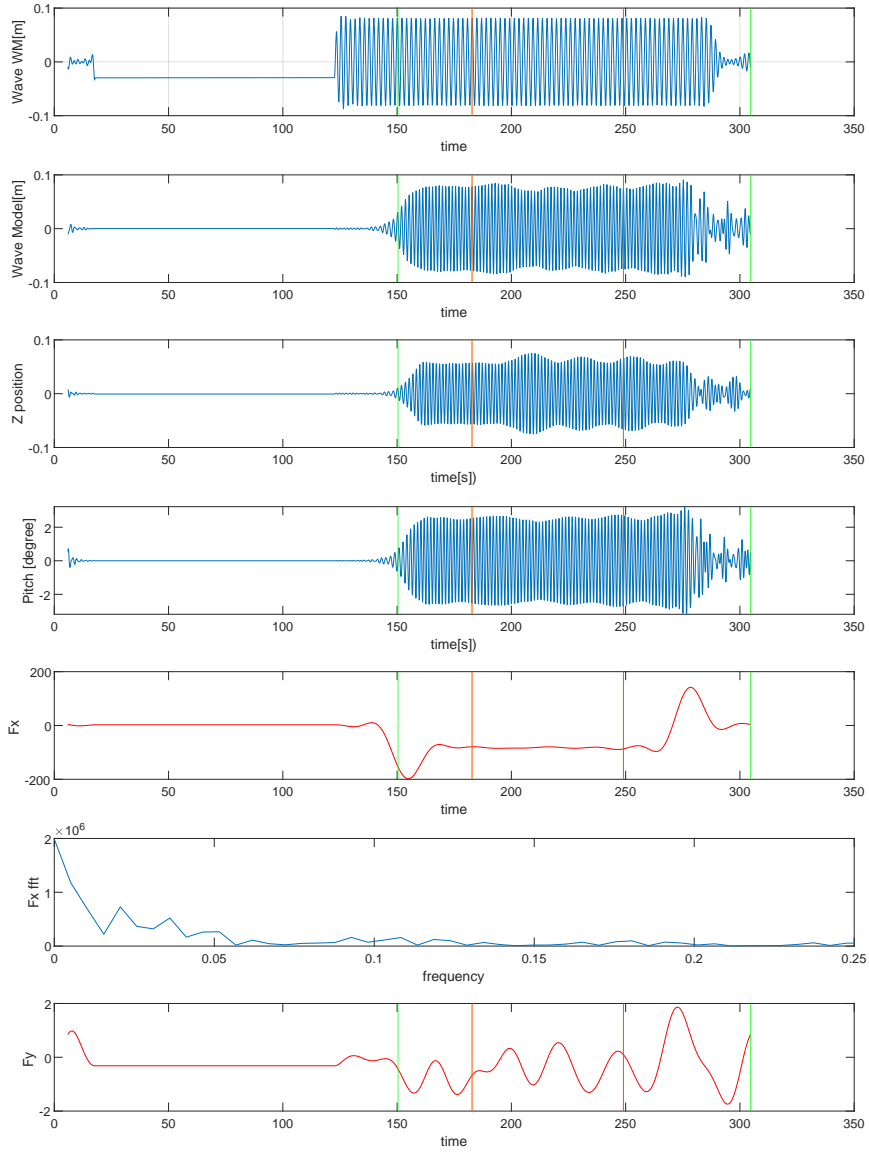
CE4140 Period(s):11.3 Lamda/L:1.05 Drift angle(deg):0 Speed(m/s):7.71



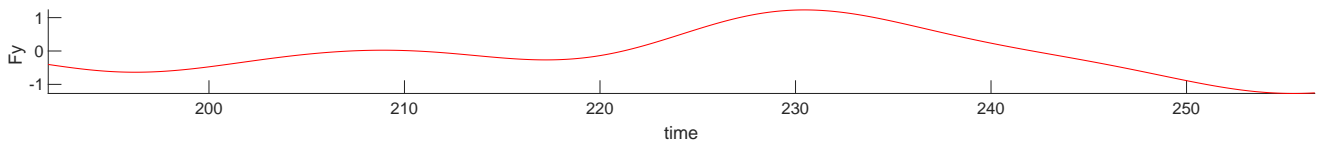
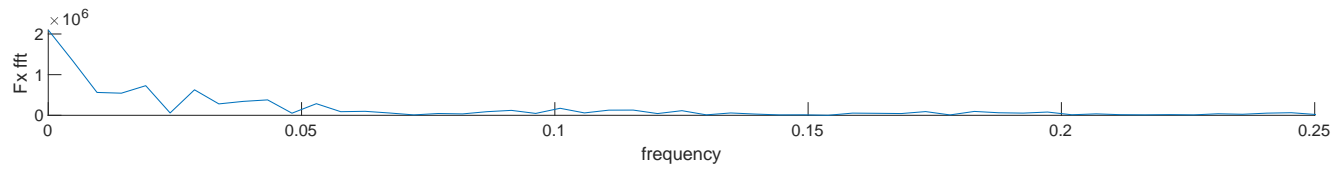
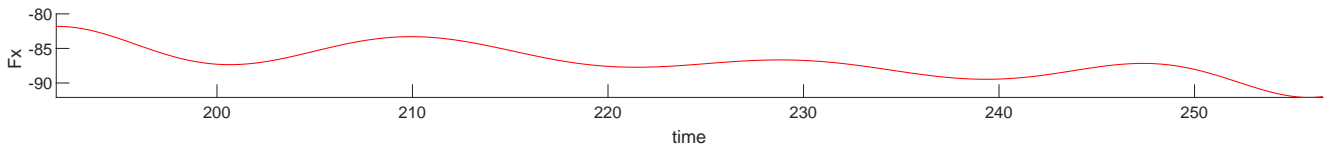
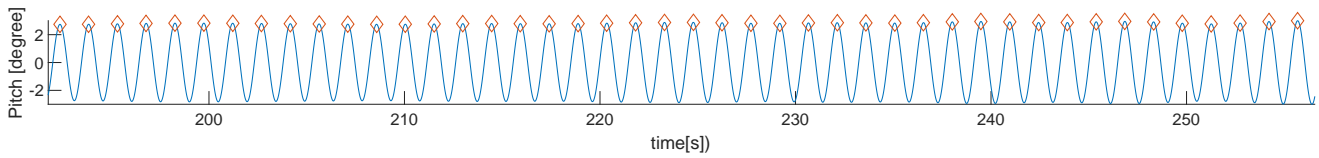
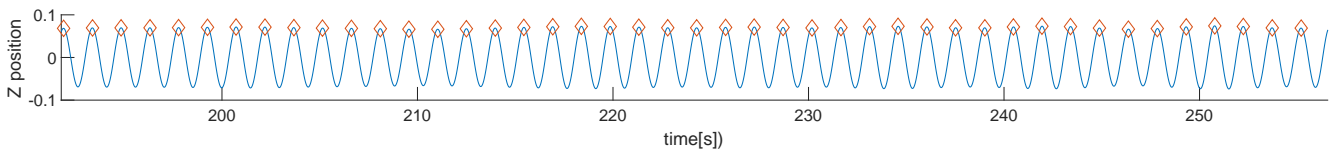
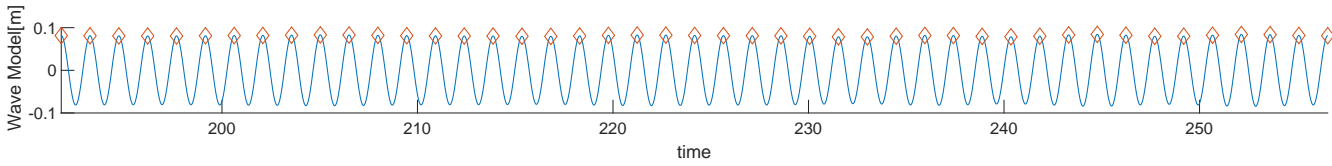
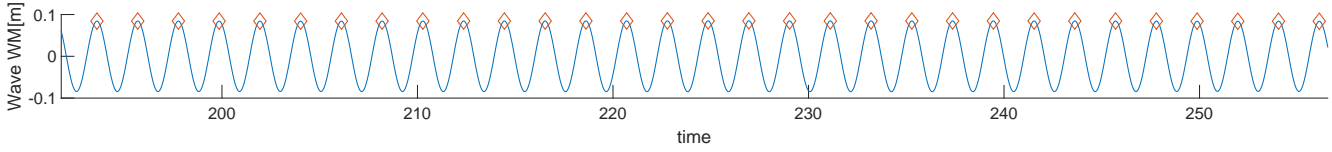
CE4150 Period(s):11.6 Lamda/L:1.11 Drift agle(deg):0 Speed(m/s):7.71



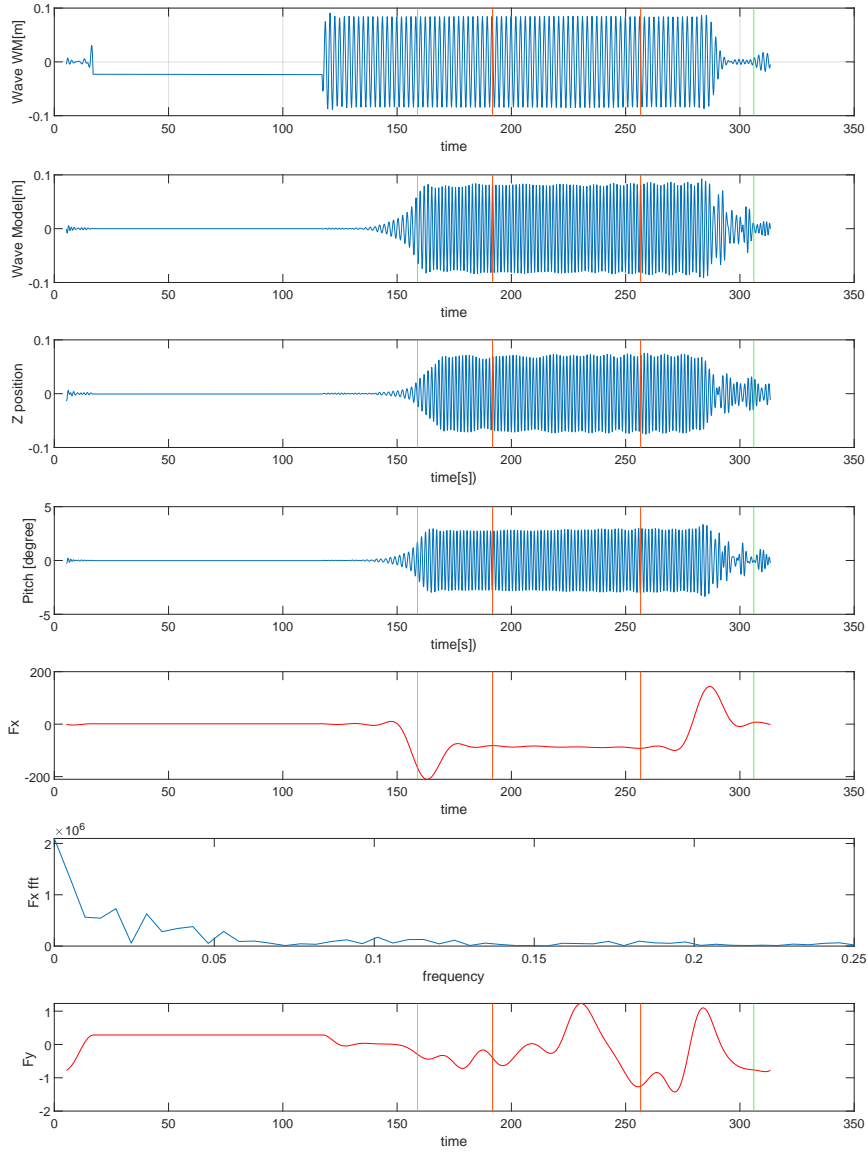
CE4150 Period(s):11.6 Lamda/L:1.11 Drift angle(deg):0 Speed(m/s):7.71



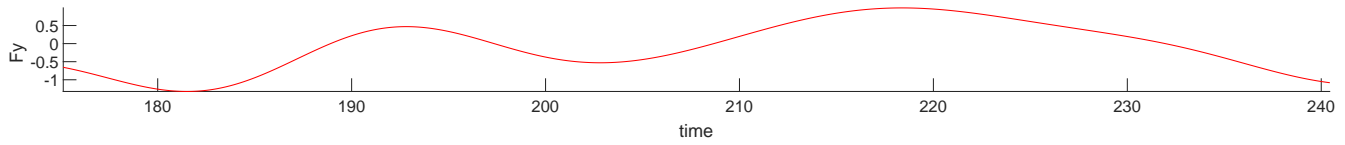
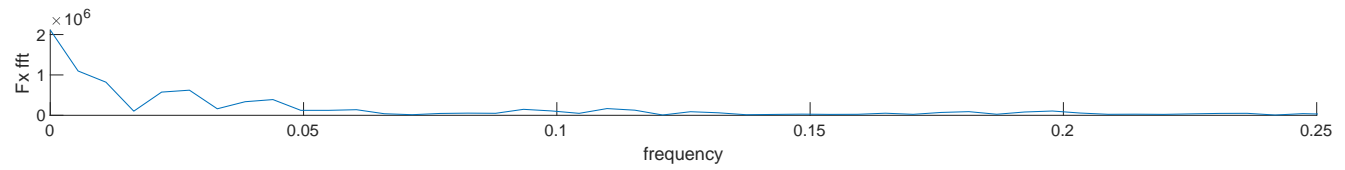
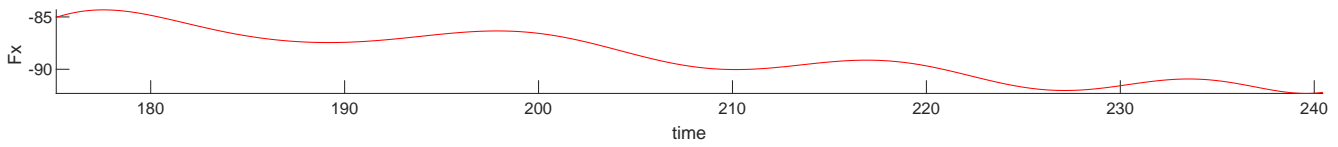
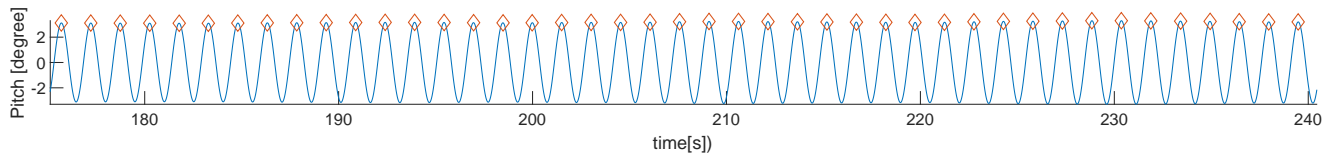
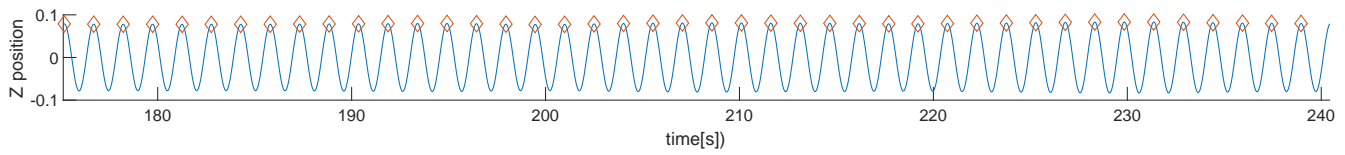
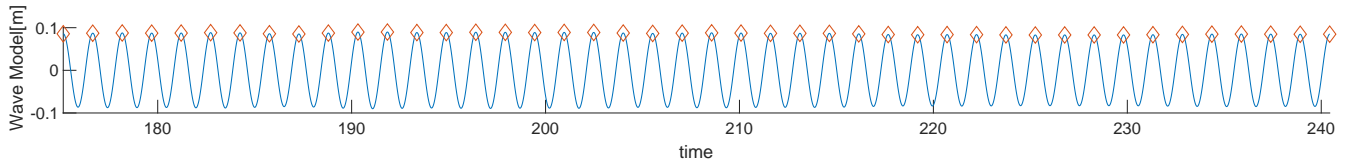
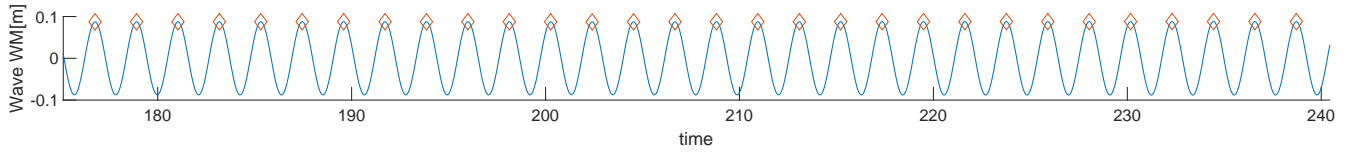
CE4160 Period(s):11.8 Lamda/L:1.14 Drift agle(deg):0 Speed(m/s):7.71



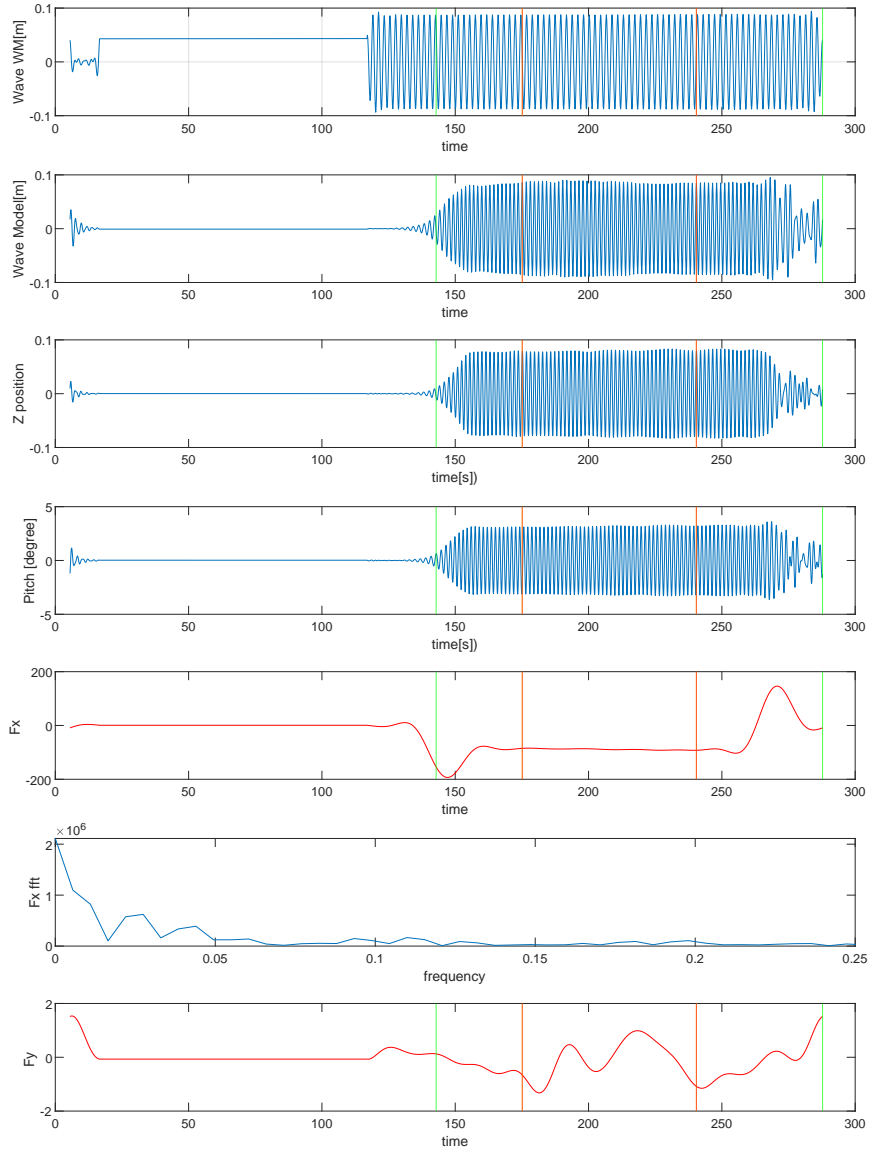
CE4160 Period(s):11.8 Lamda/L:1.14 Drift angle(deg):0 Speed(m/s):7.71



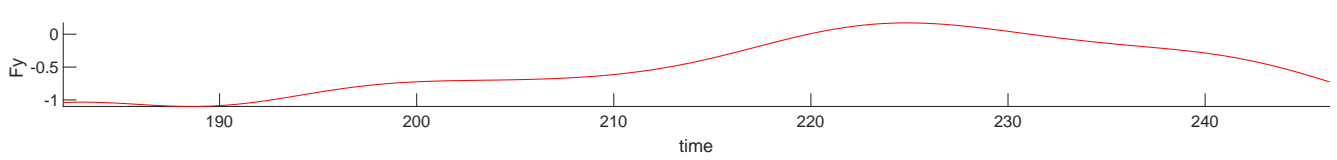
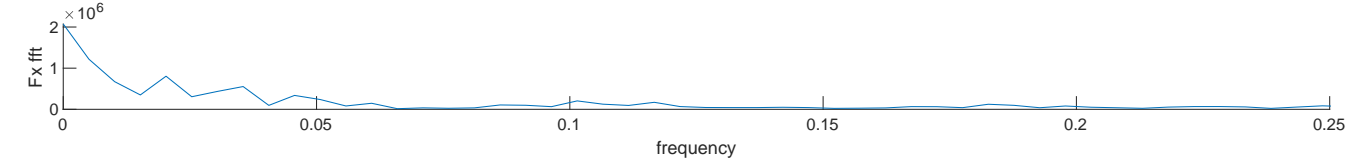
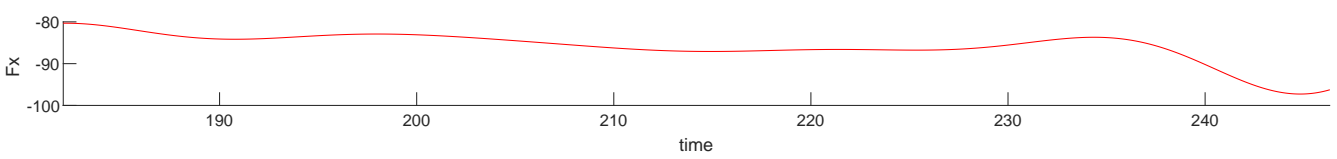
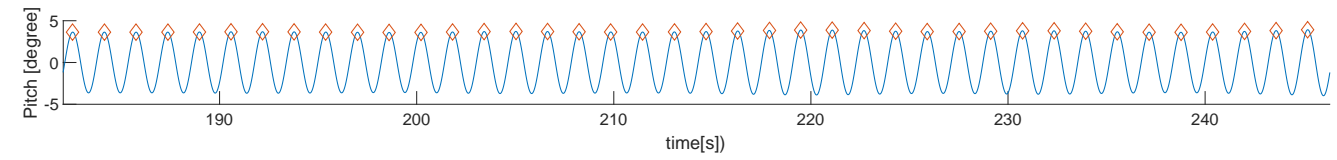
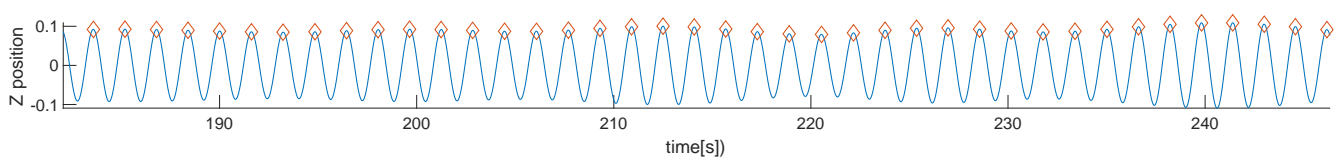
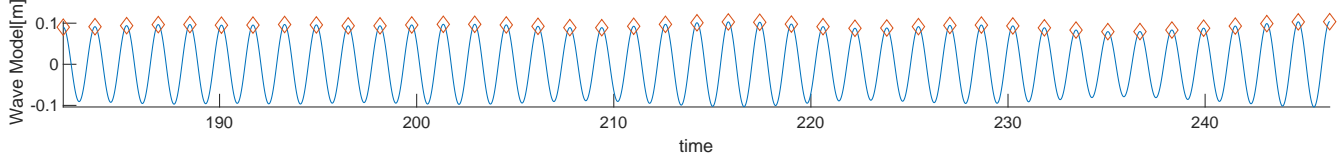
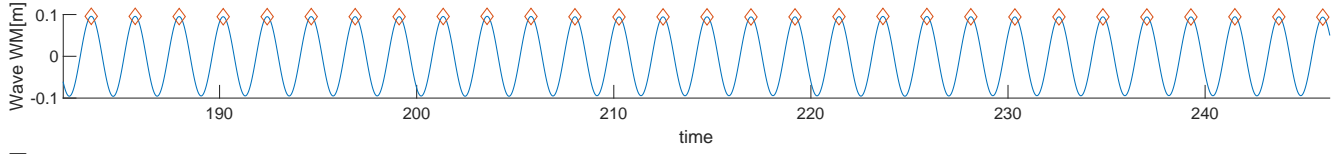
CE4170 Period(s):12.1 Lamda/L:1.2 Drift angle(deg):0 Speed(m/s):7.71



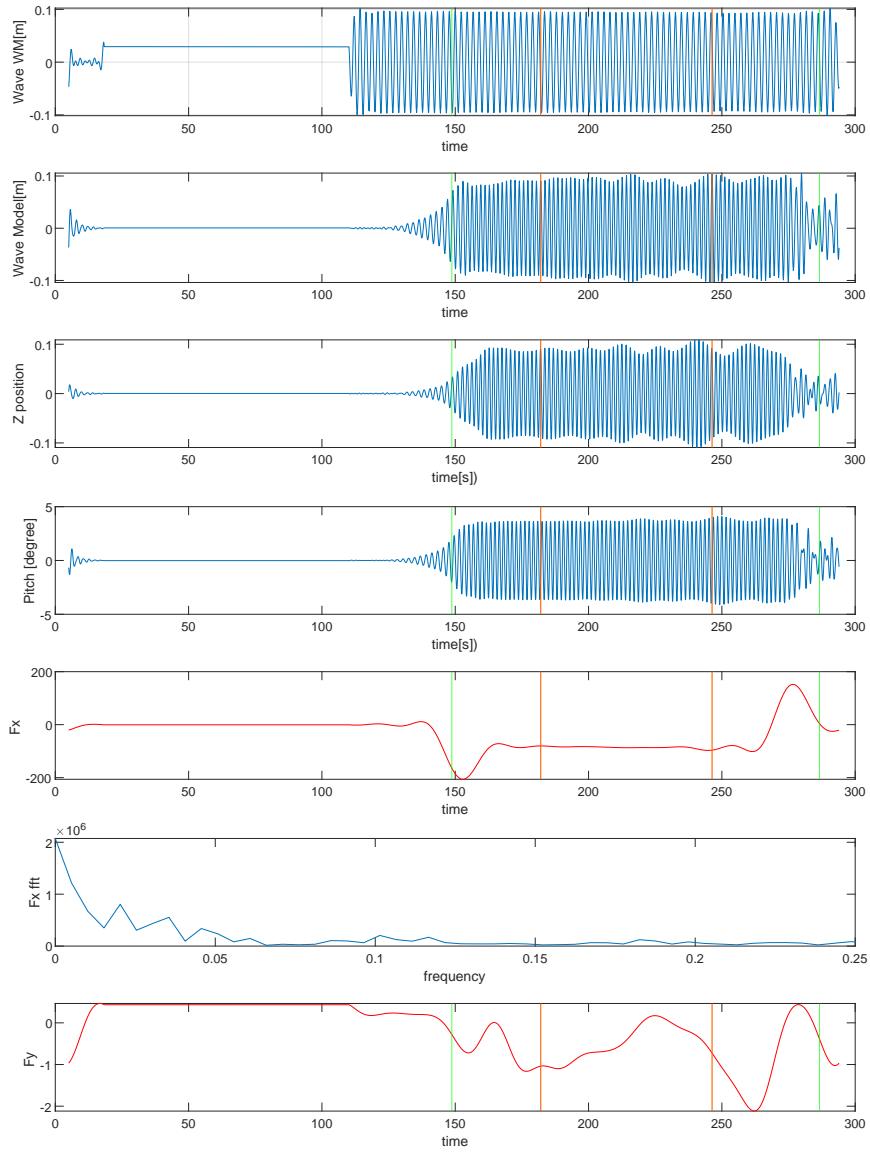
CE4170 Period(s):12.1 Lamda/L:1.2 Drift agle(deg):0 Speed(m/s):7.71



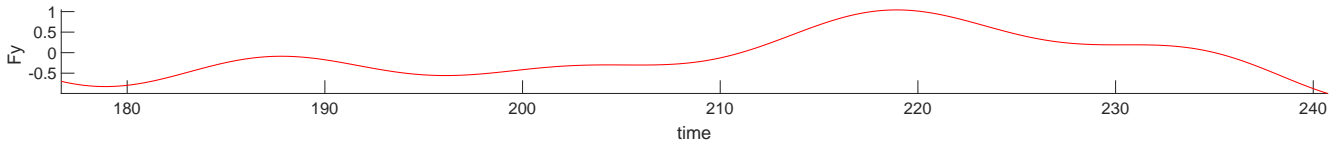
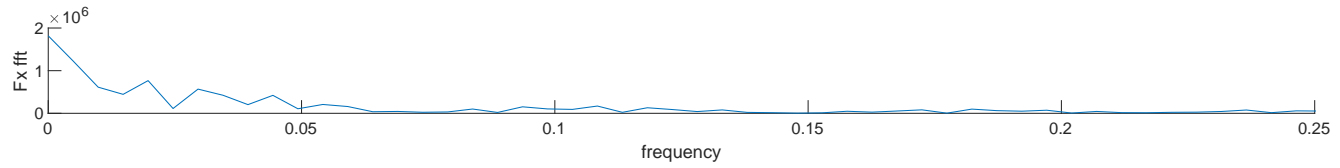
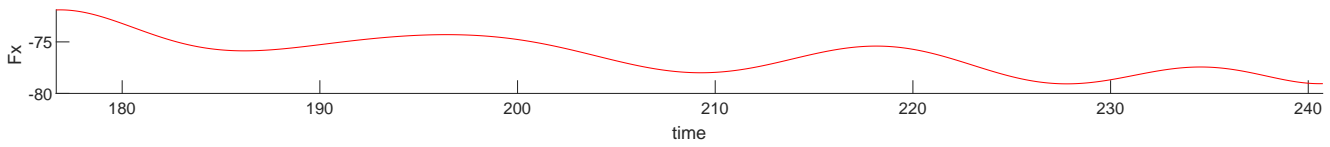
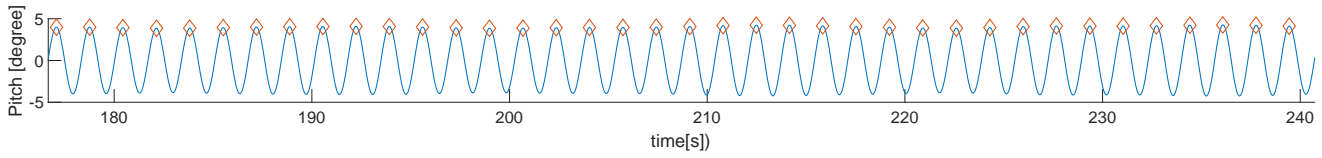
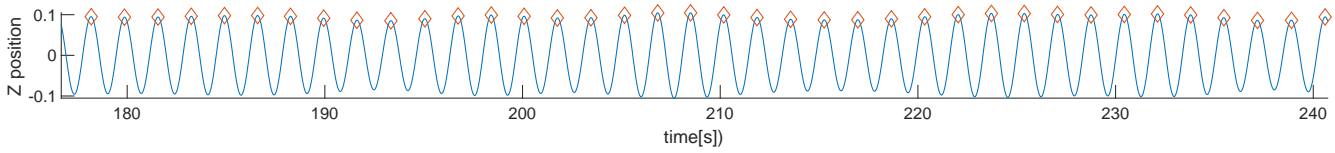
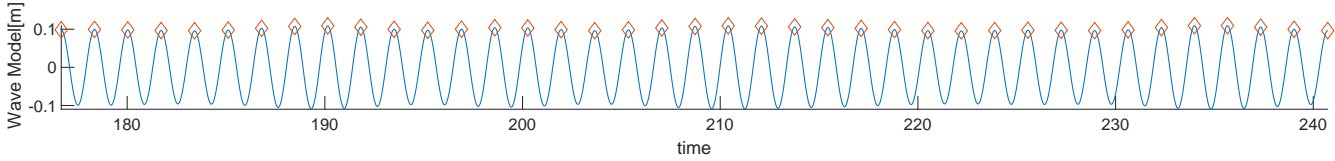
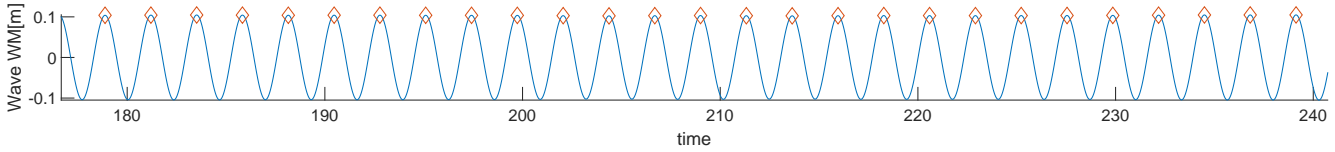
CE4180 Period(s):12.6 Lamda/L:1.3 Drift agle(deg):0 Speed(m/s):7.71



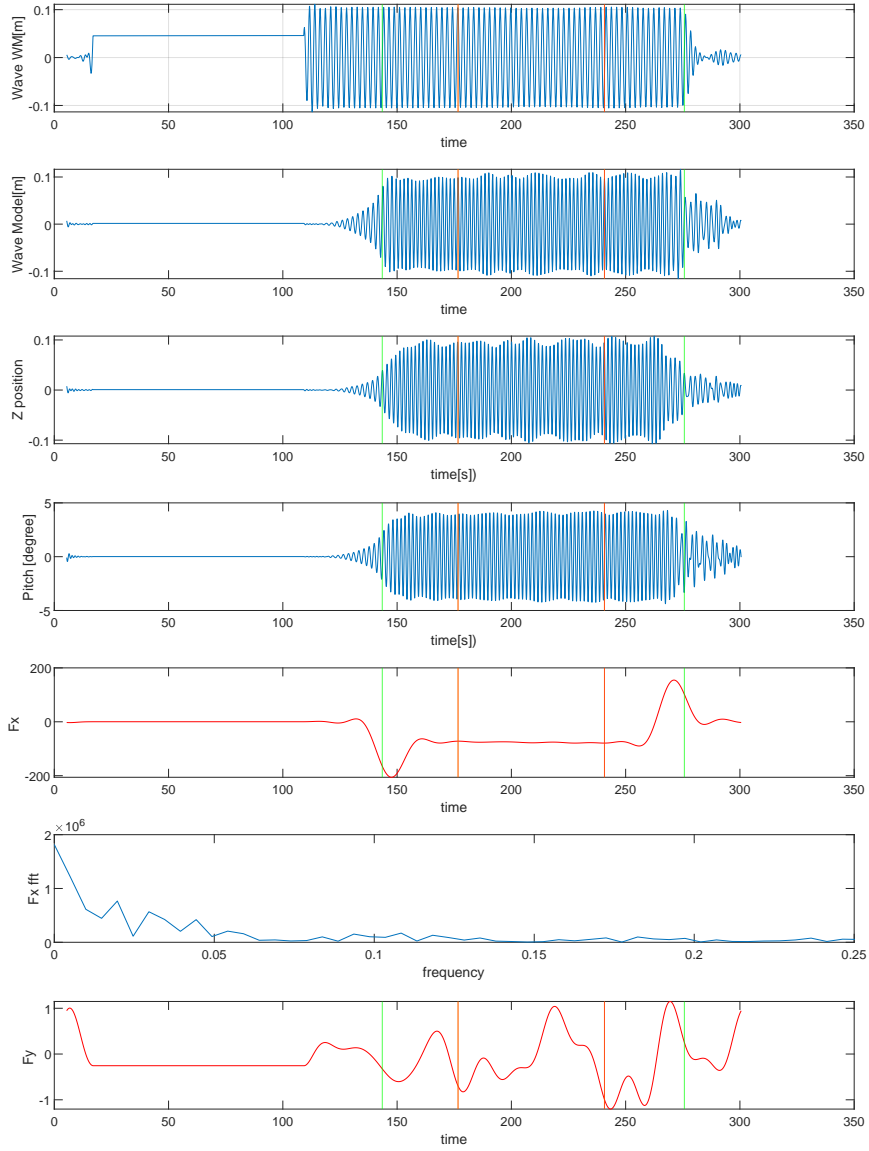
CE4180 Period(s):12.6 Lamda/L:1.3 Drift angle(deg):0 Speed(m/s):7.71



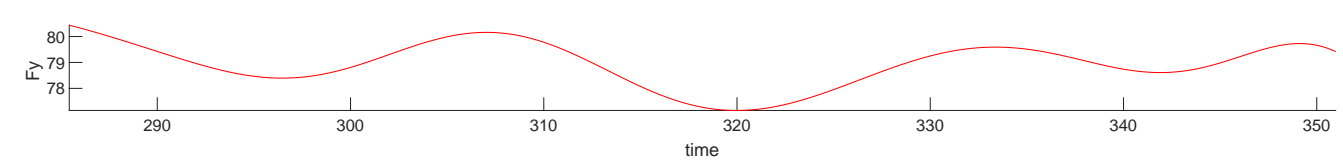
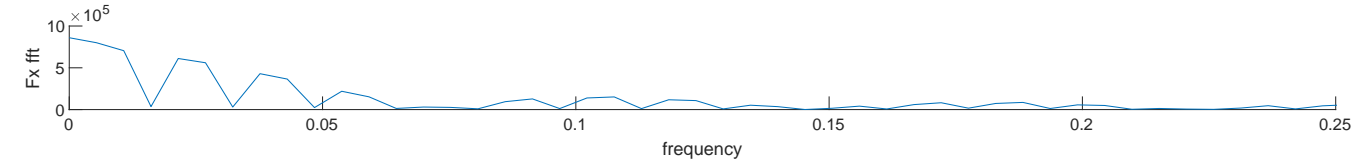
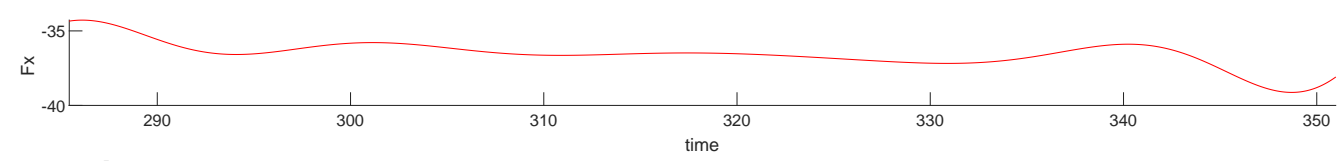
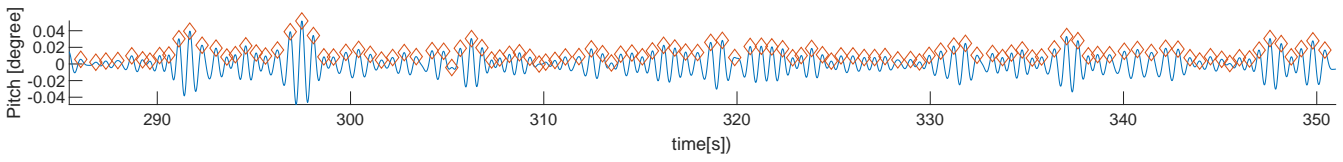
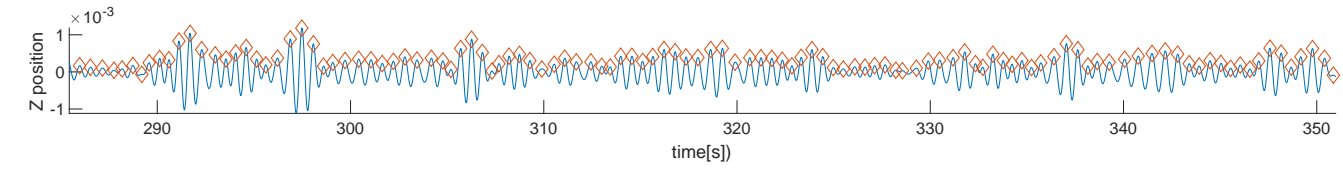
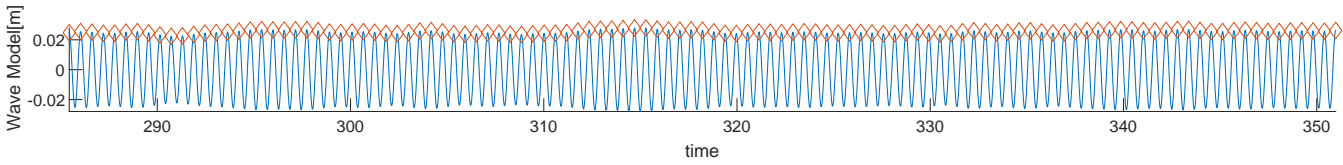
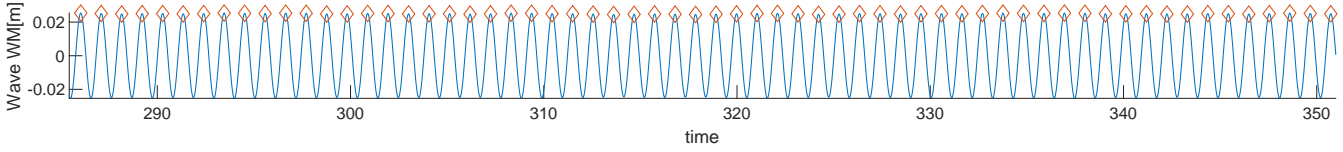
CE4190 Period(s):13.1 Lamda/L:1.41 Drift agle(deg):0 Speed(m/s):7.71



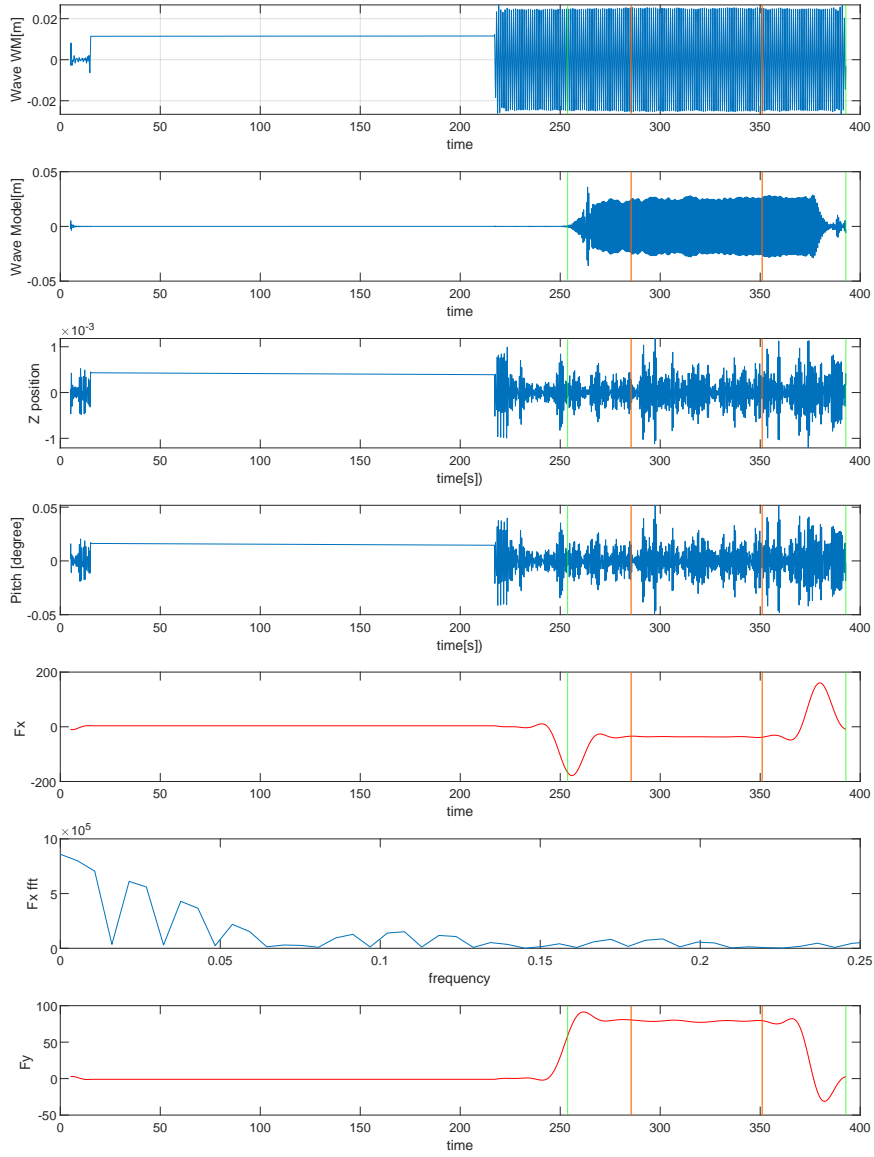
CE4190 Period(s):13.1 Lamda/L:1.41 Drift angle(deg):0 Speed(m/s):7.71



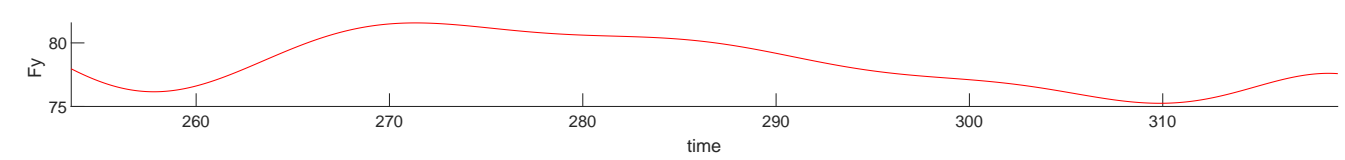
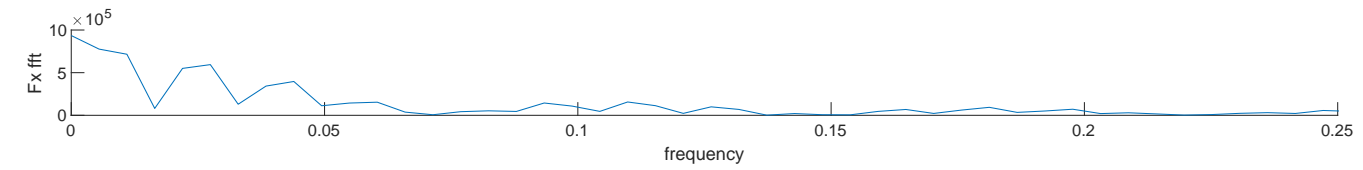
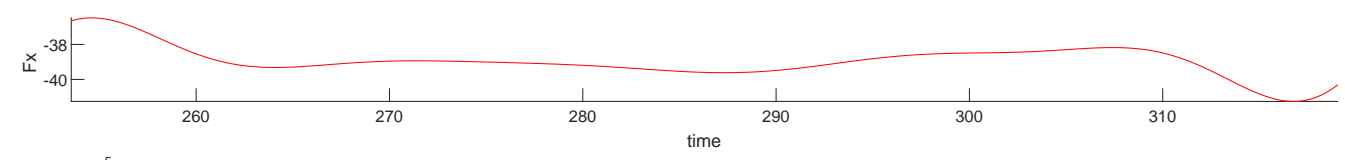
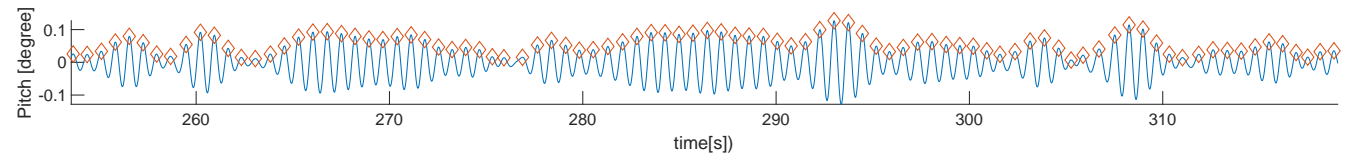
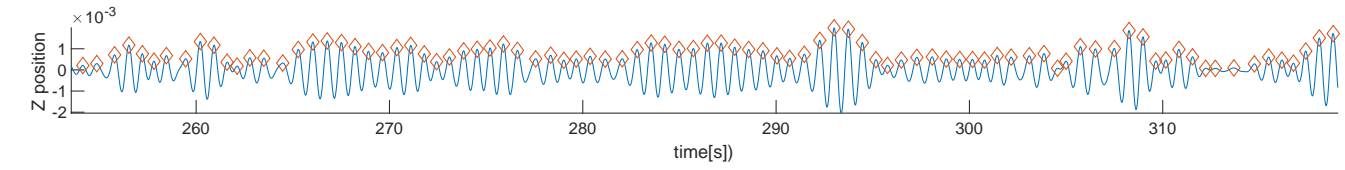
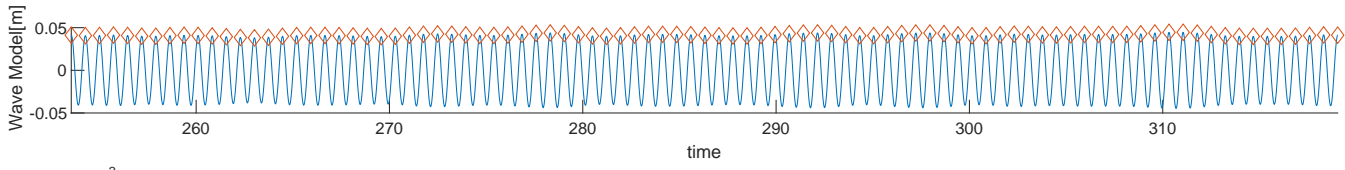
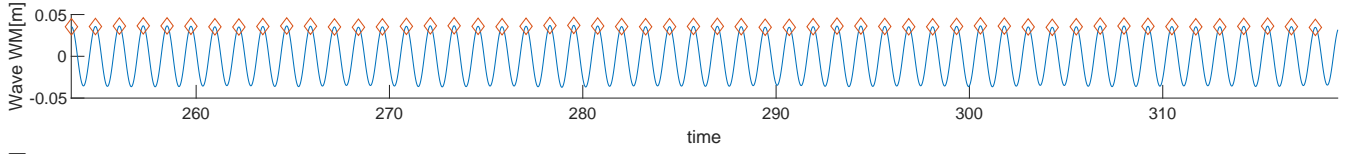
CE5000 Period(s):6 Lamda/L:0.3 Drift agle(deg):9 Speed(m/s):7.71



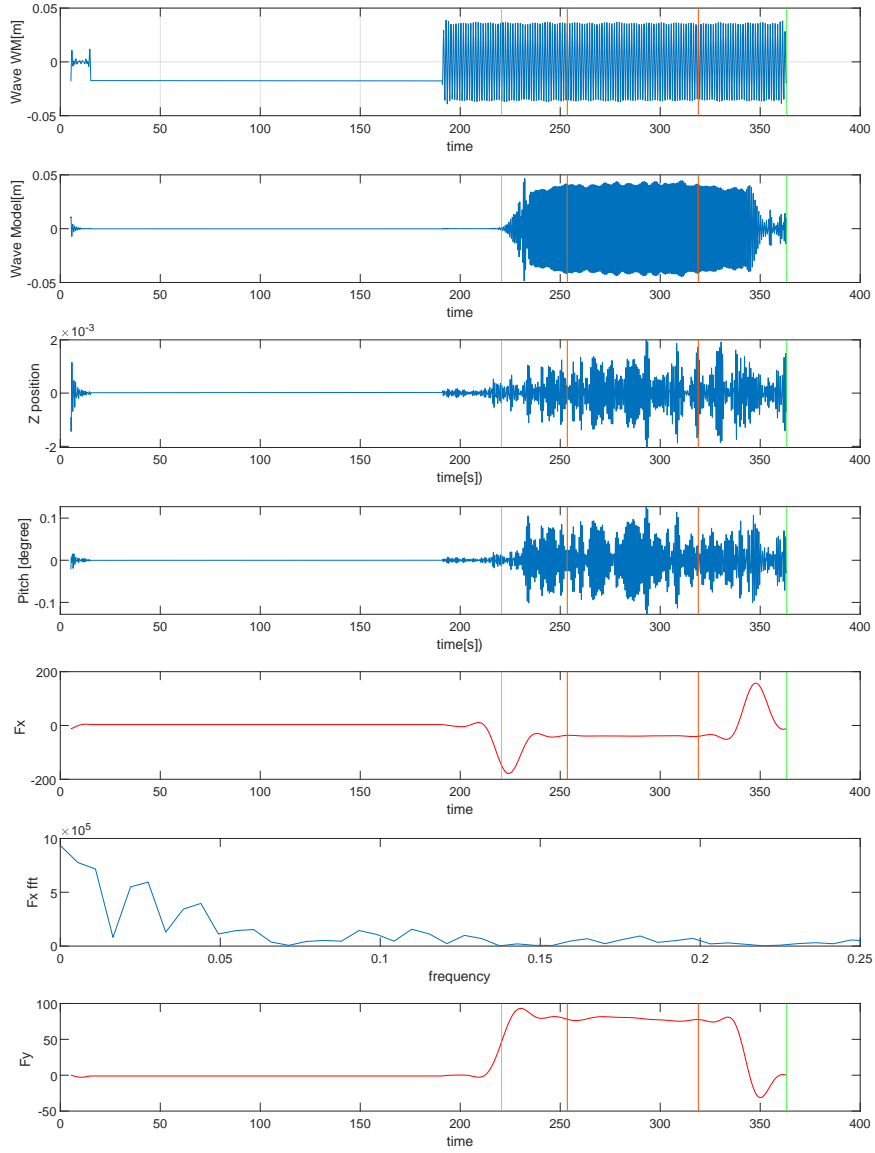
CE5000 Period(s):6 Lamda/L:0.3 Drift angle(deg):9 Speed(m/s):7.71



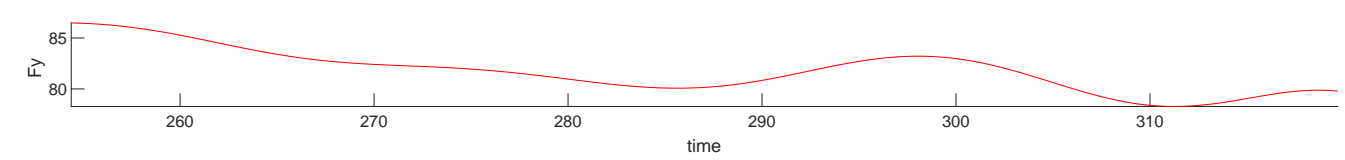
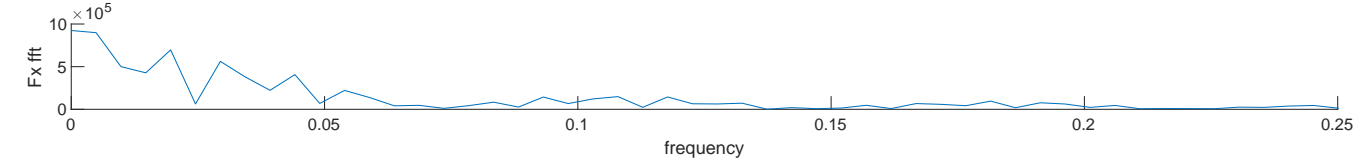
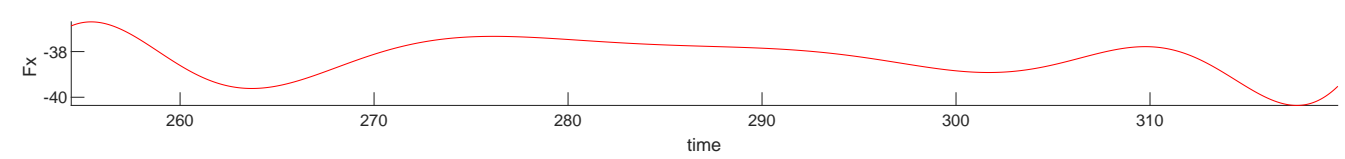
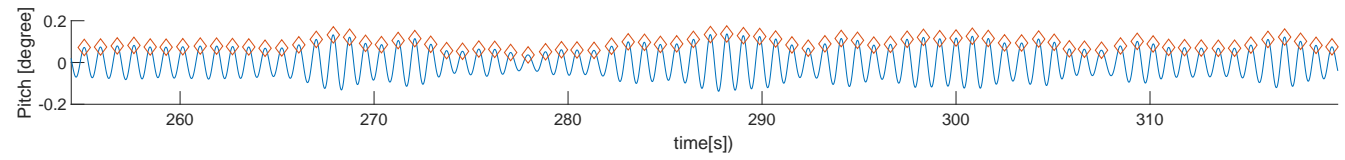
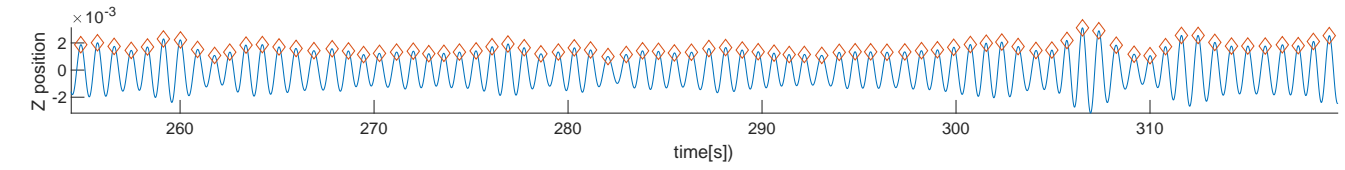
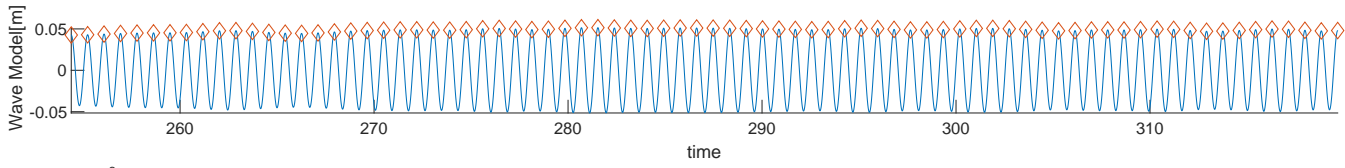
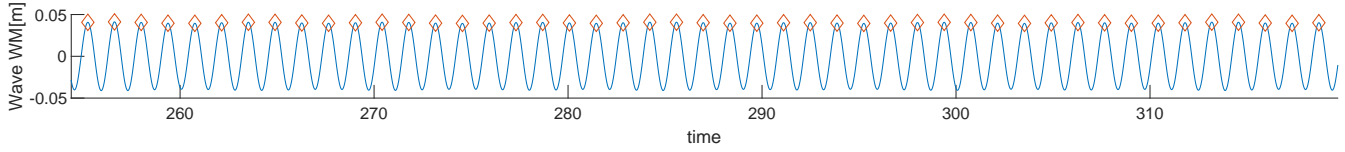
CE5010 Period(s):7 Lamda/L:0.4 Drift agle(deg):9 Speed(m/s):7.71



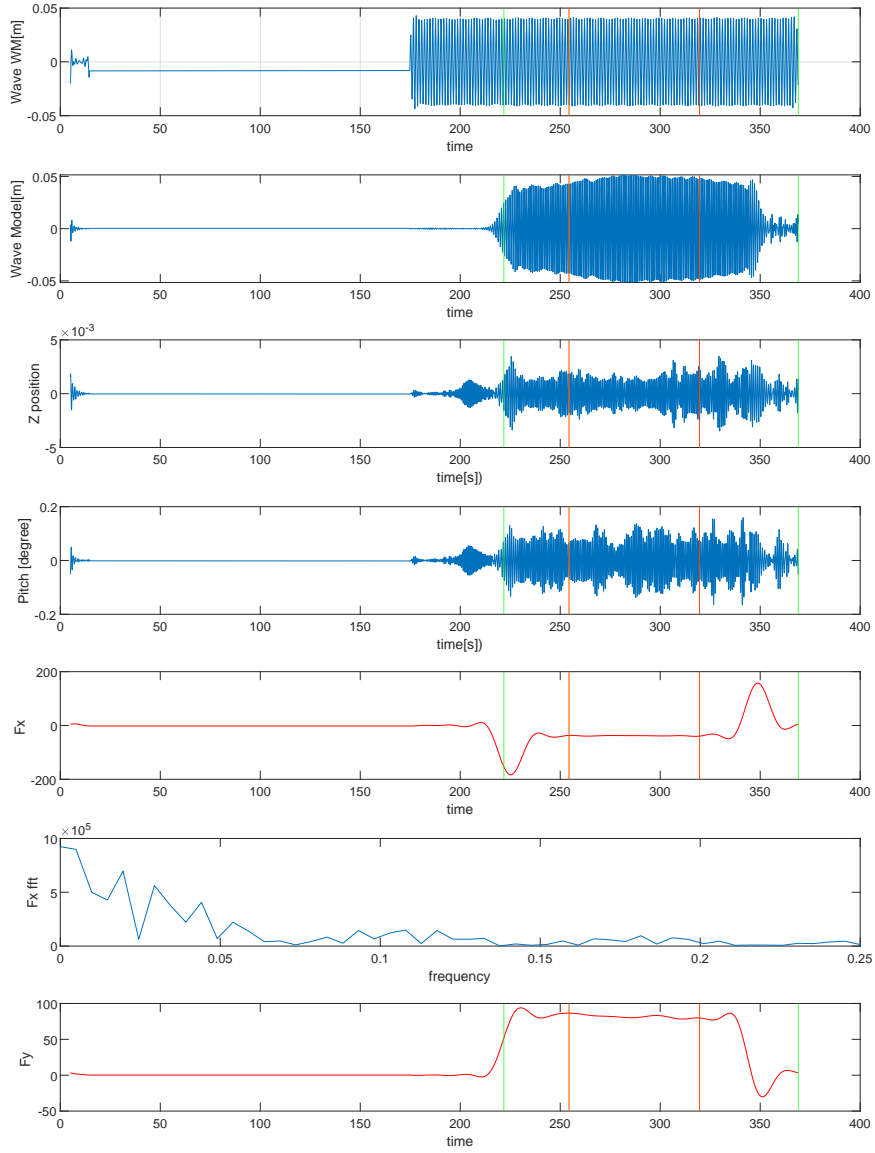
CE5010 Period(s):7 Lamda/L:0.4 Drift angle(deg):9 Speed(m/s):7.71



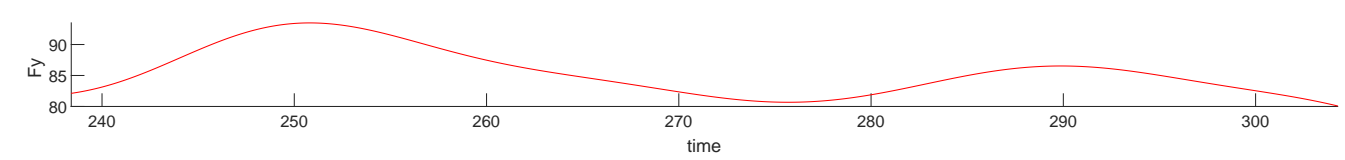
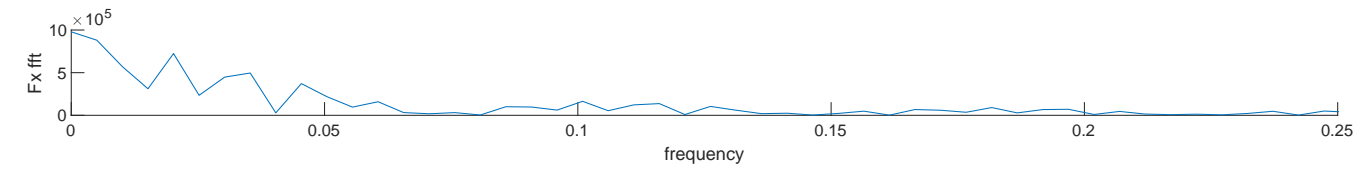
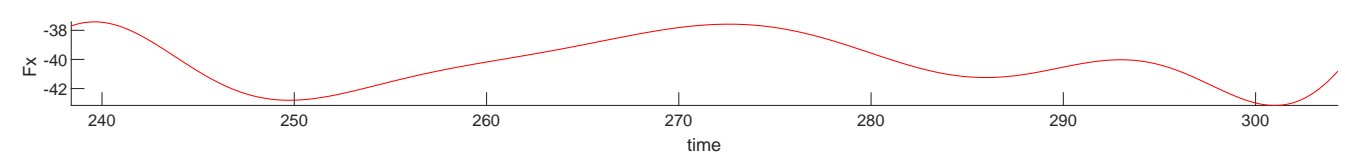
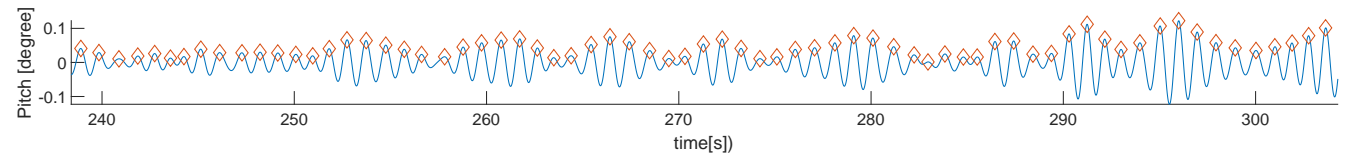
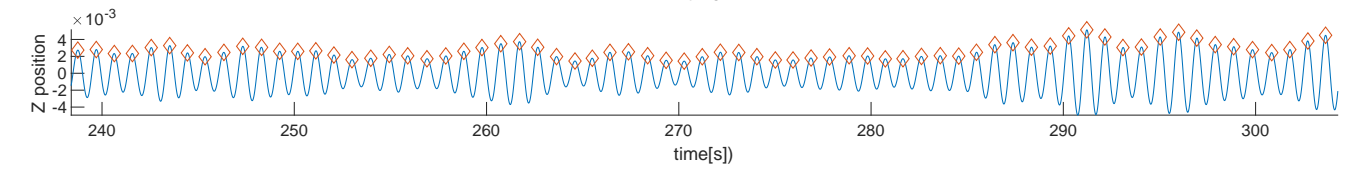
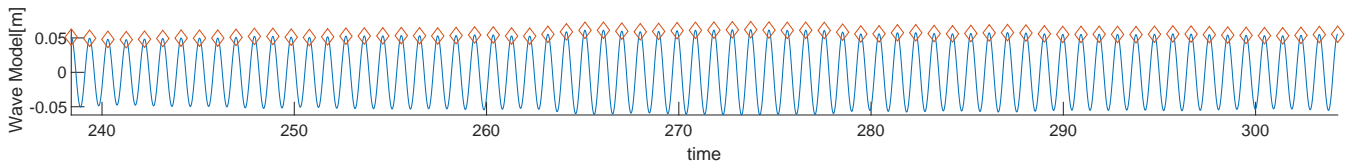
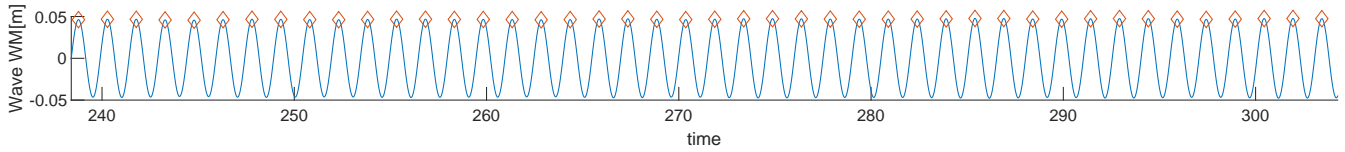
CE5020 Period(s):7.8 Lamda/L:0.5 Drift angle(deg):9 Speed(m/s):7.71



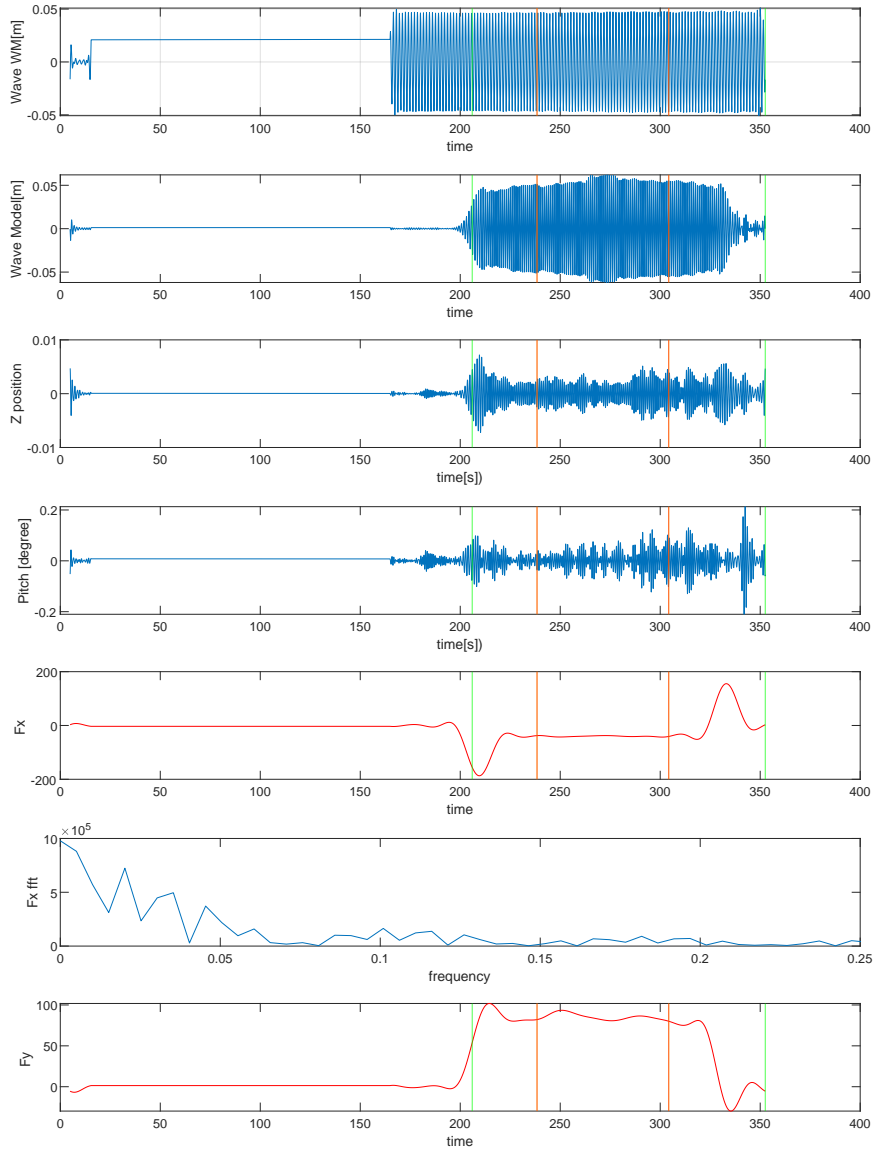
CE5020 Period(s):7.8 Lamda/L:0.5 Drift angle(deg):9 Speed(m/s):7.71



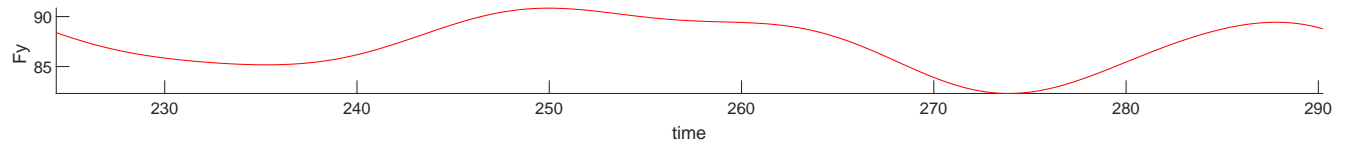
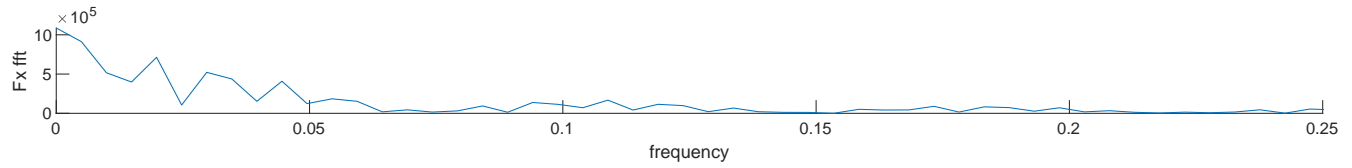
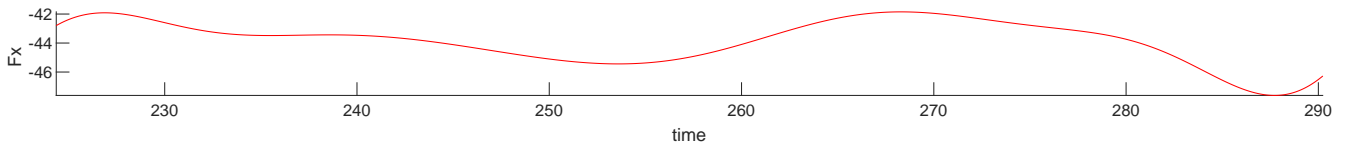
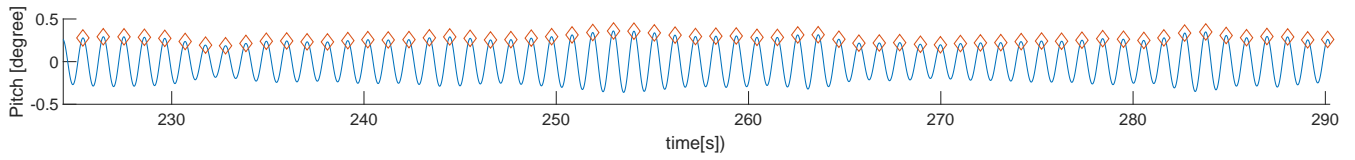
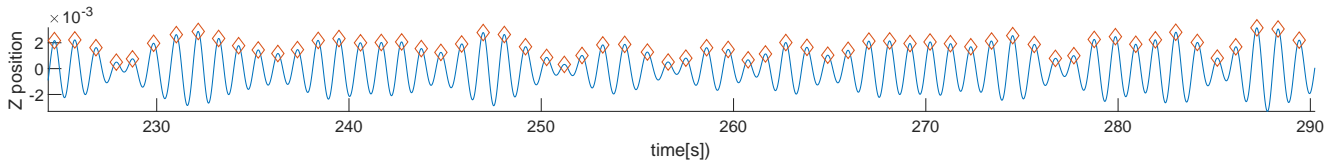
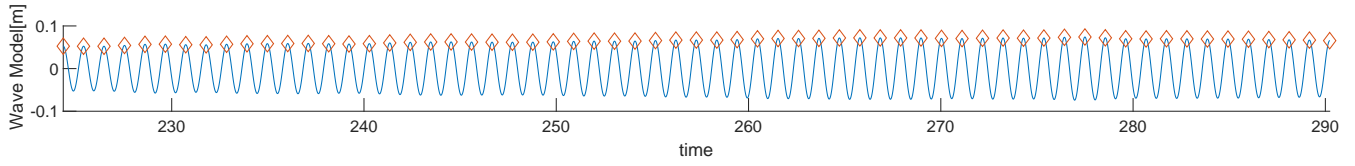
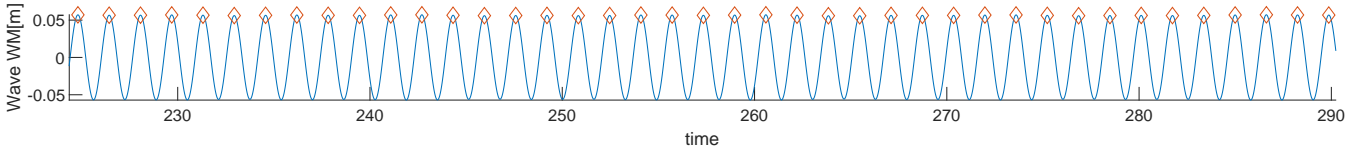
CE5030 Period(s):8.5 Lamda/L:0.59 Drift agle(deg):9 Speed(m/s):7.71



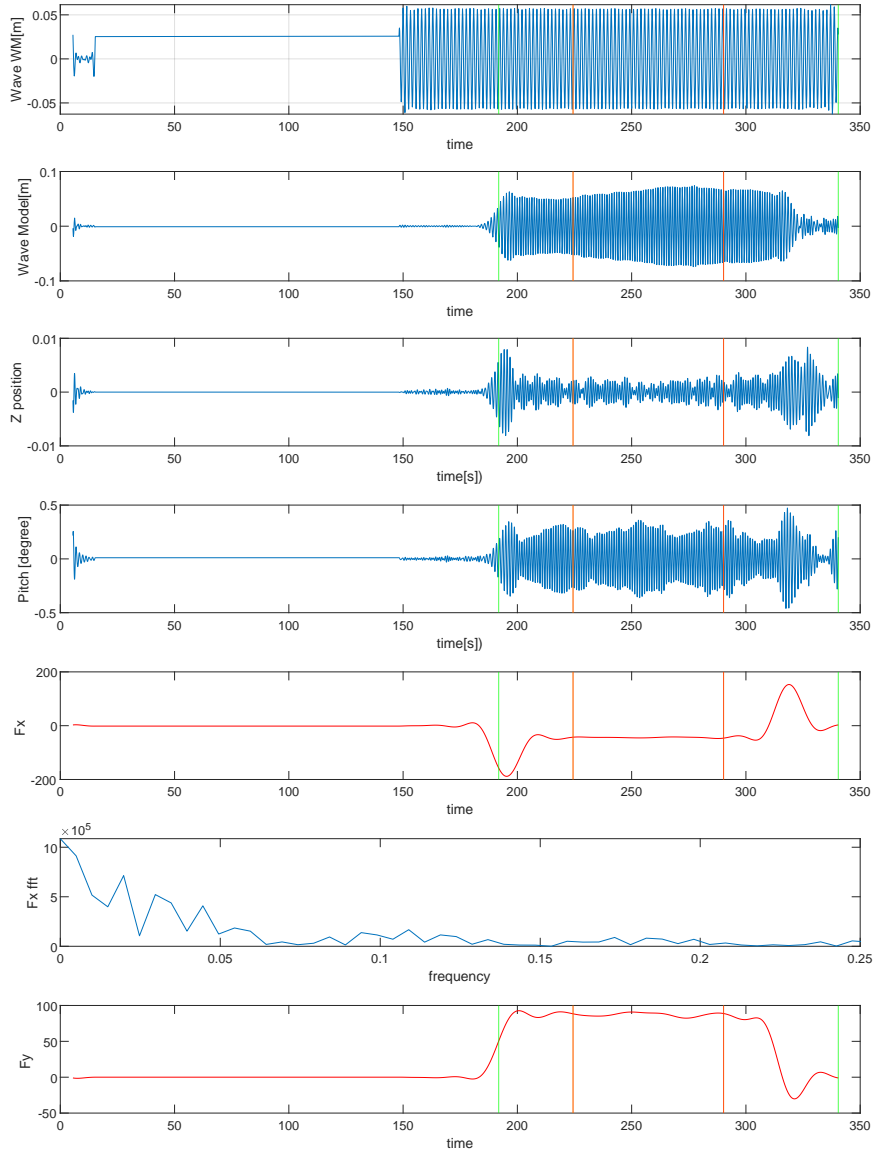
CE5030 Period(s):8.5 Lamda/L:0.59 Drift angle(deg):9 Speed(m/s):7.71



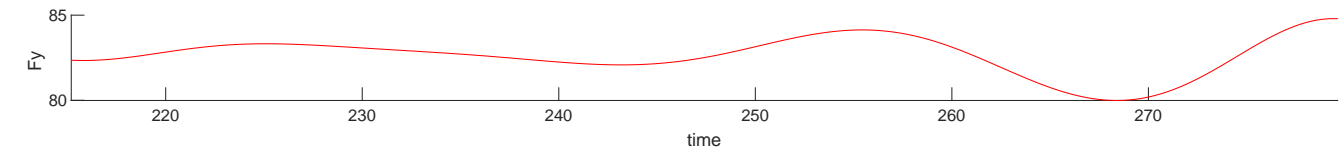
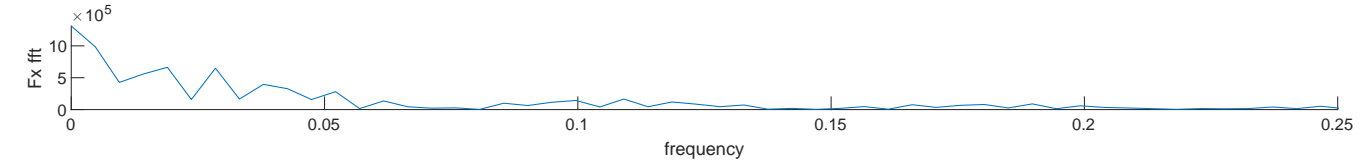
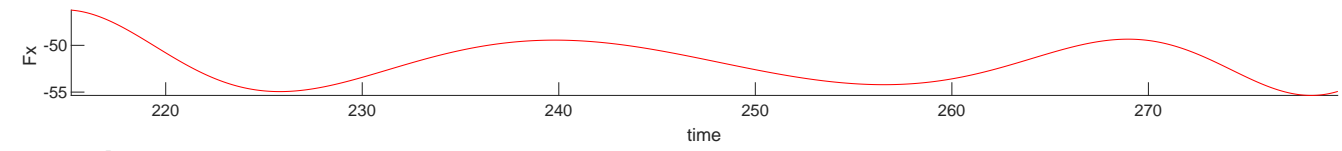
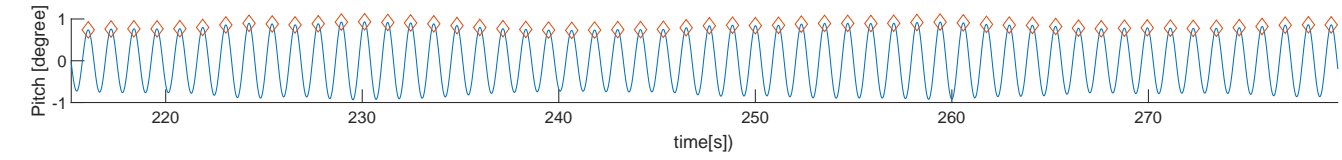
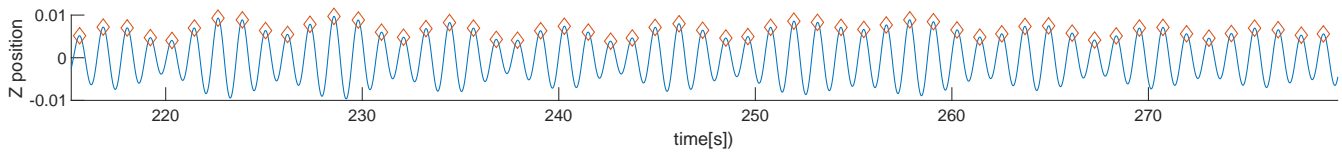
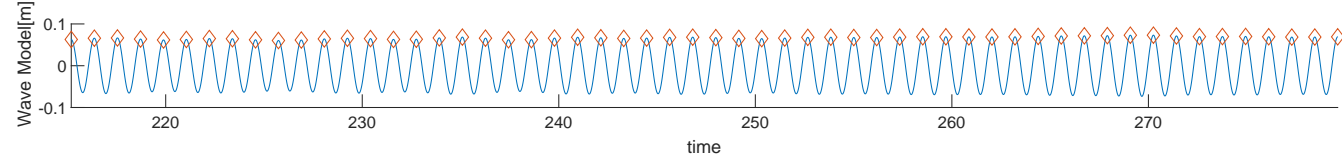
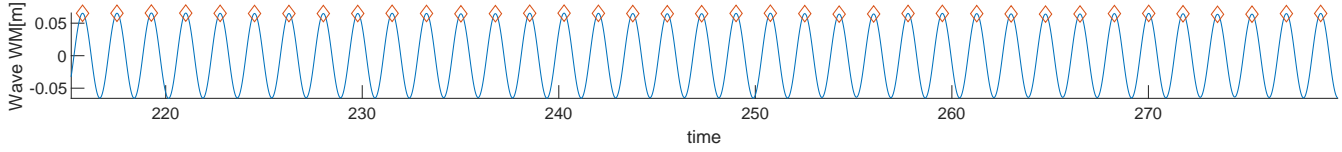
CE5040 Period(s):9.2 Lamda/L:0.7 Drift angle(deg):9 Speed(m/s):7.71



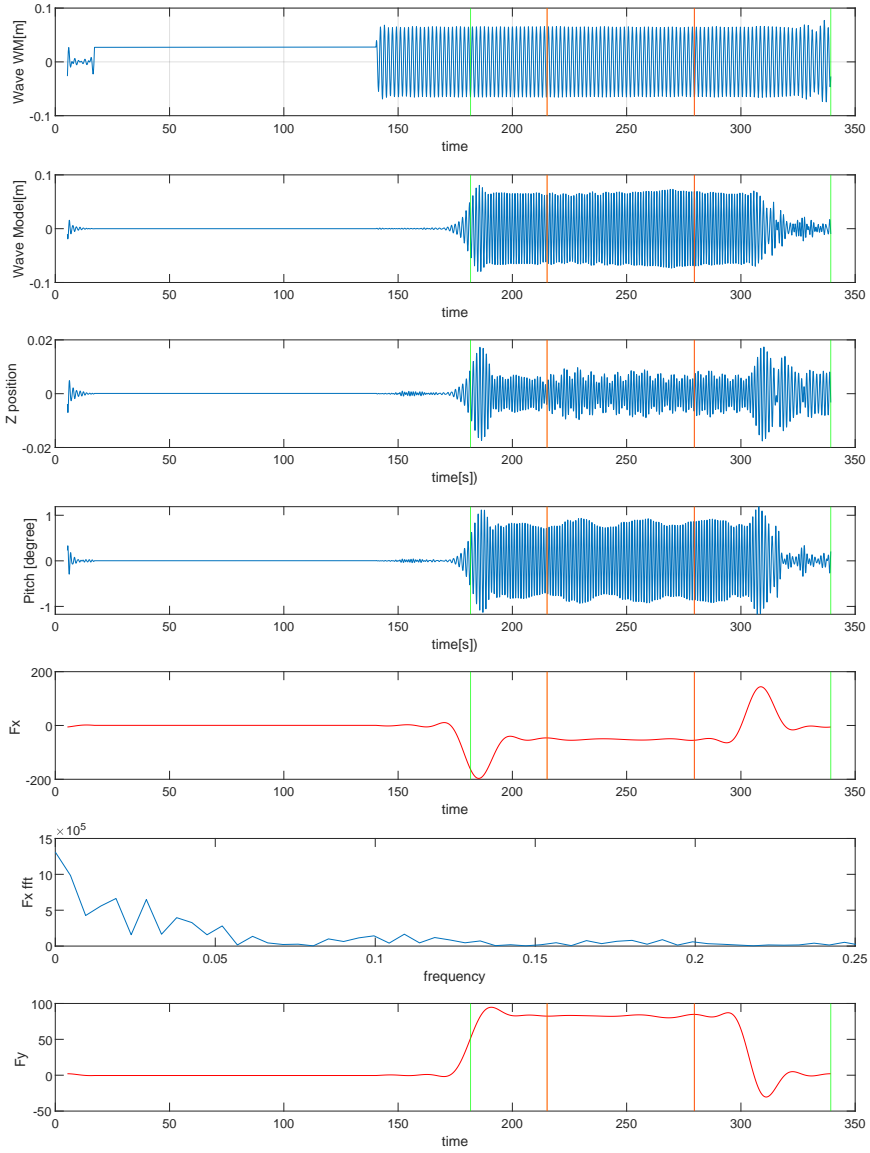
CE5040 Period(s):9.2 Lamda/L:0.7 Drift agle(deg):9 Speed(m/s):7.71



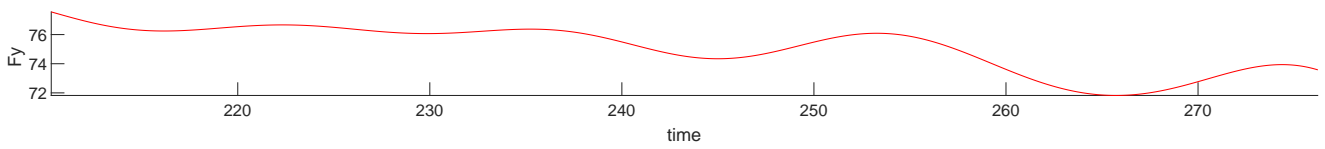
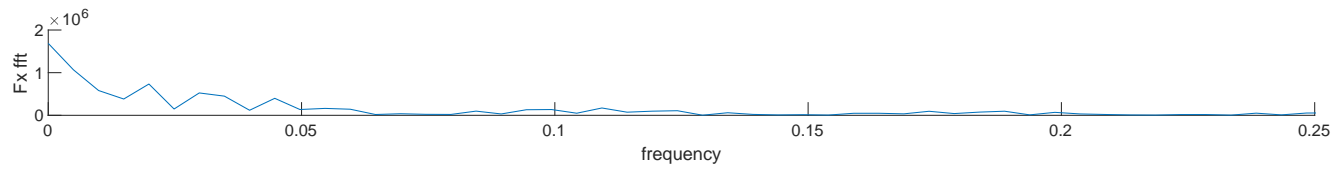
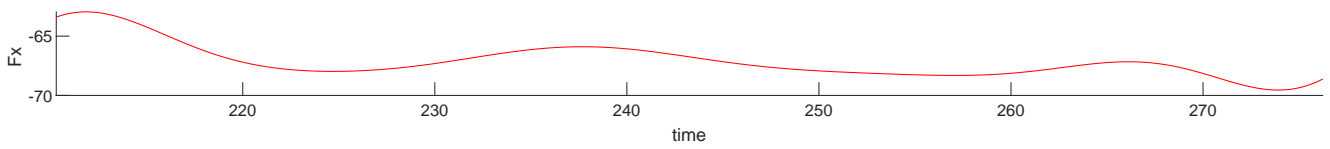
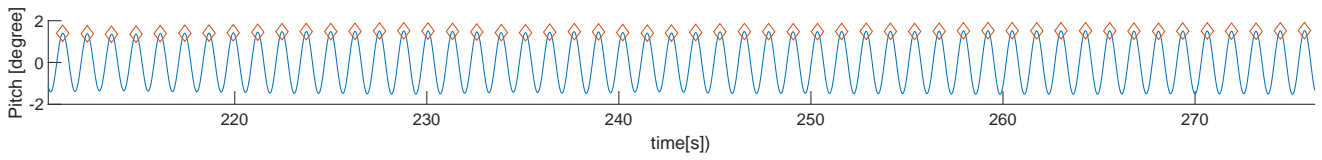
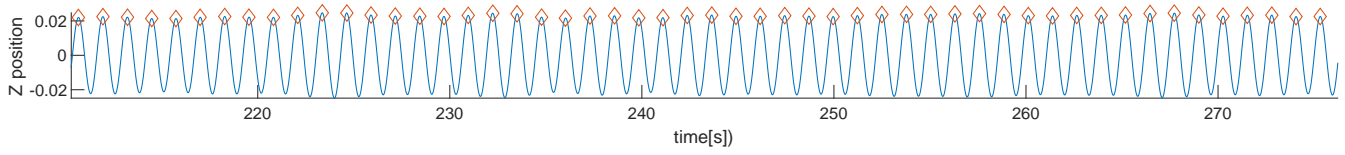
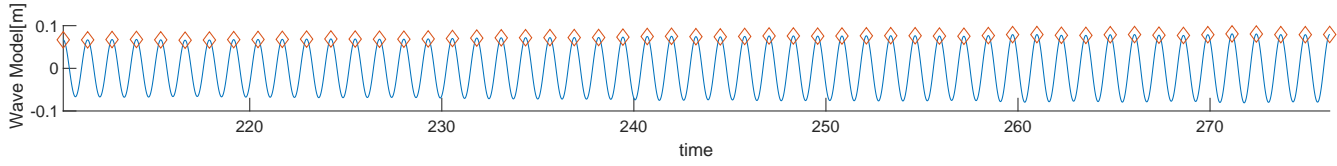
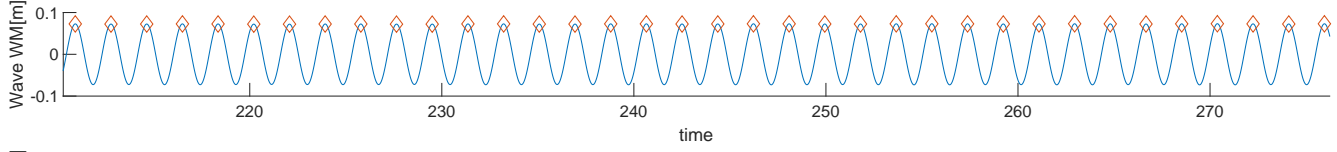
CE5050 Period(s):9.9 Lamda/L:0.81 Drift agle(deg):9 Speed(m/s):7.71



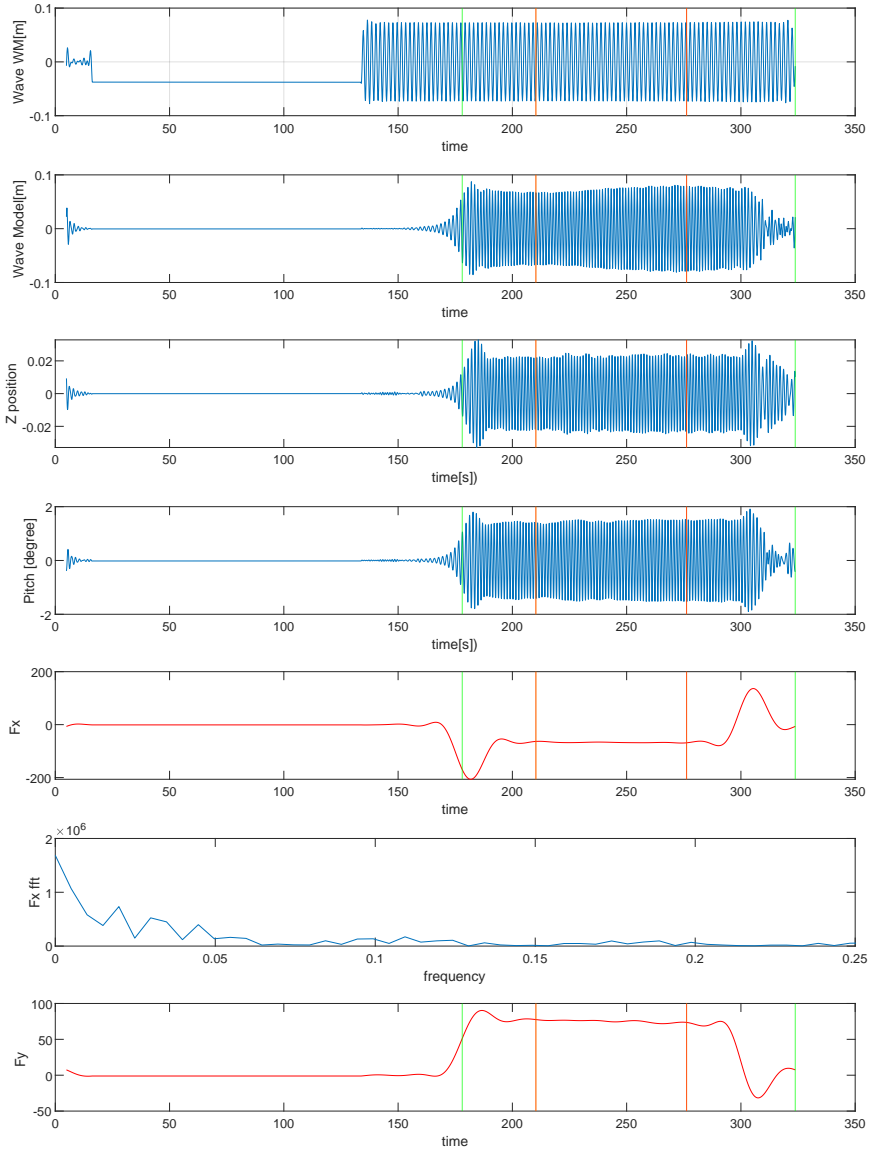
CE5050 Period(s):9.9 Lamda/L:0.81 Drift agle(deg):9 Speed(m/s):7.71



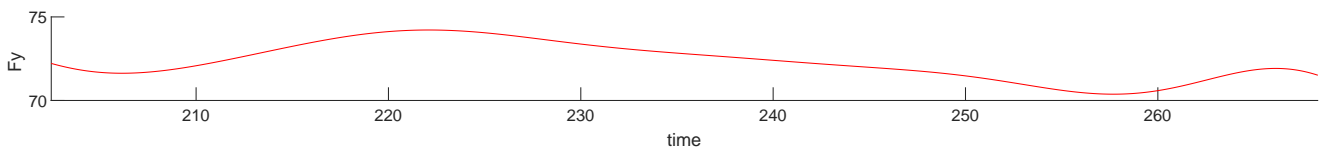
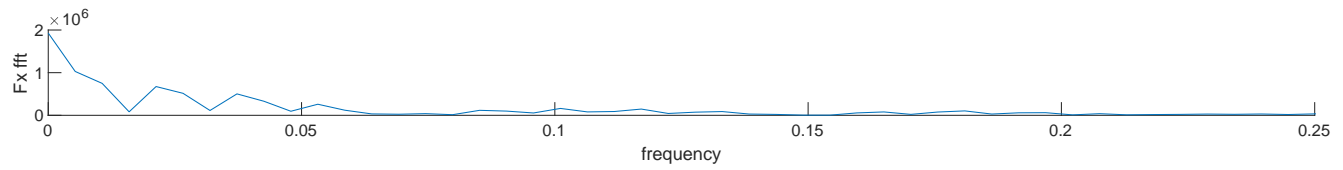
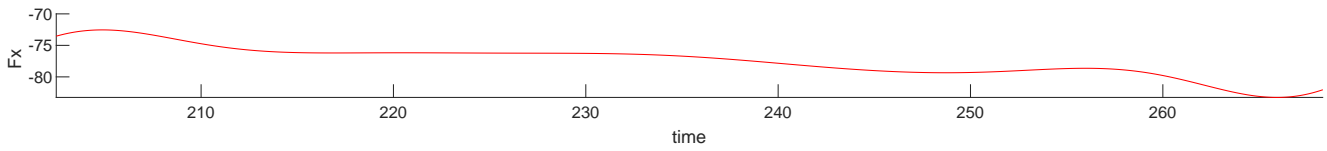
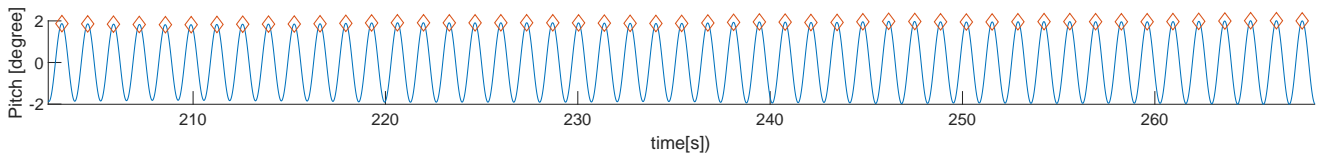
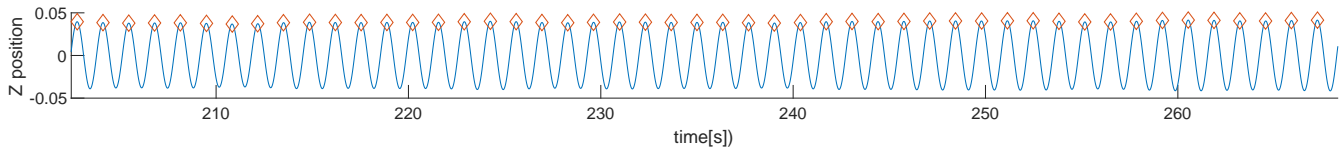
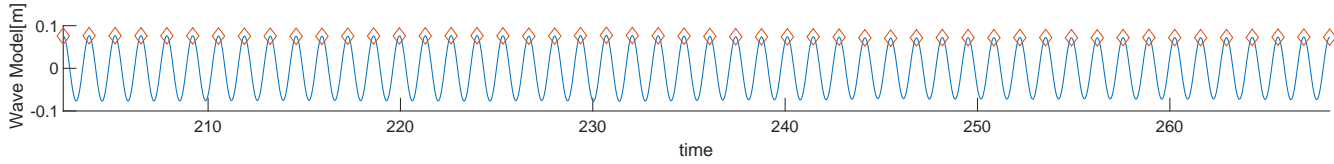
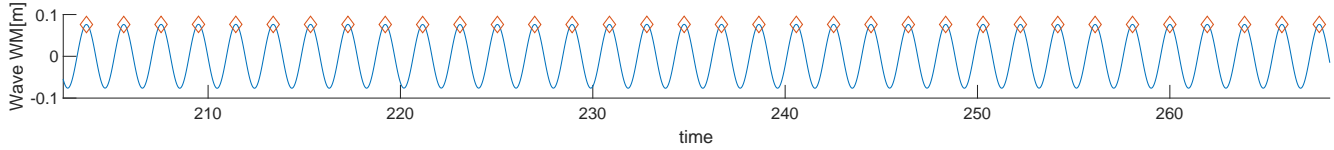
CE5060 Period(s):10.5 Lamda/L:0.91 Drift agle(deg):9 Speed(m/s):7.71



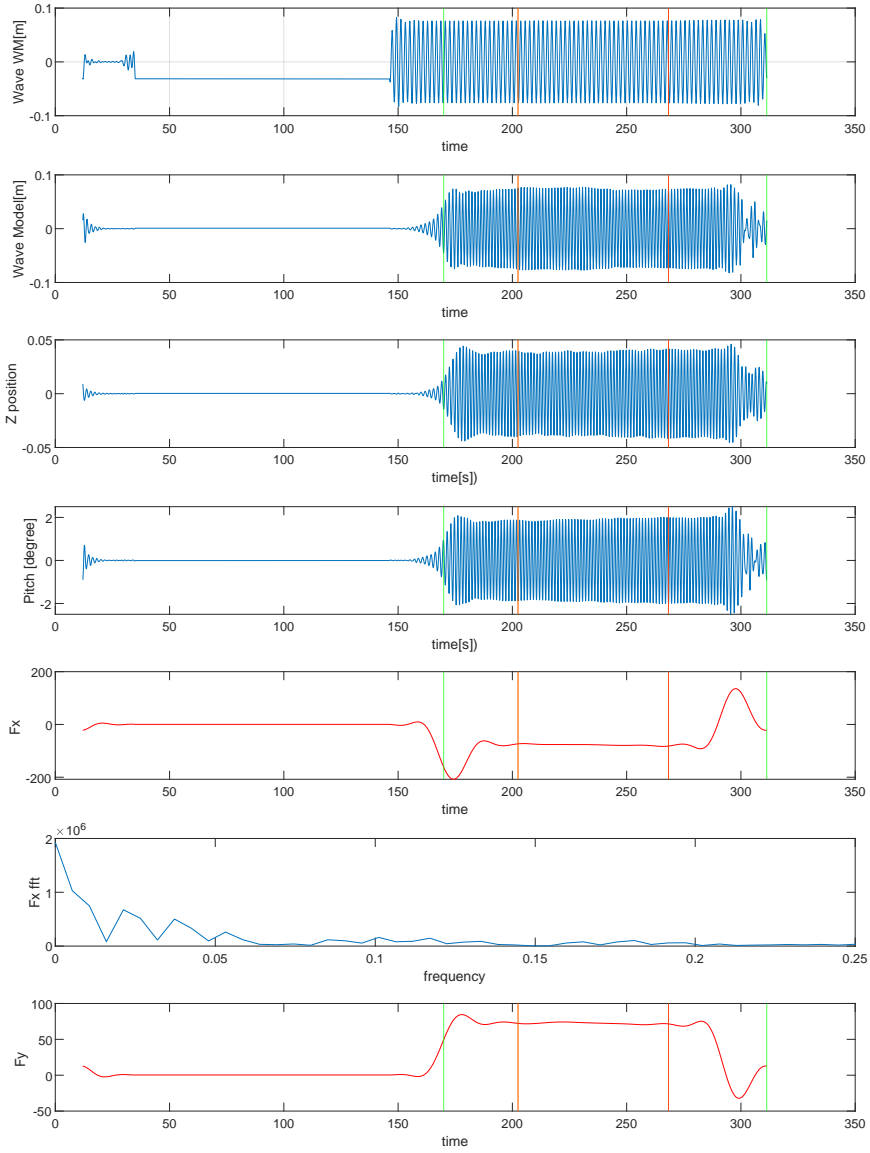
CE5060 Period(s):10.5 Lamda/L:0.91 Drift angle(deg):9 Speed(m/s):7.71



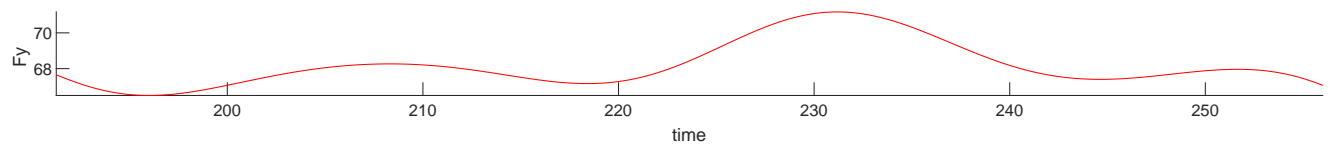
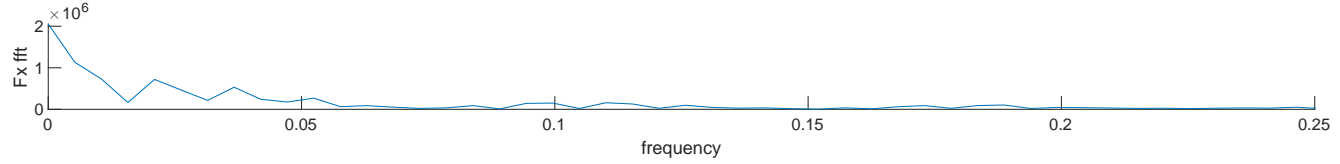
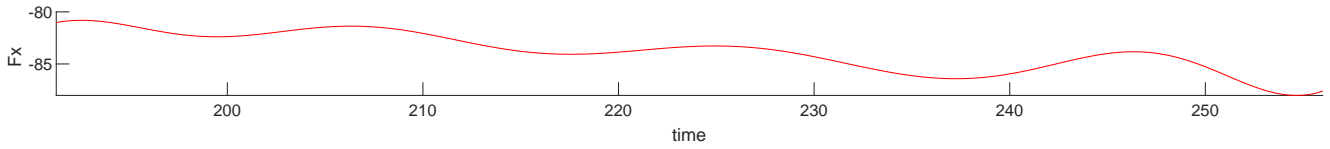
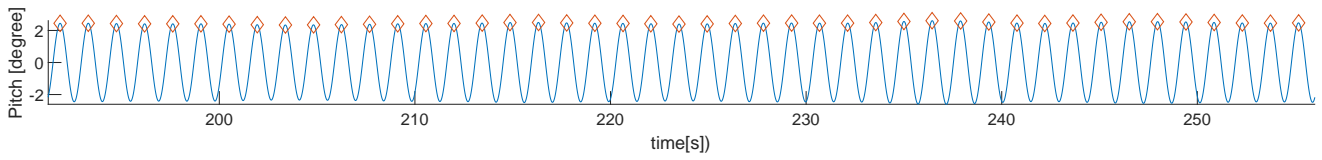
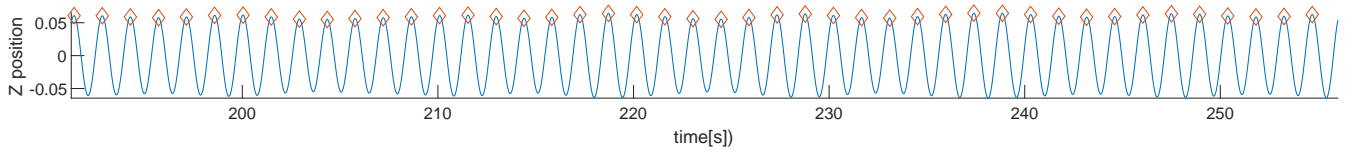
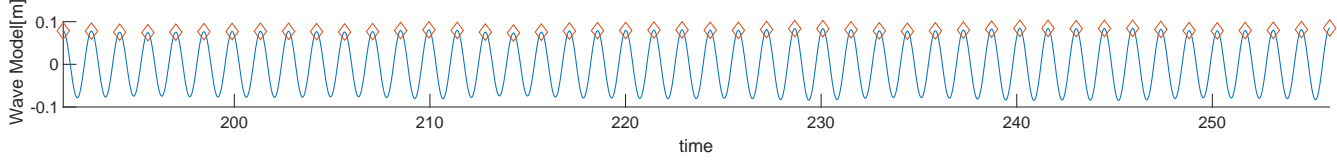
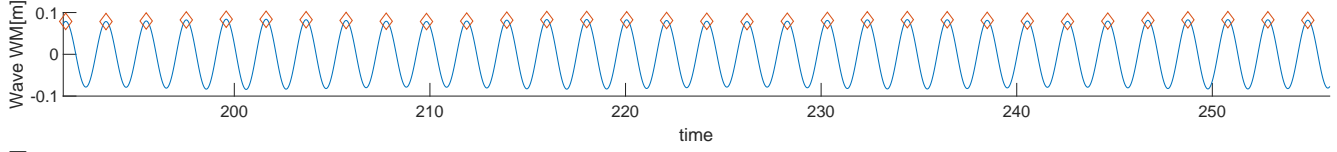
CE5070 Period(s):11 Lamda/L:0.99 Drift agle(deg):9 Speed(m/s):7.71



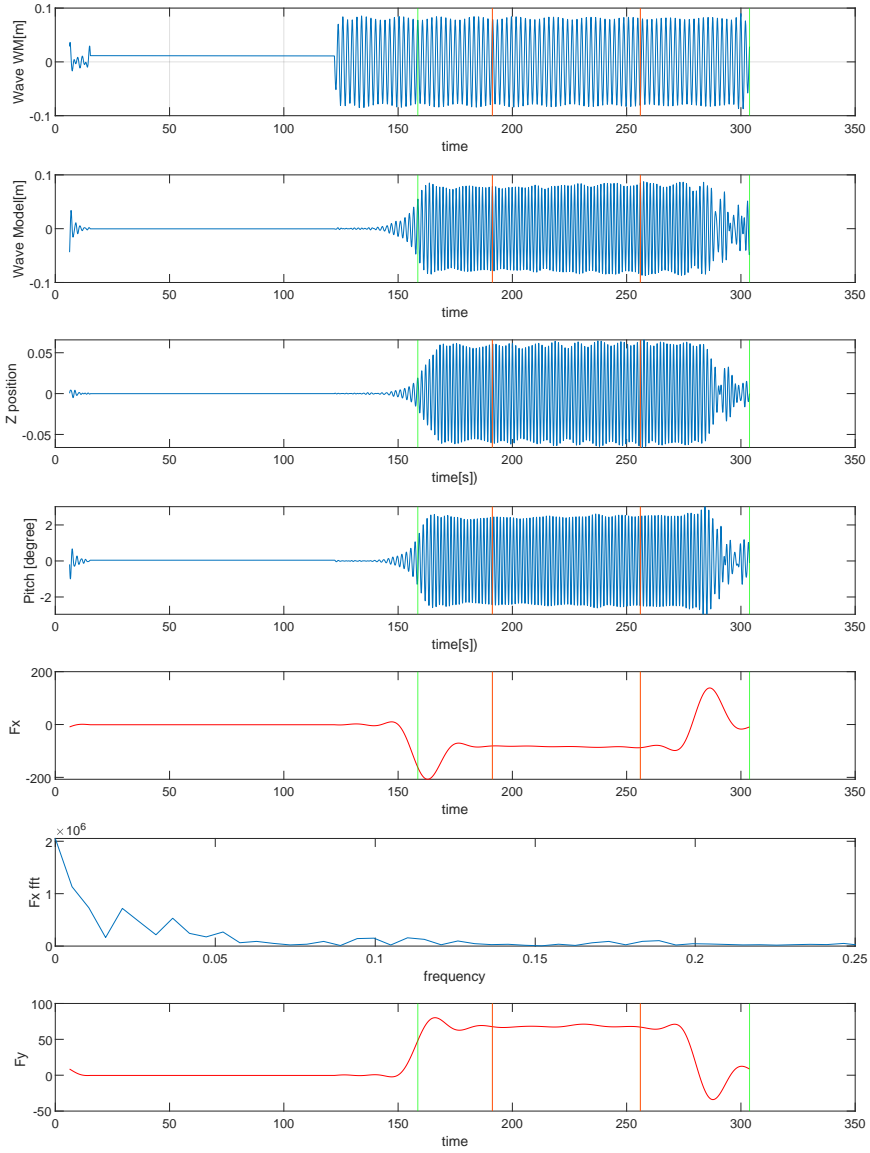
CE5070 Period(s):11 Lamda/L:0.99 Drift angle(deg):9 Speed(m/s):7.71



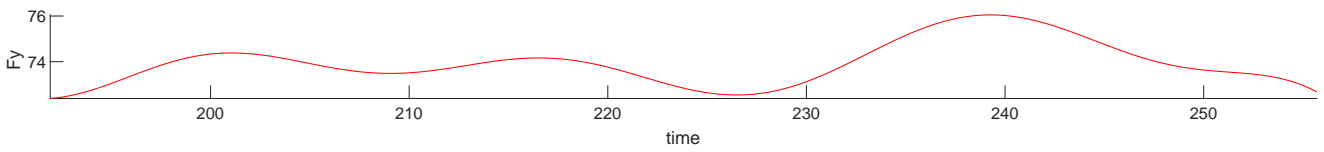
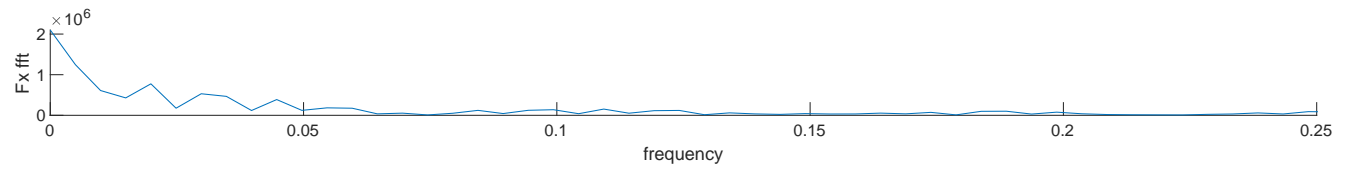
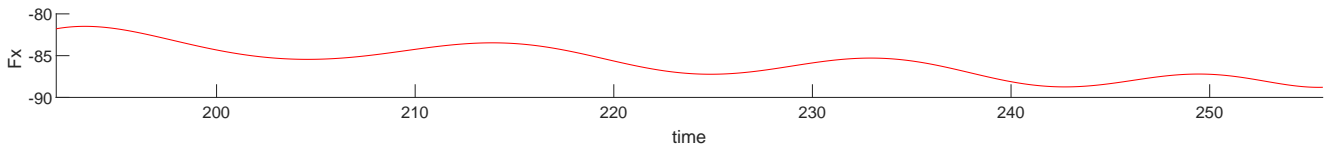
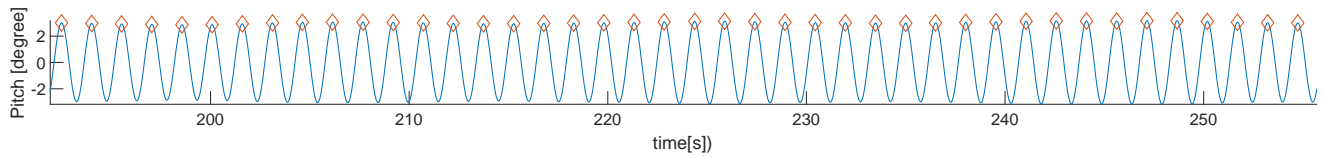
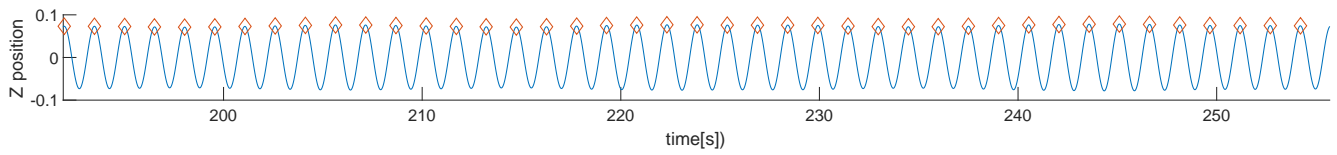
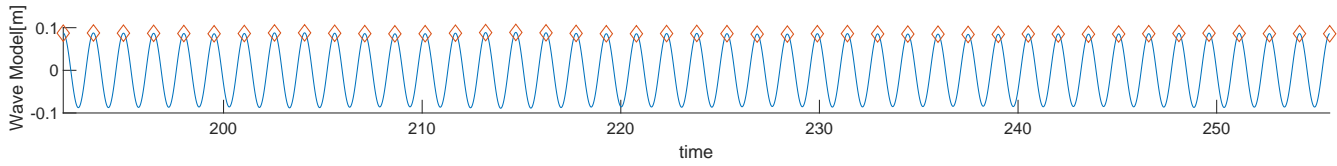
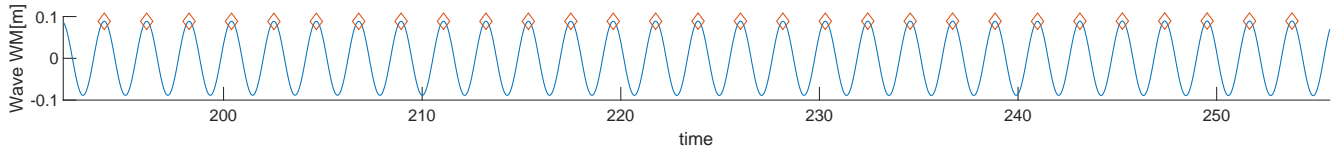
CE5080 Period(s):11.6 Lamda/L:1.11 Drift agle(deg):9 Speed(m/s):7.71



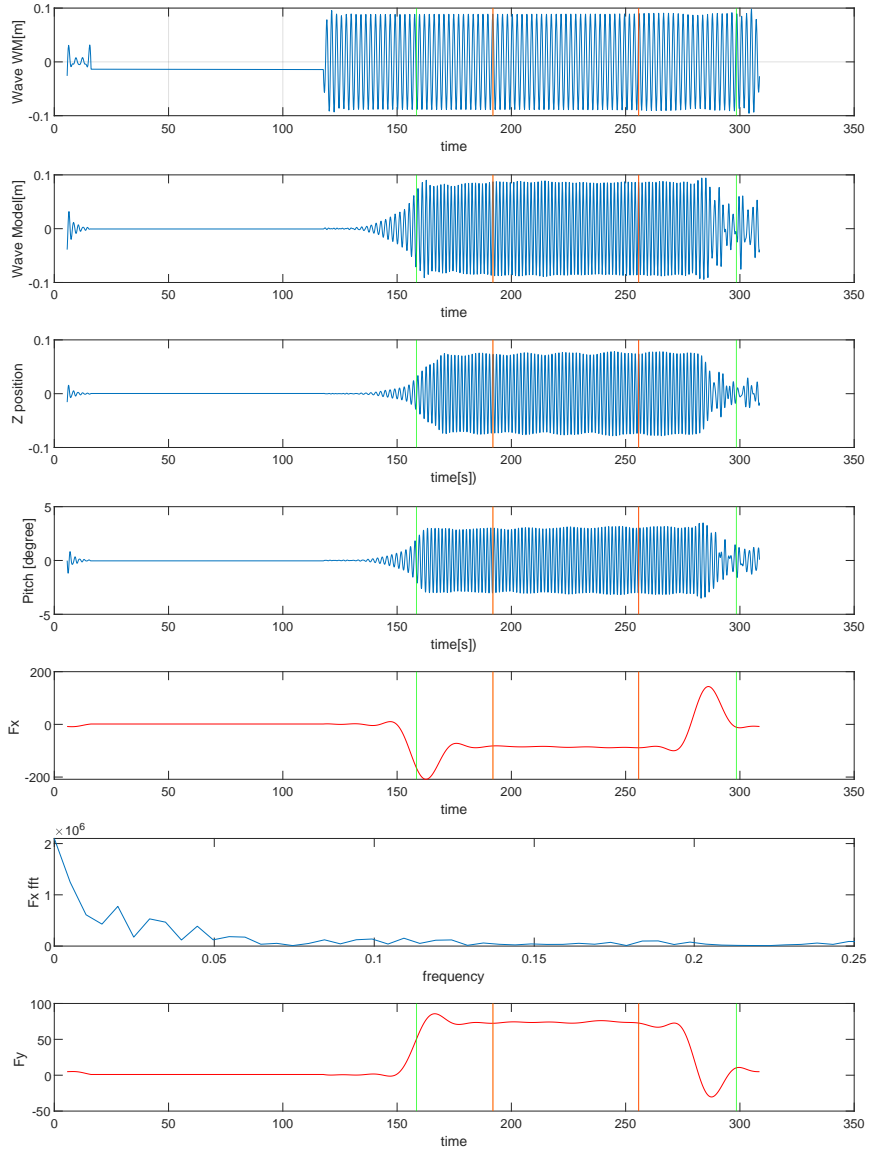
CE5080 Period(s):11.6 Lamda/L:1.11 Drift angle(deg):9 Speed(m/s):7.71



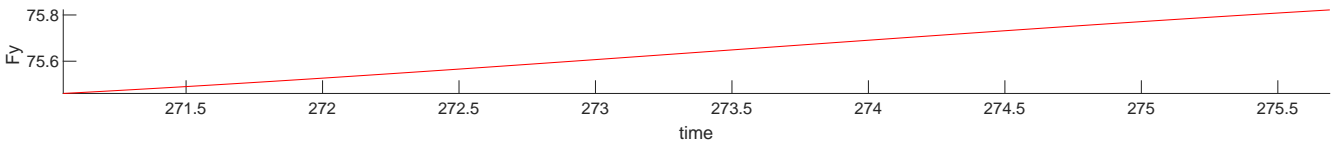
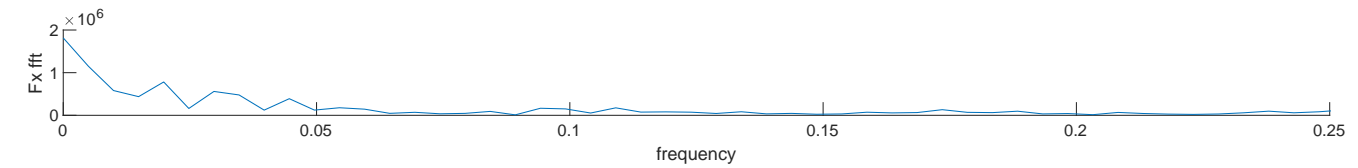
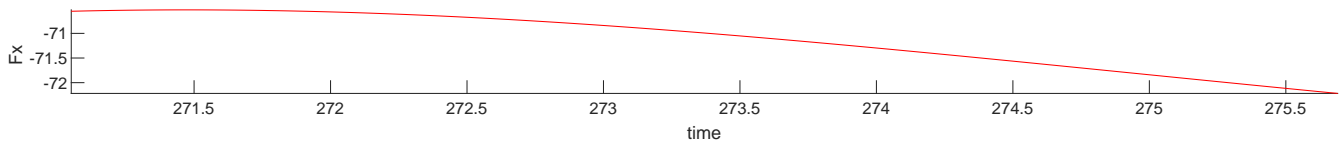
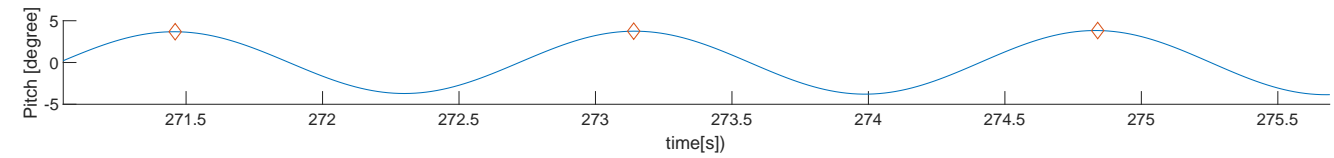
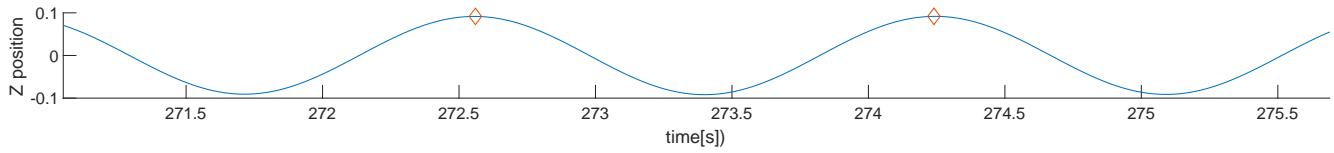
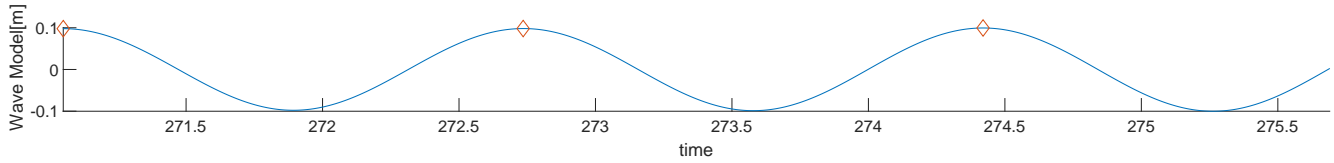
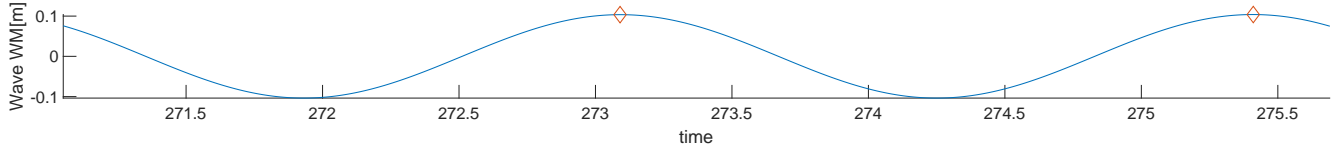
CE5090 Period(s):12.1 Lamda/L:1.2 Drift agle(deg):9 Speed(m/s):7.71



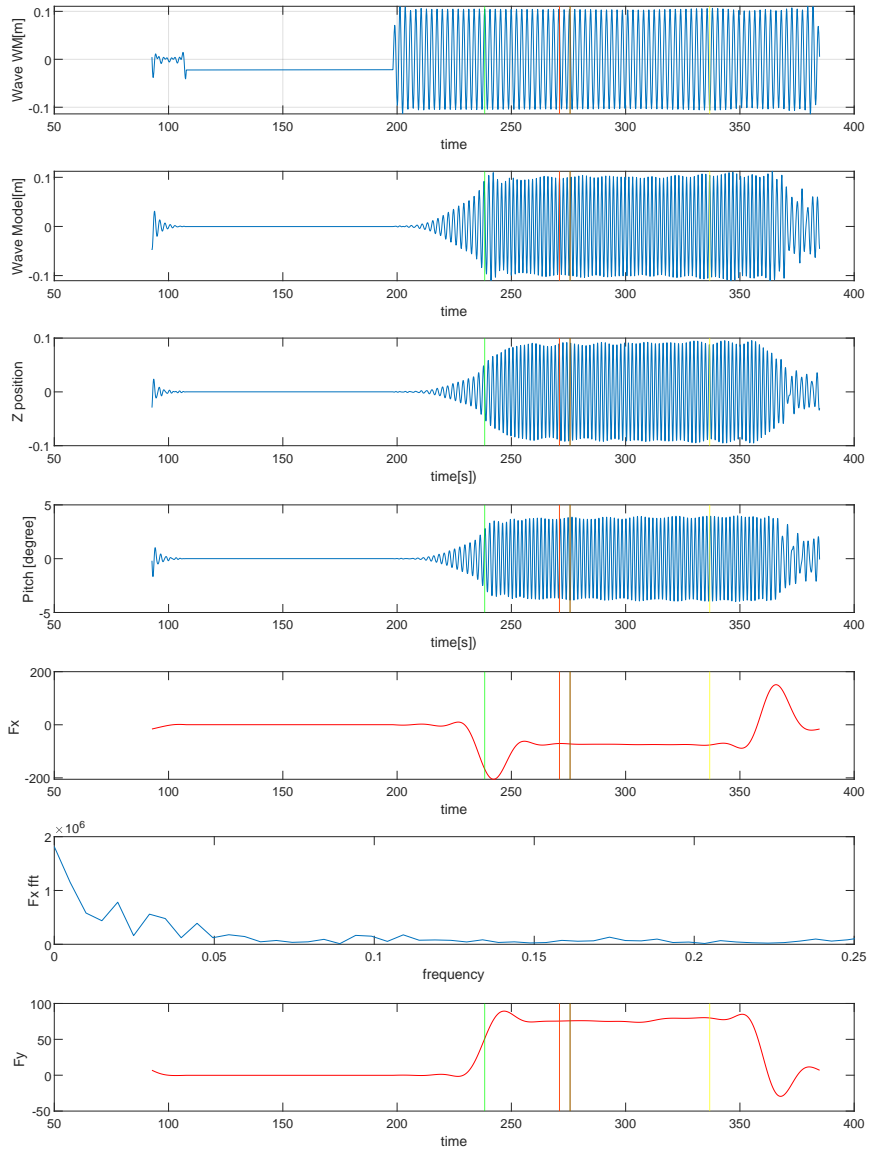
CE5090 Period(s):12.1 Lamda/L:1.2 Drift agle(deg):9 Speed(m/s):7.71



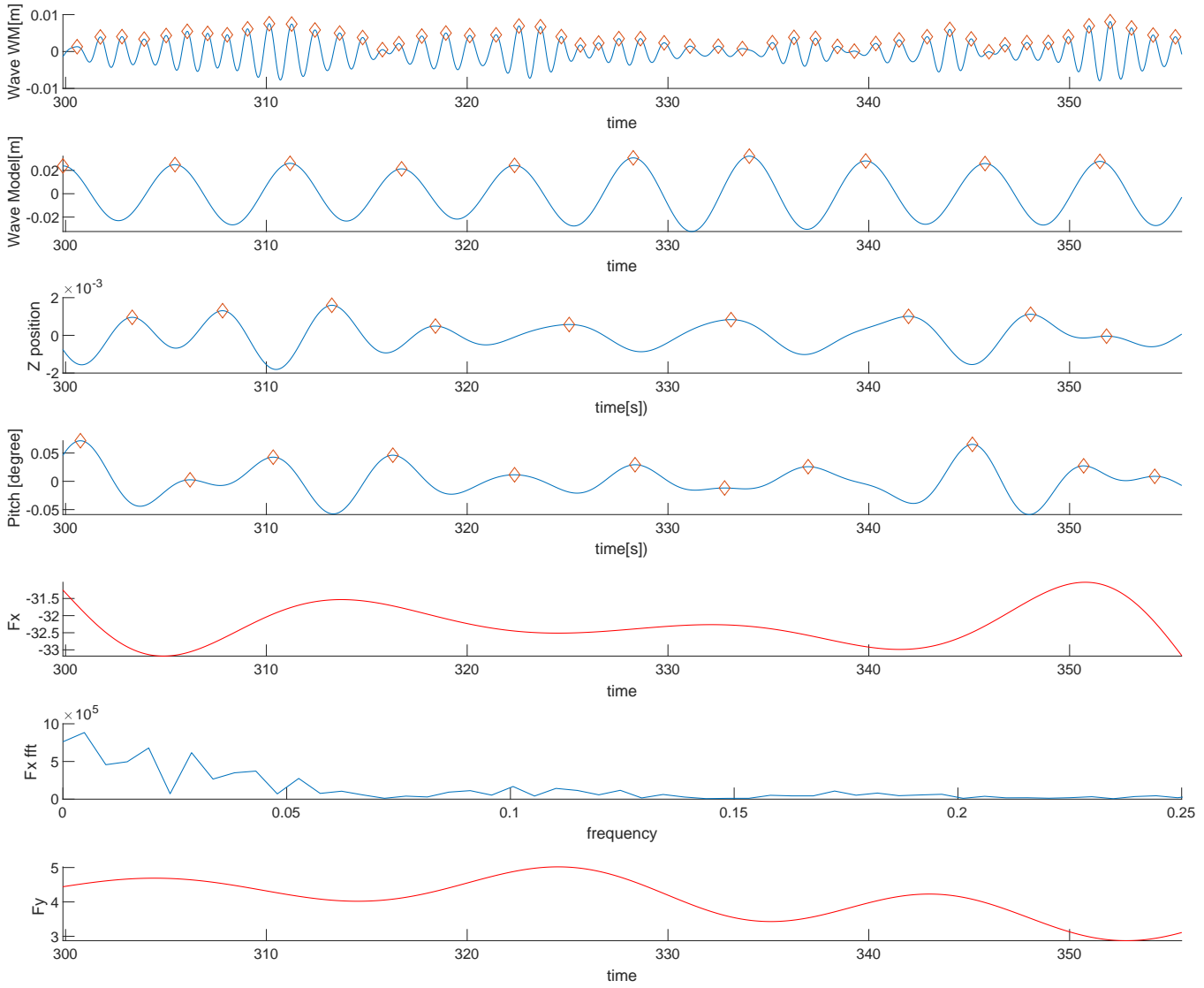
CE5100 Period(s):13.1 Lamda/L:1.41 Drift agle(deg):9 Speed(m/s):7.71



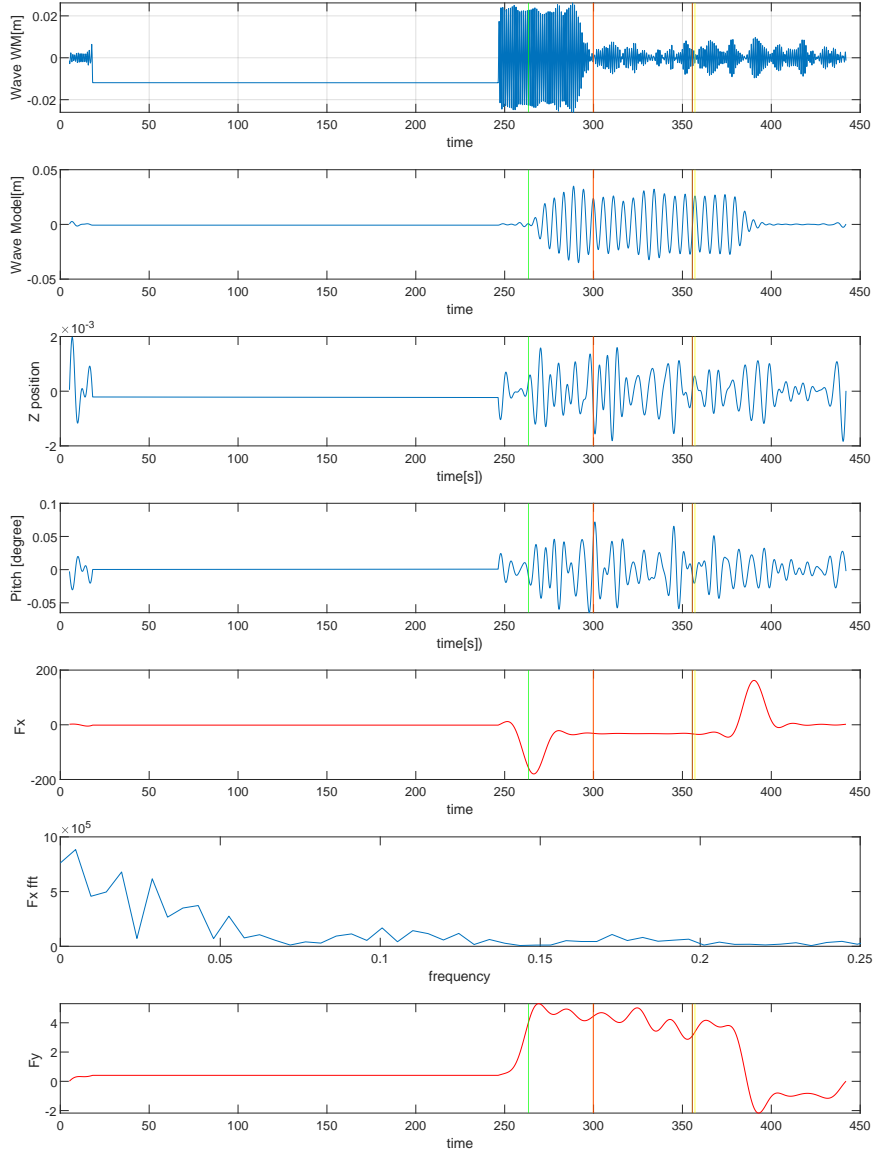
CE5100 Period(s):13.1 Lamda/L:1.41 Drift angle(deg):9 Speed(m/s):7.71



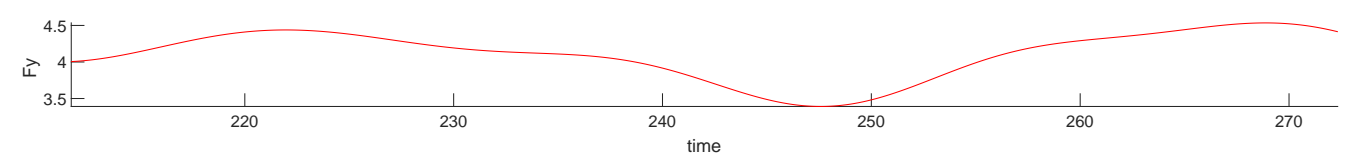
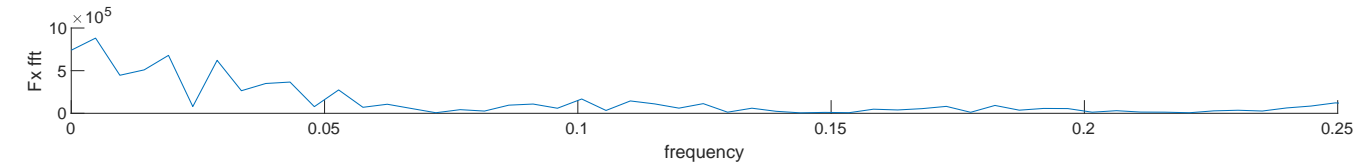
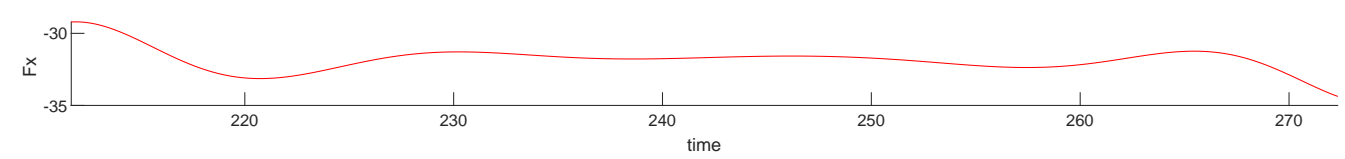
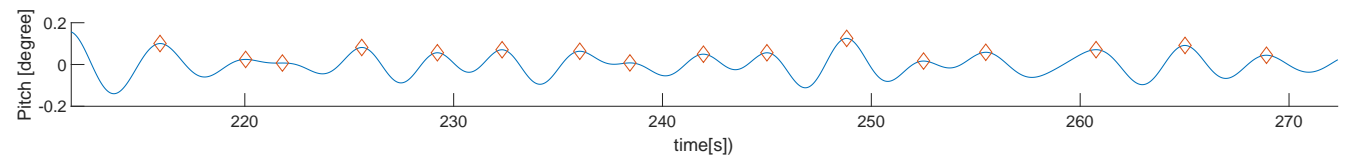
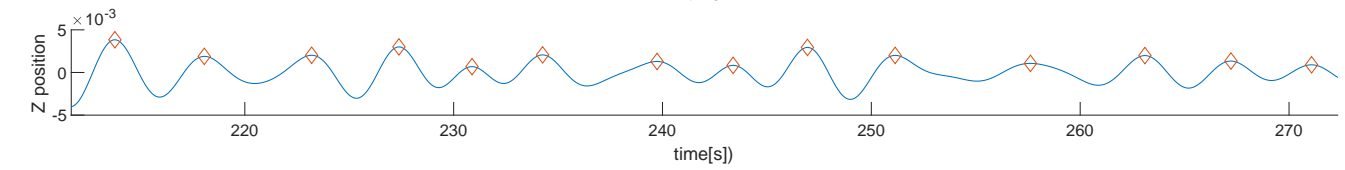
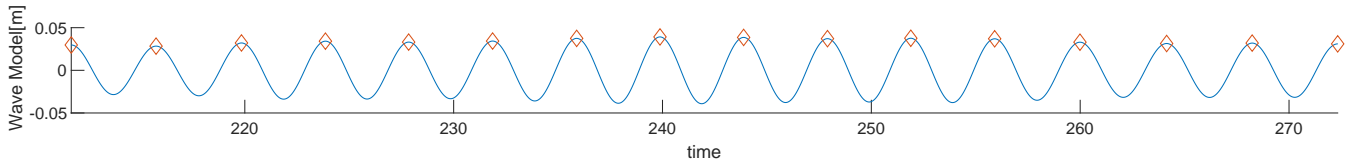
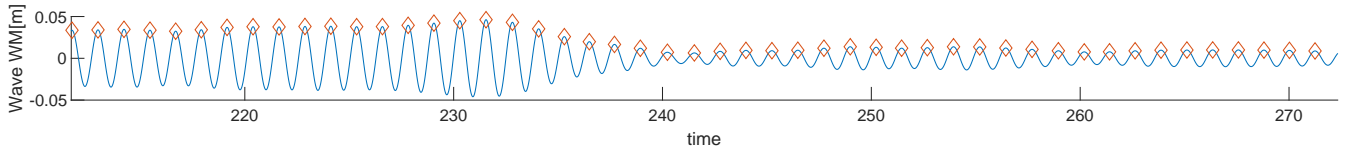
CE6000 Period(s):6 Lamda/L:0.3 Drift agle(deg):180 Speed(m/s):7.71



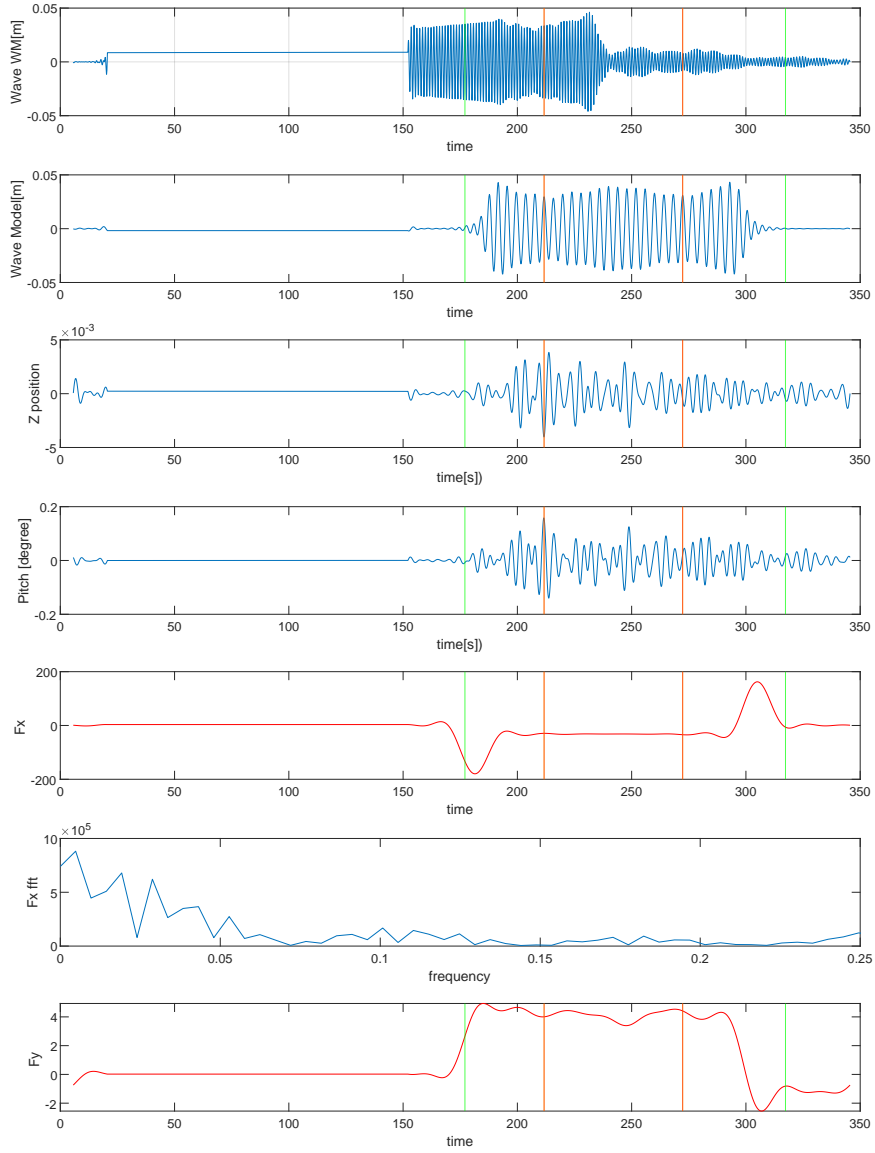
CE6000 Period(s):6 Lamda/L:0.3 Drift agle(deg):180 Speed(m/s):7.71



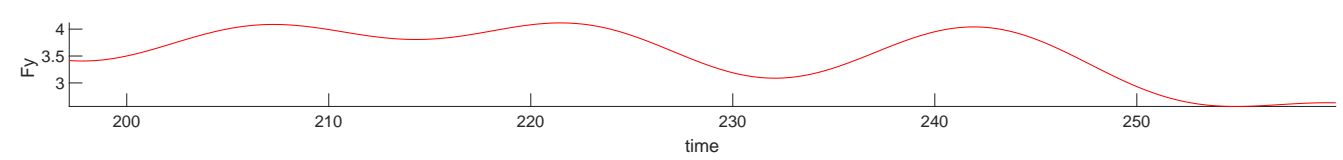
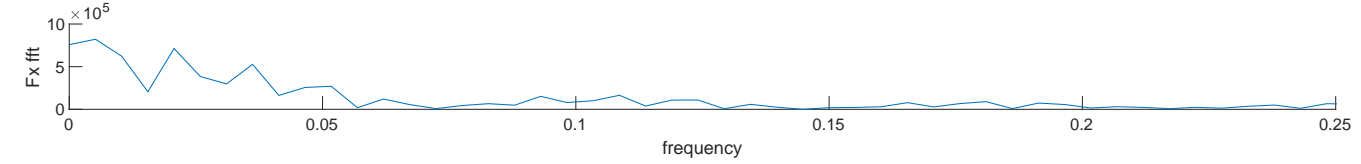
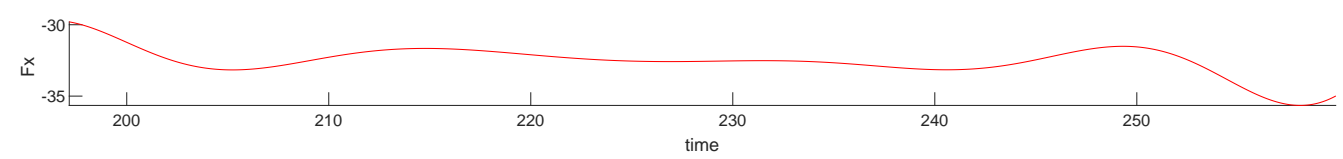
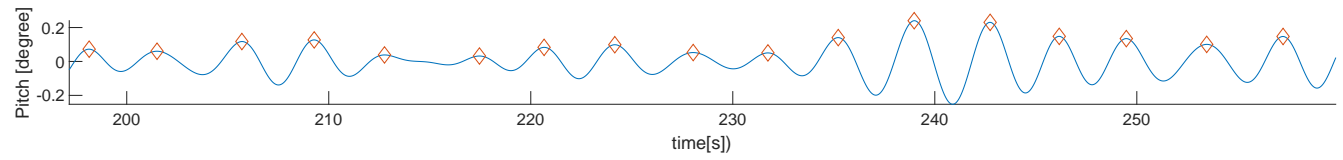
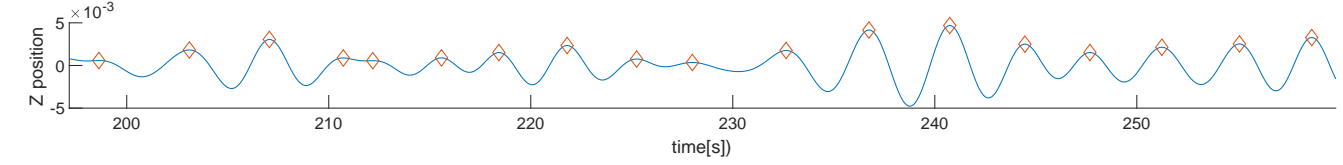
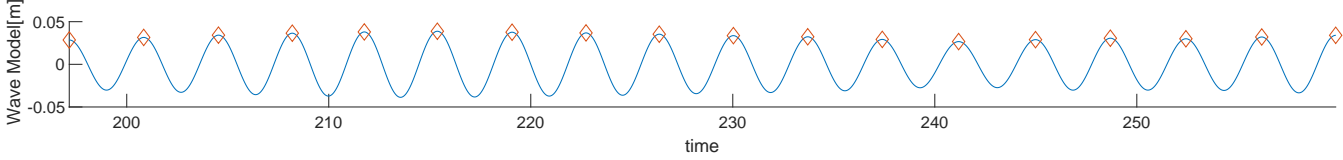
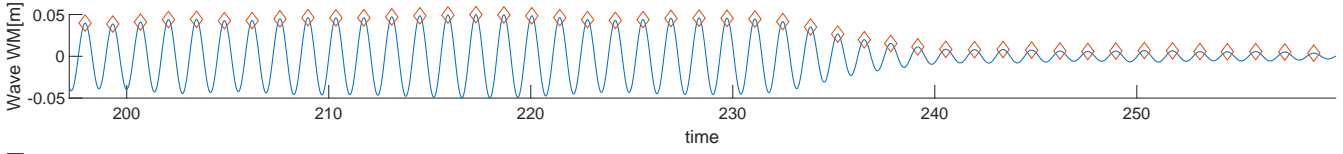
CE6010 Period(s):7 Lamda/L:0.4 Drift angle(deg):180 Speed(m/s):7.71



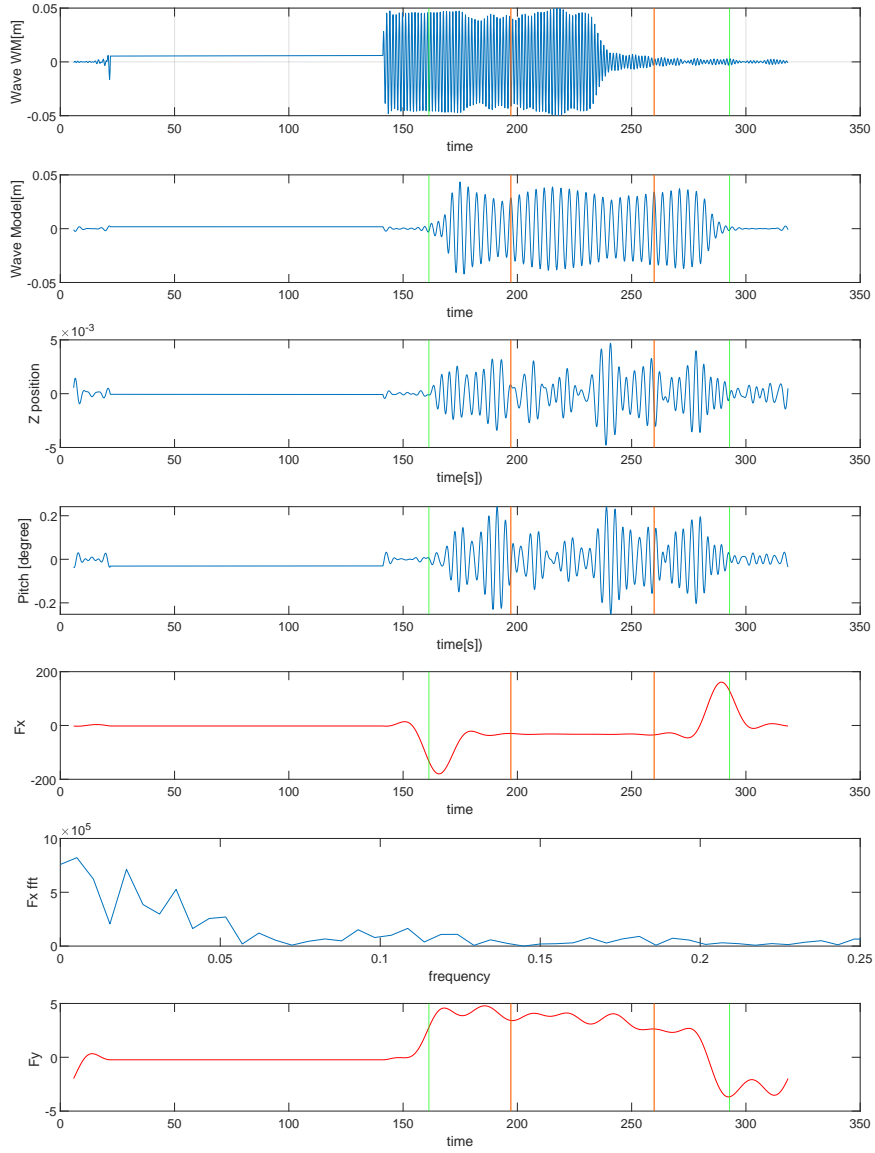
CE6010 Period(s):7 Lamda/L:0.4 Drift agle(deg):180 Speed(m/s):7.71



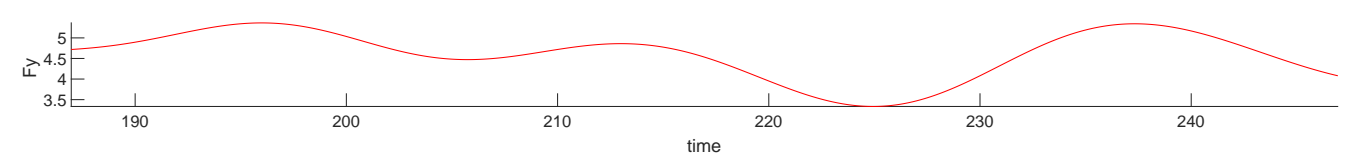
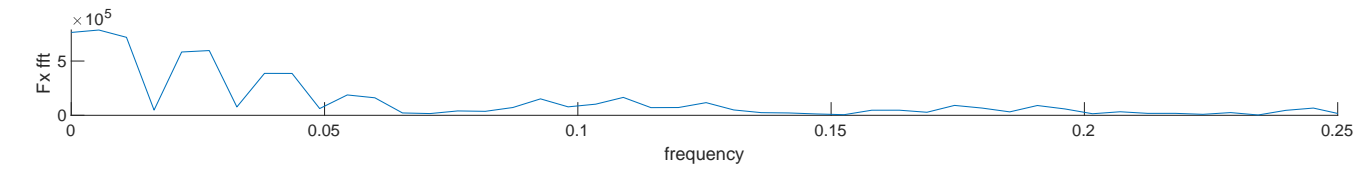
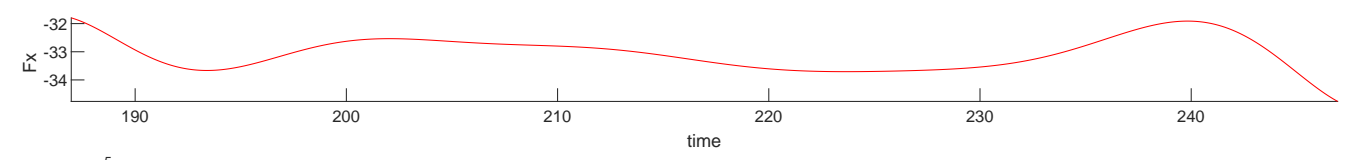
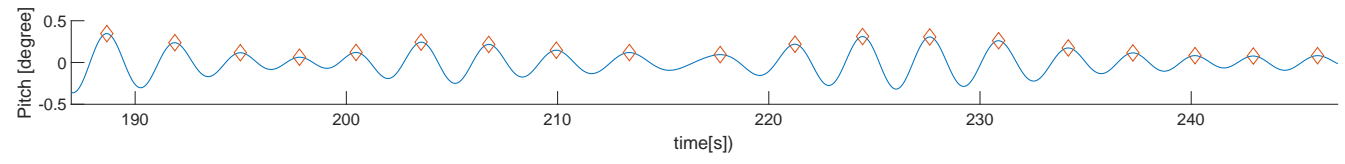
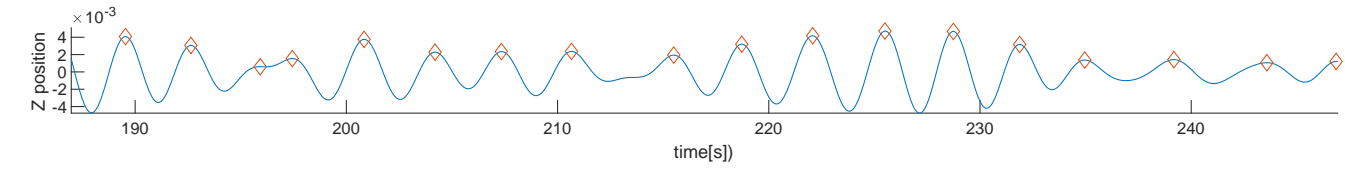
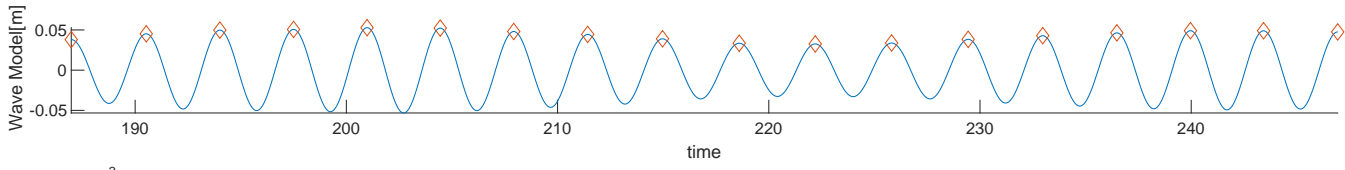
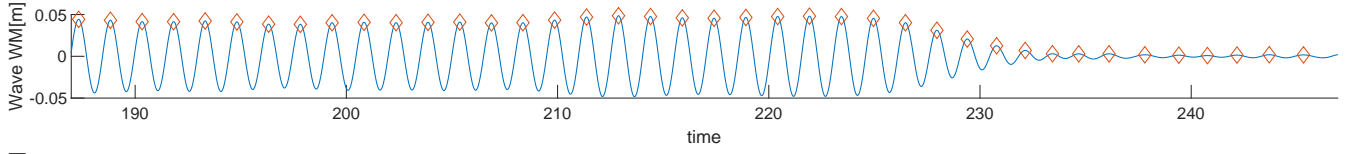
CE6020 Period(s):7.8 Lamda/L:0.5 Drift agle(deg):180 Speed(m/s):7.71



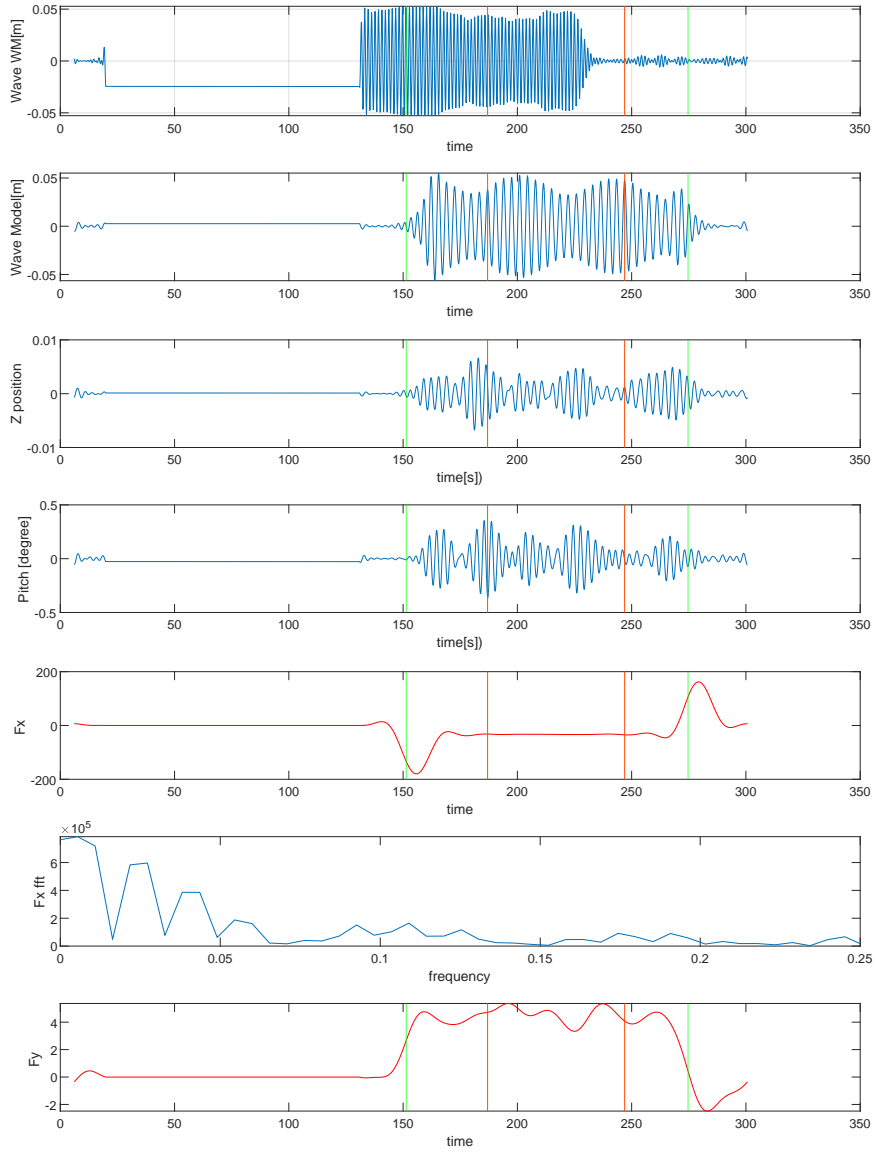
CE6020 Period(s):7.8 Lamda/L:0.5 Drift agle(deg):180 Speed(m/s):7.71



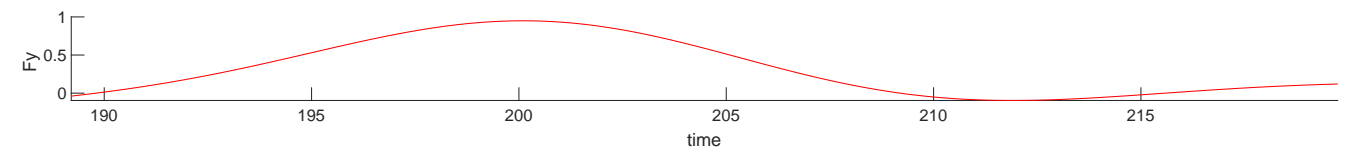
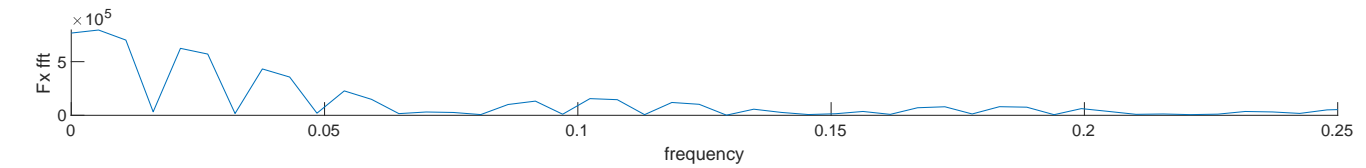
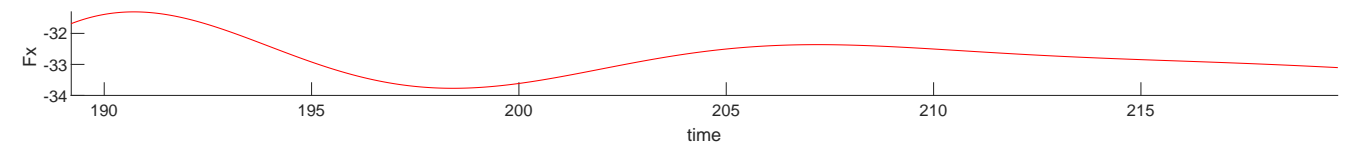
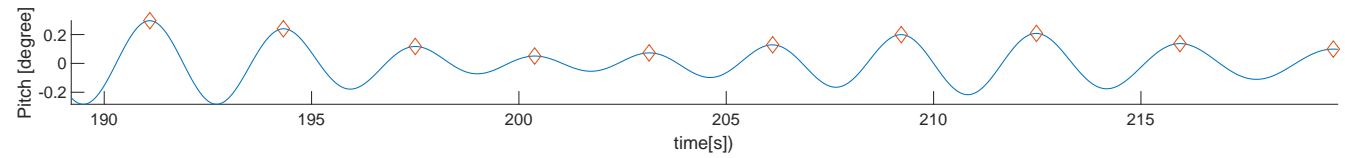
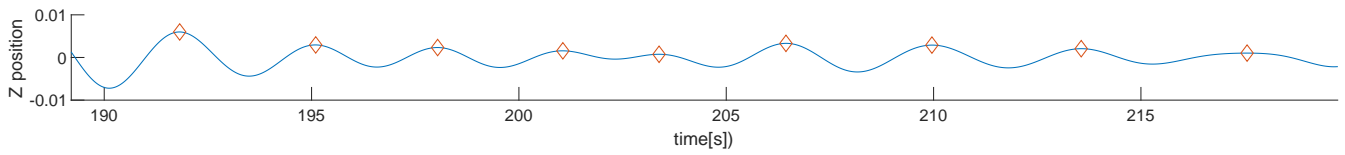
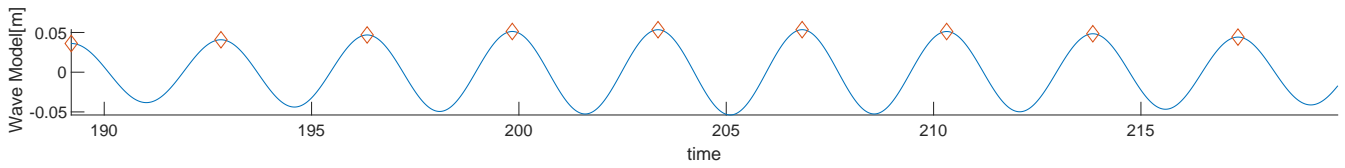
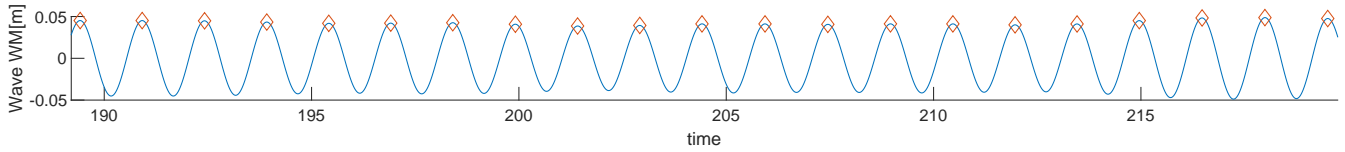
CE6030 Period(s):8.5 Lamda/L:0.59 Drift agle(deg):180 Speed(m/s):7.71



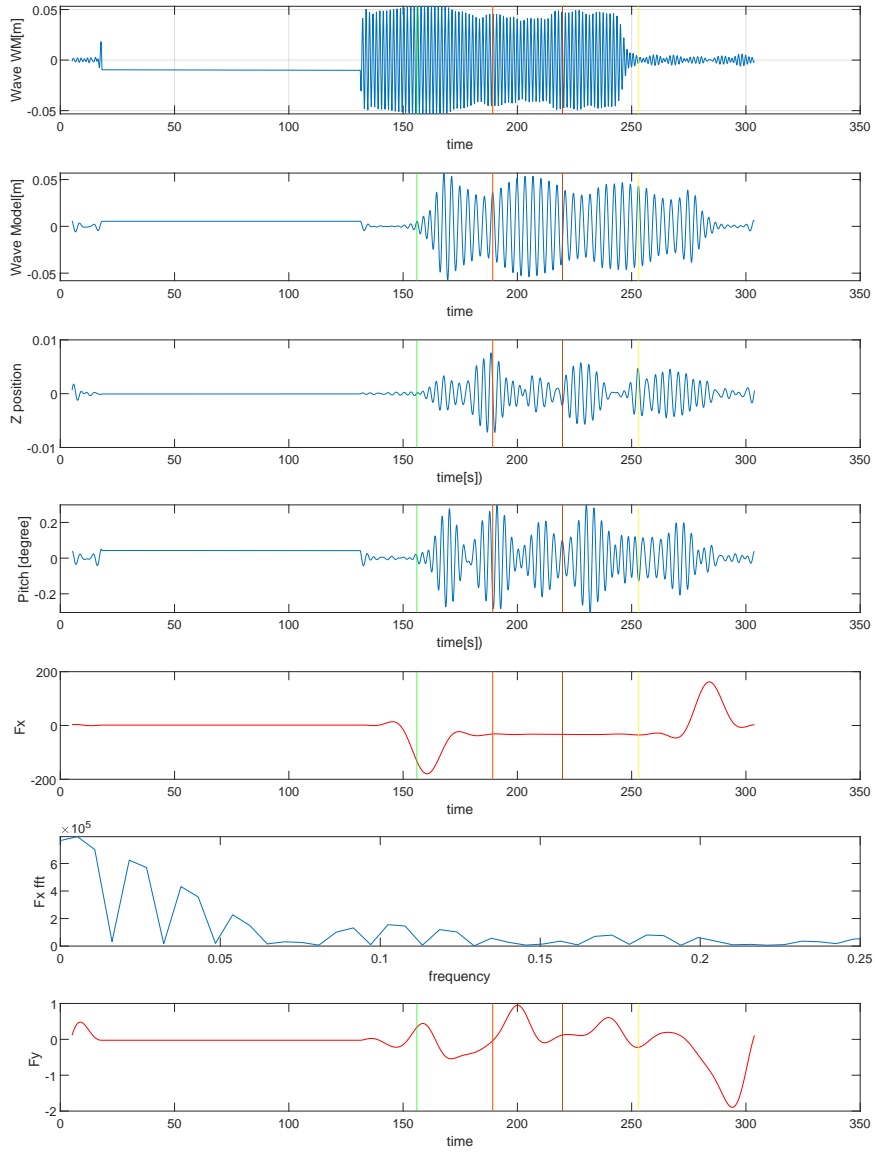
CE6030 Period(s):8.5 Lamda/L:0.59 Drift angle(deg):180 Speed(m/s):7.71



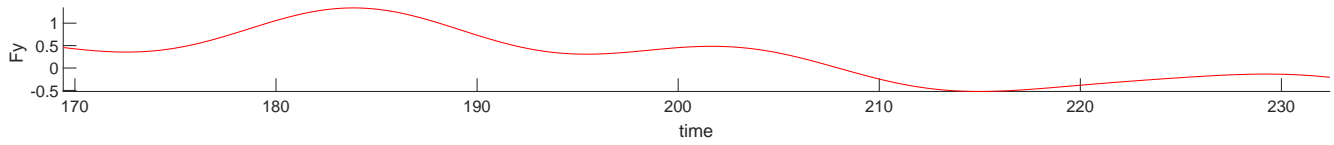
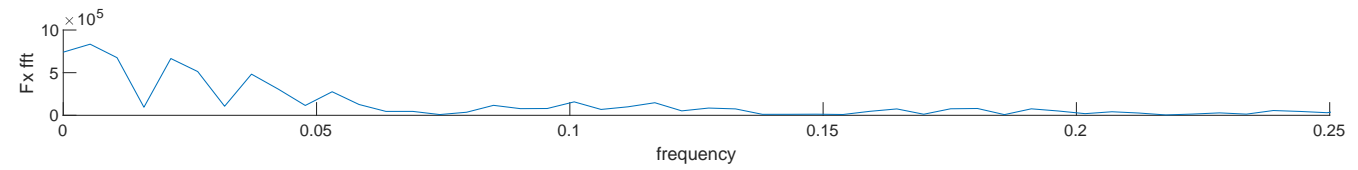
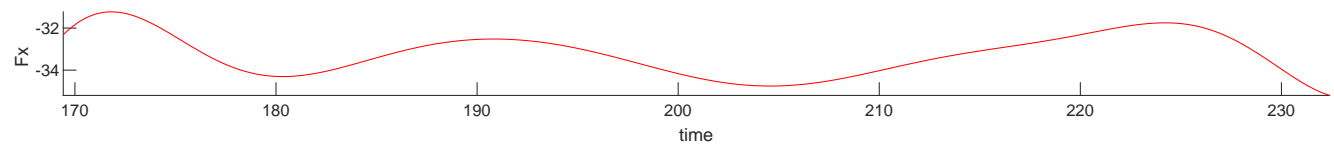
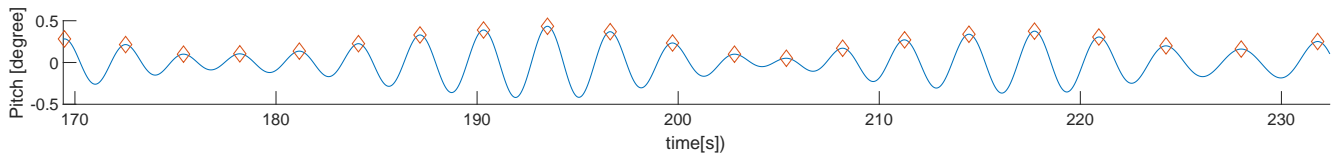
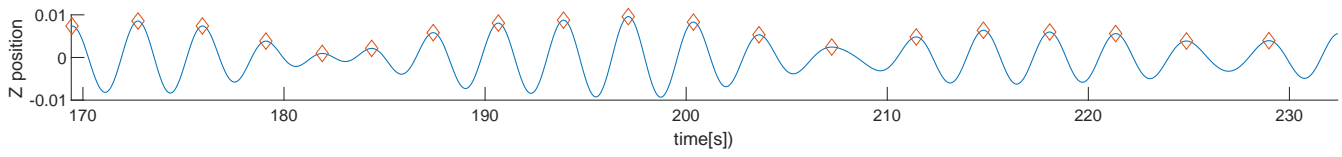
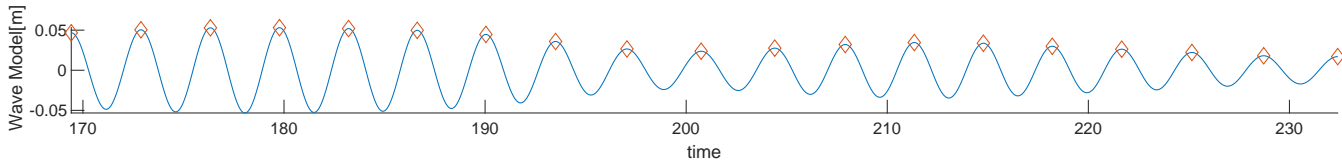
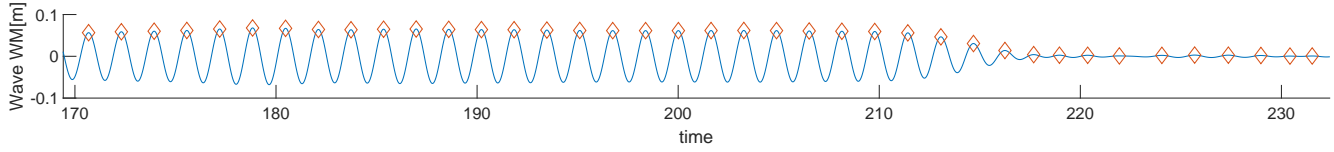
CE6031 Period(s):8.5 Lamda/L:0.59 Drift angle(deg):180 Speed(m/s):7.71



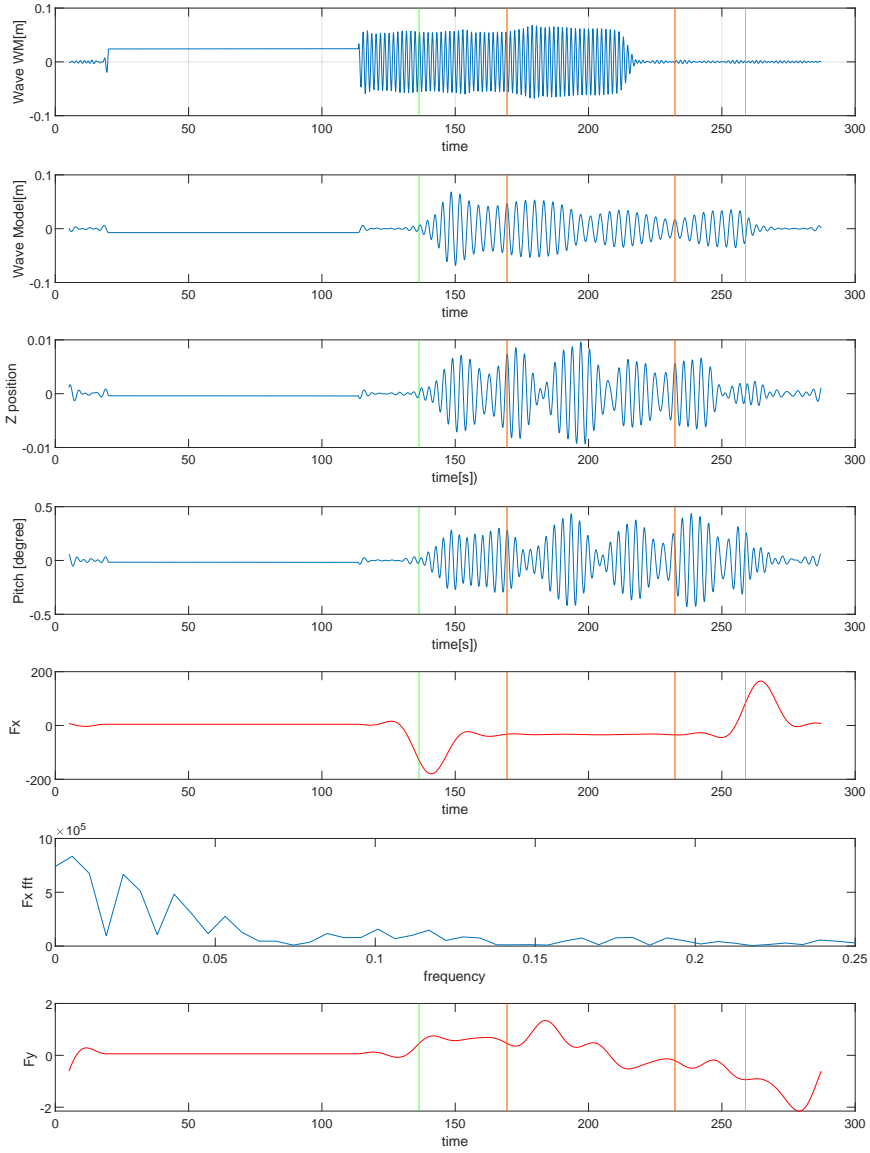
CE6031 Period(s):8.5 Lamda/L:0.59 Drift angle(deg):180 Speed(m/s):7.71



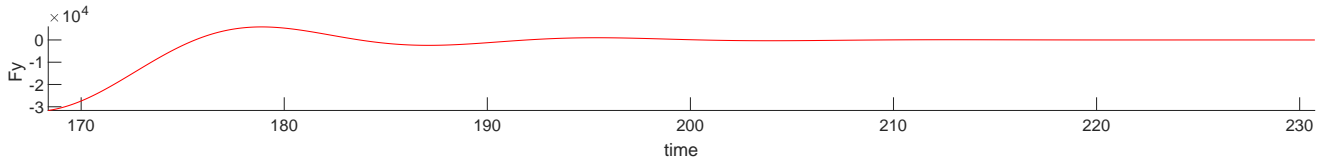
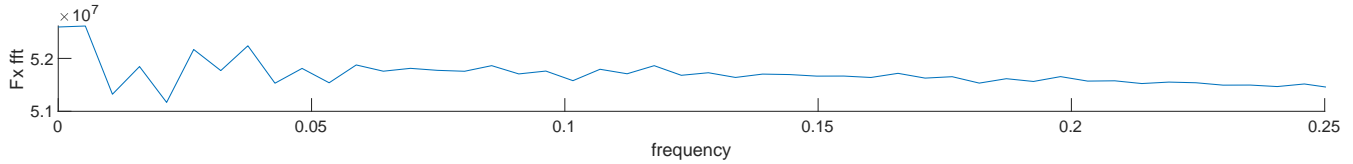
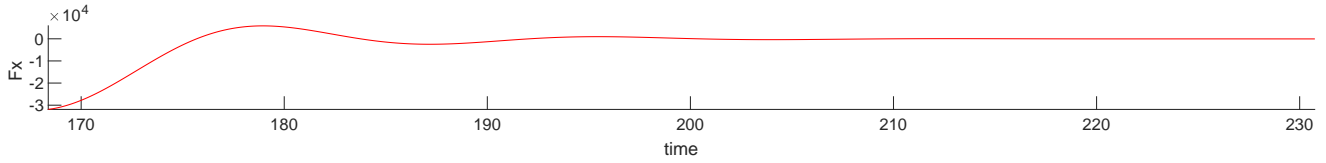
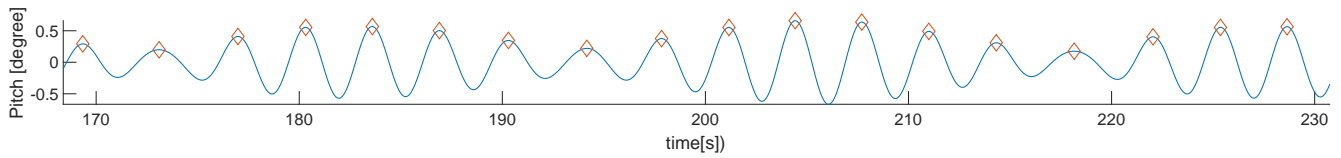
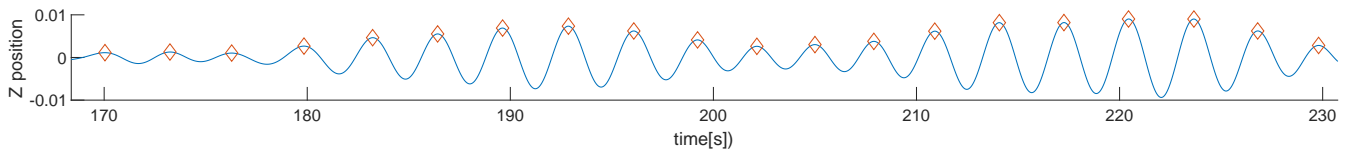
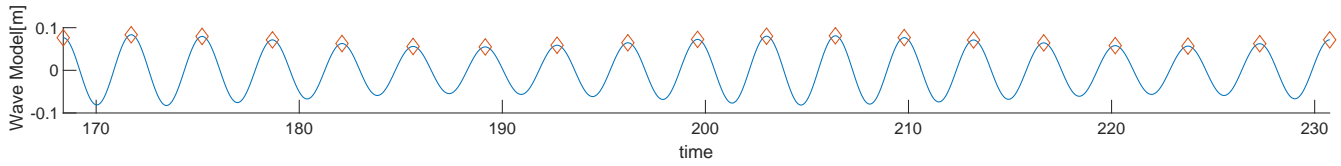
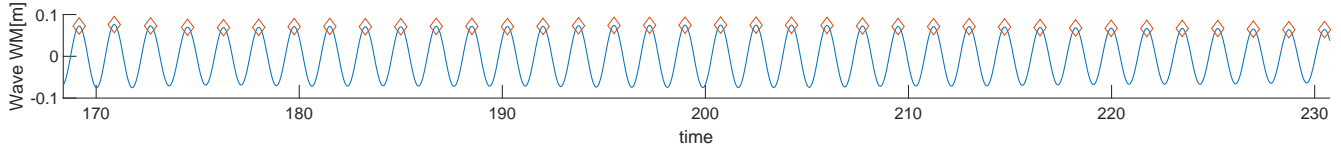
CE6040 Period(s):9.2 Lamda/L:0.7 Drift agle(deg):180 Speed(m/s):7.71



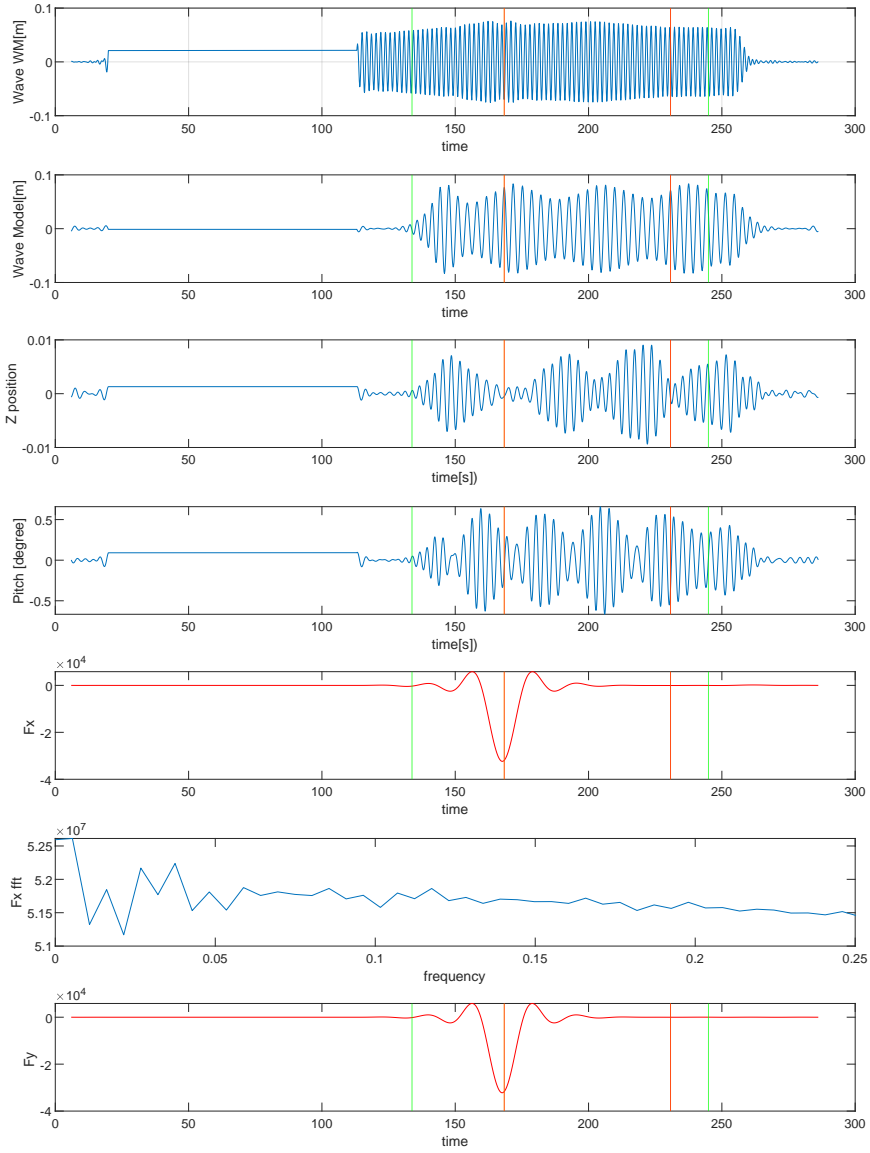
CE6040 Period(s):9.2 Lamda/L:0.7 Drift aple(deg):180 Speed(m/s):7.71



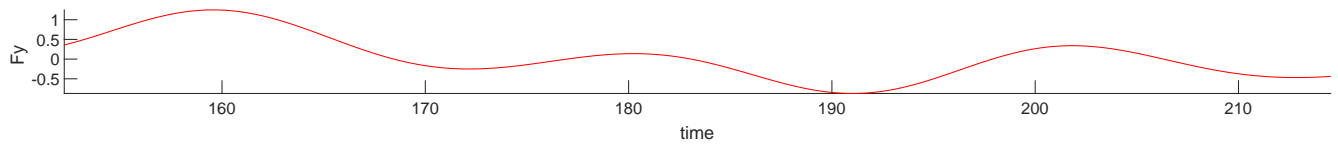
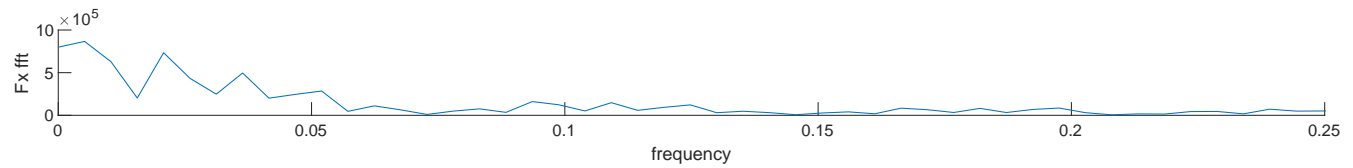
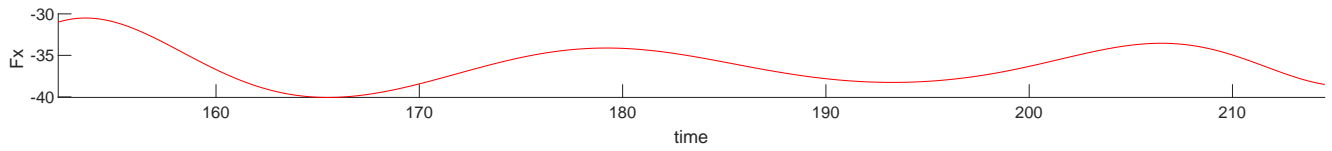
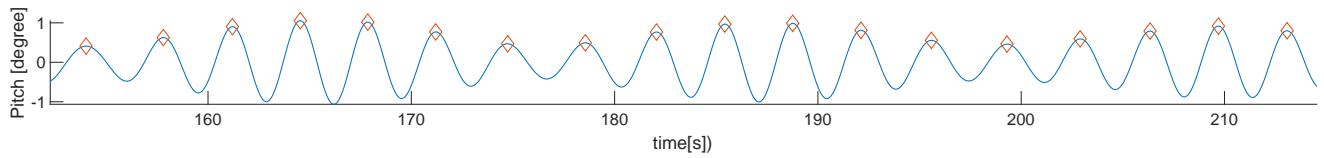
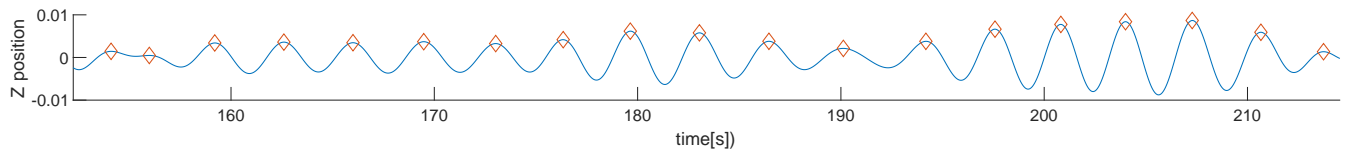
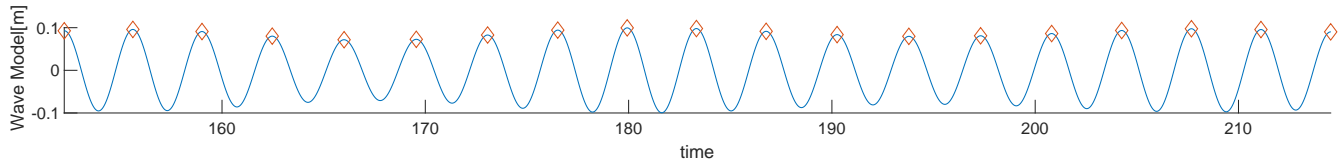
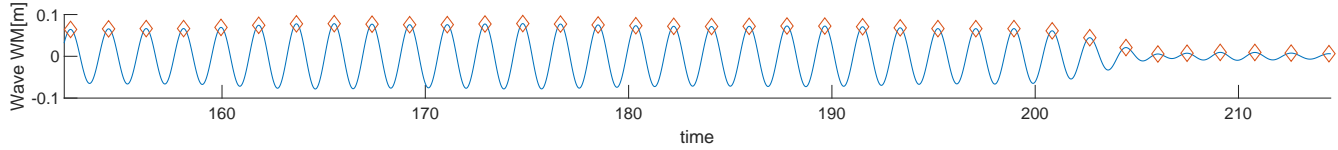
CE6050 Period(s):9.9 Lamda/L:0.81 Drift agle(deg):180 Speed(m/s):7.71



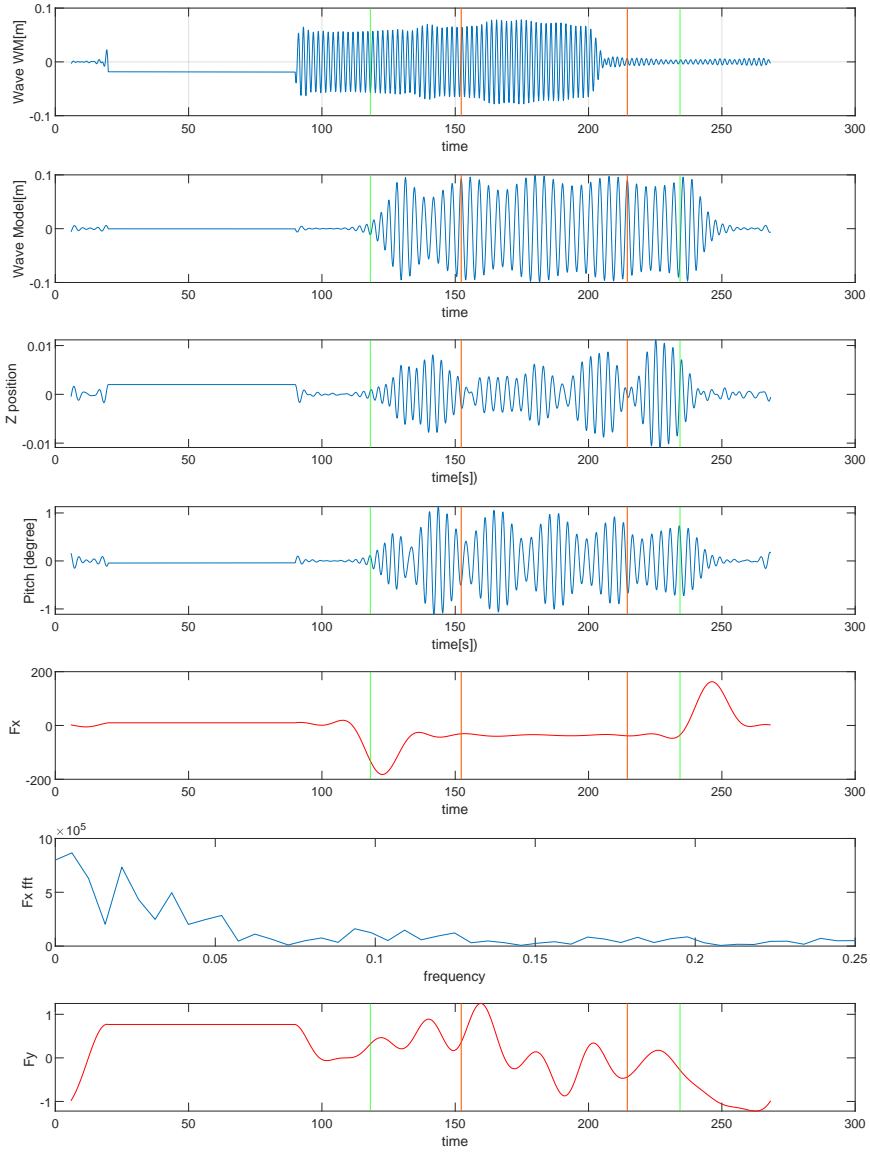
CE6050 Period(s):9.9 Lamda/L:0.81 Drift angle(deg):180 Speed(m/s):7.71



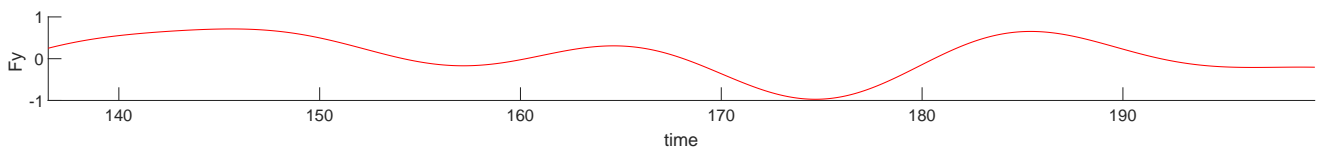
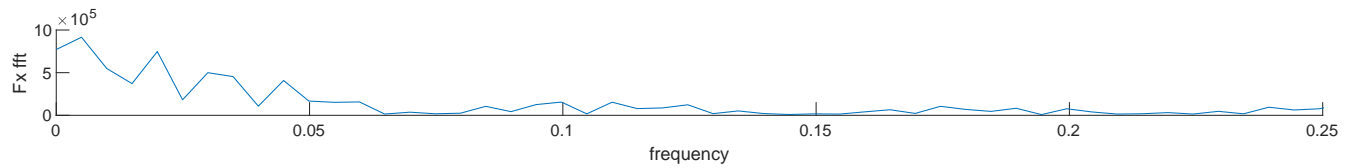
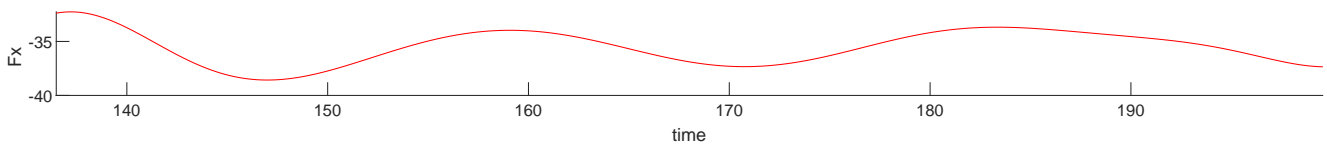
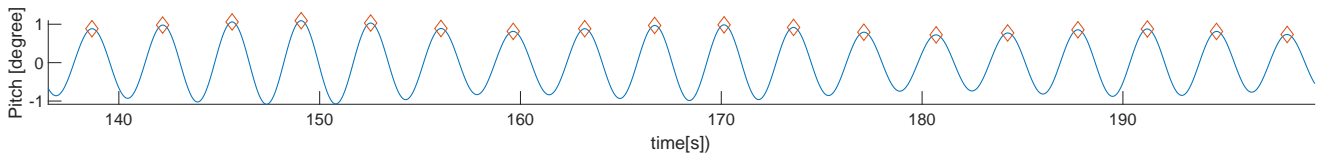
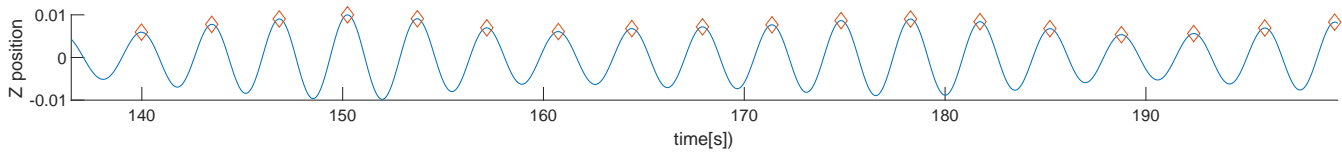
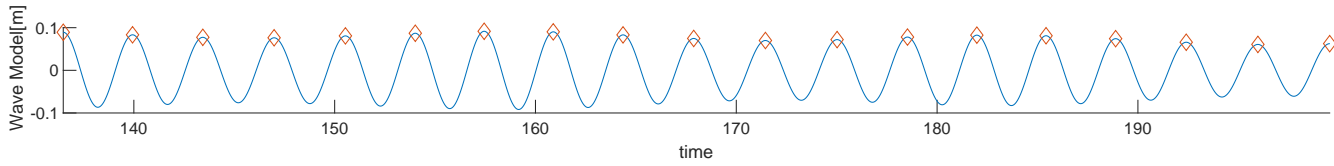
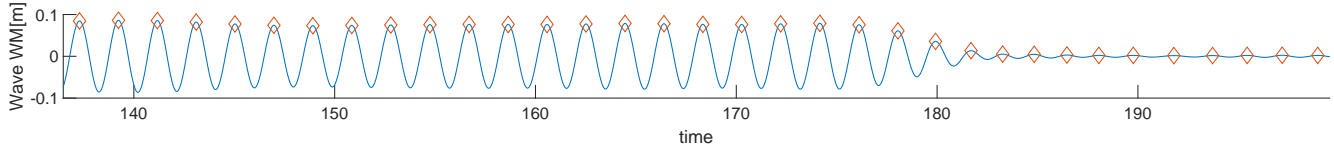
CE6060 Period(s):10.5 Lamda/L:0.91 Drift angle(deg):180 Speed(m/s):7.71



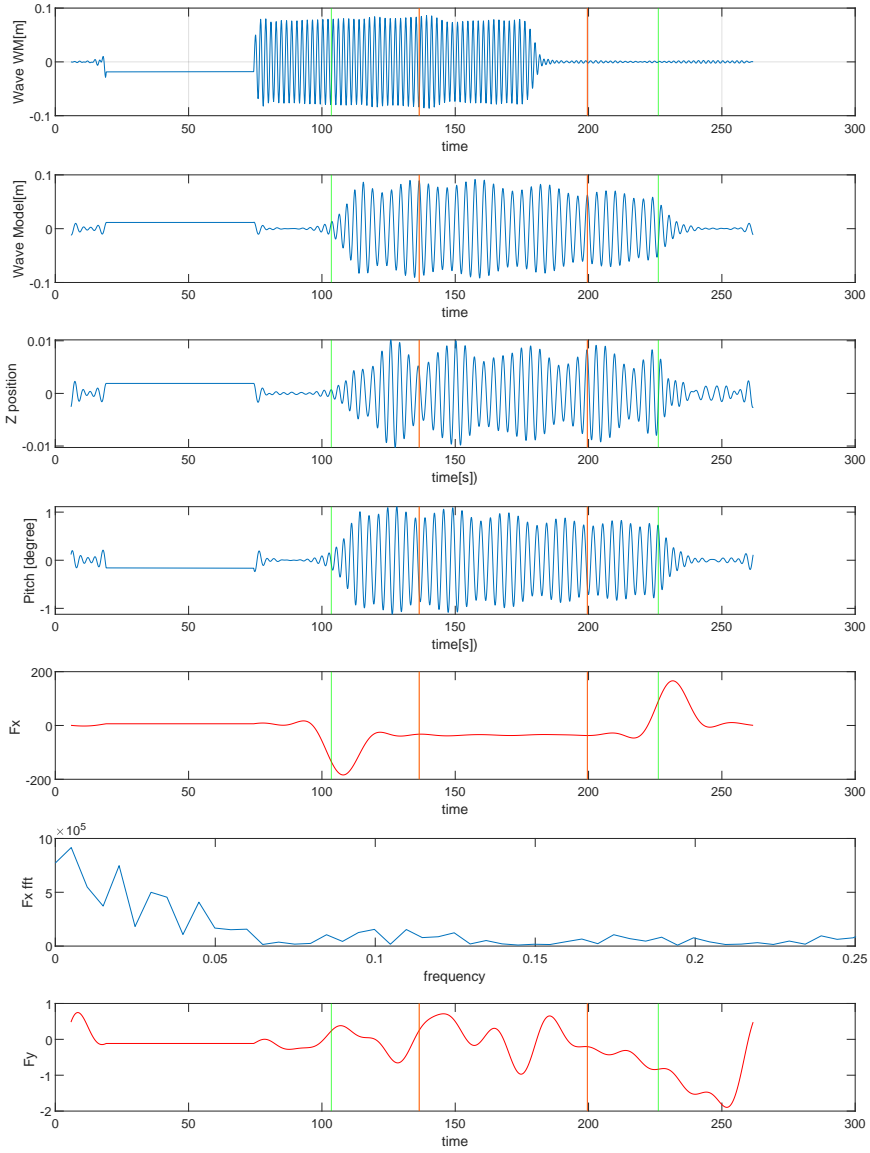
CE6060 Period(s):10.5 Lamda/L:0.91 Drift agle(deg):180 Speed(m/s):7.71



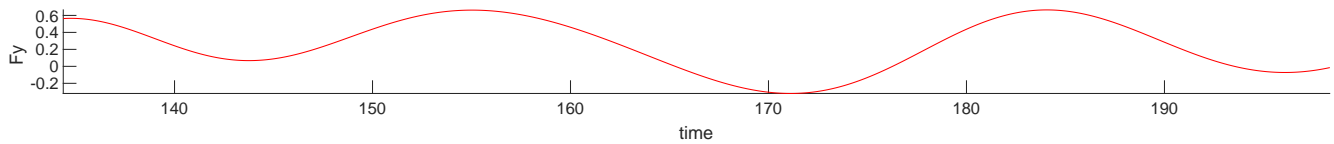
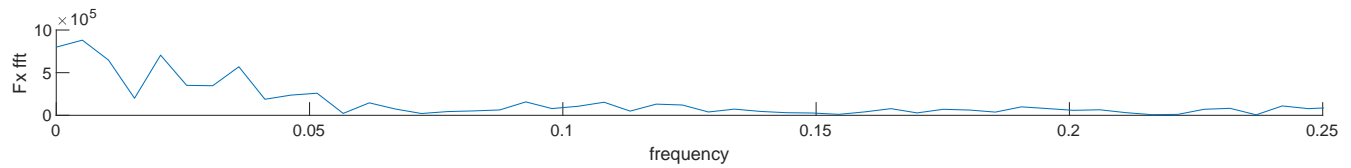
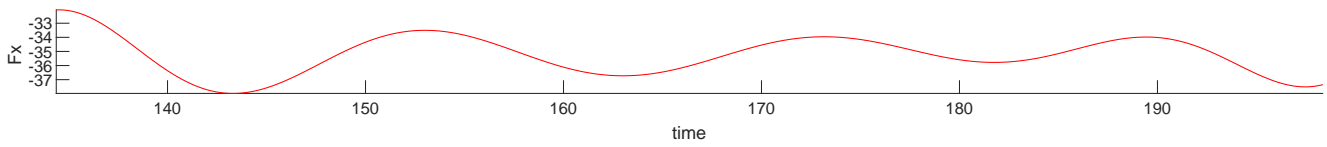
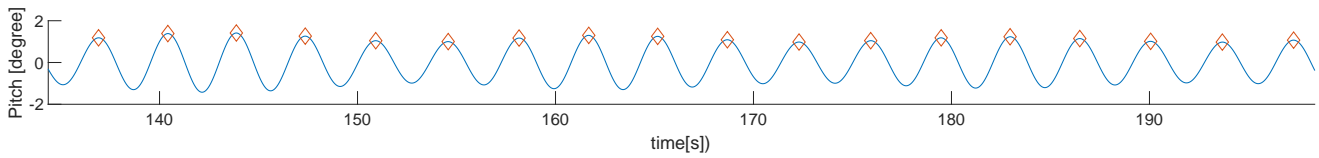
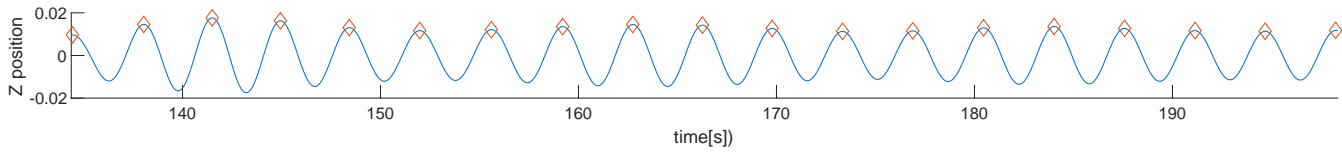
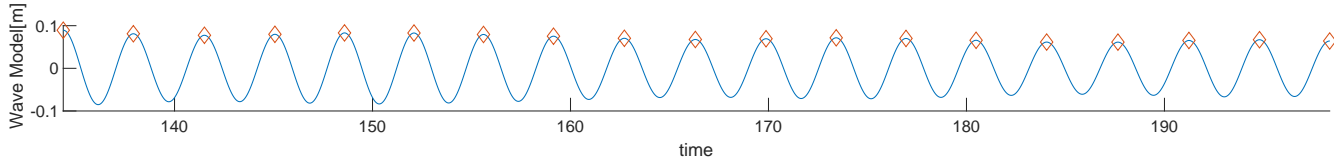
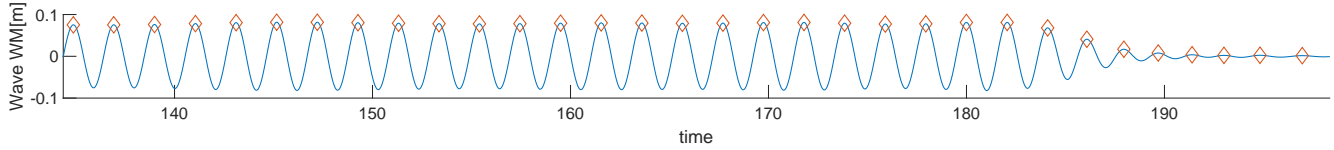
CE6070 Period(s):11 Lamda/L:0.99 Drift agle(deg):180 Speed(m/s):7.71



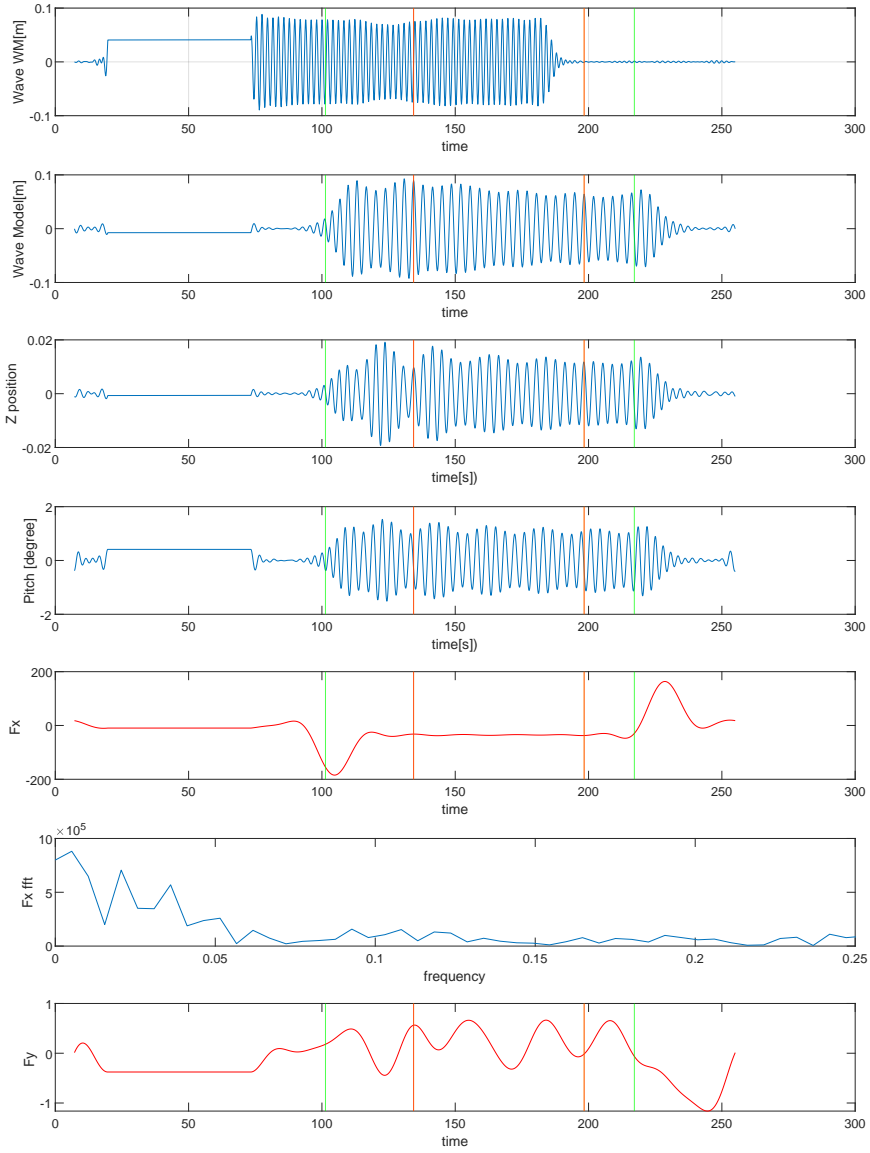
CE6070 Period(s):11 Lamda/L:0.99 Drift agle(deg):180 Speed(m/s):7.71



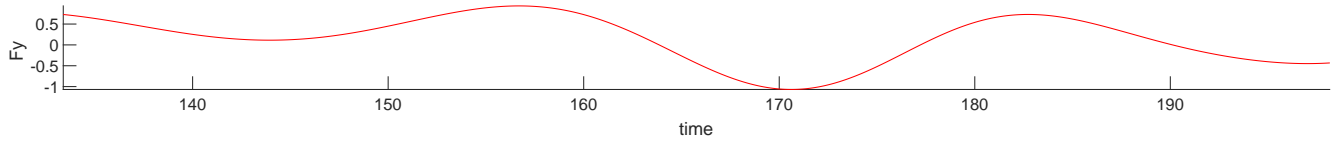
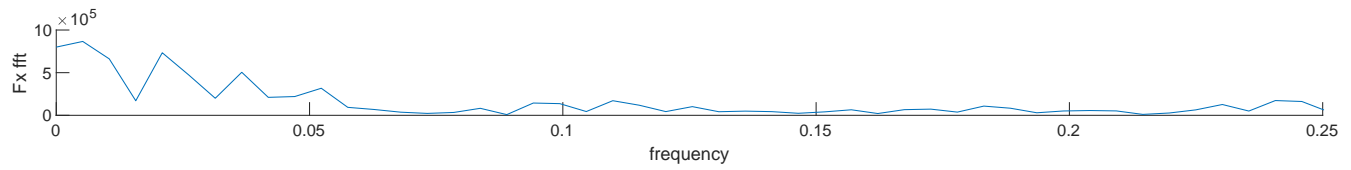
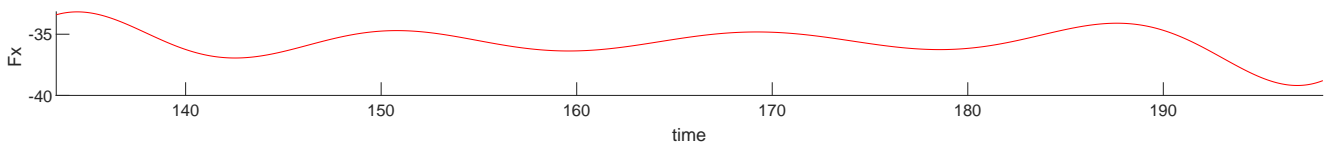
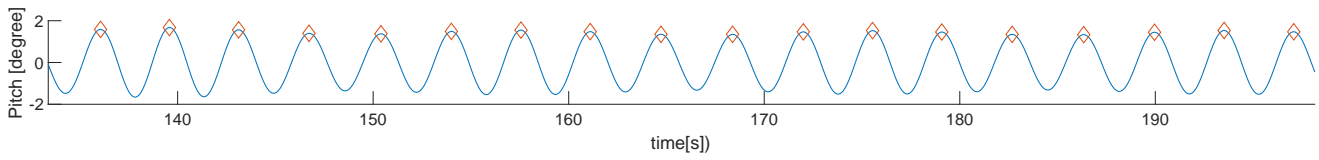
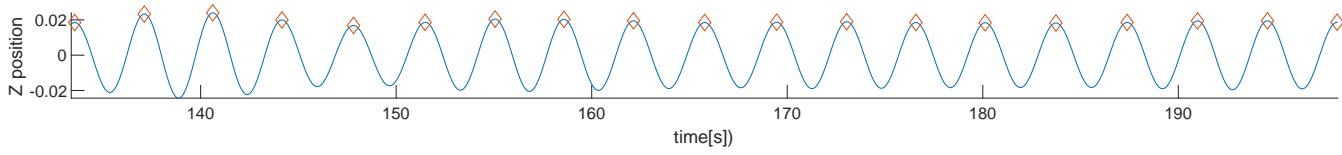
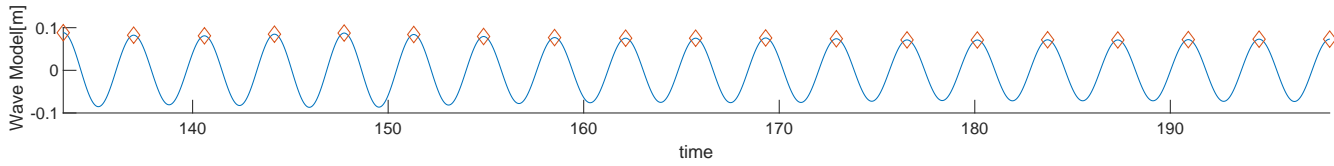
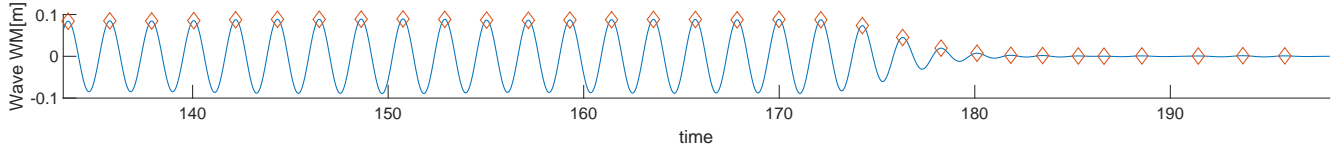
CE6080 Period(s):11.6 Lamda/L:1.11 Drift angle(deg):180 Speed(m/s):7.71



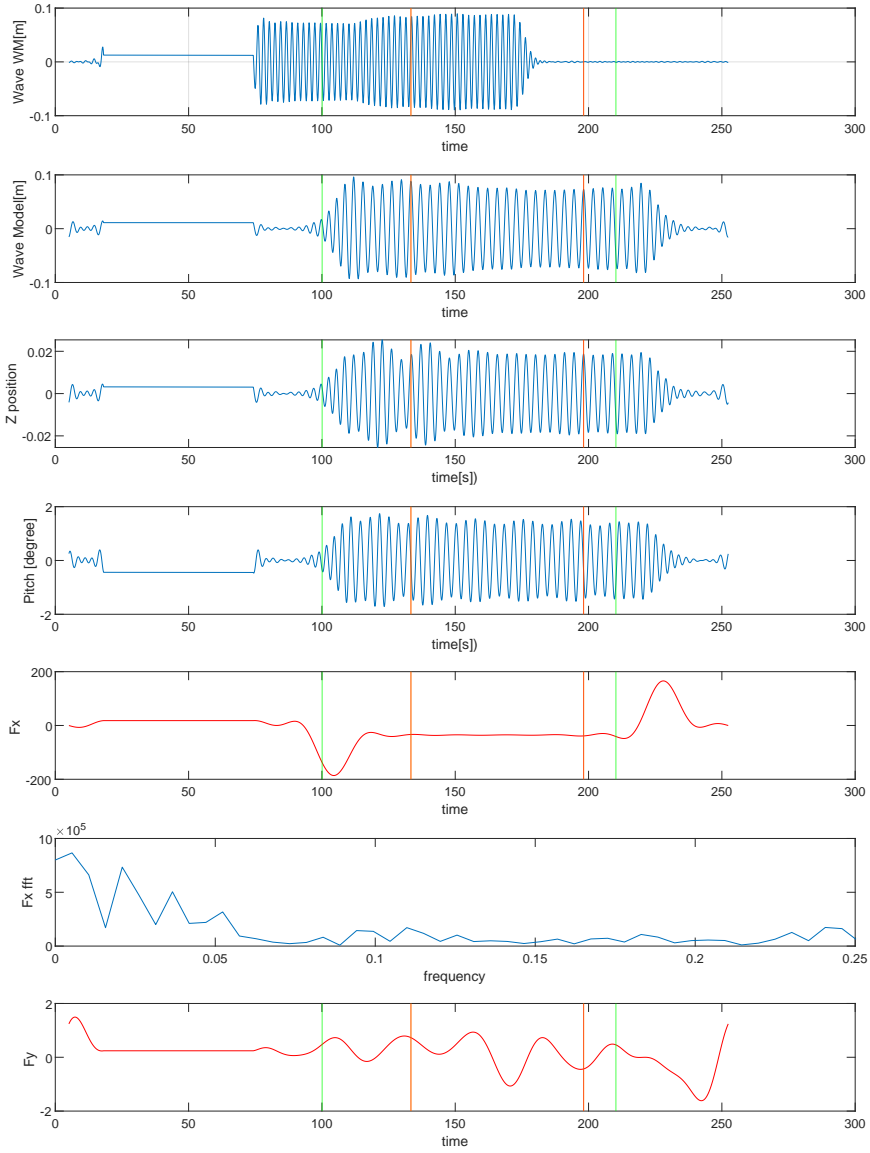
CE6080 Period(s):11.6 Lamda/L:1.11 Drift angle(deg):180 Speed(m/s):7.71



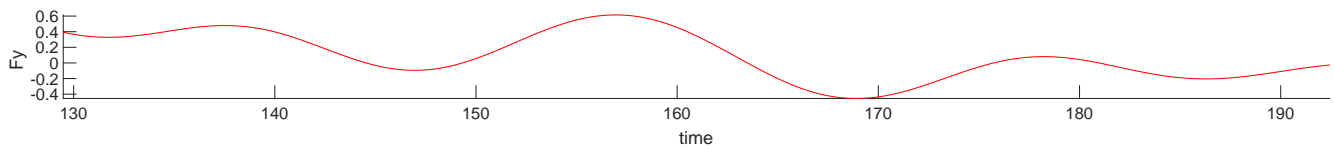
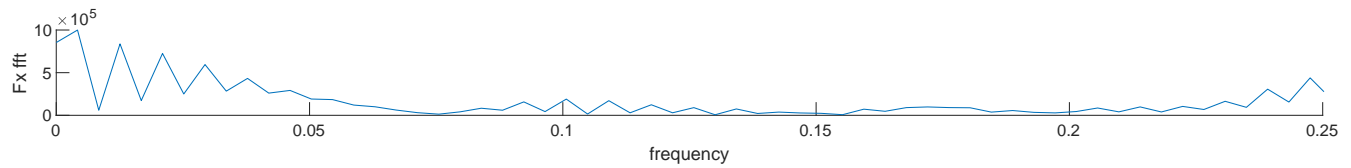
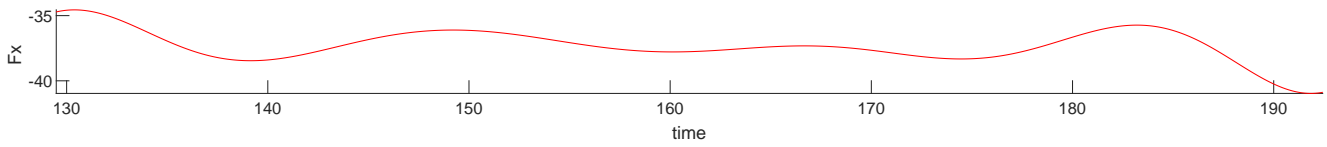
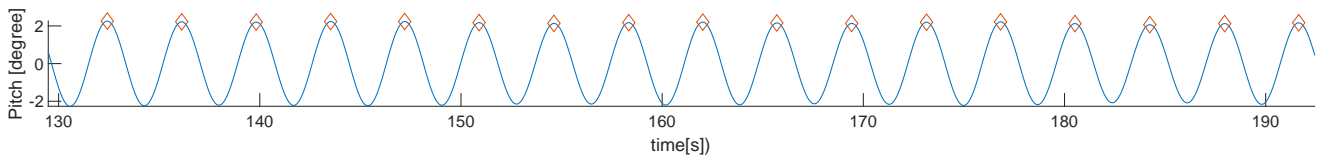
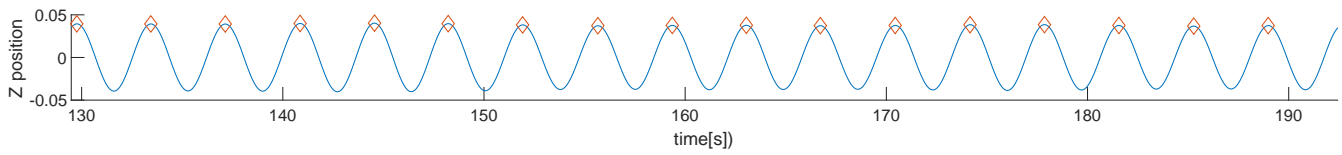
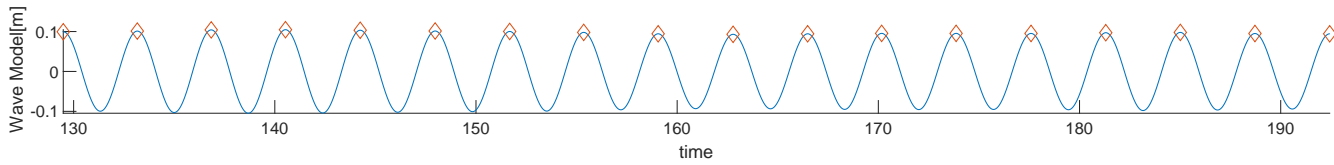
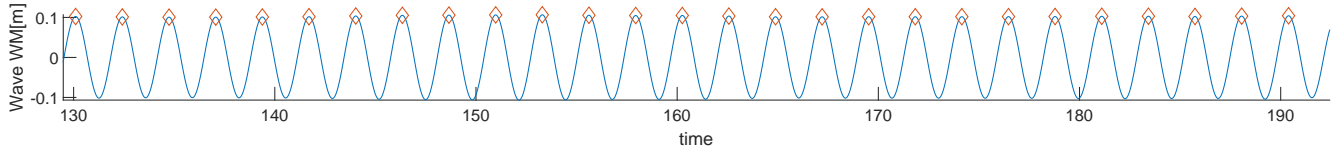
CE6090 Period(s):12.1 Lamda/L:1.2 Drift agle(deg):180 Speed(m/s):7.71



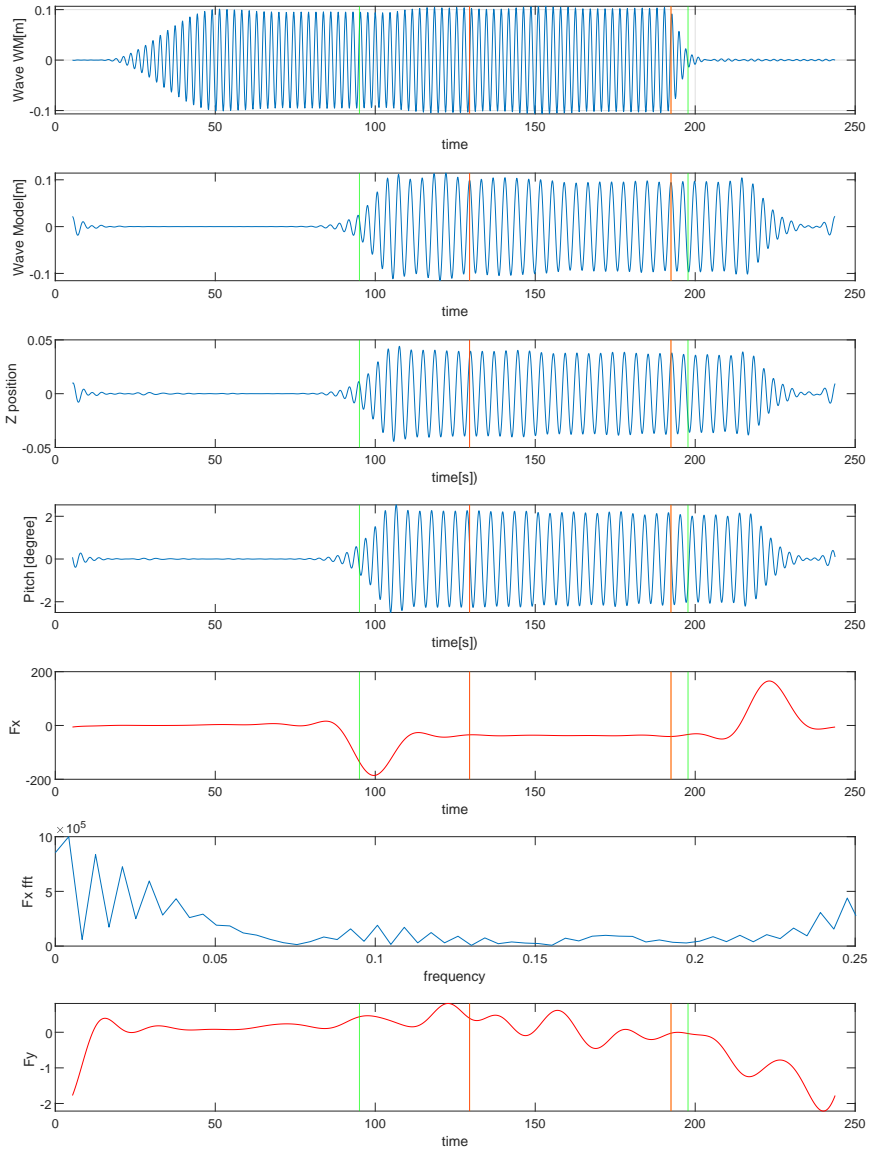
CE6090 Period(s):12.1 Lamda/L:1.2 Drift angle(deg):180 Speed(m/s):7.71



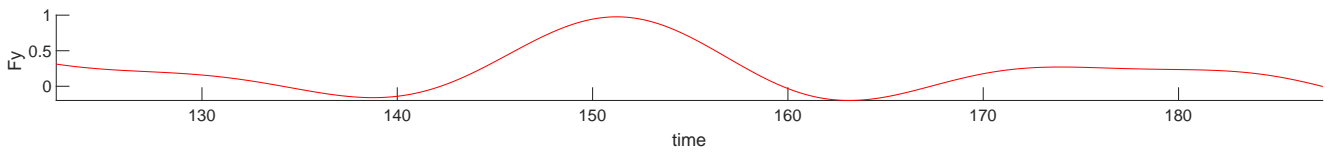
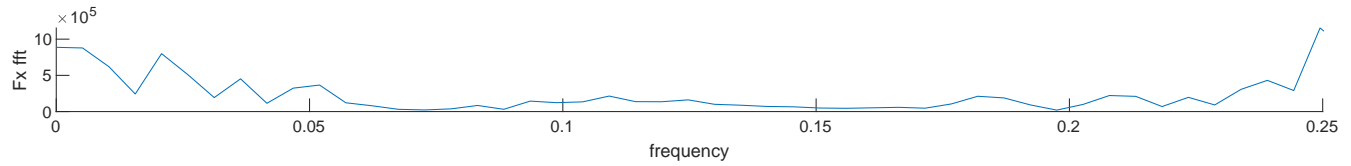
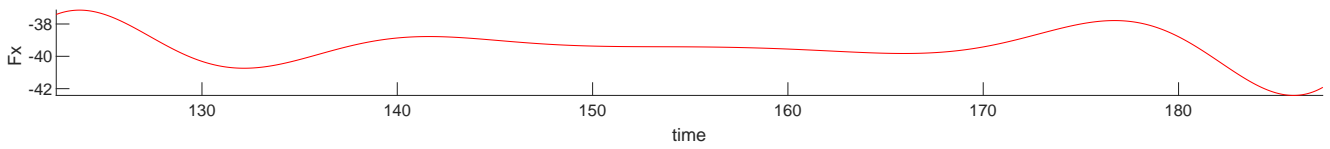
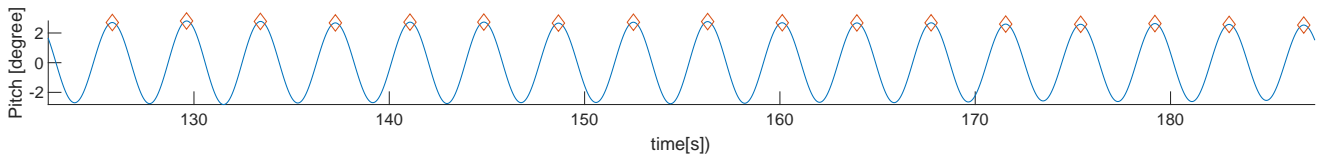
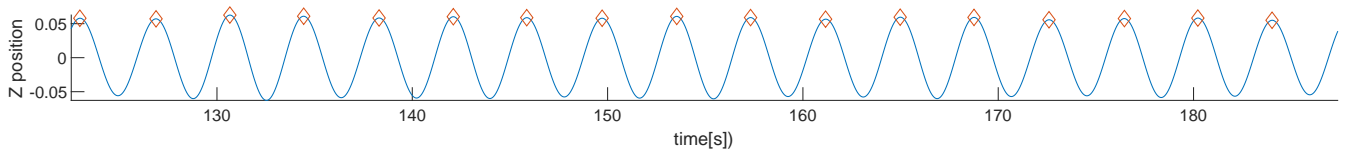
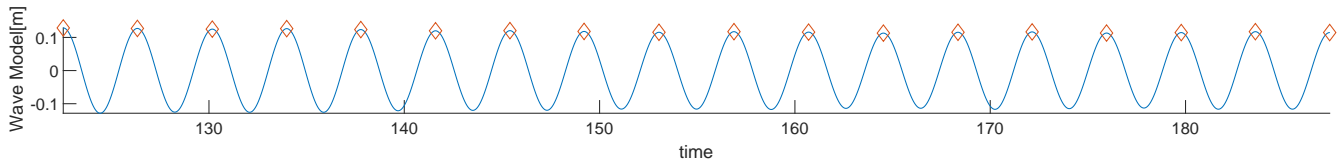
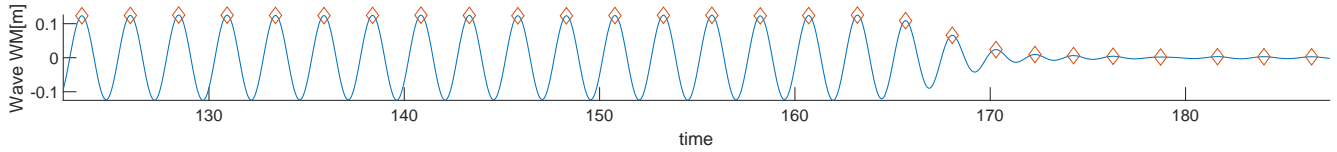
CE6100 Period(s):13.1 Lamda/L:1.41 Drift angle(deg):180 Speed(m/s):7.71



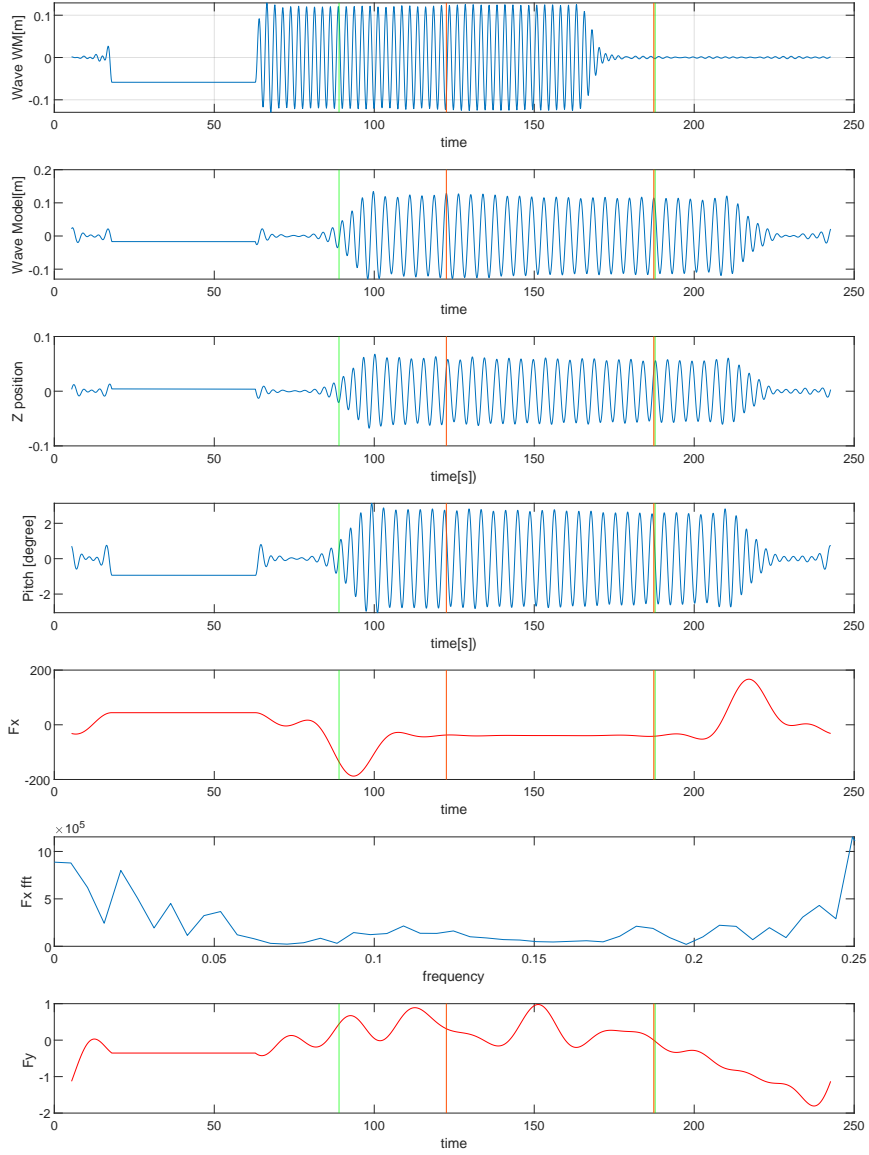
CE6100 Period(s):13.1 Lamda/L:1.41 Drift angle(deg):180 Speed(m/s):7.71



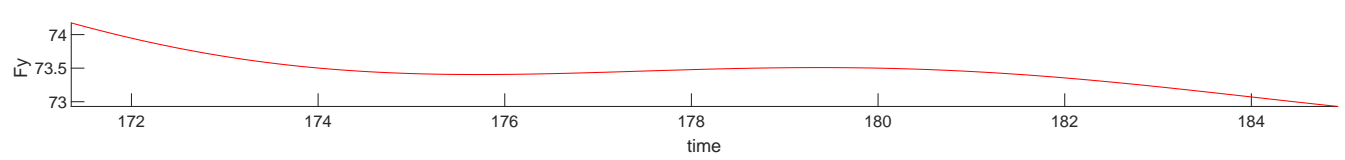
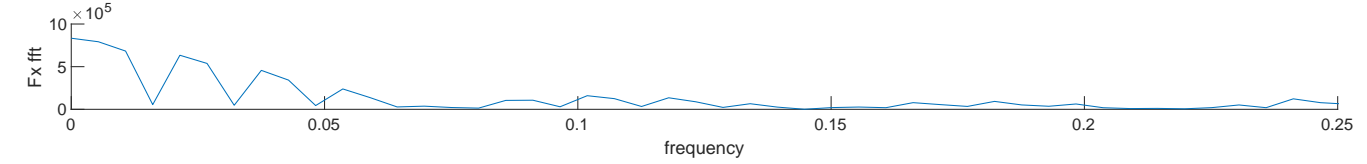
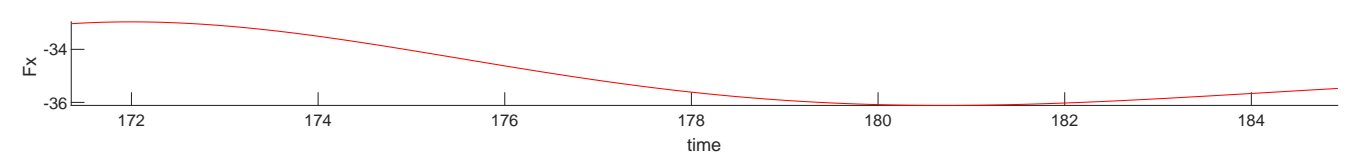
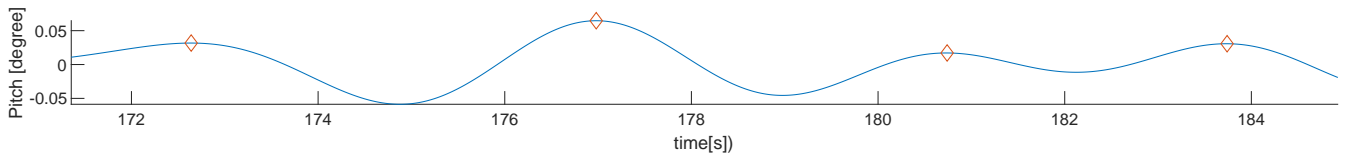
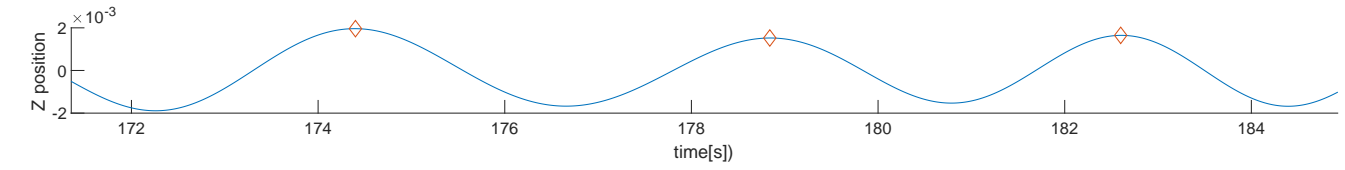
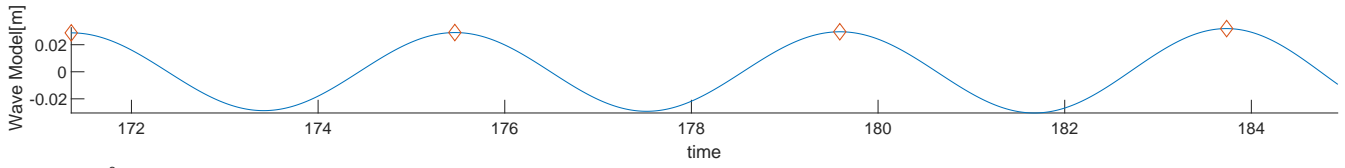
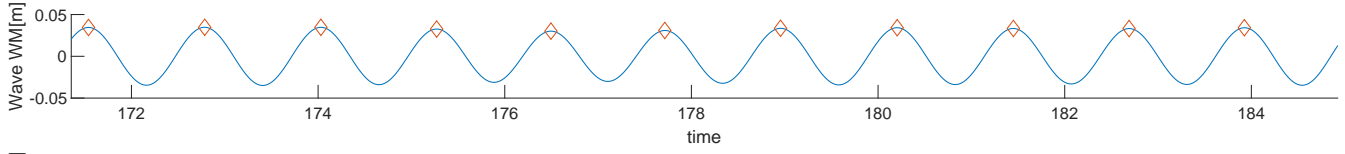
CE6110 Period(s):14 Lamda/L:1.61 Drift agle(deg):180 Speed(m/s):7.71



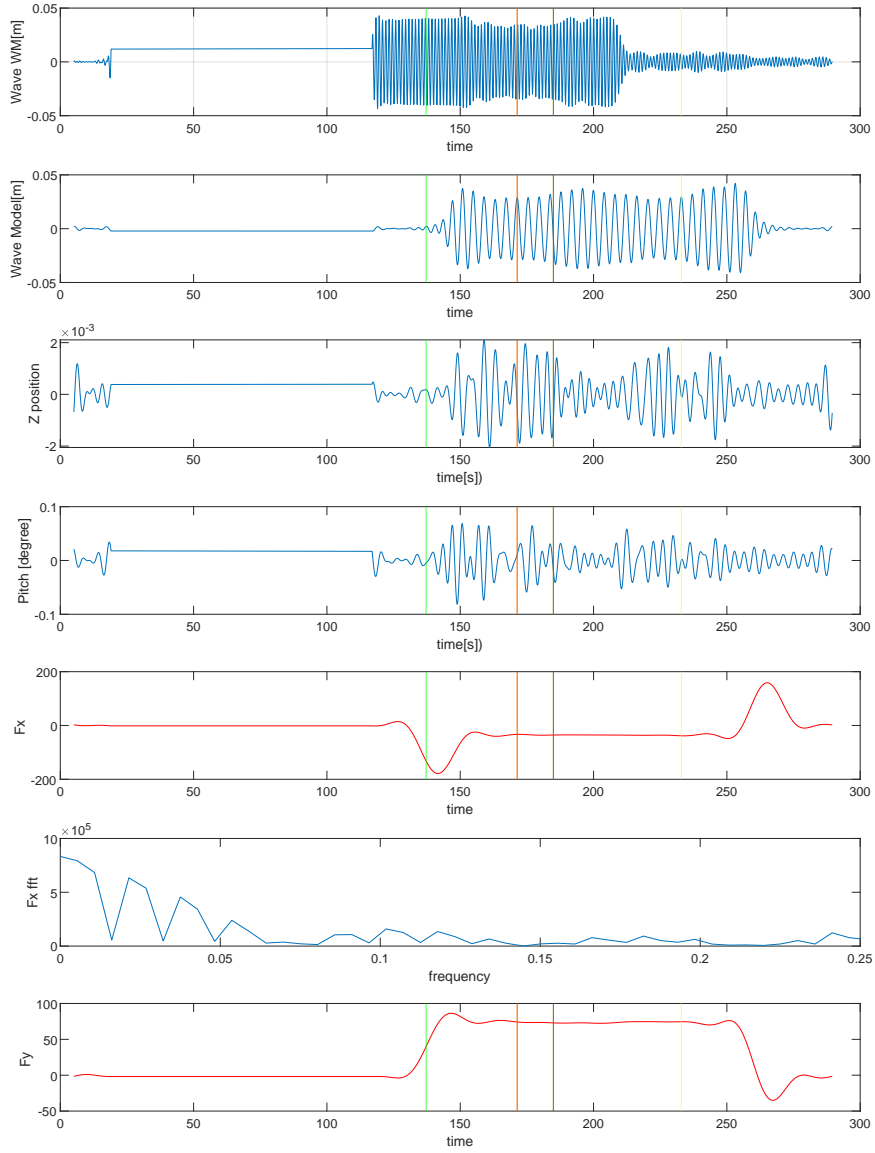
CE6110 Period(s):14 Lamda/L:1.61 Drift angle(deg):180 Speed(m/s):7.71



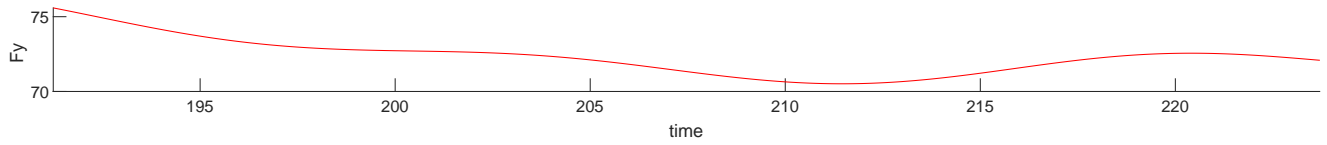
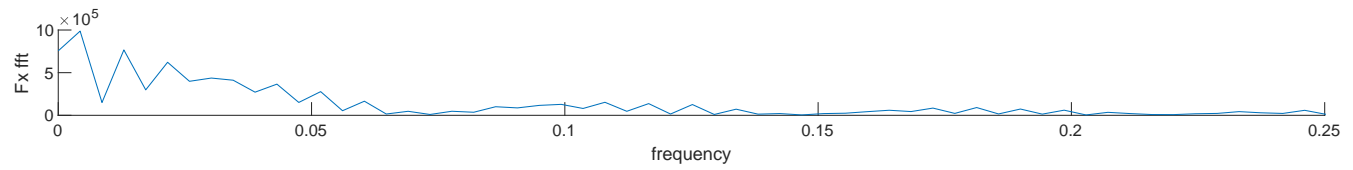
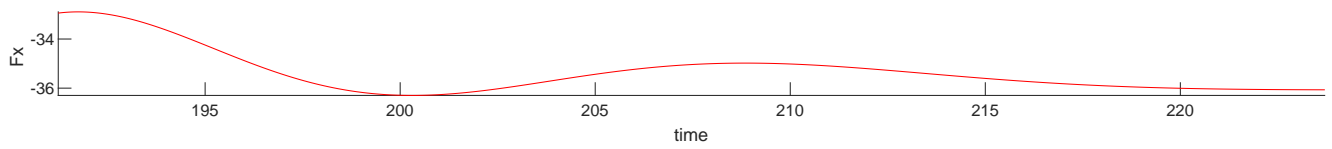
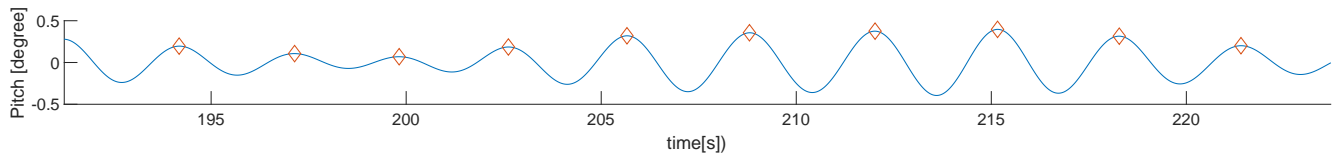
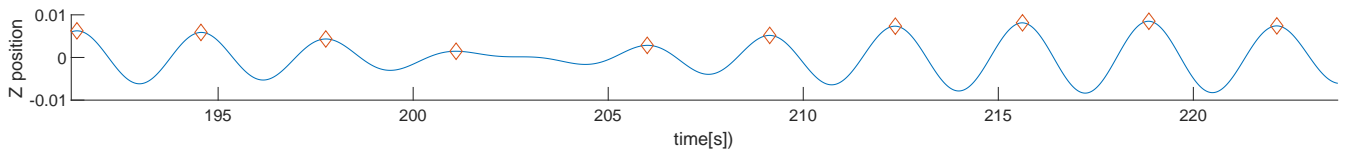
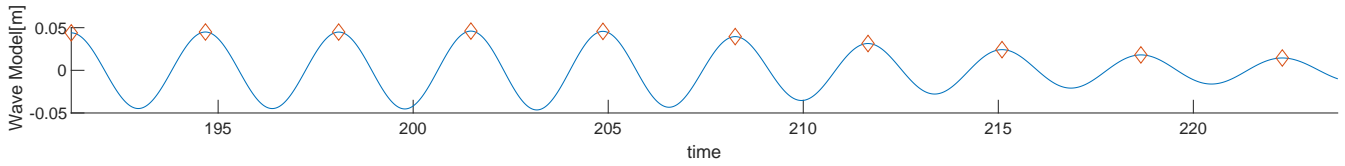
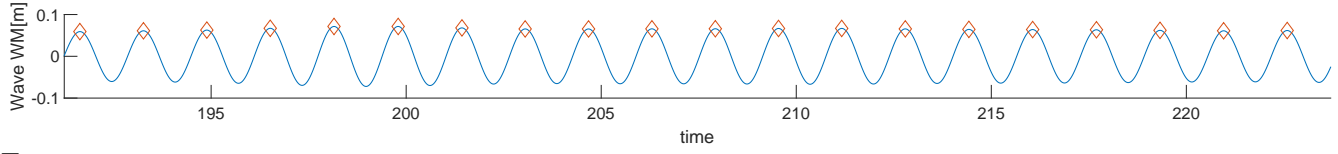
CE7010 Period(s):7 Lamda/L:0.4 Drift agle(deg):189 Speed(m/s):7.71



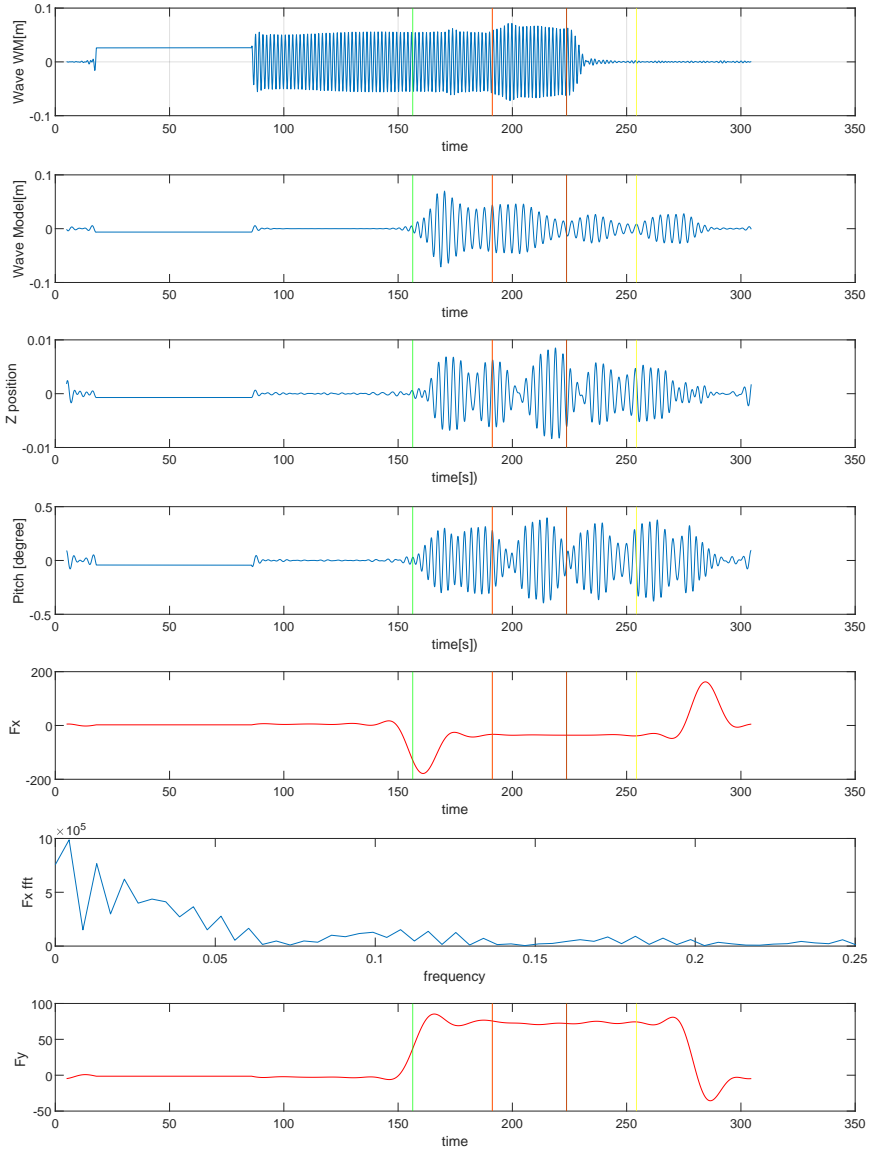
CE7010 Period(s):7 Lamda/L:0.4 Drift agle(deg):189 Speed(m/s):7.71



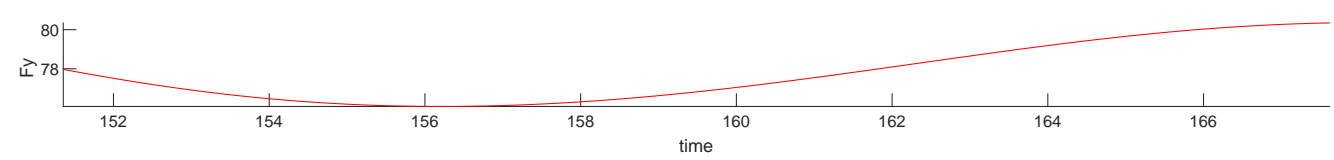
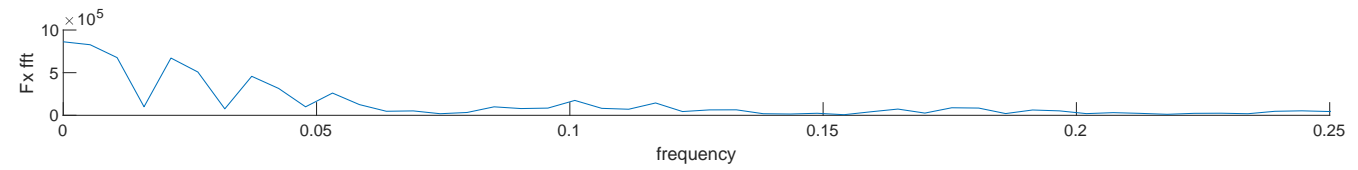
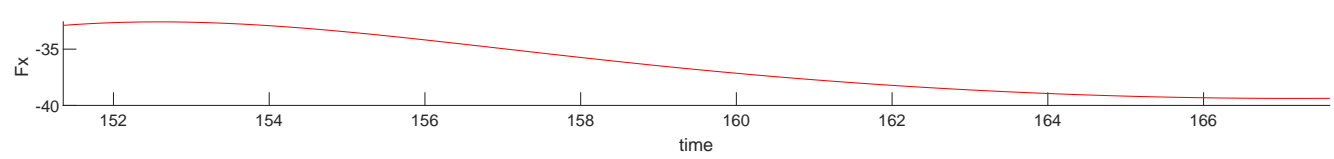
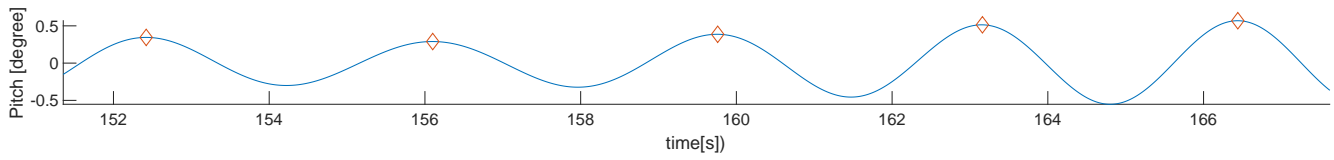
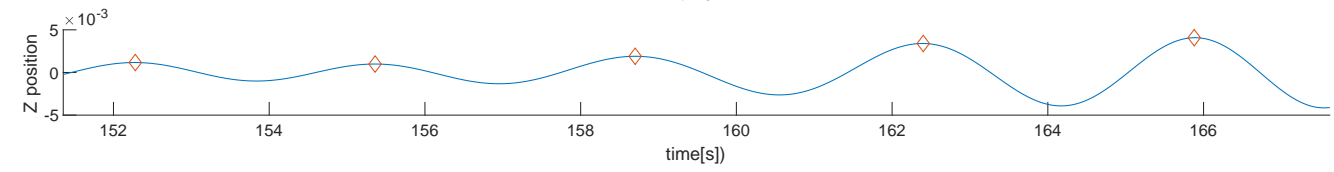
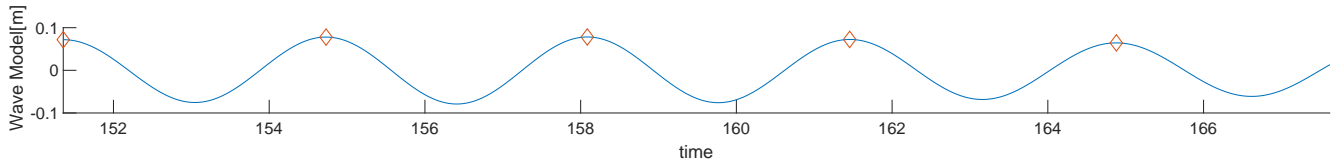
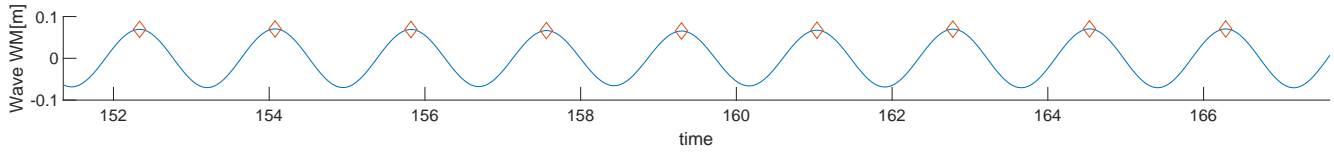
CE7040 Period(s):9.2 Lamda/L:0.7 Drift agle(deg):189 Speed(m/s):7.71



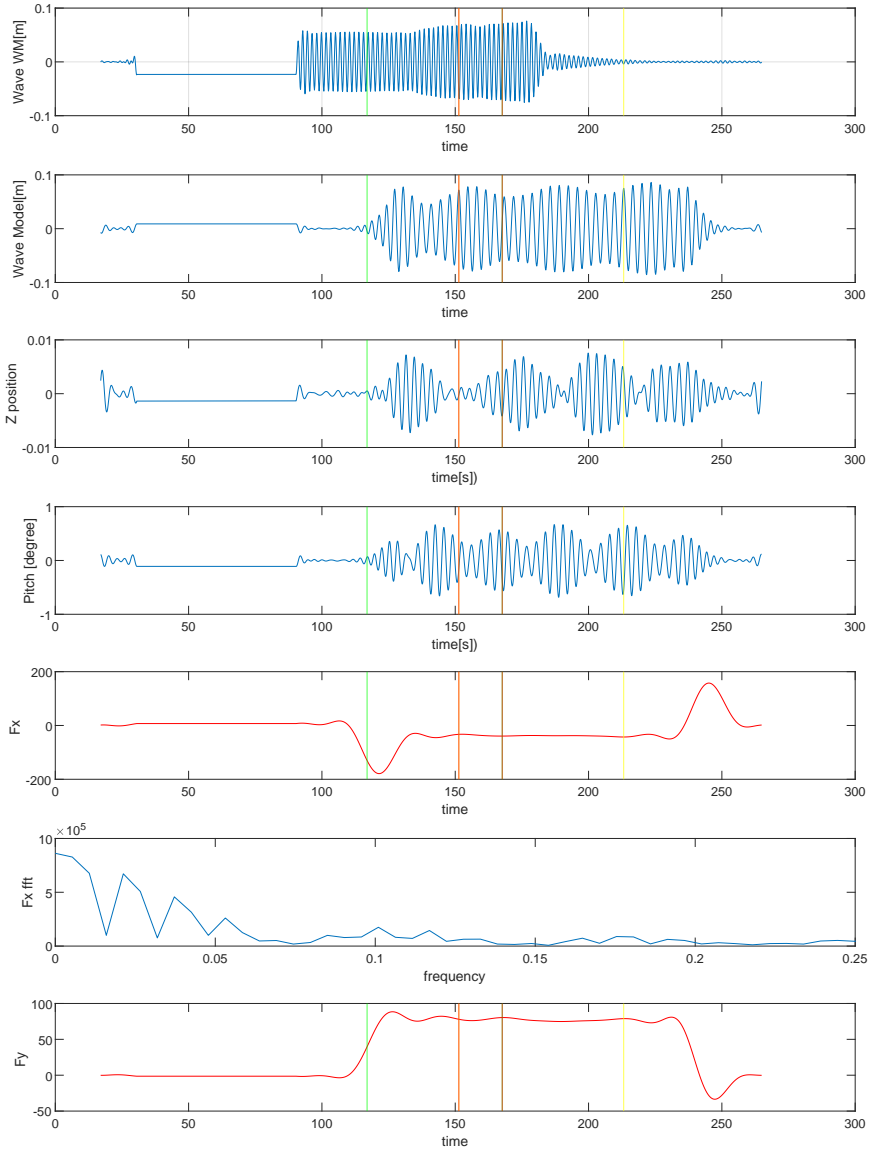
CE7040 Period(s):9.2 Lamda/L:0.7 Drift aple(deg):189 Speed(m/s):7.71



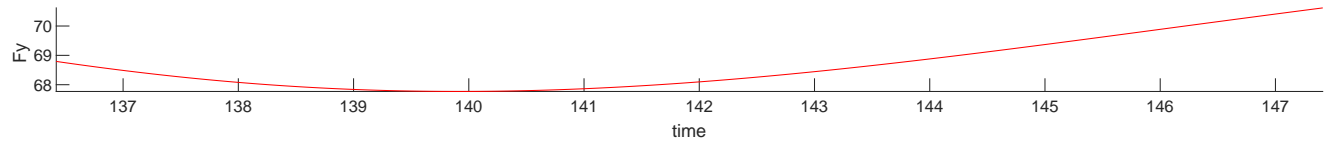
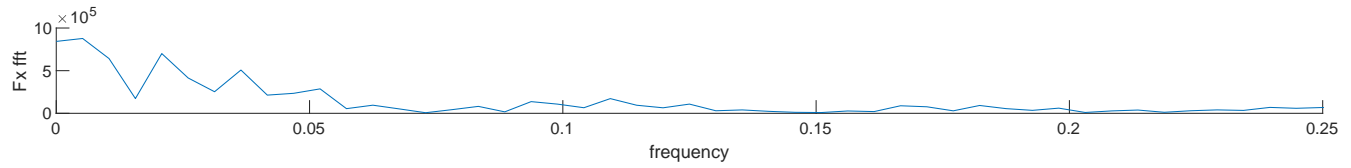
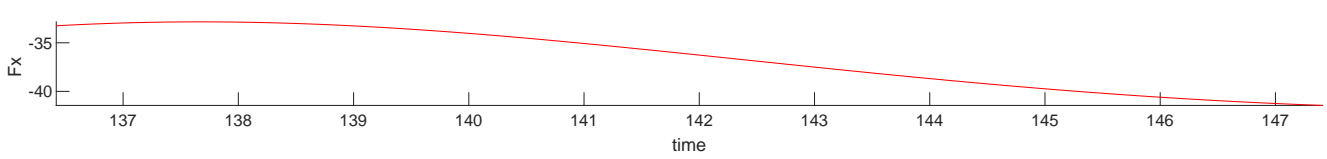
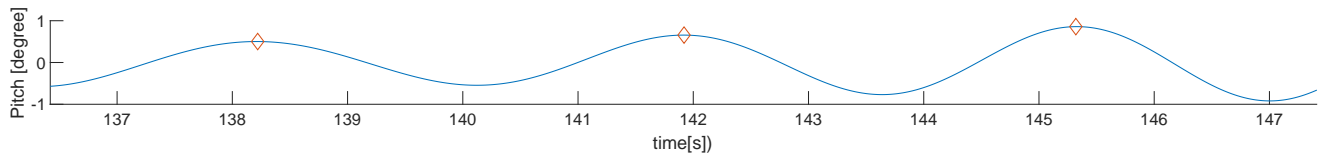
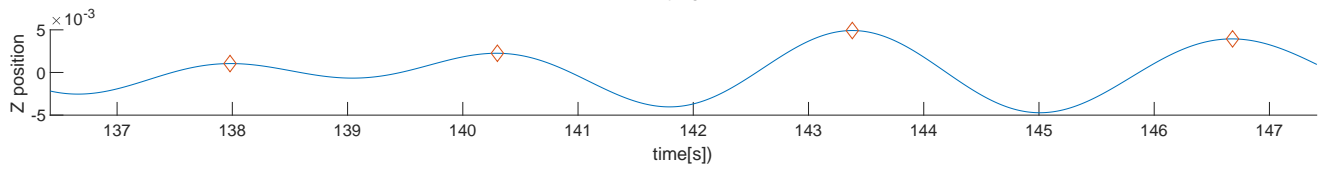
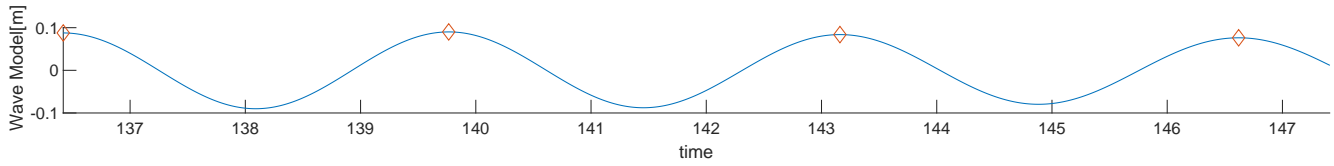
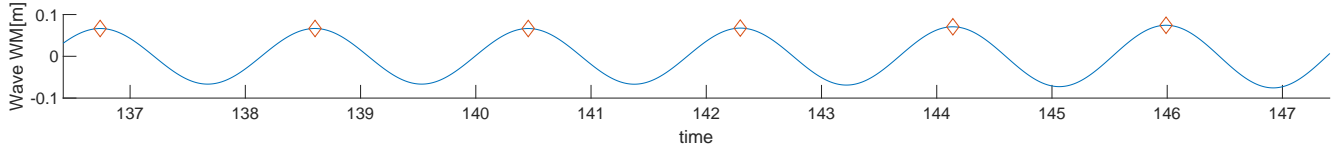
CE7050 Period(s):9.9 Lamda/L:0.81 Drift angle(deg):189 Speed(m/s):7.71



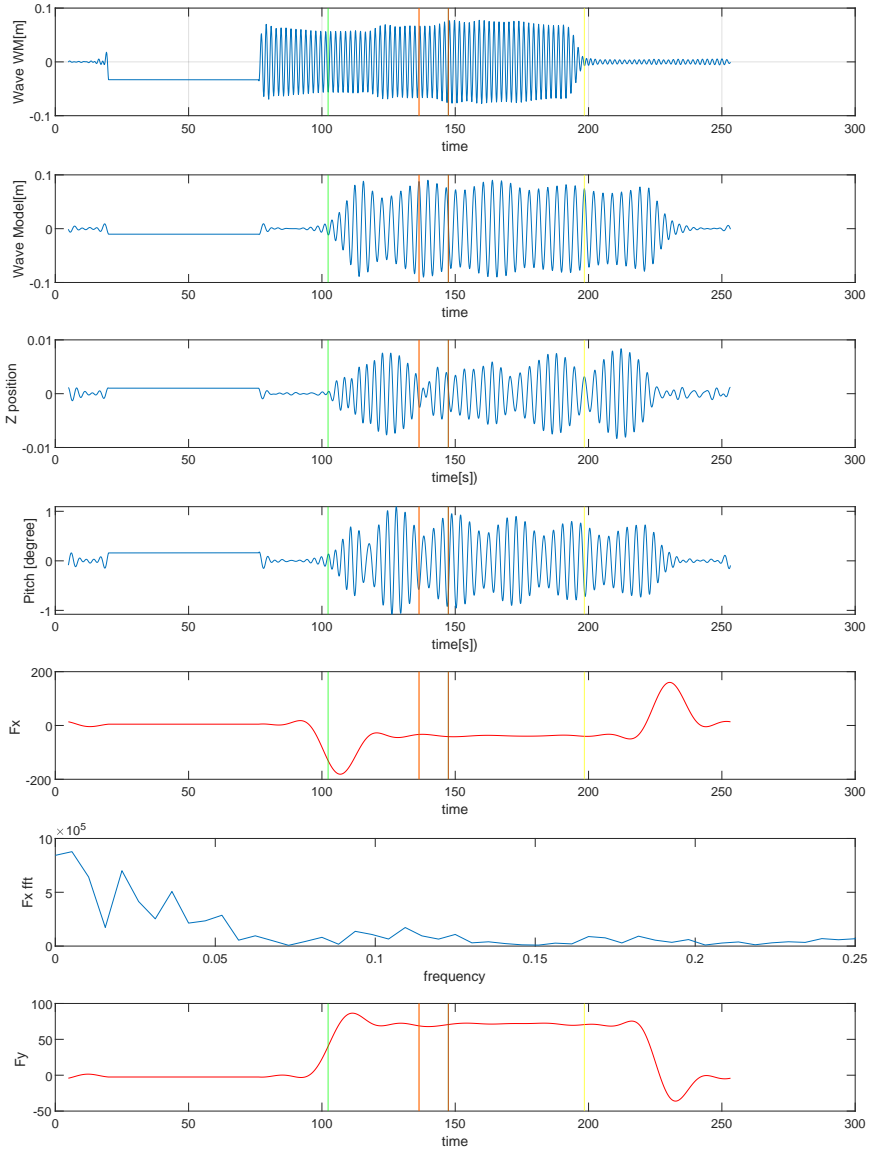
CE7050 Period(s):9.9 Lamda/L:0.81 Drift angle(deg):189 Speed(m/s):7.71



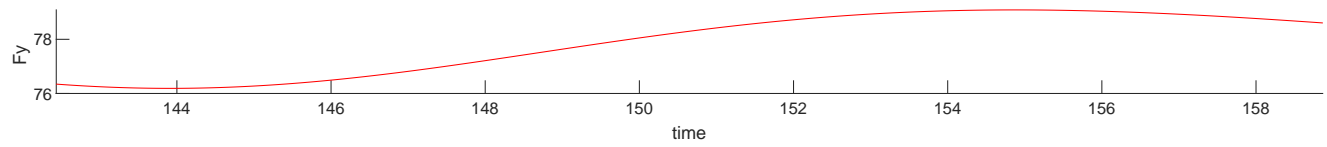
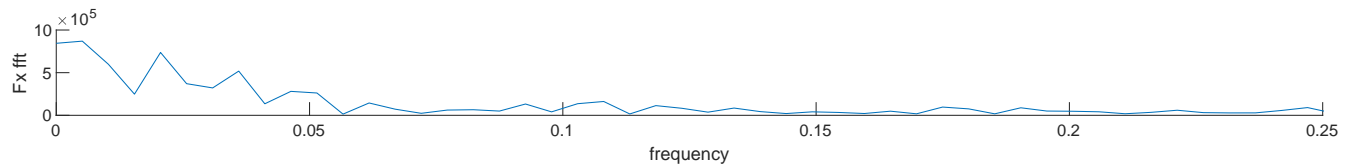
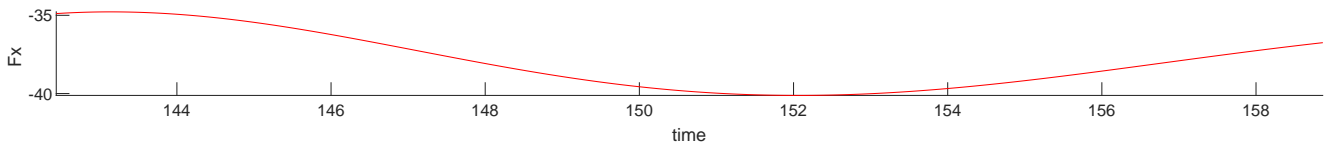
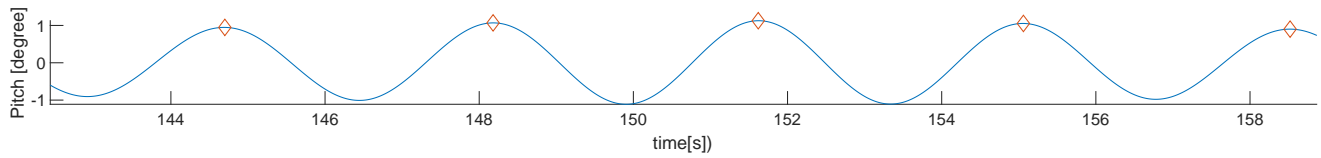
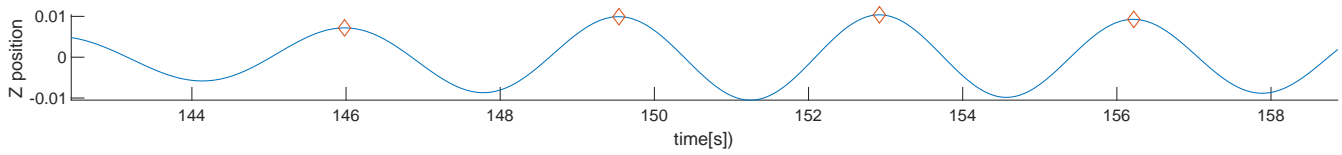
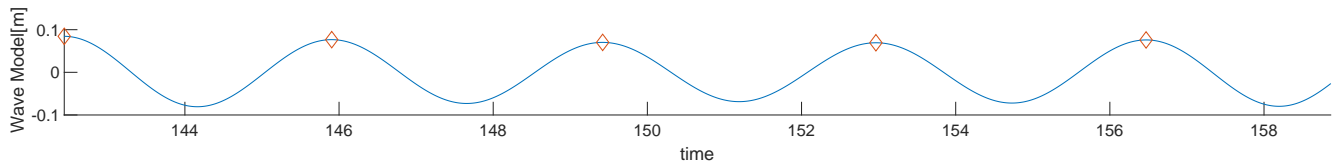
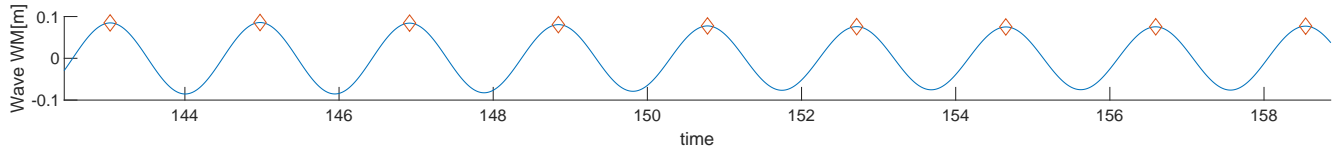
CE7060 Period(s):10.5 Lamda/L:0.91 Drift agle(deg):189 Speed(m/s):7.71



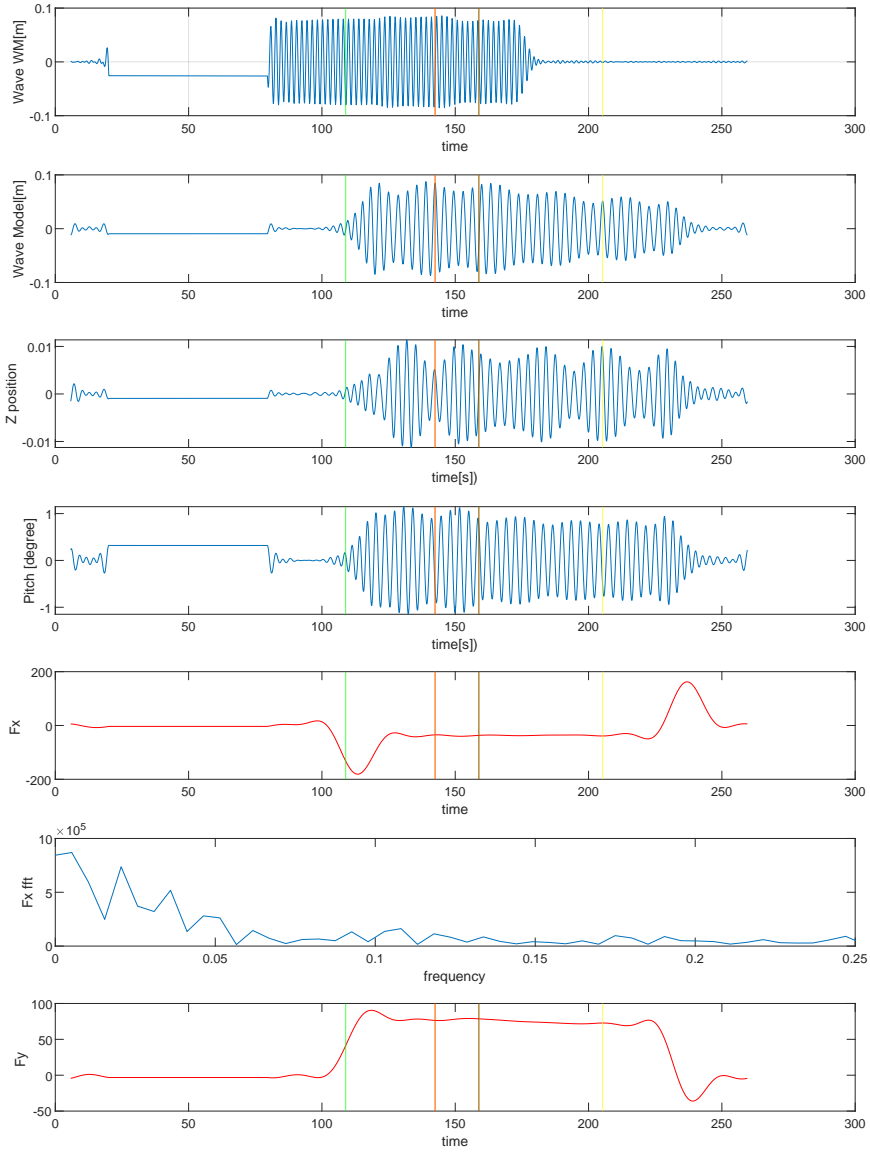
CE7060 Period(s):10.5 Lamda/L:0.91 Drift angle(deg):189 Speed(m/s):7.71



CE7070 Period(s):11 Lamda/L:0.99 Drift agle(deg):189 Speed(m/s):7.71



CE7070 Period(s):11 Lamda/L:0.99 Drift angle(deg):189 Speed(m/s):7.71



D Instrumentation

Marintek

Manual for the Large Yacht Dynamometer

1 INTRODUCTION

The large yacht dynamometer is suitable for testing models up to 900kg, for example, 1:3 scale of the America's Cup Class. The design has been developed and refined over a number of versions. Its principle characteristics are the mechanical separation of the drag and sideforce loads eliminating these interactions and their measurement in tank axes irrespective of yaw angle.

2 GENERAL DESCRIPTION

A schematic general arrangement of the dynamometer is shown in Figure 1, and photographs during commissioning shown in Figure 2 to Figure 5. The dynamometer measures resistance and sideforce on tank axes. This avoids the need to transform the data, which can lead to errors due to inaccuracies in determining the leeway angle. Heel and leeway angles are set between the model and the dynamometer at their attachment, which is within the model below the heave posts.

The forward and aft heave posts carry the side force load, and the centre post carries the drag load. The posts run in linear races which are free to pivot, but restrain the model in yaw and surge. The fore and aft posts are free to pitch and surge and thus the sideforce blocks can measure no resistance. The centre post is free to roll and sway and thus the drag force block can measure no sideforce. The result of this arrangement is the elimination of any interactions between the force measurement axes.

The sideforce blocks, in addition to measuring total sideforce by the sum of their individual forces, also provide a yaw moment measurement by the difference of their individual forces multiplied by their separation.

The model is restricted in roll by two roll beams that are latched at the desired heel angle between the quadrant and the roll beams. The total roll moment is the sum of the individual roll moments.

Heave and pitch may be measured by a pair of heave wire potentiometers located between the fore and aft heave post pivots and the associated heave post clamps. Heave at the LCG or any other longitudinal position is a function of the sum of the individual heaves and pitch is a function of the difference in heave and the separation of the posts (1000mm).

3 MAJOR COMPONENTS

The dynamometer consists of two main structures, each of which carry components, and other sub-assemblies all of which are constructed from aluminium and have a silver anodised surface finish. Components that are not interchangeable are marked to ensure correct orientation.

for locking the model in roll via the quadrants. A scribed line on the roll moment beams is used as a pointer for the determination of applied heel angle. The two Vs are 2½ degrees apart allowing intermediary angles with respect to the 5 degree increments on the quadrants.

3.7 Quadrants

The dynamometer is attached to the model by quadrants at each end. Linearly adjustable pivot pins allow dimensional tolerances in the transverse bulkhead longitudinal spacing, of the model, to be accommodated. The quadrants have notches at 5 degree increments allowing the model to be fixed at the desired heel angle.

4 MEASUREMENT RANGES

The following table sets out the design limits for the dynamometer.

Parameter	Units	Range	Resolution
Heel	degrees	+/- 40	2.5
Leeway	degrees	+/- 8	infinite
Heave	mm	+/- 400	infinite
Pitch	degrees	+/- 7.5	infinite
Drag WOL 21	Newtons	+ 1590 - 1364	infinite
Sideforce Fwd WOL 20	Newtons	+1384 -1649	infinite
Sideforce Aft WOL 22	Newtons	+1433 - 1403	infinite
Roll Moment	N.metres	+/- 2000 nominal	infinite
Yaw Moment	N.metres	+/- 2400 nominal	infinite

Note 1. The heave limit is +/-400 mm, however, this limit must also incorporate the pitching of the model at approximately 1.6 metre centres. The pitch limit is +/-7.5 which with zero heave at the centre post will produce a heave of +/-105 mm at the forward and aft heave posts.

Note 2. The sideforce blocks must also react the yaw moment.

Note 3. The sign convention for the force blocks assumes that positive is when the LVDT transducer is getting longer, e.g. for drag, positive is when the model is going forwards.

The natural frequency of the dynamometer in surge is one of the parameters to be considered when judging its performance in waves. A dynamometer with a high natural frequency is desirable as is a low inherent mass. High in this context is related to the encounter frequency of the waves, which at full scale will be less than 1 Hz.

We estimate that the natural frequency of the dynamometer with a 1:4 scale model attached to be about 4 Hz and with a 1:3 model to be about 2.5 Hz. When scaled to full scale these give 2 Hz and 1.5 Hz respectively, which in our experience, is a sufficient margin over the encounter frequency of 1 Hz.

3.1 Upper Frame

The upper frame is connected to the carriage by non-supplied fixings and should be mounted on stiff aligned cross-members. It can be mounted either way round since it is symmetric fore and aft. This frame has three pivot blocks connected to it, each of which contains linear bearings. The forward and aft pivot blocks have tapped M4 holes to allow fixing of suitable heave potentiometers, for example, Celesco SP 1-50. All three pivot blocks are in their correct orientation when the tapped M4 holes are uppermost.

3.2 Posts and Linear Bearings

The three posts each weigh 12.9kg and are sufficiently stiff so their lateral deflections under sideforce and drag loadings are not significant. The posts have moveable clamps so that they are prevented from sliding right through the linear bearings. The clamps have machined spigots to take the heave potentiometer draw wire fittings.

3.3 Force Blocks

Force blocks are mounted on the bottom of the heave posts using connector blocks. They are machined from a solid stainless steel block. They are a four bar cage design with bars that bend in contraflexure and an LVDT displacement transducer (not supplied) to sense the deflection. This arrangement results in a robust force sensor with in-built overload stops and very low interactions, which are further reduced by the isolation of forces through the arrangements of posts and pivots. The force block that senses drag does not have to transmit any roll moments since the heave post is free to roll. The force blocks that sense side force also have to transmit roll moments since the model is restrained in roll.

The blocks have serial numbers WOL 20 for the forward block, WOL 21 for the centre block and WOL 22 for the aft block. The fore and aft blocks are in the correct orientation when their transducer leads exit to starboard. The centre block, drag, is in the correct orientation when its transducer lead points forward.

Owing to the way in which the stops are incorporated the forces are relieved progressively and the table in Section 4 should be consulted to ensure overload does not occur during measurements. UNDER NO circumstances should the stop screws in the top of the force blocks be adjusted.

3.4 Top Channel

The top channel is bolted to the force blocks via the channel pivot blocks. It is marked 'FWD' at the forward end to ensure its correct orientation with respect to the bottom platform. The top channel is located on the bottom platform by a spigot and connected at the desired leeway using the four T bars and by the nature of its mounting provides an entity that is capable of transmitting resistance and side forces, a yaw moment and roll moments to ground in tank axes, whilst allowing the attached model freedom in heave and pitch.

3.5 Bottom Platform

The bottom platform is of an open frame construction, which allows access to the keel area and provides a wide base on which to clamp the top channel when the model is yawed.

The bottom platform is designated 'FWD' at its forward end to ensure correct orientation with respect to the top channel. At the forward and aft ends leeway angles are scribed every half degree up to 8 degrees.

The bottom platform is connected rigidly to the roll moment beams at the forward and aft ends. Adjustable pivots, integral to the quadrants, allow the bottom platform to rotate with respect to its fore and aft line. The linear adjustment screws allow tolerances between inner faces of the model bulkheads from the nominal 1836mm spacing.

3.6 Roll Beams

The roll moment beams are machined from a solid stainless steel block. They are a two bar cage design with in-built stops and an LVDT sensor (not supplied) to sense deflection and their characteristics are similar to the force blocks described above.

The roll moment beams are connected permanently to the bottom platform and on their top surface each have two 'Vs' incorporated in order that the roll angle latch fits snugly. These two latches, one at each end, are used

Figure 1

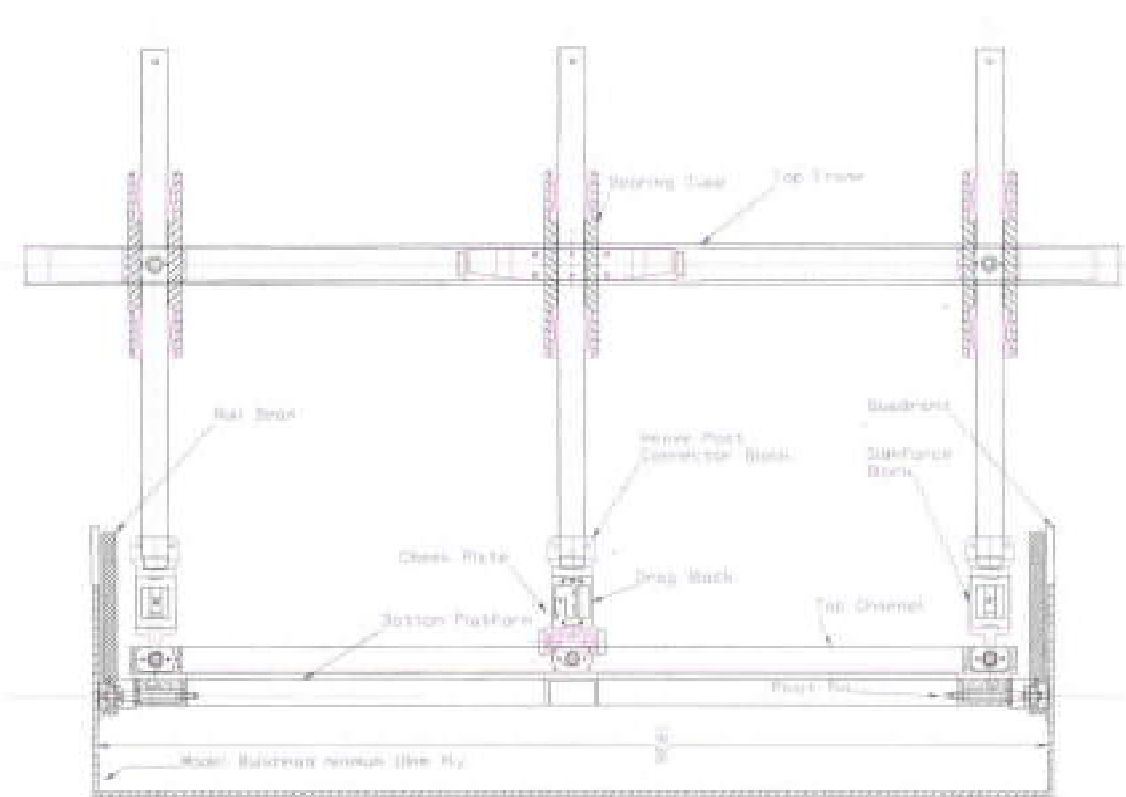


Figure 2

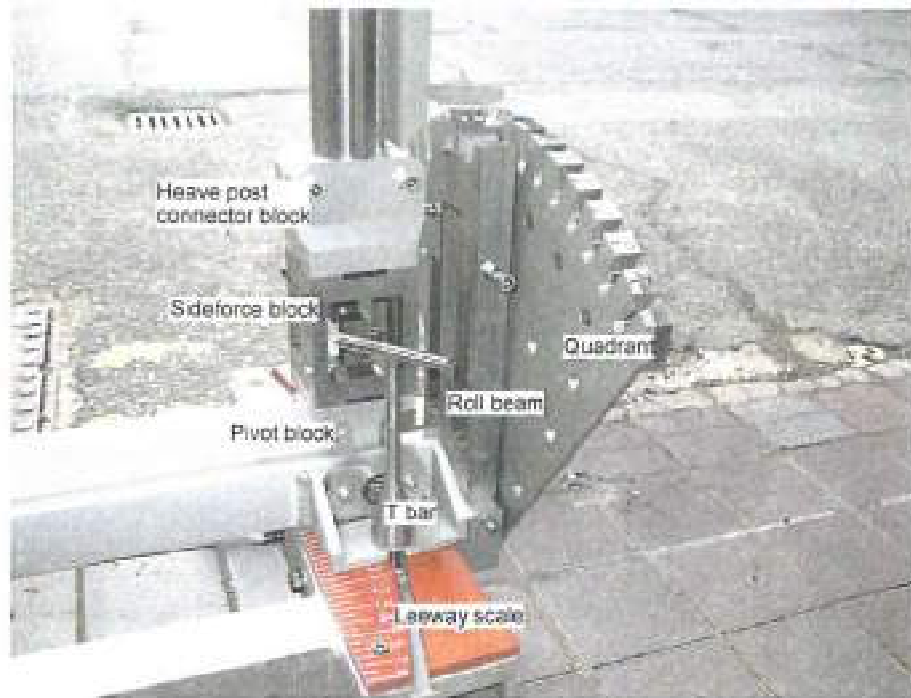


Figure 3



Figure 4

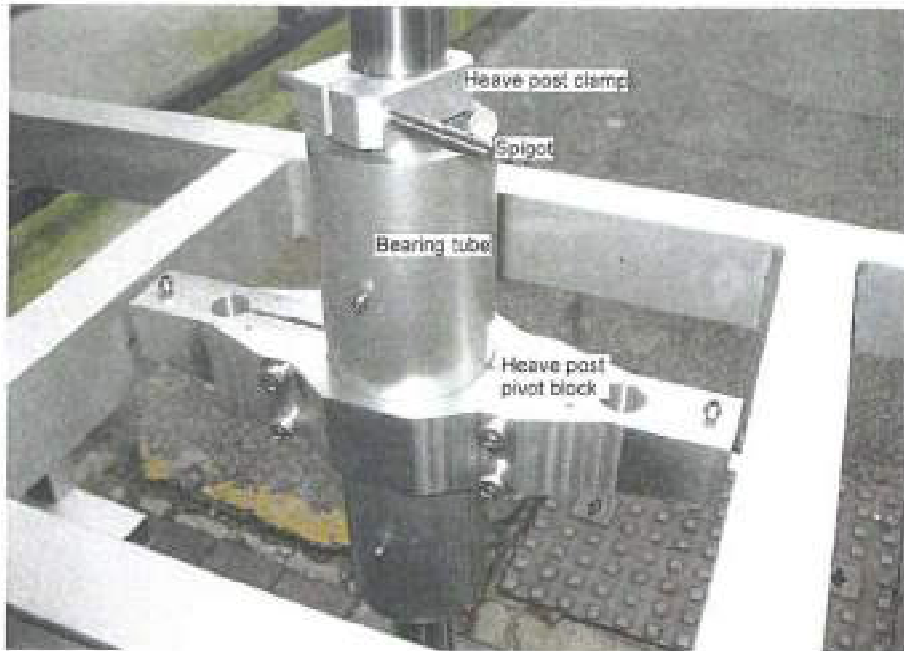
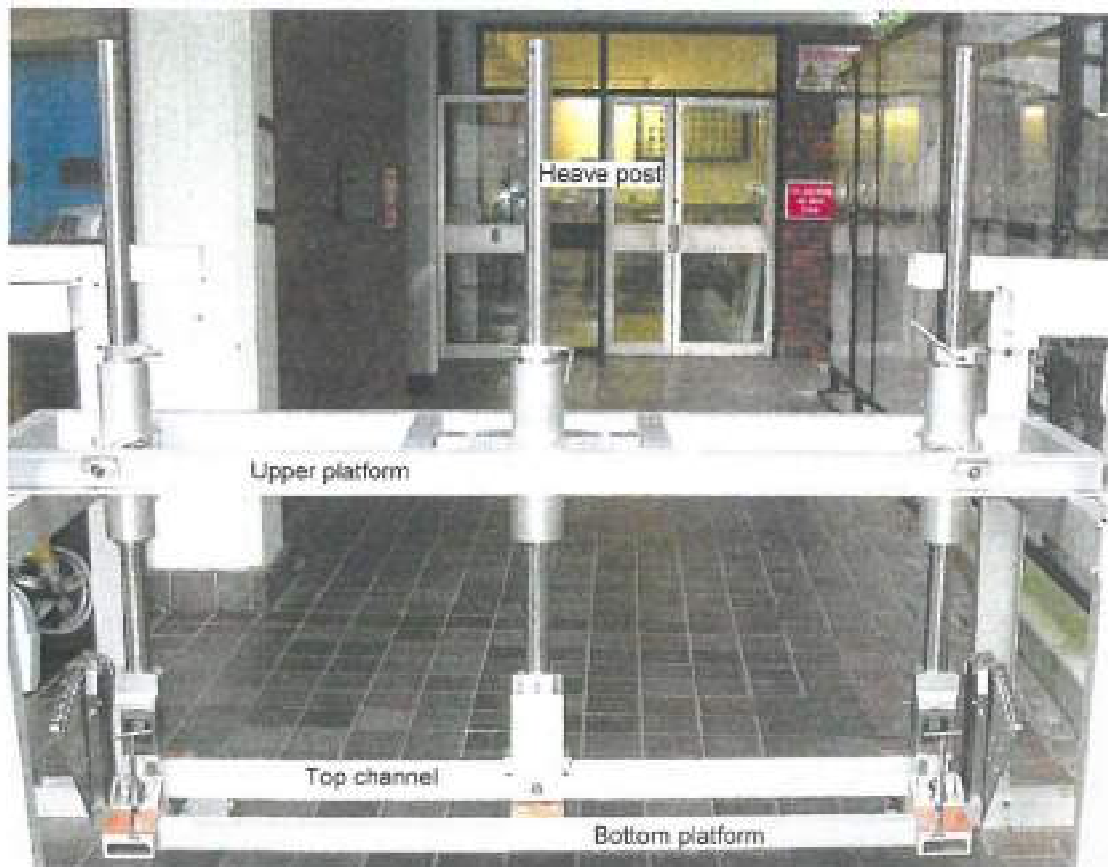
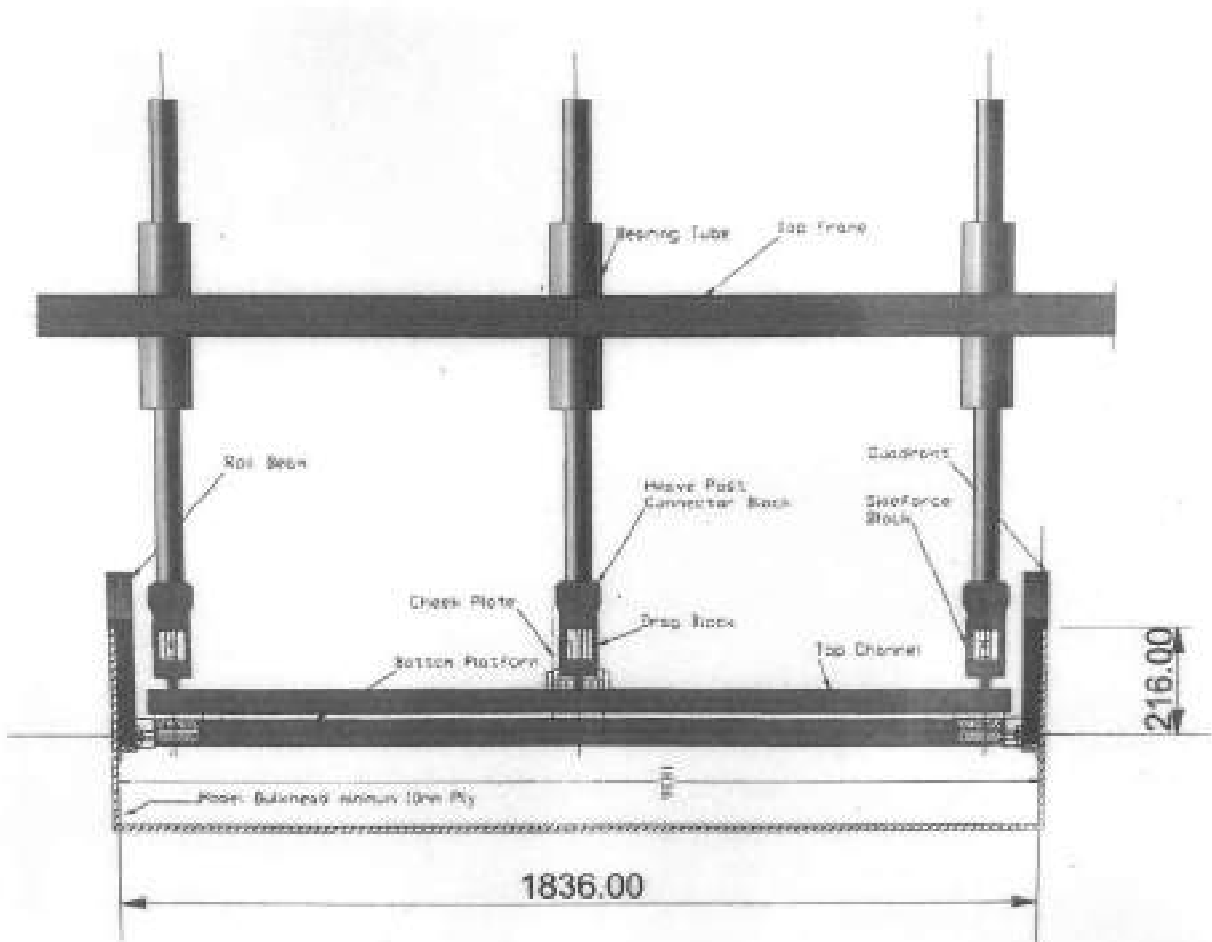


Figure 5





SPECIFICATIONS

Camera output modes	Marker coordinates, high speed video, streaming video
Built-in camera display	128 × 64 graphical high contrast OLED
Camera body	Custom, die-cast aluminium
Camera size Oqus 100	185 × 110 × 124 mm (7.3 × 4.3 × 4.9 inches)
Camera size Oqus 300/500	200 × 145 × 155 mm (7.9 × 5.7 × 6.1 inches)
Weight including optics	1.9 kg Oqus 100 - 2.1 kg Oqus 300/500 (4.2 - 4.6 lbs)
Cooling	Convection cooling
Camera protection level*	Water resistant IP67 housing available
Operating temperature	0-35 °C
Firmware	Upgradeable from host computer
Position data noise level	+/- 1 camera units
Adjustable threshold	Yes
Frame buffer speed	12.9 Gbit/second
Maximum frame buffer size	1152 Mbyte
Cabeling	Hybrid cable with Ethernet and power
Wired communication	Hubless daisy-chained Ethernet 802.3@100Mbps
Wireless communication*	WLAN 802.11b/g@54Mbps
Power supply	Daisy-chained power from mains adaptor
Power	36-72 VDC, 10-16 VDC (battery) at 30 W maximum
Battery*	Available Q4-2008
Lens types*	Standard 40 degrees HFOV (many other options available)
Strobe types supported*	Infrared, red and cyan



	1-SERIES	3-SERIES	5-SERIES
CMOS sensor size (pixels)	640×480	1280×1024	2352×1728
Maximum frame rate at full resolution and field-of-view	250 fps	500 fps	180 fps
Maximum frame rate at full resolution and reduced field-of-view	1000 fps	10000 fps	10000 fps
x-coordinate full scale range (camera units)	41000	82000	150000
y-coordinate full scale range (camera units)	31000	65000	110000
Maximum video frame rate (full resolution)	250 fps	500 fps	180 fps
Maximum video buffer capacity (full res.)	3800 frames	900 frames	290 frames
Maximum video buffer capacity (full resolution and frame rate)	15.2 s	1.8 s	1.6 s

* Optional accessory/feature

Qualisys reserves the right to change specifications without notice

QUALISYS AB

Packhusgatan 6 · 411 13 Gothenburg · SWEDEN
 Tel. +46 31 336 94 00 · Fax. +46 31 336 94 20
 e-mail: sales@qualisys.com · www.qualisys.com



measurement

Accelerometer Calibration Certificate

20642.

Measurement Specialties Inc.

PH: 1-949-716-5377

FX: 1-949-916-5677

www.meas-spec.com

vibration@meas-spec.com

Calibration Date: **October 27, 2017** By: 11972

Model: **3022-020-N** S/N: **5186-016**

With 5VDC supply and 24°C:

Input Resistance: **3.31 kΩ**

Zero Offset: **1.58 mV**

Sensitivity: **1.652 mV/g** at 80Hz

measurement

Accelerometer Calibration Certificate

20645.

Measurement Specialties Inc.

PH: 1-949-716-5377

FX: 1-949-916-5677

www.meas-spec.com

vibration@meas-spec.com

Calibration Date: **October 27, 2017** By: 11972

Model: **3022-020-N** S/N: **5186-013**

With 5VDC supply and 24°C:

Input Resistance: **3.07 kΩ**

Zero Offset: **4.93 mV**

Sensitivity: **2.330 mV/g** at 80Hz

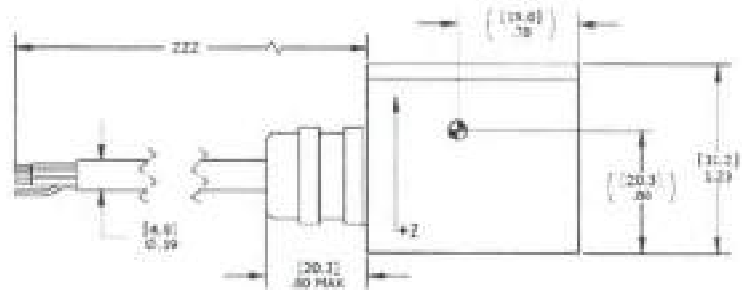
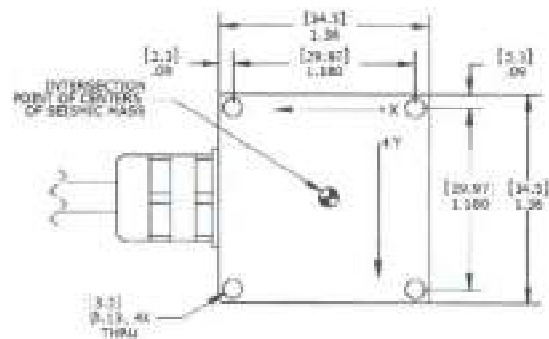
Model 4332 Accelerometer

MEMS Triaxial Accelerometer
Temperature Calibrated
IP68 Protection
Low Noise, High Resolution



The Model 4332 is a low noise triaxial accelerometer offering both static and dynamic response. The accelerometer is packaged in an anodized aluminum housing and is offered in $\pm 2g$ & $\pm 5g$ range. The model 4332 features an integral cable and is certified to IP68 protection. The accelerometer incorporates a 50Hz LP filter and an operating temperature range of $-40^{\circ}C$ to $+85^{\circ}C$.

dimensions



FEATURES

- Micro-g Resolution
- Three Independent Circuits
- Low Current Consumption
- $\pm 2g$ & $\pm 5g$ Dynamic Range
- DC Response
- Temperature Compensation

APPLICATIONS

- Transportation Measurements
- Structural Monitoring
- Bridge Monitoring
- Low Frequency Applications
- Motion Analysis

Model 4332 Accelerometer

performance specifications

All values are typical at +24°C, 10Hz and 12Vdc excitation unless otherwise stated. Measurement Specialties reserves the right to update and change these specifications without notice. Standard product parameters are described in PSC-1004 for Plug & Play DC Accelerometers.

Parameters			Notes
DYNAMIC			
Range (g)	±2	±5	
Sensitivity (mV/g)	1000	400	±10%
-3dB Cutoff Frequency (Hz)	50 +20/-0	50 +20/-0	
Rolloff Above Cutoff Frequency (dB/oct)	-40	-40	
Natural Frequency (Hz)	700	700	
Non-Linearity & Hysteresis (NFSO)	±0.5	±0.5	
Transverse Sensitivity (%)	<3	<3	<2 Typical
Damping Ratio	0.7	0.7	
Shock Limit (g)	5000	5000	
ELECTRICAL			
Zero Acceleration Output (V)	2.5 ±0.1	2.5 ±0.1	
Excitation Voltage (Vdc)	5 to 30	5 to 30	
Excitation Current (mA)	<15	<15	
Full Scale Output Voltage Swing (Vdc)	0.5 to 4.5	0.5 to 4.5	
Output Impedance (Ω)	<100	<100	
Insulation Resistance (MΩ)	>50	>50	@50Vdc
Turn On Time (msec)	<100	<100	
Residual Noise (µg)	80	50	0.1 to 100Hz
Ground Isolation	Isolated from Mounting Surface		
ENVIRONMENTAL			
Thermal Zero Shift (%FSO/°C)	±0.24		0 to +85°C
Thermal Sensitivity Shift (%/°C)	±0.24		0 to +85°C
Operating Temperature (°C)	-40 to 85		
Compensated Temperature (°C)	0 to 85		
Storage Temperature (°C)	-40 to 85		
PHYSICAL			
Case Material	Anodized Aluminum		
Cable	PVC Insulated Leads, Braided Shield, PVC Jacket		
Weight (grams)	<100		
Mounting	4x #4 or M3 Screws		
Mounting Torque	6 lb-in (0.7 N-m)		
AVG (model-4332)	6x 0.14 mm ²		
Calibration supplied:	C5-FREQ-0100	NIST Traceable Amplitude Calibration from 1Hz to 100Hz	
Supplied accessories:	4x #4-40 (1 1/2" length) Socket Head Cap Screw and Washer		
Optional accessories:	101	Three Channel DC Signal Conditioner Amplifier	

The information in this sheet has been carefully reviewed and is believed to be accurate; however, no responsibility is assumed for inaccuracies. Furthermore, this information does not convey to the purchaser of such devices any license under the patent rights to the manufacturer. Measurement Specialties, Inc. reserves the right to make changes without further notice to any product herein. Measurement Specialties, Inc. makes no warranty, representation or guarantee regarding the suitability of its product for any particular purpose, nor does Measurement Specialties, Inc. assume any liability arising out of the application or use of any product or circuit and specifically disclaims any and all liability, including without limitation consequential or incidental damages. Typical parameters can and do vary in different applications. All operating parameters must be validated for each customer application by customer's technical experts. Measurement Specialties, Inc. does not convey any license under its patent rights nor the rights of others.

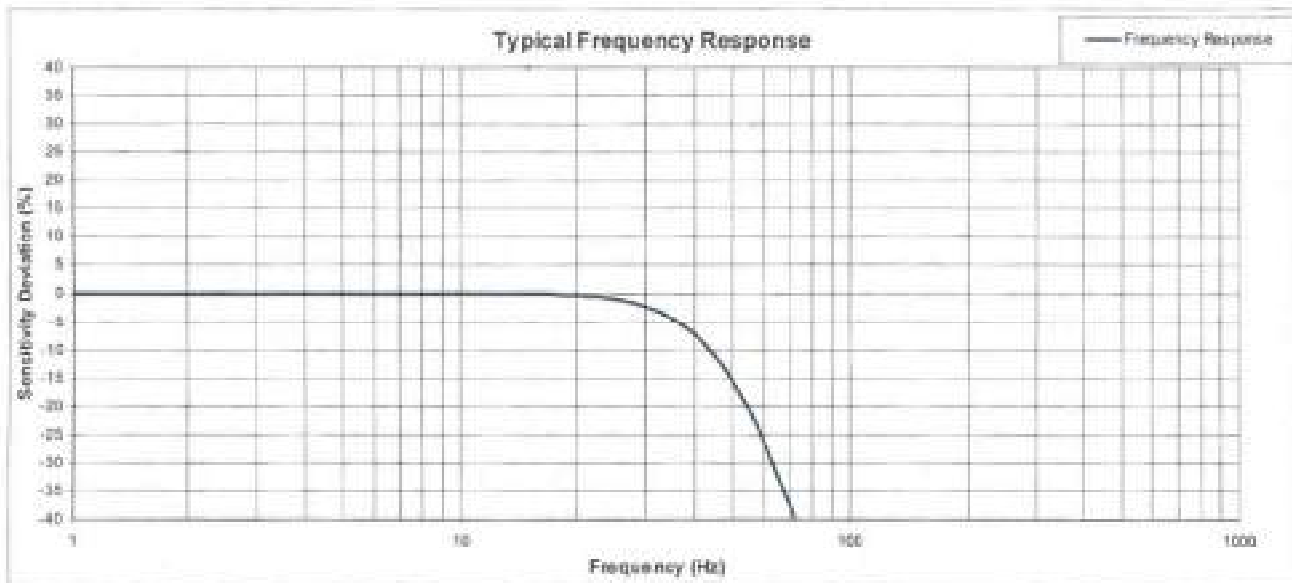
schematic

4332 Schematic

WIRE DESIGNATIONS: WHITE = INPUT (EXCITATION)
 BROWN = OUTPUT X AXIS
 GREEN = OUTPUT Y AXIS
 PINK = OUTPUT Z AXIS
 YELLOW = COMMON (CIRCUIT GROUND)
 GRAY = NO CONNECTION

Model 4332 Accelerometer

performance specifications



ordering info

PART NUMBERING - Model Number+Range+ Cable Length (as applicable)

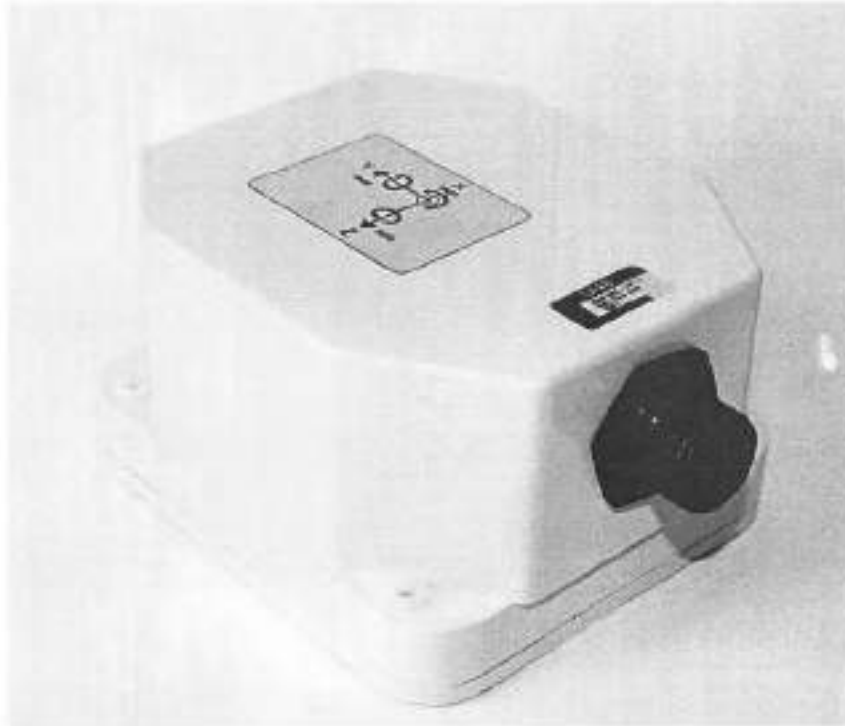
4332-000-CCC

Cable (120 is 120 inches)
Range (002 is 2g)

Example: 4332-002-120

Model 4332, 2g, 120' Cable

Specification
For
Three Axes
Rate Gyro Unit
Part No: 8088 009-141



			Redrawn	100125/ALTM-AN	Obj/Project	FOG	
			Desig/Prep	060512/OMG-DM	Ingr/Next step		Infoklass/ Classification
			Gransk/Checked	080228/OMG-AN	Lagr data/File	8088904141C.DOC	(I)
			Post/Prod	080222/OMGJ-DA	Specification Rate Gyro Unit 8088 009-141		
C	8-41627	1004	Kval/Quality	080302/OQM-BK			
B	8-41074	0807	Post/Proc				
A	Initial	0619	Serie/Serial	080229/OMG-HA			
Issue	Ad m/ECC. No.	W	Saab		no/No.	S-8088904-141	Sider/Page 1 (4)

Delta dokument utlämnat till This document issued to

Ljphövisstien till detta dokument är och förblir vår.
Documentet får inte obehörigen användas eller delgas annan.
Saab AB

The copyright ownership of this document is and will
remain ours. The document must not be used, without our
authorization or brought to the knowledge of a third party.
Saab AB

REVISION HISTORY

Issue	Date	ECO (AO)	Description
A	060512		Initial Issue
B	080213	8-41074	See AO-8-41074
C	100125	8-41627	Power @28VDC 10W <i>changed to 12W</i>

Issue		Part No.	Issue Page
C	Saab	S-8088904-141	2 (4)

Characteristics	Unit	Value	ATP
- Operating Range (OR)	°/sec	±60	X
- Tracking Range (TR)	°/sec	±20	X
- Scale Factor Nominal at TR	mV DC/°/sec	166,7	X
- SF error at TR @ RT	% of TR	±0,2	X
- SF error at OR @ RT	% of OR	±1,0	X
- SF variation over temp.-range ¹	%	±0,3	X
- Linearity error over TR	% of TR	±0,1	X
- Linearity error over OR	% of OR	±0,8	X
- Threshold	°/sec max	0,001	X
- Resolution	°/sec max	0,001	X
- Hysteresis (1/2 alg. diff)	°/sec max	NA	
- G-insensitive drift at 20°C (initial cond.)	°/h max	100	X
- Drift variation during 1 min	°/h max	5	
- Drift variation (peak to peak in -30/+70°C range)	°/h	40	X
- Bandwidth (-90° phase lag)	Hz min	100	X
- Sync Time	sec max	1	X
- Noise (up to 100Hz)	°/sec RMS max	0,02	
- Noise (100 - 1000Hz)	°/sec RMS max	0,05	
- Misalignment	° max	0,5	X
- Output Load	kΩ	80	
- Weight	gram max	1400	
- Built-in-test	VDC _{OK}	3,5-6,0	X

Power Requirements

- Supply Voltage	VDC (nom 28)	18-32	
- Power @ 28 V	W max	12	X
Tested according to MIL-STD-1275B			

Environment

- Shock (half sine)	g : msec	300 : 1	
- Shock (half sine)	g : msec	40 : 11	
- Vibration, sine	g : Hz	10: 20-2000	
- Vibration, random	g ² /Hz : Hz	0,1 : 20-2000	
- Bump	ms/g	4-7/10	
- Temperature range operating	°C	-30 - +70	
- Temperature range storage	°C	-46 - +75	

Electromagnetic Interference – Design qualified according to MIL-STD-461E

1) Change from RT to either extreme of operating temperature, max

X = Tested during ATP

OR = Operating Range

TR = Tracking Range

RT = Room Temperature (+22 ± 3°C)

OTR = Over Temperature Range

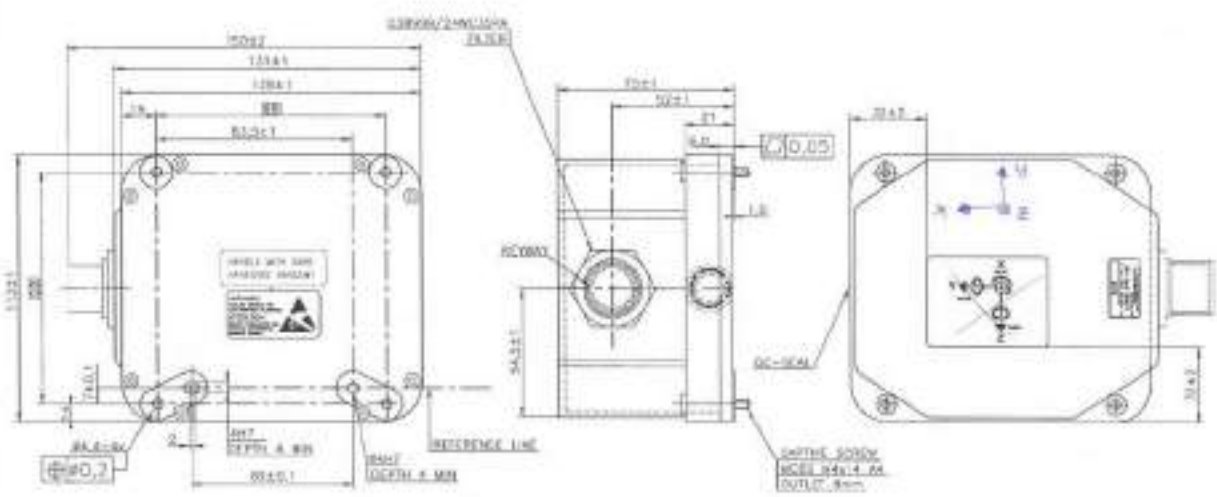
FS = Full Scale

SF = Scale Factor

ATP = Acceptance Test

Issue	Part No.	Rev/Ed	Page
C	Saab	S-8088904-141	3 (4)

Part Number: S-9088904-141
 Description: Saab
 Revision: 4 (4)
 Date: 1/1/00



KEY

1	+28 VDC
2	+28 VDC
3	0 V (28V RETURN)
4	0 V (28V RETURN)
5	CONTINUITY LOOP
6	X-AXIS OUTPUT HI
7	X-AXIS OUTPUT LO
8	X-AXIS SHIELD
9	Y-AXIS OUTPUT HI
10	Y-AXIS OUTPUT LO
11	Y-AXIS SHIELD
12	MANUFACTURER USE (30A)
13	0790 OK
14	MANUFACTURER USE (50)
15	MANUFACTURER USE (WPCN)
16	CHASSIS GND
17	050A GND
18	Z-AXIS OUTPUT HI
19	Z-AXIS OUTPUT LO
20	Z-AXIS SHIELD

NOTE:
 MATERIAL: ALUMINUM (STRESS RELIEVED)
 CHROMATING: PER MIL-C-2541 CLASS 3 OR ISO 10546 CLASS 3.
 COLOUR: PEARL WHITE RA1.101.3 SEMI-GLOSS TO GLOSS.
 POSITIVE ROTATION AS SHOWN SHALL PRODUCE POSITIVE OUTPUT SIGNALS.
 WEIGHT: 0.4 kg.

E MATLAB Code

```
”
1
2 %files to read-----
3
4 [numbers ,text ,textAndNumbers] = xlsread('testno_list_for_analysis.
   xlsx');
5 no_of_file=length(textAndNumbers(:,8));
6 filelist=string(transpose((textAndNumbers(2:no_of_file,8))));
7 fileno=string(transpose((textAndNumbers(2:no_of_file,1))));
8 period=string(transpose((textAndNumbers(2:no_of_file,4))));
9 lamda_l=string(transpose((textAndNumbers(2:no_of_file,5))));
10 drift=string(transpose((textAndNumbers(2:no_of_file,6))));
11 speed=string(transpose((textAndNumbers(2:no_of_file,7))));
12 w_e=(transpose(numbers(:,11)));
13 A=(transpose(numbers(:,12)));
14 K=(transpose(numbers(:,13)));
15 te=(transpose(numbers(:,14)));
16 tm=(transpose(numbers(:,8)));
17
18 %Essential paramaters-----
19
20 nondim_para=-1*1000*9.81*((1.009375^2)/5.9375);
21 cw_4000=-31.3134;
22 cw_5081=-34.3085;
23 cw_fy_4000=-0.377;
24 cw_fy_5081=71.1189;
25 endtime=numbers(:,2);
26
27 %Making required empty matrices
   -----
28 file_no=length(filelist);
29 startpos=zeros(file_no);
30 endpos=zeros(file_no);
31 startpos_oq=zeros(file_no);
32 endpos_oq=zeros(file_no);
33 tw1=zeros(file_no,4);
34 tw1_index=zeros(file_no,4);
35 tw2=zeros(file_no,4);
36 tw2_index=zeros(file_no,4);
37 tw_final=zeros(file_no,4);
38 tw_final_index=zeros(file_no,4);
39 comparison_tw1_force=zeros(file_no,4);
40 comparison_tw1_oq=zeros(file_no,4);
41 comparison_tw2=zeros(file_no,4);
```

```

42 slider_fx=zeros(file_no,150);
43 slider_fy=zeros(file_no,150);
44 slider_cr=zeros(file_no,150);
45 slider_cr_fy=zeros(file_no,150);
46 slider_heave=zeros(file_no,150);
47 slider_zpos=zeros(file_no,150);
48 slider_zposacc=zeros(file_no,150);
49 slider_pitch=zeros(file_no,150);
50 slider_avgheave16xxx=zeros(file_no,150);
51 slider_avgpitch16xxx=zeros(file_no,150);
52 slider_wp3=zeros(file_no,150);
53 slider_wp1=zeros(file_no,150);
54 slider_heave_rao=zeros(file_no,150);
55 slider_zpos_rao=zeros(file_no,150);
56 slider_zposacc_rao=zeros(file_no,150);
57 slider_pitch_rao=zeros(file_no,150);
58 slidingmean_fx=zeros(file_no,1);
59 slidingmean_fy=zeros(file_no,1);
60 slidingmean_zpos=zeros(file_no,1);
61 slidingmean_zposacc=zeros(file_no,1);
62 slidingmean_heave=zeros(file_no,1);
63 slidingmean_pitch=zeros(file_no,1);
64 slidingmean_wp3=zeros(file_no,1);
65 slidingmean_wp1=zeros(file_no,1);
66 slidingmean_cr=zeros(file_no,1);
67 slidingmean_cr_fy=zeros(file_no,1);
68 slidingmean_zpos_rao=zeros(file_no,1);
69 slidingmean_zposacc_rao=zeros(file_no,1);
70 slidingmean_heave_rao=zeros(file_no,1);
71 slidingmean_pitch_rao=zeros(file_no,1);
72 slidingmean_fx_std=zeros(file_no,1);
73 slidingmean_cr_std=zeros(file_no,1);
74 slidingmean_cr_fy_std=zeros(file_no,1);
75 slidingmean_zpos_std=zeros(file_no,1);
76 slidingmean_zposacc_std=zeros(file_no,1);
77 slidingmean_heave_std=zeros(file_no,1);
78 slidingmean_pitch_std=zeros(file_no,1);
79 slidingmean_heaverao_std=zeros(file_no,1);
80 slidingmean_zposrao_std=zeros(file_no,1);
81 slidingmean_zposaccrao_std=zeros(file_no,1);
82 slidingmean_pitchrao_std=zeros(file_no,1);
83 heave_mean=zeros(file_no,1);
84 fx_mean=zeros(file_no,1);
85 error_bar_fx=zeros(file_no,5);
86 error_bar_heave=zeros(file_no,5);
87 error_bar_pitch=zeros(file_no,5);

```

```

88 std_values_fx=zeros(file_no,1);
89 std_values_heave_16xxx=zeros(file_no,1);
90 std_values_pitch_16xxx=zeros(file_no,1);
91
92 %Loop starts
-----
93 for i=1:file_no
94
95
96     %select model scale cw
97     if i<19
98         cw=0;
99         cw_fy=0;
100    elseif i>=19&&i<38
101        cw=cw_4000;
102        cw_fy=cw_fy_4000;
103    elseif i>=38&&i<49
104        cw=cw_5081;
105        cw_fy=cw_fy_5081;
106    elseif i>=49&&i<61
107        cw=cw_4000;
108        cw_fy=cw_fy_4000;
109    elseif i>=61
110        cw=cw_5081;
111        cw_fy=cw_fy_5081;
112    end
113
114
115    disp('    =')
116    disp(i)
117    disp('tw1 strt_time')
118    disp(starttime(i))
119    disp('tw1 end time')
120    disp(endtime(i))
121
122
123
124    [a1,a2]=catman_read_dt(filelist(i));
125    plot_title=append(fileno(i),"    ","Period(s):",period(i),"    ","
        Lamda/L:",lamda_l(i),"    ","Drift agle(deg):",drift(i),"    ","
        Speed(m/s):",speed(i));
126
127    disp(filelist(i))
128 %---parameters for bandpass filtering
-----

```

```

129
130 motion_flow=(0.8*1/te(i));
131 motion_fhigh=(1.2*(1/te(i)));
132 force_flow=0;
133 force_fhigh=0.05;
134 wp3_flow=(0.8*(1/te(i)));
135 wp3_fhigh=(1.2*(1/te(i)));
136 wp1_flow=(0.8*(1/tm(i)));
137 wp1_fhigh=(1.2*(1/tm(i)));
138
139 %extract data to variables
-----
140 time_raw=a2(1).data; %time for force
    transducers
141 time_oq_raw=a2(2).data; %time for oqus
142
143 %Sailboat Dynamometer
144 fx_raw=a2(9).data; %Fx
145 fx_bp=bpass2(transpose(fx_raw),0.005,force_flow,force_fhigh,1,0,
    ' ',0);
146 fx_fft=fft(fx_raw);
147 force_f=0:200/length(time_raw):200-(200/length(time_raw));
148
149 fytot_raw=a2(63).data; %Fytot
150 fytot_fft=fft(fytot_raw);
151 fy_bp=bpass2(transpose(fytot_raw),0.005,force_flow,force_fhigh
    ,1,0,' ',0);
152 fyfrnt_raw=a2(8).data; %Fyfrnt
153 fyfrnt_fft=fft(fyfrnt_raw);
154 fyaft_raw=a2(10).data; %Fyaft
155 fyaft_fft=fft(fyaft_raw);
156 mz_raw=a2(64).data; %MZ_sdyn
157 mz_fft=fft(mz_raw);
158 mx_tot_raw=a2(65).data; %Mxtot
159
160 %OQUS
161 xpos1_raw=a2(25).data; %xpos1
162
163 ypos1_raw=a2(26).data; %ypos1
164
165 zpos1_raw=bpass2(transpose(a2(27).data),0.02,motion_flow,
    motion_fhigh,1,0,' ',0); %zpos1
166 roll1_raw=a2(28).data; %roll1
167
168 pitch1_raw=bpass2(transpose(a2(29).data),0.02,motion_flow,
    motion_fhigh,1,0,' ',0); %pitch1

```



```

169
170 yaw1_raw=a2(30).data; %yaw1
171
172 rollrate_raw=a2(60).data; %rollrate
173
174 pitchrate_raw=a2(61).data; %pitchrate
175 yawrate_raw=a2(62).data; %yawrate
176
177 %Accelerometer
178 acc_fpz_16316=a2(47).data;
179 acc_fpz_20642=a2(48).data;
180 acc_apz_16426=a2(51).data;
181 acc_apz_20645=a2(52).data;
182 pos_fpz_16316=acc2pos(transpose(a2(47).data),0.005,0.25);
183 pos_apz_16426=acc2pos(transpose(a2(51).data),0.005,0.25);
184 zpos_acc=(pos_fpz_16316+pos_apz_16426)/2;
185 pitch_16xxx=(pos_fpz_16316-pos_apz_16426/5.241);
186 pos_apz_20645=acc2pos(transpose(a2(52).data),0.005,0.25);
187 pos_fpz_20642=acc2pos(transpose(a2(48).data),0.005,0.25);
188 heave_20xxx=(pos_fpz_20642+pos_apz_20645)/2;
189 pitch_20xxx=(pos_fpz_20642-pos_apz_20645)/3.625;
190
191 %Waveprobes
192 WP1=a2(66).data; %WP1
193 [WP1_transpose,Tp1,FF1,Fx1] = bpass2(transpose(WP1),0.005,
wp1_flow,wp1_fhigh,0,0,'',0);
194 WP1_bm_raw=transpose(WP1_transpose);
195
196 WP2_bm_raw=a2(67).data; %WP2
197
198 WP3=a2(53).data; %WP3
199 [WP3_transpose,Tp,FF,Fx] = bpass2(transpose(WP3),0.005,wp3_flow,
wp3_fhigh,0,0,'',0);
200 WP3_car_raw=transpose(WP3_transpose);
201 WP4_car_raw=a2(54).data; %WP4
202
203 WP_us_raw=a2(68).data; %WP_ULTRA SOUND
204
205
206 car_pos_raw=a2(55).data; %carrage position
207
208
209 %% Find Peaks
210
211 [pks_wp3,locs_wp3]=findpeaks(WP3_car_raw,'MinPeakDistance',0.8*te
(i));

```

```

212 [pks_wp1,locs_wp1]=findpeaks(WP1_bm_raw,'MinPeakDistance',0.8*te(
    i));
213 [pks_zpos,locs_zpos]=findpeaks(zpos1_raw,'MinPeakDistance',0.8*te
    (i));
214 [pks_pitch,locs_pitch]=findpeaks(pitch1_raw,'MinPeakDistance'
    ,0.8*te(i));
215 [pks_zposacc,locs_zposacc]=findpeaks(zpos_acc,'MinPeakDistance'
    ,0.8*te(i));
216
217
218 %% LVL 1 Time window
219
220 %finding matching starttime and endtime lvl1
    -----
221
222 %in trnasducer time scale
223
224 %note:lvl1 is read as lvlone
225
226     lvl1_sp1=starttime(i)-0.005;
227     disp('lvlsp1')
228     disp(lvl1_sp1)
229     lvl1_sp2=starttime(i)+0.005;
230     lvl1_ep1=endtime(i)-0.005;
231     lvl1_ep2=endtime(i)+0.005;
232
233
234     for u=1:length(time_raw)
235         if time_raw(u)>lvl1_sp1&&time_raw(u)<lvl1_sp2
236
237             tw1(i,1)=time_raw(u);
238             tw1_index(i,1)=u;
239             disp('sp is')
240             time_raw(u)
241             disp('tw1 is')
242             disp('sp found')
243             break
244
245
246         else
247             tw1(i,1)=time_raw(1);
248             tw1_index(i,1)=1;
249
250
251         end
252     end

```

```

253
254
255     for u=1:length(time_raw)
256         if time_raw(u)>lvl1_ep1&&time_raw(u)<lvl1_ep2
257
258             tw1(i,2)=time_raw(u);
259             tw1_index(i,2)=u;
260             disp('ep is')
261             time_raw(u)
262             disp('tw1 is')
263             disp(tw1(i,2))
264             disp('ep found')
265             break
266
267
268         else
269             tw1(i,2)=time_raw(length(time_raw));
270             tw1_index(i,2)=length(time_raw);
271
272
273         end
274     end
275
276
277 %in oqus time scale
278
279     lvl1_oq_sp1=starttime(i)-0.02;
280     lvl1_oq_sp2=starttime(i)+0.02;
281     lvl1_oq_ep1=endtime(i)-0.02;
282     lvl1_oq_ep2=endtime(i)+0.02;
283
284     for s=1:length(time_oq_raw)
285         if time_oq_raw(s)>lvl1_oq_sp1&&time_oq_raw(s)<lvl1_oq_sp2
286             tw1(i,3)=time_oq_raw(s);
287             tw1_index(i,3)=s;
288             disp('lvl-oq_sp1 is')
289             disp(lvl1_oq_sp1)
290             disp('tw_oq is')
291             disp(tw1(i,3))
292             break
293
294         else
295             tw1(i,3)=time_oq_raw(1);
296             tw1_index(i,3)=1;
297
298         end

```

```

299     end
300     for t=1:length(time_oq_raw)
301
302         if time_oq_raw(t)>lvl1_oq_ep1&&time_oq_raw(t)<lvl1_oq_ep2
303             tw1(i,4)=time_oq_raw(t);
304             tw1_index(i,4)=t;
305             disp('lvl-oq_ep1 is')
306             disp(lvl1_oq_ep1)
307             disp('tw_oq is')
308             disp(tw1(i,4))
309             break
310
311         else
312             tw1(i,4)=time_oq_raw(length(time_oq_raw));
313             tw1_index(i,4)=length(time_oq_raw);
314
315         end
316     end
317
318
319
320
321 %% lvl 2 time window
322
323     if i<19
324
325         [min_locs_value1,min_locs_index1]=min(abs(locs_wp3-(length(
326             time_raw)-11250)));
327         tw2(i,1)=time_raw(locs_wp3(min_locs_index1));
328         tw2_index(i,1)=locs_wp3(min_locs_index1);
329
330         [min_locs_value2,min_locs_index2]=min(abs(locs_wp3-(length(
331             time_raw)-5000)));
332         tw2(i,2)=time_raw(locs_wp3(min_locs_index2));
333         tw2_index(i,2)=locs_wp3(min_locs_index2);
334
335     elseif i>=19&&i<49
336
337         for r=1:length(locs_wp3)
338             if r==length(locs_wp3)
339                 disp('not found')
340             elseif car_pos_raw(locs_wp3(r))>110
341                 tw2(i,1)=time_raw(locs_wp3(r));
342                 tw2_index(i,1)=locs_wp3(r);
343                 break

```

```

343         end
344     end
345
346     for q=length(locs_wp3):-1:1
347         if q==1
348             disp('not found')
349         elseif car_pos_raw(locs_wp3(q))<200
350             tw2(i,2)=time_raw(locs_wp3(q));
351             tw2_index(i,2)=locs_wp3(q);
352             break
353         end
354     end
355
356     elseif i>=49
357
358         for r=1:length(locs_wp3)
359             if r==length(locs_wp3)
360                 disp('not found')
361             elseif car_pos_raw(locs_wp3(r))<200
362                 tw2(i,1)=time_raw(locs_wp3(r));
363                 tw2_index(i,1)=locs_wp3(r);
364                 break
365             end
366         end
367
368         for q=length(locs_wp3):-1:1
369             if q==1
370                 disp('not found')
371             elseif car_pos_raw(locs_wp3(q))>110
372                 tw2(i,2)=time_raw(locs_wp3(q));
373                 tw2_index(i,2)=locs_wp3(q);
374                 break
375             end
376         end
377
378     end
379
380     %--finding oqus matching time for lvl 2 tw
381     -----
382     lvl2_oq_sp1=tw2(i,1)-0.02;
383     lvl2_oq_sp2=tw2(i,1)+0.02;
384     lvl2_oq_ep1=tw2(i,2)-0.02;
385     lvl2_oq_ep2=tw2(i,2)+0.02;
386
387     oq_len=length(time_oq_raw);

```

```

388
389     for z=1:oq_len
390         if time_oq_raw(z)<lvl2_oq_sp2&&time_oq_raw(z)>lvl2_oq_sp1
391             tw2(i,3)=time_oq_raw(z);
392             tw2_index(i,3)=z;
393
394             break
395         end
396     end
397     for y=1:oq_len
398         if time_oq_raw(y)<lvl2_oq_ep2&&time_oq_raw(y)>lvl2_oq_ep1
399             tw2(i,4)=time_oq_raw(y);
400             tw2_index(i,4)=y;
401
402             break
403         end
404     end
405
406 %% creating final time window
407
408 %forcestart time
409
410     if max(tw1(i,1),tw2(i,1))==tw1(i,1)
411
412         [min_locs_value3,min_locs_index3]=min(abs(locs-tw1_index(i
413             ,1)));
414         tw_final(i,1)=time_raw(locs(min_locs_index3));
415         tw_final_index(i,1)=locs(min_locs_index3);
416
417     else
418         tw_final(i,1)=tw2(i,1);
419         tw_final_index(i,1)=tw2_index(i,1);
420     end
421
422 %force endtime
423
424     if min(tw1(i,2),tw2(i,2))==tw1(i,2)
425
426         tw_final(i,2)=tw1(i,2);
427         tw_final_index(i,2)=tw1_index(i,2);
428
429     else
430         tw_final(i,2)=tw2(i,2);
431         tw_final_index(i,2)=tw2_index(i,2);
432     end

```

```

433
434 %oqus start and end points
435
436 final_sp1=tw_final(i,1)-0.02;
437 final_sp2=tw_final(i,1)+0.02;
438 final_ep1=tw_final(i,2)-0.02;
439 final_ep2=tw_final(i,2)+0.02;
440
441 for z=1:length(time_oq_raw)
442     if time_oq_raw(z)<final_sp2&&time_oq_raw(z)>final_sp1
443         tw_final(i,3)=time_oq_raw(z);
444         tw_final_index(i,3)=z;
445
446         break
447     end
448 end
449 for y=1:length(time_oq_raw)
450     if time_oq_raw(y)<final_ep2&&time_oq_raw(y)>final_ep1
451         tw_final(i,4)=time_oq_raw(y);
452         tw_final_index(i,4)=y;
453
454         break
455     end
456 end
457
458
459
460 %% sliding mean
461 slider_width_factor=10;
462 slider_width=slider_width_factor*te(i);
463
464
465 k=0;
466 while((tw_final(i,1)+(slider_width+(k*te(i)))+0.005)<tw_final(i,2)
467     )
468     k=k+1;
469 end
470
471 step_no=k;
472 slider_fx_temp=zeros(1,step_no);
473 slider_fy_temp=zeros(1,step_no);
474 slider_cr_temp=zeros(1,step_no);
475 slider_cr_fy_temp=zeros(1,step_no);
476 slider_zpos_temp=zeros(1,step_no);
477 slider_zposacc_temp=zeros(1,step_no);
478 slider_zpos_rao_temp=zeros(1,step_no);

```

```

478 slider_zposacc_rao_temp=zeros(1,step_no);
479 slider_pitch_temp=zeros(1,step_no);
480 slider_pitch_rao_temp=zeros(1,step_no);
481 slider_wp3_temp=zeros(1,step_no);
482 slider_wp1_temp=zeros(1,step_no);
483
484
485 %In force time scale
486 for x=0:step_no-1
487     if((tw_final(i,1)+(slider_width+(x*te(i)))+0.005)<tw_final(i
,2))
488         sl_sp1=(tw_final(i,1)+(x*te(i)))-0.005;
489         sl_sp2=(tw_final(i,1)+(x*te(i)))+0.005;
490         sl_ep1=tw_final(i,1)+(slider_width+(x*te(i)))-0.005;
491         sl_ep2=tw_final(i,1)+(slider_width+(x*te(i)))+0.005;
492         for a=1:length(time_raw)
493             if time_raw(a)>sl_sp1&&time_raw(a)<sl_sp2
494                 sl_startpos=time_raw(a);
495                 sl_startpos_index=a;
496             end
497         end
498         for b=1:length(time_raw)
499             if time_raw(b)>sl_ep1&&time_raw(b)<sl_ep2
500                 sl_endpos=time_raw(b);
501                 sl_endpos_index=b;
502             end
503         end
504
505 %finidng slider pos in oqus scale
506 sl_startpos_sp1= sl_startpos-0.02;
507 sl_startpos_sp2= sl_startpos+0.02;
508 sl_startpos_ep1= sl_endpos-0.02;
509 sl_startpos_ep2= sl_endpos+0.02;
510
511 for z=1:length(time_oq_raw)
512     if time_oq_raw(z)<sl_startpos_sp2&&time_oq_raw(z)>
sl_startpos_sp1
513         sl_startpos_oqus=time_oq_raw(z);
514         sl_startpos_oqus_index=z;
515         break
516     end
517 end
518 for y=1:length(time_oq_raw)
519     if time_oq_raw(y)<sl_startpos_ep2&&time_oq_raw(y)>
sl_startpos_ep1
520         sl_endpos_oqus=time_oq_raw(y);

```



```

521         sl_endpos_oqus_index=y;
522         break
523     end
524 end
525
526
527 slider_fx(i,x+1)=mean(fx_bp(sl_startpos_index:
528     sl_endpos_index));
529 slider_fx_temp(1,x+1)=mean(fx_bp(sl_startpos_index:
530     sl_endpos_index));
531 slider_fy(i,x+1)=mean(fy_bp(sl_startpos_index:
532     sl_endpos_index));
533 slider_fy_temp(1,x+1)=mean(fy_bp(sl_startpos_index:
534     sl_endpos_index));
535
536 for b=1:length(locs_wp3)
537     if locs_wp3(b)>=sl_startpos_index
538         slider_wp3_startpos=b;
539         break
540     end
541 end
542 for b=length(locs_wp3):-1:1
543     if locs_wp3(b)<=sl_endpos_index
544         slider_wp3_endpos=b;
545         break
546     end
547 end
548
549 for b=1:length(locs_wp1)
550     if locs_wp1(b)>=sl_startpos_index
551         slider_wp1_startpos=b;
552         break
553     end
554 end
555 for b=length(locs_wp1):-1:1
556     if locs_wp1(b)<=sl_endpos_index
557         slider_wp1_endpos=b;
558         break
559     end
560 end
561
562 for b=1:length(locs_zpos)

```

```

563         if locs_zpos(b) >= sl_startpos_oqus_index
564             slider_zpos_startpos = b;
565             break
566         end
567     end
568     for b = length(locs_zpos) :- 1 : 1
569         if locs_zpos(b) <= sl_endpos_oqus_index
570             slider_zpos_endpos = b;
571             break
572         end
573     end
574
575     for b = 1 : length(locs_zposacc)
576
577         if locs_zposacc(b) >= sl_startpos_index
578             slider_zposacc_startpos = b;
579             break
580         end
581     end
582     for b = length(locs_zposacc) :- 1 : 1
583         if locs_zposacc(b) <= sl_endpos_index
584             slider_zposacc_endpos = b;
585             break
586         end
587     end
588     end
589
590     for b = 1 : length(locs_pitch)
591
592         if locs_pitch(b) >= sl_startpos_oqus_index
593             slider_pitch_startpos = b;
594             break
595         end
596     end
597     for b = length(locs_pitch) :- 1 : 1
598         if locs_pitch(b) <= sl_endpos_oqus_index
599             slider_pitch_endpos = b;
600             break
601         end
602     end
603
604     slider_wp3(i, x+1) = mean(pks_wp3(slider_wp3_startpos :
605         slider_wp3_endpos));
606     slider_wp3_temp(1, x+1) = mean(pks_wp3(slider_wp3_startpos :
607         slider_wp3_endpos));
608     slider_wp1(i, x+1) = mean(pks_wp1(slider_wp1_startpos :

```

```

        slider_wp1_endpos));
607 slider_wp1_temp(1,x+1)=mean(pks_wp1(slider_wp1_startpos:
        slider_wp1_endpos));
608 slider_zpos(i,x+1)=mean(pks_zpos(slider_zpos_startpos:
        slider_zpos_endpos));
609 slider_zpos_temp(1,x+1)=mean(pks_zpos(slider_zpos_startpos
        :slider_zpos_endpos));
610 slider_zposacc(i,x+1)=mean(pks_zposacc(
        slider_zposacc_startpos:slider_zposacc_endpos));
611 slider_zposacc_temp(1,x+1)=mean(pks_zposacc(
        slider_zposacc_startpos:slider_zposacc_endpos));
612 slider_zpos_rao(i,x+1)=(slider_zpos(i,x+1)/slider_wp1(i,x
        +1));
613 slider_zpos_rao_temp(1,x+1)=(slider_zpos(i,x+1)/
        slider_wp1_temp(1,x+1));
614 slider_zposacc_rao(i,x+1)=(slider_zposacc(i,x+1)/
        slider_wp1(i,x+1));
615 slider_zposacc_rao_temp(1,x+1)=(slider_zposacc(i,x+1)/
        slider_wp1_temp(1,x+1));
616 slider_pitch(i,x+1)=std(pks_pitch(slider_pitch_startpos:
        slider_pitch_endpos));
617 slider_pitch_temp(1,x+1)=std(pks_pitch(
        slider_pitch_startpos:slider_pitch_endpos));
618 slider_pitch_rao(i,x+1)=(slider_pitch(i,x+1)/(K(i)*
        slider_wp3(i,x+1)));
619 slider_pitch_rao_temp(1,x+1)=(slider_pitch(i,x+1)/(K(i)*
        slider_wp1_temp(1,x+1)));
620 slider_cr(i,x+1)=(slider_fx(i,x+1)-cw)/(nondim_para*(
        slider_wp1_temp(1,x+1)^2));
621 slider_cr_temp(1,x+1)=(slider_fx(i,x+1)-cw)/(nondim_para*(
        slider_wp1_temp(1,x+1)^2));
622 slider_cr_fy(i,x+1)=(slider_fy(i,x+1)-cw_fy)/(nondim_para
        *(slider_wp1_temp(1,x+1)^2));
623 slider_cr_fy_temp(1,x+1)=(slider_fy(i,x+1)-cw_fy)/(
        nondim_para*slider_wp1_temp(1,x+1)^2);
624
625     else
626         break
627     end
628
629
630 end
631
632 slidingmean_fx(i)=mean(slider_fx_temp);
633 slidingmean_fy(i)=mean(slider_fy_temp);
634 slidingmean_wp3(i)=mean(slider_wp3_temp);

```

```

635 slidingmean_wp1(i)=mean(slider_wp1_temp);
636 slidingmean_zpos(i)=mean(slider_zpos_temp);
637 slidingmean_zposacc(i)=mean(slider_zposacc_temp);
638 slidingmean_pitch(i)=mean(slider_pitch_temp);
639 slidingmean_cr(i)=mean(slider_cr_temp);
640 slidingmean_cr_fy(i)=mean(slider_cr_fy_temp);
641 slidingmean_zpos_rao(i)=mean(slider_zpos_rao_temp);
642 slidingmean_zposacc_rao(i)=mean(slider_zposacc_rao_temp);
643 slidingmean_pitch_rao(i)=mean(slider_pitch_rao_temp);
644 slidingmean_fx_std(i)=std(slider_fx_temp);
645 slidingmean_zpos_std(i)=std(slider_zpos_temp);
646 slidingmean_zposacc_std(i)=std(slider_zpos_temp);
647 slidingmean_pitch_std(i)=std(slider_pitch_temp);
648 slidingmean_cr_std(i)=std(slider_cr_temp);
649 slidingmean_cr_fy_std(i)=std(slider_cr_fy_temp);
650 slidingmean_zposrao_std(i)=std(slider_zpos_rao_temp);
651 slidingmean_zposaccrao_std(i)=std(slider_zposacc_rao_temp);
652 slidingmean_pitchrao_std(i)=std(slider_pitch_rao_temp);
653 %}
654
655
656 %% Sub plots
        -----

657
658
659 figure(1)
660
661 sgttitle(plot_title)
662
663 subplot(7,1,1)
664 plot(time_raw,WP1_bm_raw)
665 xlabel('time')
666 ylabel('Wave WM[m]')
667 xline(tw1(i,1),'g')
668 xline(tw1(i,2),'g')
669 xline(tw2(i,1),'y')
670 xline(tw2(i,2),'y')
671 xline(tw_final(i,1),'r')
672 xline(tw_final(i,2),'r')
673
674
675 subplot(7,1,2)
676 plot(time_raw,WP3_car_raw)
677 xlabel('time')
678 ylabel('Wave Model[m]')
679 xline(tw1(i,1),'g')

```

```

680     xline(tw1(i,2), 'g')
681     xline(tw2(i,1), 'y')
682     xline(tw2(i,2), 'y')
683     xline(tw_final(i,1), 'r')
684     xline(tw_final(i,2), 'r')
685
686 subplot(7,1,3)
687 plot(time_oq_raw, zpos1_raw)
688     xlabel('time[s]')
689     ylabel('Z position')
690     xline(tw1(i,3), 'g')
691     xline(tw1(i,4), 'g')
692     xline(tw2(i,3), 'y')
693     xline(tw2(i,4), 'y')
694     xline(tw_final(i,3), 'r')
695     xline(tw_final(i,4), 'r')
696
697 subplot(7,1,4)
698 plot(time_oq_raw, pitch1_raw)
699     xlabel('time[s]')
700     ylabel('Pitch [degree]')
701     xline(tw1(i,3), 'g')
702     xline(tw1(i,4), 'g')
703     xline(tw2(i,3), 'y')
704     xline(tw2(i,4), 'y')
705     xline(tw_final(i,3), 'r')
706     xline(tw_final(i,4), 'r')
707
708 subplot(7,1,5)
709 plot(time_raw, fx_bp, 'r')
710     xlabel('time')
711     ylabel('Fx ')
712     xline(tw1(i,1), 'g')
713     xline(tw1(i,2), 'g')
714     xline(tw2(i,1), 'y')
715     xline(tw2(i,2), 'y')
716     xline(tw_final(i,1), 'r')
717     xline(tw_final(i,2), 'r')
718
719 subplot(7,1,6)
720 plot(force_f, abs(fx_fft))
721     xlabel('frequency')
722     ylabel('Fx fft')
723     xlim([0, 5*force_fhigh])
724
725 subplot(7,1,7)

```

```

726 plot(time_raw,fy_bp,'r')
727     xlabel('time')
728     ylabel('Fy ')
729     xline(tw1(i,1),'g')
730     xline(tw1(i,2),'g')
731     xline(tw2(i,1),'y')
732     xline(tw2(i,2),'y')
733     xline(tw_final(i,1),'r')
734     xline(tw_final(i,2),'r')
735
736 figure(2)
737
738 sgtitle(plot_title)
739
740 subplot(7,1,1)
741
742 hold on
743 plot(time_raw,WP1_bm_raw)
744 plot(time_raw(locs_wp1),pks_wp1,'d')
745     xlabel('time')
746     ylabel('Wave WM[m]')
747     xlim([time_raw(tw_final_index(i,1)) time_raw(tw_final_index(i,2))
748           ])
749 hold off
750
751 subplot(7,1,2)
752 hold on
753 plot(time_raw,WP3_car_raw)
754 plot(time_raw(locs_wp3),pks_wp3,'d')
755     xlabel('time')
756     ylabel(' Wave Model [m]')
757     xlim([time_raw(tw_final_index(i,1)) time_raw(tw_final_index(i,2))])
758 hold off
759
760 subplot(7,1,3)
761 hold on
762 plot(time_oq_raw,zpos1_raw)
763 plot(time_oq_raw(locs_zpos),pks_zpos,'d')
764     xlabel('time[s]')
765     ylabel('Z position')
766     xlim([time_raw(tw_final_index(i,1)) time_raw(tw_final_index(i,2))
767           ])
768 hold off
769

```

```

770 subplot(7,1,4)
771 hold on
772 plot(time_oq_raw,pitch1_raw)
773 plot(time_oq_raw(locs_pitch),pks_pitch,'d')
774 xlabel('time[s]')
775 ylabel('Pitch [degree]')
776 xlim([time_raw(tw_final_index(i,1)) time_raw(tw_final_index(i,2))
       ])
777 hold off
778
779
780 subplot(7,1,5)
781 hold on
782 plot(time_raw,fx_bp,'r')
783 xlabel('time')
784 ylabel('Fx ')
785 xlim([time_raw(tw_final_index(i,1)) time_raw(tw_final_index(i,2))
       ])
786 hold off
787
788 subplot(7,1,6)
789 hold on
790 plot(force_f,abs(fx_fft))
791 xlabel('frequency')
792 ylabel('Fx fft')
793 xlim([0,5*force_fhigh])
794 hold off
795
796 subplot(7,1,7)
797 hold on
798 plot(time_raw,fy_bp,'r')
799 xlabel('time')
800 ylabel('Fy ')
801 xlim([time_raw(tw_final_index(i,1)) time_raw(tw_final_index(i,2))])
802 hold off
803
804
805 orient landscape
806 set(figure(1),'Units','centimeters')
807 set(figure(1),'PaperPositionMode','auto')
808 set(figure(1),'PaperPosition',[-0.5 -0.5 9 12])
809 name3=fileno(i);
810 name3file=append(name3,"w",".pdf");
811 path3=append("J:\academics\thesis expmnt results\results\series2
            ", "\",name3file);
812 print('-dpdf','-r600',path3)

```

```

813
814
815 orient landscape
816 set(figure(2),'Units','centimeters')
817 set(figure(2),'PaperPositionMode','auto')
818 set(figure(2),'PaperPosition',[-0.5 -0.5 11 9])
819 name4=fileno(i);
820 name4file=append(name4,"t_",".pdf");
821 path4=append("J:\academics\thesis expmnt results\results\series2
      "\",name4file);
822 print('-dpdf','-r600',path4)
823
824 close all
825
826
827 end

```

”

```

1 filelist=["CE4000.bin","CE5081.bin"];
2 fileno=["CE4000","CE5081"];
3 file_no=length(fileno);
4 mean_fx=zeros(2,1);
5 mean_fy_tot=zeros(2,1);
6
7
8 for i=1:file_no
9     [a1,a2]=catman_read_dt(filelist(i));
10    fx_raw=a2(9).data;
11    fx_bp=bpass2(transpose(fx_raw),0.005,0,0.05,1,0,'',0);
12    fy_tot_raw=a2(63).data;
13    fy_bp=bpass2(transpose(fy_tot_raw),0.005,0,0.05,1,0,'',0);
14    time_raw=a2(1).data;
15    car_pos_raw=a2(55).data;
16    car_pos_len=length(car_pos_raw);
17
18    for k=1:car_pos_len
19        if car_pos_raw(k)>105
20            start_pos=time_raw(k);
21            start_pos_index=k;
22            break
23        end
24
25    end
26
27
28    for l=car_pos_len:-1:1

```



```

29     if car_pos_raw(1)<195
30         end_pos=time_raw(1);
31         end_pos_index=1;
32         break
33     end
34
35 end
36
37 mean_fx(i)=mean(fx_bp(start_pos_index:end_pos_index));
38 mean_fy_tot(i)=mean(fy_bp(start_pos_index:end_pos_index));
39
40 figure(1)
41 subplot(4,1,1)
42 plot(time_raw,car_pos_raw)
43 xlabel('time')
44 ylabel('carriage position [m]')
45 xline(start_pos,'r')
46 xline(end_pos,'r')
47
48 subplot(4,1,2)
49 plot(time_raw,fx_raw)
50 xlabel('time')
51 ylabel('Fx [N]')
52 xline(start_pos,'r')
53 xline(end_pos,'r')
54
55 subplot(4,1,3)
56 plot(time_raw,fx_bp)
57 %plot(time_raw,fy_bp)
58 xlabel('time')
59 ylabel('Fx filtered [N]')
60 xline(start_pos,'r')
61 xline(end_pos,'r')
62
63 subplot(4,1,4)
64 plot(time_raw(start_pos_index:end_pos_index),fx_bp(
        start_pos_index:end_pos_index))
65 %plot(time_raw,fy_bp)
66 xlabel('time')
67 ylabel('Fx filtered [N]')
68 %xline(start_pos,'r')
69 %xline(end_pos,'r')
70
71 orient landscape
72 set(figure(1),'Units','centimeters')
73 set(figure(1),'PaperPositionMode','auto')

```

```
74 set(figure(1), 'PaperPosition', [-0.5 -0.5 12 9])
75 name1=fileno(i);
76 name1file=append(name1, ".png");
77 path1=append("J:\academics\thesis expmnt results\results\cw2
    \"\", name1file);
78 print('-dpng', '-r600', path1)
79
80
81 end
```

